Hemanta Hazarika ·
Stuart Kenneth Haigh ·
Babloo Chaudhary · Masanori Murai ·
Suman Manandhar   *Editors*

Climate Change Adaptation from Geotechnical Perspectives

Select Proceedings of CREST 2023

Springer

Lecture Notes in Civil Engineering

Volume 447

Lecture Notes in Civil Engineering (LNCE) publishes the latest developments in Civil Engineering—quickly, informally and in top quality. Though original research reported in proceedings and post-proceedings represents the core of LNCE, edited volumes of exceptionally high quality and interest may also be considered for publication. Volumes published in LNCE embrace all aspects and subfields of, as well as new challenges in, Civil Engineering. Topics in the series include:

- Construction and Structural Mechanics
- Building Materials
- Concrete, Steel and Timber Structures
- Geotechnical Engineering
- Earthquake Engineering
- Coastal Engineering
- Ocean and Offshore Engineering; Ships and Floating Structures
- Hydraulics, Hydrology and Water Resources Engineering
- Environmental Engineering and Sustainability
- Structural Health and Monitoring
- Surveying and Geographical Information Systems
- Indoor Environments
- Transportation and Traffic
- Risk Analysis
- Safety and Security

To submit a proposal or request further information, please contact the appropriate Springer Editor:

- Pierpaolo Riva at pierpaolo.riva@springer.com (Europe and Americas);
- Swati Meherishi at swati.meherishi@springer.com (Asia—except China, Australia, and New Zealand);
- Wayne Hu at wayne.hu@springer.com (China).

All books in the series now indexed by Scopus and EI Compendex database!

Hemanta Hazarika · Stuart Kenneth Haigh ·
Babloo Chaudhary · Masanori Murai ·
Suman Manandhar

Editors

Climate Change Adaptation from Geotechnical Perspectives

Select Proceedings of CREST 2023

Editors
Hemanta Hazarika
Kyushu University
Fukuoka, Japan

Babloo Chaudhary
National Institute of Technology Karnataka
Surathkal
Mangalore, India

Suman Manandhar
Kyushu University
Fukuoka, Japan

Stuart Kenneth Haigh
University of Cambridge
Cambridge, UK

Masanori Murai
Shimizu Corporation
Tokyo, Japan

Organization

Organizing Committee

Chairperson

Prof. Hemanta Hazarika, Kyushu University, Japan

Honorary Chairpersons

Prof. Masayuki Hyodo, Professor Emeritus, Yamaguchi University, Japan
Prof. Osamu Kusakabe, International Press-in Association, Japan
Prof. Takaji Kokusho, Professor Emeritus, Chuo University, Japan
Prof. Kazuya Yasuhara, Professor Emeritus, Ibaraki University, Japan

Co-chairpersons

Prof. Gopal Santana Phani Madabhushi, University of Cambridge, UK
Prof. Mitsu Okamura, Ehime University, Japan
Prof. Anand Jagadeesh Puppala, Texas A&M University, USA
Prof. Takayuki Shimaoka, Kyushu University, Japan
Mr. Kunihiko Tanaka, Japan Foundation Engineering Co., Ltd., Japan
Mr. Hiroshi Yamada, NITTOC Construction Co., Ltd., Japan
Prof. Noriyuki Yasufuku, Kyushu University, Japan

Secretary General

Dr. Yoshifumi Kochi, K's Lab Inc., Japan

Co-secretary General

Dr. Naoto Watanabe, KFC Ltd., Japan

Members

Mr. Shunichi Ikeda, Toa Grout Kogyo Co., Ltd., Japan
Mr. Shinichiro Ishibashi, Nihon Chiken Co., Ltd., Japan
Dr. Tomohiro Ishizawa, National Research Institute for Earth Science and Disaster Resilience, Japan
Dr. Kentaro Kuribayashi, Eight-Japan Engineering Consultants Inc., Japan
Ms. Nanae Maeda, Corp Seiko, Japan
Dr. Suman Manandhar, Kyushu University, Japan
Mr. Daisuke Matsumoto, Japan Foundation Engineering Co., Ltd., Japan
Dr. Kenta Mizuno, Wakachiku Construction Co., Ltd., Japan
Dr. Masanori Murai, Shimizu Corporation, Japan
Dr. Atsunori Numata, Soil and Wood Research Institute, Japan
Mr. Yoshikazu Ochi, Kawasaki Geological Engineering Co., Ltd., Japan
Dr. Mai Sawada, Tokyo Institute of Technology, Japan
Dr. Tadaomi Setoguchi, Association of Disaster Experts in Kyushu Region, Japan
Prof. Daisuke Suetsugu, University of Miyazaki, Japan
Mr. Tsuyoshi Tanaka, Tokyo City University, Japan
Dr. Kentaro Yamamoto, Oita University, Japan

Steering Committee

Chairperson

Prof. Yasuhide Fukumoto, Kyushu University, Japan

Co-chairpersons

Prof. Haruichi Kanaya, Kyushu University, Japan
Prof. Naoaki Suemasa, Tokyo City University, Japan

Secretary General

Dr. Masanori Murai, Shimizu Corporation, Japan

Co-secretary General

Mr. Tsuyoshi Tanaka, Tokyo City University, Japan

Members

Prof. Takenori Hino, Saga University, Japan
Mr. Shinichiro Ishibashi, Nihon Chiken Co., Ltd., Japan
Dr. Yoshifumi Kochi, K's Lab Inc., Japan
Dr. Kenta Mizuno, Wakachiku Construction Co., Ltd., Japan
Ms. Tomomi Nishi, Fukuoka University, Japan
Dr. Atsunori Numata, Soil and Wood Research Institute, Japan
Mr. Yoshikazu Ochi, Kawasaki Geological Engineering Co., Ltd., Japan
Dr. Osamu Otsuka, KFC Ltd., Japan
Prof. Kazunari Sako, Kagoshima University, Japan
Mr. Taisuke Sasaki, Nihon Chiken Co., Ltd., Japan
Dr. Tadaomi Setoguchi, Association of Disaster Experts in Kyushu Region, Japan
Prof. Daisuke Suetsugu, University of Miyazaki, Japan
Prof. Yuichi Sugai, Kyushu University, Japan
Dr. Kentaro Yamamoto, Oita University, Japan

Technical Committee

Chairperson

Prof. Stuart Kenneth Haigh, University of Cambridge, UK

Co-chairpersons

Prof. Toshiro Hata, Hiroshima University, Japan
Prof. Shinya Inazumi, Shibaura Institute of Technology, Japan
Dr. Eiji Kohama, Port and Airport Research Institute, Japan
Prof. Neelima Satyam, Indian Institute of Technology Indore, India
Prof. Yuichi Sugai, Kyushu University, Japan

Secretary General

Dr. Babloo Chaudhary, National Institute of Technology Karnataka Surathkal, India

Co-secretary Generals

Dr. Kohei Araki, National Institute of Technology, Tokuyama College, Japan
Dr. Suman Manandhar, Kyushu University, Japan
Dr. Sugeng Wahyudi, NITTOC Construction Co., Ltd., Japan

Members

Dr. Lutfian Rusdi Daryono, NITTOC Construction Co., Ltd., Japan
Dr. Zentaro Furukawa, Okayama University, Japan
Dr. Yi He, Southwest Jiaotong University, China
Dr. Toshiyuki Himeno, National Institute of Technology, Oita College, Japan
Dr. Keisuke Ishikawa, Tokyo Denki University, Japan
Dr. Atsushi Koyama, University of Miyazaki, Japan
Dr. Masaaki Katagiri, Nikken Sekkei Ltd., Japan
Dr. Tomokazu Ozawa, moAI, Japan
Mr. Kenichi Sakai, Fukuoka Prefecture, Japan
Mr. Yasutaka Tabuki, Fukuoka Prefecture, Japan
Mr. Tsutomu Tsuchiya, Chemical Grouting Co., Ltd., Japan
Dr. Kyohei Ueda, Kyoto University, Japan
Prof. Kenji Watanabe, University of Tokyo, Japan
Dr. Kentaro Yamamoto, Oita University, Japan

Logistics Committee

Chairperson

Dr. Yoshifumi Kochi, K's Lab Inc., Japan

Co-chairperson

Mr. Daisuke Matsumoto, Japan Foundation Engineering Co., Ltd., Japan

Secretary General

Mr. Shinichiro Ishibashi, Nihon Chiken Co., Ltd., Japan

Members

Mr. Takashi Fujishiro, Institute of Geo-Disaster Prevention, Japan
Mr. Shunichi Ikeda, Toa Grout Kogyo Co., Ltd., Japan
Ms. Nanae Maeda, Corp Seiko, Japan
Ms. Mika Murayama, Kyushu University, Japan
Dr. Osamu Otsuka, KFC Ltd., Japan
Mr. Taisuke Sasaki, Nihon Chiken Co., Ltd., Japan
Mr. Akira Takeda, Okumura Corporation, Japan

Special Committee on SDGs

Chairperson

Dr. Atsunori Numata, Soil and Wood Research Institute, Japan

Co-chairperson

Dr. Naoki Sakai, National Research Institute for Earth Science and Disaster Resilience, Japan

Secretary General

Dr. Tomohiro Ishizawa, National Research Institute for Earth Science and Disaster Resilience, Japan

Co-secretary General

Dr. Mai Sawada, Tokyo Institute of Technology, Japan

Members

Prof. Chandan Ghosh, National Institute of Disaster Management, India
Dr. Yusaku Isobe, IMAGEi Consultant Corporation, Japan
Dr. Ik Joon Kang, Kyushu University, Japan
Prof. Taizo Kobayashi, Ritsumeikan University, Japan
Dr. Kentaro Kuribayashi, Eight-Japan Engineering Consultants Inc., Japan
Dr. Wei Feng Lee, Ground Master Construction Co., Ltd., Taiwan
Dr. Nguyen Thi Hoai Linh, Kyushu University, Japan
Dr. Mamiko Maeno, Fukuoka City Council, Japan
Ms. Alena Raymond, University of California Davis, USA
Mr. Tsuyoshi Tanaka, Tokyo City University, Japan
Dr. Tran Thi Thanh Thuy, Ho Chi Minh City, Vietnam

Special Committee on Diversity

Chairperson

Prof. Fauziah Ahmad, Universiti Sains Malaysia, Malaysia

Co-chairpersons

Dr. Naoko Kitada, Geo-Research Institute, Japan
Ms. Kyoko Ohta, Fukuoka Prefectural Assembly, Japan
Dr. Atsuko Sato, Civil Engineering Research Institute for Cold Region, Japan
Dr. Satoquo Seino, Kyushu University, Japan

Secretary General

Dr. Ryoko Senda, Kyushu University, Japan

Co-secretary General

Dr. Tomohiro Ishizawa, National Research Institute for Earth Science and Disaster Resilience, Japan

Members

Dr. Amizatulhani Abdullah, Universiti Malaysia Pahang, Malaysia
Ms. Tomomi Nishi, Fukuoka University, Japan
Dr. Tadaomi Setoguchi, Association of Disaster Experts in Kyushu Region, Japan

Sponsorship Committee

Chairperson

Mr. Hideaki Moriya, NITTOC Construction Co., Ltd., Japan

Co-chairpersons

Dr. Yusaku Isobe, IMAGEi Consultant Corporation, Japan
Dr. Nozomu Kotake, JAFEC USA, USA

Dr. Chakravarthy R. Parthasarathy, Sarathy Geotech and Engineering Services Pvt. Ltd., India
Dr. Yasuo Shirai, Kiso-Jiban Consultants Co., Ltd., Japan
Dr. Lin Wang, Chuo Kaihatsu Corporation, Japan

Secretary General

Dr. Masanori Murai, Shimizu Corporation, Japan

Co-secretary Generals

Dr. Akira Ishikawa, Shimizu Corporation, Japan
Dr. Tadaomi Setoguchi, Association of Disaster Experts in Kyushu Region, Japan

Members

Mr. Takayoshi Inukai, Zeta Sekkei Inc., Japan
Mr. Daisuke Matsumoto, Japan Foundation Engineering Co., Ltd., Japan
Dr. Kenta Mizuno, Wakachiku Construction Co., Ltd., Japan
Mr. Katsuji Takematsu, Japan Foundation Engineering Co., Ltd., Japan
Mr. Tsuyoshi Tanaka, Tokyo City University, Japan

Public Relations Committee

Chairperson

Dr. Kenta Mizuno, Wakachiku Construction Co., Ltd., Japan

Co-chairpersons

Prof. Netra Prakash Bhandary, Ehime University, Japan
Dr. Kiyoharu Hirota, Kokusai Kogyo Co., Ltd., Japan

Secretary General

Mr. Tsuyoshi Tanaka, Tokyo City University, Japan

Co-secretary Generals

Dr. Kentaro Kuribayashi, Eight-Japan Engineering Consultants Inc., Japan
Dr. Guojun Liu, Takenaka Corporation, Japan
Dr. Tadaomi Setoguchi, Association of Disaster Experts in Kyushu Region, Japan

Members

Mr. Yoshikazu Ochi, Kawasaki Geological Engineering Co., Ltd., Japan
Ms. Nanase Ogawa, GIKEN Ltd., Japan

Youth Endeavor Committee

Chairperson

Dr. Kentaro Yamamoto, Oita University, Japan

Co-chairpersons

Dr. Keita Lee, Nippon Koei Co., Ltd., Japan
Prof. Kazunari Sako, Kagoshima University, Japan
Prof. Daisuke Suetsugu, University of Miyazaki, Japan
Dr. Norimasa Yoshimoto, Yamaguchi University, Japan

Secretary General

Dr. Taichi Hyodo, Toyama Prefectural University, Japan

Co-secretary Generals

Dr. Zentaro Furukawa, Okayama University, Japan
Dr. Shintaro Miyamoto, National Defense Academy, Japan

Members

Mr. Yuta Ichikawa, Shimizu Corporation, Japan
Mr. Katsuya Ogo, Nippon Koei Co., Ltd., Japan

Preface

Climate Change Adaptation from Geotechnical Perspectives is a compilation of carefully selected and peer-reviewed papers from the 2nd International Conference on Construction Resources for Environmentally Sustainable Technologies (CREST 2023). This conference, hosted by Kyushu University, Fukuoka, Japan, was held in Fukuoka International Congress Center, Fukuoka, from November 20 to 22, 2023. It was co-hosted by the University of Cambridge, International Society for Soil Mechanics and Foundation Engineering (ISSMGE), Japan Society of Civil Engineers (JSCE), Japanese Geotechnical Society (JGS), The Japan Landslide Society, ISSMGE Technical Committee 307 (TC307), ISSMGE Technical Committee 215 (TC215), ISSMGE Asian Regional Technical Committee 1 (AsRTC1), ISSMGE Asian Regional Technical Committee 3 (AsRTC3), International Press-in Association (IPA), and Global Society for Smart Geo-Sustainnovation (GLOSS). Further support to this conference was extended by the Kyushu Regional Development Bureau, Ministry of Land, Infrastructure, Transport and Tourism, Japan, Fukuoka Prefecture, Fukuoka City, Consulate General of India Osaka-Kobe, National Research Institute for Earth Science and Disaster Resilience (NIED), UN-HABITAT Regional Office for Asia and the Pacific, Fukuoka, Kyushu Branch of Japanese Geotechnical Society (JGS), The Society of Materials Science Japan (JSMS), Japan Federation of Construction Contractors (JFCC), Japan Civil Engineering Consultants Association (JCCA), Japan Geotechnical Consultants Association (JGCA), Organization of Geowaste Technology for a Recycled Based Society, Applied Slope Engineering Association (ASERG), and the Local Resilience Research Institute (LRRI).

The principal aim of CREST 2023 was to disseminate knowledge and foster discussions concerning issues related to natural disasters and disasters associated with anthropogenic activities. Additionally, it sought to proffer solutions through the utilization of alternative resources, groundbreaking technologies, and adaptable disaster mitigation strategies. All these endeavors converged toward the common objective of establishing a resilient and sustainable society from a geoengineering perspective. The conference's themes spanned across a wide range of interdisciplinary areas that align with the Sendai Framework for disaster risk reduction (DRR).

The holistic approach, based on the Sendai Framework for DRR, includes the integration of disaster risk reduction into development strategies, thereby cultivating resilience in nations and communities against future disasters. The conference was centered on the themes of sustainability, the promotion of innovative concepts, and advancements in the design, construction, and maintenance of geotechnical structures. All these efforts were geared toward contributing to climate change adaptation and disaster resilience, in alignment with the Sustainable Development Goals (SDGs) set forth by the United Nations (UN). The conference aspires to unite scientists, researchers, engineers, and policymakers from around the world, creating a platform for robust debate and discussion on these pressing issues.

The proceedings of CREST 2023 are thoughtfully partitioned into five volumes. This volume encompasses four fundamental issues, namely (i) innovative techniques toward low carbon footprint, (ii) innovative case studies for sustainable design and construction, (iii) socio-economic and environmental aspects in sustainable construction, and (iv) geological and hydrological aspects. Comprising a total of 38 contributions. Each manuscript underwent rigorous reviews, subjected to evaluation by at least two reviewers chosen from an international panel of experts.

The publication of *Climate Change Adaptation from Geotechnical Perspectives* was made possible through the unwavering dedication of the core members of the technical committee of CREST 2023, along with the contributions of the staff from the Research Group of Adaptation to Global Geo-Disaster and Environment, Kyushu University, Japan. The editors extend their heartfelt gratitude to all those who have played a part in this endeavor. The editors also wish to convey their heartfelt appreciation to all the reviewers for generously dedicating their time and efforts to meticulously review the manuscripts, thereby enhancing the overall content.

The editors hold the hope that this book will prove valuable to students, researchers, professionals, and policymakers. The editors also firmly believe that, in the years to come, the knowledge encapsulated within this volume will contribute significantly to the realization of the UN's Sustainable Development Goals.

Fukuoka, Japan	Hemanta Hazarika
Cambridge, UK	Stuart Kenneth Haigh
Surathkal, India	Babloo Chaudhary
Tokyo, Japan	Masanori Murai
Fukuoka, Japan	Suman Manandhar

Acknowledgments

Financial Supports

Panel of Reviewers

The manuscript for each chapter included in this book was carefully reviewed for the quality and clarity of technical contents by at least two members from the review panel, consisting of the following international experts. The editors wish to express their sincere gratitude to all the reviewers for their valuable time and efforts.

Dr. Amizatulhani Abdullah, Universiti Malaysia Pahang, Malaysia
Dr. Kohei Araki, National Institute of Technology, Tokuyama College, Japan
Prof. Lilia Austriaco, Angeles University, Philippines
Dr. Babloo Chaudhary, National Institute of Technology Karnataka, Surathkal, India
Dr. Gabriele Chiaro, University of Canterbury, New Zealand
Dr. Lutfian Rusdi Daryono, NITTOC Construction Co., Ltd., Japan
Dr. Rohit Divyesh, TechFab India Industries Ltd., India
Dr. Kevin Franke, Brigham Young University, USA
Dr. Tjie-Liong Gouw, GTL Geotechnical Consultant, Indonesia
Prof. S. Mohsen Haeri, Sharif University of Technology, Iran

Contents

Innovative Case Studies for Sustainable Design and Construction

Socio-Economic and Environmental Aspects in Sustainable Construction

About the Editors

Prof. Hemanta Hazarika is currently a professor in the Graduate School of Engineering and Department of Interdisciplinary Science and Innovation, Kyushu University, Fukuoka, Japan. Professor Hazarika's research activities include disaster prevention and mitigation, soil-structure interaction, stability of soil-structures during earthquakes and tsunami, ground improvement, application of recycled waste and lightweight materials in constructions, stability of cut slopes, and landslides and their protection.

He has more than 350 technical papers in various international journals, international conferences, workshops and symposia to date. He has also authored two textbooks on soil mechanics and their Japanese versions. In addition, Prof. Hazarika served as the editor of six books on diverse topics. Prof. Hazarika has several years of experience in teaching, research as well as geotechnical practice and consulting both within and outside Japan. He is currently a foreign expert of the world's first research center in Palu, Indonesia on liquefaction research called "The National Research Center for Liquefaction." Currently, Prof. Hazarika is the chairman of Asian Technical Committee on "Geotechnical Mitigation and Adaptation to Climate Change-induced Geo-disasters in Asia-Pacific Regions" of International Society of Soil Mechanics and Geotechnical Engineering (ISSMGE). He is also Founding President of a general incorporated corporation called GLOSS (Global Society for Smart Geo-Sustainnovation).

Prof. Stuart Kenneth Haigh is a professor in Geotechnical Engineering at Cambridge University and a fellow of Trinity College. In addition, Prof. Stuart Kenneth Haigh is Assistant Director of the Schofield Centre. He has a wide range of research interests centered around physical modelling at 1g and utilizing centrifuges and numerical modelling using FE and MPM. His 25 years of experience in developing complex centrifuge experiments includes developing earthquake actuators, high-g robots, and an in-flight tunnel boring machine. He also delivered the Geotechnic Lecture on Mobilizable strength design for flexible retaining walls in November 2021. He has published more than 100 papers in several journals of repute.

Dr. Babloo Chaudhary is an assistant professor in the Department of Civil Engineering at National Institute of Technology Karnataka (NITK) Surathkal, India. He completed his Ph.D. from Kyushu University, Japan. He was a postdoctoral fellow at Kyoto University, Japan. His research activities include geo-disaster prevention and mitigation, dynamic soil-structures interaction, coastal geotechnics, renewal energy, ground improvement, energy geotechnics. His expertise extends from physical model tests, including 1g model tests and centrifuge model tests, to numerical simulation in the domain of geotechnical Engineering. He has published around 100 technical papers in various international and national journals, conferences, workshops and symposia. Dr. Chaudhary is recipient of Shri M. S. Jain Biennial Award given by Indian Geotechnical Society in 2017.

Dr. Masanori Murai has had a distinguished career as a senior engineer with Shimizu Corporation, a leading construction company in Japan, after receiving his Ph.D. from Kochi University in Japan. Throughout his career, he has specialized in the field of geotechnical engineering and has played a key role in the design, construction, and maintenance of a wide range of infrastructure projects. In addition to his work on infrastructure projects, Dr. Murai has also been involved in research and development activities related to geotechnical engineering. He has published numerous papers in peer-reviewed journals and presented at conferences around

the world, sharing his expertise and insights with other professionals in the field. Overall, Dr. Murai's career at Shimizu Corporation has been characterized by a strong focus on safety, sustainability, and innovation. His expertise in geotechnical engineering and commitment to excellence have made him an asset to the company and the field of engineering as a whole.

Dr. Suman Manandhar is a Research Fellow in the Department of Civil Engineering at Kyushu University, Japan. He completed his post-doctoral research from Kyushu University and enhanced his career from a lecturer to guest/visiting associate professor at the Institute of Lowland and Marin Research, Saga University, Japan. He also served in different academic and professional sectors in Nepal. He is one of the founder members of Global Institute for Interdisciplinary Studies (GIIS) in Nepal. He has published more than 70 papers in refereed journal and proceedings in different SCI and Scopus-indexed journals. His major research areas cover risk sensitive land use plan and multi-hazard assessments, geo-disasters, DRRM, foundation, ground improvement, stability analysis, liquefaction analysis, numerical modeling, and compaction on embankment slopes.

Innovative Techniques Towards Low Carbon Footprint

Analysis of Operational Energy Cost of Typical Residential Building (in Guwahati Located in Northeastern India) with Foam Concrete as Walling Material

Chandrashekhar Dattatray Wagh [ID]**, Indu Siva Ranjani Gandhi** [ID]**, and Vishal Shrivastava**

Abstract The building construction sector is known around the world for its huge energy consumption with a significant proportion contributed by the building's operations phase alone. This encourages us to investigate alternative building materials in order to reduce the energy consumption of buildings. Foam concrete (FC) is one such energy-saving material with special attributes such as low density (400–1850 kg/m^3) and excellent insulating characteristics. The main facet of the present study includes investigations on operational energy cost of typical G + 1 bungalow located in the Guwahati city (in Northeastern region of India) for different scenarios of walling materials (FC, autoclaved aerated concrete block (AAC) and clay brick). Experimental outcomes indicated that thermal conductivity of AAC block and FC of density 1000 kg/m^3 are found to be very much lower than that of conventional clay brick. Further results on energy simulation analysis showed that building with AAC block (density 660 kg/m^3) and FC (density 1000 kg/m^3) as walling material exhibited yearly energy consumption of 15,188.24 and 15,608.75 kWh, respectively, which is comparatively lower than that of clay bricks (16,187.13 kWh). Adding to above, use of better insulating walling material also results in reduction of CO_2 emission by 53.99 and 31.26 tons for AAC block and FC (density 1000 kg/m^3), respectively. The above results highlight that FC can serve as a better energy-efficient alternative to conventional walling material.

Keywords Thermal comfort · Life cycle · Carbon footprint

C. D. Wagh · I. S. R. Gandhi (✉) · V. Shrivastava
Department of Civil Engineering, Indian Institute of Technology Guwahati, Assam, India
e-mail: gindu@iitg.ac.in

1 Introduction

Over a period of time, building sector has turned out to be major consumer of energy. A recent survey indicates that the total energy utilization in buildings has reached 40% of the total global demand, surpassing the transportation sector. Further, this contributes to more than 30% of the worldwide greenhouse gas (GHG) emissions [1]. On a similar note, energy demand of building sector from Indian context accounts for 33%, with heating and cooling accounting for more than half of this requirement. It is expected that this energy usage will increase steadily by 8% annually in the coming years [2]. Moreover, in the present scenario, with the publication of energy-saving design standards and building energy-saving requirements becoming more stringent, there is an arduous requirement for energy-efficient solutions to reduce the operational energy of buildings [3]. In this line studies carried out by various researchers have showed that the annual energy consumption of building can be reduced significantly by 27–77% through simpler means of incorporation of better thermal insulating materials for roof and wall during construction [4, 5]. Numerous research on energy-efficient structures have demonstrated that walls with thermal insulation play a significant role in reducing the amount of energy needed for heating and cooling without relying heavily on mechanical air-conditioning, particularly during inter-seasonal months [6]. Thermal insulation in walls and roofs not only leads to a reduction in the size of the required air-conditioning system, but also reduces the building's overall operational energy demand, resulting in a decrease in the annual energy cost and carbon footprint of the buildings. In similar context, Comaklı and Yuksel's [7] investigations proved that 50% reduction in CO_2 emissions can be realized through provision of insulation of optimum thickness for external wall and through other energy-saving methods. Thus it can be inferred from above discussion that adopting the right thermal insulation walling system is one of the effective ways to reduce energy needed for cooling and heating of buildings.

Sustainability being the key trend of construction, in present scenario, various passive insulation techniques are being developed to produce energy-efficient structures. One such promising way of achieving energy efficiency is through use of foamed concrete in construction which is globally accepted as an effective thermal insulation material. Foamed concrete is a type of cellular concrete with randomly distributed air voids in the mortar or cement paste with a wide range of density ranging from 150 to 1800 kg/m^3 [8, 9]. Owning to its wide range of density, foam concrete has thermal conductivity values ranging from 0.05 to 0.90 W/mK [8]. This wide range of density and excellent thermal insulating properties has facilitated the use of foam concrete predominantly in building sector as a walling material. The present study evaluates the potential of foam concrete in reduction of operational energy consumption of G + 1 house with foam concrete as walling material.

Guwahati (26°10′ N, 92°49′ E) the capital of the Indian state of Assam is chosen as the study location for this research. This urban region is around 262 km^2 in size and has a population of approximately 12 lakh people (Census of India, 2011) expected to reach 21.74 lakh by 2025. The city's and region's general climate is warm

and humid, with wide temperature fluctuations throughout the year, with average temperatures exceeding 30 °C in the summer and hovering around 10 °C in the winter. Statistics shows that in the last 40 years, the frequency of hot days and hot nights has increased, while cold days and cold nights have decreased dramatically [10]. Further, the prediction reports states that the building energy usage is set to rise in Guwahati eventually resulting in higher carbon emissions. The above information indicates the need for adoption of sustainable energy-efficient materials in construction.

Motivated by arduous requirement of prevailing studies in this context, the present work provides an in-depth investigation into global warming potential and operational energy cost implications of employing foam concrete with varying densities (1000–1800 kg/m^3) as a walling material for G + 1 bungalow house in Guwahati taking into account the local climatic condition. Further, comparative analysis of performance of foam concrete with conventional brick walls materials is also carried out.

2 Methodology

2.1 Materials and Mix Proportioning

The freshly premade foams produced with Hingot surfactant (6% concentration) along with Xanthan gum (0.1% dosage) as a foam stabilizer are mixed with the base mix prepared from Ordinary Portland Cement of 43 grade (conforming to IS 269–2015, specific gravity 3.15) and zone 3 river sand (finer than 300 µm, specific gravity of 2.65). Three different densities of foam concrete mix, viz. 1800, 1500 and 1000 kg/m^3 are prepared for this study. The proportioning of the mixes is done as per the procedure given in ASTM C 796 [11]. As the prescribed procedure in standard serves proportioning of only cement slurry, hence the mix design procedure is modified to include the additional component of sand. A constant cement to the sand ratio of 1:2 by weight is adopted for all the mixes. The water-to-solid ratio is varied in between 0.25 to 0.35 for densities 1800 kg/m^3 to 1000 kg/m^3 correspondingly. Table 1 provides the mix proportioning details of different foam concrete mixes.

Table 1 Details of mixture proportions per m^3 of concrete

Mixture	Cement (kg)	Sand (kg)	Water (kg)	Foam weight (kg)	W/S* ratio	Foam vol. (Lit.)	Target density (kg/m^3)
FC 1000	246.91	493.83	234.31	24.95	0.35	498.98	1000
FC 1500	384.62	769.23	333.33	12.55	0.30	250.94	1500
FC 1800	480.00	960.00	353.60	6.40	0.25	127.90	1800

*W/S Water-to-solid ratio

2.2 Experimental Test Methodology

In this study, an estimated amount of pre-foamed foam is introduced into the slurry of mix components added in proper sequence thereafter mixed using a paddle-type mixer in order to obtain the homogeneous mix with desired density. The fresh density of mixes is calculated using the standard container of known volume as recommended by ASTM C796 [11]. To evaluate thermo-mechanical properties of foam concrete, cubical foam concrete specimens of size 50 mm size are casted. Specimens are then demolded after 24 h, moist cured for 25 days followed by 3 days of air curing and finally tested at age of 28 days as prescribed in ASTM C796. Compressive strength test is carried out in accordance with IS 2250:1981 [12] on compression testing machine of maximum capacity 500 KN.

Thermal conductivity is determined using transient plane source (TPS) method in compliance with ISO 22007–2 [13]. Figure 1 shows the set-up of TPS based T.C. kit for measurement of thermal conductivity. The flexible, 13 mm Kapton-based sensor is placed between a sliced samples of foam concrete, and electric current is sent through the spiral heating element of the sensor to heat the specimen samples. By measuring the current and voltage drop through the spiral sensor over time, the thermal characteristics of the specimens are computed. Thermal conductivity (W/m*k) is assessed for foam concrete of different densities and other locally available conventional walling materials like AAC block and standard clay brick for comparative analysis. This property is further used in the annual energy consumption simulation carried out using DesignBuilder software.
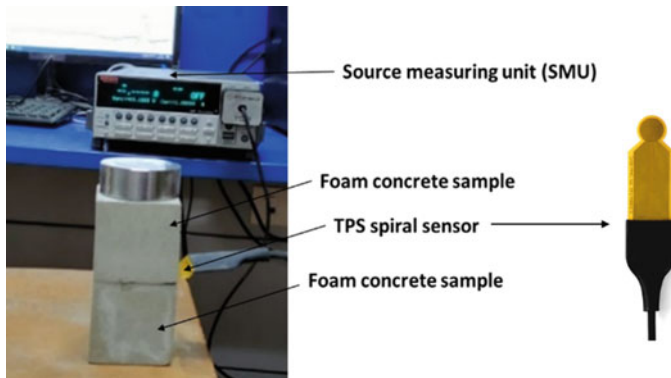
Fig. 1 TPS-based thermal conductivity kit

2.3 DesignBuilder Methodology for Operational Energy Analysis

This study focuses on the operational energy cost of a building located in a Guwahati in Northeast India experiencing hot and humid climate and cold winter. In general, most of the energy is spent for the cooling operation, and comparatively much lesser fraction is spent for heating operations as temperature usually does not fall below a certain threshold level for major part of the winter. Thus, the major consumer of energy in operational phase of the building are cooling mechanisms, day-to-day light-ings and other electrical equipment. DesignBuilder software used in this study serves as a suitable analysis tool for calculation of operational energy cost of the building. Some of the important modules in DesignBuilder which are worth mentioning are 3D Modeler, visualization module used to render image, simulation module which uses EnergyPlus simulations for energy and comfort analysis and HVAC module which provides a powerful and flexible interface to EnergyPlus HVAC. Figure 2 shows the schematic representation of methodology adopted for typical energy simulation modeling for building using DesignBuilder software. Further Fig. 3 represents the G + 1 bungalow floor plan designed on AutoCAD 2020 to be modeled in Design-Builder software for operational energy analysis. All the elements of the building are assigned with the proper layers and with corresponding properties as represented in Fig. 4. The heating and cooling design sections calculate the equipment required to meet the coldest and hottest conditions at the chosen site location. The source of energy for heating and cooling is set accordingly for the Guwahati city which is predominantly electricity from power grid. Annual energy consumption of buildings is calculated in the simulation section. Figure 4 provides the cross-sectional repre-sentation of walling materials (AAC block, foam concrete, clay brick) assigned to building model.
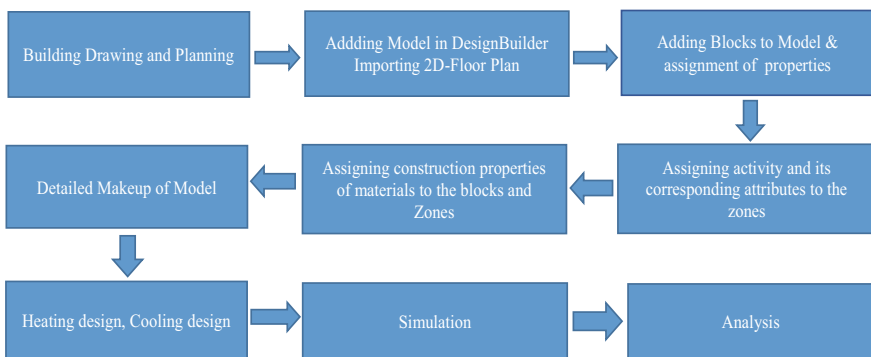
Fig. 2 Schematic representation for a typical building modeling in DesignBuilder
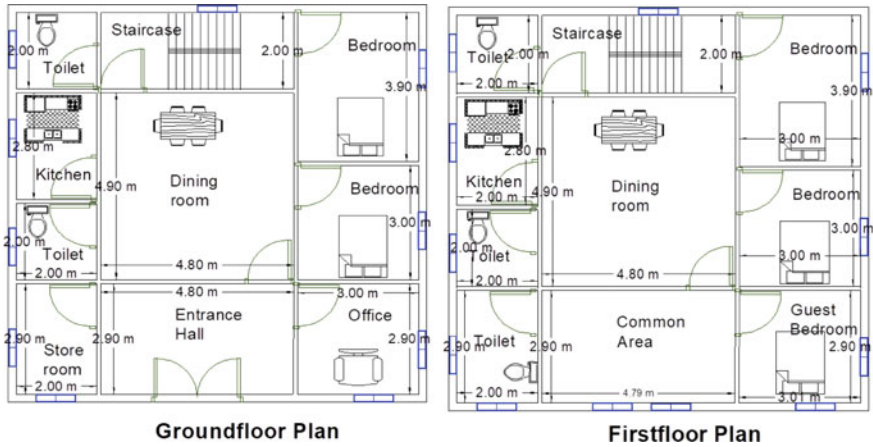
Fig. 3 G + 1 bungalow floor plan designed on AutoCAD 2020 for operational energy analysis
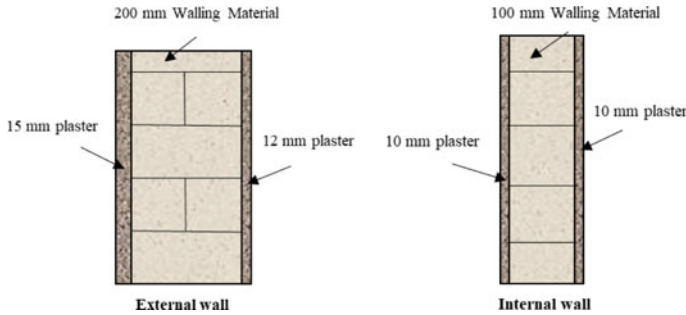
Fig. 4 Cross-sectional representation of walling materials assigned to building model

2.4 Methodology of Estimation of Global Warming Potential (GWP)

In this study, further the global warming potential (GWP) in terms of CO_2 emissions is estimated considering the annual energy consumption results obtained from simulation carried out for different walling materials. The amount of CO_2 emission in kilograms for one kWh of electricity produced and distributed by northeastern grid of India at medium voltage is calculated from the database of the Ecoinvent via SimaPro software. Ecoinvent is a life cycle inventory (LCI) database that supports a wide variety of sustainability assessments for more than 18,000 activities over a wide range of sectors including building and construction. The life cycle inventory data of the electricity produced and distributed for northeastern grid of India obtained from Ecoinvent database is used as an input parameter for calculation of CO_2 emission using the method of ReCiPe 2016 Midpoint (H) V1.06 available in SimaPro software.

ReCiPe 2016 Midpoint (H) V1.06 is chosen as it has been demonstrated to have a greater relationship with environmental flows with relatively low uncertainty [14]. Moreover, in the literature, the midpoint characterization factor for climate change is reported to be frequently employed for calculating global warming potential (GWP). Further, Hierarchist (H) perspective is selected for its ability to balance between the short- and long-term damaging effects [15]. Here it should be noted that this study limits its scope to the reduction in global warming potential obtained from the energy savings achieved in heating and cooling due to use of better insulating walling materials. However, it is to be noted that the proposed analysis does not consider the energy accounted in the process of production of the walling materials and the corresponding amount of GWP involved in the production phase. Also the source of energy used for heating and cooling of spaces is predominantly electricity for urban areas like Guwahati in India, and hence, the other sources are not considered for this study [16].

3　Results and Discussions

3.1　Compressive Strength and Thermal Properties

Figure 5 shows the results of 28 days compressive strength and thermal properties of the foam concrete of three different design densities, viz. 1000, 1500 and 1800 kg/m^3. In line with observations in other literature, both compressive strength and thermal conductivity show similar trend with variation in the density of the foam concrete [8, 9]. As expected increase in density of foam concrete resulted in significant improvement in the compressive strength of the foam concrete. The increase in density of foam concrete from 1000 to 1800 kg/m^3 resulted in sixfold improvement in compressive strength from 2.76 to 16.27 MPa, while 2.5 times increment in thermal conductivity from 0.37 to 0.924 W/mK is observed. This increase in thermal conductivity with the density of concrete resulted in the decrement of the overall insulating property of the foam concrete. It is evident from the Fig. 5 that the conventional clay brick exhibited maximum thermal conductivity, while the lowest thermal conductivity is noted for AAC block with density 660 kg/m^3. The thermal conductivity of brick is approximately 1.5 times that of foam concrete with design density of 1500 kg/m^3 and 2.6 times that of foam concrete with a design density of 1000 kg/m^3 and almost similar to the foam concrete with density of 1800 kg/m^3. Further, the lowest thermal conductivity value (0.37 W/mK) achieved for foam concrete with design density 1000 kg/m^3 in the present study is nearly 6 times lesser than that of normal concrete with density around 2400 kg/m^3 as reported by various researchers [8, 17]. The above results indicate that the foam concrete can serve as a better thermal insulation material depending upon its density. Furthermore, the above-mentioned properties of walling materials will be used as input in the DesignBuilder software for simulating
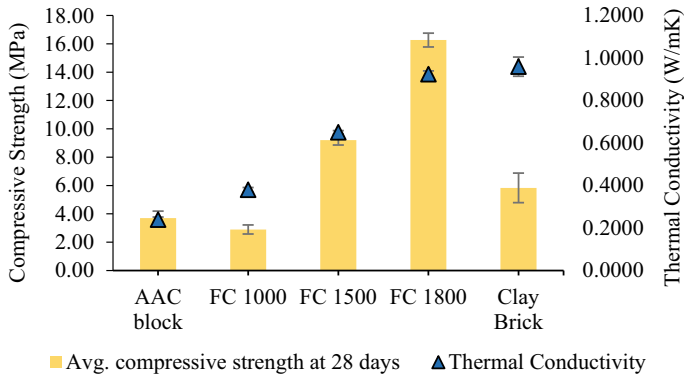
Fig. 5 Compressive strength and thermal conductivity of foam concrete

the annual operational energy consumption of G + 1 bungalow in Guwahati city, India.

3.2 *Operational Energy Analysis and Global Warming Potential*

Table 2 summarizes the energy simulation output of DesignBuilder software for a typical G + 1 bungalow model in Guwahati. It is evident that all the alternative materials used in the present study in place of clay brick exhibited lower annual energy consumption. The increased annual energy consumption of clay brick wall can be attributed to its higher thermal conductivity value, which allows higher average thermal transmittance through the structure [18, 19]. Table 2 also provides a detailed cost estimate considering the annual energy charges incurred by the building utilizing region-specific costs over the facility's lifetime. In accordance with BS 7543:2015, the building's expected lifespan is assumed as 60 years. The energy costs adopted in the estimation (IRs. 6.75/kWh for year 2022) pertain to the state of Assam and conform to LT-III housing type. In addition, ten years of financial data are analyzed, and the average rate of increase in electricity rates is determined to be 6.1% and used for cost analysis [20]. Results indicate that when compared to clay brick the life cycle operational energy cost of foam concrete is found to be relatively lower. For instance, foam concrete with target densities of 1000, 1500 and 1800 kg/m^3 resulted in cost savings of Rs. 23,06,421, Rs. 12,44,211 and Rs. 2,68,135, respectively, when compared to conventional clay brick. The operational energy cost of AAC blocks is slightly lesser than that of foam concrete with density of 1000 kg/m^3 as the AAC block used in this study is less dense than foam concrete. As anticipated and confirmed by the report, it can be concluded that foam concrete with a lower density can dramatically cut operational energy costs.

Table 2 Operational energy cost analysis and reduction in carbon footprint of building with different walling materials

Blocks	Annual energy consumption (kWh)	Life cycle operational energy cost (in ₹)	Annual GWP due to operational energy (kg)	Reduction in GWP compared to clay brick (kg)	Total reduction in GWP over the life cycle of building compared to clay brick (kg)
AAC block	15,188.24	₹ 6,05,66,532	13,682.35	899.85	53,991.09
FC 1000	15,608.75	₹ 6,22,43,410	14,061.16	521.03	31,262.06
FC 1500	15,875.12	₹ 6,33,05,621	14,301.12	281.07	16,864.48
FC 1800	16,119.89	₹ 6,42,81,696	14,521.62	60.57	3634.39
Brick	16,187.13	₹ 6,45,49,831	14,582.20	0.00	0.00

From the above Table 2 it can be concluded that the annual energy consumption of the building with standard clay brick as walling material is highest, and hence, it will result in the highest amount of global warming potential in terms of CO_2 emission [7, 21]. From the adopted methodology of ReCiPe 2016 Midpoint (H) V1.06 in SimaPro software, one kWh of electricity production and distribution resulted in 0.901 kg of carbon dioxide emission in the atmosphere. Due to significant energy savings, usage of foam concrete blocks and AAC blocks as an alternative to standard clay brick would result in sizeable amount of reduction in CO_2 emissions as represented in Table 2. The mere use of AAC block as a walling material in place of standard clay brick would reduce almost 900 kg of CO_2 emissions yearly and almost 54 tons of CO_2 emission reduction over the complete life of building assuming it as 60 years. On the similar lines, foam concrete with 1000 kg/m^3 will result in decrease in global warming potential of 521 kg annually and 31.26 tons of CO_2 over the complete life of building. This amount of reduction in CO_2 is equivalent to the CO_2 sequestration resulting from planting 112 mango trees over its life time (assuming 278.3 kg CO_2 sequestered by single mango tree) [22].

4   Conclusions

Operational energy demand and its respective cost analysis and reduction in carbon footprint of a G + 1 residential building are evaluated and subjected to use of different walling material for climatic conditions of Northeast Indian city of Guwahati. The house is studied with conventional clay bricks and alternative wall materials (AAC, FC 1800, FC 1500 and FC 1000). The study reports following conclusions:

- The thermal conductivity of foam concrete is significantly influenced by its density. The value of thermal conductivity is raised by 2.5 times from 0.37 to 0.924 W/Mk when density of foam concrete is increased from 1000 to 1800 kg/m^3.

- Annual energy consumption of G + 1 building in Guwahati with walling material as foam concrete with density 1000 kg/m^3 (15,608.5 kWh) is lesser than that of conventional clay bricks (16,187.13 kWh), but slightly higher than that of AAC blocks of density 660 kg/m^3 (15,188.24 kWh). Taking inflation of 6.1% into account with current energy rates, it is found that the usage of 1000 kg/m^3 density foam concrete will result in a saving of Rs. 23,06,421/- during a 60-year building lifespan.

- By using appropriate insulating material like AAC block and foam concrete (1000 kg/m^3) as walling material, the GWP in terms of CO_2 emission to the environment will be reduced by 54 and 36.21 tons, respectively, which is equivalent of planting 194 and 112 mango trees. This GWP can be further decreased through the use of density of foam concrete lesser than 1000 kg/m^3 and additional use of foam concrete for roof insulation.

- The above results indicate that foam concrete has the potential to significantly reduce the building's operational energy cost and the carbon footprint of building and thus proves to be an energy-efficient sustainable building material.

References

1. Costa A, Keane MM, Torrens JI, Corry E (2013) Building operation and energy performance: monitoring, analysis and optimisation toolkit. Appl Energy 101:310–316
2. GRIHA (2011) Green rating for integrated habitat assessment. TERI Press, New Delhi
3. Energy Conservation Building Code (2017) Bureau of energy efficiency (BEE). New Delhi, India
4. Mohsen MS, Akash BA (2001) Some prospects of energy savings in buildings. Energy Convers Manag 42:1307–1315
5. Marwan M (2020) The effect of wall material on energy cost reduction in building. Case Stud Therm Eng 17:100573
6. Latha PK, Darshana Y, Venugopal V (2015) Role of building material in thermal comfort in tropical climates—a review. J Build Eng 3:104–113
7. Çomakli K, Yüksel B (2004) Environmental impact of thermal insulation thickness in buildings. Appl Therm Eng 24:933–940
8. Wagh CD, Indu Siva Ranjani G, Kamisetty A (2021) Thermal properties of foamed concrete: a review. RILEM Bookseries 29:113–137
9. Ramamurthy K, Kunhanandan Nambiar EK, Indu Siva Ranjani G (2009) A classification of studies on properties of foam concrete. Cem Concr Compos 31:388–396
10. Deka RL, Saikia L, Mahanta C, Dutta MK (2018) Increasing extreme temperature events in the Guwahati City During 1971–2010. Springer International Publishing
11. ASTM C 796/C796M-19 (2019) Standard test method for foaming agents for use in producing cellular concrete using preformed foam. West Conshohocken, United States
12. Bureau of Indian Standards (1981) I.S:2250–1981. Code of practice for preparation and use of masonry mortars. New Delhi, India

13. ISO 22007–2 (2008) Plastics—determination of thermal conductivity and thermal diffusivity—Part 2: Transient plane heat source (hot disc) method. Int Stand
14. Huijbregts M, Steinmann ZJN, Elshout PMFM, Stam G, Verones F, Vieira MDM, Zijp M, van Zelm R (2016) ReCiPe 2016. Natl Inst Public Heal Environ 194
15. Van Lieshout KG, Bayley C, Akinlabi SO, Von Rabenau L, Dornfeld D (2015) Leveraging life cycle assessment to evaluate environmental impacts of green cleaning products. Procedia CIRP 29:372–377
16. van Ruijven BJ, van Vuuren DP, de Vries BJM, Isaac M, van der Sluijs JP, Lucas PL, Balachandra P (2011) Model projections for household energy use in India. Energy Policy 39:7747–7761
17. Asadi I, Shafigh P, Abu Hassan ZF, Bin Mahyuddin NB (2018) Thermal conductivity of concrete—a review
18. Aste N, Angelotti A, Buzzetti M (2009) The influence of the external walls thermal inertia on the energy performance of well insulated buildings. Energy Build 41:1181–1187
19. Ficco G, Iannetta F, Ianniello E, D'Ambrosio Alfano FR, Dell'Isola M (2015) U-value in situ measurement for energy diagnosis of existing buildings. Energy Build 104:108–121
20. Jaganmohan M (2022) Average cost of state electricity supply in India from financial year 2009 to 2020. Retrieved from https://www.statista.com/statistics/808201/india-cost-of-state-electricity-supply/. Accessed on 2022/09/08
21. Yuan J, Farnham C, Emura K (2017) Optimum insulation thickness for building exterior walls in 32 regions of China to save energy and reduce CO_2 Emissions. Sustain 9
22. Bhaskar A, Shah A, Gupta S (2017) 7.5 crore green jobs ? assessing the greenness. Indian J Labour Econ 59:441–461

Contribution of Vetiver Grass Towards Slope Stability Via Mechanical Root Reinforcement

Ujwalkumar D. Patil , **Myeong-Ho Yeo, Else Demeulenaere, Daniel Mabagos, and Surya Sarat Chandra Congress**

Abstract Soil bioengineering techniques offer an eco-friendly and practically viable alternative for slope stabilization when compared to traditional techniques. In particular, the improvement in slope stability is obtained by planting vegetation that offers an improvement in existing shear strength via mechanical root reinforcement promoted by the presence of roots along failure surface. This study was aimed at evaluating the contribution of the root cohesion for vetiver grass (Chrysopogon zizanioides) on slope stabilization in a tropical and mountainous environmental setting. Various root morphological characteristics of vetiver were obtained experimentally through field and laboratory testing. In general, the vetiver root system comprises of mostly fine roots of diameter varying between 0.11 and 2.22 mm and can offer large tensile strength between 14.4 and 2000 MPa. Results show that the tensile strength offered by vetiver roots increased with decreasing root diameter and a good power-fit relationship was obtained between root diameter and tensile strength. Furthermore, the root morphological characteristics were used with root bundle theory to translate the tensile strength offered by roots into additional root cohesion. Transient seepage analysis was performed on bare and vegetated slope to generate degree of saturation and suction profiles with respect to depth, which were incorporated into a simple infinite slope stability problem to compute the FOS with respect to depth. Analysis of results show that the FOS of shallow depths with presence of vetiver roots increased many folds as compared to bare slope, which demonstrated the potential of vetiver grass in restoration of watersheds along the hill slopes in southern Guam.

Keywords Soil bioengineering · Vetiver · Root cohesion · Root tensile strength · Slope stability

U. D. Patil (✉)
University of The District of Columbia, Washington, DC 20008, USA
e-mail: ujwalkumar.patil@udc.edu

M.-H. Yeo · E. Demeulenaere · D. Mabagos
University of Guam, Mangilao, GU 96923, USA

S. S. C. Congress
Michigan State University, East Lansing, MI 48824, USA

1 Introduction

Rainfall-induced slope failures are a common issue in tropical countries, especially, the ones which receive heavy rainfall events such as typhoons and storms [1, 2]. Slope surface protection has become a necessity to prevent further erosion of barren and already failed hill slopes. In addition, on tropical Islands like Guam the coral life along the coastal bay gets stressed and smothered due to excessive sedimentation deposited along reefs from such eroded slopes. Plants/vegetation can provide a cover to the hill slopes and prevent the direct contact of water with surficial soil, thereby preventing the dislodging of soil particles. Also, roots tend to draw water via root water uptake (RWU) from surrounding soil, which increases the suction within root-soil zone and improve the stability of unsaturated slopes. However, this beneficial hydrological effect ceases when soil becomes completely saturated during long duration rainfall because this suction reduces to zero [1]. Thus, for saturated slopes, the slope with and without vegetation behaves similarly if root reinforcement is neglected. On the other hand, once the saturated soil mass becomes unstable and starts to slide down the slope, it activates the tensile strength of roots present across the sliding mass (Fig. 1a, b).

This results in additional root cohesion along shearing plane, which increases the shear strength of soil-root matrix. Hence, grass/plants can be used as a slope stabilization treatment method. Thus, for the advancement of such ecological protection technology and increasing of our understanding of such technology more studies are encouraged. In particular, the quantification of increase in shear strength due to root reinforcement by different plants/grass becomes crucial.

Past couple of decades have seen growing popularity of using vetiver grass (Chrysopogon Zizanioides) in tropical and sub-tropical countries as a strategy to prevent shallow slope slides and erosion control [3, 4]. Several voluntary community drives have taken place to plant vetiver to control erosion in Guam. However,

(a) **(b)**

Fig. 1 **a** Exposed root-soil zone after shallow slope failure, **b** sketch showing root tensile strength activated from sliding forces in root-soil zone

there is a scarcity of studies regarding quantification of the improvement in shear strength provided by the vetiver system, especially on Island of Guam.

Patil et al. [5] conducted transient seepage coupled slope stability analysis using Acacia tree roots in soils from Ija watershed in Guam and demonstrated its positive benefits. Current study is inspired by it and uses similar procedures of root testing and analysis for testing efficacy of vetiver roots in soil from Inarajan watershed in Guam. This study presents laboratory-based tests on soil samples collected from hill slopes of Inarajan watershed in southern Guam to characterize it for geotechnical and hydrological properties. Vetiver grass was grown in nursery using native soil from Inarajan hill slopes. Tensile strength tests were conducted on 1-year-old root samples collected from each 5 cm depth below ground surface. Root bundle theory proposed by Wu et al. [6] was used to estimate the root cohesion by translating the tensile strength of roots. In addition, soil–water retention curves (SWRC), basic geotechnical properties and unsaturated permeability as a function of suction were used to perform transient seepage analysis on an idealized hill slope under a one-month worth rainfall data using SEEP/W [7, 8]. In particular, the degree of saturation (Sr) and suction (s) profiles were obtained and then used in a simple infinite slope stability problem to demonstrate the positive role of vetiver roots in improving factor of safety (FOS) of hill slopes in Guam.

2   Saturated and Unsaturated Properties of Soil Slope

For hill slope along Fintasa River in Inarajan watershed, Guam was selected for this study. A case study was conducted on a 1:1 slope ($\beta = 45°$) made from a clayey sand (SC) permeated with vetiver roots.

Soil samples were collected from hill slopes of Inarajan watershed in southern Guam to perform saturated and unsaturated soil testing. After conducting the sieve, hydrometer and Atterberg's limit analysis, the soil was classified as clayey sand (SC) as per the Unified Soil Classification System (USCS). The field unit weight of soil was 16 kN/m^3, specific gravity (G_s) was 2.81, saturated hydraulic conductivity (K_{sat}) was 0.108 m/day, and saturated volumetric water content (θ_s) was 0.6325. The consolidated drained direct shear tests on undisturbed samples revealed an effective cohesion (c') and effective friction angle (ϕ') of 4.6 kPa and 33.1°, respectively. The soil–water retention curve (SWRC) and its unsaturated parameters using [9] model are shown in the Inset in Fig. 2. The liquid limit (LL), plastic limit (PL) and hence the plasticity index (PI) were 65, 30 and 35%, respectively.
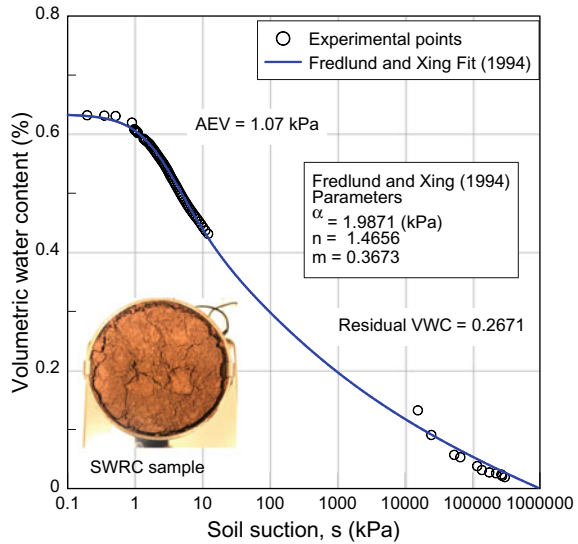
3 Morphological Characteristics of Vetiver Roots

Vetiver grass is also classified as Chrysopogon zizanioides, which is perennially
grown in tropical and sub-tropical countries [10]. It is tolerant to extreme climate
change events including prolonged drought, flood submergence, frost and fire. It is
also a resilient grass that can tolerate acidity, alkalinity and salinity [3, 4, 10]. Vetiver
roots grow vertically downward and have a fine and dense root structure (Fig. 3b),
which can reach up to 2 to 4 m in depth. It has been used in the past for watershed
restoration in Guam [11]. However, the role of roots in enhancing slope stability has
not been explored, which is the chief motivation for this research study.

Vetiver uprooted from field with a dense root structure can be seen in Fig. 3a.
Due to such fine root structure, it was difficult to uproot it from deeper depth without
breaking roots. Hence, to study the root morphological characteristics, it was grown
in plastic pipes of ~7 cm diameter at the nursery of University of Guam campus
using soil collected from southern Guam. Figure 3b shows the 1.5-year-old vetiver
root system taken out carefully from the plastic pipe. Figure 3c shows the fibrous
vetiver root system of about 65 cm length that was obtained after careful washing.
Root area ratio (RAR) was used to determine the ratio of area occupied by roots on
a certain plane, i.e., at each 5 cm depth of roots using the equation: RAR = (A_r/
A_s) × 100, where A_r = sum of the root cross-sectional area at given depth and A_s
= soil sample plan area. Figure 4 illustrates the variation of RAR with respect to
depth. This variation of RAR was best fitted with a power equation with an excellent
regression coefficient of $R^2 = 0.94$. The RAR was maximum near the ground surface
and decreased nonlinearly with increasing depth.

(a)   **(b)**   **(c)**
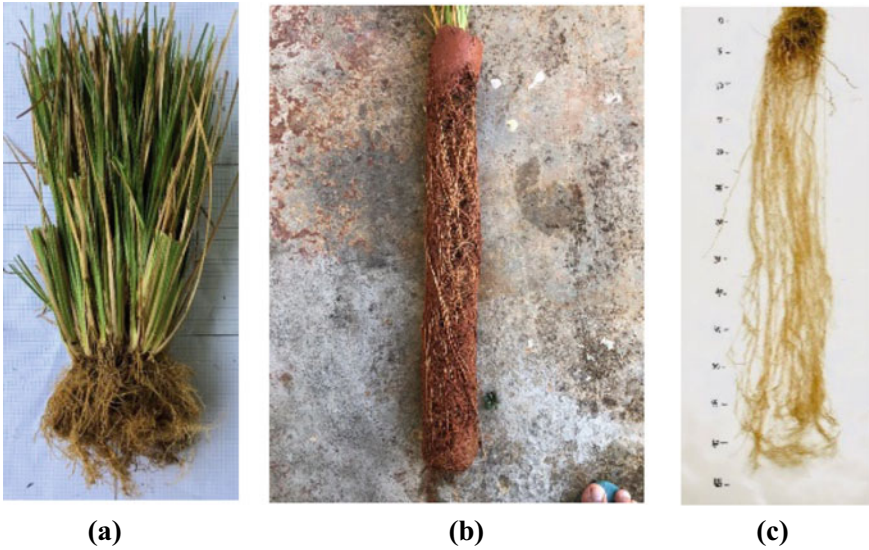
Fig. 3 **a** Uprooted vetiver grass grown along slopes in southern Guam; **b** vetiver grown in native soil inside PVC pipe; **c** washed vetiver root system

Fig. 4 Vetiver root area ratio distribution with regard to depth

$$Y = 0.0549 \, (X)^{-1.191}$$
$$R^2 = 0.94$$
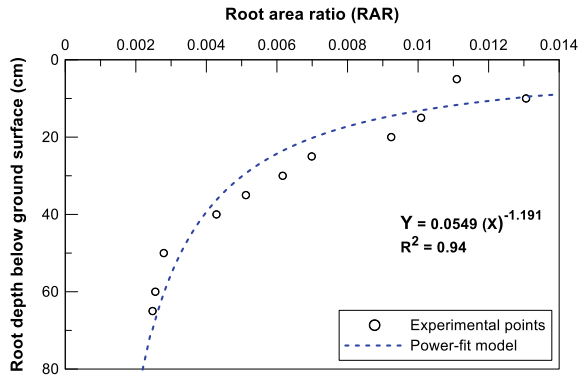
The procedure of testing roots and conducting transient seepage coupled slope stability analysis used in this paper is like the one adopted by Patil et al. [5], in which they tested role of Acacia tree roots in stabilizing hill slope failures in Ija watershed, Guam. About 50 roots with varying diameters (d_r) were chosen and cut to a length of 6cm before being tensile tested on a Universal Testing Machine. The ends of the roots were taped to grasp them inside the jaws and prevent slippage. Tensile force was applied at a 10mm/min pace, and the maximal tensile force (F_{max}) required to break the root was measured. Any trial that did not break the root in the middle was discarded. $T_r = F_{max}/(\pi/4)d_r^2$ was used to compute the maximum tensile strength (T_r) given by the root at breakage. The vetiver roots' maximum tensile strength (T_r)

Fig. 5 Variation of vetiver root tensile strength versus root diameter
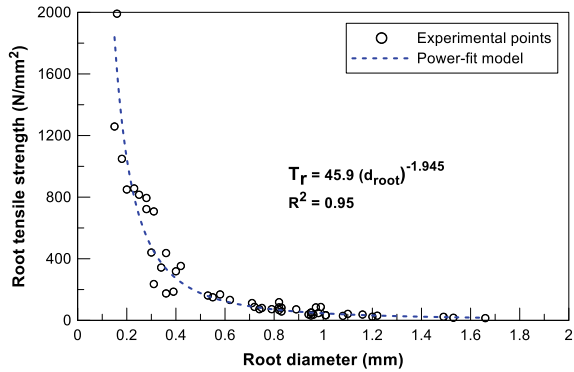
was plotted versus their root diameters, as illustrated in Fig. 5. The tensile strength of vetiver roots was found to decrease nonlinearly with increasing root diameter (d_r). It was best fit by a power-fit equation $T_r = 45.9 \, (d_r)^{-1.946}$ with an excellent correlation coefficient $R^2 = 0.95$.

The value 45.9 is the scale factor, and the value -1.946 is the rate of decrease in strength (empirical constants). The values of these empirical constants vary between plant species and hence documenting it is very important. The lowest and highest values of root diameter and tensile strength were 0.11–2.22 mm and 14.4–2000 MPa (N/mm^2), respectively.

4 Quantitative Modeling of Root Reinforcement

Several researchers have done pioneering work in the quantitative modeling of root reinforcement [6, 12]. Accordingly, the mobilized tensile resistance in the roots can be translated into an increase in shear strength in the soil, i.e., the additional cohesion (c_r). In this study, the c_r using model proposed by Wu et al. [6], which is dependent on the root tensile strength, and the root area ratio (RAR) was used in this study (Eq. 1). It also assumes that all roots are initially perpendicular to the slip surface and break at the same time.

$$c_r = T_r \frac{A_r}{A_s} (sin\theta + cos\theta tan\emptyset) \tag{1}$$

where θ is the angle of shear distortion in the shear zone, ϕ is the soil friction angle, (°) and T_r is the mobilized tensile strength of roots. The term ($sin\theta + cos\theta tan\phi$) accounts for shear distortion, and its value is set at 45°. Figure 6 shows that the value of c_r declines with depth and is best fit by a power model with a reasonable coefficient of correlation ($R^2 = 0.67$). Further study took into account the computed c_r value for each 5 cm depth below ground level. A similar procedure of analysis was adopted by Patil et al. [5] while testing Acacia roots.

Root cohesion, C$_r$ (kPa)
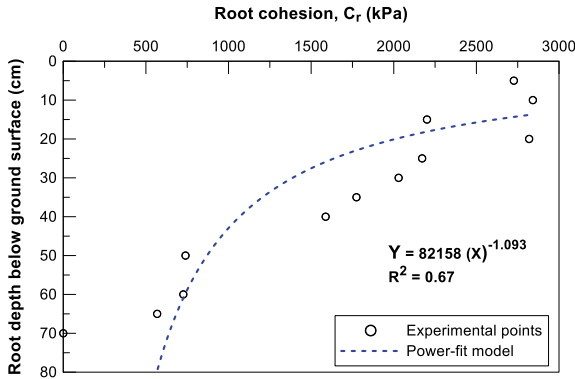
Fig. 6 Estimated root cohesion with respect to depth for vetiver roots

5 Modeling Response of Vegetated Slope to Rainfall-Induced Infiltration

In 2021, the month of October yielded maximum amount of rainfall in this watershed of Guam. Hence, 1-month rainfall, relative humidity, wind speed, solar radiation and air temperature data were collected from an onsite weather station. Also, suitable vegetation data such as variation of leaf area index versus time; plant limiting factor versus matric suction; root depth versus time, normalized root density versus normalized root depth; and soil cover fraction versus leaf area index were obtained from Patil et al. [2]. This climate and vegetation boundary condition were applied on an idealized 45° hill slope made from soil with properties described previously. Transient seepage numerical analysis was conducted by employing the finite element-based program SEEP/W [7, 8]. We considered two case studies. First was case (a): rainfall applied on bare slope and case (b) rainfall applied on vegetated (i.e., vetiver grass) slope (Figs. 7 and 8). The results of the SEEP/W 2D transient seepage study were then used to construct profiles of degree of saturation (Sr) and soil suction (s) with respect to depth at mid-slope (Figs. 7 and 8). A similar procedure of analysis was adopted by Patil et al. [5] while testing Acacia roots.

SEEP/W program utilizes modified Richard's equation and [13, 14] model to simulate the flow of fluid and root water uptake (RWU). Out of the two case scenarios, first was bare slope with rainfall, and second was vegetated slope with rainfall considering the root water uptake (RWU). It can be clearly observed that irrespective of either case, the Sr increases, and the suction reduces with time as the rainwater infiltrates the shallow stratum (i.e., top 1–2 m) of hill slope. Both Sr and s reach their maximum and minimum values, respectively, on 6th day, and hence these profiles with respect to depth were further used to calculate the factor of safety.
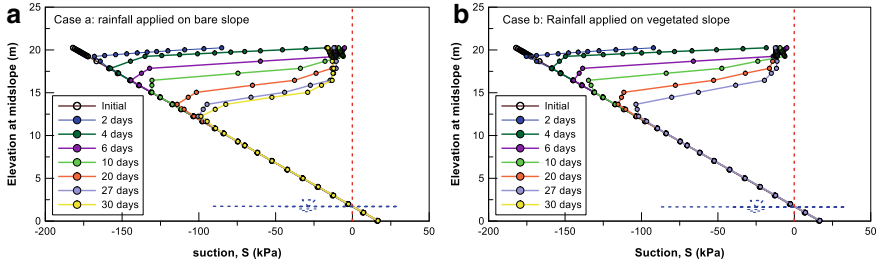
Fig. 7 Profiles of suction with depth for cases **a** and **b**
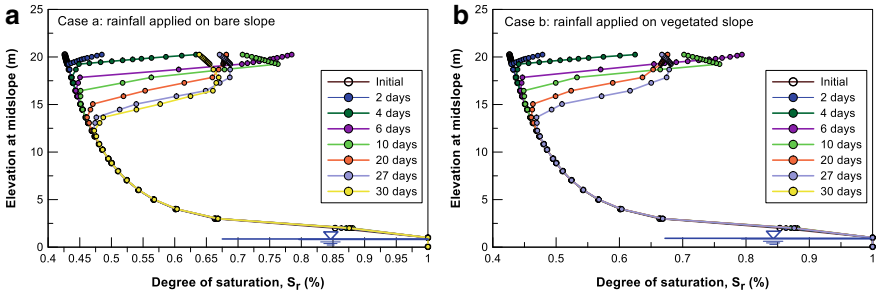
Fig. 8 Profiles of degree of saturation with depth for cases **a** and **b**

6 Example of a Simple Infinite Slope Stability Problem

A simple example was presented to illustrate the positive effect of root cohesion in improving slope stability. Cecconi et al. [15] used unsaturated shear strength equation of Vanapalli et al. [16] to compute the factor of safety (FOS) for a simple infinite slope problem, which uses S_r and s values with respect to depth. Furthermore, the FOS was computed by feeding the S_r and s profiles from Figs. 7 and 8 into Eq. (2).

$$FOS(z) = \left[1 + \frac{S_r(z)s(z)}{\gamma z cos^2 \alpha}\right] \frac{tan\emptyset'}{tan\alpha} + \frac{c' + c_r(z)}{\gamma z cos\alpha sin\alpha} \qquad (2)$$

Similar to studies conducted by Patil et al. [5] on slopes vegetated with Acacia roots, three different case situations were considered in this research. The first instance was applying rainfall to a barren slope, the second case involved applying rainfall to a vetiver vegetated slope while only considering RWU, and the third case was similar to the second situation but additionally taking vetiver root reinforcement into account. Results (Fig. 9) of this analysis illustrate the nonlinear variation of FOS with respect to depth for case 3. Clearly, the FOS was maximum and increased many folds near surface upon consideration of root tensile strength. Furthermore, FOS decreased with increasing depth, mostly because of increasing Sr and s, and decreasing RAR. Three case scenarios were presented in Fig. 9.
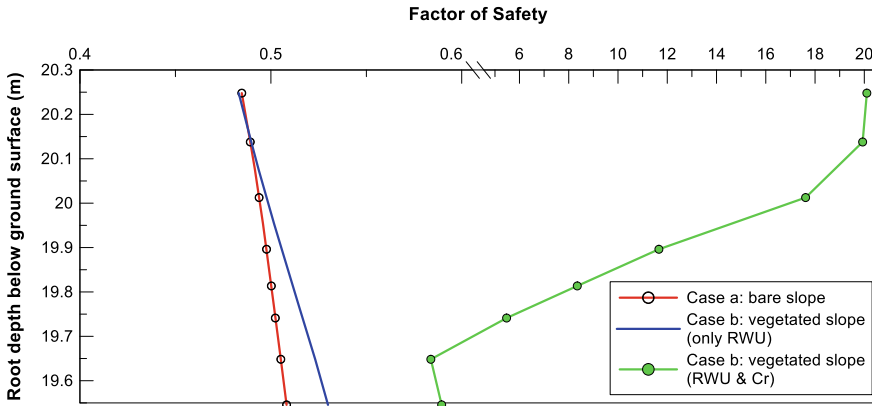
Fig. 9 Variation of the lowest FOS with respect to depth

7 Conclusion

This research records a basic infinite slope stability problem to demonstrate the beneficial effect of vetiver grass root reinforcement in preventing shallow slides. The root diameter and tensile strength of vetiver grass grown in local soil from Guam varied between 0.11–2.22 mm and 14.4–1259 MPa (N/mm^2), respectively. The best fit for the link between root diameter and tensile strength of roots was a power equation with an excellent correlation coefficient of $R^2 = 0.95$. The tensile strength of roots increased with decreasing the root diameter, which also confirmed the previous findings. This was attributed to the root chemical content, namely lignin and cellulose that are function of root diameter and are correlated with root tensile strength. Zhang et al. [17] reported increase in percentage of cellulose and decrease of lignin content with increasing root diameter to be the prime cause of reduction in tensile strength. Thus, thinner roots lead to greater strength. The tensile strength of roots was converted into a root cohesion (c_r) value, which was calculated for each 5 cm depth below ground surface. On an idealized hill slope, appropriate climate and vegetation boundary conditions were applied, and a transient seepage numerical analysis was performed to obtain S_r and s profiles with respect to depth. Finally, the computed values of S_r, s and c_r values at different depths were incorporated into a simple infinite slope stability equation to compute the FOS with respect to depth. Analysis of results shows that the FOS of shallow depths with presence of vetiver roots increased many folds, and it decreased nonlinearly with depth. Nonetheless, the presented case studies revealed the potential of vetiver grass (Chrysopogon zizanioides) as a bioengineering solution in rehabilitation of hill slopes of Guam.

References

1. Patil UD, Shelton III AJ, Aquino E (2021) Bioengineering solution to prevent rainfall-induced slope failures in tropical soil. Land (MDPI) 10(3):299
2. Patil UD, Shelton AJ, Catahay M, Kim YS, Congress SSC (2022) Role of vegetation in improving the stability of a tropical hill slope in Guam Environ Geotech, 9(8):562–581
3. D'Souza DN, Choudhary AK, Basak P, Shukla SK (2019) Assessment of vetiver grass root reinforcement in strengthening the soil. In: Ground improvement techniques and geosynthetics. Springer, Singapore, pp 135–142
4. Truong P (2006) Vetiver system for infrastructure protection. Potential applications of vetiver plan in the Gulf region, 7443, Kuwait Foundation for the Advancement of Sciences. Kuwait 2006; pp 113–123
5. Patil UD, Yeo M, Aquino E, Congress SSC, Demeulenaere E (2023) Role of acacia tree root's reinforcement in hill slope stability. In: Proceedings of the 9ICEG-9th international congress on environmental geotechnics, vol 5, Human-Induced and Natural Disaster Mitigation, 25–28 June 2023, Chania, Greece, pp 436–443
6. TH Wu WP McKinnell III DN Swanston 1979 Strength of tree roots and landslides on Prince of Wales Island Alaska Canad Geotech J 16 1 19 33
7. GeoStudio (2017) Heat and mass transfer modeling with Geostudio. First edition, Calgary, Alberta, Canada. Geoslope International ltd. Retrieved from www.geoslope.com. Accessed on 2/1/2022
8. GeoStudio (2012) Seepage Modeling with SEEP/W an engineering methodology. Geo-slope international ltd. Accessed on 2/1/2022
9. Fredlund DG, Xing A (1994) Equations for the soil-water characteristic curve. Canad Geotech J 31:521–532
10. Truong P, Van TT, Pinners E (2008) The Vetiver System for slope stabilization: an engineer's handbook. Proven Green Environ Sol 1
11. MH Golabi C Iyekar D Minton CL Raulerson JC Drake 2005 Watershed management to meet water quality standards by using the vetiver system in Southern Guam AU JT 9 1 63 70
12. LJ Waldron 1977 Shear resistance of root-permeated homogeneous and stratified soil Soil Sci Soc Am J 41 843 849
13. RA Feddes P Kowalik K Kolinska-Malinka H Zaradny 1976 Simulation of field water uptake by plants using a soil water dependent root extraction function J Hydrol 31 1–2 13 26
14. R Prasad 1988 A linear root water uptake model J Hydrol 99 3–4 297 306
15. M Cecconi P Napoli V Pane 2016 Effects of soil vegetation on shallow slope instability Environ. Geotech. 2 3 130 136
16. SK Vanapalli DE Fredlund DE Pufahl AW Clifton 1996 Model for the prediction of shear strength with respect to soil suction Can Geotech J 33 379 392
17. CB Zhang LH Chen J Jiang 2014 Why fine tree roots are stronger than thicker roots: the role of cellulose and lignin in relation to slope stability Geomorphology 206 196 202

Effect of Change in Penetration to Rotation Rate on Screw Pile Performance in Loose Sand

Adnan Anwar Malik [ORCID]**, Shekh Istiaq Ahmed, Jiro Kuwano, and Tadashi Maejima**

Abstract Sustainable engineering solutions are the key to future infrastructure development to address the devastating effects of climate change. Screw pile is a sustainable, cost-effective, and environmentally friendly piling technique that can be used more and more in future infrastructure. Therefore, this study aims to understand the effect of change in penetration to rotation rate on screw pile performance in terms of installation effort and load-carrying capacity of single-helix screw piles in loose ground conditions. Steel screw piles having a helix-to-shaft diameter ratio of 2.0 were installed into the model ground with different penetration rates; however, the rotation rate was kept the same in all the experiments to achieve different penetration-to-helix pitch ratios in one rotation. The test results showed that in all cases, the ground around the installed pile densifies with the highest densification at a penetration-to-helix pitch ratio of 1.00. The densification zone below the pile tip level is up to 2.5 times the helix diameter, but its trend is gradually decreasing. While comparing the load-settlement response of screw piles installed with different penetration-to-helix pitch ratios with no installation case, it is found that all installation ratios showed higher load-carrying capacity, with the highest for 1.00 penetration-to-helix pitch ratio.

Keywords Screw pile · Penetration-to-helix pitch ratio · Loose sand

A. A. Malik (✉)
School of Engineering, The University of Newcastle, Newcastle, Australia
e-mail: adnananwar.malik@newcastle.edu.au

S. I. Ahmed
Bangladesh Water Development Board, Dhaka, Bangladesh

J. Kuwano
Saitama University, Saitama, Japan

T. Maejima
Asahi Kasei Construction Materials Corporation, Tokyo, Japan

1   Introduction

Deep foundations are vital for the safety of future infrastructure as urbanization is expanding more vertically. Another essential factor that needs to be considered in future infrastructure is the effect of climate change. That is the reason scientists and researchers are searching for sustainable engineering solutions. In the case of deep foundations, a screw pile can be considered one of the sustainable solutions for future infrastructure. It is a displacement pile consisting of a central steel shaft with one or more helices attached [1]. This structural arrangement provides tensile, compressive, lateral, and overturning moment resistance [2, 3]. The well-known advantages of screw piles are their easiness of installation, no wastage of material, less noise and vibration, can be used in limited available spaces, removable and reusable, etc. [4–6].

The helix is one of the main components that contribute to the bearing response of the screw pile; therefore, its strength should be sufficient enough to resist the ground response. Previous studies highlighted that the deformation or deflection of the helix reduced the bearing resistance [7–11]. It was also investigated that the pressure distribution under the screw pile is different from the pipe pile due to the position of the helix from the pile tip [4, 12]. The bearing performance of the screw pile can be reduced even with a strong helix, and it is due to the advancement ratio. The advancement ratio of the screw pile is closely related to the penetration rate, rotation rate, and helix pitch. Helix pitch is the distance between the leading and tailing cutting edges. Previous studies indicated that higher performance could be achieved if the screw pile advances at one pitch penetration per helix rotation, i.e., advancement ratio [13–15]. Sharif et al. [16] observed that the pressing force required to install the pile could be reduced up to 96 % if the advancement ratio is reduced; however, this arrangement will reduce the compressive capacity but increase the tensile capacity. As limited studies are available to understand the effect of the advancement ratio; therefore, this study focused on the effect of the advancement ratio on the installation effort, surrounding ground disturbance and related bearing resistance. A screw pile with a single helix and a close-end central shaft is used in this research.

2   Methodology

To achieve the set objectives, piles were installed in loose sand under different penetration (S)-to-helix pitch (P_h) ratios (S/P_h) in a steel cylindrical model container. The S/P_h ratio varied from 0.25 to 1.25 by changing the penetration rate, i.e., the rotation rate was kept constant. The model ground was checked with the help of a thin steel needle before and after the installation and pile load test. The difference in the penetration provided the ground disturbance due to pile installation. The pile load tests were conducted, and load-settlement curves were compared under different S/P_h ratios and with reference screw pile response. The reference screw pile was not

installed in the model ground but was placed in the model ground to eliminate the installation effect.

3   Testing Equipment and Procedure

The testing was conducted on a model scale (see Fig. 1). A steel container with a diameter of 1000 mm and a depth of 1130 mm was used to prepare the loose sand (Toyoura sand, dry) model ground. The helix diameter was restricted to 1/23 times the diameter of the container so that the effect of rigid boundary on the results could be eliminated. According to [17], to avoid boundary effects, the model container should be more than 20 times the radius of the pile. Moreover, [18] used the same container to study the end-shape effect of steel pipe piles. The relative density of the Toyoura sand was kept at around 45 %. The steel screw pile having a shaft diameter (D_s) of 21.7 mm and helix diameter (D_h) of 43 mm was used in this study. The bottom end of the central shaft was closed. The pitch of the helix was 19.7 mm. A number of piles were installed by varying the penetration (S)-to-helix pitch (P_h) ratio from 0.25 to 1.25. To achieve these S/P_h ratios, the rotation rate was kept the same (1 rotation per minute), whereas the penetration rate was varied from 4.9 to 24.9 mm/min. The disturbance in the surrounding ground was monitored by checking the penetration load before (PL_B) and after (PL_A) the pile installation at distances of 1.5, 2.0, and 3.5 D_h from the centre of the pile through a thin steel needle-connected load cell. After pile installation, a pile load test was conducted using a penetration rate of 2 mm/min. For the reference pile, to avoid the installation effect, the ground was prepared first, then the pile was placed, and then the surrounding ground was prepared.

4   Results and Discussion

4.1   Installation Effort

The installation depth was kept constant in all the tests at 350 mm. The installation effort comprises installation load (press-in) and torque (rotation). It is observed that the installation load increases with the increase in the S/P_h ratio, as shown in Fig. 2. Installation load is highest when the S/P_h ratio is 1.25, and it is lowest when the is S/P_h ratio 0.25. This is because 70 rotations are required to reach the embedment depth for $S/P_h = 0.25$, which is more than the $S/P_h = 1.25$, i.e., 14 rotations. The higher rotation reduced the installation load effort. At low S/P_h ratios (0.25 and 0.50), the central pile shaft experienced tension load at greater depth. It might be due to the upward movement of soil under the screw pile during penetration, as the ground is also densifying. In the case of installation torque, it is observed that with the increase in the S/P_h ratio, the installation torque decreases, as shown in Fig. 3. This trend
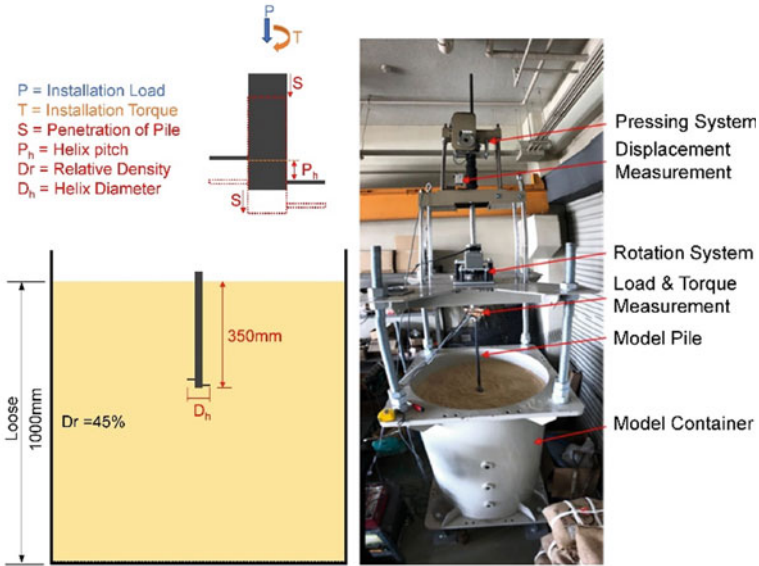
Fig. 1 Testing equipment

is due to a lesser number of rotations as the S/P_h ratio increases. The screw pile installed with the S/P_h ratio of 1.0 showed the least installation torque. This might be due to the less resistance offered by the ground as the soil particles moved along the slope face of the helix. The higher torque at the S/P_h ratio of 1.25 is because the soil particles that cannot enter the helix-sloping face generate additional resistance at the helix edges.

4.2 Surrounding Ground Disturbance

The penetration load was recorded before (PL_B) pile installation and after pile installation (PL_A) with the help of a thin steel needle. The thin steel needle is pushed into the ground with the help of a load cell attached to the penetration system. The surrounding ground disturbance is presented as a ratio, i.e., $PLR = PL_A/PL_B$. When this ratio exceeds 1, it indicates densification; less than 1 indicates the ground loosening. It is observed from the test results that the surrounding ground densifies in all the cases in which the pile is installed with different S/P_h ratios, as shown in Fig. 4. The magnitude of densification increases with the increase in S/P_h ratio, highest for $S/P_h = 1.0$. It is also observed that the general trend of densification increases with depth; however, it gradually decreases below the embedment depth. In addition, the magnitude of densification gradually decreases as it moves away from the centre of the pile (refer to Fig. 4). In other words, the influence of ground disturbance due to

Fig. 2 Installation load with varying S/P$_h$ ratios

Installation Load [kN]

Pile Penetration Depth [mm]

Legend:
- S/Ph = 0.25
- S/Ph = 0.50
- S/Ph = 0.75
- S/Ph = 1.0
- S/Ph = 1.25
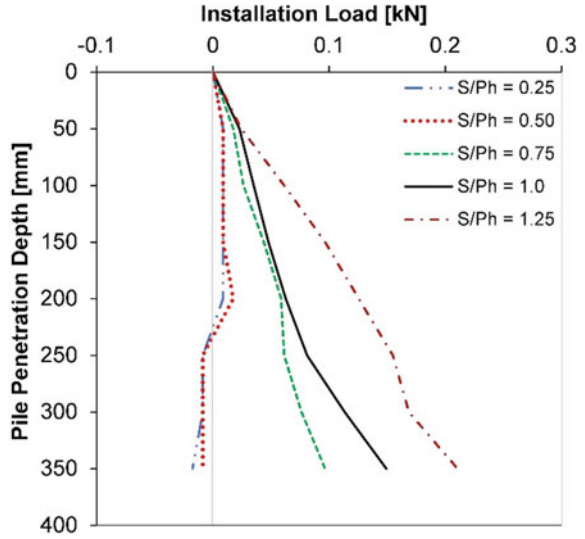
Fig. 3 Installation torque with varying S/P$_h$ ratios

Installation Torque [N-m]

Pile Penetration Depth [mm]

Legend:
- S/Ph = 0.25
- S/Ph = 0.50
- S/Ph = 0.75
- S/Ph = 1.0
- S/Ph = 1.25
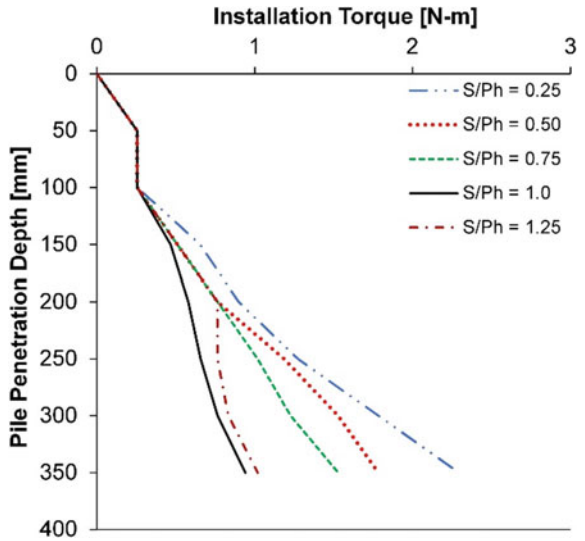
pile installation always fades out around and below the pile, and it can be observed if monitored the disturbance away from the pile boundary.
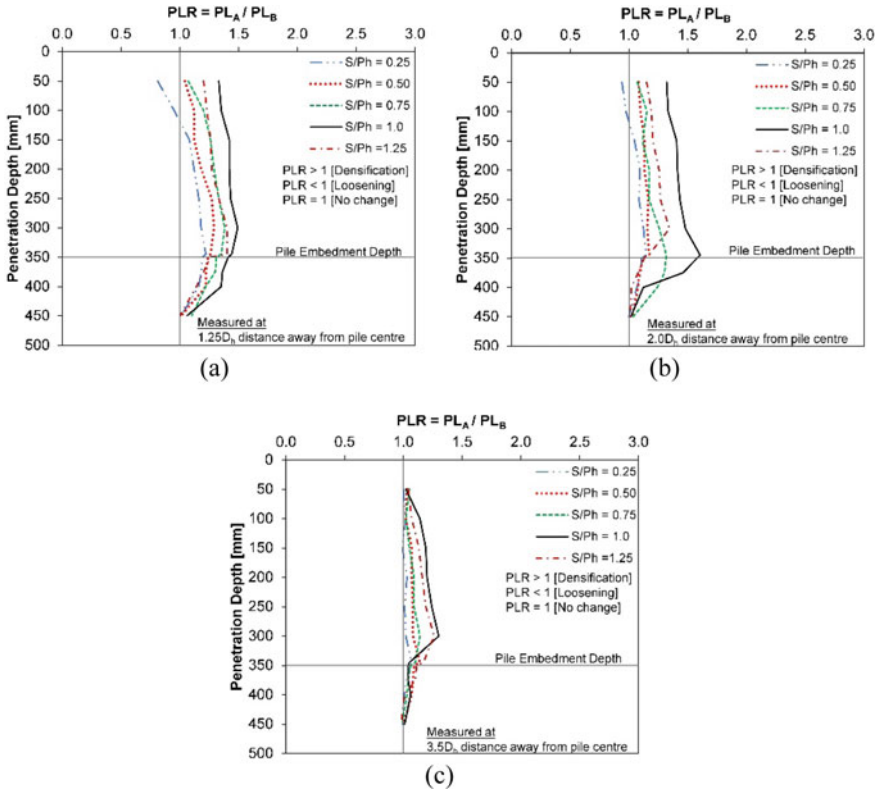
Fig. 4 Ground disturbance with varying S/P_h ratios **a** at a distance 1.5 D_h from the centre of the pile, **b** at a distance 2.0 D_h, **c** at a distance 3.5 D_h

4.3 Bearing Resistance

The load-settlement response indicates that bearing resistance increases with the increase in S/P_h ratio, highest for $S/P_h = 1$ as shown in Fig. 5. This increasing trend is closely related to the ground densification in which densification increases with the increase in S/P_h ratio, highest for $S/P_h = 1$ (refer to Fig. 4). Moreover, due to less ground densification in the $S/P_h = 1.25$ case, a lower axial load is observed than $S/P_h = 1$. While comparing the load-settlement curves for installation and without installation screw piles, it is also observed that in the loose ground, all S/P_h ratios densify the ground, which ultimately enhances the bearing resistance of the screw pile. This indicates that any S/P_h ratio can be selected in the practical field as it enhances the bearing resistance, but it is always preferable to be as close to $S/P_h = 1.0$.

Fig. 5 Load-settlement response at varying S/Ph ratios, including no installation pile response
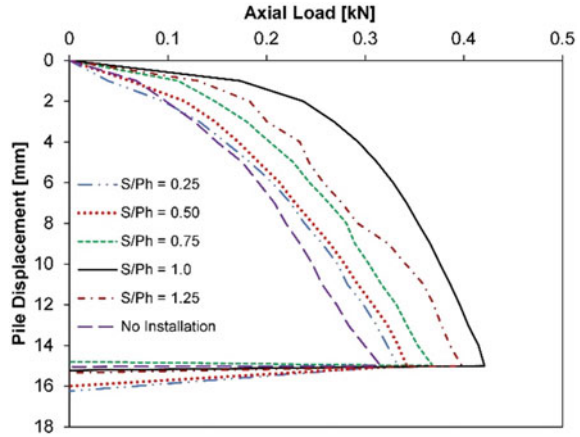
5 Conclusions

This study focused on the effect of change in penetration to rotation rate on screw pile performance in loose sand. A single-helix screw pile with a close end is used in this research. Based on the experimental results, the following conclusions can be drawn.

- The installation effort in terms of press-in load increases with the increase in penetration-to-helix pitch ratio (S/P_h). This increase is due to the lower number of rotations as the S/P_h value increases, i.e., less rotation to reach the embedment depth increases the press-in load. Meanwhile, the installation effort in terms of torque decreases with the increase in penetration-to-helix pitch ratio (S/P_h). This decrease is due to the lower number of rotations as the S/P_h value increases.
- The surrounding ground densifies in all the cases with different S/P_h ratios; however, the highest densification is observed when the pile is installed at $S/P_h = 1.0$. An increasing trend of densification is observed up to the embedment depth, whereas a gradually decreasing trend of densification is observed below the embedment depth. Moreover, the magnitude of densification decreases as it moves away from the centre of the screw pile shaft.
- Bearing resistance increases with the increase in the S/P_h ratio, which is closely related to surrounding ground densification. The highest bearing resistance is observed at $S/P_h = 1.0$, which is due to the movement of soil particles along the sloping face of the helix.
- The comparison in terms of installation and without installation effect indicates that bearing resistance increases in all the S/P_h ratios; therefore, any S/P_h ratio can be selected in the practical field. However, to achieve the optimum performance, it is preferable to be close to $S/P_h = 1.0$.

References

1. Lutenegger AJ, Tsuha CDHC (2015) Evaluating installation disturbance from helical piles and anchors using compression and tension tests. In: Proceedings for the 15th Pan-American Conference On Soil Mechanics And Geotechnical Engineering, Buenos Aires, Argentina
2. Mohajerani A, Bosnjak D, Bromwich D (2016) Analysis and design methods of screw piles: a review. Soils Found 56(1):115–128
3. Schmidt R, Nasr M (2004) Screw piles: uses and considerations. Struct Mag 29–31
4. Ho HM, Malik AA, Kuwano J, Brasile S, Tran TV, Mazhar MA (2022) Experimental and numerical study on pressure distribution under screw and straight pile in dense sand. Int J Geomech 22(9):1–13
5. Livneh B, Naggar MHM (2008) Axial testing and numerical modelling of square shaft helical piles under compressive and tensile loading. Canadian Geotechn J 45(8):1142–1155
6. Sakr M (2011) Installation and performance characteristics of high capacity helical piles in cohesionless soils. J Deep Found Inst 5(1):39–57
7. Ho HM, Malik AA, Kuwano J, Rashid HMA (2021) Influence of helix bending deflection on the load transfer mechanism of screw piles in sand: Experimental and numerical investigations. Soils Found 61:874–885
8. Malik AA, Kuwano J (2020) Single helix screw pile behavior under compressive loading/ unloading cycles in dense sand. Geotech Geol Eng 38:5565–5575
9. Malik AA, Kuwano J, Tachibana S, Maejima T (2019) Effect of helix bending deflection on load settlement behaviour of screw pile. Acta Geotech 14:1527–1543
10. Malik AA, Kuwano J, Tachibana S, Maejima T (2016) Interpretation of screw pile load test data using extrapolation method in dense sand 10(19):1567–1574
11. Yttrup PJ, Abramsson G (2003) Ultimate strength of steel screw piles in sand. Australian Geomech J 38(1):17–27
12. Malik AA, Kuwano J, Tachibana S, Maejima T (2017) End bearing capacity comparison of screw pile with straight pipe pile under similar ground conditions 12:415–428
13. Bradshaw A, Zuelke R, Hilderbranndt L, Robertson T, Mandujano R (2019) Physical modelling of a helical pile installed in sand under constant crowd. In: Davidson C, Brown MJ, Knappett JA, Brennan AJ, Augarge CE, Coombs WM, Wang L, Richards D, White DJ, Blake A (eds) Proceedings of the 1st international symposium on screw piles for energy applications, University of Dundee, Dundee, UK, University of Dundee, Dundee, UK, 109–115
14. British Standards Institution (2015) BS8004: Code of practice for foundations. British Standards Institution, London, UK
15. Perko HA (2009) Helical piles: a practical guide to design and installation. John Wiley and Sons, New Jersey, US
16. Sharif YU, Brown MJ, Cerfontaine B, Davidson C, Ciantia MO, Knappett JA, Ball JD, Brennan A, Augarde C, Coombs W, Blake A, Richards D, White D, Huisman M, Ottolini M (2021) Effects of screw pile installation on installation requirements and in-service performance using the discrete element method. Can Geotech J 58(9):1334–1350
17. Bolton MD, Gui MW, Garnier J, Corte JF, Bagge G, Laue J, Renzi R (1999) Centrifuge cone penetration tests in sand. Geotechnique 49(4):543–552
18. Saleem MA, Malik AA, Kuwano J (2020) End shape and rotation effect on steel pipe pile installation effort and bearing resistance. Geomech Eng 23(6):523–533

Experimental Study on the Bearing Capacities of Sheet Pile Foundation in Saturated Clay Ground

Xi Xiong, Jiayu Chen, Tatsunori Matsumoto, and Yukihiro Ishihara

Abstract In recent years, offshore wind power has been an important way to generate renewable energy and reduce the influence of greenhouse effect. The target of this research is to investigate the bearing capacity characteristics of steel sheet piles as foundations of offshore wind farms. In this study, a series of experiments were conducted to investigate the bearing capacity characteristics of a single steel sheet pile model and a sheet pile group foundation model in a saturated clay ground. According to experiment results, both single pile and pile group in vertical load test (VLT) show similar load-settlement behavior, which is related to the mechanical properties of the overconsolidated clay. Due to the difference in bending rigidity of sheet pile in the direction of the strong axis and weak axis, pile arrangement of pile group significantly influenced the horizontal load carried by each pile, and more effective pile arrangements need to be discussed in future studies.

Keywords Sheet pile · Pile foundation · Load test · Clay ground

1 Introduction

Renewable energy sources are gaining attention to reduce the influence of greenhouse effect, and offshore wind power is an important way to generate renewable energy. Recently, the construction of offshore wind turbines is increasing worldwide. The previous research shows that the time and cost of construction for steel sheet piles are lower than for pipe piles [1]. To design more economical and safer foundations for offshore wind power generation facilities, sheet pile foundations could be an alternative. However, the bearing capacity characteristics of steel sheet piles as the foundation of offshore wind farms has not been comprehensively clarified.

X. Xiong (✉) · J. Chen · T. Matsumoto
Kanazawa University, Kanazawa 920-1192, Japan
e-mail: xiong@se.kanazawa-u.ac.jp

Y. Ishihara
GIKEN LTD, Kochi, Japan

Table 1 Physical properties of K50S50 clay [2]

Specific gravity, G_s	2.653
Saturated density, ρ_{sat} (Mg/m^3)	1.98
Plastic limit, PL (%)	13.6
Liquid limit, LL (%)	33.9
Water content, w (%)	26.2
Void ratio, e	0.703

In this study, a series of experiments were conducted to investigate the penetration resistance and bearing capacity characteristics of a single steel sheet pile model and a sheet pile group foundation model in a saturated clay ground.

2 Experiment Description

2.1 Model Ground

The soil used as model ground was Kasaoka clay mixed with silica sand No. 6 in a weight ratio of 1:1 (K50S50 clay). Table 1 shows the physical properties of the soil. The model ground was prepared in a cylindrical chamber with a diameter of 420 mm and a height of 420 mm. A drainage line with a valve was connected to the bottom of the chamber. The bottom drainage layer was 50 mm thick and compacted to a uniform relative density of around 81% using silica sand No. 3. For the clay layer, water was then added to dry K50S50 to obtain a soil slurry with a water content w of 1.3 times the liquid limit LL. This soil slurry was poured into the soil chamber to an initial thickness of 370 mm. The soil was then consolidated with a vertical pressure of up to 100 kPa.

2.2 Model Foundations

As shown in Fig. 1, a 195 mm long acrylic plate was used to present a sheet pile wall, hereafter referred to as the single sheet pile model. Table 2 shows the specifications of the model pile (sheet pile). Strain gauges were attached horizontally and vertically both on the front and back sides at six cross-sections of the pile to measure the axial forces and bending moments.

Figure 2 shows the sheet pile group model consisting of 4 sheet piles, which is the foundation of an offshore wind farm proposed by this paper. In addition to the horizontal and vertical strain gauges, cross gauges were attached at 30 mm from the pile head to measure shear resistance. A model square raft with a side length of 100 mm and a thickness of 30 mm was used to fix the heads of 4 piles.

Fig. 1 Single sheet pile model

Right view   Left view

Unit: mm   ⊕ Strain gauge
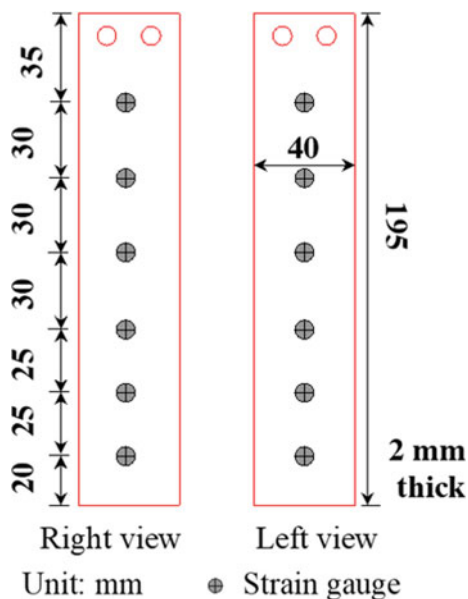
Table 2 Specifications of the sheet pile

Length, L (mm)	195
Width, B (mm)	40.00
Thickness, h (mm)	2.00
Young's modulus, E (N/mm^2)	3379.63
Bending rigidity, EI (MN · mm^2)	0.09
Bending rigidity, EI (MN · mm^2) (strong axis)	36.05
Poisson's ratio, v	0.35
Length, L (mm)	195

Though the stiffness of acrylic is smaller than that of steel, it is still much greater than that of soil. Moreover, the use of acrylic makes it easier to measure strain in model piles. Therefore, it was reasonable to utilize acrylic for model piles.

2.3 Experimental Equipment

Compression test was conducted using a static loading device (screw jack) to obtain Young's modulus and Poisson's ratio of the model pile (Fig. 3). The same screw jack was used for the pile penetration test (PPT) and vertical load test (VLT). The vertical load was measured by a load cell (LC) placed on the pile head. Vertical displacement of the pile head was measured by a dial gauge (DG).

Fig. 2 Sheet pile group model
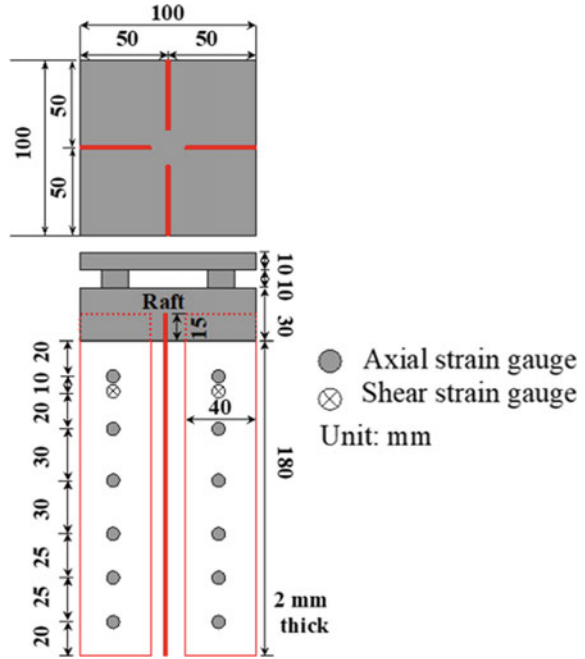
Fig. 3 Vertical load equipment
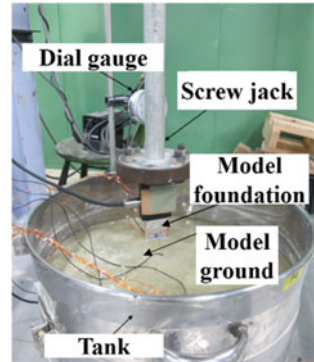
As shown in Fig. 4, in the horizontal load tests (HLT), due to the low height of the foundation, a steel rod with sufficient rigidity was fixed at the center of the model raft. The pile group model was pulled horizontally by a winch from a position 30 mm above the top surface of the raft, and horizontal load was measured with an LC connected between the rod and the winch. The horizontal displacement of the raft was measured with a DG on the opposite side connected with the rod. To measure the angle of deflection of the pile head, an accelerometer (ACC) was mounted on the top of the loading bar, which was fixed on the raft.
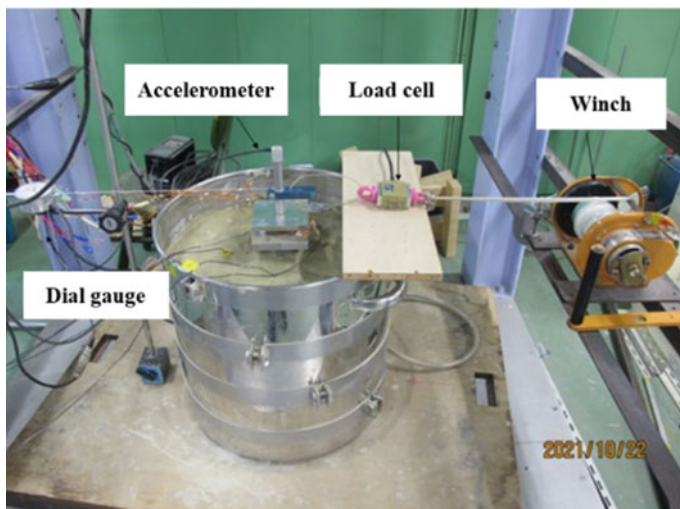
Fig. 4 Horizontal load equipment

Fig. 5 Locations of piezometers (single pile)
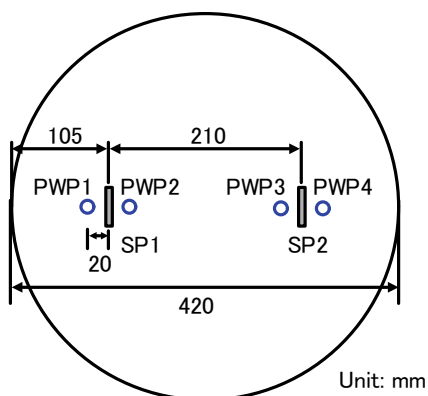
Piezometers PWP 1–4 were adopted to measure pore water pressures in the model clay ground. They were set at a horizontal distance of 20 mm from the model piles, as shown in Figs. 5 and 6. The piezometers were set at a depth of 20 mm from the ground surface.

2.4 Experimental Procedure

Load tests on two single pile models, SP1 and SP2, were conducted first. PPTs were first conducted, and the two model piles were penetrated into the model ground one

Fig. 6 Locations of
piezometers (pile group)
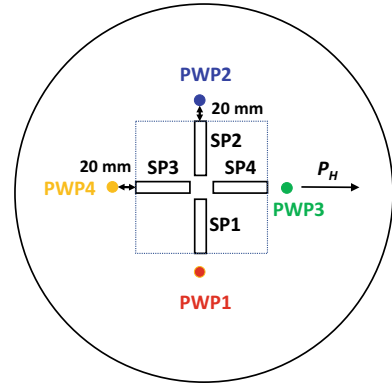
by one (Fig. 5) using the screw jack until the pile embedment length reached 150 mm.
Then, monotonic VLT was conducted on SP1 immediately and on SP2 24 h after
the installation process to investigate the consolidation (set-up) effect on the pile
capacity.

For load tests on the pile group model, the foundation was penetrated into the
model ground to the same depth as that of the single piles. VLT was carried out 24 h
after the installation process. After another 24 h, HLT was carried out considering
that offshore wind farms are subject to large horizontal loads. The horizontal loading
position was on the loading bar and 39 mm above the bottom of the raft (Fig. 4).

3 Experiment Results

3.1 Result of Single Pile

Pile Penetration Test (PPT). Figure 7 shows the relationship between vertical load
P_v and settlement (penetration depth of the pile head) w of model piles SP1 and
SP2. It is found that there is no significant difference in the vertical load between
SP1 and SP2 at the end of PPTs. Unfortunately, shaft resistance during PPT was not
successfully obtained due to a technical problem.

Figure 8 shows the relationship between excess pore water pressure p_w and pene-
tration depth w. At PWP1, the excess pore water pressure (EPWP) increased signif-
icantly from the start of penetration, reaching a peak of around 3.5 kPa at w was
30 mm, and then decreased. PWP2 and PWP3 also increased from the start of pene-
tration, peaked at w of about 30 mm, and remained almost constant thereafter. The
EPWP remained in the soil surrounding all piles after the penetration processes were
completed. The difference in the tendency of EPWP on either side of the model piles
is thought to be caused by the slight bending of the model pile during penetration. In

Fig. 7 Load-settlement behavior during PPTs on single piles
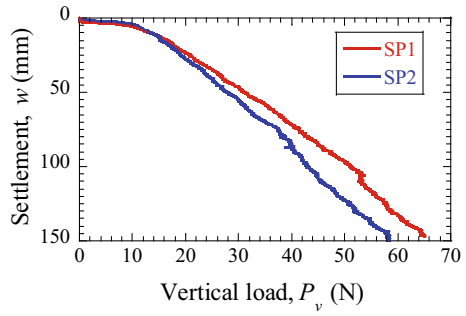
Fig. 8 EPWP-settlement behavior during PPTs on single piles
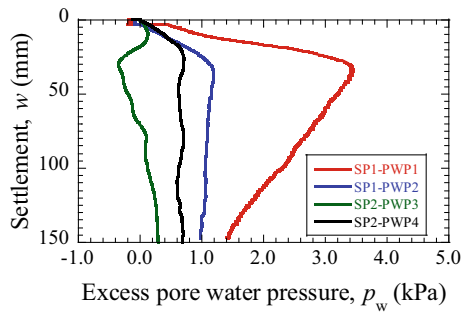
addition, the position of piezometers may be influenced by the ground deformation during pile penetration, causing discrepancies among them.

Vertical Load Test (VLT). Figure 9 shows the relationship between vertical load P_v and settlement w for SP1 and SP2. Note that w at the end of PPT was zeroed in VLT.

The yield load P_v of SP1 and SP2 was approximately 80 and 140 kN, respectively, indicating that the bearing capacity of SP2 is significantly superior. The reason is considered that EPWP generated in PPT had not yet dissipated in the soil around SP1, and it had a significant influence on the bearing capacity of a sheet pile.

Fig. 9 Load-settlement behavior during VLTs on single piles
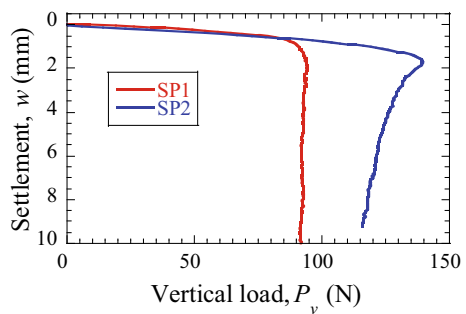
Fig. 10 EPWP-settlement behavior during VLTs on single piles
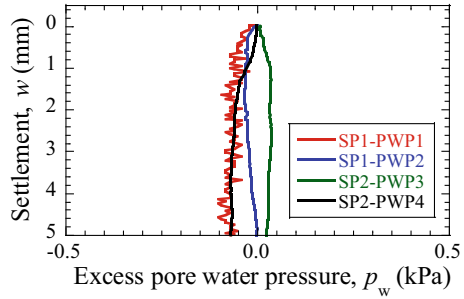
Figure 10 shows the relationship between the EPWP p_w and the settlement w during VLT. The EPWP during VLT was much smaller than that during PPT (-0.2–3.5 kPa), and the difference in different sensors was minor. This is probably because the EPWP mainly occurred near the pile tip, and for VLT, the pile tip was far away from the piezometers. Negative EPWP was also observed in some areas due to soil dilatancy.

3.2 Result of Pile Group

Pile Penetration Test (PPT). Figure 11 shows the vertical load P_v of the sheet pile group foundation during PPT. The vertical load P_v of sheet pile foundations increased almost in proportion to the pile head settlement w. P_v acting on the pile group at the end of the PPT is about 120 N. Similar to PPT on single piles, the shaft resistance of the pile group was not successfully obtained due to a technical problem.

Figure 12 shows the relationship between settlement w and EPWP p_w during PPT. The data of PWP3 was not obtained due to a technical problem. It was found that p_w increased slightly at first and then decreased gradually to negative values. It means that the soil around the piles showed compression behavior and then turned into dilatancy.

Fig. 11 Load-settlement behavior during PPT on pile group
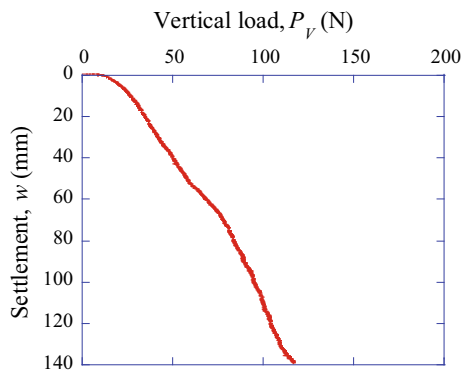
Fig. 12 EPWP-settlement behavior during PPT on pile group
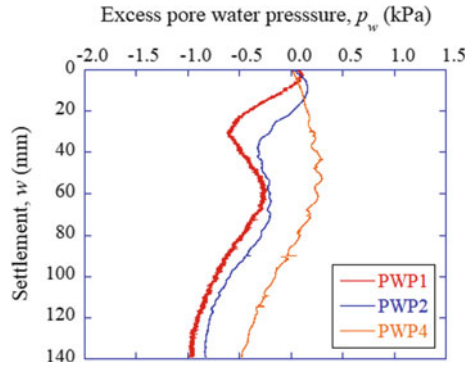
Vertical Load Test (VLT). Figure 13 shows the relationship between the pile head load P_h, pile tip resistance P_t, shaft resistance P_f, and pile head displacement w during VLT for the sheet pile group foundation. The pile head load, pile tip resistance, and shaft resistance increased with increasing pile head settlement and reached a peak, after which the pile head load and shaft resistance decreased, and the pile tip resistance was approximately constant. Hence, it is the decrease in shaft resistance that led to the decrease in pile head load after reaching the peak.

Figure 14 shows the relationship between the pile head settlement w and the EPWP p_w of the surrounding soil during VLT of the sheet pile group foundation. In the surrounding soil, negative EPWP was generated at the beginning and positive EPWP occurred at the end of VLT. Compared to the results of PPT, the behavior of the soil was reversed, and generated EPWP was smaller.

Horizontal Load Test (HLT). Figure 15 shows the relation between horizontal displacement u-horizontal load P_H. The horizontal load increased with the increase of horizontal displacement. The maximum horizontal load in the test was around 60 N at $u = 15.0$ mm. For the load carried by each sheet pile, the horizontal load of SP3 was initially lower than that of SP4, then increased significantly, and finally reached almost the same value as that of SP4. SP1 and SP2 increased slowly from the

Fig. 13 Load-settlement behavior during VLT on pile group
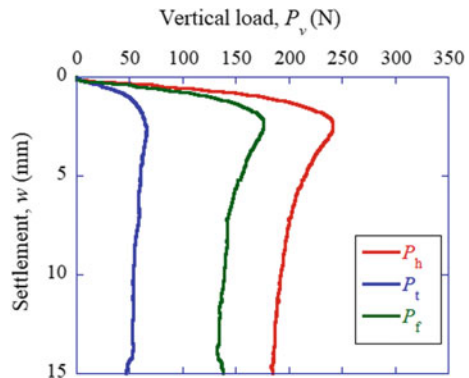
Fig. 14 EPWP-settlement behavior during VLT on pile group
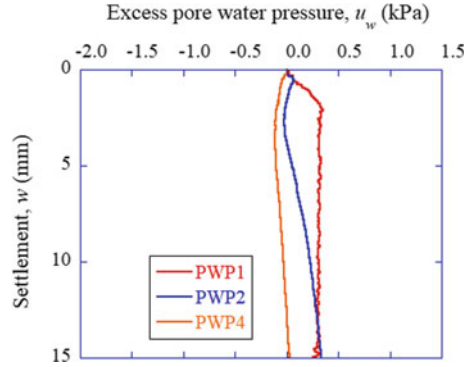
Fig. 15 Horizontal displacement-horizontal load behavior during HLT on pile group
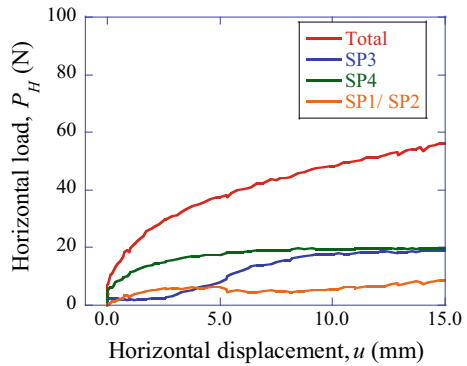
start of loading and finally reached approximately half of the values of SP3 and SP4. Therefore, due to the difference in bending rigidity of the sheet piles in the direction of the strong axis and the weak axis (Table 2), the piles in the direction of the strong axis could carry much greater horizontal load in the sheet pile group foundation. It is noted that due to the loading direction, the horizontal resistance of SP3 and SP4 is almost from the shaft resistance acting on wider lateral surfaces, while that of SP1 and SP2 is from earth pressures acting normally on wider lateral surfaces.

Figure 16 shows the relation between pile head inclination degree θ—horizontal load P_H for sheet pile group foundation. The horizontal load carried by the pile group increased with the increase in pile inclination degree, which is similar to the relation between horizontal displacement-horizontal load. The maximum horizontal load in the test was around 60 N at $\theta = 3.5°$.

Figure 17 shows the relationship between pile head inclination angle θ—horizontal displacement u of sheet pile group foundation. The relationship between the pile inclination angle θ and the horizontal displacement u was almost linear.

Figure 18 shows the bending moment M_b versus depth from the ground surface z of SP2 in the sheet pile group foundation. Please note the data of bending moments was obtained at specified horizontal loads as shown in Fig. 16. The bending moments

Fig. 16 Inclination degree-horizontal load behavior during HLT on pile group
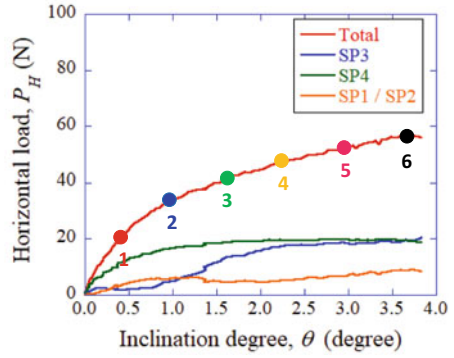
Fig. 17 Horizontal displacement-inclination degree behavior during HLT on pile group
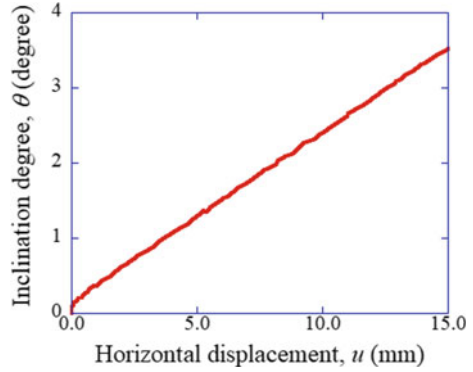
Fig. 18 Distribution of bending moment of piles in pile group at specific horizontal load
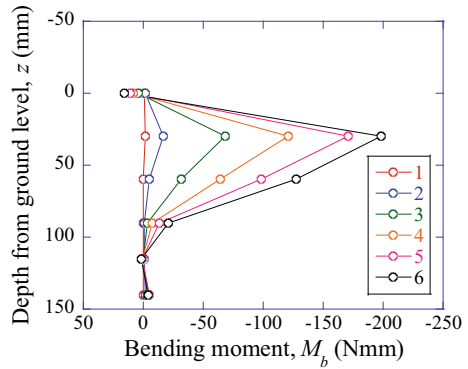
were calculated from the strains ε obtained from the strain gauges during the HLT. The bending moments at each point were obtained by subtracting the bending moment at each point at the beginning of HLT. It was found that the bending moment increased with the increase in horizontal load. It was found that the largest bending moments occur at about $z = 30$ mm.

3.3 Discussion

Comparing Figs. 9 and 13, the load-settlement behavior of single pile SP2 and pile group is similar during VLT, i.e., vertical load increased with increasing pile head settlement, reached a peak, and finally decreased gradually. The decrease in pile head load after reaching the peak was caused by the decrease in shaft resistance, which is related to the mechanical properties of the overconsolidated clay. For the stress–strain relation of the overconsolidated clay, the stress decreases with the increase in shear strain after reaching a peak. However, the pile group requires a larger settlement to reach the peak vertical load, which should be suitably considered when estimating the load-settlement behavior of the sheet pile group from that of a single sheet pile. Moreover, the group efficiency of the proposed sheet pile group subjected to vertical load is around 0.43, and for the application of the proposed foundation, more effective pile arrangements need to be discussed in future studies.

4   Conclusion

In this study, a series of load tests was conducted on a single steel sheet pile model and a sheet pile group foundation model in a saturated clay ground. The following conclusions were obtained:

Both single pile and pile group in pile penetration tests (PPTs) show that vertical load P_v increases in proportion to the penetration depth w.

In the vertical loading test on single piles, the ultimate vertical load of SP1, which was tested immediately after the penetration test, was about 60% of that of SP2, indicating that EPWPs generated during pile installation process significantly influenced the vertical bearing capacity of the steel sheet piles.

Both single pile SP2 and pile group in vertical load tests (VLTs) show that vertical load increased with increasing pile head settlement, reached a peak, and finally decreased gradually. Since the shaft resistance during VLT on pile group decreased after reaching the peak, while the pile tip resistance was approximately constant, the decrease in pile head load after reaching the peak was considered to be caused by the decrease in shaft resistance.

Pile group subjected to vertical load requires a larger settlement to reach the peak of bearing capacity, which should be suitably considered when estimating the load-settlement behavior of sheet pile group from that of single sheet pile.

Due to the difference in bending rigidity of sheet pile in the direction of the strong axis and week axis, pile arrangement of sheet pile group significantly influenced the horizontal load carried by each pile, and more effective pile arrangements need to be discussed in future studies.

References

1. Guo WT, Honda Y, Xiong X, Matsumoto T, Ishihara Y (2021) Behaviour of three types of model pile foundation under vertical and horizontal loading. In: Proceedings of the h 2021, Kochi, Japan. CRC Press
2. Hoang LT, Xiong X, Matsumoto T (2021) Performance of pressed-in piles in saturated clayey ground: Experimental and numerical investigations. In: Proceedings of the second international conference on press-in engineering 2021, Kochi, Japan. CRC Press, pp 49–159

Hydro-Mechanical Effect of Vetiver Root on Laterite Soil

T. T. Safa, D. Mahima, P. K. Jayasree, and K. Balan

Abstract Soil bioengineering is a technique that uses vegetation in engineering design. Stabilizing slopes using grass roots can be considered as a soft type disaster mitigation measure for building a sustainable and resilient society from the perspective of its socio-economic benefits. The applicability of plant roots in slope stability can be understood by studying its hydrological and mechanical attributes. Hence the aim of this study is to identify the contribution of these two factors in stabilizing slopes by considering root–soil interaction. Plant roots act as a structural element to provide mechanical reinforcement, and when transpiration becomes significant, it induces soil suction which enhances the soil shear strength and reduces the hydraulic conductivity. Out of several grass species, vetiver grass (Crysopogon zizanioides) has various predominant qualities in its availability, faster growth and root biomass which ensure its use in geotechnical and geo-environmental engineering. Hence, the effect of vetiver grass roots on soil water retention curves (SWRC), permeability (k) functions and shear strength parameters have been experimentally investigated on lateritic soil. Thus, this paper focuses on quantifying the root contribution in improving the shear strength parameters: cohesion and friction angle along with permeability functions and further to develop SWRC to measure soil suction for different root biomass. Results of this study can be used as a tool for engineers in establishing a sustainable mitigation measure for a region where the impacts due to landslides are severe and vulnerabilities are the greatest.

Keywords Vetiver grass · SWRC · Permeability · Apparent cohesion

T. T. Safa · D. Mahima (✉) · P. K. Jayasree
Department of Civil Engineering, APJ Abdul Kalam Technological University, College of Engineering Trivandrum, Thiruvananthapuram, Kerala, India
e-mail: mahimadethan@gmail.com

P. K. Jayasree
e-mail: jayasreepk@cet.ac.in

K. Balan
Rajadhani Institute of Engineering and Technology, APJ Abdul Kalam Technological University, Thiruvananthapuram, Kerala, India

1 Introduction

The bioengineering techniques are environment-friendly alternative used for slope protection and stabilization. The use of vegetation to stabilize slopes is a better alternative to many uneconomic slope improvement techniques. Though it has been practiced as an environmentally friendly way of stabilizing shallow slopes since ancient times, thorough investigations inferring the geotechnics involved have not been properly done. Reinforcement using vegetation is mainly due to its hydraulic action which is due to water removal and mechanical action by apparent cohesion and friction angle [1, 2]. Root–soil interaction as well as root content has qualitative and quantitative effects on soil water retention curve and permeability functions depending on the type of soil.

The mitigation of shallow landslides in natural and man-made slopes using vegetation can be considered as economic and ecological alternative to conventional civil engineering solutions [3]. Ruiz [4] discussed the role of vegetation in stabilizing slopes by considering the various components of root–soil interaction. Hydrological mechanism is influenced by interception by canopy and stem of the vegetation and affects soil moisture by evapotranspiration. Vegetation has the capability of inducing suction to the soil mass [5]. This increases soil shear strength but also reduces water permeability. The reduced permeability results in reduced rainfall infiltration and hence helps to preserve a greater amount of soil suction in an unsaturated soil slope [6]. The mechanical effect of vegetation in stabilizing the terrain is due to the root–soil interaction at the potential shear surface of soil slope. Vegetation increases the shear strength and pull-out resistance of the terrain [7]. Soil reinforcement by roots is influenced by factors associated root density and architecture as well as mechanical characteristics of soil and roots [8].

There are different vegetation types like trees, grass and shrubs which can be used for slope stabilization. The most commonly used vegetation is vetiver grass that has the ability to work well in various climatic conditions and protect slopes from erosion. However, the studies quantifying the effect of grass root on hydro-mechanical properties of soil are very limited. Present study analyzes the applicability of using vetiver grass roots in stabilizing laterite soil. This study also gives an idea about the variation in behavior of a vegetated soil mass with different plant ages. This can be used as a method to analyze the effectiveness of vetiver grass roots on a different soil types.

1.1 Objectives

The fundamental objective of the paper is to investigate the effect of vetiver grass (Crysopogon zizanioides) on hydraulic properties of soil and quantify the effect of grass roots on the reinforcement of soil by plant roots using laboratory experiments. The main objectives are:

- To analyze the variation of root biomass in soil with different plant ages.
- To study the effect of vetiver grass roots on soil water retention curve.
- To evaluate the variation in permeability functions of laterite soil for different root contents.
- To quantify the effect of root reinforcement on slope stability by finding root cohesion and apparent friction angle.

2 Materials and Methodology

Laterite soil is present in different parts of Kerala and is encountered in regions of slope instability. Hence, the effect of vetiver roots on the behavior of laterite soils was analyzed. The laterite soil used for the study was collected from College of Engineering Trivandrum Campus, Kerala, India. Table 1 shows the properties of soil used. Vetiver saplings were planted in tanks filled with laterite soil at a bulk density 1.71 g/cc.

The grasses were grown until reaching a certain age, differing from one to four months before testing. The spacing was fixed after considering the lateral spread of the vetiver saplings. The dimensions of the tank and spacing of vetiver saplings denoted as small rectangular sections are shown in Fig. 1.

The growth of vetiver saplings was monitored for 30, 60, 90 and 120 days. The test program involved first soaking of the tank containing the specimen for one day to attain saturation condition, which made the sampling process easier. The specimens were sampled in a split cylindrical sampler having diameter 0.15 m and height of 0.3 m as shown in Fig. 2.

The experimental program was considered to be conducted in three stages. The first stage was soil suction measurement followed by permeability test.

Table 1 Properties of soil collected

Sl. no	Properties	Result
1	Grain size distribution	
	Gravel fraction (%)	31
	Sand fraction (%)	69
	Silt fraction (%)	3
	Clay fraction (%)	7
2	Liquid limit (%)	35
3	Plastic limit (%)	23
4	Plasticity index (%)	9
5	Specific gravity	2.56
6	Maximum dry density (g/cc)	1.88
7	Optimum moisture content	18
8	Soil classification	SW-SC
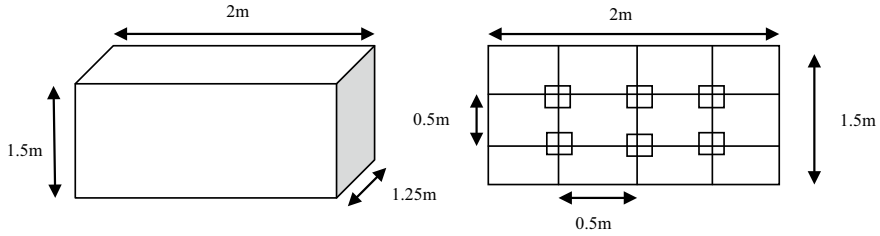
Fig. 1 Dimensions of tank and spacing of vetiver samplings

Fig. 2 Sampling of specimen

After conducting the permeability test, the sample is taken for studying the root morphology. The third set of experiment consisted of direct shear tests. The experimental procedures are performed on soil filled at a known density, and hence the results obtained are dependent on the density and soil type.

To develop soil water retention curve (SWRC) for different root biomass, the sampled specimen after each sampling was taken to suction test using point-wise method. In this technique, incremental measurement of soil suction at different moisture contents is considered.

After sampling it was possible to begin the testing immediately at the saturated condition by using two Whatman No. 42 filter papers per sample (2 at sides and 2 at the bottom). To prevent the loss or gain of moisture and obtain a stable temperature, samples were placed in Styrofoam box after wrapping in PVC plastic film and aluminum foil as shown in the Fig. 3. The samples were kept in Styrofoam box for duration of 3–4 days as per [9] for proper moisture balance. The moist filter paper was then removed from the soil specimen and weighed to one 10-thousandth of a gram in an analytical weighing machine. The measurement was taken in 3–5 s to

prevent moisture loss. After finding the suction corresponding to the saturated volumetric water content the sample was exposed to air and dried. Water content was increased by 1% in order to obtain suction at different moisture contents. Drying is attained with the exposure of sample in air, while wetting is attained by spraying water into sample. After addition of water to the sample, it was wrapped and cured till equilibrium of suction is reached. This procedure is repeated for different water content to obtain required number of points in SWRC. To determine the volumetric water content for rooted soils a new relationship considering roots is used developed by Jotisanka and Sirirattanachat [10] given in Eq. 1.

$$\theta = \frac{V_w}{V} = \frac{(W - Wr - Ws)}{V} x \frac{1}{\gamma_w} \tag{1}$$

where V is total volume, Vw is water volume, W is total weight, Ws is weight of soil particles, Wr is weight of roots, γ_w is water unit weight, and θ is volumetric water content.

For root content measurement, "root biomass per soil volume", ρ_r, kg/m^3 was determined. The sample was dismantled after sampling, and the moisture content was determined. After sampling, the roots were washed and passed through sieve of 1 mm size. Roots that passed through sieve were not considered in measuring the root biomass. Root biomass is obtained as the ratio of total dry weight of root to volume of the specimen.

To conduct the permeability test, the top portion of the specimens was trimmed off with knives, surface was leveled, and the specimen was kept undisturbed. The test procedure was according to [11]. Test was carried out for specimens with different root biomass during each interval of sampling. To determine the shear strength parameters C and ϕ, direct shear tests were conducted on bare sample and rooted sample

Fig. 3 Sample preparation for suction measurement

with different root biomass. The tests were carried out according to IS 2720 Part XII (1972). Undisturbed samples having the same dimensions of the shear box were cut out from an extruded specimen keeping the root specimen undisturbed.

3 Results and Discussions

From the detailed methodology adopted as discussed in the previous section, the following results were obtained for vetiver rooted laterite soil samples for different ages.

3.1 Soil Water Characteristic Curve

The presence of plant roots in soil directly affects soil hydraulic properties, including soil water retention. Hence, proper study of SWRC can help in analyzing the effect of plant roots in soil. Figure 4 shows the SWRC obtained for root–soil matrix with varying age.

When root density increases, transpiration becomes more effective, and consequently the suction pressure developed in the soil increases. Table 2 shows the variation of air entry value (AEV) with different root biomass corresponding to different age of the plant.

As the root biomass increased from 1.7 to 5.4 kg/m^3 there is significant changes in the nature of SWRC characteristics. It is observed from the graph that SWRC corresponding to root biomass of 3.5 and 4.42 kg/m^3 is steeper than that of lesser root content. That is for a given amount of moisture absorption, steeper SWRC will
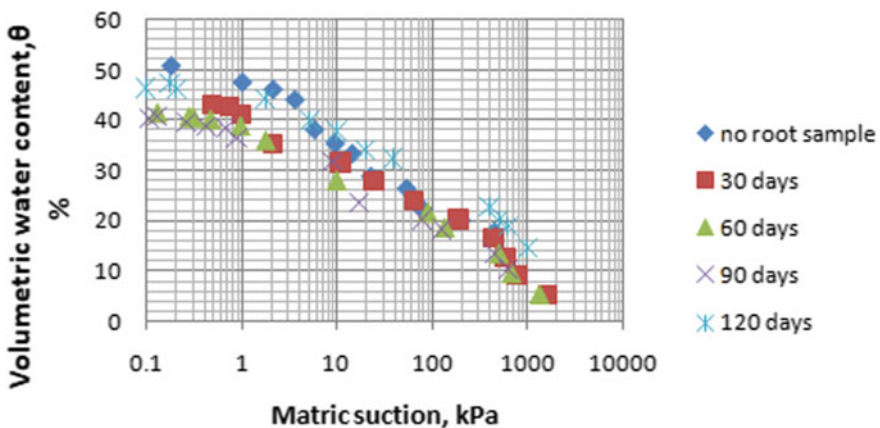
Fig. 4 Variation of SWCC with different age of vetiver saplings

Table 2 Variation of air entry value and root biomass with plant age

Sl. no	Age (days)	Root biomass (kg/m^3)	Air entry value (AEV)
1	0	0	0.7
2	30	1.716	1.3
3	60	3.5	1.6
4	90	4.42	2
5	120	5.4	1.5

induce higher suction. The decrease in saturated volumetric water content from 50 to 40% may be due to the decreased pore sizes of soil mass because of root occupying the pore spaces. The change in the behavior of SWRC primarily affect the air entry suction created in the soil. Changes in AEV have significant effect on suction regime, slope stability and time to failure of slopes during rainfall. The AEV of bare soil is estimated as 0.7 kPa which further increased up to 2 kPa with increase in root biomass from 1.7 to 4.42 kg/m^3. The increasing trend in AEV is seen only up to the threshold root biomass beyond which AEV decreased to 1.5 kPa as shown in the graph. A higher value of AEV represents a slope with greater factor of safety and longer time for slope failure, which means that vegetated slopes with sufficient quantity of root biomass can stabilize the slope.

3.2 Permeability

The value of coefficient of permeability k for bare soil sample at 70% of bulk density was 1.03×10^{-4} m/s. As the root content increased and rate of infiltration reduced the value of k also decreased to 2.87×10^{-7} m/s due to decrease in porosity as shown in Fig. 5.
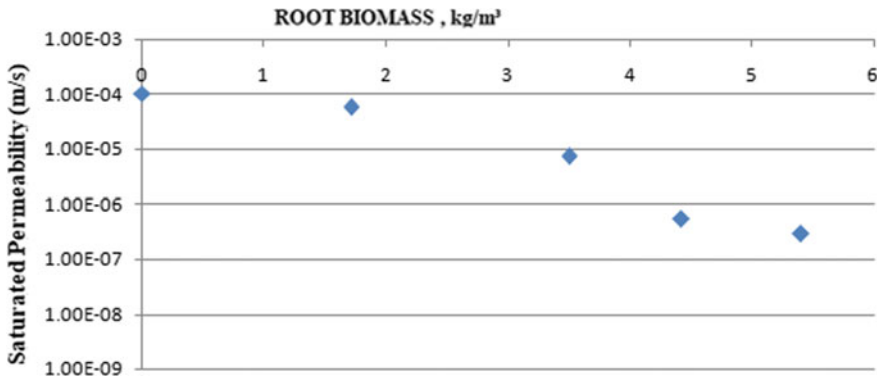
Fig. 5 Variation of permeability with root biomass

The effect of root on permeability is abrupt that with a minor increase of root content the water flow was blocked. The distribution of macro-pores would be affected by roots to a greater extend. It is also speculated from the graph that beyond the threshold root content the rate of decrease in permeability is unnoticeable which may be because of the decreased effect of soil suction due to root fragmentation.

3.3 Shear Strength

The effect of roots on cohesion and friction angle were determined using direct shear strength test on specimens with various root biomasses. The peak shear strength of the specimen increased with increase in root biomass and increase in normal stresses. Apparent cohesion (C') and apparent angle of internal friction ($\varnothing$ ') values are obtained from maximum shear stress versus normal stress plot. The increase in apparent cohesion from 7.75 kPa of bare soil to 17.98 kPa for vegetated soil plays a significant role in increasing the factor of safety of slopes. The net increase in apparent cohesion is 10.23 kPa for a root content of 5.4 kg/m^3 which is a good improvement compared to other method of slope stabilizing techniques. The increase in C' is not predominant beyond the root content of 4.42 kg/m^3 which may be due to the formation of shrinkage cracks formed due to the presence of extreme root biomass which may cause a detrimental effect to slope stability (Fig. 6).
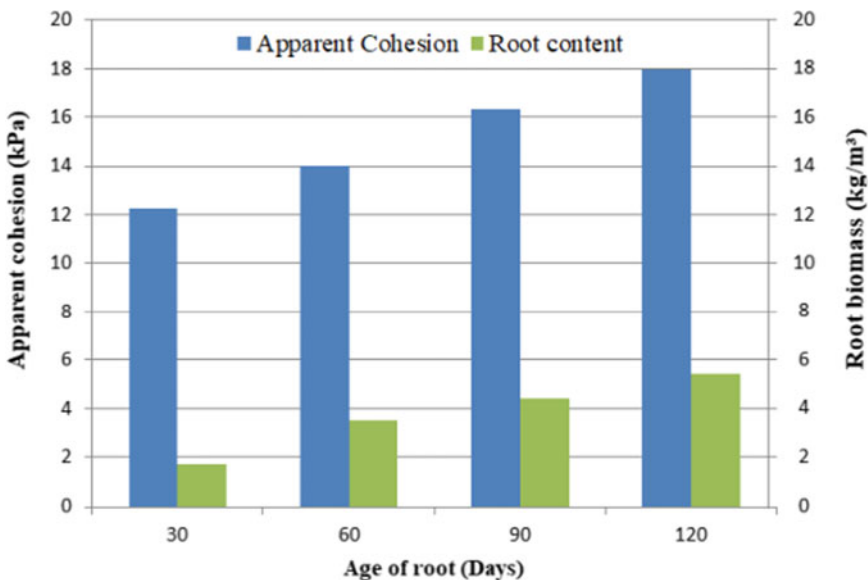
Fig. 6 Variation of apparent cohesion with root biomass and plant age
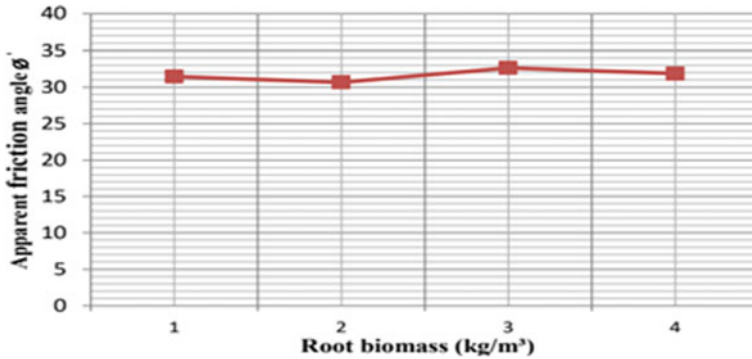
Fig. 7 Variation of apparent friction angle with root biomass

When apparent friction angle is considered, no significant variation is noticed with increase in root biomass in this study as shown in Fig. 7.

When root penetrates through soil, it densifies the soil mass, and this would increase the angle of internal friction. However, this effect is not noticed here because of the limitation in the laboratory shear strength test.

4 Conclusion

In this study the effectiveness of vetiver roots in stabilizing lateritic soil slope is investigated by conducting various laboratory experiments and studying root morphology. The analysis is carried out based on two aspects of root–soil interaction, viz., hydrological effects and mechanical effects of grass roots on soil reinforcement. Following conclusions were derived.

- Root biomass has significant effect in deciding the behavior of soil water characteristic curves of vegetated soil, with increase in root biomass SWRC became steeper and more shifted downward with AEV increasing from 0.7 to 2 kPa.
- When root biomass increased beyond 4.4 kg/m^3 SWRC shifted upward and became less steep with decrease in AEV up to 1.5 kPa.
- The additional shear strength provided by vetiver roots increased about three times with increase in root content from 1.7 to 5.4 kg/m^3.
- The permeability decreased from 1.03×10^{-4} to 2.87×10^{-7} m/s, i.e., k decreased by thousand times, and these are important parameters which predict the suitability and effectiveness of vetiver grass for shallow slope stabilization.

The rates of increase in matric suction and shear strength are only significant up to a threshold root concentration beyond which the rate became slightly smaller; hence for lateritic soil the optimum root biomass is approximately within in the range of 4.42–5.40 kg/m^3.

References

1. FH Ali N Osman 2008 Shear strength of a soil containing vegetation roots Soils Found 48 4 587 596
2. KM Briggs JA Smethurst W Powrie AS O'Brien 2016 The influence of tree root water uptake on the long term hydrology of a clay fill railway embankment Géotechnique 66 9 31 48
3. A Stokes C Atger AG Bengough T Fourcaud RC Sidle 2009 Desirable plant root traits for protecting natural and engineered slopes against landslides Plant Soil 324 1 1 30
4. Ruiz S (2021) Plant–soil modelling Fourth edition. Wiley & Sons Publishers, Southampton, UK
5. Tien H, Fellow W (2013) Study of soil-root interaction. J Geotech Eng ASCE 114(32):1351–1375
6. JJ Ni AK Leung CWW Ng W Shao 2018 Modelling hydro-mechanical reinforcements of plants to slope stability Comput Geotech 95 99 109
7. G Veylon M Ghestem A Stokes A Bernard 2015 Quantification of mechanical and hydric components of soil reinforcement by plant roots Can Geotech J 52 11 1839 1849
8. YH Chok MB Jaksa WS Kaggwa 2015 Assessing the influence of root reinforcement on slope stability by finite elements Geo-Engineering 6 12 https://doi.org/10.1186/s40703-015-0012-5
9. ASTM D 5298–10, Standard test method for measurements of soil potential (Suction) by filter paper, American Society for Testing and Materials (ASTM)
10. A Jotisankasa T Sirirattanachat 2017 Effects of grass roots on soil-water retention curve and permeability function Can Geotech J 54 11 1612 1622
11. IS 2720–17 (1986) Methods of test for soils, Part 17: Laboratory determination of permeability [CED 43: Soil and Foundation Engineering]. BIS, New Delhi

Influence of Relative Stiffness on Integral Bridge Design

Douglas G. Morley, Yazan B. Asia, Gopal S. P. Madabhushi, Indrasenan Thusyanthan, and Dennis Sakufiwa

Abstract Integral bridges are a low-maintenance form of bridge construction used worldwide. Their jointless structure eliminates bearing and expansion joint replacement bringing a reduction in lifecycle cost, carbon emissions, and socio-economic impact from road and rail disruption, therefore offering a resilient infrastructure solution in the face of a changing climate. By better understanding earth pressure ratcheting in the backfill due to repeated thermal movements of the deck, integral bridge use can increase to greater spans and skews while excessive design conservatism can be reduced. This paper explores the integral bridge problem and design code prescriptions before using analytical, numerical, and centrifuge modeling to show that soil-structure interaction, especially the relative stiffness of soil and structure, can reduce abutment bending moments by 30% and that this is largely unaccounted for in the current U.K. design code PD 6694–1. Preliminary results showed a similar influence of stiffness on seismic response.

Keywords Integral bridges · Soil ratcheting · Cyclic loading

1 Introduction

Bridges attract a significant proportion of national infrastructure maintenance expenditure, reported at around 40% in the U.S. [1]. Given the disruption caused by their maintenance, as well as the material and equipment involved, the improvement of current practice is central to providing a resilient and sustainable transport network.

D. G. Morley (✉) · Y. B. Asia · G. S. P. Madabhushi
Department of Engineering, University of Cambridge, Cambridge, UK
e-mail: dm909@cam.ac.uk

I. Thusyanthan
Gavin & Doherty Geosolutions (GDG) Ltd, Dublin, UK

D. Sakufiwa
National Highways, Birmingham, UK
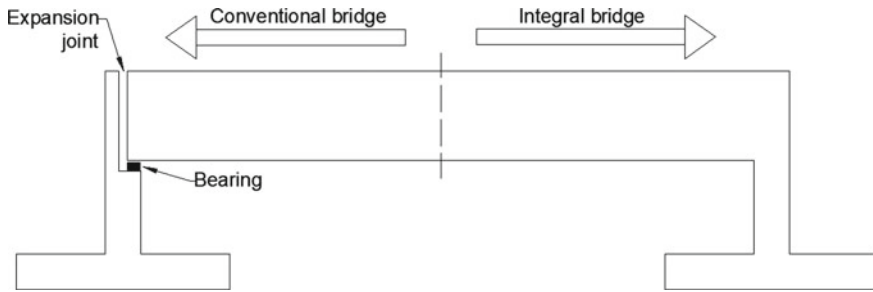
Fig. 1 Integral bridge typology

This is especially true as the environmental threat of climate change grows and the construction industry seeks to reduce its carbon emissions.

Bridge bearings and expansion joints are particularly troublesome [2]. These metallic components are susceptible to corrosion that is accelerated by deicing salts, seizing over time. The integral bridge typology is one that omits these problematic connections by creating a rigid, portal frame structure—the difference between these and conventional bridges is shown in Fig. 1. This design was first used in the U.S. over a century ago and is now used worldwide, extensively so in Europe, Canada, and Japan, with a number also built in the U.K. in the 50s [3] where they have become a first choice for moderate spans. As well as attracting low-maintenance and durability under operational loading, they also offer seismic resilience. The review by Mitoulis [4] highlights lower abutment rotation during liquefaction, while Choine et al. [5] spoke of their resistance to unseating and enhanced structural redundancy on account of deck-abutment fixity.

Integral bridges, however, attract their own maintenance concerns. Without joints to accommodate thermal movements, the deck interacts directly with the abutments and retained backfill causing so-called strain ratcheting and settlement, indicated in Fig. 2, which progresses with daily and annual cycles. A lack of reliable data characterizing these soil-structure interaction (SSI) phenomena fuels material wastage from design conservatism and is largely the cause of restrictions on spans and skews. This work explores the integral abutment backfill pressure buildup under thermal loading, focusing on the influence of soil and structural stiffness. Preliminary results also comment upon seismic response.

2 Design Prescriptions

Integral bridge design codes vary considerably. Eurocodes are limited in their guidance; hence U.K. design is governed by PD 6694–1 [6], traditionally favoring full-height abutments and used for deck spans and skews up to 60 m and 30°, respectively. Swiss and Finnish design typically follow similar limits, while much larger spans
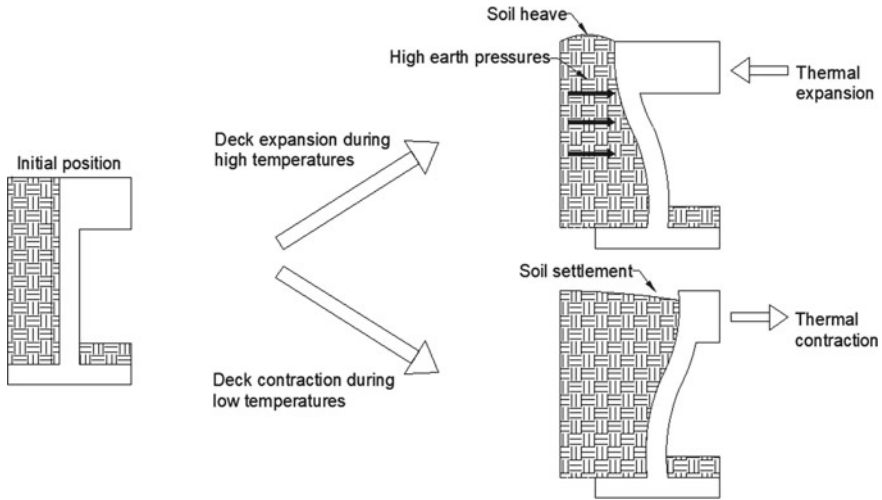
Fig. 2 Integral bridge backfill ratcheting and settlement concerns

have been used in the U.S. where integral bridges are mostly founded upon piles. Differences in international codes are to be expected, not least because deck movements are governed by temperature fluctuations of the local climate. However, variations seen in prescribed earth pressure distributions following backfill strain accumulation, and factors that influence this, have a significant bearing upon abutment design.

2.1 PD 6694–1: Limit Equilibrium Method

Section 9 and Annex A of PD 6694–1 [6] provide the current U.K. integral bridge design guidance. Within PD 6694–1, the limit equilibrium (LE) method provides the main method of assessing backfill pressures on the abutment and hence bending moments for structural design, following thermal cycles of the bridge deck. Alongside the LE method, PD 6694–1 allows the designer to carry out a more onerous SSI analysis generally followed when criteria for the LE method are not met.

Clause 9.4 of PD 6694–1 provides Eq. 1 and Fig. 3 setting out the earth pressure coefficient, K_d^*, and pressure distribution on the abutment following strain ratcheting due to repeated thermal movements of the bridge deck.

$$K_d^* = K_0 + \left(\frac{C d_d'}{H} \right)^{0.6} K_{p;t} \tag{1}$$

K_d^* is taken as the coefficient at rest, K_0, plus some proportion of passive limit pressure, $K_{p;t}$, where this proportion is influenced by the founding soil stiffness, C,

Fig. 3 PD 6694–1 lateral
earth pressure distribution
down the abutment following
ratcheting
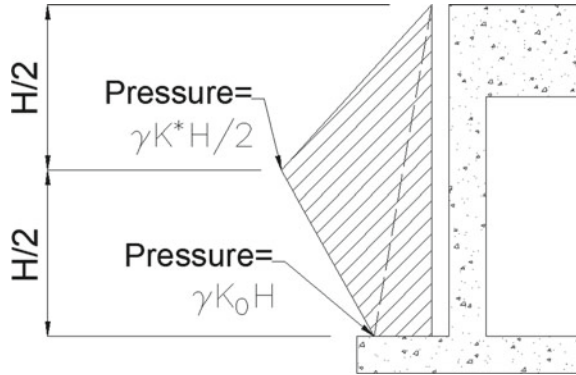
deck expansion and wall deflection, d'_d, and the height of abutment, H. The ratio d'_d/H
is equivalent shear strain; hence this term reflects that increased lateral straining of
the soil due to abutment movement mobilizes higher resistive earth pressures. This
equation has no dependence on thermal cycles and so describes pressures after a
design life of strain accumulation from soil ratcheting. The superposition of pressure
coefficients, rather than a single term reducing K from the limiting $K_{p;t}$, is unusual.
Figure 3 shows the design pressure distribution down the abutment, following K_d^* to
abutment mid-height beyond which it decreases to meet $K_0 \gamma H$, where γ is the unit
weight of the backfill. This agrees with the typical distribution for rigid abutment toe
rotation, with differences expected due to the contribution of abutment flexure and
strain ratcheting.

PD 6694–1 provides these two stipulations for abutments that deflect either in
flexure or rotation. Differences in deflected shape and hence imposed soil straining
in these cases are suggestive of the altered backfill pressure distributions that in fact
exist, with lower pressures expected toward the base of a flexible wall. Therefore,
there is seemingly a disconnect between PD 6694–1 and the SSI mechanism taking
place. This is supported by the experimental work of Wood [7] and Sandberg et al.
[8], with the latter suggesting that PD 6694–1 mischaracterizes the height and K_d^*
value leading to an overestimate of earth pressures and abutment bending moments.
This is agreeable with guidance from the Idaho Transportation Department [9], which
follows the full passive pressure coefficient, K_p, to $H/3$, rather than K_d^* to $H/2$ as
in Fig. 3.

A final doubt in U.K. guidance is the results from England et al. [10], commis-
sioned by the Highways Agency, from which Eq. 1 and Fig. 3 are largely based [11].
These come from small-scale tests performed at 1g with a pinned foundation and an
absence of founding soil. The three centrifuge experiments referenced by PD 6694–1
alongside this work raise further concern, notably: a discrepancy in results arising
from incorrect stress levels in 1g experiments [12], the impact of using a simplified
pin support on SSI response [13], and the need to model an appropriate foundation
and founding soil [14]. Further testing is required to confirm or alter design guidance.

3 Relative Soil-Structure Stiffness

Despite little mention in PD 6694–1, stiffness of the abutment and backfill are seemingly important factors in the determination of soil straining, and hence the earth pressure distribution imposed on an integral abutment following repeated deck thermal movements. Figure 4 compares the two extreme cases of a stiff and flexible secant piled wall displaced at the deck, where stiffness is relative to that of the backfill. The relatively stiff, high flexural rigidity (EI) wall is governed by base rotation, whereas the flexible, low EI wall bends to remain compatible with the deck expansion. In the case of rotation, the soil experiences a linearly decreasing lateral straining with depth, while flexure in the low EI wall sets up a nonlinear decrease reaching 0 strain generally at some point above the base. The consequence on the earth pressure coefficient, and hence the horizontal pressures acting on the abutment, is shown in the figure. Smaller K values toward the base of the flexible wall lead to a favorable decrease in lateral earth pressures, and hence abutment bending moments, that peak higher in the wall.

The numerical results of Sandberg et al. [8] agree with these concepts and imply a reduction in cross-section of around 25% could be achieved by considering relative
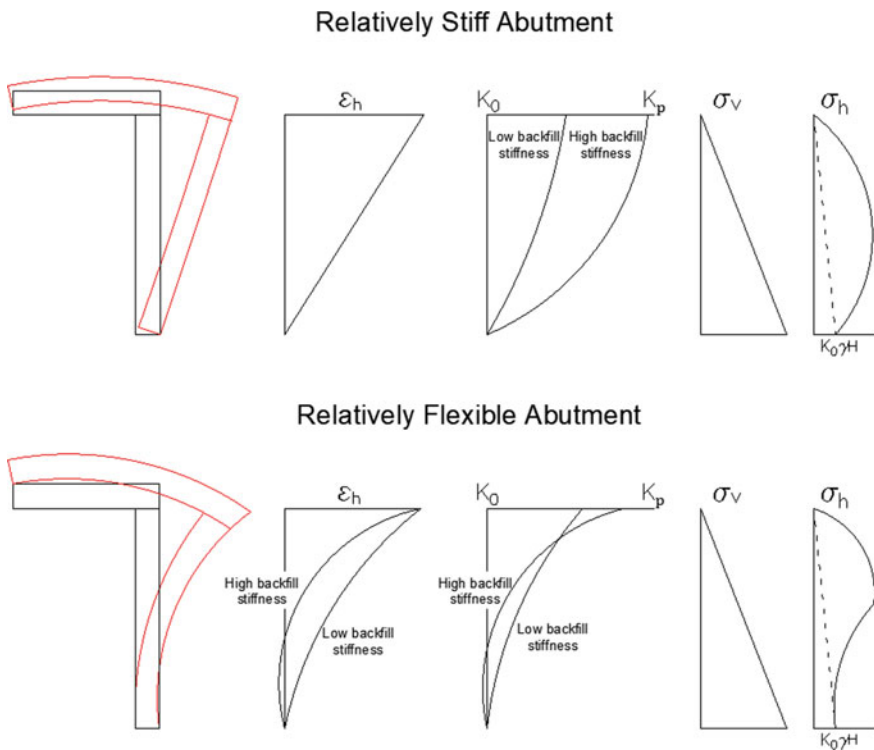
Fig. 4 Indicative influence of abutment and backfill stiffness on structure and soil response

stiffness in the pressure distribution, bringing considerable cost and carbon savings. Similarly, Bloodworth et al. [15] found a 10% reduction in earth pressures between the most flexible and rigid secant piled walls. The experimental work of Wood [7] in fact suggests that it is the soil and abutment stiffness, rather than friction angle as indicated in Clause 9.10.1 of PD 6694–1, that is dominant in integral abutment response. The importance of backfill is not only in the abutment deflected shape, but also in altering the K value mobilized, as indicated in Fig. 4. The results of both Wood [7] and Sandberg et al. [8] agree that with a higher backfill stiffness a larger earth pressure coefficient is generated toward the top of the abutment, and also that there is a lower K value toward the base as the abutment is restrained from moving.

Figure 4 sets out why the design of integral abutments is an SSI problem, influenced by relative stiffness rather than absolute values. To illustrate this point, the model was simplified ignoring pressure increase lower in the wall due to soil arching [16] and the absence of a shallow foundation, founding soil, and bridge deck which all contribute to the boundary restraints and hence deflected shape.

4   Methodology

To examine the influence of relative stiffness, a 9 m tall prototype, 1 m thick, was chosen to represent a full-height concrete integral abutment on a shallow foundation. Symmetry in the problem permitted only half the bridge to be modeled. This prototype structure was used for both the thermal and seismic testing.

4.1   Thermal Loading

Thermal deck loading in the numerical and centrifuge models was applied in displacement control, moving the abutment either side of its initial position over 120 cycles, representing a single peak expansion and contraction per year over the design life of a bridge. A 40 mm total movement was prescribed (20 mm either side of vertical), which is the maximum currently permitted in the LE method of PD 6694–1.

Numerical Modeling. The FEA software SWANDYNE was used with the Mohr–Coulomb V elasto-plastic hardening constitutive model [17] to capture the ratcheting of earth pressures as strain was accumulated over cycles. A model simulating the pin-based small-scale experiments of England et al. [10] was validated before moving onto the prototype. A mesh of 8-noded quad elements was created, shown in Fig. 5, with material properties given in Table 1. Extreme stiffness values were taken for the loose and dense backfill to investigate the role of soil stiffness on response. Roller and pin supports were imposed at the edge and base nodes, respectively. Deck thermal movements were simulated by prescribing top node displacements in a sinusoidal function between the 20 mm limits. After testing the prototype conditions, a flexible
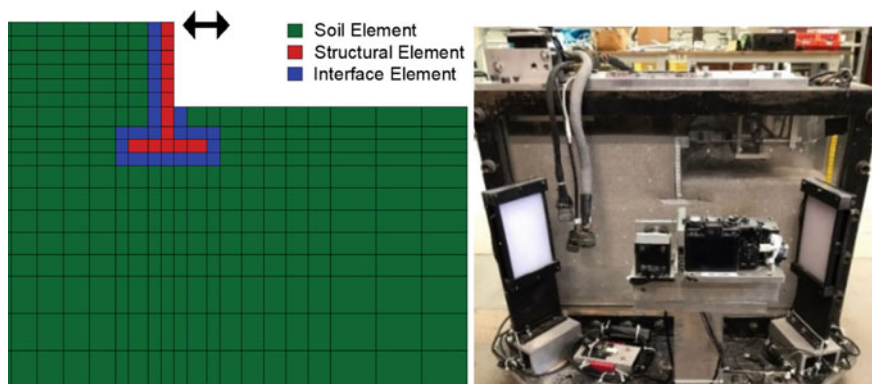
Fig. 5 Integral abutment numerical (left) and centrifuge (right) model

wall and lowered stiffness backfill were modeled independently to assess their impact on response.

Centrifuge Modeling. The prototype structure was scaled and tested in the 10 m diameter Turner beam centrifuge at the Schofield Centre, University of Cambridge [18]—the complete model is shown in Fig. 5. An enhanced gravity of 60 g was chosen as the lowest accommodating the model within the strongbox, with plane-strain conditions assumed over the 12 m prototype wall width. The aluminum abutment was scaled to a thickness of 12 mm to maintain similitude of flexural stiffness, EI. Thermal movements were applied using a mechanical actuation system capable of repeating 0.33 mm increments (20 mm prototype scale) at a maximum force of 12 kN. A clevis connected the actuator to the abutment, preventing moment transfer and meaning that the influence of moment restraint in the presence of a bridge deck was not modeled here. Instrumentation included a load cell to record deck axial force, an LVDT to measure and control bridge deck movements, strain gauges to record abutment bending moments, a Tekscan sheet to record backfill earth pressures, and PIV imaging to observe soil and abutment movements. Hoston HN31 silica sand was poured using air pluviation so that both dense and loose configurations could be tested to observe the influence of backfill stiffness. Following testing of the prototype, a flexible wall was modeled.

Table 1 Material properties used in the SWANDYNE model

	Soil	Abutment	Interface elements
Constitutive model	Mohr–Coulomb V hardening model	Elastic	Slip element
Elastic modulus	300 MPa (dense) 100 MPa (loose)	30 GPa	300 MPa
Friction angle	40°	–	40°
Dilation angle	5°	–	–
Poisson ratio	0.3	0.2	–
Hardening parameter	50	–	–

4.2 Seismic Loading

Following thermal loading, similar numerical and centrifuge models were subjected to seismic input to investigate the dynamic response. The abutment connection at deck level remained pinned in the numerical model and was supported laterally, without moment restraint, on the side of the deck in the centrifuge. A 23 m extent of backfill was sufficient to achieve dynamic absorbent boundaries, with 11 m of founding soil depth to allow input motion attenuation or amplification. A sinusoidal input motion with 10 cycles and a PGA of 0.33g was applied. Similarly to the thermal case, in the numerical analysis a flexible wall was tested alongside the prototype model for comparison.

5   Results and Discussion

Figures 6 and 7 show the influence of structure and soil stiffness on abutment response following repeated deck thermal movements. The numerical results of Fig. 6 show a 30% decrease in peak bending moment acting 1 m higher with the more flexible wall, on account of lower deflections toward the base. They also show the original wall to have mobilized a full K_p pressure coefficient from the top of abutment until almost mid-height. It follows that the pressure distribution agrees more with that of the Idaho DOT than PD 6694–1, with the latter appearing to underestimate both the height and magnitude of peak pressures. The centrifuge results in Fig. 7 agree with these numerical findings. Figure 7 also shows that with a decrease in soil stiffness there is a fall in peak bending moment by around 30% in the numerical and centrifuge data—this is agreeable with the work of Wood [7] and Sandberg et al. [8]. Finally, a comparison between the two modeling methods shows the numerical analyses to over-predict both the height and magnitude of peak bending moments in all cases, perhaps due to mischaracterization of strain ratcheting in the constitutive model.

Figure 8 shows preliminary results from seismic loading at the peak excitation amplitude. In agreement with thermal loading, a reduction in abutment stiffness lowered deflections relative to the base, which increased the height and decreased the magnitude of lateral pressures—this translated to a 40% reduction in peak bending moment. A comparison of the centrifuge and numerical results shows a similar bending moment magnitude, with the latter overestimating the height of the peak as in the thermal case.

These findings support the discussion throughout the paper, including the schematic in Fig. 4, on the importance of soil and structural stiffness on integral abutment design. They also suggest an inflexibility of current design practice, notably the U.K. design code PD 6694–1, in capturing the true earth pressure distribution following strain ratcheting. Furthermore, this work justifies the suggestion from Wood [7] that efficiencies can be made if designers provide the necessary vertical stiffness and lateral strength of an abutment, without unnecessary lateral
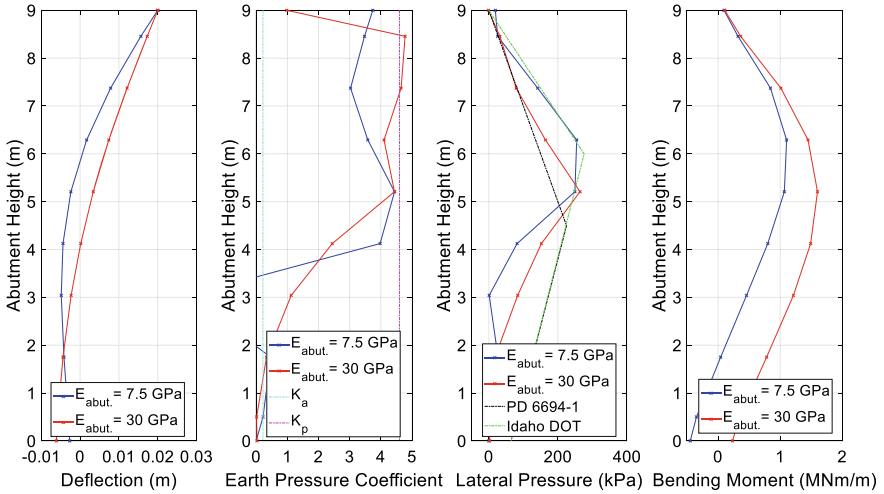
Fig. 6 Numerical results showing the influence of abutment stiffness on response

Fig. 7 Centrifuge and numerical results for altered backfill (left) and abutment (right) stiffness
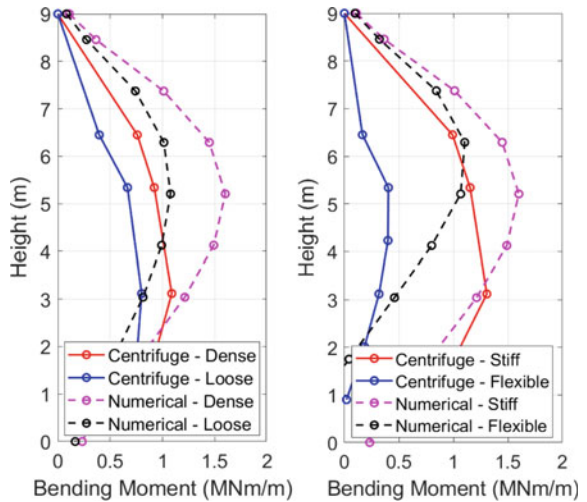
stiffness, which appears to increase applied bending moments. A final observation from centrifuge testing was the 0.6 m depth and 3 m extent of surface soil loss adjacent to the abutment following deck thermal movements. These observations stress the need for careful design and monitoring of the bridge approach with resurfacing when necessary. Minimizing this would further the durability and resiliency credentials of the integral bridge typology.
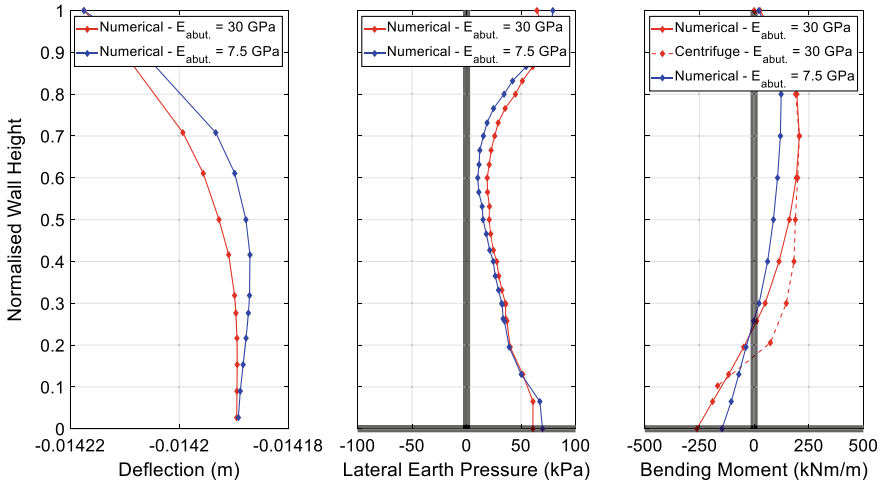
Fig. 8 Deflection, lateral pressure, and bending moment distribution at peak seismic excitation

6   Conclusion

Integral bridges are a low-maintenance form of bridge construction used worldwide. By characterizing the SSI mechanism during thermal movements of the deck, especially the lateral earth pressure distribution following backfill strain ratcheting, this low-maintenance bridge form can be made applicable for greater spans and skews, and to last longer, further reducing the operational carbon emissions associated with transport infrastructure. In doing so, the opportunity also exists to reduce material wastage through efficiencies, using the influence of relative soil-structure stiffness to reduce lateral pressures and therefore the abutment bending moments governing design.

This work has presented the variability of restrictions on global integral bridge use and critiqued the U.K. design code PD 6694–1 in its guidance on earth pressure distribution, governed by the K_d^* formula. It has highlighted inflexibility of the LE method to reduce structural demand considering soil-structure stiffness, which is thought to be of larger significance than friction angle of the backfill. Mischaracterizations caused by ubiquity of the design pressure distribution, irrespective of abutment rotation or flexure, was explored through a schematic showing the influence of deflected shape on soil response. These points were affirmed with numerical and centrifuge data. A peak bending moment reduction of 30% was found when abutment EI was lowered to a quarter of the original, as well as when backfill stiffness was decreased. Preliminary results from seismic loading also showed a 40% reduction in peak bending moment when a more flexible wall was used.

Future work should look to investigate integral bridges of different height and foundation configuration, observing how these influence the earth pressure and bending moment distribution following ratcheting. Furthermore, a portion of bridge

deck should be modeled to capture the influence of abutment top restraint and carry-over moment on response.

References

1. Sakulich AR, Bentz DP (2012) Increasing the service life of bridge decks by incorporating phase-change materials to reduce freeze-thaw cycles. J Mater Civ Eng 24(8):1034–1042
2. Office of Rail and Road (2019) Annual assessment of Highways England's performance
3. Hambly EC (1997) Integral bridges. Proc Instn Civ Engrs Transp 123, 30–38
4. Mitoulis SA (2020) Challenges and opportunities for the application of integral abutment bridges in earthquake-prone areas: a review. Soil Dynam Earthquake Eng 135
5. Choine MN, Oconnor AJ, Padgett JE (2015) Comparison between the seismic performance of integral and Jointed concrete bridges. J Earthquake Eng 19(1):172–191
6. British Standards Institute (2020) PD 6694–1:2011+A1:2020—Recommendations for the design of structures subject to traffic loading to BS EN 1997–1:2004+A1:2013. London
7. Wood DM (2004) Geotechnical modelling. Spon Press, Abingdon
8. Sandberg J, Magnino L, Nowak P, Wiechecki M, Thusyanthan I (2020) The integral bridge design concept for the third runway at Heathrow, UK. Proceed Inst Civil Eng Bridge Eng 173(2):112–120
9. Idaho Transportation Department (2008) Load resistance factor design (LRFD) bridge manua—chapter 11. Retrieved from https://itd.idaho.gov/bridge/
10. England GL, Tsang NCM, Bush DI (2000) Integral bridges—a fundamental approach to the time-temperature loading problem. Crown Copyright and Thomas Telford Limited, London
11. Denton S, Riches O, Christie T, Kidd A (2011) Developments in integral bridge design. Bridge Design to Eurocodes, UK Implementation
12. Tapper L, Lehane B (2004) Lateral stress development on integral bridge abutments. In: Australasian conference on the mechanics of structures and materials
13. Tan EL, Lehane BM (2007) Lateral stress development on integral bridge abutments. Perth
14. Springman SM, Norrish A, Ng CWW (1996) Cyclic loading of sand behind integral bridge abutments. Crowthorne
15. Bloodworth AG, Xu M, Banks JR, Clayton CRI (2012) Predicting the earth pressure on integral bridge abutments. J Bridge Eng 371–381
16. Ng C, Springman S, Norrish A (1998) Soil-structure interaction of spread-base integral bridge abutments. Soils Found 38(1):145–162
17. Chan AHC (1988) A unified finite element solution to static and dynamic problems of geotechnics. University College of Swansea
18. Schofield AN (1980) Cambridge geotechnical centrifuge operations. Geotechnique 30(3):227–268

Study on Compaction and Unconfined Compressive Strength Characteristics of Magnesium Carbonate Mixed Soils

Navya Ann Eldho and Hailong Wang

Abstract As the global urgency to stem global warming increases, the need to implement negative emissions technologies grows with it. This study takes into consideration one such proposed desalination brine conversion technology, capable of making use of its product magnesium oxide (MgO) to mineralize CO_2 and produce magnesium carbonate ($MgCO_3$). Recognizing the necessity to find feasible applications for the output non-plastic $MgCO_3$, this paper outlines the study done to evaluate the performance of $MgCO_3$ as a geomaterial by taking into account the material properties and unconfined compressive strength (q_u) characteristics of a clayey soil mixed with 0–40 wt.% $MgCO_3$. It was found that further addition of $MgCO_3$ progressively reduced maximum dry density and increased plastic and liquid limits and optimum water content. It was also noted that the q_u of soil mixtures with 10–30 wt.% $MgCO_3$ were much greater than that of pure soil (i.e., 0 wt.% case). The probable reasons were attributed to the suction effect being lower the pure soil due to the greater than optimum water content used, and the effect instead being higher in mixtures due to increase in finer particles.

Keywords Geomaterial · Magnesium carbonate ($MgCO_3$) · Unconfined compressive strength (q_u) · Compaction

1 Introduction

Climate change and global warming are some of the most pressing issues we face today. Among many other greenhouse gases, carbon dioxide (CO_2) emissions due to human activities is one of the leading causes of this worldwide phenomena. It is known with high confidence that emissions due to humans activities have caused up to 1.2 °C global temperature increase from pre-industrial times and that global warming up to 1.5 °C should be expected between 2030 and 2052 [1]. Although global warming of 1.5 °C is bound to increase climate change related risks than what

N. A. Eldho (✉) · H. Wang

Waseda University, 3-4-1 OhkuboShinjuku-Ku, Tokyo 169-8555, Japan

e-mail: navyanneldho@fuji.waseda.jp

we experience presently, it is still lower than the consequences of a 2 °C increase [1]. Therefore, according to the 2018 by the Intergovernmental Panel on Climate Change [1], limiting global warming to 1.5 °C is of utmost importance if we were to avoid 'unprecedented changes in all aspects of society' [1]. This would require reducing global anthropogenic CO_2 emissions by 45% back to pre-industrial levels by 2030 and reaching net zero emissions by 2050, which is no easy feat considering that the current reduction requirement is approximately 1–2 billion-ton/yr [2]. Given that the current reduction average is a mere 160 million mt-ton/yr [2], there is a growing urgency to develop and implement negative emissions technology capable of CO_2 extraction and storage.

Among the many developments aiming to aid achieving these lofty goals is a promising study in the form of a conversion process proposed by Myers and Nakagaki [3]. The process entails converting desalination brine into a set of widely used industrial products using entirely electricity-based evaporation and temperature control. The products, which include gypsum, salt, Glauber's salt, hydrochloric acid, and magnesium oxide (MgO), are industrially relevant and hence reduce the demand for conventional production methods. Most importantly, the product MgO is capable of direct CO_2 mineralization to produce magnesium carbonate ($MgCO_3$). This carbon capture process can prove to be particularly significant as it is said to bring about 4.5 kg-CO_2/m³-brine negative emissions [3]. If implemented, this desalination brine conversion process can bring about 231 Mt-CO_2/yr of negative emissions, a figure which is significant considering that the current requirement is 10's Gt-CO_2/y of emissions reduction [3]. As a whole, the process also results in a 22.9 kg-CO_2/m³-brine reduction when run on conventionally produced electricity and a further 43.9 kg-CO_2/m³-brine when using renewables-based electricity [3].

Recognizing the above process's immense potential to bring about climate change reduction, it became essential to improve its feasibility by considering potential applications for the product $MgCO_3$ that is bound to be produced in abundance if implemented. As a result, this study looks to evaluate the performance of $MgCO_3$ as a geomaterial by evaluating the characteristics of $MgCO_3$-mixed soils with different $MgCO_3$ percentages on the basis of their index properties and uniaxial strength patterns. The primary aims of this study were to obtain the unconfined compressive strength characteristics of soil mixtures with differing percentages of $MgCO_3$ and then compare them to those shown by pure soil.

2   Test Materials and Procedure

2.1   Test Materials

The two primary materials as shown in Fig. 1 used in this study are commercial clayey soil (TAC-1) and $MgCO_3$ fine powder. The former is classified as a low liquid limit clay with a specific gravity of 2.69, while the latter is much finer in size, non-plastic,

Fig. 1 Materials used in this study: **a** the commercial clayey soil, **b** the MgCO₃ powder
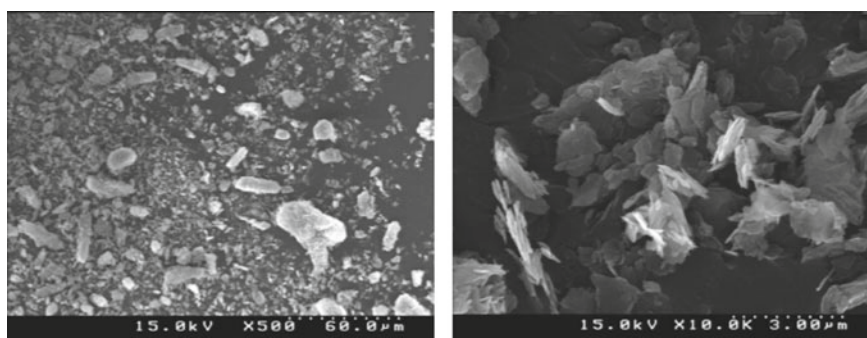
Fig. 2 SEM images of MgCO₃ fine powder

and lightweight with a specific gravity of 2.30. The scanning electron microscopic (SEM) images of the $MgCO_3$ powder are shown in Fig. 2.

The plastic and liquid limit index properties of soil mixtures with 0–40 wt.% $MgCO_3$ were evaluated using the standard procedure outlined in JIS A 1205:2009 [4]. The obtained result for each case is illustrated in Table 1.

Compaction characteristics of soil mixtures with 0–40 wt.% MgCO3 were also evaluated using the standard Proctor compaction test. The soil used for test was firstly passed through a 4.75 mm sieve to ensure the use of soil of size 4.75 mm or finer. The mold used for the test had a 9.7 cm diameter and a 12.8 cm height. The soil was

Table 1 Plastic and liquid limits of soil with 0–40% MgCO₃

MgCO₃ percentage (wt.%)	0	10	20	30	40
Plastic limit (wt.%)	28.1	32.7	38.2	48.9	57.8
Liquid limit (wt.%)	46.6	57.6	63.8	79.1	83.8

compacted into the mold in three layers. To ensure the compaction uniformity, soil poured into the mold was adjusted to have an approximate height of 4.6 cm each layer, 1.0 cm higher than the mold. Every layer was compacted by employing 25 blows using a compacting rammer, which was placed at a 30 cm height.

2.2 Procedure

Uniaxial compression tests were conducted on $MgCO_3$ and soil mixtures by varying $MgCO_3$ percentage of 0, 10, 20, 30, and 40 wt.%. The soil mixtures for the specimens were made by mixing the soil with the $MgCO_3$ fine powder at each required percentage. Water was also added in such that the water content corresponded to the optimum water content of the particular soil mixture. However, for the pure soil (i.e., 0% $MgCO_3$) case, a slightly higher water content, 26%, was used, since at the beginning, optimum water content was not well defined.

The specimens were then made using these mixtures. At least 4 specimens were made for each $MgCO_3$ percentage case having different void ratios corresponding to compaction degrees in the range of 80–95%. This was ensured by initially setting a target compaction degree for each specimen and then accordingly determining the total mass for each specimen.

Once the total mass of each specimen was determined, the specimen was created. Having dimensions of 10 cm in height and 5 cm in diameter, the specimen was prepared using a detachable cylindrical mold and by compacting the soil in 10 layers, each with 1 cm height and 1/10th of the total mass to ensure the uniformity. The topmost layer of each specimen was slightly trimmed to maintain a flat surface and ensure a uniform load distribution while undergoing testing. The specimens were then wrapped in film and sealed in airtight bags (to prevent water loss) for 3–7 days. In total, 24 specimens were created in this way to be tested.

Thereafter, the specimen was placed in the uniaxial compression testing device and made to undergo unconfined uniaxial loading at an axial strain rate of 1%/min until clear signs of failure were observed. The testing device itself has a load cell and a displacement sensor with solutions of 1.28 kPa and 0.01 mm, respectively, to measure the axial stress and axial strain, respectively. Examples of specimen with different $MgCO_3$ percentages and those after failure can be seen in Figs. 3 and 4. After testing, the water content of each specimen was measured.

3   Results and Discussion

The obtained data on the plastic and liquid limits were plotted against their respective $MgCO_3$ percentage, as seen in Fig. 5. It was deduced that as the $MgCO_3$ percentage in the soil mixture increased, both the plastic and liquid limit increased as well. When the obtained liquid limit values were plotted onto the standard plasticity chart
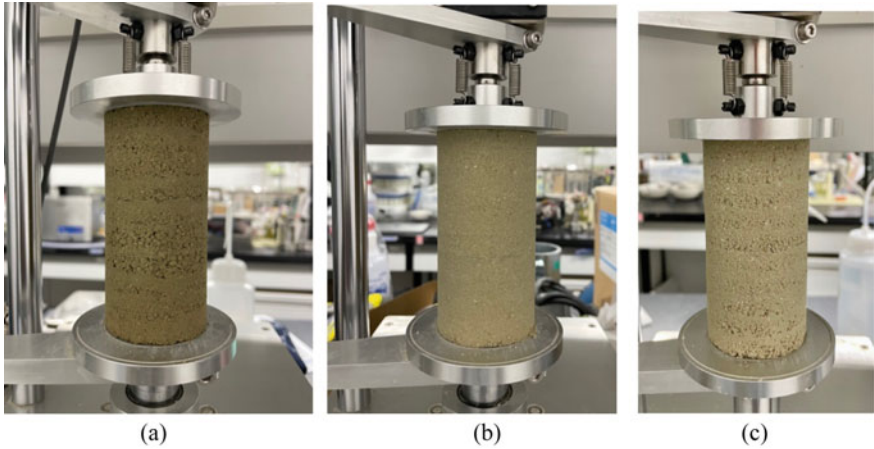
Fig. 3 Specimens for compression tests having $MgCO_3$ of **a** 0 wt.%, **b** 20 wt.%, **c** 40 wt.%
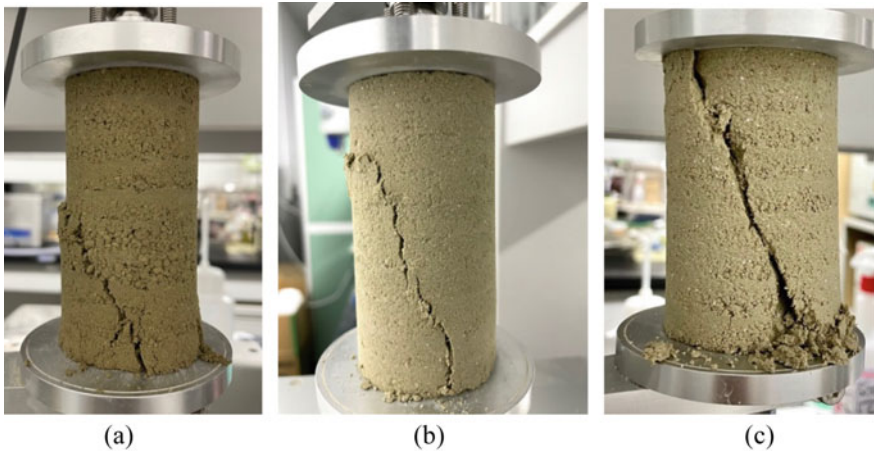
Fig. 4 Specimens at failure when having $MgCO_3$ of **a** 0 wt.%, **b** 20 wt.%, **c** 40 wt.%

typically used to classify clayey and silty soils (Fig. 6), it was observed that further addition of $MgCO_3$ transforms the soil mixture from that of low plastic limit clay (CL) to that of high plastic limit silt (MH). This could be indicative of the water retention properties of the soil increasing upon increase in $MgCO_3$ percentage.

The compaction curves, which show the relationship between dry density and water content, were plotted graphically for each $MgCO_3$ percentage case (Fig. 7). It was observed that all curves are very flat similar as typical compaction curves of clayey soils, while it becomes slightly sharp at $MgCO_3$ of 40 wt.% case. The maximum density and optimum water content were summarized in Table 2. The maximum dry densities of the pure soil case were generally much higher than those
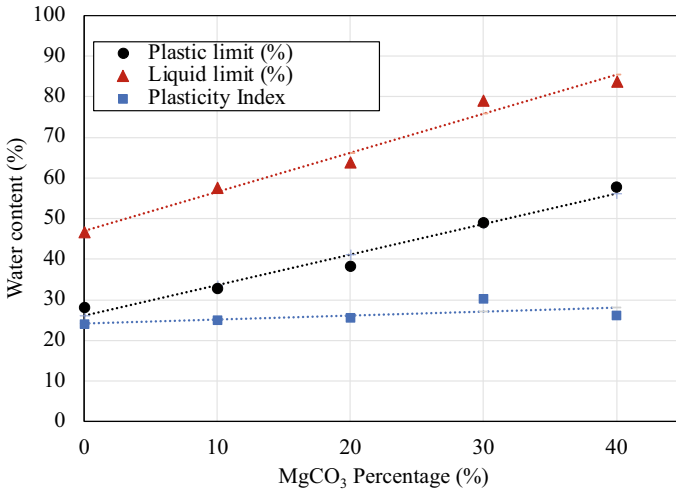
Fig. 5 Plastic and liquid limits of soil mixed with 0–40 wt.% MgCO₃

Fig. 6 Plasticity chart showing classifications of soils having 0–40 wt.% MgCO₃
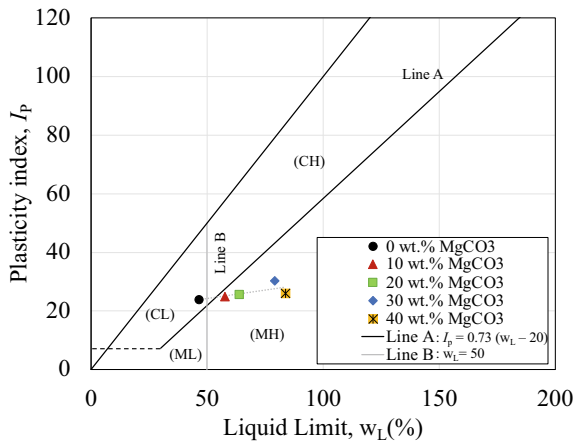
with MgCO₃. It reduces upon an increase in the MgCO₃ percentage. This can be attested to the increased addition of the lighter MgCO₃ particles, as evidenced by its lower specific gravity in relation to the pure soil.

During the uniaxial compression tests, load and deformation data were collected and the stress–strain relation and unconfined compressive strength (q_u) were calculated. Firstly, the axial strain and vertical stress relations are shown in Fig. 8 for each MgCO₃ percentage case. It can be seen that for the same MgCO₃ percentage, q_u increases as D_c increases as expected.

To compare the q_u among all tested cases, the relations between q_u and compaction degree (D_c) and void ratio are shown in Figs. 9 and 10, respectively. From Fig. 9,
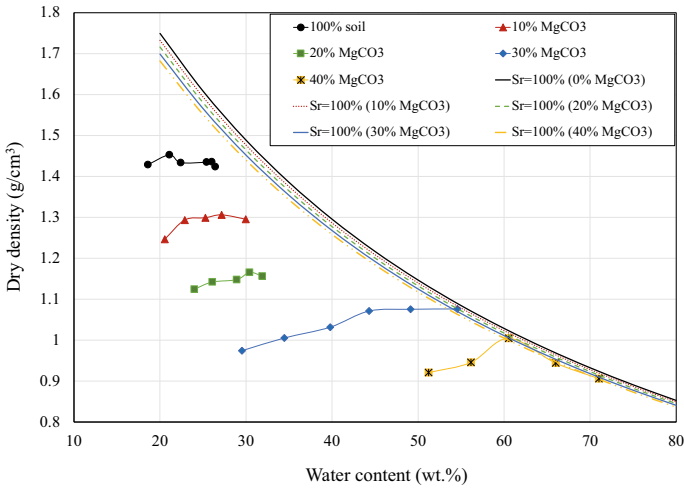
Fig. 7 Compaction curves of soil with 0–40% $MgCO_3$

Table 2 Maximum dry density data of soil with 0–40% $MgCO_3$

$MgCO_3$ percentage (%)	0	10	20	30	40
Maximum dry density, ρ_d (g/cm³)	1.453	1.306	1.166	1.077	1.004
Optimum water content (wt. %)	21.1	27.2	30.4	54.6	60.5

it was observed that the q_u of the soil mixtures with 10–30 wt.% $MgCO_3$ generally tended to be higher than those of pure soil at higher D_c (i.e., 87–95%). While $MgCO_3$ percentage increased to 40 wt.%, q_u dropped down to a lower level. From Fig. 10, it is expected that if all $MgCO_3$ mixtures were compacted to a void ratio comparable to pure soil case, their q_u must be higher than pure soil. One explanation for relatively lower q_u of pure soil case could lie in the use of a higher than optimum water content for making the pure soil specimens. It is possible that the suction effect in the pure soil case was reduced as a result, and hence producing lower q_u values. On the other hand, it is also possible that since the specimens were in an unsaturated condition, a complex energy state as a result of suction effect could have been created by the soil particles, $MgCO_3$ particles, pore air, and pore water. This suction effect could have greatly increased when the much smaller-sized $MgCO_3$ particles were introduced to the sample. This is understandable since the introduction of such smaller-sized particles could have led to an increase in the amount of pores, thus giving way for greater capillary action and, in turn, a greater suction effect. The increase in pore number can be seen by increasing void ratio upon further addition of $MgCO_3$ in Fig. 10. Therefore, further studies in this regard will be hereafter conducted to confirm this reasoning with greater confidence.
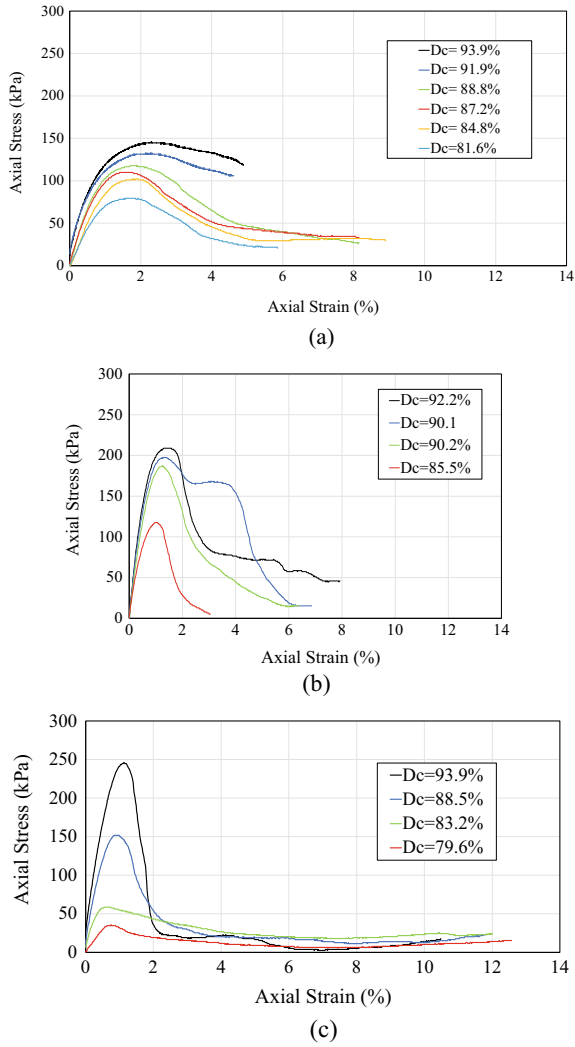
Fig. 8 Axial stress–strain relations at MgCO$_3$ percentage of **a** 0 wt.%, **b** 10 wt.%, **c** 20 wt.%, **d** 30 wt.%, **e** 40 wt.%

(d)

(e)
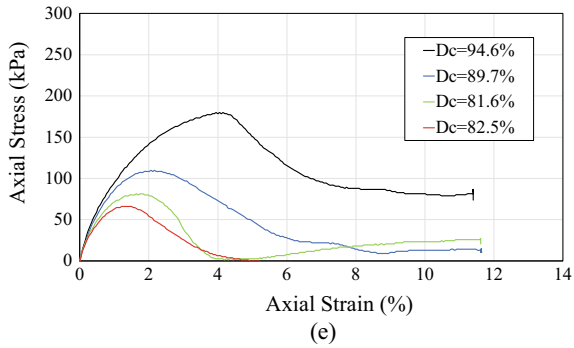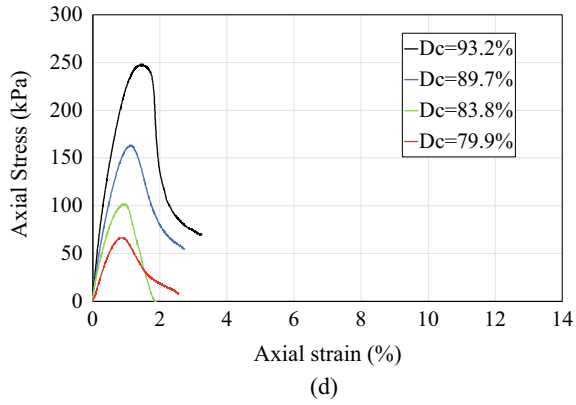
Fig. 8 (continued)
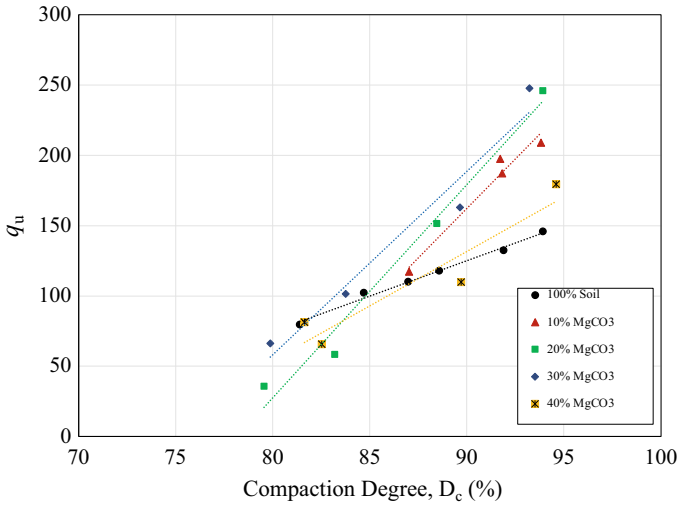
Fig. 9 qu versus compaction degree graphs for cases having 0–40 wt.% MgCO$_3$ percentage
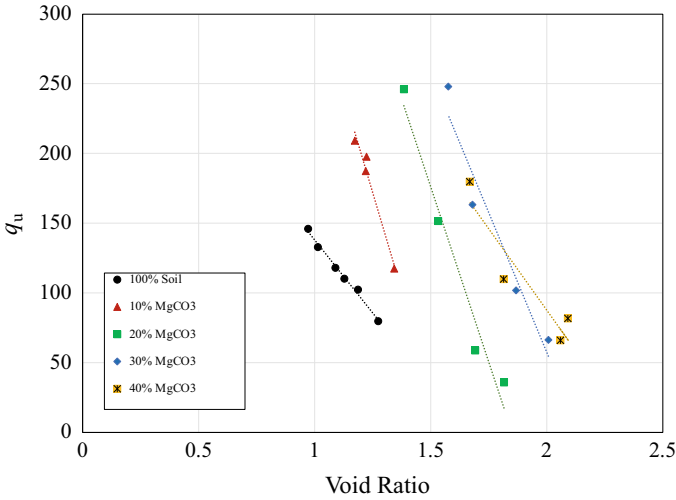
Fig. 10 qu versus void ratio graphs for cases having 0–40 wt.% MgCO₃ percentage

4   Conclusion

This paper introduced a negative emission technology with the potential to aid global warming reduction. In order to ensure its feasibility, there is a necessity to consider potential applications for the product $MgCO_3$. Therefore, this study aims to evaluate the performance of $MgCO_3$ as a geomaterial by firstly evaluating the characteristics of $MgCO_3$-soil mixtures via their general properties and finally examining the strength properties of the mixtures through a series of uniaxial compression tests. It was firstly found that the plastic and liquid limit increased upon increase in $MgCO_3$ percentage. In terms of the observed dry density properties, it was found that the pure soil had the highest dry density, and it constantly reduced upon further increase in $MgCO_3$ percentage. Finally, it was observed that the q_u characteristics of soil mixtures with 10–30 wt.% $MgCO_3$ were much higher than that of pure soil at high D_c. This could be as a result of the use of a water content higher than the optimum water content for the pure soil case or due to the increased suction effect arising from the increase in the pore spaces. From hereafter, it is necessary to conduct Life Cycle Assessment studies to assess the feasibility of this application, along with further study to confirm the suction effect theory.

References

1. IPCC (2018) Summary for Policymakers. In: Global Warming of 1.5°C. An IPCC Special Report on the impacts of global warming of 1.5°C above pre-industrial levels and related global greenhouse gas emission pathways, in the context of strengthening the global response to the threat of climate change, sustainable development, and efforts to eradicate poverty. Cambridge University Press, Cambridge, UK and New York, NY, USA, pp 3–24. https://doi.org/10.1017/9781009157940.001
2. University of East Anglia Communications (2021) Global carbon emissions need to shrink 10 times faster. Stanford Earth Matters Magazine, Stanford University
3. Myers C, Nakagaki T (2021) Negative emissions using Mg sourced from desalination brine or natural evaporate deposits. In: 15th international conference on greenhouse gas control technologies, GHGT-15, Abu Dhabi, UAE
4. Japanese Geotechnical Society (JGS) (2009) Test method for liquid limit and plastic limit of soils. JIS A 1205

Sustainable Handling of Soft Soils During the Design of Major Infrastructure Projects

Martin Tanderup [ID]**, Michael Rosenlund Lodahl** [ID]**, Kristina Thomassen, and Lars Bo Ibsen** [ID]

Abstract   This paper investigates whether cement stabilization of weak soft soils is a sustainable foundation solution, compared to traditional Danish methods used when weak soft soils are deemed unfit. Traditionally, a mass exchange, piled foundation, or pre-consolidation of the soil would be used. The paper is focused on a fictitious highway construction near Aalborg in Denmark, with a 6-m soft soil deposit below it. The effects of cement stabilization are investigated by casting specimens consisting of in-situ soft soil mixed with different cement amounts. Specimens with Aalborg Portland's Basis cement and CO_2-reduced FutureCem cement were subjected to oedometer and triaxial tests to determine stiffness and strength. To determine the CO_2 emission from each foundation solution, Life Cycle Assessments (LCAs) are performed. Based on the experiments performed, it is concluded that 37.5 kg/m^3 FutureCem gained a sufficient stiffness increase, why this cement was used in the LCA. The LCAs showed that cement stabilization could lower the CO_2 emission by 85% compared to a mass exchange, 77% for piled foundation, and 58% for pre-consolidation. Thus, cement stabilization can be a sustainable alternative to conventional soft soil remediations, and it is important to consider multiple solutions for a project to reduce CO_2 emissions.

Keywords   Cement stabilization · Soft soils · Life cycle assessment · Oedometer tests

M. Tanderup (✉) · L. B. Ibsen
Aalborg University, Aalborg, Denmark
e-mail: mntp@cowi.com

M. Tanderup · M. R. Lodahl · K. Thomassen
COWI A/S, Aalborg, Denmark

81

1 Introduction

One of the largest environmental concerns globally is the emission of carbon dioxide, CO_2. CO_2 emissions need to be reduced by 45 percent by 2030 from 2010 levels and reach net-zero emissions by 2050 to limit global warming effects well below 2 °C above pre-industrial levels according to The United Nations' 13th Sustainable Development Goal [1]. To reach this goal, all industries need to consider their carbon footprint.

The carbon footprint also has an increased focus in the geotechnical society. Multiple solutions can be investigated to incorporate CO_2 emission considerations into a geotechnical project. The carbon footprint can be investigated during different construction stages by performing Life Cycle Assessments, LCAs.

This project seeks to investigate how different foundation solutions for a fictitious highway construction near Aalborg City affect the carbon footprint. The highway is planned to be built on top of a soft Holocene gyttja layer, which is associated with large settlements. Traditional Danish solutions would be a mass exchange, piled foundation, or pre-consolidation. All of these solutions are however associated with severe transportation of materials. The project is inspired by the upcoming highway construction associated with the 3rd fixed link crossing of the Limfjord, which is expected to begin in 2025.

The hypothesis behind this project is that a solution with cement stabilization of the gyttja can reduce the carbon footprint compared to the traditional Danish foundation solutions for highways. When cement stabilization is used, none of the weak soil needs to be removed and replaced with other materials, because the cement is added directly on-site by using deep mixing techniques. Another reason cement stabilization could be beneficial is that the cement manufacturer Aalborg Portland is located in Aalborg, where the highway project takes place. Furthermore, Aalborg Portland in 2021 launched their new FutureCem cement, which reduces the CO_2 emission of the production by up to 30% compared to other cement types [2].

Cement stabilization of soft soil is not a new technique but has been used in, e.g., Sweden and Norway for decades. Mixing cement and other binders into soft soils can increase the undrained shear strength dramatically and has been proven to increase the shear strength by a factor of 10 + [3]. The stiffness generally also increases significantly due to the cementitious bonds formed between the soil particles [4]. The increase in strength and stiffness depends on the soil type, water content, and binder used.

The LCAs performed in this project will investigate the first construction stages of the highway construction usually referred to as A1–A5. These stages cover the raw material extraction (A1), transport during production (A2), manufacturing (A3), transport to the construction site (A4), and installation (A5). The usage and end-of-life stages are not considered as these are considered comparable for all solutions.

2 Highway Construction and Soil Conditions

The highway is assumed to be a four-tracked highway placed on top of a soft gyttja layer. This assumption is based on soil conditions reflecting the current state of Northern Jutland where Aalborg is located, which is characterized by pockets of soft soil deposits. The gyttja layer below the highway is challenging because this highly organic soil type often results in remarkable settlements. Based on Danish highway guidelines, two lanes including an emergency lane and edge lane result in a pavement width of 12 m and a road width of 14.5 m including shoulders at each side. The full highway will therefore be 29 m wide [5]. A section of 200 m is investigated.

The assumed soil conditions for the road section are stated in Table 1. The soil stratigraphy is based on a geotechnical site investigation from 1992 just outside of Aalborg city. The strength and water content are based on values from nearby borehole logs.

Gyttja samples from a site in Aalborg were collected to investigate the stiffness and strength parameters of cement-stabilized gyttja. The properties of the substitutional soil used for experiments are seen in Table 2.

The undrained shear strength increases with depth. The values are found from shear vane tests which are corrected according to Eq. (1) [6]. The plasticity index, I_P, is determined to be approximately 42% based on plasticity tests.

$$c_u = \frac{1.2 \cdot c_{fv}}{1 + 0.01 \cdot I_P} \left(c_u \leq c_{fv} \right) \tag{1}$$

Table 1 General soil conditions expected below the investigated highway section

Depth	Soil type	Water content [%]	Shear vane strength c_{fv} [kPa]
0–1	Topsoil	–	–
1–7	Gyttja	40–100	10–40
7–8	Sand	–	–
8–	Clay	–	100

Table 2 General soil properties for gyttja used during experiments

Water content (%)	Organic content (%)	Undrained shear strength c_u (kPa)
65.2	6.3	16–27

3   Experiments

To investigate the effect of mixing cement into gyttja, seven oedometer, and seven triaxial tests were performed, where one of each test was conducted on the in-situ material. The gyttja–cement specimens were cast in pairs and cured for 7 days and contained either 150 kg/m^3, 75 kg/m^3, or 37.5 kg/m^3 Basis or FutureCem cement.

The gyttja–cement mixtures were made by stirring the in-situ material to a remolded sample, whereafter cement was added to the mix. The mixture was then cast in a metal cylinder according to the in-situ density and stored in a zip lock back. Inside the zip lock back, the metal cylinder was wrapped in a wet cloth to obtain 100% humidity.

3.1   Stiffness and Strength Increase Due to Cement Stabilization

Stiffness. The stiffness increase was investigated by performing seven oedometer tests: one on the in-situ material and six on gyttja–cement specimens with respectively Basis and FutureCem cement.

The oedometer load program used for the presented test results is 10 kPa, 20 kPa, 40 kPa, 10 kPa, 20 kPa, 40 kPa, 80 kPa, and 160 kPa load steps. This program was designed to capture the in-situ stress, which before the tests was assessed to be approximately 40 kPa. The steps are used to capture the virgin consolidation and unloading–reloading behavior close to the expected stress level for the road during service life.

Figure 1 shows the results from the in-situ and FutureCem 37.5 kg/m^3 test. When the in-situ material is exposed to a stress of 160 kPa, it undergoes a strain of approximately 18.5%. The specimen mixed with FutureCem, however, only experiences a strain of approximately 0.5% when exposed to the same load, which is a significant stiffness increase. The other gyttja–cement specimens with different cement types and contents experienced a similar stiffness increase; hence, these are not considered. This is because FutureCem 37.5 kg/m^3 results in the lowest CO_2 emission since the foundation design is considered a settlement issue.

Table 3 shows the stiffness and drainage parameters from the oedometer tests shown in Fig. 1. The modified compression index, $C_{\varepsilon c}$, and oedometer modulus, E_{oed}, describe the stiffness of the soil. When calculating settlements according to Danish practice, the modified compression index is usually used [7]. The modified compression index describes the slope of the graphs in Fig. 1, where a gyttja often lies between 15 and 50% and a Holocene clay lies between 5 and 25% [8]. Compared to this, the gyttja–cement specimen is very stiff, and the in-situ specimen behaves as expected. Furthermore, the coefficient of consolidation, c_v, shows no significant change.
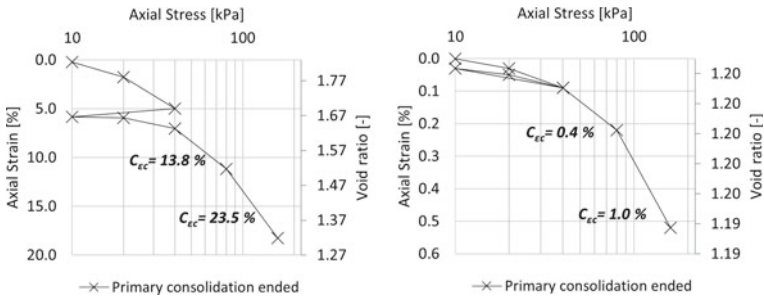
Fig. 1 Consolidation results from oedometer tests. Left: In-situ material from a cylinder sample from 3.0 to 3.5 m depth. Right: Cement stabilized specimen with 37.5 kg/m^3 FutureCem cement

Table 3 In-situ and gyttja–cement oedometer parameters. Load step 40–160 kPa

Material	Load (kPa)	c_v (m^2/s)	$C_{\varepsilon c}$ (%)	E_{oed} (MPa)
In-situ	40 (Reloading)	2.1E − 08	3.7	1.8
	80 (Loading)	1.6E − 08	13.8	1.0
	160 (Loading)	1.5E − 08	23.5	1.1
Gyttja–cement	40 (Reloading)	6.0E − 08	0.1	50.0
	80 (Loading)	2.0E − 08	0.4	30.8
	160 (Loading)	4.6E − 08	1.0	26.7

Strength. The increase in undrained shear strength was investigated by performing seven triaxial tests. However, this was of minor interest since settlements were the main challenge. The in-situ strength of ~ 19 kPa increased from ~ 73 kPa ranging to ~ 357 kPa.

4 Foundation Solutions

In the following, four different foundation solutions are investigated to assess the CO_2 emission from each solution. The solutions are listed below:

- Mass exchange: The soft soil is exchanged with sand to avoid settlements.
- Piled foundation: Piles are installed to deeper soil layers to avoid settlements.
- Pre-consolidation: A surcharge load is placed on the soft soil to increase strength and decrease future consolidation settlements.
- Cement stabilization: Cement is mixed into the soft soil to reduce settlements.

Each solution is designed based on the same criteria. The criteria are (1) sufficient undrained and drained bearing capacity in the ultimate limit state and (2) settlements below 50 mm in the serviceability limit state.

Table 4 Pavement structure for the investigated highway section, 200 m, A1–A5

	Description	(Kg CO_2 equivalent)
Pavement structure	Delivery and built-in, transport 50 km	~ 140,600
Soil excavated	4,800 m^3 topsoil, transport 80 km	~ 121,800
Total		262,400

InfraLCA is used as the primary tool to investigate the carbon footprint of each foundation solution. InfraLCA is an LCA program from Vejdirektoratet (The Danish Road Directorate) which is based on generic EPDs that fit Danish projects [9]. However, some of the data needed are not included in InfraLCA as default. These data will be added manually based on EPDs from the manufacturer.

In the LCA analysis, only construction stages A1–A5 are considered. This accounts for the CO_2 emission from the extraction of the raw materials until construction on the site is complete. InfraLCA uses the unit [tkm] for calculating CO_2 emissions from transport. The km here represents the transport to the site, where a factor of 1.75 is used to take the trip back into account.

Life Cycle Assessment of Pavement. Table 4 represents LCA calculations for the pavement structure based on InfraLCA. The pavement structure is assumed to be 1 m thick and replaces the topsoil. The pavement structure consists of a 0.55 m subgrade, 0.2 m subbase, 0.16 m base course, 0.065 m binder course, and 0.025 m surface cover. The amount of topsoil excavated is based on two pavement structures of 12 × 1 m. Soil removed between and beside the lanes during construction is assumed to be re-used.

The soil excavated is transported 80 km to Randers Harbor since this possibly is polluted. The pavement materials are transported from different gravel pits in a radius of 50 km. All soil transport in InfraLCA is calculated with the same 26 tons diesel truck. The LCA result for the pavement structure will be added to each solution discussed.

4.1 Solution 1: Masse Exchange

One of the typical solutions when encountering soft soils is a mass exchange. The soft soil is replaced by engineered fill, typically sand. Usually, this method is not used at greater depths because of the complications and extent when excavating.

If the gyttja is not exchanged, the settlements will be ~ 100 mm at the end of primary consolidation, which is unacceptable according to the applied criteria. The settlements are determined by a one-dimensional settlement analysis [7]. The bearing capacity of the engineered fill is sufficient based on the general bearing capacity formula [10].

However, if the upper 5 m of the gyttja is exchanged with sand, the settlements of the last meter of gyttja will be ~ 40 mm which is found acceptable.

Table 5 Solution 1 carbon footprint for the investigated highway section, 200 m, A1–A5

	Description	(Kg CO_2 equivalent)
Soil excavated	47,600 m^3 soil, transport 80 km	~ 968,800
Soil built-in	47,600 m^3 soil, transport 50 km	~ 854,800
Total		1,823,600
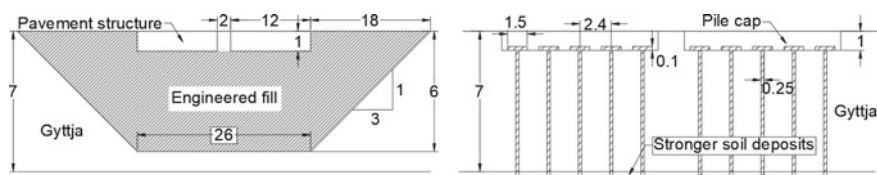
Fig. 2 Left: Excavation volume for solution 1 (hatched area), horizontal scale 1:3. Right: Piled foundation for solution 2, horizontal scale 1:1.5. Measurements in meters

Life Cycle Assessment. The carbon footprint is determined according to Table 5. The excavation volume is based on the measurements in Fig. 2. The excavation is assumed to be above the groundwater table and with an excavation slope of 1:3. The density of the gyttja is set to 1.6 t/m^3 and the sand/topsoil is set to 2.0 t/m^3.

A situation with excavation below the groundwater level would require groundwater lowering which would likely increase the CO_2 emission (operation of pumps, etc.).

4.2 Solution 2: Piled Foundation

Another typical foundation solution for roads on soft soil is a piled foundation. Piles are installed to stronger soil deposits to ensure bearing capacity and minimize settlements. The bearing capacity is determined by the skin friction and end-bearing [10]. The main issue is that the gyttja layer is a weak Holocene deposit and will drag the pile down when exposed to compressive loads (negative skin friction or dragdown). To reduce the negative skin friction, the upper 6 m of the piles are covered in bitumen. The piles are designed to be 16 m long and installed with a center-to-center distance of 2.4 m. Settlements of the piles are neglected since the pile end is installed into late glacial deposits of significant strength and stiffness (Table 6).

Life Cycle Assessment. The carbon footprint is determined according to Table 7. The pile caps are cast as squares according to Fig. 2 and are assumed to need 58.5 kg reinforcement per pile cap (~ 3.5% of cement volume). Concrete is transported from Unicon in Aalborg and steel from Poland. Approximately 1670 piles of 16 m are used for the whole section. The upper 6 m of the piles are covered with bitumen. The installation time for each pile is determined to be 17.5 min, and the diesel use is 16 L per hour. Piles are delivered from Centrumpæle in Vejle, Denmark.

Table 6 Solution 2 carbon footprint for the investigated highway section, 200 m, A1–A5

	Description	(Kg CO$_2$ equivalent)
Pile caps	378 m^3 concrete, transport 7 km, and 98 ton reinforcement, transport 1160 km	~ 271,800
Piles [11]	1,670 piles, transported 180 km	~ 787,000
Installation	7,840 l diesel used during installation	~ 26,100
Total		1,084,900

Table 7 Solution 3 carbon footprint for the investigated highway section, 200 m, A1–A5

	Description	Kg CO$_2$ equivalent
Pre-load	1,626 m^3 soil, transport 50 km	~ 201,000
Soil excavated	1,626 m^3 soil, transport 80 km	~ 284,000
Wick drains	16,884 m wick drains, transport 870 km	~ 2,700
Installation	4,498 l diesel used during installation	~ 4,500
Total		492,200

4.3   Solution 3: Pre-consolidation

Another method used when encountering soft soils is pre-consolidation. Here a load is placed on top of the soft soil, after which the soil is left to consolidate. When the degree of consolidation is deemed sufficient, the pre-load is removed, and the construction can begin. The soil is now over-consolidated for the future service load (yielding smaller settlements). By using this method, the settlements from the traffic load will only result in settlements in the over-consolidated stress regime, yielding significantly smaller settlements compared to the soil left in the normally consolidated state. The bearing capacity is verified by the general bearing capacity formula in the case [10].

To avoid large settlements, a pre-load of 40 kPa is placed on the surface. This is equivalent to 2 m of sand. The consolidation process is deemed sufficiently effective after 1 year of using wick drains or after 2.5 years without wick drains, as the effective stresses centrally in the soft deposit at this point exceed the serviceability stresses.

Life Cycle Assessment. The carbon footprint is determined according to Table 7. The carbon emission is calculated based on a pre-load of 2 × 26 m with a slope of 1:2, see Fig. 3. Furthermore, wick drains with a length of 7 m and a center-to-center distance of 1.5 m are installed. These are assumed to be transported from the Netherlands.
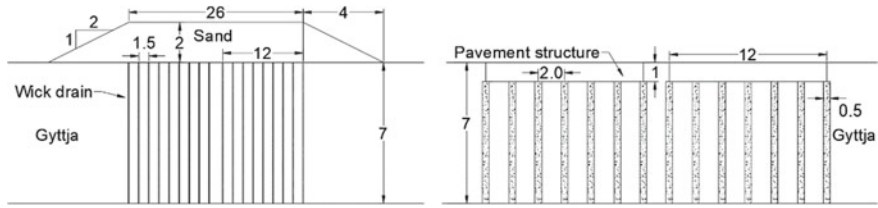
Fig. 3 Left: Pre-consolidation load for solution 3, horizontal scale 1:3. Right: Cement-stabilized columns for solution 4, horizontal scale 1:1.5. Measurements in meters

4.4 Solution 4: Cement Stabilization

Cement stabilization is a form of deep soil mixing where a rod with a mixing tool at the end is pushed through the soil. When the mixing tool reaches a specified depth, cement is expelled while the rod is withdrawn with the mixing tool rotating. This results in stabilized columns. The columns are assumed to have a diameter of 0.5 m.

The bearing capacity is investigated by using the general bearing capacity formula [10]. The strength increase from cement stabilization is calculated as a ratio between the stabilized and non-stabilized area; hence, it works as an area stabilization [3].

The settlements are based on an elastic-perfect-plastic load model [3]. The load is distributed by taking the maximum strength of the stabilized columns into account. The settlements of the stabilized and non-stabilized soil are set to be equal to ensure that the soil is acting as a stabilized area and deforms as one continuum.

By using 7 columns below each pavement structure with a center-to-center distance of 2.0 m, the settlements can be reduced from ~ 100 mm to 15 mm. It was not possible to increase the center-to-center distance further, due to load transfer effects from the pavement. The design mixture is 37.5 kg/m^3 FutureCem cement due to sufficient stiffness and strength increase.

Life Cycle Assessment. The carbon footprint is determined according to Table 8. Approximately 1,400 columns of 6 m should be installed to ensure reduced settlements. Each column consists of 44 kg FutureCem cement which gives a total mass of 62 tons. During installation, the machine on average uses 40 L per hour to install 82.5 m an hour. The foundation solution with measurements is seen in Fig. 3.

Table 8 Solution 4 carbon footprint for the investigated highway section, 200 m, A1–A5

	Description	Kg CO_2 equivalent
Cement [12]	62 tons FutureCem, transport 15 km	~ 37,200
Installation	4,072 l diesel used during installation	~ 13,600
Total		50,800

5 Discussion

Figure 4 shows the total CO_2 emission from each foundation solution. This includes the emission from the construction of the pavement structure as well. It can be concluded that cement stabilization is the solution with the lowest CO_2 emission. Compared to mass exchange, cement stabilization reduces emissions by 85%.

The emission from cement stabilization can potentially be reduced even further if investigations with lower cement amounts and longer curing periods are performed. Generally, 28 days of curing increases strength and stiffness significantly compared to 7 days [4]. It was, however, evident from the serviceability calculations of solution 4 that the full stiffness of the columns could not be utilized because the center-to-center design criterion was the load transfer from the pavement to the columns.

Even though everything is not included in these LCAs analysis, it is evident that a preliminary CO_2 emission investigation can reveal some major differences in the choice of foundation solution. The emission ranking in Fig. 4 is unlikely to change in this project, even if a detailed design is performed. It is however important to be critical when the preliminary CO_2 emission is calculated. If highly emissive factors are excluded, this can have a huge impact on the emission later on. It is therefore crucial to have an overview of the whole project at the beginning.

One of the things that has a major impact on the results is the mean of transportation and distance (A4). One of the reasons why cement stabilization has a lower CO_2 emission is because the transportation emission is minimal. Solution 1 shows how CO_2 emissive transportation is since this solution is ~ 93% transportation according to InfraLCA. CO_2 emissions are therefore highly affected by where a project takes place. New LCAs should be performed on new projects since previous LCAs on the same solutions do not necessarily reflect the new conditions.
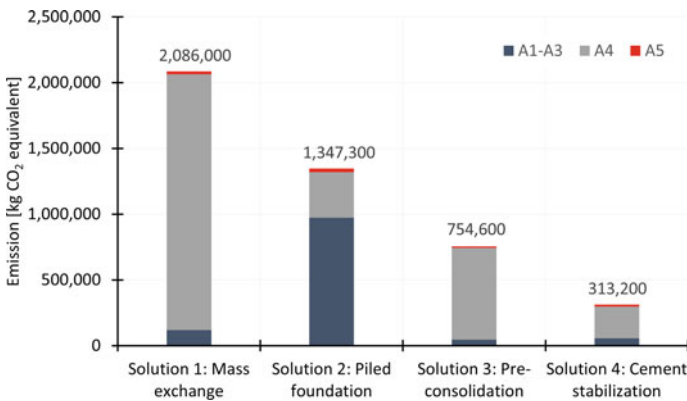
Fig. 4 Total carbon footprint for all solutions for the highway section, 200 m, A1–A5

6 Conclusion

It can be concluded that LCAs can give an extra dimension to a project. The carbon footprint is highly affected by the solution chosen. In this example, cement stabilization with 37.5 kg/m^3 FutureCem cement increased the stiffness sufficiently to avoid a large mass exchange, a pre-consolidation, or a piled foundation. Compared to mass exchange, the carbon footprint is reduced by 85%, pre-consolidation by 77%, and piled foundation by 58%. Further testing could reduce the CO_2 emission even further.

Based on this, using cement stabilization on Aalborg gyttja with the innovative FutureCem cement is proven to reduce CO_2 emissions significantly. Basis cement could not reduce the CO_2 footprint as much due to lower stiffness and larger emission.

Since the CO_2 emission is much lower for the cement stabilized solution, this technique could be used to lower the CO_2 footprint of other infrastructure projects on other soil types as well, in both Denmark and globally.

References

1. United Nations, https://unstats.un.org/sdgs/report/2021/goal-13. Last accessed 19 Apr 2023
2. Aalborg Portland, https://www.aalborgportland.dk/produkter/futurecem-cement. Last accessed 19 Apr 2023
3. Larsson R (2006) Djupstabilisering med bindemedelsstabiliserade pelare och masstabilisering—En vägledning. Svensk Djupstabilisering, Linköping
4. Al-Jabban W (2019) Soil Modification by adding small amounts of binder—a laboratory study. Luleå University of Technology, Luleå
5. Larsen et al (2021) Tværprofiler i åbent land. Vejdirektoratet, København
6. Bjerrum L (1973) Problems of soil mechanics and construction on soft clays and structurally unstable soils (collapsible, expansive and others). In: Proceedings of the 8th international conference on soil mechanics and foundation engineering. Moscow, pp 111–159
7. Terzaghi et al (1996) Soil mechanics in engineering practice, 3rd edn. Wiley, Canada
8. Andersen JD (2012) Prediction of compression ratio for clays and organic soils. In: Proceedings of the 16th Nordic geotechnical meeting. Copenhagen, pp 303–310
9. Vejdirektoratet, https://vejdirektoratet.dk/infralca. Last accessed 19 Apr 2023
10. Trafik-, Bygge- og Boligstyrelsen: DS/EN 1997-1 DK NA: 2021. Dansk Standard. (2021)
11. Centrumpæle: steel-reinforced foundation pile in concrete environmental product Declaration. EPD Danmark (2021)
12. Aalborg Portland: future CEM environmental product declaration. Bureau Veritas (2021)

Transient Simulation of Ground Source Heat Pump in Tropical Region Considering Groundwater Flow

Arif Widiatmojo and **Youhei Uchida**

Abstract Southeast Asian countries have been experiencing rapid economic growth for decades. As a result, the regional per-capita energy demands are also increasing. Concerns about regional energy sustainability are growing as most of the electricity supplies in the region come from fossil fuels. On the other hand, space cooling is essential to electricity demands. In addition to finding the solution for sustainable energy generation, the conservation of end-user energy utilization is also an important consideration. The use of a Ground Source Heat Pump (GSHP) may be a solution to improve household cooling efficiency in tropical regions. However, study on its application in such climate conditions is limited. This paper discusses the potential application of the GSHP system for space cooling, considering regional climate, ground temperature, and groundwater flow. The numerical simulation evaluates the performance of the GSHP system for a typical detached office building. The ground thermal parameters, building thermal properties, and climate conditions were based on the field data. A year of GSHP cooling was simulated, considering different cases of groundwater flow velocities. The simulation results indicate that the GSHP system can provide a 3.66–3.79 average Coefficient of Performance (COP) over a year of a cooling period in the tropical climate. Furthermore, the results show the effect of groundwater flow in enhancing the COP over a prolonged time.

Keywords Ground source heat pump · Space cooling · Southeast Asia

1 Introduction

Southeast Asian countries are experiencing economic growth in recent decades. The demand for space cooling increases as air conditioners and electricity prices become more affordable for the people in the region. The electricity demand is also increasing, raising environmental and sustainability concerns because most of the electricity in

A. Widiatmojo (✉) · Y. Uchida
Renewable Energy Research Center, National Institute of Advanced Industrial Science and Technology (AIST), 2-2-9 Machiikedai, Koriyama-shi 963-0298, Fukushima-ken, Japan
e-mail: arif.widiatmojo@aist.go.jp

the region comes from fossil fuels. The conventional or typical air conditioner system, also referred to as Air Source Heat Pump (ASHP), is believed to have reached its full potential in terms of efficiency. Alternatively, the Ground Source Heat Pump (GSHP) system can potentially provide higher thermal efficiency than ASHP. Principally, a GSHP is similar to ASHP, except for its heat sink/source. A GSHP extracts or rejects heat to the ground. In most four seasons countries, the air temperature fluctuates depending on the seasons and other weather activities. On the other hand, the average ground temperature between 15 and 100 m depth is stable around 15–17 °C, providing a stable heat sink/source regardless of the seasons. The high ground heat capacity also allows seasonal energy storage between winter and summer.

The application of GSHP in tropical countries faces two main issues: high ground temperature and the use for cooling with no heating requirement. According to the research by Yasukawa et al., the average annual ground temperature in Bangkok falls within the range of ground temperature at 0–50 m depth [1]. On the other hand, the tropical seasons require no heating, even during the lowest temperature season. Later studies focused on obtaining thermal efficiency data on GSHP in Tropical countries have found that despite the abovementioned issues, GSHP still has potential advantages over conventional ASHP based on the short-term performance data [2–4]. However, the performance analysis based on the long-term performance data is yet to be available. The long-term performance analysis is essential to evaluate the long-term sustainability of the GSHP system, as well as to estimate the system's economic feasibility and potential energy saving. As the field data is limited, this paper attempts to provide an analysis of GSHP performance in tropical climates based on the transient numerical model.

2   Numerical Model

2.1   Transient Model

To further evaluate the expected performance of GSHP in a more extended period, the transient model of GSHP cooling of a typical detached office building is simulated by using TRNSYS 18. TRNSYS is software with modular structures capable of simulating transient systems. It is used to simulate transient phenomena of coupled thermal and other energy systems, such as Heating, Ventilation and Air Conditioning (HVAC). Various GSHP studies have been carried out by using this software [5–8]. The TRNSYS's dynamic link library structures allow users to develop user-specific models. In addition, TRNSYS can be coupled with other applications such as MATLAB, Microsoft Excel, and Engineering Equation Solver (EES).

2.2　The Moving Line Source (MILS) Analytical Model for Borehole Heat Exchangers (BHEs)

The TRNSYS has a built-in BHE model (Type 557a), which is based on the Duct Storage (DST) model proposed by Hellstrom [9]. However, the model does not account for the groundwater velocity. The DST model assumes the combined effect of heat dispersion and convection of the surrounding ground by the apparent thermal conductivity. The apparent thermal conductivity is typically measured by the Thermal Response Test (TRT), considering the Infinite Line Source (ILS) theory. Thus, the apparent thermal conductivity represents diffusive and convective heat transfer in a single value. While heat transfer by thermal diffusion and convection are two different phenomena, failure to account for the convective heat transfer may lead to erroneous error, especially for the area with high groundwater flow.

In this simulation, an extension of ILS solution referred to as Moving Infinite Line Source (MILS) analytical model is used. The MILS model is programmed into MATLAB and coupled to the TRNSYS 18 main software.

According to Diao et al. [10] the temperature change at a specific location in a polar coordinate system, t second after heat extraction/rejection q (Wm^{-1}), is expressed as:

$$T(r, \varphi, t) - T_0 = \frac{q}{4\pi\lambda} \exp\left(\frac{ur}{2D}\cos\varphi\right) \int\limits_0^{r^2/4Dt} \frac{1}{\eta} \exp\left[-\frac{1}{\eta} - \frac{u_{\text{eff}}^2 r^2 \eta}{16D^2}\right] d\eta \qquad (1)$$

where $\eta = 4D(t - t')/r^2$, u(ms^{-1}) is the groundwater velocity, D(m^{2}s^{-1}) is the thermal diffusion coefficient proportional to thermal conductivity and inversely proportional to the ground volumetric heat capacity.

The following equation is introduced by assuming a homogeneous borehole temperature to obtain a relationship between the borehole temperature and the average fluid temperature:

$$\overline{T}_f(t) = \frac{1}{2\pi} \int\limits_0^{2\pi} T(r_{bh}, \varphi, t)\mathrm{d}\varphi + q.R_{bh} \qquad (2)$$

where R_{bh} (mKW^{-1}) is the borehole heat resistance. The above analytical solution is valid under the following assumption:

- The ground is infinite and homogenous.
- The physical and thermal properties of the heat medium (ground) are independent of time.
- The effect of ground surface temperature is negligible, and the initial ground temperature is homogeneous.

The main problem in solving Eq. 1 is that the temperature is calculated based on the given amount of heat rate, q, at each time step. However, the transient output from the GSHP model is the temperature and flow rate of heat exchanger fluid. Moreover, the amount of q varies because of the thermal interaction between boreholes. We proposed a numerical scheme to find the BHE fluid exit temperatures for each borehole based on the entering fluid temperature.

2.3 Building and GSHP Model

A model of a small-size office building was created and imported into TRN Build. The building had two floors and a total footprint area of 200 m². 85.5% of which (171 m²) was treated as thermal zones. The thermal zones are divided into five main rooms with a 171 m² footprint area, 85.5% of the total building area. The external wall heat transfer coefficient was set to 0.386 Wm^{-2} K^{-1}.

Figure 1 shows the relative humidity, RH (%), ambient temperature range, and average ground temperature range in Bangkok city. The ground temperature range is obtained from the groundwater observation surveys by Yasukawa et al. [1]. Other parameters to calculate the building's thermal load are presented in Tables 1 and 2. An hourly annual Bangkok weather data is used to simulate the influence of ambient temperature, solar radiation, and humidity on the building cooling load. Further, it is assumed that the GSHP works 9 h daily from 8 am to 5 pm during weekdays. A schematic diagram of the model is shown in Fig. 2.

For the GSHP model, the built-in TRNSYS module, Type 919 was used. A GSHP model with a total of 10.5 kW cooling capacity was used. The GSHP performance data is obtained from the manufacturer catalog.

A borehole configuration with three different groundwater velocities are considered, resulting in a total of three cases. Further, it is assumed that the groundwater flows in the direction parallel to the BHE column (see Fig. 3 and Table 3).

3 Results and Analysis

A standard parameter used to evaluate the heat-pump performance is the coefficient of performance (COP), which is the total cooling or heating rate ratio to the required electrical power.

$$\text{COP} = \frac{Q_T}{W_T} = \frac{Q_R - \varepsilon W_C}{W_T}, \quad \text{where} \begin{cases} \varepsilon = 1 (\text{Cooling}) \\ \varepsilon = -1 (\text{Heating}) \end{cases}, \tag{3}$$
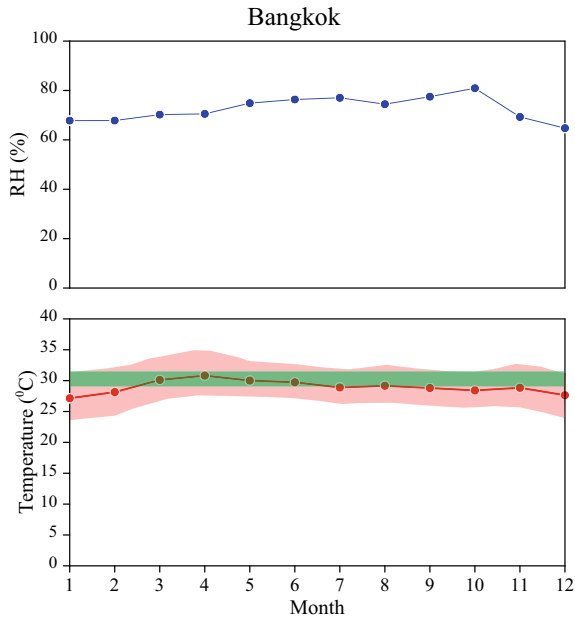
Fig. 1 Annual data of monthly averaged relative humidity, ambient temperature range and average (red shade and red line), and ground temperature range in Bangkok (green shade)

Table 1 Building thermal parameters

Parameters	
Area	Building area: 200 m^2 Thermal zone area: 171 m^2
Internal heat sources	Human, PCs, Lightings, Refrigerator
Heat pump set temp	23 °C
Air exchange rate	0.4 ACH (bedrooms, living room), 0.7 ACH (kitchen)

Table 2 Internal heat sources

Parameters	Heat load	Quantity	Daily duration
PC	100 W	10	8 h
Human (light activity)	130 W	10	8 h
Lighting	5 Wm^{-2}	− 1	8 h
Refrigerator	90 W	1	24 h

Here, Q_R [W] is the heat extraction or rejection rate from/to the ground, Q_T [W] is the rate of heat added to or removed from the building, and W_T [W] is the total electrical power consumption, such that
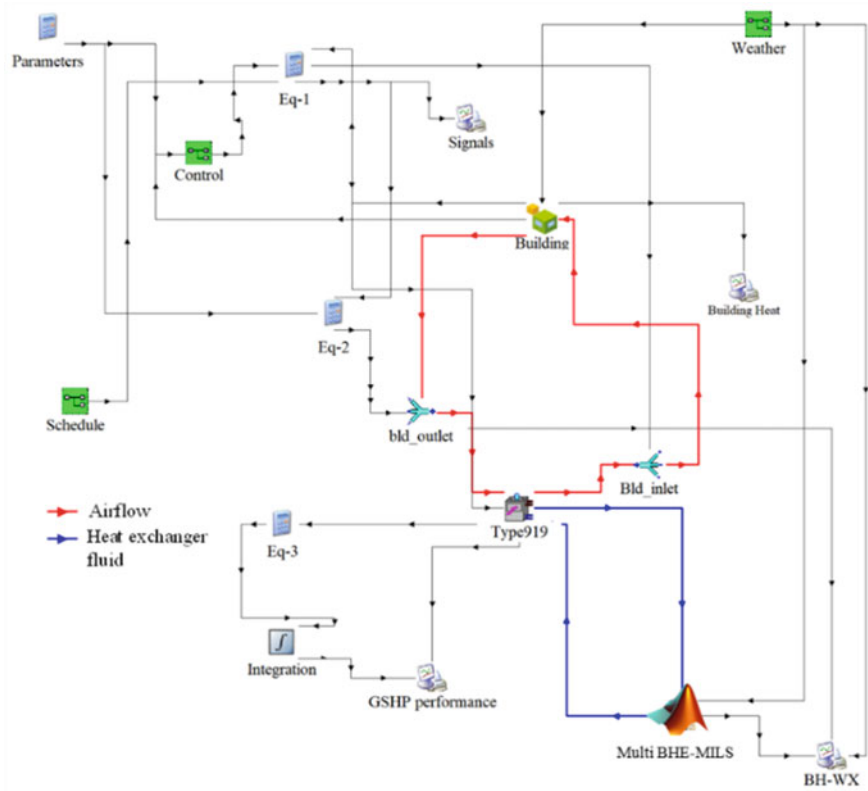
Fig. 2 Schematic figure of numerical model

Fig. 3 BHE configurations and groundwater flow direction
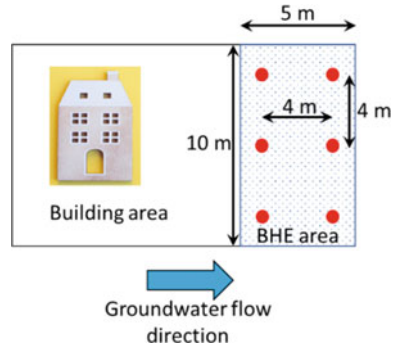
Table 3 Number of BHEs, configurations, and the groundwater velocities

	0 ms^{-1}	1.55E-07 ms^{-1}	3.1E-07 ms^{-1}
4 × 2 (8 BHEs)	Case A	Case B	Case C

Table 4 Simulation parameters

Parameter	Value	Unit
BHE radius	0.08	m
BHE length	50	m
BHE resistance	0.137	mKW^{-1}
Initial ground temperature	27	°C
Ground thermal conductivity	1.82	$Wm^{-1} K^{-1}$
Ground volumetric heat capacity	2.4	$kJm^{-3} K^{-1}$
Fluid volumetric heat capacity	4.18	$kJm^{-3} K^{-1}$
Number of boreholes	2.4	–

$$W_T = W_C + W_F + W_P, \tag{4}$$

$$Q_R = \varepsilon(\text{LWT} - \text{EWT})\rho c V_m, \quad \text{where} \begin{cases} \varepsilon = 1(\text{Cooling}) \\ \varepsilon = -1(\text{Heating}) \end{cases}, \tag{5}$$

where W_C, W_F, and W_P are, respectively, the electrical power consumption of the compressor, fans, and fluid pump; ρ [kg m^{-3}] is the fluid mass density. While c [J kg^{-1} C^{-1}] and V_m [m^3 s^{-1}] are the fluid's specific heat capacity and volumetric flow rate, respectively.

Table 4 lists the thermal and other simulation parameters. It is noted that the thermal conductivity is set based on the TRT results and analysis from the previous study in 2018 [11], while the initial ground temperature is set based on the average value obtained by Yasukawa et al. [1]. Figure 4 shows the COP of all four cases during a year cooling period. All cases indicate less variation of COP during the early period, followed by declining trends. The declining COP is caused by the thermal build-up in surrounding BHEs due to the heat rejection. Further examination at the end of the cooling period shows that the rate of COP decline varies.

Figure 5 explains the reduction of COP between the first month and the last month of operation. The cases with higher groundwater flow provide less COP reduction due to convective heat transfer. Further, the average annual COPs are 3.66, 3.71, and 3.79 for Case 1, Case 2, and Case 3, respectively. These results suggest the significant role of convective heat transfer due to the groundwater flow.

The simulation result also provides information that despite the high ground temperature, the system can still provide better thermal performance than a regular air conditioner with typical COP between 2 and 3.5. However, long-term performance simulation is required to analyze the GSHP performance over a longer period. The long-term performance estimation is critical to consider whether GSHP is a good option for investment against the standard air conditioner system.
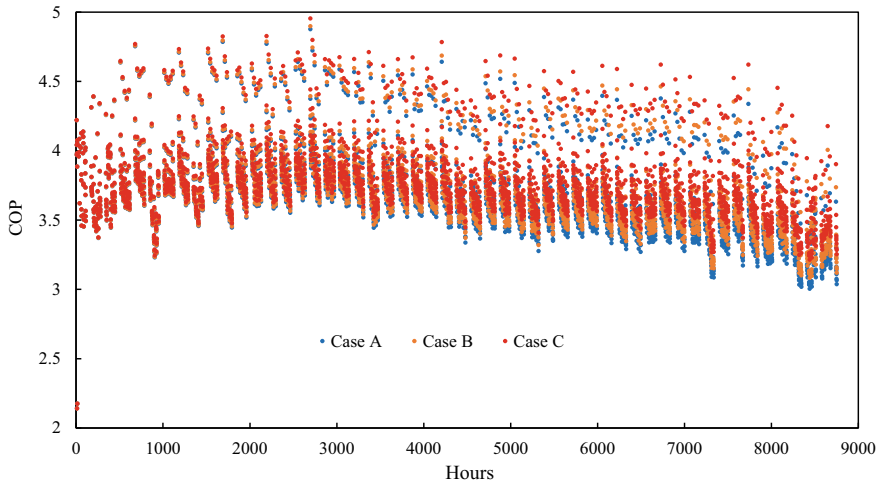
Fig. 4 COP change during a year of cooling for all cases
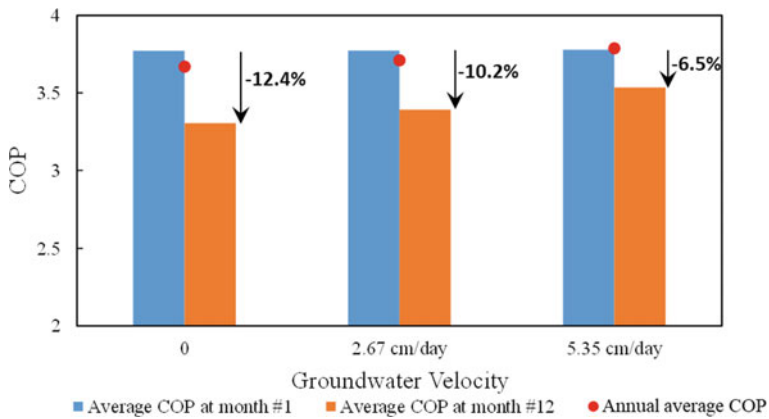
Fig. 5 Annual average COP and COP difference between the first and last month of operation

4   Conclusion

In this study, the effect of groundwater flow on the GSHP performance in a tropical region has been investigated. The numerical model incorporates the transient cooling demand of a typical detached office building with the analytical model of the borehole heat exchanger. The results suggest the decline of COP over a year of cooling operation. However, it is found that the rate of COP reduction between the first and last month of operation is affected by the groundwater flow. The average annual COPs are found to be 3.66, 3.71, and 3.79 for Case 1, Case 2, and Case 3, respectively.

Further, it is necessary to perform long-term simulations to evaluate the long-term advantages or disadvantages of GSHP over the conventional air conditioner system.

References

1. Yasukawa K, Uchida Y, Tenma N, Taguchi Y, Muraoka H, Ishii T (2009) Groundwater temperature survey for geothermal heat pump application in tropical Asia. Bull Geol Survey Jpn 60:459–467
2. Widiatmojo A, Chokchai S, Takashima I, Uchida Y, Yasukawa K, Chotpantarat S (2019) Ground-Source heat pumps with horizontal heat exchangers for space cooling in the hot tropical climate of Thailand. Energies 12:1274
3. Chokchai S, Chotpantarat S, Takashima I, Uchida Y, Widiatmojo A, Yasukawa K (2018) A pilot study on geothermal heat pump (GHP) use for cooling operations, and on GHP site selection in tropical regions based on a case study in Thailand. Energies 11:2356
4. Shimada Y, Uchida Y, Takashima I, Chotpantarat S, Widiatmojo A, Chokchai S, Charusiri P, Kurishima H, Tokimatsu K (2020) A study on the operational condition of a ground source heat pump in Bangkok based on a field experiment and simulation. Energies 13(1):274
5. Liu Z, Zhang Y, Xu W, Yang X, Liu Y, Jin G (2020) Suitability and feasibility study on the application of groundwater source heat pump (GWSHP) system in residential buildings for different climate zones in China. Energy Rep 6:2587–2603
6. De Rosa M, Ruiz-Calvo F, Corberán JM, Montagud C, Tagliafico LA (2015) A novel TRNSYS type for short-term borehole heat exchanger simulation: B2G model. Energy Convers Manage 100:347–357
7. Jonas D, Theis D, Felgner F, Frey G (2017) A TRNSYS-based simulation framework for the analysis of solar thermal and heat pump systems. Appl Solar Energy 53:126–137
8. Widiatmojo A, Uchida Y, Fujii H, Kosukegawa H, Takashima I, Shimada Y, Chotpantarat S, Charusiri P, Tran TT (2021) Numerical simulations on potential application of ground source heat pumps with vertical ground heat exchangers in Bangkok and Hanoi. Energy Rep 7:6932–6944
9. Hellstrom G (1989) Duct ground heat storage model manual for computer code
10. Diao N, Li Q, Fang Z (2004) Heat transfer in ground heat exchangers with groundwater advection. Int J Thermal Sci 43:1203–1211
11. Widiatmojo A, Shimada Y, Takashima I, Uchida Y, Chotpantarat S, Charusiri P, Navepham J, Tran TT (2021) Evaluation and short-term test on potential utilization of ground source heat pump for space cooling in Southeast Asia. In: Hazarika H, Madabhushi GSP, Yasuhara K, Bergado DT (eds) Advances in sustainable construction and resource management. Lecture Notes in Civil Engineering, vol 144. Springer, Singapore

Innovative Case Studies for Sustainable Design and Construction

2D Model Tests of Sheet Pile Reinforcement Method for Existing Pile Foundations

Takatoshi Sagawa, Tsubasa Ohata, and Hidetoshi Nishioka

Abstract The sheet pile (SP) reinforcement method can be utilized to realize a sustainable society because it is more economical, environment friendly, and easier to construct in narrow areas than conventional methods of reinforcing pile foundations. Furthermore, the method can be used as a foundation reinforcement technique. In this study, static horizontal loading tests were conducted on a model ground using various separations between the piles and SP. Additionally, we studied the effects of increasing the overall resisting force of the foundation and the effect of decreasing the load supported by the existing piles. The results confirmed that when the distance between the existing piles and SP is small, the SP reinforcement effectively reduces the cross-sectional forces acting on the existing piles. By contrast, when the separation is large, the SP reinforcement effectively increases the bearing capacity of the entire foundation. Thus, the interaction between the pile and SP perimeter soil changed when the separation varied, and the reinforcement effect varied with the separation.

Keywords Pile foundation · Sheet pile reinforcement · Subgrade reaction

1 Introduction

Many older structures do not meet the current seismic performance standards in Japan and require seismic reinforcement. The 1995 Hyogo-ken Nanbu Earthquake caused many structures to collapse, resulting in severe damage. Additionally, many structures were damaged at their foundations, triggering a major change in seismic design standards. The safety of new railroad structures is necessary to ensure against large

T. Sagawa · T. Ohata
Chuo University Graduate School, Tokyo 112-8551, Japan

H. Nishioka (✉)
Chuo University, Tokyo 112-8551, Japan
e-mail: a18.fj66@g.chuo-u.ac.jp

Fig. 1 Overview of SP
reinforcement method [3]
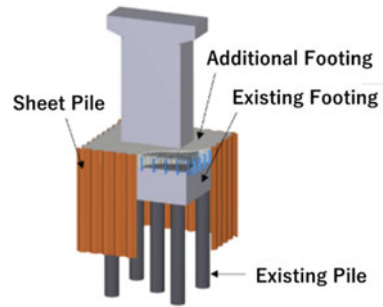
seismic motions called L2 earthquake motion. Additionally, for existing structures, seismic reinforcement work should be prioritized.

However, many structures that were designed based on old design standards before the Hyogo-ken Nanbu Earthquake still exist. In the case of seismic reinforcement of existing structures (e.g., piers), priority is given to the reinforcement of the superstructure frame, and progress in seismic reinforcement of foundations is lagging. Existing foundations have been reinforced primarily by adding new piles or by strengthening the surrounding ground. However, the issue with these reinforcement methods is that reinforcing the structure is extremely challenging while it is in service, and the large footing requirements make construction impossible when the site is restricted. Therefore, seismic reinforcement of structural foundations is generally more challenging to implement from cost and construction standpoints because it is more extensive than above-ground work, and progress in this area is slow. Therefore, an economical foundation reinforcement method must be developed that does not significantly impact existing structures, is easy to install in narrow areas, and is environment friendly. The sheet pile (SP) reinforcement method (Fig. 1) satisfies these conditions, in which steel SPs are driven into the ground around existing pile foundations and are integrated with footings.

In Japan, the SP reinforcement method has been developed primarily for seismic reinforcement, and it can also be used as a general foundation reinforcement technology in countries with fewer earthquakes. However, there are concerns that disasters such as super typhoons will increase because of climate change caused by global warming.

The sheet pile reinforcement method is expected to play an active role in addressing these problems, but a rational method for reinforcement design has not yet been established.

This study aims to establish a reasonable design method, suitable for the purpose of reinforcement by varying the spacing between the piles and SPs. Static horizontal loading experiments were conducted on a model to determine the effects of increasing the resistance of the foundation and reducing the load acting on the piles. These experiments include an analysis of the two-dimensional behavior with reference to previous studies [1, 2]. Additionally, the interaction between the two piles as a group of piles is discussed based on the ground displacement obtained by image analysis.

2 Experimental Procedure

2.1 Creation of Ground Model

An aluminum laminate rod apparatus was used for the ground model. Three types of aluminum rods, each 150 mm long with diameters of 1.5, 2, and 3 mm were mixed at a weight ratio of 1:1:1 and piled up to 700 mm wide and 430 mm high while compacted to the unit volume weight of $\gamma = 21.8$ kN/m^3.

2.2 Model Specifications

Aluminum plates (Young's modulus $E = 73$ GPa) were used for the model piles and model SPs. The model pile had a plate thickness of 1 mm, width of 190 mm, and a length of 440 mm, while the model SP had a plate thickness of 0.5 mm, width of 200 mm, and a length of 225 mm. The characteristic values of the piles for both models were obtained using the Chang equation [4] (Eq. 1) from the load–displacement relationship at 4 mm displacement when the pile and SP were loaded independently.

$$y_t = \frac{(1 + \beta \bullet h)^3 + \frac{1}{2}}{3EI \bullet \beta^3} H \tag{1}$$

where y_t is the horizontal displacement of the loading point, H is the loading load, I is the section's secondary moment, and h is the height of the loading point.

Independent loading tests were conducted as preliminary experiments using both models. The product of the load and displacement at a horizontal displacement of 1 mm, βL, was obtained from the relationship between load and displacement. Therefore, $\beta L = 6.29$ for the model pile and $\beta L = 4.56$ for the model SP. Furthermore, the condition $\beta L > 3$, which is typically applicable to a semi-infinite length pile, was satisfied.

The characteristic value of the pile, β (calculated from Chang equation) was used to describe the similarity law between the model pile and the model SP, and the ratio of the value of $1/\beta$ was matched to that of the real structure. The model structure is a combination of the cast-in-place-pile with a diameter of 1.0 m and the Type-IV steel sheet pile, and the ratio of the value of $1/\beta$ of the two model pile combinations used in the experiment is almost equivalent to that of the real structure.

2.3 Model Installation

The apparatus after the installation of the model is shown in Fig. 2a. The model pile was installed to a depth of 200 mm before being penetrated to the bottom of

(a) Model equipment　　　　　(b) Outline drawing after installation
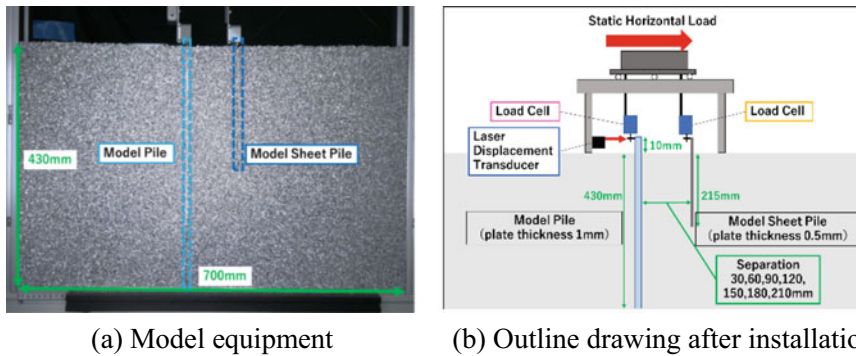
Fig. 2 Overview of loading equipment

the model, and the remaining aluminum rods were piled up to the specified root penetration length (430 mm). After the stacking of the aluminum rods, the model SP was penetrated to the prescribed root penetration length $\angle = 215$ mm using different separations of 30, 60, 90, 120, 150, 180, and 210 mm from the pile model for each experiment.

2.4　Loading Method

An overview of the loading method is shown in Fig. 2b. The model pile and the model SP were not rigidly connected, and two load cells for the model pile and one load cell for the model SP were placed on top of each model (10 mm above the ground surface). The distance between the two models was fixed, and static horizontal loads in one direction were applied until the displacements were approximately 4 mm, for both models.

2.5　Test Case

Experiments were conducted in eight cases: two cases of preliminary tests in which the pile and SP were loaded independently and six cases of primary tests in which the model pile and model SP were loaded simultaneously with separations from the model pile of 30, 60, 90, 120, 150, 180, and 210 mm.

2.6 Measuring Method

During loading, the horizontal displacements of the model pile and model SP at the loading point height were measured using a laser displacement meter. Load cells were used to measure the resistance force supported by both the pile and SP. The total resistance force of the entire foundation was obtained by summing the values measured by the load cells of the piles and SP.

2.7 Estimation of Ground Reaction Force Distribution

The ground reaction force distribution was estimated using a polynomial approximation in Microsoft Excel [5]. First, the bending moment distribution was calculated by multiplying the strain values and the calibration coefficient obtained from the bending test. The strain values were measured using strain gauges attached to the model pile at 20 mm intervals. Additionally, the bending moment distribution was approximated by a sixth-order polynomial equation. Finally, the distribution of the subgrade reaction force was calculated using the second-order derivative of the sixth-order polynomial equation with regard to the distance from the pile head.

3 Experimental Results and Discussion

3.1 Experimental Results

The results of the load–displacement relationship of the entire foundation for each case are shown in Fig. 3, and the figure illustrates the results of the pile-only loading as a comparison. Figure 4 shows the breakdown of the loads supported by the pile and SP at a 4 mm displacement. Additionally, Fig. 4 represents the results of the pile and SP loadings separately for comparison.

The load supported by the pile and SP increased with increasing separation; at a sufficiently large separation of 210 mm, the interaction between the pile and SP disappeared and the pile and SP bore approximately the same load as if each had been loaded independently.

When the separation was < 210 mm, the load capacity of the model pile decreased, implying that the model piles were reinforced in terms of reducing the cross-sectional force generated by the model piles. By contrast, the SP burden tended to increase as the separation distance increased, but the SP burden increased and decreased repeatedly after 90 mm of separation, showing no significant change with the separation distance.
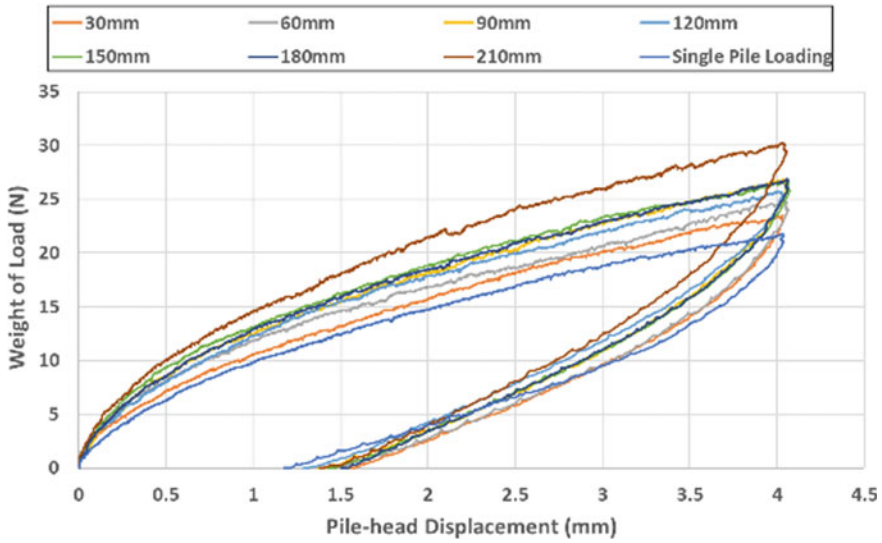
Fig. 3 Relation between loading weight and displacement after reinforcement

Fig. 4 Ratio of borne load at 4 mm pile head displacement
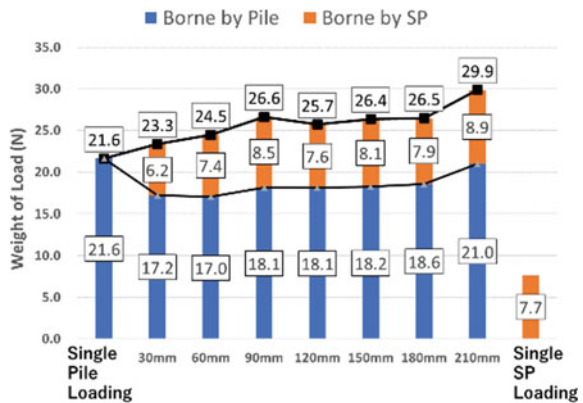
By contrast, the SP burden, which increased the overall resistance, was equivalent to the SP loading alone up to 90 mm of separation, then the SP burden decreased with the separation.

3.2 Ground Reaction Force Distribution

The distribution of ground reaction forces is shown in Fig. 5, in which no significant difference due to the size of the separation is shown for the seven cases after SP
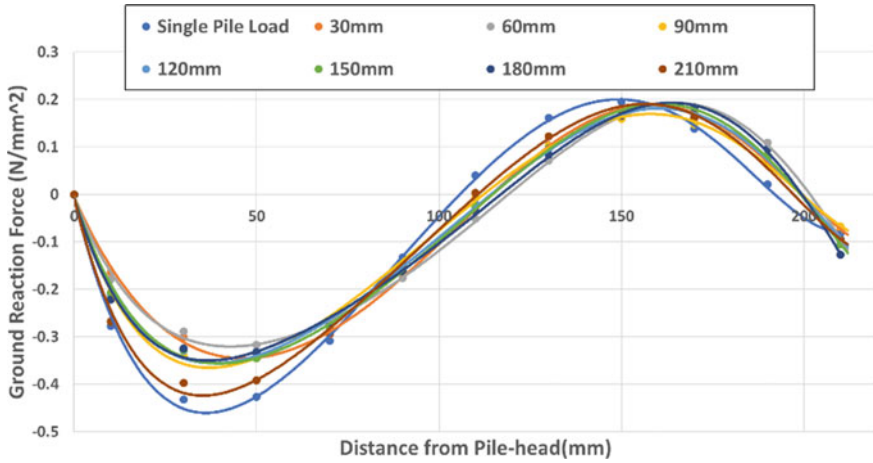
Fig. 5 Distribution of subgrade reaction force acting on pile at 4 mm pile head displacement

reinforcement. However, the ground reaction forces acting on the piles in the seven cases after SP reinforcement reduced more than those for the piles loaded alone where the ground reaction forces were at a peak (Depth of 30–50 mm). For the 210 mm separation case shown in Figs. 4 and 5, we observed that the load supported by the piles was equivalent to that of the pile-alone loading case; however, the ground reaction force was reduced.

3.3 Ground Strain Distribution

To examine the influence of the separation on the reinforcement effect, image analysis was performed on the model ground using the DippStrain (Detect Co., Ltd.) digital image correlation method. The results of the analysis are shown in Fig. 6, which shows the vertical strain distribution in the horizontal direction between 0 and 4 mm of horizontal displacement and the location of each slip surface estimated from the strain distribution of the pile and SP loading alone.

From Figs. 4 and 6, we observe that the magnitude of the resisting force of the entire foundation depends on the area of the zone of influence of the ground surrounded by the slip surface. For example, with 30 mm separation, the influence area by SP overlapped the influence area by the piles, which was considered the reason for the decrease in the SP burden due to the smaller influence area of the foundation as a whole. By contrast, with 210 mm separation, no significant overlapping was observed between the active slip surface of the pile and the passive slip surface of the SP, and the strain was generated in a wide area. Therefore, the resistance force of the entire foundation was the largest.

Fig. 6 Image analysis
results (horizontal vertical
strain distribution up to 4 mm
pile head displacement)
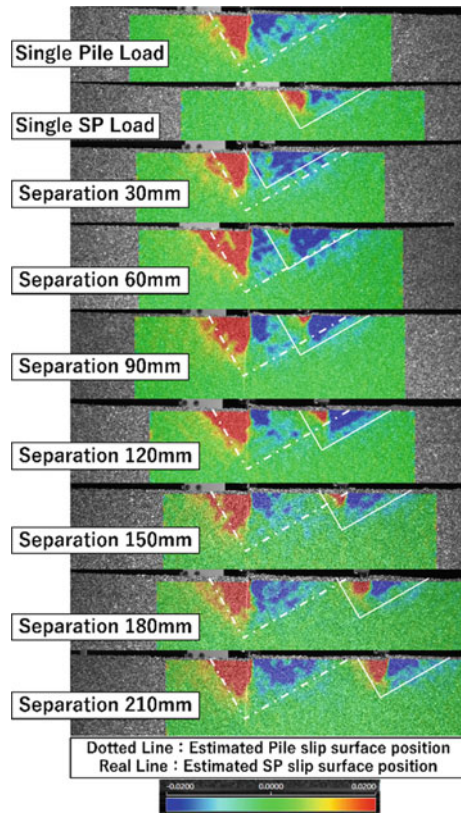
With 60–90 mm of separation, the passive slip surface of the pile passed near the starting point of the primary active slip surface of the SP, and the model SP had a positional relationship to suppress the sliding displacement of the passive slip surface of the pile. Hence, the model SP was positioned in such a way that it suppressed the sliding displacement on the passive slip surface of the pile. With 150 mm of separation, the passive slip surface of the pile overlapped with the primary active slip surface of the SP behind the SP, and the passive soil mass of the pile was reduced.

3.4 Earth Pressure Coefficient and Discussion from Image Analysis Results

The linear distribution of the ground reaction force near the ground surface was considered to be the range where the front ground resistance reached the passive earth pressure state. The coefficient of earth pressure, K_a, was calculated by dividing

Table 1 Coefficients of horizontal earth pressure acting on the existing pile

Case	Coefficient of horizontal earth pressure	Reduction factor for single pile load
Single pile load	4.40	1.00
Separation 30 mm	3.07	0.70
Separation 60 mm	2.94	0.67
Separation 90 mm	3.47	0.79
Separation 120 mm	3.35	0.76
Separation 150 mm	3.33	0.76
Separation 180 mm	3.31	0.75
Separation 210 mm	4.05	0.92

the slope connecting the two points at depths of 0 and 30 mm by the unit volume weight, γ. The calculated results for each case are listed in Table 1. The results showed that the value of K_a was higher for the cases of pile loading alone and with 210 mm of separation. Figure 6 shows that the area where the pile exerts compressive action on the ground (indicated by the dotted blue line) is larger in cases where the coefficient of earth pressure, K_a, is large for the pile-alone loading and 210 mm separation.

No clear difference in the coefficient of earth pressure was observed in the cases with separations between 30 and 180 mm; however, the coefficient of earth pressure was approximately 30% smaller in these cases.

This indicates that the magnitude of the coefficient of earth pressure acting on the pile is related to the spreading of the strain distribution in the ground around the pile due to horizontal loading.

4 Conclusion

This study confirmed that the separation between steel SP and an existing pile significantly affects the reinforcement effect of the SP reinforcement method.

A larger separation increases the horizontal resistance of the entire foundation while a smaller separation reduces the cross-sectional forces generated by the piles and the ground reaction forces acting on the piles.

Image analysis demonstrated that the difference in the effect on the ground caused by the difference in the separation size is related to the difference in the reinforcement effect of the entire foundation.

References

1. Nishioka H, Model test on the effectiveness of seismic reinforcement of existing pile foundations using sheet piles. Geotech Eng J 5(2):251–262
2. Nishioka H, Mogi Y (2021) Model test on sheet pile reinforcement method for existing pile foundation—effect of separation between pile and sheet pile on reinforcement effect. In: 2021 Annual civil engineering society national conference
3. Railroad Technical Research Institute: Sheet pile reinforcement method for pile foundations in liquefied ground. Found Soil Struct Lab
4. Public Interest Incorporated Association, Geotechnical Engineering Society of Japan: Horizontal loading test method for piles. Explanation p. 32. Maruzen Publishing Co. (2010)
5. Kikuchi Y (2003) Information on port and airport technology institute, Chapter 3. A method for estimating the distribution of subgrade reaction forces acting on a pile from the distribution of bending moments

Application of Phase Change Materials for Thermal Stabilization of Soils in Cold Regions

Ekaterina Kravchenko and **Charles Wang Wai Ng**

Abstract   With increasing climate change, the sustainability of geotechnical infrastructure in cold regions has become a global issue. Phase Change Material (mPCM) absorbs and releases energy in the form of latent heat under varying ambient temperatures. Hence, mPCM is an alternative to stabilizing the temperature regime of an embankment, and it improves the mechanical performance of soils under freeze–thaw cycles. This paper aims to investigate the effectiveness of using PCM as a thermal controller in stabilizing the temperature regime of an embankment. Soils in seasonally frozen and degrading permafrost regions were selected in this study. Firstly, the soil temperature in these two regions was analyzed. After that, a comparative analysis of the effectiveness of various mPCM's was performed based on the thermogram of the differential scanning calorimetry test. At last, a PCM-soil model was developed to simulate the thermophysical properties of reinforced soil mixture in both regions. The results show that mPCM was the most effective in soil temperature control during its phase transition. The maximum temperature rise in the mPCM soil layer was 1.4 °C under seasonal freezing conditions. With the presence of mPCM, a decrease in the maximum seasonal freezing rate and depth was observed. Under permafrost conditions, the application of mPCM at a depth of 1.2 m led to the reduction of soil temperature by 1.2 °C. This study demonstrates the thermoregulatory effects of mPCM on the reduction of the embankment's temperature and therefore by the application of mPCM the degradation of permafrost is prevented.

Keywords   mPCM · Peak Temperature · Embankment Soil · Thermo-regulation

E. Kravchenko (✉) · C. W. W. Ng
The Hong Kong University of Science and Technology, Hong Kong Special Administrative Region, Hong Kong, China
e-mail: kravchenko@ust.hk

1 Introduction

Climate change has made the sustainability of man-made structures in permafrost regions a global issue, with their reduced structural stability having significant social, economic, and environmental consequences. In recent decades, increased temperatures of permafrost soils have been recorded worldwide [1], with increased air temperatures in the Arctic having a strong ongoing effect on the region's soil temperatures and, therefore, on the spread of permafrost [2]. In seasonally frozen regions, soils experience at least one freeze–thaw cycle (F–T) each year. This F–T cycling can significantly change the soil's structure, altering its mechanical properties and thereby decreasing the ground's bearing capacity for man-made structures [3]. Seasonal freezing and thawing of the soil can produce stress–strain states in embankments, foundations, and other structures that exceed their designed tolerances. The conditions of F–T cycling also negatively influence other important engineering properties, such as the water content, soil bearing capacity, and permeability [4]. Thus, in seasonally frozen regions, engineers must ensure that soil is effectively protected from freezing, while in permafrost regions, they must ensure the stability and prevent degradation of frozen soil.

Current subgrade thermal stabilization methods need regular maintenance. An innovative way to stabilize the temperature regime of soils in cold regions can be the use of materials that independently accumulate thermal energy. For example, microencapsulated phase change materials (mPCMs) are latent thermal storage materials that can store a large amount of thermal energy during their phase changes [5]. mPCMs can stabilize soil temperature by storing and releasing energy during phase changes [6], resulting in a stable soil temperature range. Due to the property of accumulating latent heat, mPCMs have various uses in building construction, textiles, solar energy storage, and other industries [7–11]. These materials have great potential and attract the attention of scientists with the aim of introducing them into various spheres of human activity that require smoothing out temperature drops or accumulating energy. In laboratory freezing/thawing tests of a soil mixture with different concentrations of PCM with butyl stearate and paraffin core material, it was revealed that four main platforms can be distinguished on the temperature curves of samples containing different PCMs: a solidification phase change period, moisture freezing period, melting phase change period, and moisture melting period [12]. The first and third platforms, which are determined by the phase change of PCM materials, help to reduce the rate of change in soil temperature, fulfilling its main task - soil temperature regulation within a certain temperature interval. It also was observed that the unconfined compressive strength of soil treated with pure mPCM increased with the mPCM content [13]. A previous laboratory study of the thermal behavior of a silty clay mixture with different contents of mPCMs showed a significant decrease in the freezing rate of samples with the addition of mPCMs [14]. In particular, the addition of 2% and 4% mPCM (percentage from the weight of the dry soil) increased the temperature of silty clay during freezing at the time of the phase change of water in the soil. It was noted that a higher percentage of additive content resulted in a

greater decrease in silty clay temperature. When conducting a numerical simulation of a micro-model of a soil cube with added mPCM with a changing external temperature, it was observed that the amplitude of temperature fluctuations of the soil mixture significantly decreases when 4% PCMm is added [15]. In addition, it was reported that the inclusion of mPCM in the soil contributed to a decrease in the thermal conductivity of the mixture [12, 14, 15]. Determining the thermal properties of soil is of great practical importance in the field of design, operation, and construction of motor roads, building foundations, and underground heating networks in cold regions. Data on the thermal conductivity of soil are important in many engineering areas [16–18]. In seasonally frozen regions, natural soils are blended with different materials to reduce frost heave damage and to improve the thermal conductivity of the soil. For instance, fibers, geotextile materials, Portland cement are added to the soil to alter the thermal conductivity and to prevent frost heave in road pavements [4, 19]. However, the use of such additives is limited only by changes in the thermal conductivity of the soil, while mPCM is capable of accumulating thermal energy.

mPCMs have demonstrated great potential for applications in thermal energy storage and temperature regulation and have attracted significant interest from numerous research areas. However, the use of mPCMs for the thermal stabilization of embankment soil in cold regions requires further research. Therefore, this paper assesses the applicability of mPCMs for road construction in cold regions based on modeling the temperature behavior of embankment soil.

2　Materials and Methods

For this study, the commercially available mPCMs were used. Two types of mPCM (both white, odorless powders) were selected for their respective phase transition temperatures of 3 °C and − 2 °C. The mPCMs were transported and stored in a vacuum container without moisture access. The PCM consists of a core of noctadecane paraffin encapsulated in a polymeric shell. Previous studies have reported that the polymeric shell is robust enough to withstand the mixing process during mixture preparation. Differential scanning calorimetry (DSC) was used to analyze the thermal properties of the two types of mPCM. In the temperature range from − 25 °C to 20°C was only one endothermic peak during the endothermic process, and there was one exothermic peak during the cooling process for both mPCM materials. Obviously, the mPCM underwent only one phase change in one vector of the scan temperature change. The physical and thermal properties of the mPCMs are presented in Table 1. The soil parameters used for this study are described by Kravchenko et al. [14]. A Quickline-30 thermal properties analyzer was used to determine the thermal properties of the soil–mPCM mixture (1% dry weight of the soil) via a testing procedure described in a previous study [20].

Table 1 Physical and thermal properties of mPCM

Property	mPCM (3ºC)	mPCM (− 2ºC)
Specific gravity (20ºC)	0.76	0.78
Mean particle size (micron)	18–22	17–20
Temperature Range (ºC)	1.7 to 4.3	− 0.9 to − 3.6
Melting process		
Peak temperature (ºC)	3.2	− 1.5
Enthalpy (J/g)	166.5	186.5
Thermal Conductivity (W/(m K))	0.67	0.79
Specific Heat (kJ/kg°C)	2.26	4.02
Crystallization process		
Peak temperature (ºC)	2.7	− 2.6
Enthalpy (J/g)	189.2	215.3
Thermal conductivity (W/(m K))	0.83	2.21
Specific heat (kJ/kg°C)	1.78	2.10

3 Numerical Model

Two regions were chosen for numerical simulations: (1) a section of the Wushu–Xining roadway on the Qinghai–Tibet Plateau with high-temperature unstable permafrost and (2) a section of seasonally frozen soils in Central Russia. Material properties used in the modeling were obtained from laboratory and field experiments presented in studies by Tai et al. [21, 22] and Liu et al. [3]. The characteristics of materials used for modeling seasonally frozen soil were presented in a previous study [23]. Numerical modeling techniques can be used to predict temperature variations in soils during freezing and thawing. In this study, a numerical model of heat transfer in an embankment with a soil–mPCM layer was implemented using COMSOL Multiphysics software.

Figure 1 shows a cross section for two embankments, where cross-section B includes the mixed soil–mPCM layer. mPCMs with phase change temperatures of 3 °C and − 2 °C were used for the seasonal and permafrost soil models, respectively. Input parameters for the numerical analysis are presented in Table 2. The thermal boundary conditions of the numerical models were constant temperatures of 8°C and − 1°C applied at the bottom of the seasonally frozen and permafrost soil models, respectively, with the sides of the subgrade set to be adiabatic. For the top boundaries of the models, temperatures were set equal to the average monthly air temperature of the respective regions, as presented in Table 2. Table 3 shows the following thermal properties of the roadbed, soil, and soil–mPCM mixture: the density of the solid particles ρ; the specific heat capacities C and the thermal conductivity of the materials λ.

Seasonal temperature variation on a highway pavement induces heat transfer in its embankment. According to Fig. 1, it is assumed that the embankment consists of horizontal soil layers with different thermal properties. In each layer, the soil
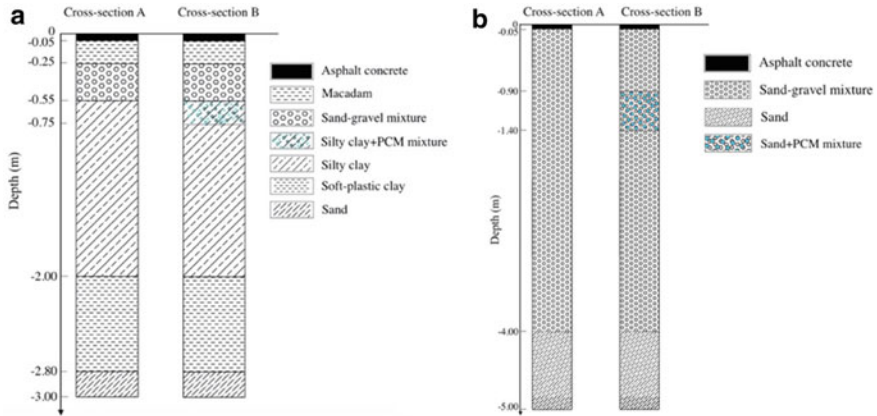
Fig. 1 Cross section of the embankment model: **a** for seasonally frozen soil and **b** for permafrost soil

Table 2 Average monthly air temperature (T_0, °C)

Month	I	II	III	IV	V	VI
T_0 for seasonally Frozen model	− 10	− 12	− 2	3	8	14
T_0 for permafrost model	− 16	− 18	− 10	0	3	5
Month	VII	VIII	IX	X	XI	XII
T_0 for seasonally frozen model	16	16	9	6	− 7	− 9
T_0 for permafrost model	5	6	2	− 5	− 6	− 14

Table 3 Input parameters in numerical analysis

ET[a]	Lithology	ρ, kg/m^3	λ, W/(m·K)	C, Jkg^{-1} °C^{-1}
Seasonally frozen soil	Asphalt	2200	1.10	1400.0
	Macadam	2250	0.79	1050.0
	Sand-gravel	1800	1.17	1254.2
	Silty clay	1400	0.83	1460.2
	Silty clay with mPCM	1400	0.81	1467.0
	Soft plastic clay	1620	0.81	2350.0
	Sand	1400	0.79	1466.0
Permafrost soil	Asphalt	2200	1.10	1400.0
	Sand-gravel	1800	1.17	1254.2
	Sand	1400	0.79	1466.0
	Sand with mPCM	1400	0.75	1490.0

[a] *ET* Embankment type

is assumed to be a saturated, isotropic porous medium. During the freezing and thawing processes, three zones can be distinguished in the soil: the unfrozen zone, consisting of soil particles and water pores; the partially frozen zone, consisting of soil particles, water pores, and ice pores; and the fully frozen zone, consisting of soil particles and ice pores. mPCM solid particles mixed into the soil constitute an additional phase in the porous media. PCM absorb and store energy, changing from solid to liquid as the outside temperature rises. Also, these materials have the ability to release previously accumulated energy when the temperature decreases during the change from a liquid to a solid state [24]. Therefore, depending on the mPCM phase change temperature, unfrozen or partially frozen zones can be divided into zones with mPCMs in liquid and solid states, which are connected by the transition zone of the mPCM. According to the energy conservation law, the heat transfer in soils can be described by the thermal conduction equation with equivalent thermal properties. To capture the latent heat released and absorbed during the water–ice phase transition and the phase transition of the PCM microcapsules, the apparent heat capacity method was adopted. Also, it is supposed that the thermal properties of the PCM microcapsules are negligible change due to the phase transition. The "Phase Change Material" module in COMSOL Multiphysics software provided the following thermal conduction equation:

$$\rho C \frac{\partial T}{\partial t} + \text{div}(-\lambda \text{grad} T) = 0 \tag{1}$$

where C is the volumetric heat capacity of the soil and ρ and λ are the equivalent density and thermal conductivity of soil. The volumetric heat capacity of the soil mixture is expressed as

$$\begin{aligned} C = \frac{1}{1+e}[&C_s \theta_s + C_{PCM(s)} \theta_{PCM} S_{PCM} \\ &+ C_{PCM(l)} \theta_{PCM}(1 - S_{PCM}) + C_w e(1 - S_i) + C_i e S_i] \end{aligned} \tag{2}$$

where C_s, C_i, and C_w are the volumetric heat capacities of soil grains, ice (is given as 2090 kJ/m^3 °C) and water (is given as 4180 kJ/m^3 °C), respectively; e is the void ratio of the soil mixture; $C_{PCM(s)}$ and $C_{PCM(l)}$ are the volumetric heat capacities of the PCM particles in the solid and liquid states, respectively; θ_s and θ_{PCM} are the volumetric fraction soil and PCM, respectively; S_i and S_{PCM} are the ice saturation and a function that indicates the state of the PCM particles, respectively. The ice saturation can be expressed through the mass moisture content w as

$$S_i = 1 - \frac{\rho_s}{\rho_w e} w \tag{3}$$

where ρ_s and ρ_w represent the densities of PCM reinforced soil and water, respectively. The volumetric fraction of PCM can be estimated as follows:

$$\theta_{\text{PCM}} = \frac{V_{\text{PCM}}}{V_{\text{tot}}} \tag{4}$$

where V_{PCM} and V_{tot} are the volume of PCM particles and the total volume of the soil mixture, respectively. The indicator function can be estimated as follows:

$$S_{PCM} = \begin{cases} 0, & T - T_{f,\text{PCM}} > \Delta T/2 \\ p(T), & -\Delta T/2 \leq T - T_{f,\text{PCM}} \leq \Delta T/2 \\ 1, & -\Delta T/2 < T - T_{f,\text{PCM}} \end{cases} \tag{5}$$

where $T_{f,\text{PCM}}$ is the freezing temperature of the PCM, ΔT is a small part of the transition zone, and $p(T)$ is a cubic polynomial. The heat released during the phase transition of the PCM particles can be determined as follows:

$$Q_{\text{pcm}} = L_{\text{PCM}} \rho_{\text{PCM}(s)} \theta_{PCM} \frac{\partial S_{\text{PCM}}}{\partial t} \tag{6}$$

where L_{PCM} is the latent heat of the phase transition of PCM; $\rho_{\text{PCM}(s)}$ is the density of solid PCM.

4   Results and Discussions

Figure 2 shows the computed soil temperature at different depths in the seasonally frozen region. Frost heave and thaw settlement occur mainly at the beginning and end of the cold season. Therefore, ΔH_1, ΔH_2, and ΔH_3 show the rise of the soil temperature zero point for external air temperatures of $-3\,°C$, $-5\,°C$, and $-7\,°C$ for March, November, and December, respectively. The effect of the inclusion of mPCM in the composition of the soil is most pronounced in the temperature range of the phase change of the mPCM. The results of the DSC thermogram showed that the mPCMs have a phase change temperature range, but not a point temperature, which is usually specified by the manufacturer. The difference in depth for the zero temperatures are 0.16 m, 0.08 m, and 0.12 m for the March, November, and December temperature regimes, respectively. From the data on the distribution of soil temperature with depth in December $(-9\,°C)$, it can be concluded that the mPCM application keeps the soil temperature far below $0\,°C$, with a maximum temperature rise of $1.4\,°C$. These results confirm that mPCMs can have a positive effect on the thermal field of embankment soils at the beginning of the cold season. The positive effect of the mPCM on the soil temperature distribution at $T_0 = -3\,°C$ (i.e., at the end of the cold season) demonstrates the cumulative effect of mixing mPCM into the soil. At the beginning of the cold period, the mPCM increases the soil temperature as it approaches the phase change interval of the mPCM, which keeps the soil temperature far below $0\,°C$ until the end of the cold period. Notably, the mPCM is most useful for thermal control at its own phase change temperature. This indicates that the mPCM

Fig. 2 Computed results of soil temperature distribution for seasonally frozen soil
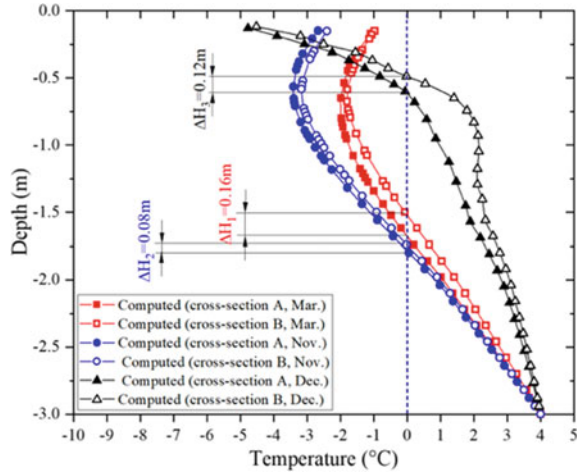
should be selected for a phase change temperature appropriate for the climate of the construction region.

Figure 3 shows the simulated soil temperatures of embankments at 120 cm, 160 cm, and 220 cm depth in the permafrost region with and without mPCM inclusion. At the 120 cm depth, the embankment without mPCM shows seasonal freezing and thawing of the active layer. In contrast, the 120 cm depth point is approximately in the middle of the soil layer when the mPCM is present. The effect of the mPCM at this depth is greatest in the third year of simulating the embankment's operation. The difference in soil temperatures at this depth for two cross sections is $\Delta T_{120}^3 = 0.88\,°C$. During the first two years of the summer months, the effect of the mPCM at this depth is not significant, potentially because the soil temperature is far below the mPCM's phase change temperature. The 160 cm depth point is located under the soil–mPCM layer in the sand–gravel mixture; notably, this depth is the permafrost table for the embankment, with and without mPCMs, for the climate of the region under study. At this depth, the addition of mPCM reduced the soil temperature rise in hot months by 0.47 °C, 0.97 °C, and 1.25 °C for the first, second, and third years of simulation, respectively. This demonstrates a cumulative effect from cycle to cycle because of the absorption and release of accumulated heat by the mPCM. At the 220 cm depth, there is a smooth time-dependent change in soil temperature. The maximum effect of mPCMs was recorded during hot periods of the first and second years of the simulations, with differences in soil temperatures $\Delta T_{220}^1 = 0.56\,°C$ and $\Delta T_{220}^2 = 0.37\,°C$ respectively; in March of the third year, the temperature difference $\Delta T_{220}^3 = 0.46\,°C$. The effect of mPCM on the temperature fluctuations at the 220 cm depth did not tend to increase. This can be explained by the large separation between this monitoring depth point from the soil–PCM layer and the influence of the underlying layers of permafrost. The results demonstrate the potential of using mPCMs to help prevent the temperature rise at embankments from degrading permafrost. However, the decision to use these materials should be based on an analysis of changes to the
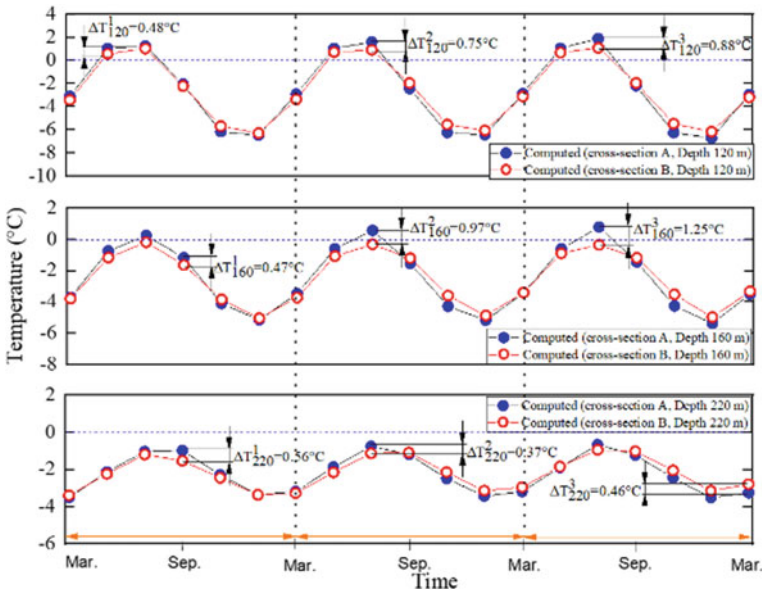
Fig. 3 Soil temperature changes of the embankment center with depths of 120, 160, and 220 cm in the permafrost region

permafrost table influenced by climate change and selected for the temperature range within which thermoregulation is required.

The region of seasonally frozen soil considered in this work is characterized by deep seasonal freezing of the embankment soils. In the course of this study, on the basis of monitoring the external temperature and soil temperature at different depths, the required temperature range was identified, within which temperature regulation is necessary for the embankment soils in this region. This temperature range is in good agreement with the paraffin mPCM temperature peaks determined by the DSC thermogram. The results of modeling the behavior of mPCM in a layer of the embankment, operated in a seasonally frozen region, confirm the presence of a cumulative effect of mPCM material in the soil. This effect allows to lower peak soil temperatures and stabilizing the soil temperature field and reduces the depth of seasonal freezing. The results also indicate that the mPCM materials are most useful in thermal control at their own phase change temperature. At the same time, for a region with degrading permafrost, the use of mPCM in the embankment layer may become a new way to maintain a negative soil temperature.

5   Conclusions

PCMs release and absorb latent heat during their phase transitions, which could help solve problems associated with seasonal freezing and thawing, as well as prevent the degradation of permafrost soil. From modeling two types of embankments, a positive effect of a mixed soil–mPCM layer on the soil temperature in a cold region was demonstrated. The simulations showed how including mPCM in the soil layer increased the maximum frozen depth during seasonal freezing and thawing. The maximum temperature increase in the soil–mPCM layer was 1.4 °C, which decreased the rate and depth of soil freezing in the cold season. Analysis of the temperature regime in the permafrost embankment showed that the inclusion of mPCM contributed to smoothing out the peak values of the temperature change amplitudes. These results indicate how applying an mPCM can improve the soil temperature stabilization during the degradation of permafrost. A cumulative effect of the mPCM on the ground temperature was observed, which increased from cycle to cycle. Further studies of mPCMs are needed for these applications, specifically to examine the morphological features in the soil structure and to identify the cost-effectiveness of using mPCMs in the construction of subgrade. Commercially available mPCM should be selected according to the manufacturer's stated melting point and latent enthalpy based on local climate data and target temperature for maximum performance. In the future, the use of mPCMs could become an effective alternative method for stabilizing the temperature regimes of soils in cold regions.

References

1. Wu Q, Zhang T (2008) Recent permafrost warming on the Qinghai-Tibetan Plateau. J Geophys Atmos 113
2. Biskaborn BK, Smith SL, Noetzli J, Matthes H, Vieira G, Streletskiy DA, Schoeneich P, Romanovsky V, Lewkowicz A, Abramov A et al (2019) Permafrost is warming at a global scale. Nat Commun 10:264
3. Liu J, Tai B, Fang J (2019) Ground temperature and deformation analysis for an expressway embankment in warm permafrost regions of the Tibet plateau. Permafrost Periglac Process 30(3):208–221
4. Orakoglu E (2017) Study on the thermal and mechanical properties of fiber- reinforced soil. Doctoral dissertation. Beijing Jiaotong University China, Beijing. http://en.njtu.edu.cn/
5. Ma B, Adhikari S, Chang Y, Ren J, Liu J, You Z (2013) Preparation of composite shape-stabilized phase change materials for highway pavements. Constr Build Mater 42:114–121
6. Peng G, Dou G, Hu Y, Sun Y, Chen Z (2020) Phase change material (PCM) microcapsules for thermal energy storage. Adv Polym Technol 2020:1–20
7. Konuklu Y, Ostry M, Paksoy HO, Charvat P (2015) Review on using microencapsulated phase change materials (PCM) in building applications. Energy Buildings 106:134–155

8. Paksoy H, Kardas G, Konuklu Y, Cellat K, Tezcan F (2017) Characterization of concrete mixes containing phase change materials. IOP Conf Series: Mater Sci Eng 251(1):012118

9. Alva G, Lin Y, Liu L, Fang G (2017) Synthesis, characterization and applications of microencapsulated phase change materials in thermal energy storage: a review. Energy Buildings 144:276–294

10. Arshad A, Jabbal M, Yan Y, Darkwa J (2019) The micro-/nano-PCMs for thermal energy storage systems: a state of art review. Int J Energy Res 43(11):5572–5620

11. Zhang X, Wang X, Wu D (2016) Design and synthesis of multifunctional microencapsulated phase change materials with silver/silica double-layered shell for thermal energy storage, electrical conduction and antimicrobial effectiveness. Energy 111:498–512

12. Rao Y, Liu J, Chang D, Kravchenko E (2021) Effects of microencapsulated phase change material characteristics on the thermal performance and mechanical behaviour of silty clay. Transp Geot 29(4):100584

13. Mahedi M, Cetin B, Cetin KS (2019) Freeze-thaw performance of phase change material (PCM) incorporated pavement subgrade soil. Constr Build Mater 202:449–464

14. Kravchenko E, Liu J, Chang D, Rao Y, Krainiukov A (2020) Study of the thermal field of a mixture of soil and PCM materials with simulation of the warming effect during a phase change. Const Build Mat 262

15. Kravchenko E, Liu J, Li X (2021) Numerical modeling of the thermal performance of soil containing microencapsulated PCM. Constr Build Mater 298(9):123865

16. Chen S (2008) Thermal conductivity of sands. Heat Mass Transf 44:1241

17. Zhang Y, Li C, Trettin C, Li H, Sun G (2002) An integrated model of soil, hydrology, and vegetation for carbon dynamics in wetland ecosystems. Global Biogeochem Cycles 16:1061

18. Miehle P, Lively SJ, Feikema PM, Li C (2006) Arndt, SK: Assessing productivity and carbon sequestration capacity of Eucalyptus globulus plantations using the process model Fores-DNDC: Calibration and validation. Ecol Model 192:83–94

19. Hejazi S, Sheikhzadeh M (2012) A simple review of soil reinforcement by using natural and synthetic fibers. Constr Build Mater 30:101–106

20. Orakoglu ME, Liu J, Niu F (2016) Experimental and modeling investigation of the thermal conductivity of fiber-reinforced soil subjected to freeze-thaw cycles. Appl Therm Eng 108:824–832

21. Tai B, Liu J, Wang T, Tian Y, Fang J (2017) Thermal characteristics and declining permafrost table beneath three cooling embankments in warm permafrost regions. Appl Therm Eng 123:435–447

22. Tai B, Liu J, Chang D (2020) Experimental and numerical investigation on the sunny-shady slopes effect of three cooling embankments along an expressway in warm permafrost region China. Eng Geology 269:105545

23. Burgonutdinov A, Kleveko V (2021) Monitoring of changes in the thermal regime in the road structure. J Phys: Conf Ser 1928(1):012047

24. Da Cunha SRL, De Aguiar JLB (2020) Phase change materials and energy efficiency of buildings: a review of knowledge. J Storage Mater 27:101083

Case Study on Application of an Innovative Method of Pulling Out the Earth Retaining Pile with Less Ground Surface Settlement

Michiho Taoka, Yoshinori Fukubayashi, Hiroaki Watanabe, and Yasuhiko Nishi

Abstract Temporally constructed steel sheet piles to retain the excavated ground wall at neighboring construction sites have been often left in the ground even after the backfill at the open-cut was completed. This is because the pull-out of steel sheet piles causes the non-negligible subsidence of the surrounding ground. In order to suppress ground deformation caused by the extraction, "A method of pulling out the earth retaining pile and filling filler at the same time" was developed and has been applied in more than 530 cases where the surrounding ground deformation was especially concerned. In this paper, a method of pulling out the earth retaining pile and filling filler at the same time is introduced, and its application is described. From the same case, the validity of the prediction of settlement of the surrounding ground during pull-out of steel sheet pile by the simple method is examined. As an initial step to develop three-dimensional elasto-plastic finite element method for evaluating ground deformation during the application of the simultaneous pull-out filling method, the mechanical properties of the filler are investigated taking curing period into account through uniaxial compression tests.

Keywords Earth retaining · Pulling out · Simultaneous filling

1 Introduction

When performing the excavation work associated with constructing underground structures, the pile retaining method utilizing steel sheet piles is used to prevent the collapse of the surrounding ground and to prevent the impact on surrounding ground settlement and structures. Once the underground structure is constructed and the excavation is backfilled, the retaining structure ends its role. Therefore,

---
M. Taoka · Y. Fukubayashi (✉)
University of Miyazaki, Miyazaki Prefecture, Japan
e-mail: fukubayashi@cc.miyazaki-u.ac.jp

H. Watanabe · Y. Nishi
Masters Cooperative, Osaka Prefecture, Japan

although the removal of the steel sheet piles has been considered, it is known that the ground loosens and deforms due to the adhesion of sediment to the steel sheet piles during extraction. Horiuchi and Shimizu measured the subsidence of the surrounding ground throughout the entire process from the placing of sheet piles to excavation, installation of structures, and backfilling work until sheet pile withdrawal. As a result, it was found that 60–90% of the settlement measured throughout the whole process occurred during the extraction of the sheet piles [1, 2]. Therefore, there are many cases in which steel sheet piles are left to remain in consideration of the influence on the adjacent structures. However, recent increases in the prices of construction materials, adaptation to a recycling society, and the achievement of SDGs [3] have made it necessary to pull out and reuse steel sheet piles even in adjacent construction work.

In order to pull out and reuse steel sheet piles, various measures have been taken to suppress ground deformation caused by the extraction. For example, Umezaki et al. [4] have developed a method to apply a liquid coating agent in which a special binder resin and a water-absorbent polymer are dispersed in an organic solvent in order to reduce the amount of sediment deposited on the steel sheet pile at the time of sheet pile extraction. In addition, after pulling out the entire length of the steel sheet pile, the gaps in the pull-out site are filled with sand, and chemical grouting is carried out. On the other hand, the newly developed "A method of pulling out the earth retaining pile and filling filler at the same time [5]," makes it possible to fill simultaneously the voids caused by pulling out of steel sheet piles with a filler that develops strength quickly once stagnant, following the extraction of the steel sheet pile. This method has been adopted mainly in areas where the surrounding ground deformation is a problem when using the conventional method, and it has been applied to more than 530 cases so far.

The purpose of this study is to develop a quantitative evaluation method of soil deformation using the finite element method for pull-out of steel sheet piles using a method of pulling out the earth retaining pile and filling filler at the same time [5] under various ground and environmental conditions. In this paper, the outline of the earth retaining member pull-out simultaneous filling method [5] is described, and the adoption case of this method is shown. Then, the validity of the prediction of settlement of the surrounding ground during pull-out of steel sheet pile by the simple method is examined from the construction case. As one of the initial steps to application of the three-dimensional elasto-plastic finite element method to the quantitative evaluation of soil deformation during the application of the simultaneous pull-out filling method [5], the uniaxial compression test results for modeling fillers are shown. Then, the direction of future research is shown.

2 Overview of the Method of Pulling Out the Earth Retaining Pile and Filling Filler at the Same Time

Figure 1 shows the construction procedure for the method of pulling out the earth retaining pile and filling filler at the same time [5]. In this method, the filler is injected from the filler pipe installed along the steel sheet pile in advance every time the steel sheet pile is pulled out 50 cm. The difference from conventionally applied ground deformation control methods, such as cement bentonite (CB) grouting, is that it simultaneously injects fillers and fills voids created by withdrawal, rather than pressuring chemicals into the soil particle voids. Because this newly developed method injects the fillers from the bottom edge of the sheet pile at the same time as it is pulled out, there is less time difference between the extraction and filling, and the settlement of the ground can be reduced. Eventually, the filler reaches the ground surface due to the negative pressure caused by the extraction. The filler remains in a liquid state while flowing and hardens as it stays in place and stagnant. Therefore, even if the gap caused by the extraction of steel sheet piles is filled with the filler in order from the edge of the steel sheet pile in the ground, it is considered that the filler will be reached to the ground surface by maintaining the liquid at the place where the filler is flowing. This filling phenomenon has been verified through full-scale model tests and field experiments. Photo 1 shows the solidified filler in the shape of the sheet pile found after removal of ground material in the full-scale model tests.
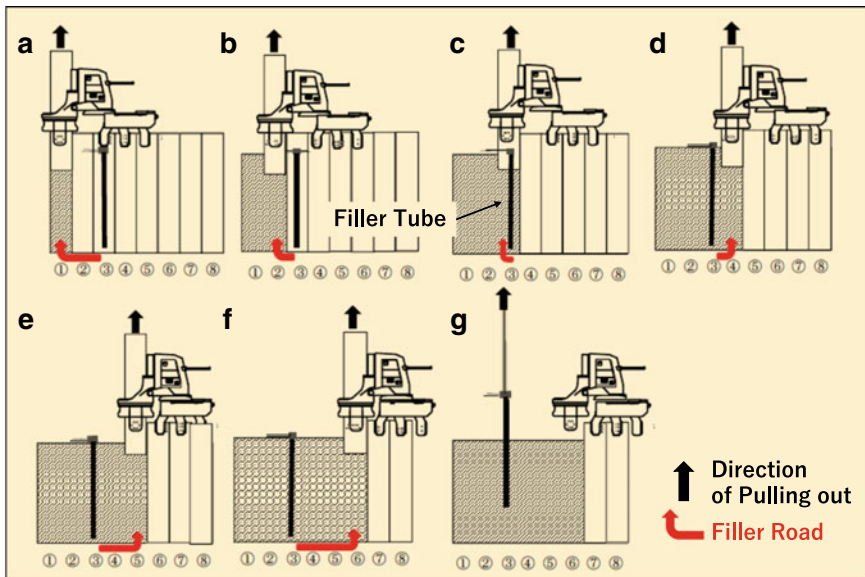
Fig. 1 Construction procedure for simultaneous pull-out of earth retaining members
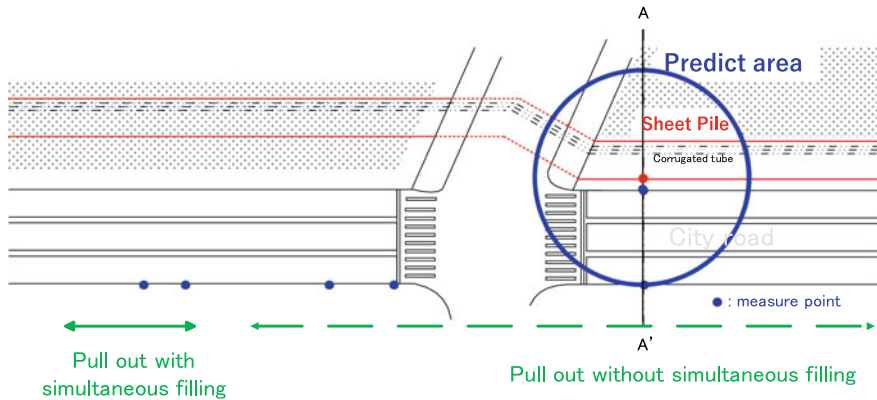
Photo 1 Solidified filler in the shape of the sheet pile found after removal of ground material

3   Application of the Simultaneous Pull-Out Filling Method for Each Retaining Members

The method of pulling out the earth retaining pile and filling filler at the same time is often applied at neighboring construction work, where the displacement and influence area of the surrounding ground needs to be controlled. It is also applicable to the removal of earth retaining structures placed in and around rivers and reservoir aiming to reduce piping phenomena. In addition, the impermeable filler-hardened walls left after the earth retaining walls have been removed with this method can prevent contaminants from leaking into adjacent areas after soil contamination suppression work.

A case of the application of this method to extracted steel sheet piles at a nearby the city road in service is shown in this chapter. Firstly, by the simple method, which is developed empirically, the influence range and settlement at the time of extraction by the conventional method was estimated and the estimated settlement was compared with the measured one. The measured settlement was then reported when the simultaneous pull-out filling method for earth retaining members was adopted at the same site.

3.1   Estimation of the Range of Influence and Settlement of Surrounding Ground During Extraction of Steel Sheet Piles Using the Simple Method

Firstly, the ground deformation was predicted using the current simple method, and its adaptability was evaluated.

According to the technical standards for neighboring construction [6], the range of influence for the ground deformation caused by soil retention and extraction is defined as the inside of a straight line connecting the bottom edge of the sheet pile to the ground surface at an angle of $(45° + \varnothing/2)$ from the horizontal [7, 8]. However, Horiuchi and Shimizu [7] reported that this method of prediction underestimated the settlement of the surrounding ground based on the results of settlement measurement in several earth retaining construction projects. They also proposed the application of the relationship diagram between the horizontal distance from the sheet pile and the amount of ground surface settlement (hereafter, "settlement diagram") summarized by Peck [9]. Peck [9] classified the relationship between the excavation depth and the amount of settlement of the background based on a wider range of actual values and proposed a settlement diagram categorized with the type of ground and the stability factor. In the settlement diagram of Peck [9], the relationship between the dimensionless amount of surface subsidence (S), which is the distance (D) from the earth retaining wall divided by the excavation depth (H), is shown. Peck's method was also proposed in the Standard Specifications for Tunnels as a simple method for predicting the displacement of the surrounding ground to examine the effect on the surrounding ground and its structures. Horiuchi and Shimizu [7] proposed a normalized and organized settlement diagram (hereinafter referred to as a modified settlement diagram) by dividing by the length of the steel sheet pile in the soil (L) instead of the excavation depth (H). Modified settlement diagram is classified into three types according to the type of ground, from region I to region III. Here, region I is sand and soft-hard clay, region II is very soft clay, region III is extremely soft clay, and the ground where there is deep clay below the bottom of the excavation is shown.

3.2 Construction Example

Figure 2 shows the plan view of the site of open-cut construction. A type III steel sheet pile with a length of 17.5 m in the soil was installed at this site. There were concerns about the influence on the city road located about 2.5 m away from the sheet pile when pulling out this steel sheet pile (AA' cross section in Fig. 2). Therefore, the settlement at the edge of the city road 12.28 m away from the soil retention due to pull-out was examined using a modified settlement diagram. This position was selected in order that the results are compared with the settlement measurements at this position. A cross section of the earth retaining wall is shown in Fig. 3 along with the soil types. Because the bearing layer is located at very deep, to be friction pile, the end of the pile is rooted 8 m into the soft clay layer with an average N value of 1. The upper layer consists of a sand layer with an average N value of 6 and an embankment layer with a thickness of 4 m. Since the average N value is less than 10 in all layers, this was assumed to be soft ground, and a study was carried out using area II of the modified diagram. As a result, as shown in Fig. 4, the predicted settlement was 228 mm. The measured settlement at the same distance from the earth retaining
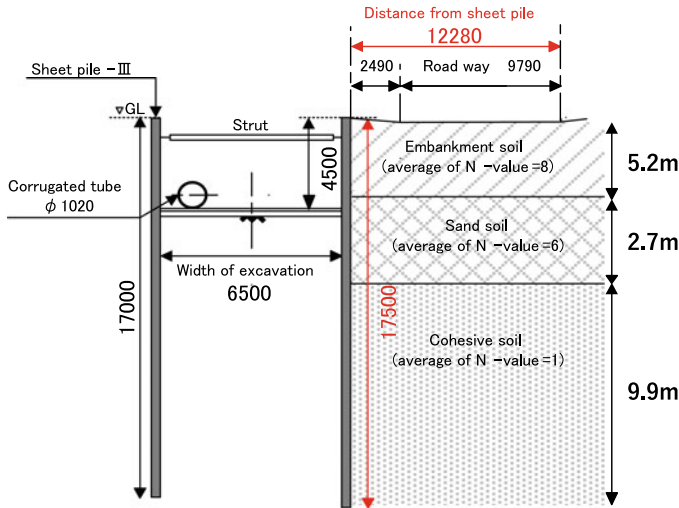
Fig. 2 Open-cut construction site (plan view)
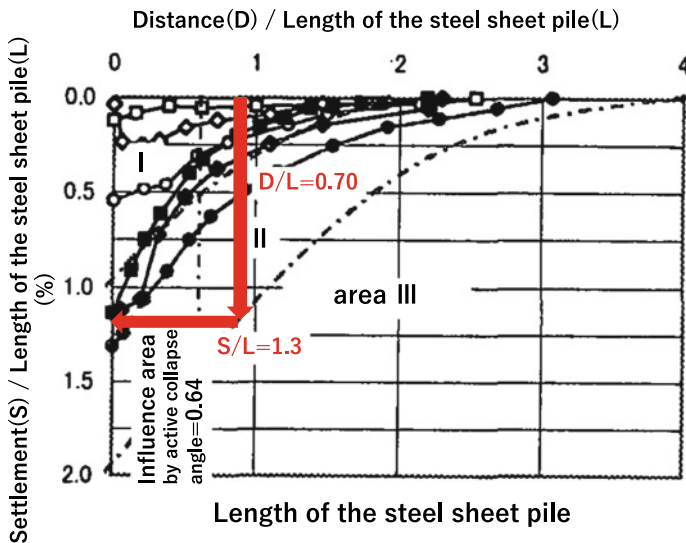
Fig. 3 Open-cut construction site (cross section)

was 201 mm. The settlement prediction using the modified settlement diagram was, therefore, considered to be reasonable.

On the other hand, a method of pulling out the earth retaining pile and filling filler at the same time [5] was adopted in another construction zone across the crossroad.

Fig. 4 Diagram of the process of studying the predicted settlement using a modified settlement diagram
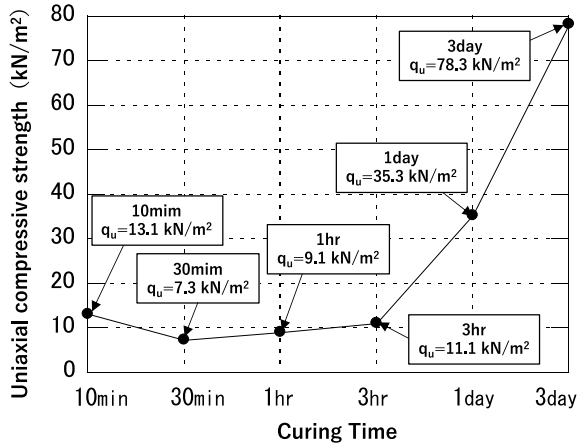
The amount of settlement at the same distance from the earth retaining wall was about 20 mm, confirming the effectiveness of this method.

In this construction case, the simple prediction was reasonably agreed with the actual settlement. However, if the displacement predicted by the simple method is considered to affect the surrounding ground, or if the simple method cannot sufficiently predict it due to complexity at the construction site, it is necessary to perform numerical analysis to measure the influence, such as generated stress and deformation, on the surrounding ground and existing structures in detail. Therefore, the authors have been conducting research to understand the deformation of the surrounding ground during pull-out by three-dimensional elasto-plastic finite elements and to quantitatively evaluate the deformation suppression effect of the pull-out simultaneous filling method. In the next section of this paper, as an initial step, an attempt in order to understand the mechanical properties of fillers is reported.

4   Basic Initiatives for Development of Ground Deformation Evaluation Methods for Simultaneous Extraction and Filling by FEM Analysis

Uniaxial compression tests were carried out to understand the strength characteristics of the filler. The filler is made by mixing two agents, one is a cementitious accelerator solution the other an aqueous curing solution. The specimens were cured in a constant temperature room at 75% humidity and room temperature of 18 °C. The curing times were 10 min, 30 min, 1 h, 3 h, 24 h, and 3 days. Three specimens were prepared for each curing time, and the average value was calculated after performing uniaxial compression tests.

Fig. 5 Transition of uniaxial compressive strength
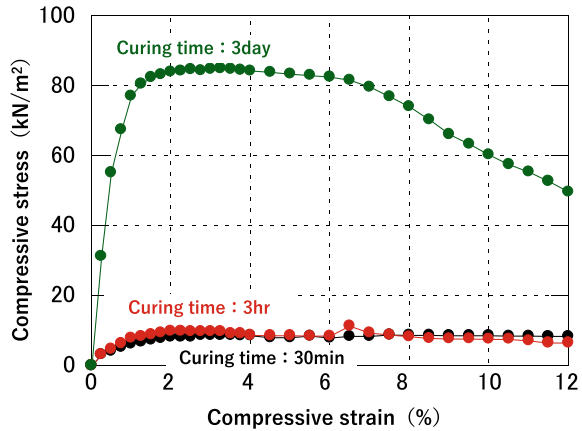
The transition of the uniaxial compressive strength with the curing period is shown in Fig. 5. Even after 10 min of curing, the uniaxial compressive strength exceeded 10 kN/m^2, and the strength increased to 80 kN/m^2 after three days of curing. This solidified filler after three days is with a moderate consistency of approximately 4–8 in terms of N-value conversion. It is observed that the uniaxial compressive strength after 10 min of curing was bit higher than that after 30 min and 1 h of curing. This might be due to inconsistency of in the stirring time and temperature during the preparation of the specimen.

Figure 6 shows the stress–strain relationship during uniaxial compression tests for specimens cured for 30 min, 3 h, and 3 d. After curing for 3 d, the compressive stress increased remarkably compared to other curing times. The specimens at each curing time showed linear elastic behavior at the initial stage of loading and yielded up to 2% strain. After that, it demonstrated constant strength. When the strain was more than 6%, the 3-day cured sample softened. Therefore, it is necessary to consider the modeling of the filler in the ground, taking into account the curing time.

5 Summary

(1) Through the model and in-situ tests, it was confirmed that the filler was injected and solidified into the shape of the steel sheet pile.
(2) A modified settlement diagram with reference to Peck's method was used to predict the amount of settlement that would occur during withdrawal without simultaneous filling. The settlement measured in the case presented was close to the predicted value.
(3) The conventional method and simultaneous filling and pulling out were conducted in a 300-m-long plot. The settlement on the surrounding ground was reduced by the adoption of the simultaneous pull-out filling method.

Fig. 6 Stress–strain relationship

(4) Uniaxial compression tests of fillers cured for 30 min, 3 h, and 3 d were carried out to investigate the stress–strain relationship.

Moving forward, we shall examine the reproduction method of pull-out and pull-out simultaneous filling in terms of three-dimensional elasto-plastic finite element analysis. Based on data from more than 530 actual construction projects to date, the results of the calculations are compared with the measured settlement to verify the validity and applicability of the numerical calculation method.

References

1. Ichikawa A, Imori H, Fujimaru T, Tsuruoka I (2009) Settlement of surrounding ground due to extraction of sheet piles and its countermeasure. In: 2009 Annual conference of Japan society of civil engineers Kansai Branch, vol VI
2. Horiuchi T, Shimizu M (1997) Settlement of ground by braced excavation and damage of wooden houses in vicinity. Environ Eng Res 35
3. United Nations, Department of Economic and Social Affairs, Sustainable Development; https://sdgs.un.org. 05 Nov 2022
4. Umezaki T, Kawamura T, Okamoto K, Hattori A, Kobayashi Y (2018) Swelling properties and coefficient of permeability of friction-reducing polymer for pull-out of temporary sheet piles. Soils Found 58(4):797–807
5. GEOTETS society https://www.hikinuki.jp. 21 Oct 2022
6. Ministry of Construction Public works research institute: The guideline for design and construction of proximity foundation (1983)
7. Horiuchi T, Shimizu M (2001) Influences on ground displacements caused by pulling out the sheet piles walls. In: Proceedings of the symposium on underground space, vol. 4. JSCE
8. Shimizu, M, Hayakawa K, Kaji Y (2004) Issues in evaluating the impact of surrounding ground subsidence pictures in earth retaining open cut construction in soft ground. In: The 59th annual conference of Japan society of civil engineers, p 9
9. Terzaghi T (ed) (1996) Settlement due to extraneous causes. In: Soil mechanics in engineering practice, Chapter10, Wiley. A Wiler-Interscience Publication, pp 457–473

Case Studies of Vibration Method to Evaluate Residual Tensile Force of Ground Anchors

Naoto Ogawa ⓘ **, Takamasa Niibe** ⓘ **, Hideki Saito** ⓘ **, Mitsuru Yamazaki** ⓘ **, and Atsushi Yashima** ⓘ

Abstract In the maintenance of slopes and infrastructures stabilized by ground anchors, it is important to evaluate the residual tensile force of the anchors. Generally, a lift-off test is used to measure the residual tensile force. The test is performed by placing a hydraulic jack on the extra part of the PC steel wire at the anchor head and loading a tensile force. The measurement principle of the test is clear, and the results are reliable. However, the test has the following problems: (1) anchors have the risk of breaking or ejection, so safety equipment is needed to protect operators from the ejection of anchors, (2) the cost of the test is expensive. To solve these problems, our group developed a non-destructive and non-loading test method to determine the residual tensile force by measuring the resonant frequency of the free part of the wire. We named the new test method "non-lift test", and we are working toward the practical application of this method and are conducting measurements to determine its applicability. We conducted measurement tests on several standards of anchors. As the results, it is found that the discrepancy between the residual tensile forces obtained by lift-off and non-lift tests is less than 10%.

Keywords Ground anchor · Residual tensile force · Non-destructive measurement · Resonant frequency

N. Ogawa (✉) · T. Niibe · H. Saito
OYO Corporation, Saitama 3310812, Japan
e-mail: ogawa-naoto@oyonet.oyo.co.jp

M. Yamazaki
Central Nippon Highway Engineering Nagoya Co., Ltd., Nagoya 4600003, Japan

A. Yashima
Gifu University, Gifu 5011193, Japan

1 Introduction

Ground anchoring was introduced to Japan from Europe in the late 1950s and has now become an indispensable construction method to reinforce infrastructures and slopes.

In order to stabilize the ground, a number of anchors are installed on a slope. To maintain the stabilizing function of the anchors, it is necessary that the anchors are not corroded and maintain residual tensile force within the expected range. In particular, to maintain the residual tensile force, it is important to inspect the residual tensile force periodically and to apply tension again or relax the tension as necessary. Furthermore, the stability of the anchoring slope can be evaluated by investigating the residual tensile force of some ground anchors and estimating the surface residual tension distribution of the slope.

Maintenance of ground anchors is often performed in the following order in Japan [1]. First, check the anchor visually and by hammering at regular inspections. If an abnormality of the anchor is found by the inspection, detail surveys will be conducted, which include the appearance survey of the anchor head, the exposure survey of the anchor head, lift-off test, and so on. Among these surveys, the lift-off test is the one which measures the residual tensile force of the anchor. The test is performed by placing a center-hole hydraulic jack on the extra part of the PC steel wire at the anchor head and loading a tensile force. The measurement principle of the test is clear, and the results are reliable. The hydraulic jacks for construction have been used for a long time. But performing the test by using the jacks requires temporary scaffolding and cranes to carry in and out due to their weight, and in some cases, traffic restriction on the road, which makes the survey large scale. To solve these problems, a small and lightweight SAAM jack was developed [2]. By using SAAM jacks, the survey cost per anchor and the number of tests per day were greatly improved compared to hydraulic jacks for construction.

Although the development of SAAM jacks has improved efficiency of the test, the following problems remains in the lift-off test.

- Anchors have the risk of breaking or ejection, so safety equipment is needed to protect operators from the ejection.
- The test cannot be performed on significantly rusted anchors due to a risk of rupture of the anchor.
- Anchors in a state of overstrain do not lift off even when loaded to near the yield tensile force of the tendon. In that case, the residual tensile force cannot be determined even by the lift-off test.

In order to solve these problems, our group developed a non-destructive and non-loading test method to determine the residual tensile force by measuring the resonant frequency of the free part of the tendon [3]. We named the new test method "non-lift test", and we are working toward the practical application of this method and are conducting measurements to confirm its applicability. In this paper, we report the field measurement results of the non-lift test and compare them with the results of the lift-off test.

2 Principle of Non-lift Test

When the free length of tendon vibrates in the lateral direction, two restoring forces act: one due to bending rigidity and the other due to tensile force. The free length vibrates like a "beam" when the effect of bending rigidity is large, and vibrates like a "string" when the effect of bending rigidity is small and the restoring force due to tensile force is dominant. Shinke et al. proposed relational equations between the tensile force and the natural frequency [4]. The equations are classified by the value of the parameter ξ defined by Eq. (1).

$$\xi = \sqrt{\tfrac{T}{EI}}L \tag{1}$$

where T is tensile force, L is free length of tendon, E is Young's modulus, and I is the moment of inertia.

The ξ indicates the influence of the bending rigidity. If ξ is sufficiently large, the effect of bending rigidity is small and the free length vibrates like a string. On the other hand, when ξ is small, the effect of bending rigidity increases and the free length vibrates like a beam.

The equations Shinke et al. proposed are following Eqs. (2)–(4).

When $3 \leq \xi \leq 17$,

$$T = 4L^2 f^2 \mu \left\{ 0.857 - 10.89 \left(\tfrac{c}{f} \right)^2 \right\} \tag{2}$$

When $17 \leq \xi \leq 100$,

$$T = 4L^2 f^2 \mu \left\{ 1 - 2.2 \left(\tfrac{c}{f} \right) - 2 \left(\tfrac{c}{f} \right)^2 \right\} \tag{3}$$

When $\xi > 100$,

$$T = 4L^2 f^2 \mu \tag{4}$$

where f is natural frequency, μ is line density, and c is defined by Eq. (5).

$$c = \sqrt{\tfrac{EI}{\mu L^4}} \tag{5}$$

Our group confirmed the validity of these equations by conducting small and full-scale model experiments that allowed direct measurement of free length vibration [5]. We confirmed that resonant vibration was excited in the tendon by applying vibration at the extra length of the anchor, and that the resonant frequency could be measured at the extra length.

3   Measurement Procedure of Non-lift Test

The non-lift test was performed with a small vibrator and accelerometers attached to the steel extra length of the anchor head. A schematic diagram of the measurements is shown in Fig. 1.

   We performed the non-lift test by following procedure. First, we place a small vibrator and accelerometers on the extra part of the wire at the anchor head. The waveform generated by the vibrator is a sweep waveform whose frequency of a sinusoidal wave increases continuously with time. The vibration is applied for 60 or 120 s with a frequency increase rate of 1 oct/min or less. In anchors with multiple steel wires, accelerometers are attached to the vibrated steel wire and the adjacent steel wires.

   Figure 2 shows an example of measurement data and analysis. This is a record that a steel wire at K-1 anchor in Table 1 described later was vibrated, and the vibration was received at the adjacent steel wire. The sweep frequency was 0.4 octave from 15 to 21 Hz, and the sweep time was 2 min. The upper right of the figure is the time history waveform, the lower right is the spectrogram obtained by the running spectrum analysis, and the lower left is the Fourier spectrum of each time window during the running spectrum analysis. An isolated peak on the spectrogram at 18.9 Hz was determined as a resonant point, which showed the resonant frequency. For anchors with multiple steel wires, we measured the resonant frequency for each vibrated steel wire, and obtained the resonant frequency of the anchor by averaging over the number of steel wires. We consider the measured resonant frequency as the natural frequency of the free part of the wire and calculate the residual tensile force from it by using Eqs. (2)–(4). The calculated residual tensile force is expressed as P in later chapters.
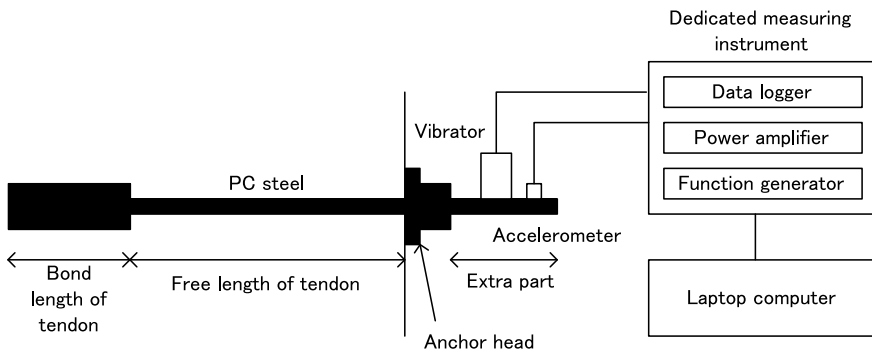
Fig. 1 Schematic diagram of the ground anchor and the measuring systems for non-lift test
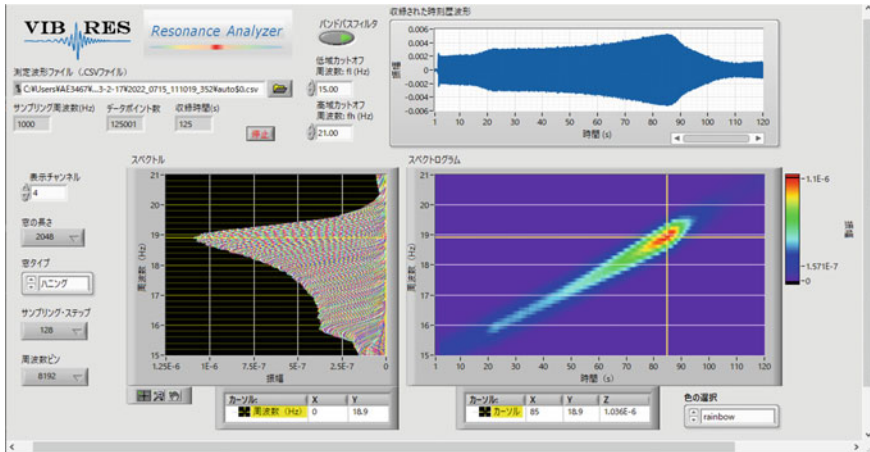
Fig. 2 An example of analysis to obtain the resonant frequency (18.9 Hz). The data was measured at K-1 anchor in Table 1 described later

4 Field Test

In order to compare the results of lift-off test and non-lift tests, we performed non-lift tests on ground anchors that were actually installed.

4.1 Dataset

A total of 28 anchors were investigated on 12 slopes from A to L in Japan, as shown in Table 1. The tests were performed on the following seven types of anchors; SEEE, KP, VSL, SHS, FLO, SFL, and EHD. The free lengths ranged from 4.0 to 15.5 m. Lift-off tests were performed on all anchors, and residual tensile force was determined for 26 of these anchors. Anchors B-3 and B-4 did not "lift off" after 250 kN of tensile force loading, and no residual tensile force was determined because there was a risk that the anchor would break if we loaded it any further.

4.2 Result

The residual tensile forces estimated from the non-lift test (P) and measured by the lift-off test (Pe) are shown in Table 1, and the comparison of Pe and P is shown in Fig. 3. The relationship between Pe and P is approximately 1:1, and the error of P with respect to Pe is within $\pm$ 10% at most. There is no systematic difference in error due to differences in anchor type or tendon free length.

Table 1 Results of lift-off test and non-lift test on target anchors

Slope	Anchor number	Anchor standard	The free length of the tendon (m)	The residual tensile force measured by lift-off tests Pe (kN)	The residual tensile force estimated by non-lift tests P (kN)	Error (P–Pe)/Pe (%)
A	A–1	SEEE F70U A	7.2	321.8	320.0	− 0.6
	A–2		7.2	310.0	306.8	− 1.0
	A–3	SEEE F100U A	13.1	344.0	343.4	4.6
	A–4		13.1	378.7	356.0	− 9.3
	A–5		13.1	376.6	236.0	− 5.5
B	B–1	KP 5–2	7.5	225.0	174.0	4.9
	B–2		7.5	172.0	251.0	1.2
	B–3		7.5	> 250	284.0	–
	B–4		8.0	> 250	163.1	–
C	C–1	VSL E 5–3	5.5	170.0	251.6	− 4.1
	C–2		4.0	243.2	195.1	3.5
D	D–1	VSL E 5–3	5.5	194.7	281.0	0.2
	D–2		13.5	283.6	249.1	0.9
	D–3		9.5	253.7	243.5	− 1.8
	D–4		15.0	291.4	262.7	− 2.5
E	E–1	SHS S5–3	13.5	258.0	275.2	− 5.6
	E–2		15.5	252.0	259.0	4.2
	E–3		15.5	253.0	246.0	8.8
F	F–1	VSL E 5–4	10.0	250.0	242.0	3.6
G	G–1	FLO E −3	6.0	266.0	246.0	− 7.5
	G–2		6.0	265.0	242.	− 8.7
H	H–1	VSL E 5–2	8.0	119.0	126.0	5.9
I	I–1	SFL–1	13.0	62.0	57.0	− 8.1
	I–2		9.0	35.0	36.0	2.9
J	J–1	VSL E 5–3	4.0	200	185.0	− 7.5
K	K–1	EHD 5–4	9.5	421.0	408.0	− 3.1
	K–2		14.5	386.0	409.0	6.0
L	L–1	EHD 5–3	10.0	202.0	201.0	− 0.5
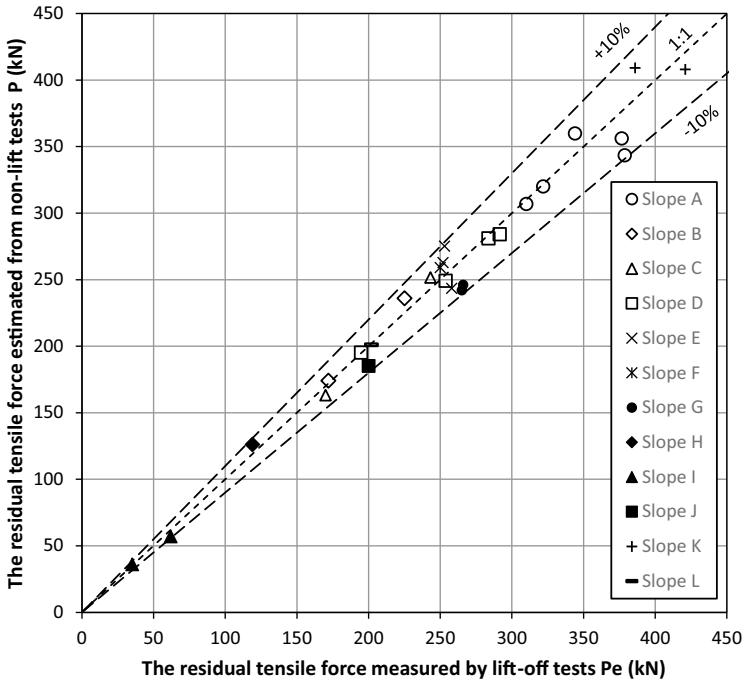
Fig. 3 Comparison of the result of lift-off tests (Pe) and non-lift tests (P)

4.3 Discussion

In B-3 and B-4, where the residual tensile force could not be determined by the lift-off test, the residual tensile force higher than the maximum load in lift-off test was estimated by the non-lift test. This method is characterized by its ability to safely estimate the residual tensile force even for such over-tensioned anchors.

In the example recordings shown in Fig. 2, the resonant points are clearly seen as sharp spectral peaks. On the other hand, there were data in which multiple peaks were observed and data in which the resonant point was unclear. In the future, standardization of the method for reading resonant frequencies will be necessary.

Also, we are studying whether it is possible to measure the residual tensile force with accuracy that does not cause practical problems even if the test is performed using a simplified procedure. If the tensile force can be measured in a short time by improving the procedure, the survey cost will be reduced and more anchors can be measured. That would facilitate sustainably maintaining infrastructure.

5   Conclusion

The field applicability experiments have shown that the non-lift test is applicable to seven types of anchors. We believe that the results of the field application experiments demonstrate the effectiveness of this test method. We consider that the effectiveness of this test has been demonstrated because the estimated residual tensile force is within the range of 10% error.

In the future, in order to disseminate this test method, we believe that it is necessary to standardize the method of identifying the resonant frequency and improve the test procedure so that it can be performed in a shorter time.

References

1. Public Works Research Institute, Japan Anchor Association, Mie University, and NEXCO Research Institute Co. Ltd. (eds.): Ground Anchor Maintenance Manual. Gihodo Shuppan, Tokyo (2020). (in Japanese)
2. Japan Geotechnical Consultants Association: Lift-off Test Manual Using SAAM Jacks for Ground Anchor Maintenance (2008). (in Japanese)
3. Saito H, Yamazaki M, Yashima A, Nawa I, Aoike K, Sone Y (2021) Estimation of ground anchor tension by vibration method. J Jpn Soc Civil Eng Ser C (Geosphere Eng) 77(3):213–232 (2021). (in Japanese)
4. Shinke T, Hironaka K, Zui H, Nishimura H (1980) Practical formulas for estimation of cable tension by vibration method. J JSCE 294:25–32 (in Japanese)
5. Nawa K, Yashima A, Murata Y, Kariya K, Saito H, Aoike K, Sone Y, Yamazaki M (2021) Evaluation of ground anchor residual tension by vibration method. In: Hazarika H, Madabhushi GSP, Yasuhara K, Bergado DT (eds) Advances in sustainable construction and resource management. Lecture notes in civil engineering, vol 144. Springer, Singapore, pp 271–282

Centrifuge Modeling of Highway Embankment Improved by Hybrid Type Reinforcement

Chengjiong Qin, Hemanta Hazarika, Yoshifumi Kochi, Masanori Murai, Hideo Furuichi, Guojun Liu, Naoto Watanabe, Shinichiro Ishibashi, and Daisuke Matsumoto

Abstract The 2016 Kumamoto Earthquakes destroyed a few highway embankments of the Kyushu Expressway in the Kumamoto province, located at the saturated, loose sandy foundation. To reduce the potential risk of earthquake-induced damage, such as these embankment failures, an innovative low-cost hybrid type reinforcement was developed, consisting of vertical and inclined piles. This study presents a series of centrifuge tests modeling the performance of highway embankments subjected to embankment failure. The sinusoidal wave with a peak shaking amplitude of 0.2 g was adopted. Several aspects regarding the behaviors of excess generation of pore water pressure, pile bending moment and embankment settlement under four configurations were revealed and discussed. The centrifuge test results illustrate the hybrid type reinforcement with the angle (55°) between the vertical and inclined pile which has the greater performance during the dynamic loading.

C. Qin (✉) · H. Hazarika
Kyushu University, Fukuoka, Japan
e-mail: qinchengjiong@yahoo.co.jp

Y. Kochi
K's Lab Inc., Yamaguchi, Japan

M. Murai
Shimizu Corporation, Tokyo, Japan

H. Furuichi
Adachi Architectural Design Office Co., Ltd., Tokyo, Japan

G. Liu
Takenaka Corporation, Chiba, Japan

N. Watanabe
KFC Ltd, Nagoya, Japan

S. Ishibashi
Nihon Chiken Co., Ltd, Fukuoka, Japan

D. Matsumoto
Japan Foundation Eng., Co., Ltd., Fukuoka, Japan

1 Introduction and Background

In the process of an earthquake, saturated loose sand is characterized by a significant increase in excess pore water pressure, which results in a drastic loss of strength and stiffness. When the excess pore water pressure reaches the initial effective overburden stress, liquefaction occurs, which often results in severe damage. Recently, the NEXCO report [1] cited an example of a liquefaction-induced embankment failure, in which a road embankment in the town of Mashiki, Kumamoto region, suffered severe damage as a result of the 2016 Kumamoto Earthquakes. Previous centrifuge tests indicate the main reason for road embankment failure is the liquefaction of the lower saturated loose soil layer [2].

To reduce the potential risk of liquefaction-induced damage, such as these embankment failures, an innovative low-cost hybrid type reinforcement was developed [3, 4], consisting of vertical and inclined piles. The vertical piles are used to suppress the lateral deformation of embankment slope failure, and inclined piles are installed at the top of vertical piles, fixed to each other, providing an additional restraining force to the vertical piles against lateral loading, reducing soil movement due to dynamic loadings. 1 g shaking table tests and 2D numerical analysis with the model size were produced by Hazarika et al. [3] to examine the effectiveness of this proposed technique during two different sine waves. Qin et al. [4] continued to investigate this new countermeasure in the prototype size subjected to the 2016 Kumamoto Earthquakes using FEM analysis in the two dimensions. This study presents a series of centrifuge model tests to determine the performance of hybrid type reinforcement to prevent road embankment failure during earthquake loadings.

2 Experimental Methods

2.1 Experimental Setup and Produces

A series of centrifuge model tests were carried out at DPRI (Disaster Prevention Research Institute), Kyoto University, Japan, using a beam type geotechnical centrifuge machine, which has an effective radius of 2.5 m. This machine has the maximum reachable centrifugal acceleration of 200 g for static and 50 g for dynamic tests. The input motion for the dynamic test was operated using a displacement control system. Therefore, the calibration test, which has a similar weight to model tests, was performed using the accelerometer to examine several input motions with the desired amplitude and frequency. More details about the centrifuge facility at DPRI were introduced by Ueda et al. [5].

2.2 Model Description

If conventional scaling laws were applied for the centrifuge model tests, the highway embankment was too large for the centrifuge machine (arm's length = 2.5 m). To model a large-scale prototype subjected to earthquake loadings with current centrifuge facilities, Iai et al. [6] have proposed a generalized scaling law by combining the existing 1 g scaling scale [7] with the scaling rules of centrifuge model tests. Tobita et al. [8, 9] validated the generalized scaling law for dry and saturated sand by conducting a series of centrifuge model tests. The prototype-to-model ratio (λ) was chosen as 120, and the centrifuge tests were carried out in the gravity field of 40 g. The generalized scaling law ($\mu = 3$ and $\eta = 40$) was adopted to determine the various parameters for the earthquake loadings, as shown in Table 1.

The internal dimensions of the rigid soil container, which was used for the tests, are 550 mm (L) X 162 mm (W) X 400 mm (H). Figure 1 presents the top and front views of the centrifuge model test (hybrid type reinforcement). The model foundation consisted of a 70 mm thick loose Toyoura sand layer underlain by a 100 mm thick dense Toyoura sand layer. The lower soil layer was of relative density, approximately Dr = 90%, assumed as hard strata representing bedrocks. The upper soil layer was of relative density, around Dr = 60%, which was filled using the sand raining method to obtain a uniform relative density throughout the depth. After two sand layers were prepared, centrifuge test models were saturated with viscous fluid, made by Metolose, to reach a viscosity of 91.2 cSt following the generalized scaling laws. It took around 24 h to complete the saturation for each case. The soil used was a mixture of Toyoura sand and Kaolin clay at 9:1 according to dry weight to construct the highway embankment after the foundation saturation. The density of

Table 1 Scaling factors (=prototype/model) in physical-model tests

Items	Scaling factors for 1 g test		Scaling factors for centrifuge test		Generalized scaling factors	
Length	μ	3	η	40	$\mu\eta$	120
Density	1	1	1	1	1	1
Time	$\mu^{0.75}$	2.3	η	40	$\mu^{0.75}\eta$	91.2
Stress	μ	3	1	1	μ	3
Pore pressure	μ	3	1	1	μ	3
Displacement	$\mu^{1.5}$	5.2	η	40	$\mu^{1.5}\eta$	207.8
Acceleration	1	1	η^{-1}	0.025	η^{-1}	0.025
Frequency	$\mu^{-0.75}$	0.44	η^{-1}	0.025	$\mu^{-0.75}\eta^{-1}$	0.011
Permeability	$\mu^{0.75}$	2.3	η	40	$\mu^{0.75}\eta$	91.2
Viscosity	$\mu^{-0.75}$	0.44	η^{-1}	0.025	$\mu^{-0.75}\eta^{-1}$	0.011
Bending stiffness	$\mu^{4.5}$	140.3	η^4	2.6×10^6	$\mu^{4.5}\eta^4$	3.6×10^8
Bending moment	μ^4	81	η^3	6.4×10^4	$\mu^4\eta^3$	5.2×10^6

Unit: mm (Prototype size in parentheses, Unit: m)
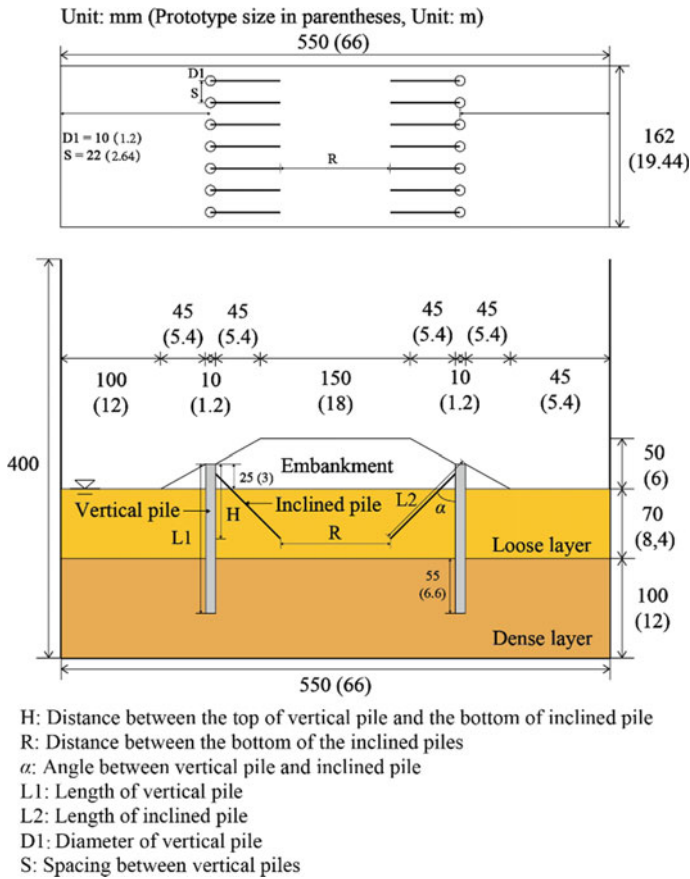
Fig. 1 Centrifuge model test for model and prototype sizes in top and front view (hybrid type reinforcement)

this soil was 2.0 g/cm^3 with a water content of 15% using the viscous fluid. The upper embankment was relatively loose not to disturb the loose sand layer.

Further details about the physical properties of vertical and inclined piles are shown in Table 2. The configurations of each model test are referred to in Fig. 1 and Table 3. Centrifuge model tests were conducted for four different configurations of highway embankment and foundation: (Case 1) unreinforced foundation of embankment, (Case 2) only two rows of vertical piles to support embankment, (Case 3a) hybrid type reinforcement (angle between the vertical and inclined pile, $\alpha = 45°$) and (Case 3b) hybrid type reinforcement ($\alpha = 55°$).

Instrumentations for the tests are shown in Fig. 2. Six pore water pressure gauges (P1–P6) were installed in the loose and dense layers; one sensor (P6) in the free field, two sensors (P1 and P5) below the toe of the embankment slope and three sensors (P2, P3 and P4) in the middle line of the embankment. Five accelerometers (A1–A5)

Table 2 Physical properties of the aluminum vertical and inclined pile

Property	Vertical pile	Inclined pile
Outer diameter	10 mm	2 mm
Inner diameter	8 mm	–
Length	150 mm	106/131 mm
Young's modulus	70 GPa	70 GPa
Second moment of area, I	289.8 mm^4	0.8 mm^4

Table 3 Test program, Unit: mm (Prototype size in parentheses, Unit: m)

Tests	Vertical pile	Inclined pile	H	L2	R	α
Case 1	✗	✗	–	–	–	–
Case 2	○	✗	–	–	–	–
Case 3a	○	○	75(9)	106(12.7)	110(13.2)	45°
Case 3b	○	○	75(9)	131(15.7)	46(5.5)	55°

were used to record at different locations of the model. An accelerometer (A5) is attached to the bottom of the soil container and is used to record the input motion. Figure 3 displays two piles (piles 1 and 2) at the center of the row instrumented with the strain gauges to record the bending moments under dynamic loadings. In addition, soil displacement was obtained by processing the digital images taken in the front view from a high-speed camera.

2.3 *Dynamic Loadings*

The sinusoidal acceleration wave was applied at the bottom of the soil container. The input motion was of acceleration amplitude of 8.0 g (corresponds to 0.2 g in the prototype scale). Figure 4 illustrates the time history of acceleration, recorded at the bottom (A5) in Case 1.

3 **Experimental Results**

3.1 *Excess Pore Water Pressure*

Figure 5 shows time histories of excess pore water pressure (EPWP) and the effective vertical stress for 4 cases in six different locations (P1–P6) during the earthquake loading. The condition of soil liquefaction is defined as excess pore water pressure
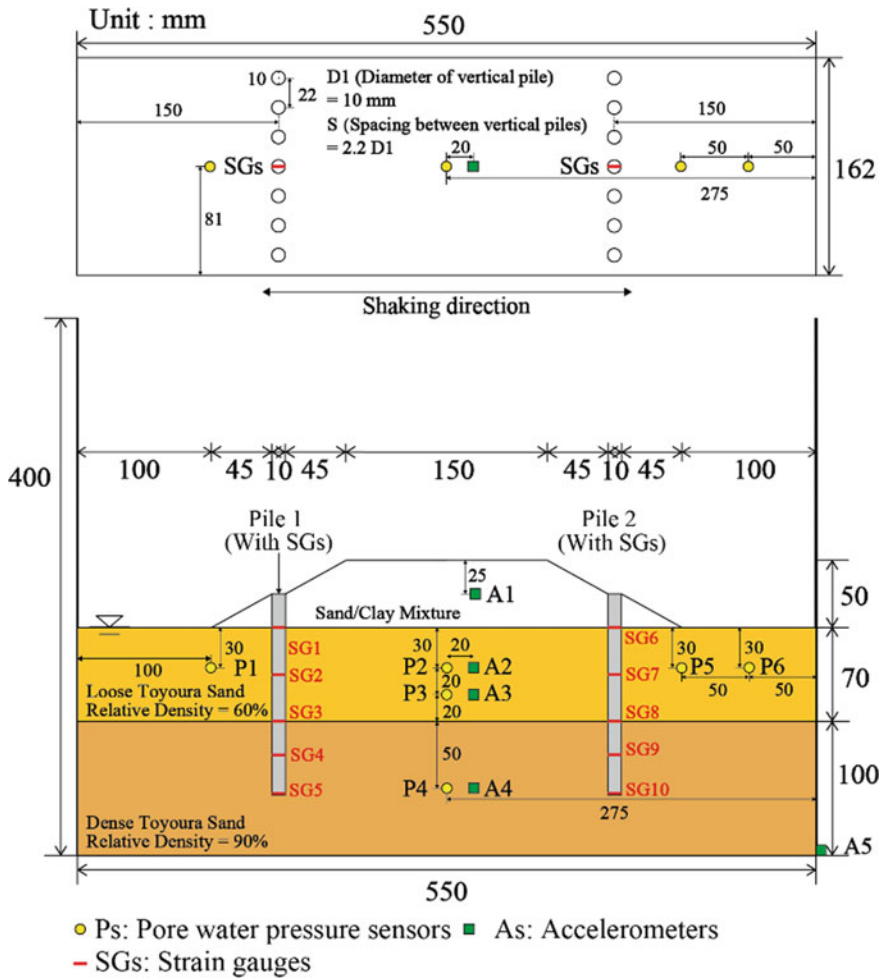
Fig. 2 Test setup and instrumentations for case 2 in the top and front view
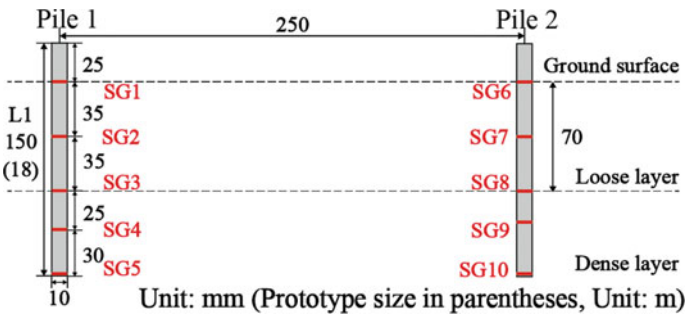
Fig. 3 Pile layout

Fig. 4 Input motion achieved at the bottom of soil container in case 1
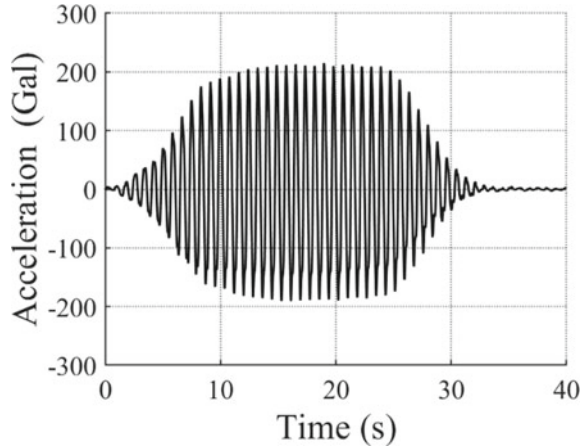
ratio ($Ru = u/\sigma'$) = 1.0, where u is the excess pore pressure generated under earthquake loading and σ' is the initial effective vertical stress. An important observation is that the process of soil liquefaction is initiated in the free field, which occurred more quickly with a few loading cycles with the increase of the shaking intensity. It is interesting to note that the dissipation occurred lately after the dynamic loadings. It was found that the excess pore water pressures, which were recorded at P1, P5, and P6, with both positive and negative amplitude, developed in the vicinity of the ground surface. The negative excess pore water pressure was observed at P2 in Fig. 5 due to the capillarity of the upper unsaturated embankment. In addition, the soil below the toe of the embankment slope did not reach liquefaction due to the soil improvement by installing vertical piles. The maximum excess pore water pressures were observed in the dense layer (P4). The responses (P2 and P3) show Case 3a and 3b have lower excess pore water pressures during earthquake loading, demonstrating the reinforcing effect of the hybrid type reinforcement in the middle line of the embankment.

3.2 Settlement

The vertical deformation of the foundation was analyzed using the DIPP-Motion cineradiography system with a high-speed camera. The time histories of vertical deformation, located at the middle point of the upside loose layer, are depicted in Fig. 6. In the case of the unreinforced embankment, the vertical deformation shows the most considerable magnitude during the earthquake loading when compared with the other cases. The rapid increase in vertical deformation in the unreinforced case (Case 1) is due to soil consolidation and soil displacement induced by liquefaction in the free field and the area near the toe of the embankment slope. Furthermore, Case 2 has a reduction (approximately 10%) of the vertical deformation compared to the
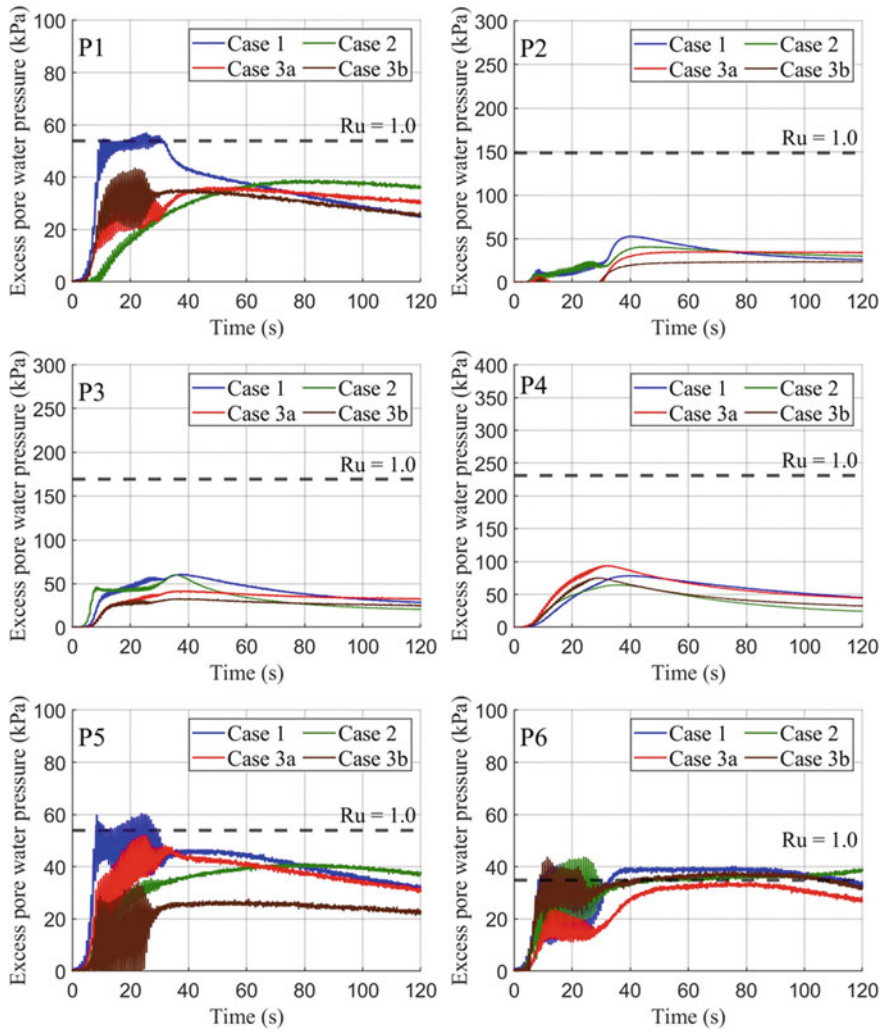
Fig. 5 Time histories of excess pore water pressure ratios of ground in 4 cases: (1) P1 and P5 below the toe of the embankment slope; (2) P2, P3, and P4 in the middle line of the embankment; (3) P6 in the free field

unreinforced case. Additionally, vertical displacement for Cases 3a and 3b decreased by approximately 55%, indicating the effectiveness of the hybrid type reinforcement in stabilizing embankment slopes.

Fig. 6 Time histories of vertical deformations for four cases
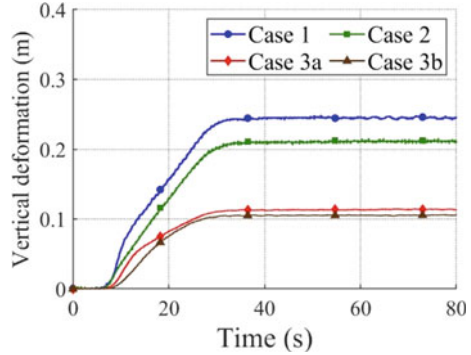
Fig. 7 Distribution of maximum bending moments of Row 1 and Row 2 during earthquake loading
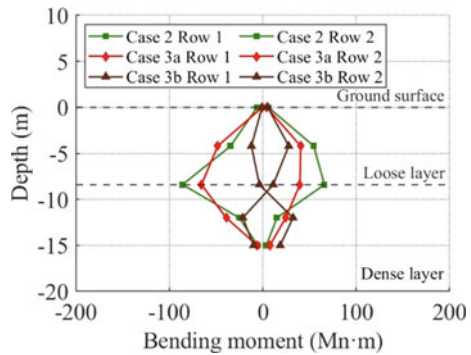
3.3 Bending Moment of Vertical Pile

Figure 7 shows the kinematic bending moment response for two rows of vertical piles for three cases, where the locations of strain gauges are shown in Fig. 3. The maximum bending moments for Case 2 were found to occur near the bottom of the loose layer during the shaking event. Due to the more area reinforced by the inclined pile, the maximum bending moments for Case 3b recorded at the middle of the loose layer illustrated the better reinforcing effect of the hybrid type reinforcement ($\alpha = 55°$).

4　Conclusions

The performance of a highway embankment on the liquefiable ground under cyclic sine wave loading has been evaluated. Furthermore, a new reinforcement technology has been developed, which can reduce the damage caused by the failure of the foundation during earthquakes. Based on the outcome of the centrifuge model test, the following conclusions can be drawn:

1. Under the condition that no reinforcement technology is used, the generations of excess pore water pressure near the saturated free field and near the toe of the embankment slope cause the soil strength reduction, which leads to excessive settlement and lateral displacement and instability of the embankment.

2. Since all the reinforcement measures did not provide any reinforcement to the embankment in the central part (even Case 3b has 5.5 m in the prototype size), the vertical deformation of 0.1 m in Case 3b was still obtained during earthquake loadings. From the smaller values in the maximum bending moments in 3b, the highway embankment reinforced by Case 3b has better stability among the four cases.

3. The area in the free field is in the stage of liquefaction, and the central area below the road has excess pore water pressure, resulting in instability of the embankment and foundation, which can also be observed from the maximum bending moment during the earthquake loading. However, the embankments improved by hybrid type reinforcement (Case 3a and 3b) could suppress the development of excess pore water pressure and reduce the settlement during the earthquake loading.

The stability of the embankment and foundation could be better improved by hybrid type reinforcement ($\alpha = 55°$). To explore the better reinforcing effect of this developing method, we need to continue a progressive study; for example, inclined piles should reinforce more areas. Studies are clarifying the seismic performance of the proposed technology using FEM analysis in three dimensions.

References

1. West Nippon Expressway Company Limited: Kumamoto Earthquake Response Committee WG2 Report: About earthquake resistance performance of highway embankment (2017)
2. Maharjan M, Takahashi A (2014) Liquefaction-induced deformation of earthen embankments on non-homogeneous soil deposits under sequential ground motions. Soil Dyn Earthq Eng 66:113–124
3. Hazarika H, Qin CJ, Kochi Y, Furuichi H, Ogawa N, Murai M (2022) Hybrid type reinforcement of highway embankment against earthquake induced damage. In: Wang LM, Zhang JM, Wang R (eds) Proceedings of the 4th international conference on performance based design in earthquake geotechnical engineering. Springer, Cham, pp 472–499

4. Qin CJ, Hazarika H, Rohit D, Ogawa N, Kochi Y, Liu GJ (2022) Numerical simulation of seismic performance of road embankment improved with hybrid type steel pile reinforcement. In: Wang LM, Zhang JM, Wang R (eds) Proceedings of the 4th international conference on performance based design in earthquake geotechnical engineering. Springer, Cham, pp 1332–1339
5. Ueda K, Sawada K, Wada T, Tobita T, Iai S (2019) Applicability of the generalized scaling law to a pile-inclined ground system subject to liquefaction-induced lateral spreading. Soils Found 59:1260–1279
6. Iai S, Tobita T, Nakahara T (2005) Generalized scaling relations for dynamic centrifuge tests. Geotechnique 55(5):355–362
7. Iai S (1989) Similitude for shaking table tests on soil-structure-fluid model in 1g gravitational field. Soils Found 29(1):105–118
8. Tobita T, Escoffier S, Chazelas JL, Iai S (2012) Generalized scaling law for settlements of dry sand deposit. In: Proceedings of the 15th world conference on earthquake engineering, Lisbon, Portugal (No. 4104)
9. Tobita T, Iai S, Tann LV, Yaoi Y (2011) Application of the generalised scaling law to saturated ground. Int J Phys Model Geotech 11(4):138–155

Comparative Study of Evaluations of Bearing Capacity Using Conventional Method and Finite Element Method

Suman Manandhar , **Sunny Karmacharya, Panich Vootripruex, and Salisa Chaiyaput**

Abstract Kathmandu Clay, also called the black clay, found near the sub-surface of the valley sediments, incorporating with its low strength and high compressibility. In this research, the vertical bearing capacity of strip footing on Kathmandu Clay was analyzed using Mohr–Coulomb soil model both in drained and undrained conditions through finite elements. The analyses were focused on the failure patterns of the footing for both drained and undrained conditions. The failure analyses showed a varying degree of effects of the friction angle of the soil both in drained and undrained conditions. The results were further compared with Vesic's and Prandtl's methods of evaluating bearing capacities. Hence, obtained results of simulated failure plane and the conventional one preceded by Prandtl show a good agreement between each other and validated the results.

Keywords Kathmandu clay · Strip footing · Finite element method · Bearing capacity

S. Manandhar (✉)
Kyushu University, Fukuoka 819-0395, Japan
e-mail: geosuman27@gmail.com

S. Karmacharya
Global Institute for Interdisciplinary Studies (GIIS), 3084 Kathmandu, Nepal

P. Vootripruex
Department of Teacher Training in Civil Engineering, Faculty of Technical Education, King Mongkut's University of Technology North Bangkok, Bangkok, Thailand

S. Chaiyaput
School of Engineering, King Mongkut's Institute of Technology Ladkrabang, Bangkok 10520, Thailand

1   Introduction

Black Clay of Kathmandu which is also named as Kathmandu Clay is one of the most problematic soils known which is distributed at the central part of the Kathmandu Valley fed with lacustrine deposit. It is found in different parts of the valley at different depths and in varying thickness. In this research, the main objective has been set up to evaluate the bearing capacity of this black clay of Kathmandu Valley using Vesic's conventional method and compare with numerical analysis using FEM. The research on black clay at this location is very limited and constructions have been carried out in ad hoc basis. Few literatures such as Khadka [1], Danai, and Acharya (the fine soil at Kupondol in the Kathmandu Valley consists of 75% silt and 25% clay) [2] can be delineated in order to understand the behaviors of this clay. According the Khada [1], the undrained shear strength of clay seemed to be increased with depth. Further, it is mentioned that the bearing capacity of soil from different parts of Kathmandu Valley were as low as 50 kPa in context to Danai and Acharya [2]. With these limitations, this study is intended to focus on the evaluation of bearing behaviors of shallow foundation on black clay of Kathmandu Valley by both conventional and numerical methods respectively using displacement method with axisymmetric model in PLAXIS 2D.

Usually, the bearing capacity of shallow foundations is computed by using several existing most popular theories elucidated by Terzaghi [3], Meyerhof [4], and Skempton [5]. The bearing capacity was first developed for a strip footing where the length of the footing is very long compared to its breadth. The methods were later modified to accommodate different shapes of footings with shape factors by many authors such as Meyerhof [6]; Hansen [7]; Vesic [8]. The bearing capacity with Vesic's formula is calculated with the equation:

$$q_u = cN_cs_cd_ci_c + qN_qs_qd_qi_q + 0.5\,B\gamma N_\gamma s_\gamma d_\gamma i_\gamma \tag{1}$$

where q_u is the bearing capacity, c is the cohesion, q is the uniformly distributed surcharge acting as the overburden soil at the level of the base of the foundation, c is the cohesion, B is the foundation width, γ is the unit weight of the soil, N_c, N_q, and N_γ are the bearing capacity factors which depend on the friction angle of the soil φ, s_q, s_c, s_γ are the shape factors which depend on the shape of the foundation, i_q, i_c, i_γ are inclination factors for the load inclined at an angle to the vertical, and d_q, d_c, d_γ are the depth factors. For a strip footing with purely vertical loading, the shape factors and the inclination factors are equal to unity.

Proceeding, there is an extensive literature regarding the numerical analyses of the bearing capacity of foundations by pioneer researchers such as Taiebat and Carter [9, 10], Salgado [11], Gourvenec and Randolph [12], and Gourvenec et al. [13]. The introduction of the finite element methods for the calculation of bearing capacity has allowed the comparison of the obtained results with the predictions from the conventional methods. Griffith [14] concluded that the finite element method can be used to predict the bearing capacity of surface footing with satisfactory results. The

study of bearing capacity with finite elements has been extended to soils with multiple layers in accordance with Burd and Frydman [15, 16], Merifield and Nguyen [17]. Vilas and Moniuddin [18] found fair comparison between the results from the finite element method and Terzaghi's method for the bearing capacity of square footings. Conte et al. [19] performed analysis of failure mechanism of footings using finite element analyses. Prandtl type failure mechanism was found with slip surface starting at the edges of the foundation and a wedge-shaped zone below the foundation. Li et al. [20] showed that shear plane for uniform soils is symmetrical. The failure initially is developed at the bottom corners of the foundation which develops downward until a weak layer of soil is encountered.

2   Method of Research

2.1   *Material Properties*

In order to evaluate the bearing behaviors of the black clay (Kathmandu Clay), a total of four samples were extracted from the western part of the Kathmandu Valley. Samples T1 and T2 were collected from Tokha and samples D1 and D2 were collected from Dhapasi site. Four undisturbed samples were extracted using Shelby tube with internal diameter 90 mm and tube thickness 2.0 mm from 2.0 m depth, and subsequently extruded the samples and tested in the geotechnical laboratory. The results of index properties of the samples are listed in Table 1. The grain size analyses showed that silt represents predominate portion of the black clay (Table 1 and Fig. 1). Soil parameters such as modulus, physical and strength parameters used for the finite element analyses for the Mohr–Coulomb soil modeling are summarized in Table 2. For the model analyses, oedometer elastic modulus was obtained from the oedometer test, and the shear strength parameters of the soils were obtained from direct shear test.

Table 1 Summary of the index properties of black clay

Soil	NMC (%)	Grain size distribution			Atterberg limits			Bulk density g/cc	Specific gravity
		Sand, (%)	Clay, (%)	Silt, (%)	LL (%)	PL (%)	PI (%)		
D1	51.75	5.44	8	86.56	64.03	48.47	15.06	1.638	2.60
D2	53.61	4.78	8	87.22	55.04	45.45	9.89	1.624	2.60
T1	23.65	27.36	12	60.64	36.65	21.08	15.58	1.969	2.57
T2	25.16	1.46	25	73.58	65.27	34.13	31.03	1.916	2.55
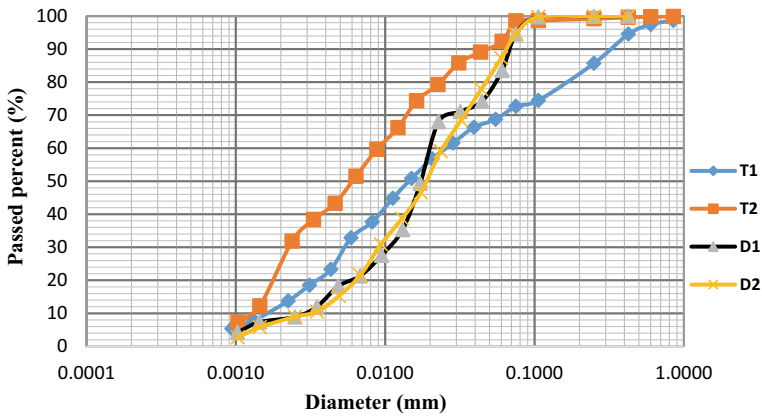
Fig. 1 Grain size distribution curve from four different sites

Table 2 Summary of the physical properties and strength parameters of black clay

Parameters	T1	T2	D1	D2	Units
Soil type criterion	Mohr–Coulomb	Mohr–Coulomb	Mohr–Coulomb	Mohr–Coulomb	
Unsaturated unit weight (γ_{bulk})	19.69	19.16	16.38	16.24	kN/m^3
Saturated unit weight (γ_{sat})	19.74	19.63	17.26	17.13	kN/m^3
Elastic modulus (E_{oed})	5058	6428	5058	5000	kN/m^2
Poisson's ratio (ν)	0.3	0.3	0.3	0.3	
Cohesion (c)	6.87	20.72	12.09	10.72	kN/m^2
Friction angle (φ)	22.39	21.70	25.2	26.76	°
Angle of dilation (ψ)	0	0	0	0	°

2.2   Model Description

To obtain the ultimate vertical bearing resistance, the footing is subjected to a single vertical load under two-dimensional finite element analysis. A strip foundation of 2.0 m width is kept at different depths (0 m, 1.0 m, and 2.0 m). The vertical load was subjected to increase until complete failure occurs which was characterized by
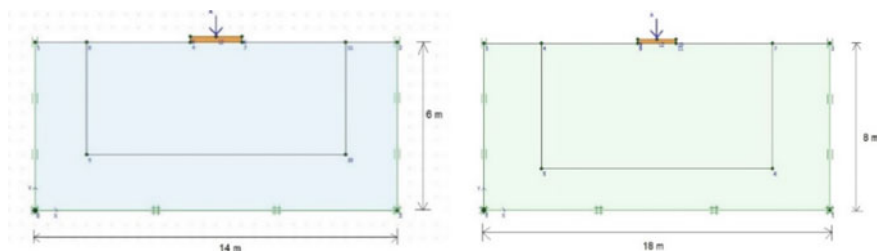
Fig. 2 Model geometry for undrained (left) and drained (right) analyses

the load–displacement curve. The analysis showed that the displacement increases rapidly without significant increase in load. Both drained and undrained analyses were performed to analyze gradual and rapid load bearing capacity failures. The effect of the ground water is not considered in the analysis since it was assumed that the water table would encounter in deeper part where the zone of influence of the footing would not meet to represent the effects. The model geometry was chosen such that the boundaries do not affect the analyses as shown in Fig. 2. The model geometry of 14 m × 6 m was chosen for undrained analysis, while the model geometry of 18 m × 8 m was chosen for drained analyses. This is because the failure surface tends to reach deeper in drained analyses in comparison to undrained condition.

3 Results of Analyses

Bearing capacity of strip footing was calculated by using FEM and conventional Vesic's method for different depths. The analyses with FEM included both drained and undrained analyses for each black clay. Undrained analyses were carried out assuming conditions of rapid loading with no time of drainage. Figure 3 shows the comparison of the bearing capacity calculated from conventional Vesic's method to the results obtained from FEM. The results obtained from FEM for drained conditions are lower than the values predicted by Vesic's method. Also, the comparison is made between the ultimate capacity of the soil at drained and undrained conditions. The results showed that the sample D2 has the highest bearing capacity in drained condition while the sample T2 has the highest load carrying capacity in undrained condition.

Table 3 shows the comparison of bearing capacities obtained at 2 m depth in drained and undrained conditions in PLAXIS 2D. It is clear that in drained conditions, the bearing capacity of the soil with high friction angle is higher with compared to the bearing capacity with low friction angle. However, in undrained condition, soils with higher cohesion have received more load bearing capacity regardless of the value of friction angle which is clarified by the values corresponding to D2 and T2. Soils of D1 and D2 show high load bearing capacity despite having low cohesion and unit
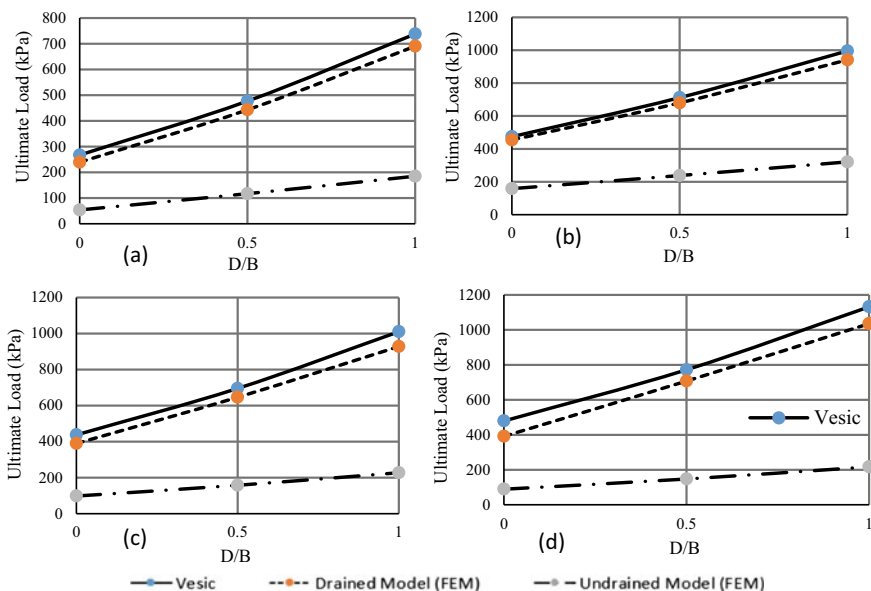
Fig. 3 Results of bearing capacity by FEM and Vesic's method for samples **a** T1, **b** T2, **c** D1, **d** D2 respectively

Table 3 Bearing capacity at 2.0 m depth obtained from PLAXIS 2D

Soil Sample	Unit weight (kN/m^3)		Friction angle (°)	Cohesion (kN/m^2)	Bearing capacity (PLAXIS)	
	γ_{unsat}	γ_{sat}			Drained	Undrained
D1	16.38	17.26	25.2	12.09	936.82	227.26
D2	16.24	17.13	26.76	10.72	1035	217
T1	19.69	19.74	22.39	6.87	690.47	185
T2	19.16	19.63	21.71	20.72	927.50	320.97

weight. Whereas, in case of undrained analyses, both D1 and D2 govern low bearing capacities compared to T2 which has high cohesion value.

The settlement of the foundations must not exceed the allowable settlement value. Hence, the bearing pressure at the allowable settlement value must be calculated. Bearing capacity of the isolated strip footings in drained conditions was calculated using the prescribed settlements of 25 mm and 40 mm in different D/B ratios. The effect of ground water table was not taken into consideration in this analysis. The comparisons of the bearing pressures obtained from the failure criteria and settlement criteria from PLAXIS 2D is shown in Table 4. The least value of the bearing pressure obtained is taken to be the actual bearing capacity of the foundation. T2 shows the highest bearing capacity while D1 has the lowest bearing pressure.

Table 4 Bearing capacity obtained from failure criteria and settlement criteria

Soil sample	D/B	Bearing capacity (kPa)		
		Failure Criteria	Settlement criteria	
			25 mm	40 mm
T1	0.0	239.5	40.85	60.97
	0.5	443.1	50.55	73.42
	1.0	690.0	64.25	93.25
T2	0.0	454.48	253.69	344.87
	0.5	679.50	318.06	429.37
	1.0	941.25	318.06	503
D1	0.0	389.68	40.01	57.61
	0.5	646.0	49.77	77.41
	1.0	927.68	63.02	98.27
D2	0.0	391.58	38.25	55.99
	0.5	707.25	49.25	77.41
	1.0	1035.25	64.21	99

3.1 Load Settlement Curves

With reference to elastic-perfectly plastic model of Mohr–Coulomb, as load increases, the soil under the foundation deforms elastically. Once it crosses its elastic limit, it behaves as a perfectly plastic material where large deformation occurs at constant pressure. This is the ultimate load bearing capacity of the soil as shown in Fig. 4.

Figure 5 represents the deformation–load relationship in drained condition. The curves show that as depth of the foundation increases, less deformation occur at same pressure. As the material is drained, more settlement is allowed, compared to undrained conditions, before total collapse of the soil occurs. The curves for drained models resemble the load settlement curve subject to local shear failure.

4 Conclusions

The research was carried out for the determination of shallow bearing capacities of black clay (Kathmandu Clay) using conventional Vesic's method and compared with FEM using PLAXIS. Through the study, following specific conclusions can be drawn in detail.

i. The bearing capacities calculated by conventional Vesic's method obtain higher values compared with results obtained by FEM. The ultimate load bearing capacity tends to increase as the depth of the footing increases.
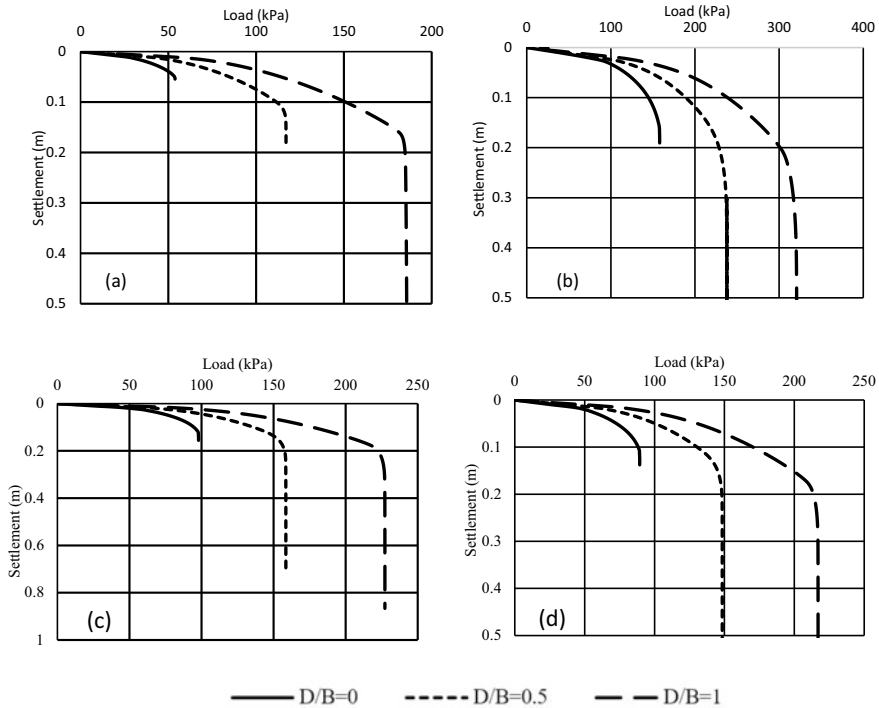
Fig. 4 Load settlement curve for **a** T1, **b** T2, **c** D1, **d** D2 in undrained conditions

ii. The trend of increase in bearing capacity with depth is similar in drained condi-
tions for both Vesic's method and the FEM. It is observed that the bearing
capacity evaluation of the clay can be performed by FEM very effectively.

iii. The value of load bearing capacity in undrained conditions obtained from
PLAXIS is lower compared to the drained analysis. This implies that in case of
constructions that require rapid loading with no time of drainage in clays, the
undrained bearing capacity should be considered.

iv. The drained analyses revealed the higher role of ϕ. The bearing capacity
obtained from settlement analysis was found to be lower than the bearing
pressure obtained from failure criteria. T2 shows higher bearing capacity with
compared to other soil. This may be caused due to the higher modulus of elas-
ticity. The results show that the bearing capacity obtained from the settlement
analysis is more realistic and practical.

v. The load settlement curve of undrained analyses has a characteristic sharp rise
in load with little deformation followed by a perfectly plastic stage where
large deformation occurs with little change in the load. This is a character-
istic curve obtained in a Mohr–Coulomb soil which assumes the material as
elastic-perfectly plastic.
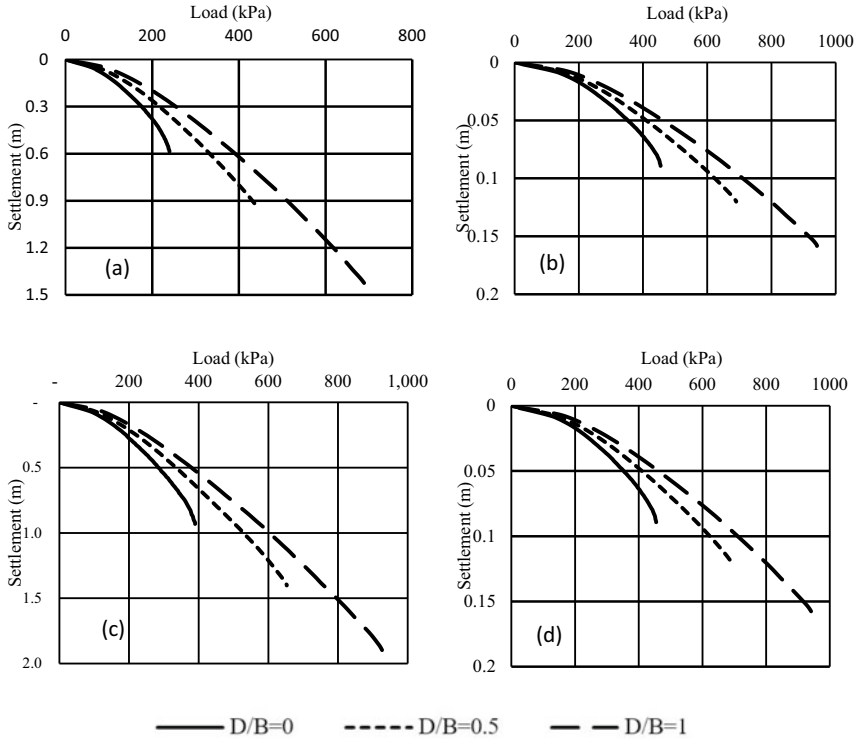
Fig. 5 Load settlement curve for **a** T1, **b** T2, **c** D1, **d** D2 in drained conditions

vi. The amount of deformation is also dependent upon the elastic modulus of the soil. Higher the value of the elastic modulus, lesser the deformation will occur. The load–deformation curve for drained analyses does not show large perfectly plastic stage. The curve shows more or less linear relationship of load and settlement in this case indicating that the soil is in elastic state until failure occurs.

vii. With increasing D/B ratio, the amount of deformation tends to be lesser for the same load applied. Therefore, it can be concluded that deeper the foundation, lesser will be the settlement under the similar loading condition.

References

1. Khadka PB (2011) Stress-strain behavior of undrained organic soil in Kupondol Kathmandu. J Inst Eng 8(1):151–162

2. Danai RK, Acharya I (2018) Bearing capacity analysis and zoning of Kathmandu for shallow foundations. Adv Coll Eng Manage 4:111–117

3. Terzaghi K (1943) Theoretical soil mechanics. Wiley, New York, N.Y.

4. Meyerhof GG (1951) The ultimate bearing capacity of foundations. Geotechnique 2:301–332

5. Skempton AW (1951) The bearing capacity of clays. In: Proceeding, building and research congress, vol 1, pp 180–189, London

6. Meyerhof GG (1963) Some recent research on the bearing capacity of foundations. Can Geotech J 1(1):16–26

7. Hansen JB (1961) A general formula for bearing capacity. Dan Geotech Inst Bull 11

8. Vesic AS (1973) S Analysis of ultimate loads of shallow foundations. J Soil Mech Found Div ASCE 99(SM1):45–73

9. Taiebat HA, Carter JP (2000) Numerical studies of the bearing capacity of shallow foundations on cohesive soil subjected to combined loading. Geotechnique 50(4):409–418

10. Taiebat R, Sloan S, Yu HS (2004) Two and three-dimensional bearing capacity of foundations in clay. Geotechnique 54:297–306

11. Salgado HA, Carter JP (2002) Bearing capacity of strip and circular foundations on undrained clay subjected to eccentric loads. Geotechnique 52(1):61–64

12. Gourvner S, Randolph M (2003) Effect of strength non-homogeneity on the shape of failure envelopes for combined loading of strip and circular footings on clay. Geotechnique 53:575–586

13. Gourvner S, Randolph M, Kingsnorth O (2006) Undrained bearing capacity of square and rectangular footings. Int J Geomech 6(3):147–157

14. Griffith DV (1982) Computation of bearing capacity factors using finite elements. Geotechnique. Geotechnique 32(3):195–202

15. Burd HJ, Frydman S (1996) Discussion on bearing capacity of footings over two-layer foundation soils. J Geotech Eng ASCE 122(8):699–700

16. Burd HJ, Frydman S (1997) Bearing capacity of plane-strain footings on layered soils. Can Geotech J 34:241–253

17. Merifield RS, Nguyen VQ (2006) Two and three dimensional bearing capacity solutions for footings on two layered clays. Geomech Geoengineering 1(2):151–162

18. Vilas M, Moniuddin Md (2015) Finite element analysis of soil bearing capacity using Plaxis. Int J Eng Tech Res 4

19. Conte S, Donato A, Troncone A (2013) Progressive failure analysis of shallow foundations on soils with strain-softening behavior. Comput Geotech 54:117–124

20. Li L, Tian Y, Cassidy M (2015) Failure mechanism and bearing capacity of footings buried at various depths in spatially random soil. J Geotechn Geoenvironmental Eng 141(2):1–11

Effects of Climate Change on Landslide Slope Stability and Case Studies

Shiro Ota, Masafumi Okawara, Nobuo Sakakibara, and Takamasa Yamaji

Abstract In recent years, disasters caused by torrential rains and floods that exceed the planned scale are occurring in Japan due to climatic change. In response to it, Japan has been improving and reinforcing existing infrastructure to withstand more severe disasters. For example, in river projects, widening river width through channel excavation to increase flow capacity, and in road projects, lane widening and reinforcement of existing embankments to enhance the traffic network during disasters are occurring. At these project sites, there is concern that artificial topographic modification (changes in stress conditions due to excavation and embankment), which was conducted as a countermeasure, will affect potential weak surfaces in the ground, which, combined with the effects of increased rainfall caused by climate change, will destabilize the existing slopes and cause new slope changes (Kaneko in A collection of papers from the China Branch of Geotechnical Society, pp.161–168, 2018). In this wise, the demand for the assessment of landslide slope stability associated with increased rainfall caused by climate change and artificial modification is increasing; in this study, we examined a method for the assessment of landslide slope stability that takes into account the change in the strength of the slip surface associated with increased rainfall and artificial modification targeting a landslide area near a planned site for excavation of a river channel.

Keywords Climate change · Landslide · Slope stability analysis

S. Ota (✉)
Kawasaki Geological Engineering Co., Ltd. Planning and Technical Headquarters, Minato-ku, Tokyo, Japan
e-mail: ohtas@kge.co.jp

M. Okawara
Faculty of Science and Engineering, Iwate University, Morioka, Iwate Prefecture, Japan

N. Sakakibara
Kawasaki Geological Engineering Co., Ltd. North Japan Branch, Miyagino-ku, Sendai, Miyagi Prefecture, Japan

T. Yamaji
Kawasaki Geological Engineering Co., Ltd. Kyusyu Branch, Hakata-ku, Fukuoka, Fukuoka Prefecture, Japan

1   Introduction

In addition to the occurrence of new landslide disasters caused by rainfall increased due to climate change, there are landslides occurred that have stabilized due to the implementation of countermeasures and have changed in the past and are now inactive. Landslide reactivation is feared. To predict and assess the risk of slope instability associated with increased rainfall properly, it is necessary to estimate the increase and distribution of pore water pressure on slopes associated with increased rainfall accurately. However, pore water pressure on slopes is often determined based on groundwater level observation data in Japan, and if there is no record of heavy rainfall during the observation period, it may not be possible to estimate properly the pore water pressure for increased rainfall. Therefore, in this study, we examined a method for estimating the increase in pore water pressure due to rainfall above the observed rainfall in a landslide facing a river using seepage flow analysis.

In Japan, road widening (excavation) and river widening to prevent river flooding are being promoted as measures to create a country resilient to climate change. It is often accompanied by excavation and embankment modification, which causes the stress state of the slope to change, the strength of the slip surface to decrease due to the progress of displacement and water absorption expansion, and the slope to become unstable. Therefore, in this study, a method for setting slip surface strength considering water absorption expansion by indoor shear test and a method for slope stability evaluation by 3D stability analysis were investigated.

2   Outline of the Target Landslide

2.1   Outline of the Landslide

In the target area, when a landslide occurred in Block B (length 126 m, width 138 m) shown in Fig. 1 during the construction to widen the river in the past, the head soil removal work was conducted. In the adjacent Block A (length 380 m, width 295 m), no landslide deformation was observed in visual and field observations, but two water collecting wells were installed to improve safety and maintain stability. However, the widening of the river was required to increase the water flow of the river, and the countermeasure was pending issue.

As shown in Fig. 2, Block A of the landslide shows a characteristic landslide topography in which the bedrock of the monoclinal structure (cuesta landform) bent in the middle and rose at the end. Since the crushing of the bedrock consisting of the landslide mass was localized, differentiation of the landslide block was not approved, and no clear deformation was observed in the field monitoring, it is now considered to be a primary landslide in an inactive condition. The geology of the subject area consists of Neogene Miocene tuff (mudstone, tuff, and alternating layers of tuffaceous

Fig. 1 Bird's-eye view of topography

Fig. 2 Schematic cross-sectional view
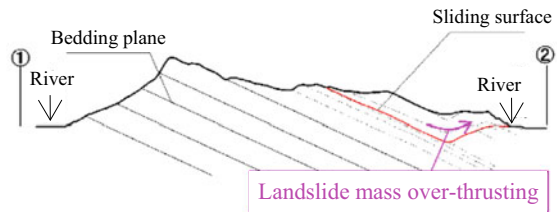
Fig. 3 Topographic shadow diagram
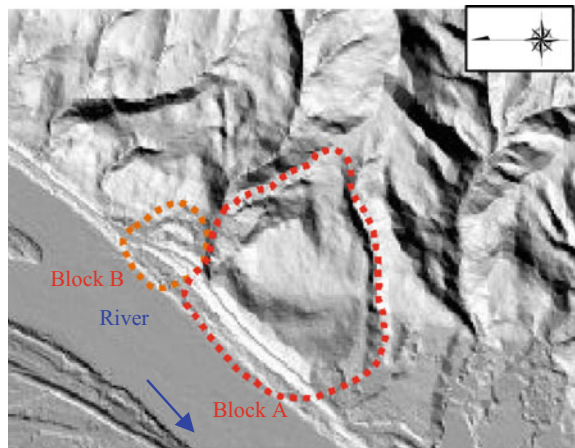
sandstone and mudstone) distributed with north–south strike and gentle west-dipping monoclinic structure in the west area and steep cliffs in the east area, and the direction of the movement is 25° oblique to the river direction (Figs. 3 and 4).
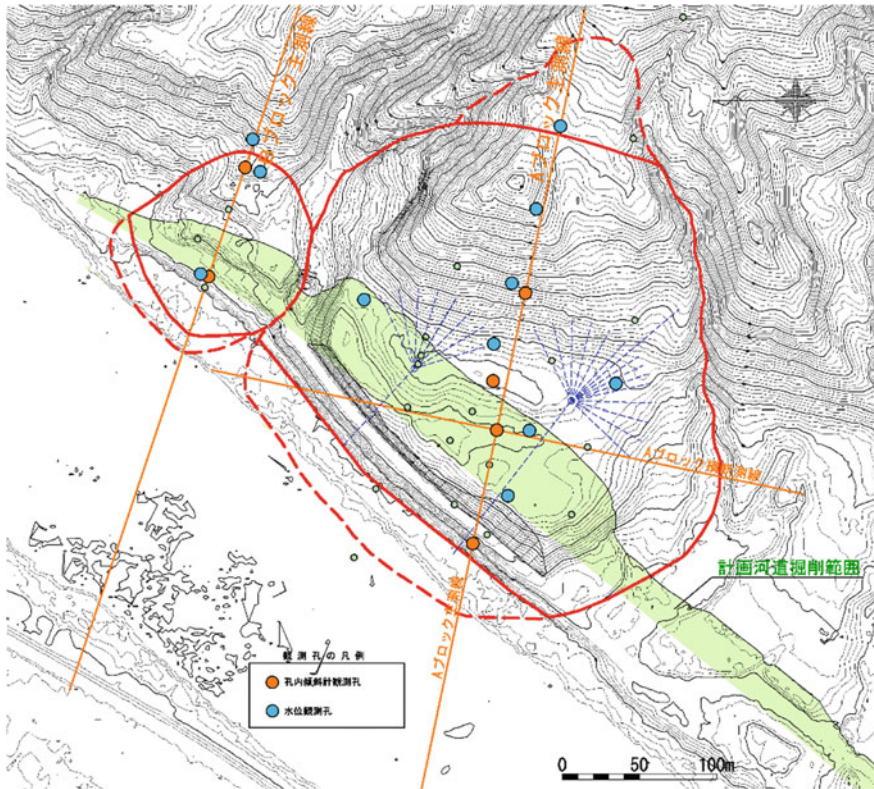
Fig. 4 Excavation plan for landslide terminus

2.2 Recognition of Slip Surfaces

A geological survey was conducted to identify the geologic stratigraphy and the inclination direction of the geologic boundary, and the clay layer was extracted as a slip surface. Then, based on the presence or absence of mirror skin and striations, and the inclination angle, the slip surface was defined by the method shown in Photo 1 and Fig. 5.

A cross-sectional view of the landslide is shown in Fig. 5. The slip surface was estimated to slope down to the riverside from the head to the bend and to ride up to the riverside from the bend to the riverside. At the foot of the landslide, an unconsolidated sand and gravel layer of the old riverbed was observed directly under the moving soil mass, and from its distribution range, the amount of movement caused by the landslide was estimated to be 80 m or more. On the other hand, since the crushing of the mobile soil mass was limited along the slip surface from the bend to the head, the majority of the mobile soil mass was massive bedrock with few cracks, and no subsurface movement was confirmed by dynamic monitoring, it was presumed to be

Photo 1 Slickensides and striations
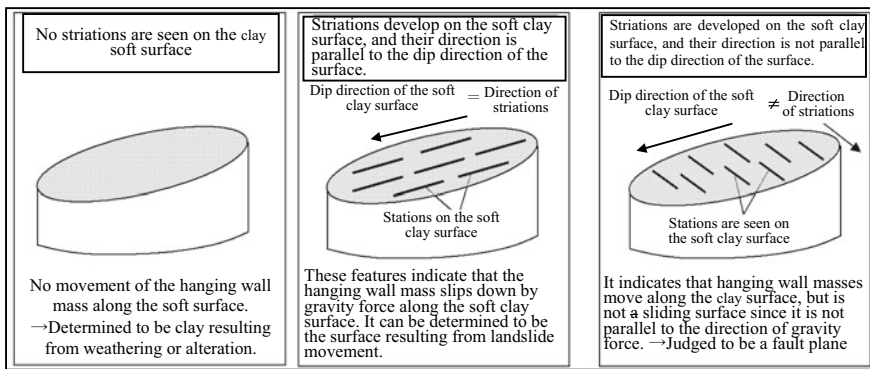
Fig. 5 Conceptual diagram of landslide surface certification

a primary slip caused by external factors such as an earthquake with large movement, and it was judged to be in a state of arrested movement at present (Fig. 6).

3 Slip Surface Strength from Cyclic Box-Shear Tests

3.1 Test Conditions

In this study, the following innovations were used to determine the strength of the slip surface in cyclic one-sided shear tests.

Fragile areas around the slip surface were crushed and slurried, and the specimens (6 cm diameter and 2 cm high) were compacted under a pressure equivalent to the thickness of the overburden. The specimens were then unloaded at a load equivalent
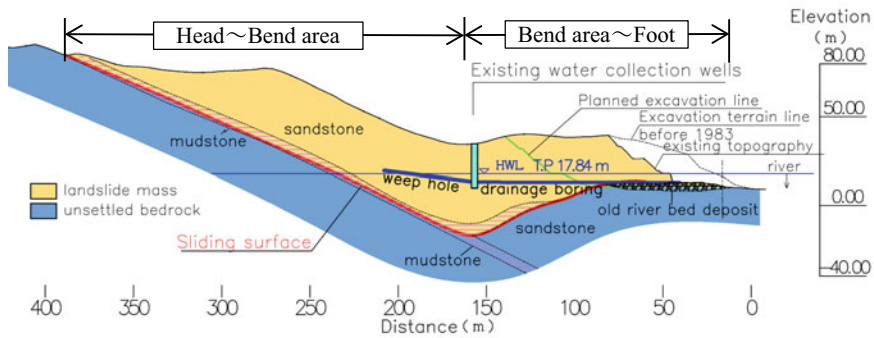
Fig. 6 Schematic diagram of landslide cross-section

to the height of the river excavation (10 m), dried at 60 °C for 24 h, and subjected to shear tests after water absorption. The residual strength was determined as the fully softened strength when recompacted by residual soil or when the slip surface was completely separated due to high shear displacement [2]. For comparison, shear tests were also carried out at natural water content.

3.2 Tests Results

The shear strength of several specimens was compared under natural water content conditions and underwater absorption and dewatering conditions. The test results in underwater absorption and dewatering conditions showed that the shear resistance angle Φ decreased by 1° to 2° due to the increased saturation state caused by water absorption. The variation in both the fully softened strength and residual strength was reduced because the saturation state became constant due to water absorption. Based on the test averages of all 15 sample's underwater absorption and dewatering conditions, the degrees were set as follows: fully softened strength: c = 21.8 (kN/m^2), ϕ = 15.2°; residual strength: c = 0.0 (kN/m^2), ϕ = 13.8° (Table 1).

3.3 Slip Surface Strength Zoning

In the practice of stability assessment of landslide slopes in Japan, shear strength (c, Φ) of the slip surface for 2D stability analysis using the limit equilibrium method is rarely obtained from soil tests. The adhesion force (c) is obtained from the maximum thickness of the landslide soil mass, and the shear resistance angle Φ is set by back-calculating the initial safety factor Fs = 0.95 to 1.05 from the existing topography depending on the situation. However, since the properties and strength are expected

Table 1 Repeated cyclic box-shear tests results

Statistics	Forced water absorption state			
	Fully softened strength		Residual strength	
	Cohesion	Angle of shear resistance	Cohesion	Angle of shear resistance
	$c(kN/m^2)$	$\varphi(°)$	$c(kN/m^2)$	$\varphi(°)$
Maximum value	50.9	27.2	0.0	24.7
Minimum value	0.0	10.9	0.0	10.6
Median value	17.2	14.2	0.0	13.0
Average value	21.8	15.2	0.0	13.8
Number of test	15		15	

to differ depending on the location of the slip surface of the landslide in question, and there is concern that the strength may decrease with excavation, zoning according to soil test results and the properties of the slip surface [3] is appropriate.

Definitions of Shear Strength Obtained from Soil Tests

Fully softened strength. It is the peak strength obtained by regular consolidation from kneading and recompressing clay and the strength of an active slip surface in which rocks and clays were destroyed by an initial landslide and released from the effects of previous consolidation or reconsolidated by overburden loads for some time after activity was stopped.

Residual strength. This is the minimum shear strength when a large shear displacement has been applied, and a residual condition has been reached, such as when a slickenside is formed on the slip surface.

Slip Surface Strength Zoning Results

From the head to the bend in the landslide mass, the slip surface is straight and completely clayed by the large shear displacement during the initial landslide. The strength of the slip is judged to be equivalent to "residual strength" because a slickenside and striations are observed. The area from the bend to the end of the landslide shows hard clay mixed with gravel, which indicates that the moving soil mass rode up on the immovable ground and riverbed during the initial landslide and was crushed and clayed, and then reconsolidated by soil overburden load or horizontal compressive force. Although slickensides and striations are recognized in some parts, no clear separation surface is recognized as a whole, and therefore, its strength is judged to be equivalent to "full softened strength" (Fig. 7 and Tables 2 and 3).

3D stability analysis [4] was used to determine the factor of safety of the landslide slope at the highest observed water level. For the case of total residual strength, Fs = 0.93, which is inconsistent with the absence of landslide movement in Block A. For the total complete softening strength, Fs = 1.34, which is inconsistent with the situation where Block B collapsed due to past river channel excavation and Block A has no margin. Compared to the safety factor when the strength is set by the inverse
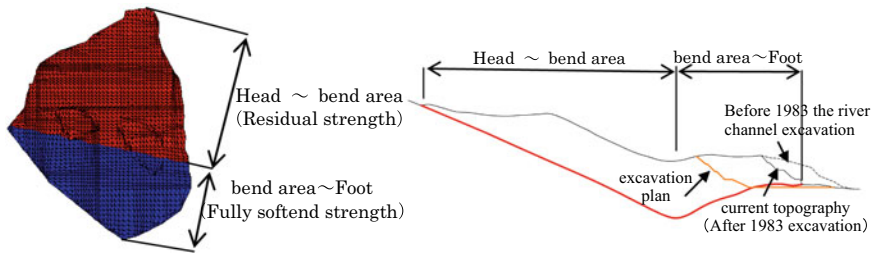
Fig. 7 Planar and longitudinal sectional maps of slip surface strength

method, the safety factor is the same for the current topography and before the past excavation, but the safety factor is calculated as 10% lower for the future excavation plan due to zoning. It is considered that the zoning set the slip surface strength at the time of excavation to the full softening strength and excavated the area of higher resistance, resulting in a greater degree of reduction in the safety factor. From the above, it is judged that the strength setting by zoning is an appropriate method that reflects the local landslide conditions.

4 Slope Stability Assessment for Inexperienced Heavy Rainfall

4.1 Prediction of Groundwater Level by Quasi-3D Seepage Flow Analysis

Since the landslide in question consists of three permeable zones: the slip surface (impermeable layer), the moving soil mass (permeable layer), and the existing catchment well (highly permeable layer), a quasi-3D seepage flow analysis [5] was applied, which reduced calculation labor while considering the 3D extent of the aquifer and the multiple aquifers. The predictive model was determined by setting the hydraulic conductivity and porosity based on the results of field permeability tests conducted for each formation and then fitting the hydraulic conductivity within the range of the test values so that the error between the calculated and observed water levels during actual rainfall would be within $\pm$ 3 m. The model was then finalized (Figs. 8 and 9).

4.2 Evaluation of Slope Stability During Heavy Rainfall

The rainfall waveforms input to the seepage flow analysis were stretched from existing observation waveforms to an arbitrarily set maximum daily rainfall, and rainfall probabilities were calculated using the widely used "Iwai equation" (Fig. 10)

Table 2 Features of the slide surfaces and strength classifications

Strength classification	Head ~ bend area	Bend area ~ Foot
Photogragh	Residual strength c = 0.0(kN/m²) φ = 13.8(°)	Fully softened strength c = 21.8(kN/m²) 3000φ = 15.2(°)
Soil features	Clay (soft). There are slickensides and slickenlines	Gravel-bearing clay (reconsolidation). There is no slickenside and slickenline
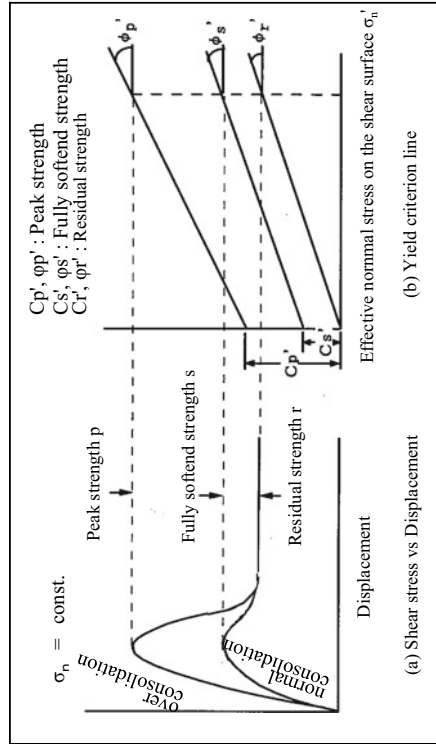
Concept of shear strength obtained from soil tests

(a) Shear stress vs Displacement   (b) Yield criterion line

Table 3 Safety factor based on 3D stability analysis

Setting method for the strength of the sliding surface	Safety factor based on three-dimensional stability analysis						Remarks
	Before 1983 the river channel excavation		Current topography (After 1983 excavation)		Future excavation (Plan)		
Zoning by the both strength (adopted)	1.37	100%	1.07	100%	0.67	100%	Highest observed groundwater level (Equivalent to 1/60th probability precipitation)
Residual strength all	1.23	90%	0.93	87%	0.58	87%	$c = 0kN/m^2$ $\varphi = 13.8°$
Fully softened strength all	1.69	123%	1.34	125%	0.85	127%	$c = 21.8N/m^2$ $\varphi = 15.2°$
Inverse calculation method (at current topography, Fs = 1.05)	1.38	101%	1.05	98%	0.74	110%	$c = 25kN/m^2$ $\varphi = 11.22°$
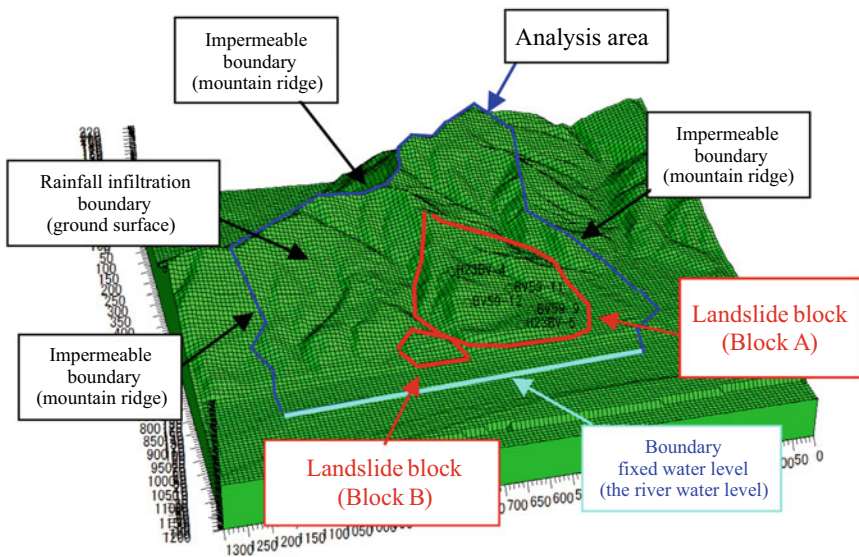
Fig. 8 Schematic diagram of the seepage flow analysis model
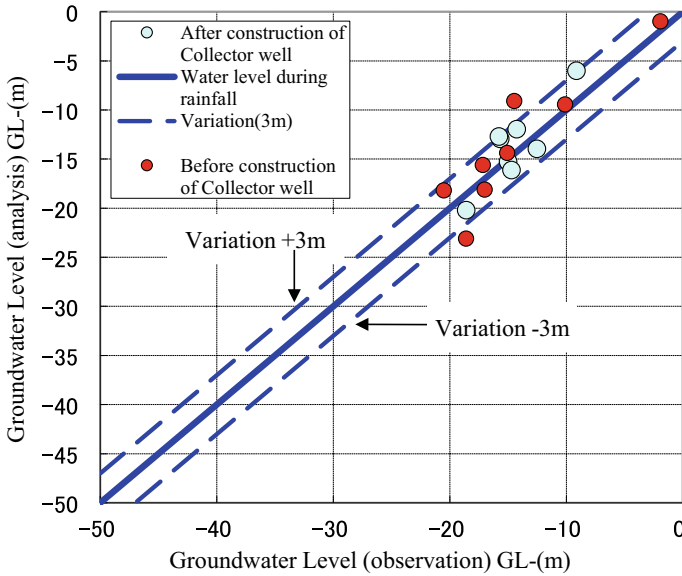
Fig. 9 Comparison of predicted and measured groundwater levels

[6]. Based on this rainfall waveform, groundwater levels were predicted by quasi-3D seepage flow analysis, and stability was evaluated by 3D stability analysis. This resulted in a predicted critical daily rainfall of 224.7 mm (1/350), which was sufficient to maintain stability (Fig. 11).

The slip factor of safety for existing slopes (Table 4) showed a significant degree of decrease with increasing rainfall, reflecting the increase in the groundwater level of the landslide soil mass as rainfall increases. On the other hand, the safety factor was less than 1.0 in the river widening plan to improve the flow capacity of the river, as shown in Table 3. Therefore, sediment removal works with a safety factor of Fs = 1.05 or higher were considered, and the results of rainfall and safety factors are shown in Table 4. Since most of the landslide soil mass was removed (Fig. 12) and there was little room for the groundwater table to rise, it was determined that there was an upper limit to the decrease in the factor of safety with increasing rainfall and that the stability of the slope could be improved.

Fig. 10 Chart for
calculating probable rainfall
precipitation using the Iwai
method
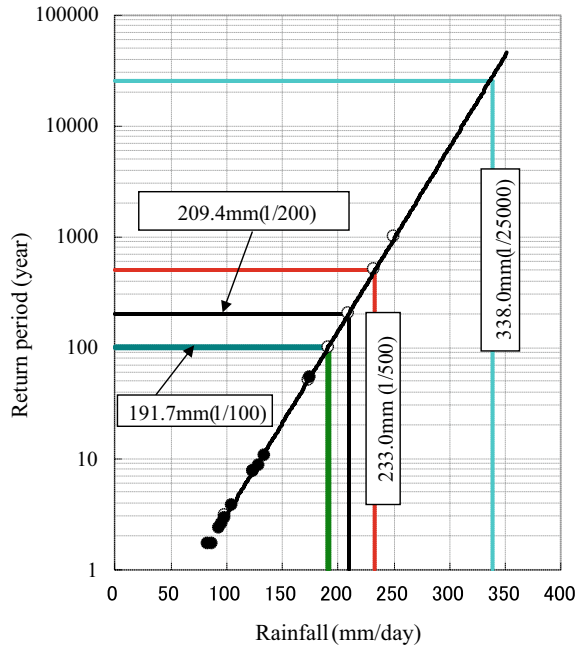
Fig. 11 Chart for
calculating the critical
rainfall that maintains slope
stability
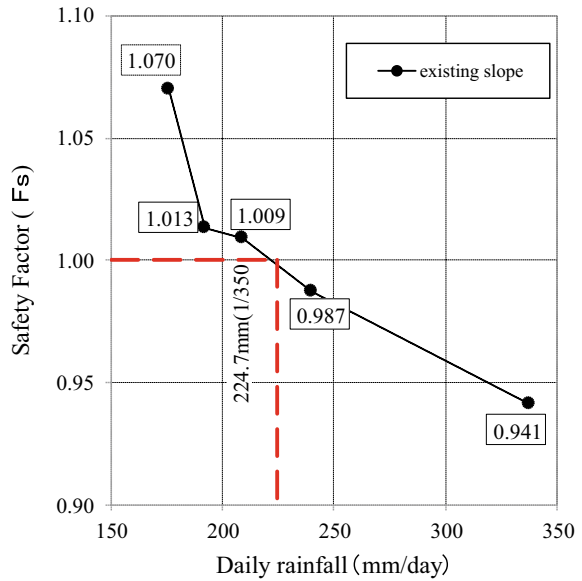
Table 4 Safety rate during heavy rain

Case	Collector well	Safety factor(Fs)				
		176 mm/day(1/60)	192 mm/day(1/100)	209 mm/day(1/200)	233 mm/day(1/500)	338 mm/day(1/25,000)
Existing slope	2 wells (Existing)	1.070 (Observed water level)	1.013	1.009	*0.987*	*0.941*
River widening and Earth removal work	Ignore effects	–	1.064	1.058	1.051	1.033
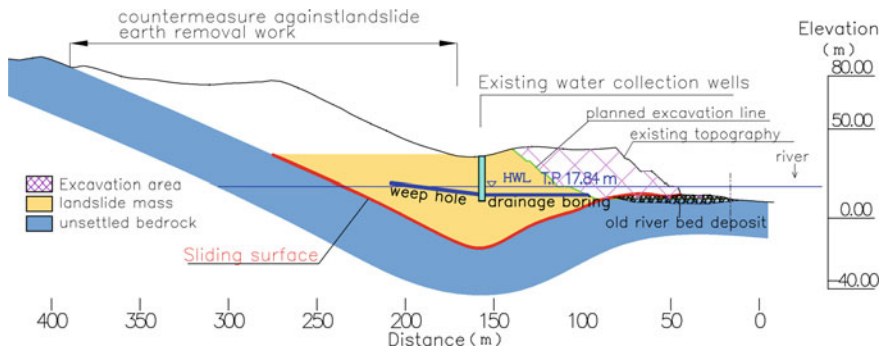
Fig. 12 Landslide prevention work for river widening

5 Conclusion

Several methods based on 2D analysis have been proposed for predicting the stability of landslide slopes with increased rainfall [7], but there are few established examples of 3D analysis combining seepage flow analysis and slope stability analysis. The quasi-3D seepage flow analysis and 3D stability analysis techniques presented in this report were put to practical use in the 1990s and are used, for example, in tunnel construction for the prediction of groundwater impacts associated with excavation and the evaluation of tunnel entrance slope stability. In this study, quasi-3D seepage flow analysis and 3D stability analysis were combined to predict the stability of landslide slopes with increasing rainfall. As the geological composition and distribution of slip surfaces in the target area were well known, modeling of the geological formations and parameter fitting using observation data were relatively easy. Future case studies will be conducted in different regions to clarify the scope and limitations of the methodology used in this study and to explore its application to a wide range of slope hazard assessments for increased rainfall due to climate change.

References

1. Kaneko M (2018) Comprehending the landslide plale and residual strength of the re-slide type landslide, and the result of the slope stability analysis. A collection of papers from the China Branch of Geotechnical Society, pp 161–168
2. The Landslide Engineering Society of Japan Tohoku Branch (2001) Method for determining strength constants for landslide stability analysis, pp 99–110
3. Mima K (2007) Stability analysis method for ensuring safety during construction of landslide terminus cuttings. In: The 42nd geotechnical engineering research meeting of geotechnical society (Nagoya, Japan), pp 1931–1932
4. Yoshimatsu Y (1995) 3-D slope stability analysis of landslides (modified Hovland method)
5. Kosaka N (1982) Quasi-3-D infiltration analysis of wide-area groundwater by finite element method. JSCE Annual Academic Lecture Summary, Part 3:531–532
6. Iwai S (1970) Applied hydrodynamic statistics. Morikita Publishing Co, Chiyoda-ku, Tokyo
7. Ohtsuka S (2004) Slope stability analysis considering seepage property of slope. In: JSCE proceedings of the second symposium on landslides, pp 165–170

Efficient Construction of Groundwater Level Observation Holes for Monitoring of Slope Disasters

Yoshikazu Ochi and Atsushi Sonoda

Abstract Slope disasters caused by heavy rain are triggered by an increase in pore water pressure due to a rise in groundwater level. Therefore, by understanding the relationship between rainfall on the slope and rise in the groundwater level, the signs of a disaster are monitored in order to detect the possibility of slope disasters. For general groundwater level monitoring, a observation hole with a water level meter installed in the drilling hole is used. However, the installation of the observation hole by drilling requires procedures such as bringing in the machine and drilling by the boring machine, and due to budgetary concerns, it is often limited to implementation at several representative points. Therefore general method, even when the area where there is a risk of landslides blocks or surface collapse is wide, it is difficult to grasp the whole picture because the observation results are predicted from limited information. Instead of drilling, we will introduce a method of making a observation hole by inserting a φ10 mm water level meter into the screw weight sounding test hole. The screw weight sounding test is a test that can evaluate the hardness, tightness, and soil layer composition of the ground by measuring the number of rotations at the time of penetration, and can penetrate up to about 10 m. The work efficiency is good and it is possible to install at multiple locations in a day. The observation hole was installed on the slope using this method and the groundwater level rise was observed, it was confirmed that the groundwater level was formed near the surface layer in conjunction with the rainfall.

Keywords Water level gauge · Slope disaster · Groundwater

Y. Ochi (✉) · A. Sonoda
Kawasaki Geological Engineering Co., Ltd. Kyusyu Branch, Hakata-Ku, Fukuoka, Fukuoka, Japan
e-mail: ochiy@kge.co.jp

1   Introduction

In recent years, heavy rainfall exceeding 150 mm per day has occurred frequently in Japan due to the development of linear rainfall belts. In Japan, where there are many slopes such as mountains, heavy rains cause slope disasters, and the current situation is that the lives of local residents are threatened.

Slope disasters such as landslides and slope failures caused by heavy rainfall are triggered by an increase in pore water pressure due to a rise in groundwater level. Therefore, by grasping the relationship between rainfall and groundwater level fluctuations on slopes, we monitor signs of disaster occurrence in order to detect the possibility of slope disaster occurrence in advance.

In the event of a disaster, prompt emergency response is required to prevent further disasters from occurring. There are a wide variety of emergency response methods, and appropriate methods are selected to ensure stability on slopes in accordance with the factors and triggers of disaster occurrence. There are various factors that cause slope disasters, such as topographic alteration, load increase, water level rise, and earthquakes. Therefore, when considering countermeasures, it is necessary to grasp in detail the predisposing factors and triggers of disaster occurrence on the target slope through site reconnaissance in advance. Among various factors, groundwater level fluctuations are difficult to visually observe and estimate, so monitoring using installed observation equipment is necessary. However, the installation of the observation equipment requires pre-drilling with a boring machine, which takes several days. Therefore, there is currently a time lag between the occurrence of a disaster and the completion of installation of observation instruments for groundwater level monitoring. Therefore, in this presentation, we will introduce an efficient method of installing a groundwater level observation instrument that can be installed in less than half the time of the conventional method.

2   The Conventional Groundwater Level Monitoring Method

2.1   Installation Method of Groundwater Level Observation Hole Instrument

Common groundwater level monitoring uses observation holes with water level gauge installed in boreholes. However, installation of observation holes by drilling requires procedures such as carrying in a machine and drilling by machine. Therefore, in the general method, even if the range of landslide block or surface failure is large, the whole picture is assumed from the observation results predicted based on limited information. Therefore, instead of drilling a hole, we introduce a method of making

a water level observation hole by inserting a φ10 mm water level gauge into a screw weight sounding test hole.

2.2 Specifications of the Water Level Gauge

The water level gauge used is the JSTA series manufactured by Soksho Giken Co., Ltd. This water level gauge can be installed in a PVC pipe VP13, which has an outer diameter of 18 mm and an inner diameter of 13 mm [1]. In addition, depending on the specifications of the loggers to be connected, it is possible to build monitoring system, and it is also possible to set an alarm to be issued when the water level exceeds the reference level.

2.3 Groundwater Level Meter Installation

The screw weight sounding test can estimate the hardness and softness of the ground, the degree of compaction, and the composition of the soil layer by measuring the number of revolutions during penetration [2]. In addition, since this test can be conducted at multiple locations in one day, it is possible to install groundwater level observation holes more efficiently than drilling. Therefore, it is possible to measure the depth of unstable layers that are in danger of collapsing at the same time as drilling water level observation holes (Fig. 1).

3 On-Site Observation

3.1 Observation Site

The observation site is Asakura City, Fukuoka Prefecture, Japan. In July 2017, short-term torrential rain occurred frequently in the area, causing a serious slope disaster (Fig. 2). The heavy rainfall in this area was caused by the development of linear rainfall belts, and accumulated precipitation in 9 h exceeding 700 mm was recorded at many points in the city [3]. On the collapsed slope, a groundwater level observation hole was installed by the method introduced above (Fig. 3), and rainfall and groundwater level fluctuation were monitored.
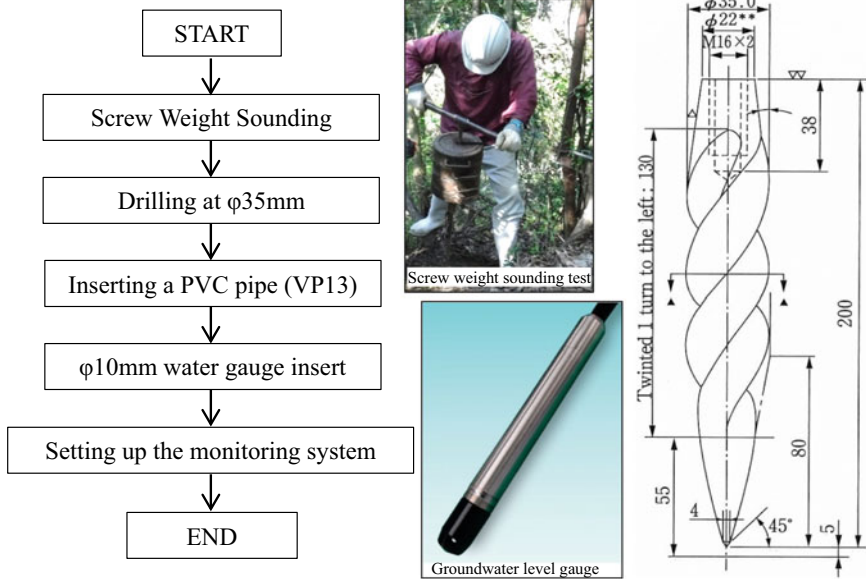
Fig. 1 Flow chart on the conventional installation method
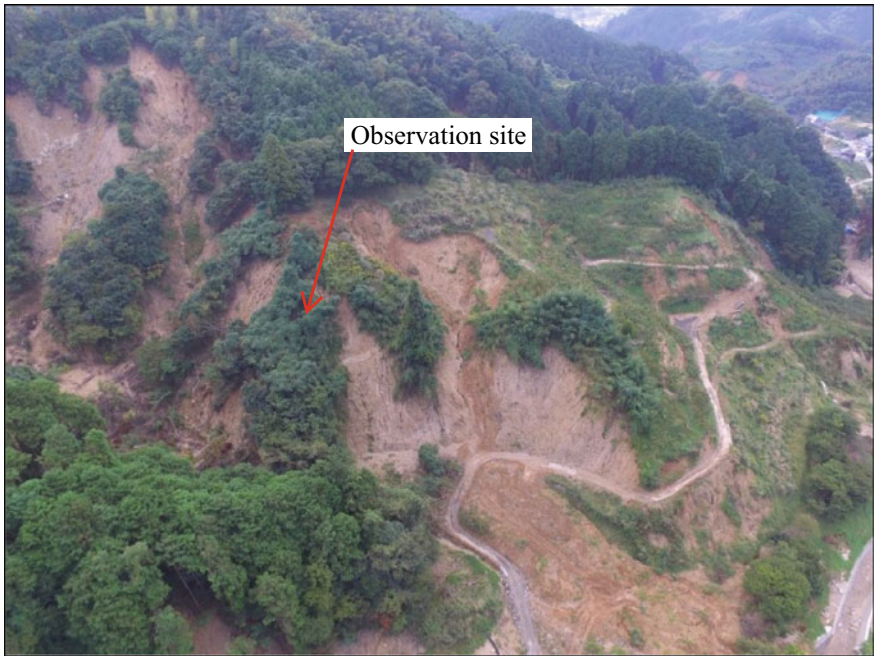
Fig. 2 Observation site
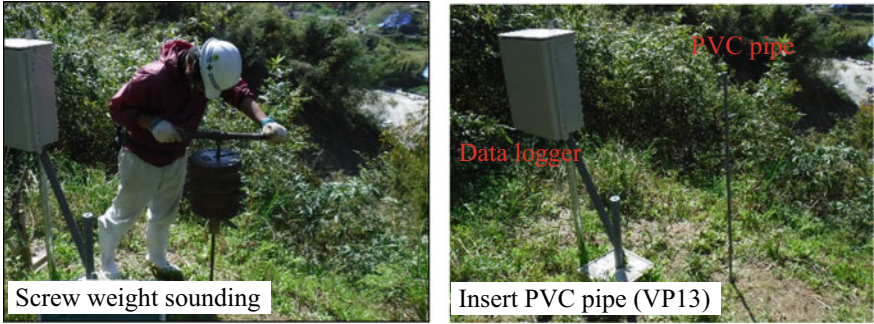
Fig. 3 Installation groundwater observation hole

3.2 Monitoring Results

The monitoring results are shown in Fig. 4. As a result of monitoring, the groundwater level in normal times is deeper than the bottom of the hole, but when there was a rainfall of 250 mm or more on July 6, 2020, the water level inside the hole was confirmed. It was confirmed that the same trend as the water level observation hole installed by the conventional method of drilling by mechanical boring can be obtained.

This conventional installation method takes about half day to install the drilling method by screw weight sounding test.
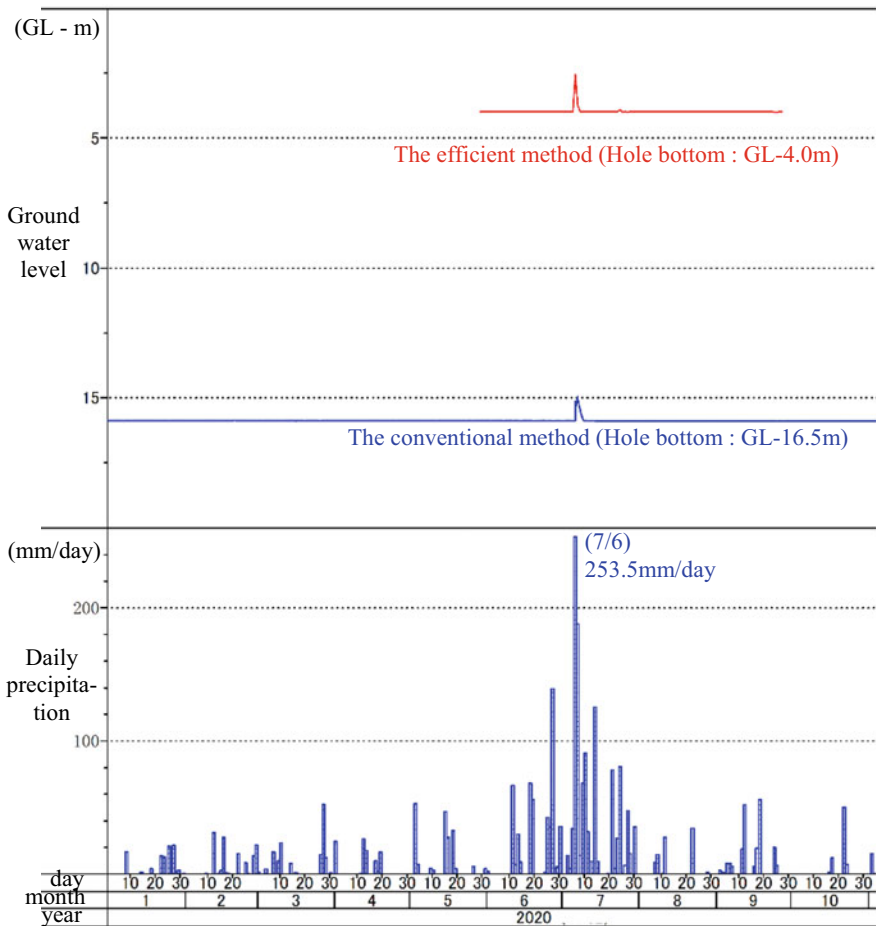
Fig. 4 The monitoring results

4   Conclusion

The water level observation hole installation method using a φ10mm water level gauge introduced this time is a method that can be installed more quickly than the drilling method using a boring machine. Because of penetration by screw weight sounding, it is not suitable for deep drilling, but it is possible to install several meters near the surface layer, and it is possible to install multiple places in a day.

In the field observation, it was confirmed that the groundwater level was formed near the surface layer in conjunction with rainfall as in the conventional method. However, since this method requires manual excavation, it may be difficult to excavate hard strata and uses a time consuming manually driven drill. Although machine

operated drill has excellent penetrating ability, the most of sites are difficult access and this limits the use of a machine operated drill.

Therefore, please consider adopting it based on the situation such as the local geology.

References

1. Soksho Giken Co., Hompage (2022) http://sokusho-giken.co.jp/jsta.html. Last Accessed 13 Nov 2022
2. Fukai A, Oshima A, Yasuda K, Matsutani Y (2020) Comparison between results of Swedish Weight sounding test stated in JIS and weight test stated in ISO. Japanese Geotech J 15(3):635–642
3. Asakra city Hompage (2022) https://www.city.asakura.lg.jp/www/contents/1560226180900/index.html. Last Accessed 13 Nov 2022

Evaluation Case of Characteristics for Improved Soil by Elastic Wave Velocity Test

Takaaki Ariki

Abstract In Japan, quality inspection of ground improvement is based on strength to confirm the required performance. Since strength is the target, the testing method is limited to unconfined compression test, and there is no alternative testing method, nor is there a clearly defined method for analyzing the factors that may cause the lack of required performance. Because of this, there is a problem of economic sustainability, such as re-executing a series of work from core sampling to testing. Therefore, we decided to study a method to deal with this problem by adding criteria such as defect factors to the inspection target. The purpose of this paper is to collect basic data for analyzing the factors that cause variations in strength and defects in quality inspections, as well as for analyzing and evaluating the results of such analysis and evaluation methods. The results of elastic wave velocity and needle penetration tests, in addition to unconfined compression test, on core specimens taken from the improved ground were briefly analyzed. The results indicated that one of the factors causing the variation in unconfined compression strength was the occupancy of voids and clods on the shear surface, which could be analyzed by the elastic wave velocity test. The correlation between unconfined compression strength and elastic wave velocity was also obtained, which could be used to estimate the unconfined compression strength. These results may suggest that the elastic wave velocity test is an effective alternative method to the unconfined compression test.

Keywords Ground improvement · Core of improved soil · Elastic wave velocity test · Unconfined compression test

1 Introduction

The inspection target of quality inspection of improved ground in Japan is defined as the unconfined compression strength of cores taken by all-core sampling satisfying the required performance [1, 2]. Confirmation that the inspection target in

---

T. Ariki (✉)
Wakachiku Construction Co., Ltd, Chiba, Japan
e-mail: takaaki.ariki@wakachiku.co.jp

quality inspection satisfies the required performance, which is a quality standard, is an indispensable item in construction management. On the other hand, there is no alternative method or method to identify the cause in cases where the required performance is not satisfied. Therefore, if the required performance is not satisfied, the entire process from core sampling to testing must be repeated, thereby causing a problem in terms of economic sustainability. The reason for not being able to clearly establish a method for identifying the cause of defects in ground improvement is that there are many factors that may cause variations in strength and defects to ground improvement, and it may be difficult to identify the main cause of the variations and defects. However, if the evaluation criteria for defect factors could be added to the inspection target, the repetitive works could be avoided, and thus, the problem of economic sustainability would be solved. The purpose of this study is to collect basic data for analyzing the factors that cause variations and defects of strength in quality inspections, as well as the methods for evaluating such variations and defects. In addition to unconfined compression test, elastic wave velocity test and needle penetration test were conducted on core specimens taken from the improved ground to conduct a simplified analysis of the factors causing the defects.

2 Testing Method of Elastic Wave Velocity

2.1 Elastic Wave Measuring System

There are two methods [3, 4] for laboratory elastic wave velocity tests in the Japanese Geotechnical Engineering Society (JGS) standard. In the elastic wave velocity test using a Bender Element (BE) for improved soil [3], Ismail and Rammah [5] mentioned that the specimen was disturbed because a trench was dug to insert the BE, and that the inserted BE was significantly affected by inequality of stress inside the specimen. To solve this problem, the test apparatus shown in Fig. 1 is designed to directly contact and hold the oscillator and receiver to the upper- and lower-end surfaces of the specimen, as in the elastic wave velocity test [4], in which the BE is not inserted into the specimen. The load applied to clamp the specimen between the oscillator and the receiver can be set by measuring it with a load cell attached to the loading axis.

As shown in Fig. 1, the measuring system including this test apparatus consists of a function generator that generates and transmits the input waveform, a bipolar power supply that amplifies the generated waveform, and a digital oscilloscope that measures the input wave and the received wave. A thickness vibrator and a thickness-slip vibrator are built into the oscillator and receiver, each of which corresponds to the oscillation and reception of P- and S-waves, respectively.
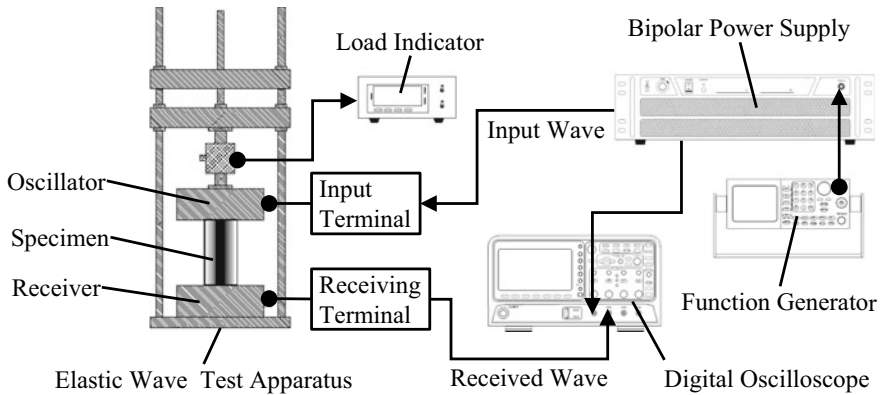
Fig. 1 Elastic wave measuring system

2.2 Testing Method

The specimen clamping pressure for elastic wave measurement was set at 6 kN/m^2 (40 N of load) and adjusted so that it did not change during the series of tests. The input waveform was a one-wavelength sine wave with an amplitude of ± 3 V and a frequency range of 7 frequencies between 1 and 100 kHz using a function generator. The amplitude of this waveform was amplified to ± 75 V via a bipolar power supply at the time of input to the specimen. To help identify the initial rise of the received wave, two phases of the input wave at the same frequency were used: 0 deg. and 180 deg. The S-wave was measured after the P-wave was measured.

2.3 Calculation Method for Elastic Wave Velocity

Figure 2 shows a schematic diagram of the input and received waves measured by the elastic wave measuring system and the method of obtaining the travel time. In this paper, the start-to-start method, which takes the difference between the input wave's rise time (point **S** in Fig. 2) and the received time (point **R** in Fig. 2), is used in the time domain method to obtain the travel time of the elastic wave. The travel time was determined by averaging the travel times of the initial rise of the received wave obtained by the method of crossing the forward and reverse phases. The elastic wave velocity was obtained by substituting the length of the specimen, the travel time of the initial rise, and the delay time of the entire measuring system into Eq. (1).

$$v = L/(\Delta t_\mathrm{s} - \Delta t_\mathrm{d}), \tag{1}$$
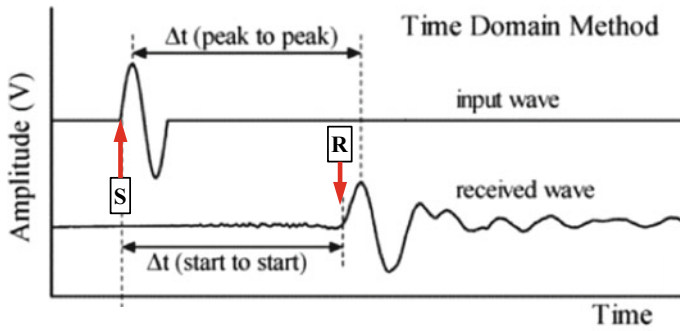
Fig. 2 Schematic diagram of the time domain method redrawn to [6]

where, v: velocity of elastic wave [m/s], L: length of specimen [m], Δt_s: travel time of initial rise by start-to-start method [s], Δt_d: delay time of the entire measuring system [s].

2.4 Specimens for the Tests

In this paper, the five core specimens taken by all-core sampling with an outer diameter of 116 mm from the improved by the high-pressure jet mixing method were used. The parallelism of the end faces was checked when each specimen was installed in the test apparatus. Those that did not ensure parallelism were shaved with a straight edge so that parallelism was ensured. As exemplified in Fig. 3, remaining voids and clods can be seen even after cutting and mixing by the high-pressure jet mixing method. In addition, wood chips and shells that had been mixed in were also confirmed. Table 1 summarizes the physical properties of the core specimens used in the tests.

3 Testing Results

3.1 Elastic Wave Velocity Test

An example of the received waveforms corresponding to the input waveforms of each frequency is shown in Fig. 4. As exemplified in Fig. 2, the rise time of the input wave is represented as 0 s. Note that the input waveforms are omitted from Fig. 4. The travel time of the received wave by the start-to-start method shown in Eq. (1) is represented in Fig. 4 as the average value obtained by the crossing method, where the input waveforms are in forward and reverse phases. These averaged travel times are indicated by dotted line in each figure.
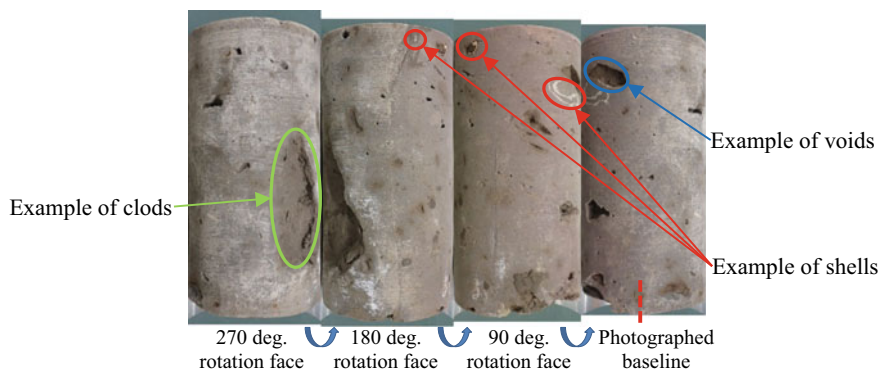
Fig. 3 Core specimen No.3 taken from improved by the high-pressure jet mixing method

Table 1 Physical properties of core specimen used in the tests

Core specimen No	1	2	3	4	5
Diameter [mm]	91.39	91.31	91.38	91.27	91.36
Length [mm]	178.17	180.86	178.78	178.61	179.18
Wet density [g/cm^3]	1.440	1.424	1.401	1.382	1.422
Dry density [g/cm^3]	0.819	0.852	0.840	0.805	0.812
Water content [%]	75.7	67.2	66.8	71.6	75.1

3.2 Unconfined Compression Test and Needle Penetration Test

Unconfined compression test [7] and needle penetration test [8] of the cores were conducted in accordance with the test methods of the respective JGS standards. The unconfined compression test was conducted at a compression rate of 1%/min until the applied load was reduced to 2/3 of the maximum compressive stress. Needle penetration test was conducted at a penetration rate of 2 mm/min until the penetration reached 10 mm, using the desktop type. The positions of the needle penetration test were set as shown in Fig. 5a for the upper- and lower-end faces of the core, and the needle penetration gradient was the harmonic mean of 42 measuring points for one specimen.

The test results of the five core specimens taken from all-core sampling No.3 (AC-3) in this paper are shown in Fig. 6. For comparison, the depth distributions of the unconfined compression test results and the results of needle penetration test of the other core specimens of AC-3 and the core specimens taken from AC-1 and AC-2 in different holes of the same improved ground as AC-3 are also shown in Fig. 6. The test positions for the portable type of needle penetration test were set as shown in Fig. 5b, and the needle penetration gradient was the harmonic mean of 12 measuring points for one specimen.
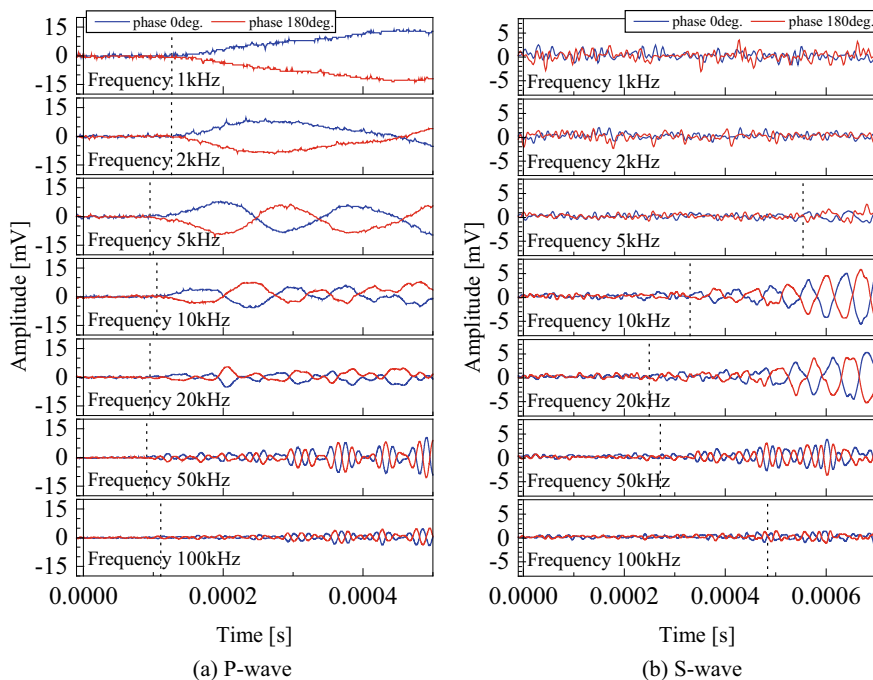
Fig. 4   Sample of received waveform by elastic wave velocity test (No. 3)
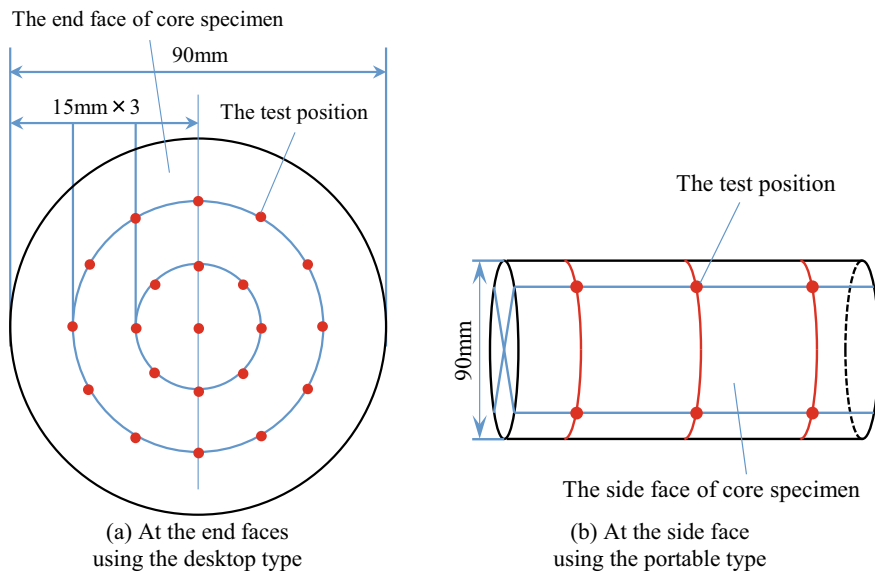
Fig. 5   Positions of the needle penetration test for the core specimen
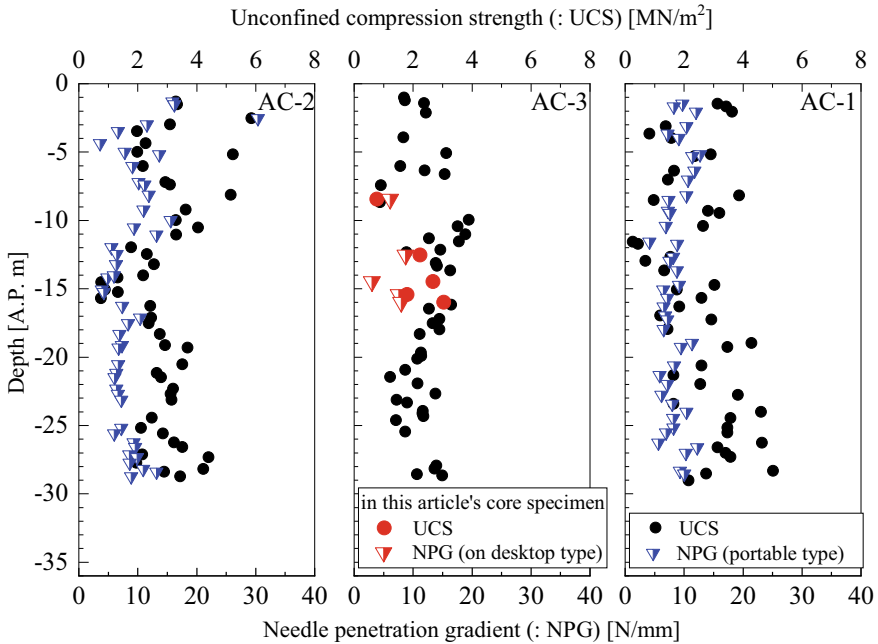
Fig. 6 Depth distribution of unconfined compression strength and needle penetration gradient

The trends of unconfined compression strength and needle penetration gradient in the depth direction shown in Fig. 6 were generally similar. The unconfined compression strength of this paper and the test results of other core specimens in AC-3 were generally equivalent. Although there seems to be a correlation between unconfined compression strength and needle penetration gradient, it might be inferred that there are some areas where the variation is large. The needle penetration gradient is obtained as the average gradient up to 10 mm penetration and is then a local penetration resistance force. As shown in the frequency distribution in Fig. 7, the individual needle penetration gradients are generally the same except for extremely small measuring points such as the clods. The needle penetration gradient of core specimen No. 1 is smaller than that of the other specimens. On the other hand, the unconfined compression strength is the average compression strength of the specimen or the shear resistance at the shear or failure surface. It would be possible to evaluate the correlation between unconfined compression strength and needle penetration gradient for a uniform specimen, but it would be difficult to consider the effect for a core specimen with voids or clods.

Fig. 7 Frequency
distribution of the needle
penetration gradients
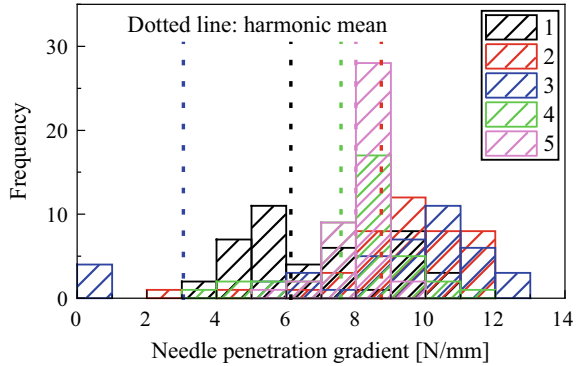
3.3 Observation of Core Specimens

For the five core specimens shown in Table 1, observations were conducted on the
end and side surfaces of the specimens before testing and on the shear or failure
surfaces after the unconfined compression test. An example of a shear or failure
surface observed is shown in Fig. 8. The voids and clods that were not cutting and
mixed were observed in the shear or failure surface, and these areas are indicated
by the red circles in Fig. 8. Table 2 shows the percentage of voids and clods in the
projecting cross-sectional area of the end, side, and shear surface of the specimen.
Occupancy was estimated for each of the upper- and lower-end faces of the specimen,
with the occupancy being the larger value.

3.4 Consideration of Testing Results

This section mainly considers the relationship between unconfined compression
strength and elastic wave velocity, as well as the relationship between voids and
clods occupancy. The relationship between elastic wave velocity and unconfined
compression strength at an input frequency of 10 kHz is shown in Fig. 9, where
the test results obtained from the uniform laboratory-mixed specimens are used as
a reference to compare the general trend. The laboratory-mixed specimens were
prepared by blending a mixed sample of Toyoura sand and Kaolin with blast furnace
cement type B. The laboratory-mixed specimens were tested in the similar method
as the core specimens. Figure 9 shows the test results of a laboratory-mixed uniform
specimen as a comparative example. The relationship between elastic wave velocity
and unconfined compression strength of the core specimens is close to that of the
laboratory-mixed specimens, so it is indicated that there is a correlation between the
two.

Figure 10a shows the relationship between the voids and clods occupancy and
the unconfined compression strength shown in Table 2, and Fig. 10b shows the
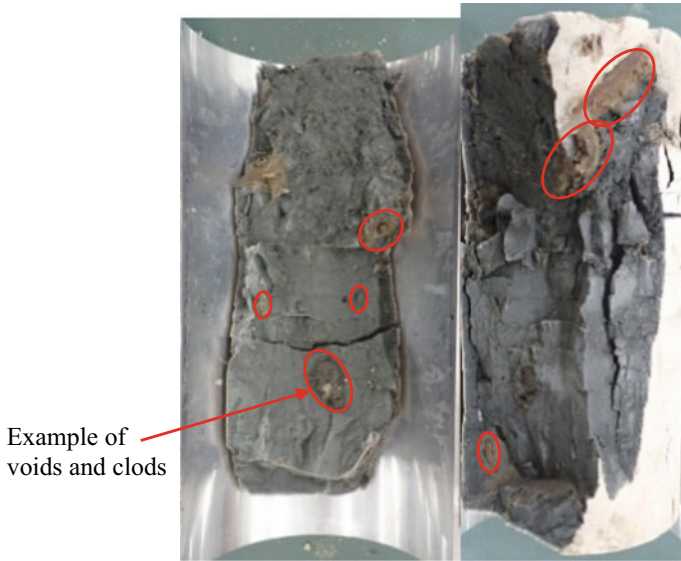
Fig. 8 Sample photograph of shear surface (No. 2)

Table 2 Occupancies of voids and clods of core specimens

Core specimen No		1	2	3	4	5
Occupancy of voids and clods [%]	Shear surface	35	12	6	16	3
	End surfaces	3	18	31	20	0
	Side surface	24	20	21	16	2

(a) Primary wave velocity

(b) Secondary wave velocity
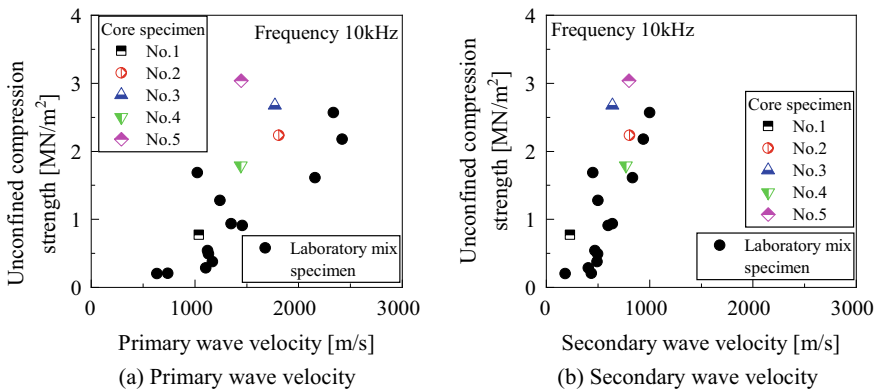
Fig. 9 Relationship between elastic wave velocities and unconfined compression strength
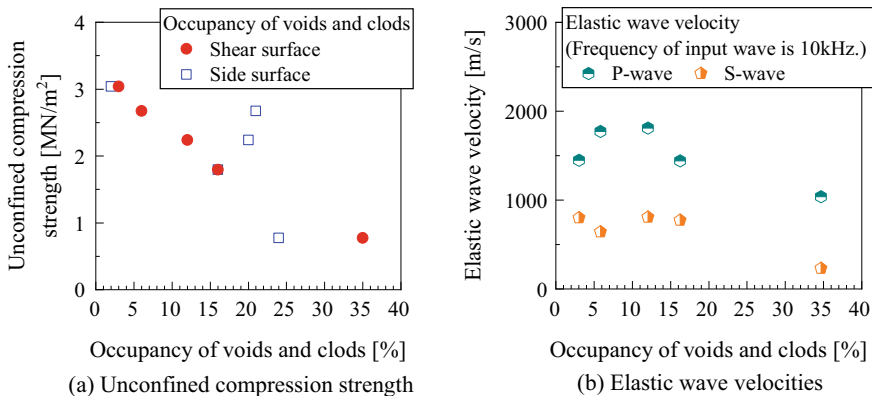
Fig. 10 Relationship between occupancies of voids and clods of the core specimens

relationship between the voids and clods occupancy on the shear surface and the elastic wave velocity. As shown in Fig. 10a, the unconfined compression strength clearly decreases with increasing voids and clods occupancy on the shear surface. This is assumed to be because the unconfined compression strength is caused by the shear resistance force at the shear surface or the cracking surface. The failure mode of the core specimens was observed as shear or crack failure. On the other hand, as shown in Fig. 10b, both P- and S-wave velocities tended to decrease when the occupancy of voids and clods exceeded about 20%.

These results provide a possibility of estimating the unconfined compression strength and the internal condition of the specimen by measuring the elastic wave velocity. These estimation results may contribute to the analysis of the causes of variation in unconfined compression strength.

4   Conclusion

The purpose of this paper is to collect basic data for analyzing the factors that cause variations and defects in the strength of individual core specimens in quality inspections, as well as for analyzing and evaluating the results of such analyses. Using core specimens taken from improved ground, needle penetration and elastic wave velocity tests were conducted in addition to the unconfined compression test, which is the usual evaluation method, to conduct a simple analysis of the factors that affect the failure of the specimens.

The results indicate that one of the factors influencing the variation in unconfined compression strength is the occupancy of voids and clods on the shear surface. Also, there was a correlation between the elastic wave velocity and the unconfined compression strength. Furthermore, the elastic wave velocity tended to decrease as the voids and clods occupancy on the shear surface increased. Therefore, it is

expected that the elastic wave velocity test can be used as an alternative method to the unconfined compression test and that the factors affecting the variation of unconfined compression strength can be analyzed.

To confirm these trends, it will be necessary to accumulate test results using specimens in various conditions.

References

1. Public Works Research Center: Design and construction manual for cement deep mixing method (in Japanese) (2022)
2. Costal Development Institute Technology: Technical manual of cement deep mixing method for port and airport (in Japanese) (2018)
3. Japanese Geotechnical Society: Method for laboratory measurement of shear wave velocity of soils by bender element test, Japanese Geotechnical Society Standards Laboratory Testing Standards of Geomaterials (2018) vol 3
4. Japanese Geotechnical Society: Method for laboratory measurement of ultrasonic wave velocity of rock by pulse test, Japanese Geotechnical Society Standards Laboratory Testing Standards of Geomaterials (2018) vol 3
5. Ismail MA, Rammah KI (2005) Shear-plate transducers as a possible alternative to bender elements for measuring G_{max}. Géotechnique 55(5):403–407
6. Satoshi Y, Takayuki K, Yukio N, Takeko M, Teruyuki F, Satoru S (2009) Interpretation of international parallel test on the measurement of G_{max} using bender elements. Soils Found 49(4):631–650
7. Japanese Geotechnical Society: Method for unconfined compression test of soils, Japanese Geotechnical Society Standards Laboratory Testing Standards of Geomaterials (2015) vol 1
8. Japanese Geotechnical Society: Method for needle penetration test, Japanese Geotechnical Society Standards Geotechnical and Geoenvironmental Investigation Methods (2018) vol 3

Groundwater Control Measures for Deep Excavation of Bangkok MRT

Pastsakorn Kitiyodom, Woraphon Wiriyatharakij, and Anucha Yamchoo

Abstract Over the past few years, Mass Rapid Transit (MRT) Projects have been implemented in Bangkok as part of a master plan for the city and its surrounding areas. However, the underground construction of the MRT in Bangkok has become increasingly complicated due to the effects of the groundwater rebound in underlaid sand layers, which has posed a significant challenge in designing and building underground structures. Most of underground structures in the MRT projects are located deeper than the piezometric profile within the sand aquifer, which is currently at approximately 13 m deep from the ground level, making them vulnerable to hydraulic uplift and piping failures. Depending on factors such as station configuration, excavation level, and soil strata at the site, various methods including diaphragm cut-off wall, staged excavation, blanket grouting, and dewatering have been considered on a site-by-site basis and presented in this paper. This paper focuses on groundwater control measures for the MRT Blue Line Extension Project Contract 2 and the MRT Orange Line East Project Contract E1 and E2 and aims to serve as a reference for practitioners in the construction industry who are involved in deep excavation work with high groundwater pressure.

Keywords Deep excavation · MRT station · Groundwater · Grouting

1 Introduction

The implementation of construction projects in Bangkok has become increasingly complex, particularly in the design and construction of underground structures due to the rebound of piezometric pressure in the underlaid sand aquifer. This paper aims to report on a groundwater control method adopted in the MRT projects.

P. Kitiyodom (✉)
ATT Consultants Co., Ltd, Bangkok, Thailand
e-mail: pastsakorn_k@attconsult.com

W. Wiriyatharakij · A. Yamchoo
Geotechnical and Foundation Engineering Co., Ltd, Bangkok, Thailand

1.1 Background of the Projects

The MRT Blue Line Extension has been implemented by the Mass Rapid Transit Authority of Thailand (MRTA) as part of the government's policy to develop a comprehensive mass electric train system network to enhance the quality of life of Bangkok's residents. The major components of MRT Blue Line Extension Project Contract 2 comprise approximately 2.6 km of infrastructure, including two underground stations, intervention shaft, cut-and-cover tunnel and twin bored tunnels. Construction was completed in 2018.

The MRT Orange Line East Project Contract E1 and E2 comprises approximately 9.73 km of infrastructure, including seven underground stations, a cut-and-cover tunnel, ventilation and intervention shafts, depot accesses, and twin bored tunnels. Construction began in 2017 and was completed in 2022.

The construction of both Blue Line Extension and Orange Line East involved deep excavation that utilizes a diaphragm wall as a retaining structure through the top-down construction method. The foundation system of the deep station excavation consisted of the diaphragm walls, base slab, and bored piles or barrettes. Ensuring the economical design without compromising safety is of utmost importance and can be achieved through a well-designed concept of deep excavation works and effective groundwater control methods.

2 Geological Condition of Bangkok Subsoil

2.1 Geology

Bangkok city is in a low-lying area known as the Chao Phraya plain, where the subsoil profile is consistent across different parts of the city. The existing ground elevations range from 0 to 2 m above mean sea level and are composed of marine deposits. The subsoil profile typically consists of up to 3 m of made ground, followed by a layer of Bangkok Soft Clay that ranges from 10 to 15 m thick with its undrained shear strength of about 10–25 kPa. Between the soft clay and the underlying stiff clay, a layer of medium stiff clay measuring 2–4 m thick can be observed with its undrained shear strength of about 25–50 kPa. Further down, alternating layers of stiff to hard clay with its undrained shear strength range from 50–200 kPa and dense to very dense sand with its SPT-N value range from 20–50 are found. The geological profile of the MRT Blue Line Extension Contract 2 and MRT Orange Line Contract E1 and E2 can be seen in Figs. 1, 2 and 3, respectively.
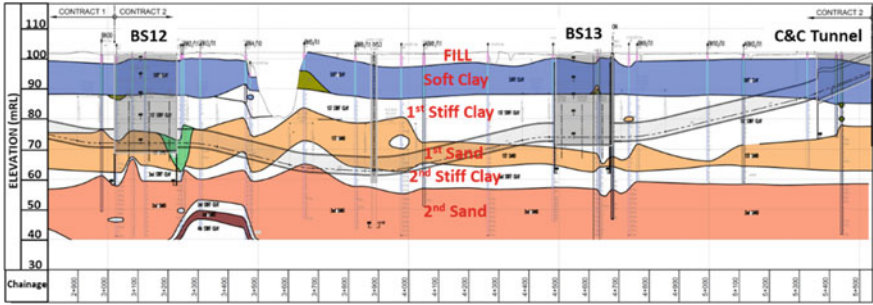
Fig. 1 Geological soil profile for MRT blue line extension project contract 2
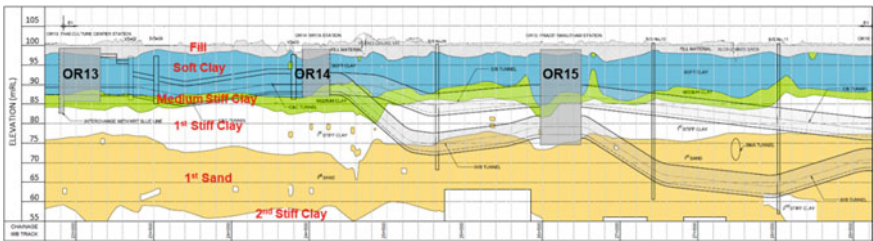
Fig. 2 Geological soil profile for MRT orange line project contract E1
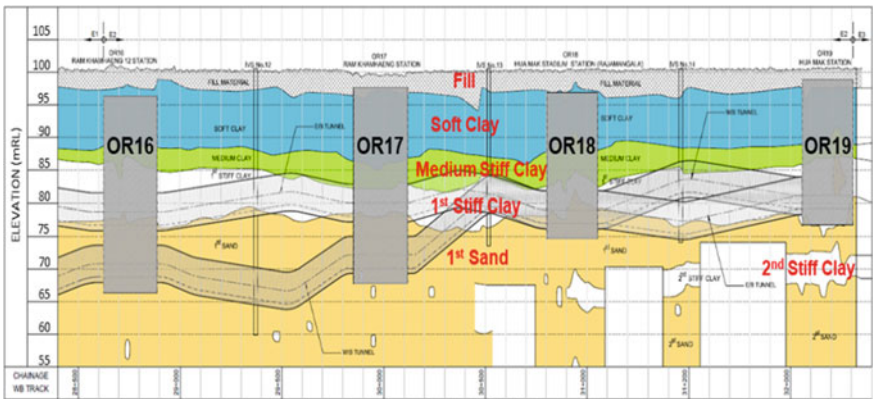
Fig. 3 Geological soil profile for MRT orange line project contract E2

2.2 Hydrology

Starting in the 1970s, Bangkok has experienced land subsidence due to the extraction of water from the upper and lower confined sandy layers (First and Second Sand strata). This lowering of the groundwater table has led to significant and ongoing consolidation settlement throughout the metropolitan area [1].

As a result, measures have been taken to control groundwater extraction within urban areas, starting with the implementation and enforcement of the Groundwater Act in Bangkok. Mitigation measures have included the expansion of tap water supply and strict enforcement of groundwater laws, which have led to a reduction in groundwater use.

The Department of Groundwater Resources has been continuously monitoring groundwater levels at various locations, and the data collected indicates that the groundwater piezometric levels in the sand layer have been increasing over time.

The rebound of groundwater has successfully addressed the serious issue of land subsidence in Bangkok. However, this has the potential to cause adverse effects on existing structures and ongoing underground construction works. It should be noted that the piezometric pressures within the first sand layer and below are still showing a slight recovery in groundwater pressure when compared to data recorded in the past.

During the design and construction stages of MRT Blue Line Extension Project, piezometric pressure in sand layer was observed at approximately 15 m below ground level with gradually rising up from time to time.

Consequently, during construction of MRT Orange Line East Project, the variation of piezometric profile with depth was observed as shown in Fig. 4. The proposed short-term design piezometric profile, at 12.9 m depth below ground level, was intended to provide a conservative estimate of the groundwater pressures that could potentially affect the construction of underground structures during the project's duration. This allows for proper design and implementation of groundwater control measures to prevent any adverse effects on the construction. It is important to note that the piezometric profile may continue to change over time, and regular monitoring and adjustments to the groundwater control measures may be necessary to ensure the safety and stability of the underground structures.

In the long term, it is expected that the piezometric pressures will continue to recover due to the control of groundwater extraction. Therefore, the design of underground structures should consider the full hydrostatic piezometric pressure profile from the ground level. This will ensure the safety of underground structures in long term.

Fig. 4 Monitored
piezometric pressure with
depth for MRT orange line
east project
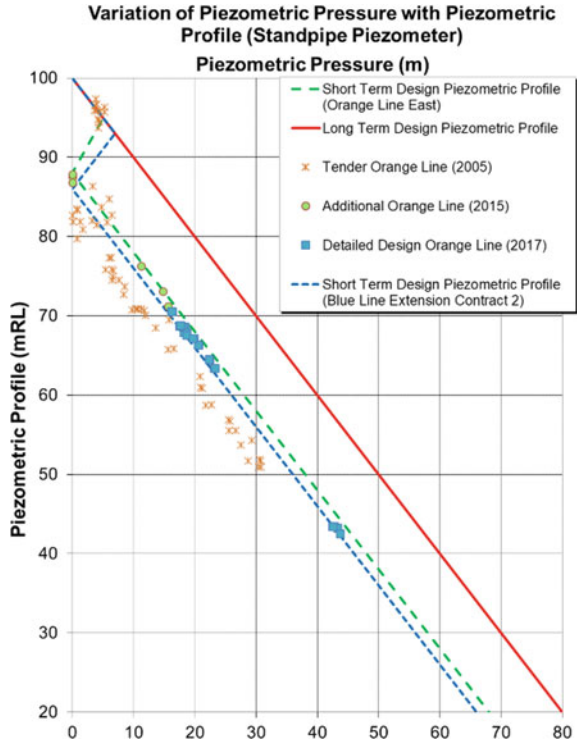
3   Stability of Excavation Base

3.1   Base Failure Due to Groundwater Pressure

To facilitate the deep excavation works in Bangkok subsoil, diaphragm wall (D-wall) as embedded earth retaining structure is known as one of the most suitable solutions [2]. Groundwater control is a critical aspect of excavation work, since the stations and intervention shafts are often situated below the piezometric level of the sand aquifer. Groundwater control measures are implemented to prevent piping/boiling in sands and blow-out in clays, which can lead to instability. Another mode of failures is also taken into consideration to ensure that the excavation base remains stable.

Hydraulic Uplift Stability (Blow-out Failure). In cases where there is a permeable layer under an impermeable layer below the excavation surface, the permeable layer can be lifted by the high groundwater pressure, as shown in Fig. 5. If the water pressure at the bottom of the clay layer exceeds the weight of the overburden soil, the bottom of the excavation may "blow out." The factor of safety can be determined using a basic weight balance equation, as follows:

$$FS = \gamma_s H_s / U, \qquad (1)$$
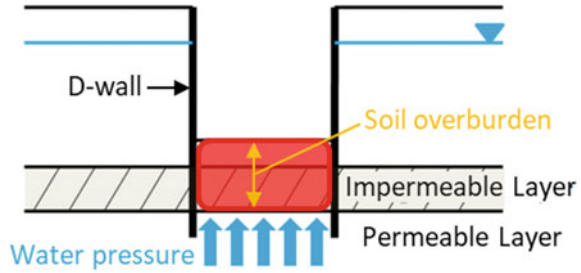
where γ_s is total unit weight of overburden soil, H_s is thickness of overburden soil layer above sand aquifer, and U is groundwater pressure in sand aquifer. A usually applied minimum FS is 1.2.

4 Groundwater Control Measures

This section describes the possible methods to control base instability issue for deep excavation in Bangkok subsoil condition.

4.1 Staged Excavation Approach

The staged excavation approach involves dividing excavation works for the base slab level in small areas. The small-sized excavation area is bounded by a higher soil surcharge and a concrete slab around the perimeter. This method improves the stability of the excavated soil base against "blow-out" by increasing the side shear resistance of the soil along the perimeter.

The excavation at BS13 Itsaraphap Station during the MRT Blue Line Extension Contract 2 Project also encountered issues related to uplift stability at the base. To address this, a modified staged excavation approach was implemented. The staged excavation works were successfully completed without any problems related to uplift stability. Moreover, three-dimensional analysis by finite element software was performed to verify the behavior of staged excavation approach [3].

To address the hydraulic uplift stability issue during the excavation works for MRT Orange Line East OR19 Hua Mak Station, preventive measures have been taken due to the marginal deficiency of factor of safety against hydraulic uplift stability. The proposed solution is to conduct a staged excavation approach.

An extensive soil investigation program was conducted at OR19 Station, which revealed the presence of a 2nd stiff clay layer with a thickness ranging from 2 to 7m
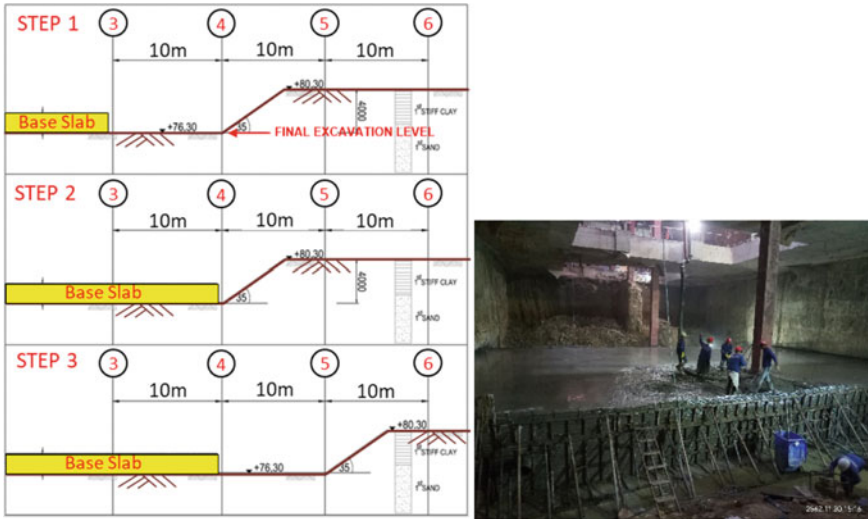
Fig. 6 Staged excavation sequences for OR19 Station

throughout the station. This layer was considered to be an impermeable layer and served as a barrier for the staged excavation works.

The stability of the excavation works at OR19 is critical, and several alternatives have been considered to ensure safety during construction. The chosen method involved carefully strip excavating starting from the first section with an adjacent safety berm that is 4m high. The excavation was conducted step by step, as shown in Fig. 6, to ensure stability throughout the process.

The proposed modifications to the excavation sequences have resulted in a higher factor of safety for all excavation stages, exceeding the required minimum value. The analysis of stability showed that the proposed sequences are safe for the construction of OR19. However, it is crucial to monitor and control the piezometric pressure in the 2nd Sand Layer before beginning any excavation activities.

4.2 Extension of Unreinforced D-wall

When constructing structural D-walls in a thick sand layer, excavating in sand with high piezometric pressure can be dangerous. In this scenario, if a stiff clay layer (impermeable layer) is present below the sand layer, the diaphragm wall toe level can be extended to penetrate into those impermeable layers (2nd stiff clay or 3rd stiff clay) to cut off groundwater pressure inside the excavation area. Deep well pumps can be used to control the groundwater level inside the excavation area during excavation. This technique can improve the factor of safety against hydraulic uplift failure.

Reference has been made to Orange Line East OR15 station; most of the final excavation level (25 m depth) was located in thick 1st/2nd sand layer with high piezometric pressure. Therefore, groundwater control measure was applied to ensure the stability of the excavation and safety during the construction. Various groundwater control measures were considered based on design and construction requirements. The extension of unreinforced D-wall was selected as this method can be performed simultaneously with the structural D-wall construction. The D-wall was extended to the impermeable 3rd stiff clay layer below the sand layer. However, as the depth of the 3rd stiff clay layer varies, the toe level of the extended D-wall also differs accordingly. A schematic of the extended D-wall and toe levels is presented in Fig. 7.
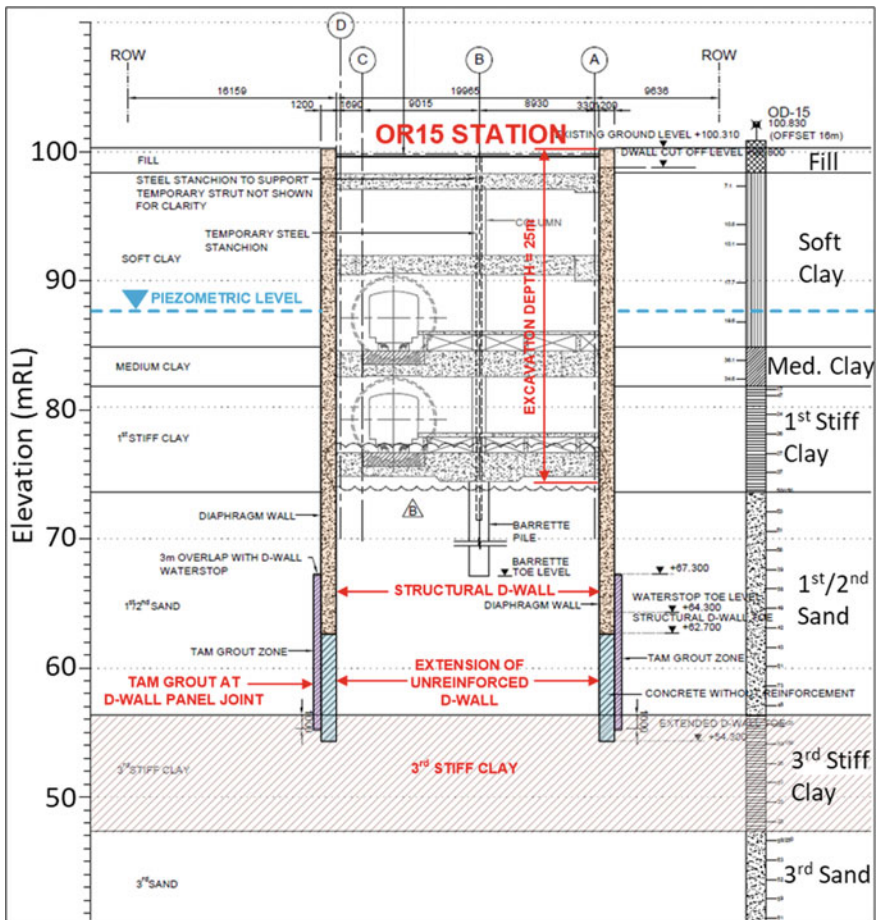
Fig. 7 Station OR15 cross-section with extension of D-wall for groundwater cut-off

4.3 Tube-A-Manchette Grouting

The Tube-A-Manchette (TAM) method is an effective chemical grouting technique that can be used to decrease the permeability of the sand layer. TAM grouting can be implemented in either a blanket arrangement or a D-wall joint grout arrangement, which serves as a waterproof barrier in the excavation area.

To reduce potential leakage at the joint of the D-wall panels, ground treatment by TAM grouting is applied to the outer joints of the D-wall panels. After the TAM grouting is completed, a pump test and dewatering scheme are conducted to ensure that the amount of groundwater in the sand layer is within a safe range.

Additional grouting is prepared in case it is needed during the excavation. Structural and ground movements are monitored to prevent any damage to the station or nearby structures.

Reference has been made to BS12 main station box of Blue Line Extension Project where the TAM grout was adopted in blanket arrangement. A 4 m thick TAM grout covering the area more than 5000 m^2 was performed in 2nd sand layer at depth of approximately 53 m from ground. Construction was successfully completed without any adverse event during excavation (Fig. 8).

Fig. 8 Tube-A-Manchette (TAM) grouting operation at BS12 station box
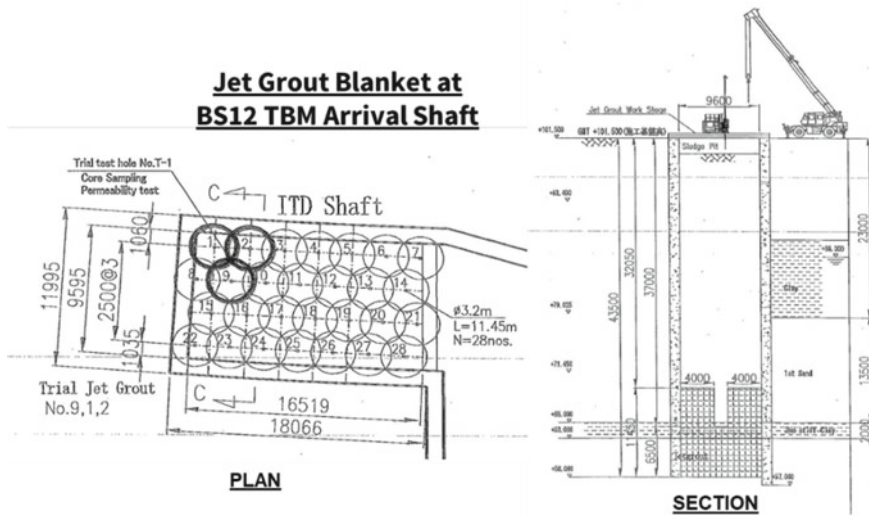
Fig. 9 Jet grouting in blanket arrangement at BS12 TBM arrival shaft

4.4 Jet Grouting

When deep excavations are to be made in thick sand layers and high piezometric pressures are present, it may not be safe to excavate in such conditions. To ensure safety, jet grouting can be utilized to create a watertight barrier around the excavation area. The thickness of the jet grout block is determined by checking for punching shear, shear stress, and bending stress. High-pressure cement grouting is used to improve the strength and water-tightness of the soil, which also aid in the design of the diaphragm wall.

At the TBM arrival shaft at BS12 Station of Blue Line Extension Project, jet grouting in blanket arrangement with thickness of 11.45 m was conducted for groundwater control purpose. A large 3.2 m diameter with a total of 28 nos. of overlapping jet grout columns was formed as a watertight barrier to ensure stability against hydraulic uplift and piping as shown in Fig. 9.

Table 1 provides a summary of the groundwater control methods that were implemented for the MRT Blue Line Extension Project Contract 2 and MRT Orange Line Project Contract E1 and E2. The selection of an appropriate method was based on careful consideration of both the design and construction aspects of the project.

Table 1 Summary of groundwater control method adopted for MRT blue line extension project contract 2 and MRT orange line project contract E1 and E2

Project	Station No	Groundwater control method adopted
MRT blue line extension project contract 2	BS12 Station	TAM blanket grouting (station box) Jet grouting (TBM arrival shaft)
	BS13 Station	Staged Excavation
MRT orange line project contract E1 and E2	OR13 Station	Not required due to shallow excavation
	OR14 Station	Not required due to shallow excavation
	OR15 Station	Extension of unreinforced D-wall coupled with TAM grouting at D-wall joint
	OR16 Station	Extension of unreinforced D-wall coupled with TAM grouting at D-wall joint
	OR17 Station	Extension of unreinforced D-wall coupled with TAM grouting at D-wall joint
	OR18 Station	Extension of unreinforced D-wall coupled with TAM grouting at D-wall joint
	OR19 Station	Staged Excavation

5 Conclusion

The design and construction of underground structures for the MRT project in Bangkok face significant challenges related to the resurgence of piezometric pressure in sand layers. However, valuable lessons have been learned from the completion of previous MRT projects, which can be applied to the planning and construction of the MRT Orange Line East. This paper provides a brief overview of various methods for managing groundwater during construction and outlines the groundwater control measures employed for the MRT Blue Line Extension and MRT Orange Line East Project. Given the situation of rising groundwater, it is anticipated that these measures will be crucial for the success of the underground construction works in Bangkok's MRT system.

References

1. Phienwej N, Giao PH, Nutalaya P (2006) Land subsidence in Bangkok, Thailand. Eng Geol 82:187–201
2. Aye ZZ, Boonyarak T, Thasnanipan N, Prongmanee N (2015) Diaphragm wall support deep-excavations for underground space in Bangkok subsoil. In: Proceedings of the international conference and exhibition on tunneling and underground space (ICETUS2015), 3–5 March 2015, Kuala Lumpur, Malaysia
3. Wiriyatharakij W (2016) MRTA station excavation under situation of space constraint and potential hydraulic uplift at base: cases of Sanamchai & Itsaraphap stations. Master Thesis, Asian Institute of Technology, Thailand

Influence of Nano-Clay on Microstructure and Mechanical Properties of Fiber-Reinforced Cement Mortar at Elevated Temperature

S. Kiran, Sadath Ali Khan Zai, Mallikarjun. A. Indi, and Amruth.R. Naik

Abstract A detailed experimental studies on use of cement as partial replacement with ground granulated blast furnace slag along with nano-clay and polypropylene fibers to improve bonding properties and shrinkage properties of cement mortar at elevated temperature were carried out in the Department of Civil Engineering, Bangalore University, Bangalore, Karnataka, India. The testing specimens casted and tested as per IS specifications, cubes (70.6 mm), cylinders (100 mm diameter and 200 mm height), prisms (160 mm length, 40 mm width, and 40 mm depth), with cement mortar mix 1:3, and polypropylene fibers (0.25% by weight of cement) all the test specimens are subjected to at elevated temperature varying from 200, 400, 600 and 800 °C, respectively. Retention time of 2 h is considered in the oven with respect to temperature and then strength properties at normal temperature as well as at elevated temperature were studied. The test results show that there is significant resistance in the strength properties can be resisted up to 400 °C then decrease in strength with rise of temperature. Scanning electron microscope and EDX were considered for morphology and mineral composition of modified cement mortar at normal temperature and elevated temperatures.

Keywords Nano-clay · Polypropylene fibers (PPF) · Elevated temperature

1 Introduction

Homogeneous cement mortar can be made by mixing the proper amounts of cement, sand, and water. Mortar is a working substance that hardens and is used to fill spaces between building materials like stones, bricks, and concrete masonry units, bind them

S. Kiran (✉)
Department of Civil Engineering, UVCE, Bangalore University, Bangalore-560056, Karnataka, India
e-mail: kiran14ask@gmail.com

S. A. K. Zai · Mallikarjun. A. Indi · Amruth.R. Naik
Department of Civil Engineering, UVCE, Bangalore University, Bangalore-56, Karnataka, India

together, distribute their weight evenly, and adorn masonry walls with beautiful colors or patterns. There are significant energy and environmental losses as a result of the massive amounts of raw materials and natural resources needed to produce cement and concrete. A large amount of carbon dioxide, a naturally occurring greenhouse gas, is also released during this process. Modifications and improvements to the current concrete production methods are needed to address these environmental and cost issues. This has led to researchers in the field of concrete engineering and technology researching into and identifying various by-product materials. This can be used in place of the constituent parts for preparing cement mortar and concrete at high temperatures. Due to their unique physical and chemical characteristics, nanoparticles are receiving more and more attention and are being used in numerous fields to develop novel materials with cutting-edge functionality.

2 Literature Review

The compressive strength, flexural strength, and [1] tensile strength of mortar were increased by 11%, 5%, and 9%, respectively, by 2% optimized nano-clay by weight of cement. The mortar also had water binder ratios of 0.55 and cube specimens of 50 mm that were water cured for 7 and 28 days. Images created utilizing replacement will be more homogeneous and denser when seen using a scanning electron microscope (SEM) [2]. OPC 43 was substituted in cement mortar with varying concentrations, from 0.5 to 2% by cement weight, and it had positive effects on the mortar's durability and mechanical properties, CM 1:3 water-cured mixture having a 0.40 water-to-cement ratio. In a mortar cube of 50 mm for compressive strength and 85 mm*50 mm for durability parameters, 1.5% of nano-silica and 2% of nano-clay increased the compressive and split tensile strengths, superior strength, permeability, and resistance to the control mix [3]. Strength and microstructure of cement mortar using nano-clay by replacement are 0%, 1%, 3%, and 5% by weight of cement with OPC, the cube specimen of 50 mm, flexural prism of 40*40*160 mm casted and water cured for 28 and 90 days, the compressive strength and flexural strength enhancement is 15.2% and 30%, respectively. The improvement in the residual strength up to 5% use of nano-clay when it is subjected to elevated temperature. SEM and X-ray diffraction (XRD) results prove that stable structure matrix even after the mortar is exposed to 250 °C. The results also point to a greater production of CSH gel, which improves residual strength even at high temperatures [4]. Cube specimens of 70.6 mm with 8, 10, 12, 14 and 16 molar concentrations of sodium hydroxide and sodium silicate are used, together with 10% GGBS, over a range of temperatures between 600 and 900 °C, the cubes are cured with water for 3, 7 and 28 days, geopolymer mortar utilizing M Sand has gained higher strength compared to geopolymer mortar using natural sand, and oven curing is the most effective technique of curing geopolymer concrete. The improvement in compressive strength for 28 days is 6.6% at 8 molar concentration [5]. Mechanical properties of cement mortar with polypropylene fibers of 1% and nano-materials 3% by weight of cement, CM 1:3 of 50 mm cube specimens

are cast for 3, 7 and 28 days. Improvement in compressive strength is marginal for all curing periods, but tensile strength is greater with the addition of 1% fibers. However, increasing the fiber content tends to cluster and to generate more micro-defects in the mortar matrix, and curing in microwaves further deteriorates in the properties.

3 Research Significance

The research work signifies the investigation on optimization of nano-clay, GGBS in cement mortar mix 1:3 to obtain maximum compressive strength to be used in different construction practices, the main focus of this studies are to study the hardened properties of mortar such as compressive, split tensile, flexural strength at normal and elevated temperature and also to analyze the surface morphology Scanning electron microscope (SEM), are performed for Mix 1 (Cement 100% + M Sand 100%), Mix 2 (Cement 70% + M Sand 100% + 30% GGBS), Mix 3 (Cement 67% + M Sand 100% + 30% GGBS + 3% nano-clay) and Mix 4 (Cement 67% + M Sand 100% + 3% nano-clay + 30% GGBS + 0.25% PPF) under consideration for actual applications, sustainable with long term performance even after subjected to elevated temperature of 800 °C when mixed with nano-clay; with experimental studies, it is evident that there may be increase in strength, and also, it will increase service life of mortar which in turn lead economic aspect consideration.

4 Materials

In this present research investigation Ordinary Portland Cement (OPC- 43 Grade) Ramco cement, manufactured sand (M Sand) passes through a 4.75 mm sieve and retained on 150μ (zone II), nano-clay (1nm-200nm) (Montmorillonite), ground granulated blast furnace pulverized slag of specific gravity 2.38, polypropylene (Recron 3s 6mm), and water (ordinary potable water) were used with cement mortar 1:3.

5 Test Specimens

For the experimental program, there are four different mixes with series of 900 testing specimens out of which 300 number of cubes (70.6 mm), 300 number of cylinders (100 mm diameter and 200 mm height), 300 number of prisms (160 mm length, 40 mm width, and 40 mm depth), with cement mortar mix 1:3, and polypropylene fibers (0.25% by weight of cement). Further to study the surface morphology of the cement mortar, The final mixes used in the main experimental program are as follows:

Mix 1 = (Cement 30% + River Sand 70%)

Mix 2 = (Cement 29.925% + 0.075% PPF + M Sand 70%)

Mix 3 = (Cement 20.925% + 0.075% PPF + 9% GGBS + M Sand 70%)

Mix 4 = (Cement 20.025% + 0.075% PPF + 9% GGBS + 0.9% Nano clay + M Sand 70%).

6 Test Program

The experimental investigation involves the determination of mechanical properties of cement mortar for mixes: Mix 1 (control mix), Mix 2, Mix 3 and Mix 4 for flexural, compressive, and split tensile strength for 3, 7, 28, 56, and 90 days, and the outcomes are summarized.

Mixing nano-powder with cement as blended composite. Dry mixing of fine aggregate and PPF, water is added and mixed until to homogeneous mix. The test samples are casted, molded, cured, and exposed to elevated temperature for 200, 400, 600 and 800 °C.

7 Results and Discussions

Hardened properties of cement mortar

Compressive Strength (Table 1)

From experimental results, it is clear that for 28 days, increase in compressive strength for Mix 1, Mix 2, Mix 3, and Mix 4 from 26° to 400 °C is 23.37%, 26.16%, 21.72%, and 35.34%, respectively. It is also noticed that from 600 to 800 °C, the strength is reduced by 63.28%, 64.34%, 65.67%, and 66.41%, respectively (Table 1 and Fig. 1).

It is found that for 28 days, increase in split tensile strength for Mix 1, Mix 2, Mix 3, and Mix 4 from 26° to 400 °C is 14.19%, 10.97%, 15.35%, and 16.67%, respectively. It is also observed that from 600 to 800 °C, the strength is reduced by 76.33%, 71.58%, 72.25%, and 74.67%, respectively (Table 2 and Fig. 2).

Table 1 Average compressive strength (N/mm^2) of Mix 1 to Mix 4 at elevated temperature

Mixes Temp	Mix 1	Mix 2	Mix 3	Mix 4
26°	47.36	54.27	60.66	67.51
200°	48.85	64.73	72.81	82.42
400°	58.43	68.47	78.84	91.37
600°	35.16	40.06	43.56	47.19
800°	17.39	19.35	20.82	22.67
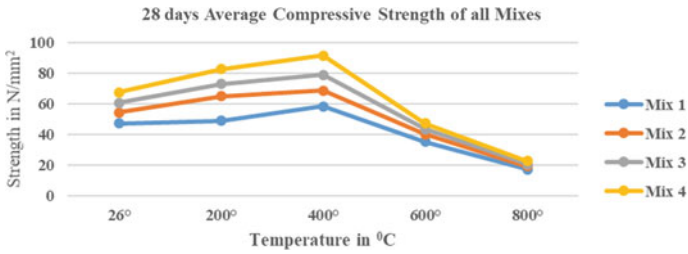
Fig. 1 Comparison of compressive strength of all mixes at elevated temperature

Table 2 Average split tensile strength (N/mm^2) of Mix 1 to Mix 4 at elevated temperature

Mixes Temp	Mix 1	Mix 2	Mix 3	Mix 4
26°	4.86	5.56	5.73	7.62
200°	5.32	6.13	6.39	8.55
400°	5.55	6.17	6.61	8.89
600°	3.15	3.5	3.53	4.53
800°	1.15	1.58	1.59	1.93
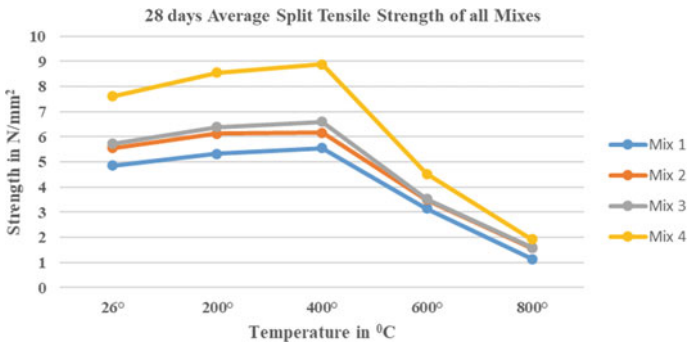
Fig. 2 Comparison of split tensile strength of all mixes at elevated temperature

It is noticed that for 28 days, increase in flexural strength for Mix 1, Mix 2, Mix 3, and Mix 4 from 26 to 400 $^\circ$C is 17.75%, 18.24%, 18.99%, and 21.19%, respectively. It is also observed that from 600 to 800 $^\circ$C, the strength decreased by 68.22%, 64.80%, 67.52%, and 68.40%, respectively (Table 3 and Fig. 3).

Table 3 Average flexural strength (N/mm^2) of Mix 1 to Mix 4 at elevated temperature

Mixes Temp	Mix 1	Mix 2	Mix 3	Mix 4
26°	5.35	6.25	8.53	10.38
200°	6.08	7.13	9.78	12.02
400°	6.3	7.39	10.15	12.58
600°	3.65	4.25	5.66	6.83
800°	1.7	2.2	2.77	3.28

Fig. 3 Comparison of flexural strength of all mixes at elevated temperature
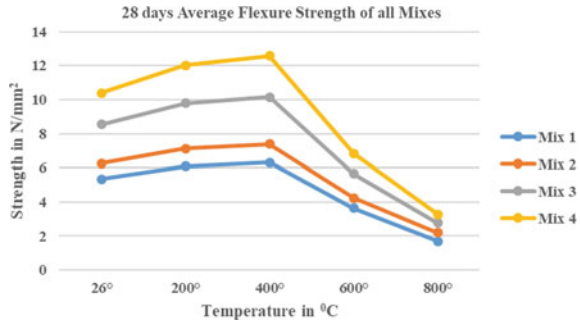
8 Microstructure Analysis

Scanning electron microscope is an instrument used to examine the morphology of the solid samples, which prepares images of a sample by scanning the top surface with a focused beam of electrons, and it gives magnification with greater depth. The test is performed in BMS College of Engineering Bull Temple Road, Basavanagudi, Bengaluru 560,019. The SEM images have magnification of 10X for 200, 400, 600 and 800 °C.

From Fig. 4 S-E-M images, the inclusion of nano-clay increases the compactness and less pore present in SEM images; thus, the strength is increased, and the presence of polypropylene fibers prevents the development of cracks. The development of more Calcium Silicate Hydrate (C-S-H) Gel is obtained from the hydration of cement and is observed in Mix 4 (Fig. 5) which leads to improvement of transition zone bonding of cement slurry between the nano-clay, GGBS, and PPF; moreover, the cracks propagation is also less because of the polypropylene fibers. Even though the fibers will melt at higher temperature, it creates a gel-like structure, covers the pore to make the structure hard, fills the gaps between the particles. Consequently, the modified cement mortar of Mix 4 gives overall effective compactness in the contribution of strength and is more as compared to the other mixes under considerations.
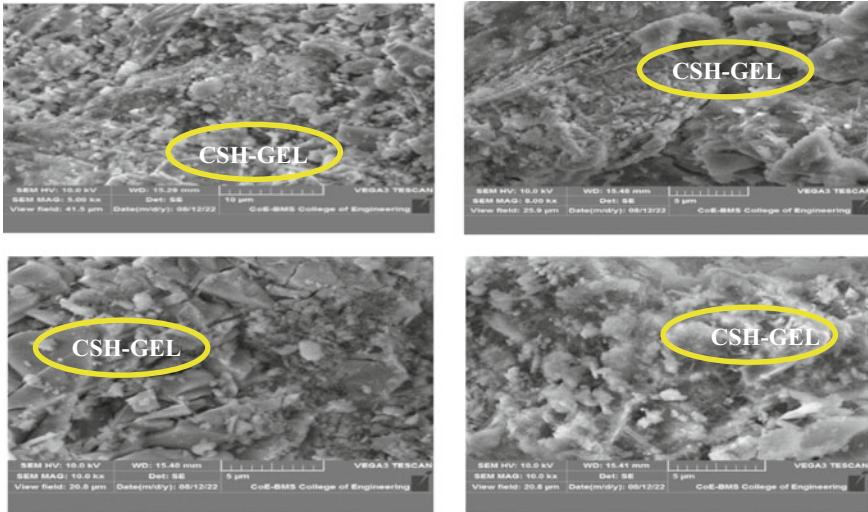
Fig. 4 SEM images of normal and elevated temperature of mix 4 with 10X magnification
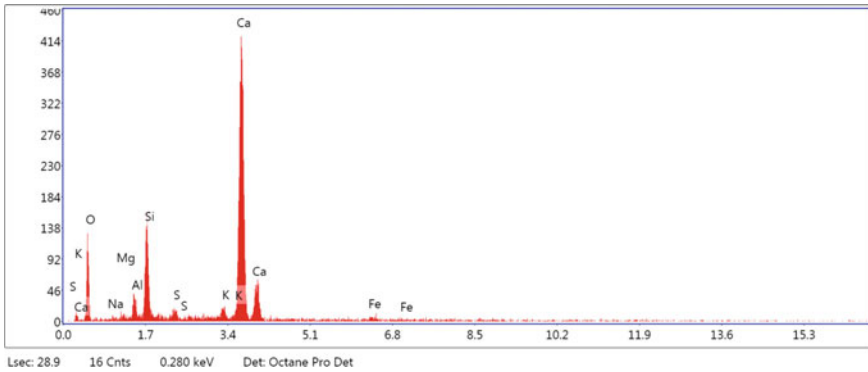
Fig. 5 EDX images of mix 4

9 Conclusion

- The incremental increase in compressive strength from 26 to 400 $^\circ$C for MIX 1 to MIX 4 ranges between 20 to 35% for 28 days which indicates that with increasing temperature up to 400 $^\circ$C, there is more improvement in the compressive strength behavior. Beyond 400 $^\circ$C up to 800 $^\circ$C, the strength reduced between 60 to 70%.
- For 28 days, the increase in the split tensile strength from MIX 1 to MIX 4 ranges between 10 to 20% for 26° to 400 $^\circ$C; above that, there is decrement in strength from 600 to 800 $^\circ$C is about 64 to 69%.

220   S. Kiran et al.

- From the experimental results, it is proved that the increase in flexural strength for 28 days from 26° to 400 °C for MIX 1 to MIX 4 ranges from 17 to 22%, and after that, for 600 to 800 °C, the strength decreased between the ranges of 64–70%.
- From SEM and EDX analysis for MIX 4, it is evident that the maximum percentage of calcium and silicate shows the possibility of more C-S-H Gel production and hence enhancement in the strength @ 400 °C as compared with MIX 1.
- The higher deformation temperature makes the grain size larger and dislocation density decreases. Hence, strength increases.
- The free water starts evaporating rapidly. In the temperature ranges from 100 to 400 °C, dehydration of ettringite takes place followed by decomposition of gypsum.
- The decrease in strength when the temperature reaches 400 °C; the chemically bound water starts evaporating; thus, the strength decreases above 400 °C.

References

1. Irshidat MR, Al-Saleh MH (2018) Influence of nanoclay on the properties and morphology of cement mortar. KSCE J Civil Eng 22(10):4056–4063. ISSN 1226-7988, eISSN 1976-3808. www.springer.com/12205
2. Ashok et-al (2017) Strength and durability study on cement mortar containing nano materials. Adv Nano Res 5(2):99–111. https://doi.org/10.12989/anr.2017.5.2.099
3. Safa Alani et-al (2020) Effects of elevated temperatures on strength and microstructure of mortar containing nano-calcined montmorillonite clay. Construct Build Mater 263:120895, journal homepage: www.elsevier.com/locate/conbuildmat
4. Bhavana et-al (2019) Examination on GGBS based Geopolymer Mortar at elevated temperatures. Int J Innov Technol Explor Eng (IJITEE) 9(2) ISSN: 2278-3075
5. Alameer SAA et-al (2020) Investigating the effect of polypropylene fibre on mortar mechanical properties with the aid of microwave curing. In: 3rd International conference on engineering sciences, IOP conference series: materials science and engineering, vol 671. 012130

Predicting Hydro-Thermal Environment Characteristics in Underground Spaces of a Tumulus Mound

Mai Sawada , **Sumire Tani, and Mamoru Mimura**

Abstract Cultural properties, such as mural paintings in underground spaces, are sensitive to hydro-thermal environments. Heat transfer analysis is useful for elucidating the mechanism behind the environment-induced deterioration of cultural properties and developing countermeasures. This study measured the temperature in the stone chamber of a tumulus mound for 500 days and validated the numerical simulation of heat transfer in the tumulus mound using the response factor method. The numerically predicted temperature values were almost consistent with the measured values. However, a numerical model that does not consider the solar radiation effects causes minor deviations from the measured values in the high-temperature period. In addition to temperature prediction, the water vapor transfer and dew condensation on the stone surfaces were calculated. The results indicated that the faces where dew condensation occurred varied seasonally. A larger amount of dew is generated on the ceiling that is not covered with soil compared with other faces, which indicates that excavation of the tumulus mound for exhibition of the stone chamber can promote dew condensation and damage the stone surfaces. The heat transfer analysis conducted in this study is useful for developing measures to sustainably control the hydro-thermal environment in the stone chamber to achieve a good balance between preservation and exhibition.

Keywords Heat transfer analysis · Dew condensation · Field monitoring

M. Sawada (✉)
Tokyo Institute of Technology, 2-12-1-M1-9 Ookayama, Meguro-Ku, Tokyo, Japan
e-mail: sawada.m.af@m.titech.ac.jp

S. Tani · M. Mimura
Kyoto University, C1-2 Kyotodaigaku-Katsura, Nishikyo-Ku, Kyoto, Japan

1 Introduction

Mural paintings and other cultural properties have existed for more than a millennium to date in stable hydro-thermal environments in underground spaces or caves. Changes in the hydro-thermal environments upset the balance in the physicochemical and biological systems in underground spaces, which cause serious deterioration in the cultural properties. For example, inside the Takamatsuzuka Tumulus in Nara, Japan, the temperature in the stone chamber was significantly affected by annual and daily changes in atmospheric temperature due to the excavation of the tumulus mound after its discovery in 1972. In addition, the annual mean temperature has increased by 1 °C over the 30 years since 1972 owing to global warming [1]. These artificial and natural thermal environment changes activated the propagation of fungi on mural paintings in the stone chamber. Damage to the mural paintings became serious, and the stone chamber was finally dismantled in 2007 to repair the mural paintings in a museum [2]. Moisture-related phenomena promoted by temperature variations, such as dew condensation, salt crystallization, and freeze–thaw cycles, also damage mural paintings and stones [3].

To elucidate the mechanism behind such damages caused by hydro-thermal environment changes and develop countermeasures, predicting the temperature that cultural properties experience is the first and most important task to accomplish. Li et al. [4] numerically simulated the temperature in the stone chamber of the Takamatsuzuka Tumulus for three years from 1972 using three-dimensional hydrothermal coupled analysis. They estimated the amount of dew condensation on the stone surfaces, as well as the temperature, and concluded that it was preferable to keep the temperature difference in the whole chamber at less than 4 °C to protect the mural paintings against dew condensation. Using air conditioners or cooling pipes is effective in controlling the temperature in underground spaces; however, it is limited by the cost of system installation and maintenance. Sawada and Mimura [5] focused on using soil covers with high heat insulation, which could be a low-cost, widely applicable, and sustainable countermeasure. They numerically investigated the influence of density, degree of saturation, and thickness of the soil cover on the temperature in the stone chamber using the response factor method. The numerical model was validated by comparing the calculated and measured annual temperature variations in the Takamatsuzuka Tumulus. However, the measured values obtained at several-week intervals yielded only a rough validation, despite the deteriorations occurring in stone chambers being very sensitive to temperature. Therefore, a more accurate validation using temperature monitoring data obtained at smaller intervals is necessary.

This study aims to obtain high-quality temperature monitoring data in an underground space and validate the heat transfer analysis using the response factor method. The temperature was measured every hour for 500 days in the stone chamber and mound of the Nakaoyama Tumulus in Nara, Japan, and the results were compared with the numerically predicted values. Furthermore, water vapor transfer and dew condensation on the stone surfaces, which can cause deterioration in the stones, were

estimated based on the calculated temperature. The tumulus mound is planned to be partially excavated in the future for the exhibition of the stone chamber. Predicting the temperature and dew condensation will be useful for evaluating the influence of future excavation on the hydro-thermal environment in the stone chamber and developing measures to achieve a good balance between preservation and exhibition.

2 Methodology

2.1 Heat Transfer Analysis

The heat transfer analysis using the response factor method [6] is schematically shown in Fig. 1. The response factor method uses a theoretical solution for one-dimensional heat flows through multi-layered walls. This method is advantageous when calculating costs compared to approximate solutions, although it cannot be used for hydro-thermal coupled analysis. The one-dimensional heat flow through multi-layered walls for a triangle-shaped unit temperature is referred to as the response factor. The response factor for the heat transfer to the outside or inside of the wall can be theoretically obtained, which is governed by the thickness and thermal properties of each layer comprising the wall. The unsteady ambient temperature variation can be expressed by the superposition of triangles with various heights; thus, the heat flow through the wall can be obtained by the superposition of the response factor for each triangle-shaped temperature change. The heat flow inside the wall after t s from the start, namely $q(t)$ is expressed as follows:

$$q(t) = \sum_{j=0}^{\infty} f(t - j\Delta t)\varphi_t(j\Delta t),\tag{1}$$
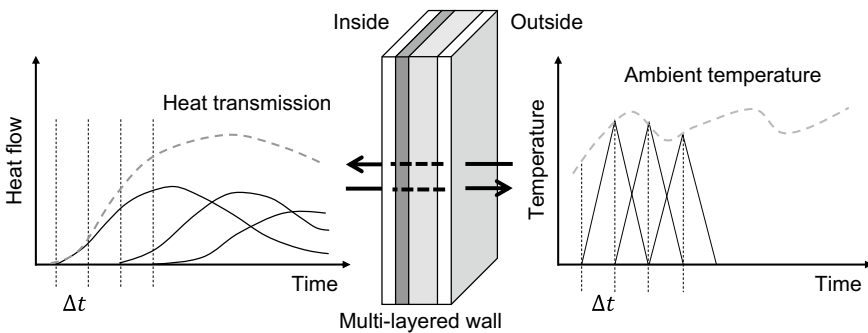
Fig. 1 Concept of heat transfer analysis using the response factor method
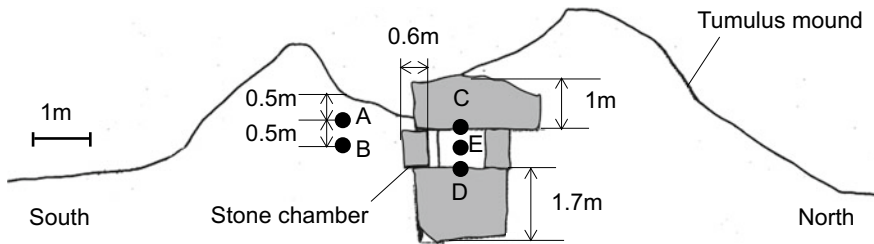
Thermocouples: A-D, Thermo-hydrometer: E

Fig. 2 Cross-sectional view of the tumulus and measurement points

where $f(t - j\Delta t)$ is the height of a triangle that arises after $t - j\Delta t$ s from the start and $\varphi_t(j\Delta t)$ is the heat transmission at $j\Delta t$ s after the triangle occurrence.

The total heat inflow to a room through six faces (i.e., the four sidewalls, ceiling, and floor) is calculated by adding the heat flow transmitted through each face. The total heat outflow is calculated in the same manner. The temperature of the room can be determined by assuming that the total heat inflow and outflow are maintained at an equilibrium.

Figure 2 shows a cross-sectional view of the Nakaoyama Tumulus [7]. The stone chamber consisted of four tuff sidewalls, a granite ceiling, and a granodiorite floor. The stone chamber with inner dimensions of 0.9 m × 0.9 m × 1.3 m is covered with soil, while the top of the stone chamber is exposed. Figure 3 shows the numerical models of the multi-layered walls surrounding the stone chamber used for heat transfer analysis. The thickness of the soil layers adjacent to the sidewalls was determined by reading the approximate distance between the sidewalls and mound surface, as shown in Fig. 2. The temperature at the bottom of the model at a depth of 10 m remains constant throughout the year (namely isothermal layer), which is generally equal to the annual mean air temperature [8]. The heat transfer layer between the atmosphere and soil or stone layer transmits heat through radiation and convection. The heat capacity was zero, and the coefficient of heat transfer was 9 and 23 W/m²K on the inside and outside of the wall, respectively [9]. The ambient temperature measured at the Nara Observatory of the Japan Meteorological Agency was used for analysis [10]. The effects of water transfer, namely evaporation and rainfall infiltration, solar radiation and nocturnal radiation were not considered because temperature variation caused by these factors can cancel out when annual soil-atmosphere heat balance is maintained.

2.2 Thermal Properties

The thermal diffusivity of the soil was measured using the cylindrical method [11]. The tumulus mound soil with a natural water content of 28.46% was compacted at
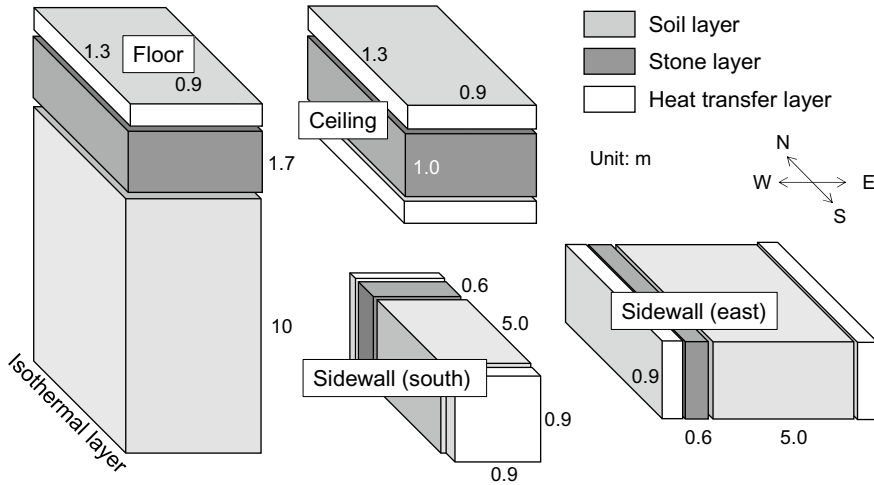
Fig. 3 Multi-layered walls surrounding the stone chamber

the equivalent dry density of the mound (i.e., 1.2 g/cm^3) in cylindrical aluminum holders 33 cm in length and 5 cm in diameter. Thermocouples were installed at the center of the specimens. Then, the specimens were soaked in a constant-temperature water bath (30 °C). The thermal diffusivity was inversely calculated using the theoretical solution for the heat conduction in an infinite cylinder and measured center temperature.

The measured thermal diffusivity was 0.32 mm^2/s. The volumetric heat capacity of the soil was determined as 2402 kJ/m^{3}K based on the specific heat of quartz (0.84 kJ/kgK) and water (4.18 kJ/kgK) [8]. The thermal conductivity of the soil was 0.77 W/mK, which was estimated using the relationship between thermal diffusivity and volumetric heat capacity. The thermal diffusivity, volumetric heat capacity, and thermal conductivity of the stone were determined as 0.88 mm^2/s, 2900 kJ/m^{3}K, and 2.56 W/mK, respectively, by referencing an earlier study based on the thermal properties of saturated tuff stones used in stone chambers [12].

2.3 Temperature Monitoring

To validate the heat transfer analysis, the temperature in the tumulus mound and stone chamber was measured for 500 days from March 27, 2021, to August 8, 2022. The thermocouples (Points A to D) and thermo-hygrometer (Point E) were installed at the measurement points shown in Fig. 2 when the tumulus was excavated for archeological investigations. The thermocouples at Points C and D were attached to the stone surfaces using aluminum tape. The thermocouples and thermo-hygrometer were connected to the data loggers fixed on the mound surface. The measurement
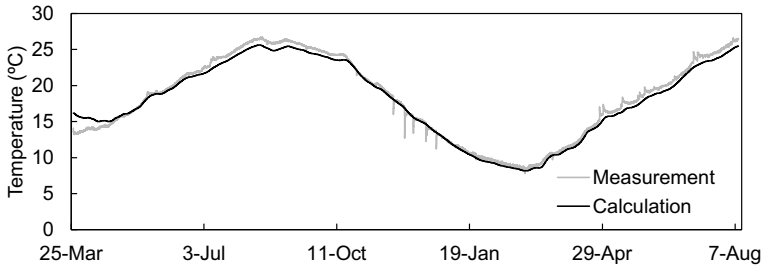
Fig. 4 Comparison between the measured and calculated temperature values at Point B

interval was set to an hour. Temperature monitoring was started when the tumulus mound was reburied after the investigation.

3 Results and Discussions

3.1 Validity of Soil Thermal Properties

The validity of the mound soil thermal properties was assessed by comparing the measured ground temperature and numerically simulated temperature values at Point B. One-dimensional heat flow between Point A at a depth of 0.5 m, where the temperature was measured, and isothermal layer at a depth of 10 m was calculated using the finite difference method. The temperature at the isothermal layer was set to the annual mean air temperature determined in 2021 (16.16 °C).

Figure 4 shows a comparison between the measured and calculated temperatures at Point B. The calculated temperature was higher than the measured values during the first two months because the initial ground temperature was assumed to be uniform. However, the calculated temperature is consistent with the measured values for the rest of the period, although the datum of the calculated temperature is slightly low because the assumed temperature at the isothermal layer can be lower than the actual value. This indicates that the experimentally obtained thermal properties of the mound soil can be used for the heat transfer analysis.

3.2 Temperature in Underground Stone Chamber

In the heat transfer analysis using the response factor method to predict the temperature at Point E in the stone chamber, the calculation period must be sufficiently long to reduce the influence of the tentative ground temperature distribution provided as the initial condition. Thus, the calculation was performed over 20 years from August

9, 2002, to August 8, 2022. Accordingly, the results for the last five years, where the initial condition has little impact on the results, were discussed. The time step was set to 24 h because the temperature in the underground stone chamber was not sensitive to the daily ambient temperature variation. Then, the temperature values of the ceiling, sidewalls, and floor during the five years were calculated using the finite difference method.

Figure 5 compares the measured and calculated temperatures at Points C, D, and E for 500 days from the start of temperature monitoring. The measurement at Point E was interrupted after the 70th day from the start because the thermo-hygrometer stopped working owing to dew condensation on the sensor; however, the temperature at the other points was successfully obtained. The calculated temperature was nearly consistent with the measured values on the ceiling and floor, which agreed well with each other, particularly during the low-temperature period. The average deviation from the measured value was 6.7% on the ceiling and 3.8% on the floor throughout the 500 days. However, the difference between the measured and calculated values was relatively large during the first several days and high-temperature period. This initial difference can be attributed to the excavation of the tumulus mound. The stone chamber was exposed to the atmosphere just before the tumulus mound was reburied and temperature monitoring started, which might have increased the temperature in the stone chamber during the first several days. The difference in the high-temperature period can be owing to the numerical model that does not consider the effects of solar radiation, which increases the heat inflow into the ground, particularly in the summer.

3.3 Water Vapor Transfer and Dew Condensation

The relative humidity measured at Point E increased to 100% over two days from the start and remained constant until the thermo-hygrometer stopped working. This indicates that the vapor pressure in the stone chamber was always fully saturated, and dew condensation occurred when the surface temperature of the stones was slightly lower than that of the atmosphere. Dew condensation on each stone surface, namely q_v was calculated using Eq. (2), which expresses water vapor transfer in the atmosphere [9].

$$q_v = \alpha'(f_r - f_w). \tag{2}$$

Here, α' is the moisture transfer coefficient (i.e., 16.7 g/m^{2}h mmHg), f_r is the atmospheric water vapor pressure in the stone chamber, and f_w is the water vapor pressure on the stone surface. The f_r and f_w were estimated using Goff–Gratach's equation, which depicts the experimentally obtained relationship between the ambient temperature and saturated water vapor pressure. Dew is generated on the stone surface when f_w is lower than f_r, whereas water evaporates from the stone surface when f_w is higher than f_r.
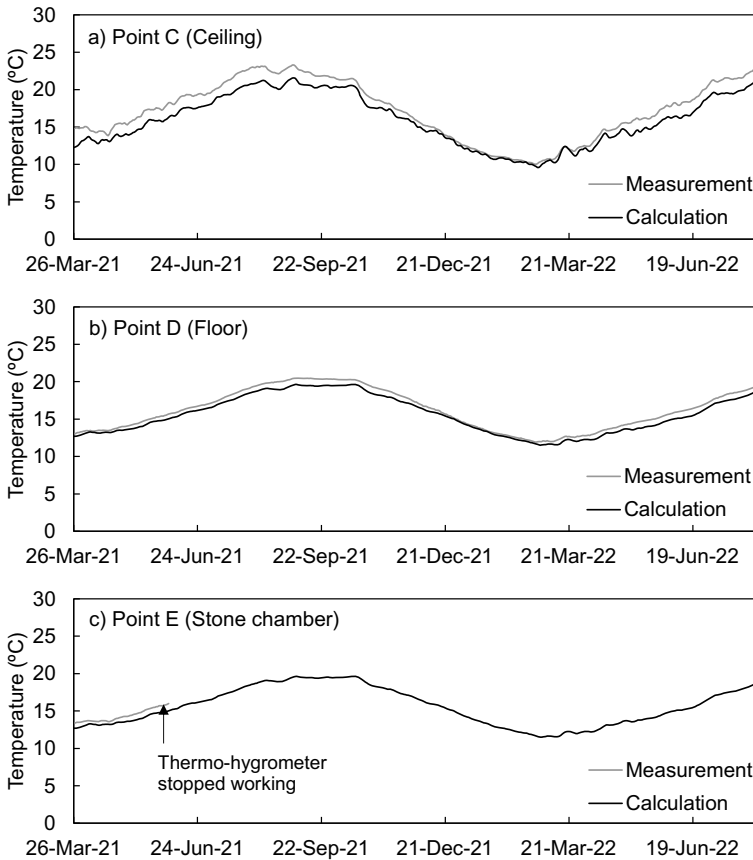
Fig. 5 Comparison between the measured and calculated temperature values at **a** Point C, **b** Point D, and **c** Point E

Figure 6 shows the amount of dew condensation per unit area on the ceiling, sidewalls, and floor during the five years between 2017 and 2022. The faces where dew condensation occurred varied seasonally. Dew was generated on the ceiling from October to April, when the ceiling was cooled down by the outdoor ambient air. During the rest of the year, when the temperature of the ceiling was relatively high, dew was generated on the sidewalls and floor, where the surface temperature was slightly affected by the outdoor ambient temperature variation. Dew condensation was significant on the ceiling compared to other faces because the ceiling that was not covered with soil was easily affected by the outdoor ambient temperature variation. This indicates that the excavation of the tumulus mound for exhibition of the stone chamber increases the temperature difference in the stone chamber, which results in dew condensation and evaporation on the stone surfaces.
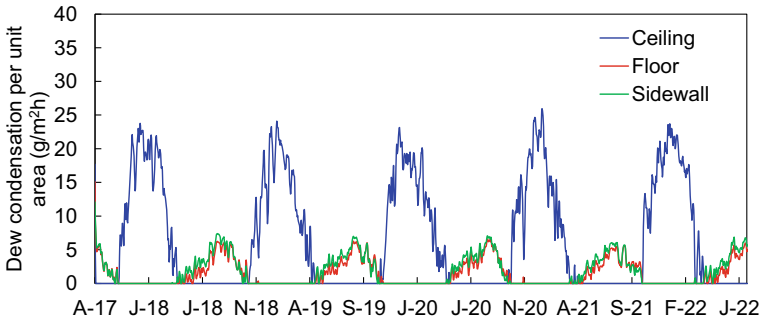
Fig. 6 Estimated dew condensation over five years from 2017 to 2022

4 Conclusions

This study numerically predicted the temperature in an underground stone chamber using the response factor method; subsequently, the prediction results were validated by comparison with the measured values. The calculated temperature was nearly consistent with the measured values; the average deviations from the measured values were 6.7% on the ceiling and 3.8% on the floor throughout the 500 days. However, the deviation was relatively large during the high-temperature period. This can be attributed to the numerical model, which does not consider the effects of solar radiation. This setback must be addressed for a more accurate prediction.

Furthermore, water vapor transfer and dew condensation in the stone chamber were predicted based on the measurements, indicating that the water vapor pressure in the stone chamber remained saturated. The results indicated that the faces where dew condensation occurred varied seasonally. A larger amount of dew was generated on the ceiling that was not covered with soil, which indicates that excavation of the tumulus mound for exhibition can promote dew condensation and damage stone surfaces. The heat transfer analysis validated in this study is useful for developing methods for controlling the hydro-thermal environment in stone chambers to achieve a good balance between preservation and exhibition. Additional calculations are underway to evaluate the influence of future excavation on the hydro-thermal environment in the stone chamber and effectiveness of countermeasures using soil covers.

References

1. Miura S, Ishizaki T, Akamatsu T (2005) Temperature changes in 30 years at Takamatsuzuka Tumulus. Sci Conserv 44:141–148 [in Japanese]
2. Mimura M, Yoshimura M (2009) Stability of the chamber stones and the compacted earth mound of Takamatsuzuka Tumulus during dismantling process. J Japan Soc Civil Eng Ser C 65(3):597–608 [in Japanese]
3. Agency for Cultural Affairs: Report of working group on exhibition and conservation of decorated stone chambers of tumuli (2014) [in Japanese]
4. Li Y, Ogura D, Hokoi S, Wang J, Ishizaki T (2014) Predicting hygrothermal behavior of an underground stone chamber with 3-D modeling to restrain water-related damage to mural paintings. J Asian Architect and Build Eng 13(2):499–506
5. Sawada M, Mimura M (2017) Environment control in a burial chamber by covering with an earth mound—evaluation of temperature and dew condensation in a burial chamber associated with the overlying tumulus mound. J Japan Soc Civil Eng Ser C 73(4):368–381 (2017) [in Japanese]
6. Nakamura Y (1984) New Architecture 10 environmental physics, Shokokusya, Tokyo (1984) [in Japanese]
7. Asuka Village of Board of Education: Excavations report in the Nakaoyama Tumulus. (1975) [in Japanese]
8. Jury WA, Horton R (2004) Soil physics. Wiley, New Jersey
9. Hokoi S, Ikeda T, Nitta K (2002) Architectural environment engineering II. Asakura Publishing, Tokyo [in Japanese]
10. Japan Metrological Agency: Past weather data (2022). https://www.data.jma.go.jp/obd/stats/etrn/index.php. (Accessed 10 Oct 2022)
11. Noborio K, Tokumoto I, Mukaida Y (2005) Estimating thermal diffusivity of soil packed in a cylinder using an analytical solution. J Japanese Soc Soil Phys 101:5–10 [in Japanese]
12. Ishizaki T, Miura S, Inukai M, Khalil M (2006) Examination and choice of cooling methods for the mound of Takamatsuzuka Tumulus as protective measures against fungi in the stone chamber. Sci For Conserv 45:59–68 [in Japanese]

Prediction of Failure of Embankment on Soft Clay from Construction Control Chart

M. Bhanuchitra, V. Padmavathi, and P. N. Rao

Abstract The stability of an embankment during and after construction is mainly dependent on the displacements under the embankment. There are numerous studies on the detrimental effect on the behavior of the proposed embankment or adjacent structures around the embankment. Different ground treatment techniques are implemented, and concurrent ground instruments are also deployed to control immense effects such as huge displacements and the collapse of embankments. Matsuo et al. (1977) proposed a stability chart to control the failure of the embankment based on the settlements at the center and lateral deformations at the toe of the embankment. The present study analyzed the data provided by different case studies on embankments and found the displacements using finite element software PLAXIS 2D. The lateral displacements and settlements obtained from PLAXIS 2D are plotted in the Matsuo stability chart to know the factor of safety at each stage of construction. Hence, the prior prediction of failure of the embankment can be possible with the Matsuo plot by observing the displacements. The lateral displacements and settlements from finite element analysis (FEA) are compared with the parameter obtained from the experimental, numerical, and observational methods existing in the case histories.

Keywords Embankment · Soft clay · Slope stability · Construction control chart · Finite element analysis

M. Bhanuchitra (✉) · V. Padmavathi
JNTUH College of Engineering Hyderabad, Hyderabad, Telangana 500085, India
e-mail: bhanumaheshwaram@gmail.com

P. N. Rao
Department of Civil Engineering, BITS Pilani-Hyderabad Campus, Hyderabad 500078, India

231

1 Introduction

In the last few decades, the growth of urbanization has significantly larger worldwide and there is a necessity to develop infrastructure in critical site conditions. The development of urbanization leads to the building of new communication infrastructure in coastal regions, where the soft soil deposits are encountered. Construction of embankments in such soils is a very difficult task due to unfavorable geotechnical conditions such as low shear strength and high compressibility. The most difficult problem is a prediction of failure during the construction of an embankment on soft clay. The observational methods stipulate (Peck 1969) many benefits over conventional design methods, including potential savings in time or cost and greater safety assurance. There are different theoretical approaches available to evaluate the stability of an embankment, but the selection of the method of approach has a great impact on the stability of the embankment. Leroueil (2001) reviewed different empirical methods of approach to evaluate the stability of an embankment. These conventional methods are based on the properties of foundation soil and embankment soil. Bejjerum (1973) evaluated the fundamental properties of soft clays and the correlation between plasticity index and undrained shear strength and their implication for practical design procedures. The process of data monitoring and careful review during the construction of an embankment play a significant role in the prediction of the failure of an embankment. The measured data of vertical and lateral displacements may not be a reliable approach for the prediction of failure. Failure can happen without any warning based on simple displacement data. Matsuo [5] proposed a construction control chart based on the combination of vertical and lateral displacements which is the most suitable approach to predict the failure of embankments on the soft ground during construction. Because it clearly demonstrates that the process of displacement in construction progress in failure cases is approaching the failure criteria line although differences in the geometrical and mechanical properties of the embankment soil and soft clay layer thickness. There is a tendency to be distant from this curve in non-failure cases. Three case studies are discussed in the present study which includes the performance of embankments during construction and the prediction of failure using approach. Wu et al. (2019) described the application of instrumentation monitoring and applied the Matsuo approach for monitoring the stability of the embankment. Chin (2005) presents guidelines for the design of embankments by various methods as well as construction control of embankment stability based on the Matsuo approach. Finite element analysis of PLAXIS 2D software is chosen with plain strain conditions to simulate the actual conditions. Further, the material model is considered as Mohr–Coulomb for the foundation and the embankment soil with the variation of drainage conditions such as undrained and drained, respectively. The soil parameters for the foundation and embankment soil include bulk unit weight (γ), undrained shear strength (S_u), undrained modulus of elasticity (E_u) for soft clay, drained modulus of elasticity (E) for embankment soil, Poisson's ratio (ν), and coefficient of lateral earth pressure (k_0) which are tabulated in Table 1 for embankment soil and foundation soil. The observed field data is compared with the result obtained

Table 1 Soil parameters for embankment soil and foundation soil in FEA

Name of the embankment	Depth (m)	Unit weight of soil,γ (kN/m^3)	Undrained Young's modulus E_u (MPa)	Poisson's ratio (ν)	Undrained shear strength (kPa) S_u	Effective friction angle, ϕ (°)	K_0
Kurashiki	0.0−0.4	18	2.4	0.3	0	30	0.5
	0.4−6.3	16	3.6	0.495	19.6	0	0.55
	6.3−40	18	4.5	0.3	1	30	0.5
	Embankment fill	18	5.0	0.3	1	32	0.5
Muar	0.0−2.0	15.5	8.7	0.495	35.0	0	0.8
	2.0−5.0	14.5	1.8	0.495	8.0	0	0.8
	5.0−10.0	15	4.1	0.495	18.0	0	0.8
	10.0−20.0	15.5	4.4	0.495	22.0	0	0.8
	20.0−40.0	18	35	0.495	13.2	37	0.39
	Embankment fill	20	5.1	0.3	14	31	0.48
St. Alban	0.0−0.3	17.0	10.0	0.3	0	28	0.53
	0.3−3.0	14.4	4.0	0.495	10	0	0.75
	3.0−6.0	16.5	6.0	0.495	15	0	0.75
	6.0−9.7	17.5	8.0	0.495	20	0	0.75
	9.7−25.0	19.0	30.0	0.3	5.0	32	0.47
	Embankment fill	18.5	20	0.3	5	44	0.30

from the FEA. The FEA result is used to find the factor of safety of the embankment utilizing the Matsuo construction control chart which is shown in Fig. 1.

2 Case Studies

2.1 Case 1: Kurashiki Trial Embankment

The Ministry's Okayama office for Highway Construction built an instrumented trial embankment in Kurashiki, Japan, to assess its performance. The trail embankment was built on typical soft ground with a rate of construction 0.1 m/day in 57 days to a height of 5.0 m and a base width of 22 m. The plan and elevation of the trial embankment are shown in Fig. 2. The measured data in terms of lateral displacements and settlements of the Kurashiki trial embankment was provided by Mochizuki

Fig. 1 Matsuo's Stability chart Ref [5]
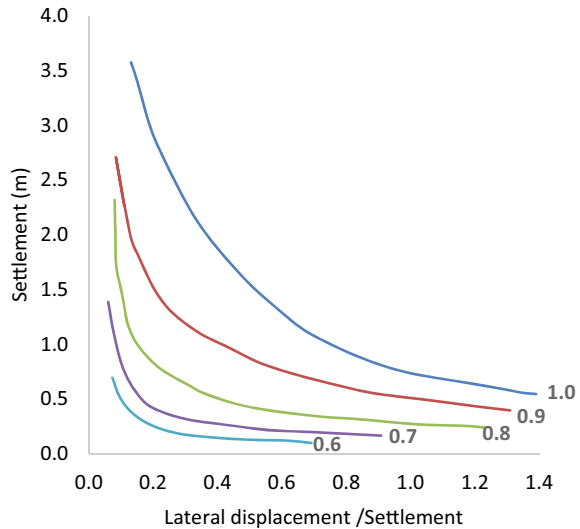
et al. (1980). Shibata and Sekiguchi (1982) performed a detailed elasto visco-plastic analysis for assessing deformations of the same embankment and compared it with the measured values of Mochizuki et al. (1980). Later, Saichi and Kamei (1996) analyzed deformations based on soil parameters estimated from the plasticity index as well as permeability. The foundation of the Kurashiki trial embankment consists of a 0.4 m thick of sand which was placed on the original ground surface one year before the construction of the embankment. A soft alluvial clay deposit of 5.9 m thick underlain by sand extended up to a depth of 33.4 m. The undrained shear strength of the foundation area with respect to the depth shown in Fig. 3. In the present case, FEA is performed in undrained conditions, and the soil parameters considered in the analysis are given in Table 1.

2.2 Case 2: Muar Trial Embankment

The Malaysian Muar trial embankment was located at the Muar flat in the valley of the Muar River. The west coast of peninsular Malaysia constitutes a coastal plain of 10–20 m soft clay deposits and has low shear strength. Consequently, there were frequent instability problems during the construction of the embankment. A large full-scale trial embankment was constructed with proper instrumentation to examine the detailed behavior of clayey soil. The Muar embankment was constructed in 100 days with a rate of construction of 0.4 m/week, and subsequent data was recorded. The geometry of the searchers and engineers to predict the deformations of the embankment prior to its construction. The "Class A" (Lambe 1973) predictions of the embankment is shown in Fig. 4. The Malaysian highway authority (MHA) invited
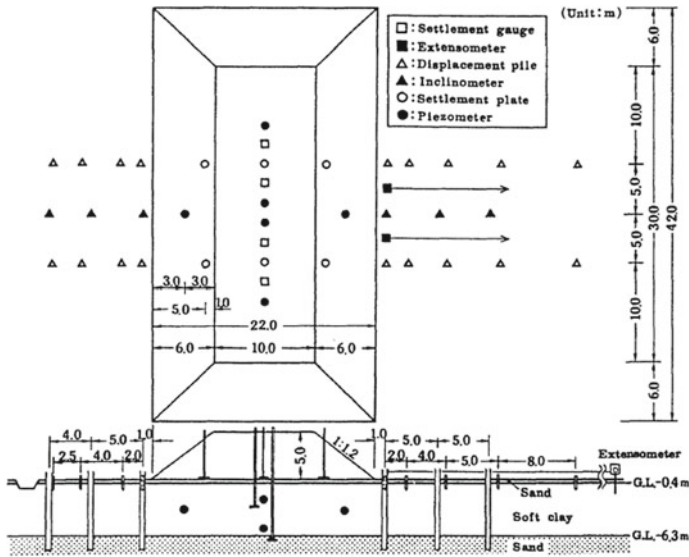
Fig. 2 Plan and elevation of the embankment Ref. [8]
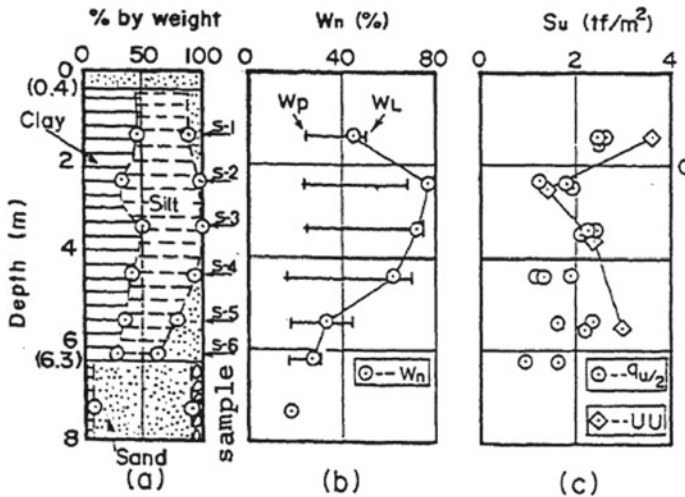
Fig. 3 Soil profile for Kurashiki embankment Ref. [8]

re-performed in different approaches to predict the failure height of the embankment which is compared with the actual failure height of 5.4 m. An international symposium was held by MHA on "Trial embankment on Malaysian Marine clays" in November 1989, the predictions and the observed data are well documented in the proceedings. The prediction of failure height is in the range of 3.0–5.0 m which was
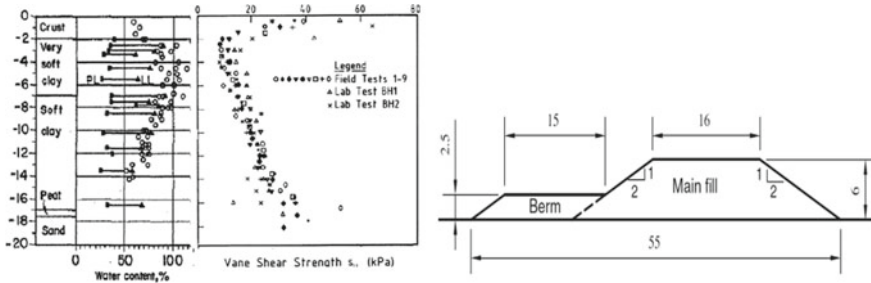
Fig. 4 Soil profile and geometry of Muar embankment Ref. [6]

determined by different analyses such as limit equilibrium (Brand 1990), centrifuge model test (Nakase and Takemura 1989), finite element method of total and effective stress analysis (Poulos et al. 1991), and CRISP program of modified cam clay method (Balasubramaniam 1992) were performed. Qu et al. (2007) mentioned the difference in results of 2D and 3D finite element analysis which are compared with the measured data. The soil profile of the test site consists of a weathered crust of 2.0 m thick underlined by 5.0 m thick of very soft clay followed by 8 m thick of soft clay. The lower clay layer is overly a 0.5 m thick peat, 3.5 m sandy clay, and then dense sand. The actual field and laboratory test results are shown in Fig. 4. In the present analysis, the 20 m clay deposit is divided into four layers, and the properties are tabulated in Table 1.

2.3 Case 3: Saint Alban Test Embankment

A large portion of eastern Canada is covered by Champlain-sensitive clay deposits. Laval University's geotechnical group conducted a research program to investigate the failure conditions of a test embankment by observing the magnitude and rate of settlement of the structure. Four test embankments were built in Saint Alban, Quebec. One of the embankments was built up to the point of failure, and the geometry of the test embankment is depicted in Fig. 5. Deformations were measured up to the embankment's failure by installing deformation measuring instruments. The expected height of the embankment was 4.6 m, but the failure occurred at 3.89 m. The detailed results of the report presented by LaRochelle et al. [4]. The effect of strength anisotropy (Zdravkovic et al. 2002) on embankment behavior and the 3D effects using elastoplastic analysis (Guangfeng Qu et al. 2007) were also investigated. A detailed geotechnical investigation was carried out, and laboratory tests were performed on the soil sample. The soil profile is composed of a 1.8 m thick weathered clay crust below topsoil of a surface of 0.3 m. The crust layer is underlain by an 8.0 m thick, soft marine clay layer, which is followed by a soft sensitive clayey
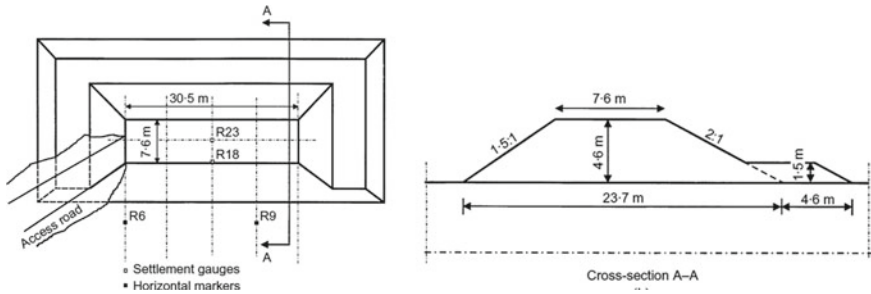
Fig. 5 Plan view and cross section of Saint Alban test embankment Ref. [4]

silt layer between 9.7 and 13.7 m depth. A dense fine to medium sand deposit was found in lower depths from 13.7 to 24.4 m.

3 Results and Discussion

The measured settlements and lateral displacements from the field data and predicted from FEA for the embankments in all the three cases at each stage of construction are depicted in Figs. 6 and 7. The settlements are measured and predicted at the center of the embankment for all three cases. The lateral displacements are measured and predicted at the toe of the embankment for Kurashiki and Muar cases whereas in the case of St Alban lateral displacements are measured at the R6 location which is shown in Fig. 5. The present study compares measured and predicted results, as well as previous studies by different authors for the same case histories.
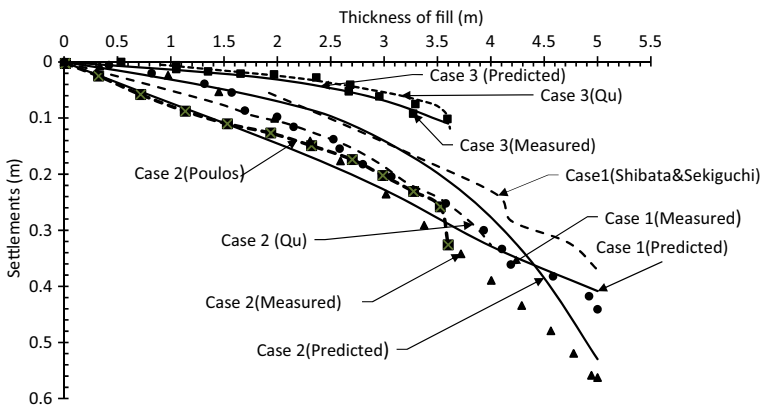
Fig. 6 Settlement at the center of the embankment for three case studies
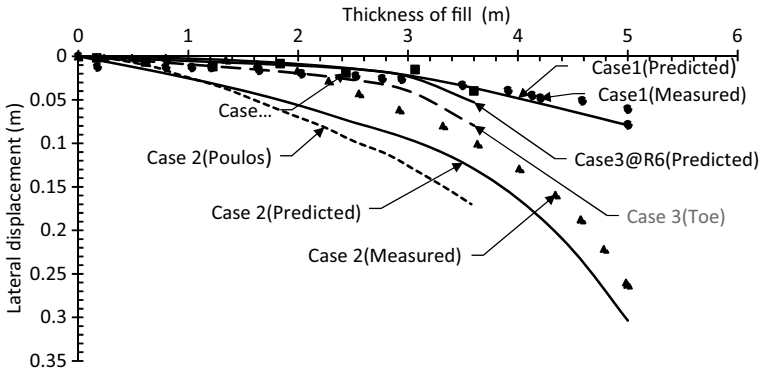
Fig. 7 Lateral displacements at the toe of the embankment for three case studies

3.1 Settlements

Case 1: Kurashiki Trial Embankment The settlements were plotted based on both measured and predicted values until the end of embankment construction, which was up to a height of 5.0 m. Shibata and Sekiguchi [8] used the FEA with drained parameters to predict the settlements and these are underestimated when compared to measured values and which are presented in Fig. 6. The difference may be due to the consideration of drained parameters during the staged construction of the embankment.

3.2 Case 2: Muar Trial Embankment

The predicted settlements agree with measured settlements at the initial stage and at the end of construction, as the embankment height increases the settlements are decreases in comparison to the measured settlements. The comparison of predicted and measured settlements as well as by Poulos et al. (1991), and Qu et al. (2007) predictions using FEM analysis are shown in Fig. 6. The actual failure height of the Muar embankment is 5.4 m, and the predicted failure height in the present study is 5.0 m. The comparison made with Poulos et al. (1991), and Qu et al. (2007) predictions, it should be noted that the failure heights differ by 3.6 m and 4.0 m, respectively. The difference in the analysis is due to the inclusion of soil parameters, specifically the variation of undrained modulus (E_u) in the present and previous predictions. Poulos et al. (1991) considered E_u as 190 S_u, and Qu et al. (2007) reported it as 8.0 MPa. The E_u considered in the present analysis is calculated using the parameters of the plasticity index (PI) and the over-consolidation ratio (OCR) [1]. Based on the field and laboratory investigation data, the PI is assumed to be greater

than or equal to 50 and the OCR is assumed to be 1, (Balasubramaniam 2007). Hence, E_u is considered as 230 to $250S_u$, where S_u is the selected undrained shear strength.

3.3   Case 3: Saint Alban Trial Embankment

The predicted and measured settlements, as well as predictions by Qu et al. (2007), are shown in Fig. 6. The difference in the settlement plot between the present and previous studies is caused by differences in the value of the undrained modulus of elasticity. The observed value of E_u/S_u from Champlain clay block samples is less than 500 (La Rochelle 1970), and for cemented clays in the eastern Canada region is in the range of 300 to 600. Based on these observations, the undrained modulus of elasticity considered in the present study is 400 times S_u, whereas Qu et al. (2007) reported a value of 25 MPa. Hence, the difference in the settlements is 20 mm higher when compared to the present study.

3.4   Lateral Displacement

3.4.1   Case 1: Kurashiki Trial Embankment

The in situ lateral displacements were measured using inclinometer tubes located on both sides of the embankment and are compared to the FEA results, which show less displacements at the initial stage of construction. The difference in the lateral displacements from measured and FEA is negligible when the embankment height increases which is depicted in Fig. 7.

3.5   Case 2: Muar Trial Embankment

The comparison of measured and predicted lateral displacements is shown in Fig. 7. The prediction by Poulos et al. (1991) is compared with the present study for a height of 3.6 m which shows 30 mm higher when compared with the present study. The difference is due to the assumption of a lower modulus of elasticity in the analysis.

3.6   Case 3: Saint Alban Trial Embankment

The lateral displacements were measured at a location of R6, as shown in Fig. 3. The comparison of measured and predicted values is shown in Fig. 7, which shows 14 mm more than the measured values. The lateral displacement at the toe of the

embankment is also shown in Fig. 7 as significantly greater than predicted the at R6 location. Hence, the gauge R6 is located outside the failure region the lateral displacements are less in both measured and predicted.

3.7 Matsuo Construction Control Chart

Matsuo's stability chart plots the ratio of lateral displacement by settlement at the center of the embankment as abscissa and settlement beneath the center of the embankment as ordinate. The predicted (solid line) and measured results (dashed line) for the current case studies are plotted in Matsuo's chart shown in Fig. 8, except for case 3 (St Alban), where the measured results are not plotted due to the non-existence of lateral displacements at the toe of the embankment. According to Matsuo's construction control chart, the failure is indicated by the points moving away from the center and toward the top. The factor of safety of the Kurashiki embankment is estimated as 1.4 from the chart, and it is agreed to the field condition that the failure did not occur during construction. In the case of the Muar trial embankment, the control chart shows that the deformations are accelerating, moving toward the top, and approaching failure with a safety factor of 1.15. In comparison with the actual site situation, the embankment failed under additional loading such that the height of the embankment was 5.4 m. Hence, the Matsuo chart provided a reasonable agreement with the site situation. The safety factor for the Saint Alban embankment computed from the chart is in the range of 1.6–1.5, but there is some deviation from the actual site condition because the embankment failed during construction.
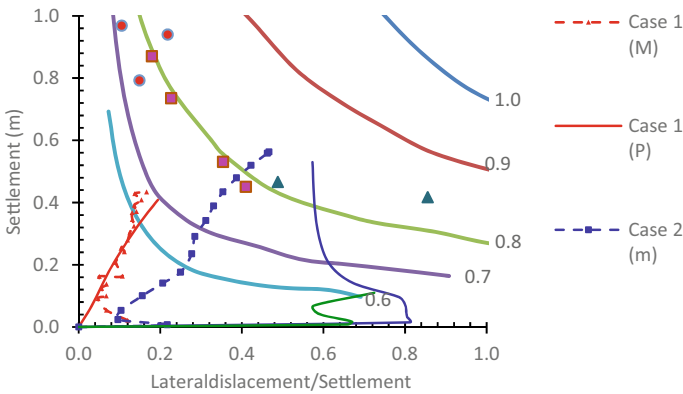
Fig. 8 Matsuo's construction control chart (Ref. Figure 1) for three cases

4   Conclusions

The measured performance of embankment case histories is compared to the predicted values based on FEA. The findings of this study are summarized as follows.

1. The settlements from FEA are comparable with the measured values of case studies.
2. When comparing previous predictions to the current study, the assumption of undrained modulus of elasticity (E_u) has a significant influence on vertical and lateral displacements to obtain acceptable results.
3. Failure prediction is possible using the construction control chart, which provides a clear warning before failure based on the factor of safety.
4. A detailed evaluation of additional case studies in the selection of soil parameters for FEA is required to predict failure from Matsuo's construction control chart.

References

1. Duncan JM, Buchignani AL (1976) An engineering manual for settlement studies. Department of Civil Engineering, University of California, Berkeley
2. Guangfeng Q, Hinchberger S, Lo KY (2009) Case studies of three-dimensional effects on the behavior of test embankments. Can Geotech J 46(11):1356–1370
3. Indraratna B, Balasubramaniam AS, Balachandran S (1992) Performance of test embankment constructed to failure on soft marine clay. J Geotech Eng 118(1):12–33
4. La Rochelle P, Trak B, Tavenas F, Roy M (1974) Failure of a test embankment on a sensitive Champlain clay deposit. Can Geotech J 11(1):142–164
5. Matsuo M, Kawamura K (1977) Diagram for construction control of embankment on soft ground. Soils Found 17(3):37–52
6. Poulos HG, Lee CY, Small JC (1990) Predicted and observed behaviour of a test embankment on Malaysian soft clays. Research Report—University of Sydney, School of Civil and Mining Engineering
7. Sakajo S, Kamei T (1996) Simplified deformation analysis for embankment foundation using elasto-plastic model. Soils and Foundation 36(2):1–11
8. Shibata T, Sekiguchi H (1984) Performance of trial embankment on soft clay. In: International conference on case histories in geotechnical engineering. St Louis, vol 2. pp 599–607

Proposed Classification of Degradable Muddy Rocks Using Physical and Chemical Properties

Koji Yamashita, Xiangyu Wang, and Noriyuki Yasufuku

Abstract It is well known that muddy rocks such as mudstone and shale are susceptible to degradation over time, as symbolized by slaking, which can cause problems in the maintenance and management of earthwork structures such as cut slopes. In addition to the chemical properties of the clay minerals contained in the mudstone, which have been shown in many previous studies, the accelerated deterioration may be due to the effects of heavy rainfall, earthquakes, and stress release during and after construction. However, while there are cut slope faces with similar mudstone distribution that have achieved long-term stability without any measures, there are also cases in which the cut slopes have collapsed over time. Against this background, the authors have been conducting research on "classification of mudstone susceptible to deterioration using physical and chemical properties," "effect of stress release on shear strength of mudstone discontinuities, "and" evaluation of the soundness of cut slope surfaces" for mudstones distributed in Miyazaki. This paper presents the physical and chemical properties and unconfined compression strength of mudstones, summarizes the relationships among them, and proposes a classification method of mudstones susceptible to degradation that reflects these results and discusses its usefulness.

Keywords Degradable muddy rocks · Physical and chemical properties · Water absorption · Slaking

K. Yamashita (✉)
Kiso-Jiban Consultants Co., Ltd, Fukuoka, Japan
e-mail: yamashita.koji@kiso.co.jp

X. Wang · N. Yasufuku
Kyushu University, Fukuoka, Japan

1 Introduction

1.1 Current Status of Research on Degradation of Muddy Rock

Previous studies on the correlation between physical and chemical properties of rocks and degradation include a study by Murakami (2000) on the relationship between physical properties of rock materials and slaking properties, which identified natural water content ratio and rate of increase in water absorption as physical properties that are highly correlated with slaking properties. In addition, a study by Wang et al. [16] on the evaluation of Miyazaki mudstone weathering degree focusing on Ignition loss shows that the existing slaking tests are highly correlated with each other and are both valid tests and finds that the pore ratio and water absorption rate each have a good relationship with Ignition loss values.

Regarding chemical weathering, there are many previous studies attributed to swelling clay minerals such as smectite, as well as a study by Chigira [9], who clarified the weathering mechanism of mudstones of the Pleistocene Haizume Formation. According to this study, the mechanism of chemical weathering is that pyrite is oxidized and lost in the oxidation front to form sulfuric acid, and chlorite is converted to smectite.

Furthermore, some studies [2] have developed the weathering characteristics into the evaluation of cut slope stability.

On the other hand, there is no established classification method for muddy rocks susceptible to deterioration, and even now, in civil engineering projects in areas where muddy rocks are distributed, these issues are taken into account by engineers in their experience during the investigation and design phases. In addition, various countermeasure methods are used in the construction phase.

1.2 Civil Engineering Problems and Issues Caused by Muddy Rocks

With the increase in the number of large civil engineering projects involving muddy rock, civil engineering problems caused by muddy rock are also emerging. In particular, most of the cut slope construction problems that the author often comes in contact with in the course of his work are considered to be collapses. In cut-and-fill surfaces, the kind of degradation that is the focus of this paper occurs over time, i.e., the cut-and-fill process causes stress release and slaking due to rainfall and other factors, resulting in rapid deterioration of the muddy rock. This results in the collapse of the cut slope. It is believed that the influence of swelling clay minerals such as smectite, which induce the slaking phenomenon, is prominent in the muddy rock that exhibits this slaking phenomenon. Muddy rocks are generally soft, high water

content rocks that tend to soften and become clayey at depth, and are also prone to long-term deterioration (so-called weathering). The deterioration of mudstone over time is a characteristic of mudstone, and it is very important to establish a classification method of mudstone susceptible to deterioration based on its physical and chemical properties in order to deal with the problems associated with construction of cut slope.

2　Investigation of Laboratory and in Situ Tests for Classification of Degradable Muddy Rock Samples

2.1　Muddy Rock Samples

Geological classification. The Cenozoic Paleogene and Neogene Muddy Rocks of the Kyushu area are relatively coherently distributed in northern, northwestern, central, and southern Kyushu. In this study, Muddy Rocks of the Miyazaki Group, which are also treated in the study by Wang [16], are targeted. Figure 1 shows a map of sampling locations.

In geological terms, mudstone is classified into mud, mudstone, shale, slate, crystalline schist, and gneiss in descending order of metamorphic grade, with metamorphic rocks generally being those that are more metamorphic than crystalline schist. In this study, mudstone and shale, which are relatively less metamorphic, are the main targets, and some sandstone is also treated to confirm the differences in physical and chemical properties between mudstone and shale. On the other hand, from a geotechnical engineering viewpoint, there are classifications such as soft rock, medium-hard rock, and hard rock based on the hardness of the rock fragments, as well as classifications based on the fracture intervals that develop in the rock. Based
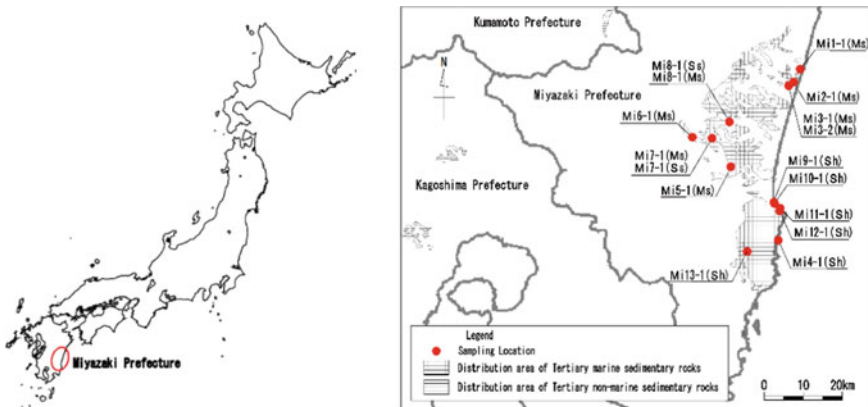
Fig. 1　Distribution map of Tertiary strata around Miyazaki and sampling locations

Fig. 2 Distribution Outcrops from which Muddy Rock samples were collected. (Left: Mudstone, Right: Shale)

on the above, the geotechnical classification of mudstone and shale used in this study is defined as follows: mudstone is defined as having few cracks (no cracks within 10 cm) in the outcrop, and shale is defined as having relatively many cracks (cracks at intervals of several centimeters) (Fig. 2).

Classification of unweathered and weathered Muddy Rocks. Groundmass has undergone weathering over a long period of geologic time. Chigira [9] classified the weathering zones of mudstone by chemical composition and other factors and noted that the chemical composition, pH, and porosity of the groundmass changed markedly between the unweathered and weathered zones. According to this classification, a zone with a pH of 7.7 ± 0.3 and a porosity of $41.4 \pm 4\%$ is defined as an unweathered zone, and a zone where iron oxide FeO_3 and H_2O is acquired, the pH becomes acidic, and the porosity increases is defined as a weathered zone.

In addition to the above classification, it is also necessary to consider the weathering of the ground immediately after the cut in the cut slope where degradable muddy stone is distributed. Figure 3 shows an example of the physical weathering classification by Taga et al. [7]. This corresponds to ① in Fig. 3. Next, when the ground is excavated, the excavation surface is disturbed by heavy machinery and blasting, and its strength is reduced by swelling due to stress release. This is included in ② in Fig. 3. This process ends relatively early, but what continues indefinitely is the so-called secondary weathering caused by repeated dry and wet weathering and freezing and thawing. This is shown in Fig. 3 ③. The susceptibility to deterioration in this study refers to this secondary weathering.

2.2 Laboratory and in Situ Tests Conducted to Classify Muddy Rock Susceptible to Degradation

With reference to the aforementioned research results on the degradation of muddy rocks, we examined laboratory and in situ test items for classification of muddy rocks
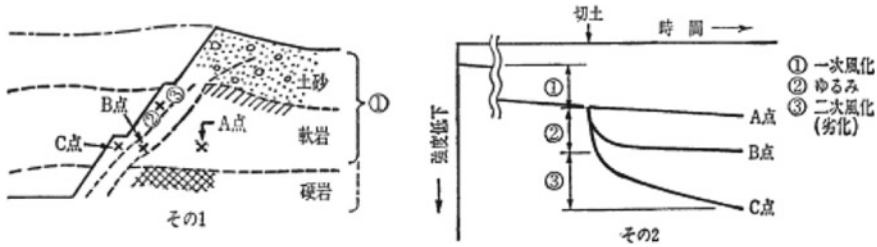
Fig. 3 Conceptual diagram of weathering and loosening deterioration [7]

susceptible to degradation, focusing on the fact that the results can be obtained in a relatively short period of time and in a simple manner.

First, as laboratory tests, a slaking test and an ignition loss test were conducted to define the susceptibility to degradation. In addition, physical tests were conducted to determine the density, particle size, and liquid/plastic limit of soil particles, which are correlated with the natural water content and rate of increase in water absorption, which are considered to have a high correlation with slaking characteristics based on previous studies, and X-ray diffraction analysis to determine the presence of swelling clay minerals. In situ needle penetration tests were also conducted to obtain in situ test values that provide an indication of unconfined compression strength.

The laboratory and in situ tests conducted in this study can be organized in order of simplicity as follows: needle penetration test, density test of soil particles, water content ratio test, grain size test, liquid and plastic limit test, ignition loss test, water absorption test, X-ray diffraction analysis, and slaking test.

3 Physical and Chemical Properties of Muddy Rocks Susceptible to Degradation

3.1 Physical and Chemical Properties and Unconfined Compression Strength of Muddy Rocks

Table 1 lists the physical properties by sample, and Table 2 lists the physical properties by rock type. For mudstone and shale, the density of soil particles ρ_s is slightly larger in shale, and the natural water content ratio W_n, effective porosity, and water absorption ratio Q are higher in mudstone. The ignition loss test values L_i, which indicate the degree of rock weathering, are all small, ranging from $L_i = 4.1$ to 5.0%. The slaking index, which suggests degradation characteristics, varied from 1 to 4 for the mudstone and 1 to 3 for the shale.

Next, Table 3 and Fig. 4 show the results of X-ray diffraction analysis. All of the samples contain trace amounts of the swelling clay minerals chlorite and smectite, indicating that in the weathered mudstone Mi3-2(Ms) the smectite content increases

Table 1 Physical properties of muddy rocks materials (by sample)

Sample No	Rock name	Density of soil particles ρ_s 3000 (g/cm³)	Natural water content W_n (%)	Effective porosity (%)	Liquid limit W_L (%)	Plastic limit W_p (%)	Plasticity index I_p	Water absorption Q (%)	Ignition loss Li (%)	Slaking index*
Mi 1–1(Ms)	Mudstone	2.725	27.3	43.7	57.7	19.0	38.7	28.7	5.1	1
Mi 2–1(Ms)	Sandy mudstone	2.725	21.6	44.2	46.7	22.5	24.2	26.1	4.7	1
Mi 3–1(Ms)	Mudstone	2.702	26.2	42.2	50.9	20.9	30.0	27.9	4.2	4
Mi 3–2(Ms)	Weathered mudstone	2.716	23.9	35.5	46.9	20.9	26.0	25.8	4.0	4
Mi 4–1(Sh)	Shale	2.722	4.3	10.1	38.4	18.1	20.3	7.4	5.5	1
Mi 5–1(Ms)	Mudstone	2.695	5.5	15.7	31.5	15.3	16.2	7.0	5.5	3
Mi 6–1(Ms)	Mudstone	2.690	7.2	34.6	31.4	16.3	15.1	9.8	4.9	4
Mi 7–1(Ms)	Mudstone	2.673	6.8	17.4	32.2	15.4	16.8	8.9	5.0	4
Mi 7–1(Ss)	Sandstone	2.667	3.0	6.8	–	–	–	1.8	4.6	0
Mi 8–1(Ms)	Mudstone	2.667	12.9	26.0	49.1	17.4	31.7	14.2	6.8	3
Mi 8–1(Ss)	Sandstone	2.649	12.9	29.9	34.1	21.6	12.5	15.2	3.6	4
Mi 9–1(Sh)	Shale	2.713	1.8	14.4	36.7	16.8	19.9	6.1	3.6	2
Mi 10–1(Sh)	Shale	2.721	6.0	16.1	37.4	15.9	21.5	7.1	4.6	3
Mi 11–2(Sh)	Low weathered shale	2.746	11.6	17.1	40.7	17.6	23.1	7.7	4.2	3
Mi 12–1(Sh)	Shale	2.738	4.4	12.3	34.3	15.5	18.8	5.2	4.8	2
Mi 13–1(Sh)	Shale	2.727	0.4	10.3	–	–	–	4.2	5.5	2

Table 2 Physical properties of muddy rocks materials (by rock type)

Rock name	Weathering classification	Density of soil particles ρ_s 3000 (g/cm^3)	Natural water content W_n (%)	Effective porosity (%)	Liquid limit W_L (%)	Plastic limit W_p (%)	Plasticity index I_p	Water absorption Q (%)	Ignition loss L_i (%)	Slaking index※
Mudstone	Unweathered	2.697	15.4	32.0	42.8	18.1	24.7	17.5	5.2	3
	Weathered	2.716	23.9	35.5	46.9	20.9	26.0	25.8	4.0	4
Shale	Unweathered	2.724	3.4	12.6	36.7	16.6	20.1	6.0	4.8	2
	Low weathered	2.746	11.6	17.1	40.7	17.6	23.1	7.7	4.2	3
Sandstone	Unweathered	2.658	8.0	18.4	34.1	21.6	12.5	8.5	4.1	2

※The slaking index shall be the slaking classification 24 h after the initial immersion of the specimen

with the disappearance of chlorite. The degree of weathering, W_d, determined by X-ray diffraction intensities of meta-haloysite and plagioclase, yielded small values of $W_d \leq 2.4\%$ (1) [14].

$$W_d = (I_{mh}/(I_{mh} + I_{pl}) \times 100 \tag{1}$$

Wd: Weathering Degree (%)
Imh: X-ray Diffraction Intensity of Meta-Haloysite
Ipl: X-ray Diffraction Intensity of Plagioclase

In addition, Fig. 5 shows the unconfined compression strength, qu, obtained from laboratory unconfined compression tests and needle penetration tests for each rock type. According to these tests, the unweathered mudstone has $qu = 782$ to 7400 kN/m^2, while the unweathered shale has higher $qu = 7750$ to $18,200$ kN/m^2, which is consistent with the geological classification of mudstones into mudstone and shale, in order of increasing metamorphic grade. On the other hand, the qu values of both rock types decreased significantly as weathering progressed. The ratios of unconfined compression test values to needle penetration test values ranged from 0.46 to 1.13 for unweathered mudstone, 0.65 to 1.35 for unweathered shale, and 1.73 for weakly weathered shale.

3.2 Relationship Between Physical and Chemical Properties and Susceptibility to Deterioration

This section discusses the relationship between the physical and chemical properties of mudstones and their susceptibility to degradation.

Since the degradation in this study mainly refers to secondary weathering caused by repeated dry and wet weathering, the slaking index, which is synonymous with secondary weathering, is used as a classification index for the susceptibility to degradation. A slaking index of 0 to 3 was defined as resistant to degradation, and a slaking index of 4 was defined as susceptible to degradation. For this reason, each characteristic value in the correlation chart shown below is organized by slaking index.

Figure 6 shows some correlograms of characteristic values that have a marked tendency to deteriorate. The figure indicates that the natural water content Wn, water absorption Q, effective porosity, degree of weathering Wd, ignition loss Li, and uniaxial compressive strength qu are strongly correlated with the susceptibility to deterioration.

Table 3 Degree of weathering by X-ray diffraction intensity W_d

Sample No.	Whole rock analysis (quartz index)											Stoichiometric analysis	Degree of weathering W_d (%)
Mi 1–1(Ms)	18.7	3.7 (8.0)	< 0.2	< 0.2 (<0.2)	0.2	0.5	< 0.2	0.6		0.4	0.2	● ○ ○ ○ ○ ○	1.2
Mi 2–1(Ms)	15.9	8.1 (8.7)	0.4	< 0.2 (<0.2)	0.3	0.4	< 0.2	1.4			0.2	● ○ ○ ○	1.1
Mi 3–1(Ms)	27.0	5.5 (7.3)		< 0.2 (<0.2)	0.4	0.7	< 0.2		0.2	0.5		● ○ ○ ○ ○	1.4
Mi 3–2(Ms)	24.4	3.7 (4.4)		< 0.2 (<0.2)	0.3	< 0.2	0.2					● ○ ○ ○	2.2
Mi 4–1(Sh)	14.5	2.4 (4.1)		< 0.2 (<0.2)	0.3	0.5	< 0.2	1.4	0.5			● ○ ○	2.4
Mi 5–1(Ms)	18.4	4.1 (4.8)		< 0.2 (<0.2)	0.7	1.3	< 0.2	1.0				● ○ ○	2.0
Mi 6–1(Ms)	24.5	6.5 (8.8)		< 0.2 (<0.2)	0.7	1.3	< 0.2					● ○ ○	2.2
Mi 7–1(Ms)	26.9	6.3 (10.9)		< 0.2 (<0.2)	0.7	1.2	< 0.2	1.0				● ○ ○	1.8
Mi 7–1(Ss)	38.2	9.1 (9.7)		– (×)	0.3	0.6	< 0.2	7.1				● ○ ○	0.0

Table 3 (continued)

Sample No.	Whole rock analysis (quartz index)							Stoichiometric analysis				Degree of weathering W_d (%)
Mi 8–1(Ms)	35.8	5.5	–	0.4	0.7	<0.2	0.6	×	○	○	○	0.0
Mi 8–1(Ss)	33.2	6.9 (5.6)	–(×)	0.5	0.9	<0.2	0.6	●	○	○	○	0.0

· Values in parentheses are quartz indices after hydrochloric acid treatment (only feldspar and meta-haloysite are shown)
· Legend ○: Confirmed by stereotaxic analysis
●: Confirmed by hydrochloric acid treatment
× : Confirmed to be below detection limit by hydrochloric acid treatment
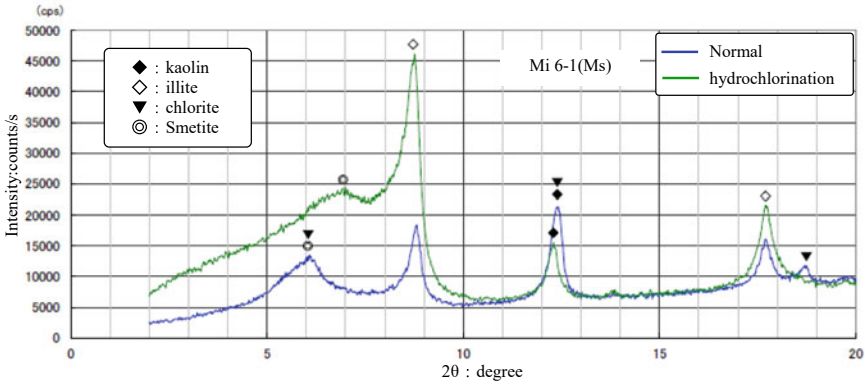
Fig. 4 Example of X-ray diffraction analysis results of muddy rock, wich is easily degraded
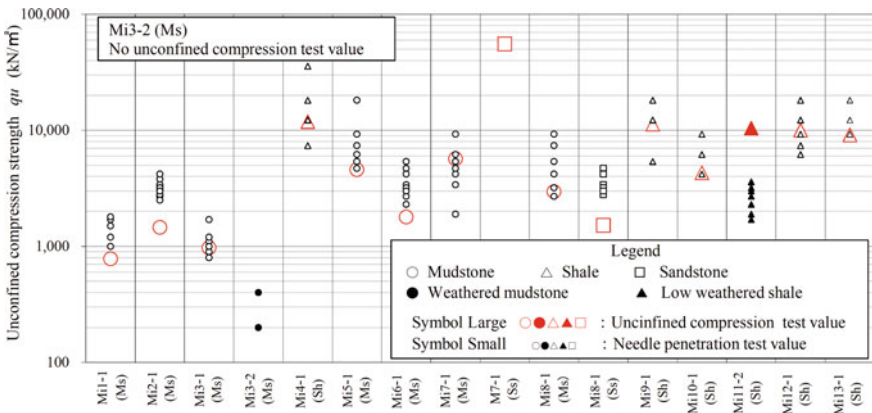
Fig. 5 Unconfined compression strength, *qu*, by indoor unconfined compression test and needle penetration test

4 Conclusion

In this study, physical and chemical properties were determined for Cenozoic Paleogene and Neogene mudstones. Mudstones with a slaking index = 4 were defined as mudstones prone to degradation, and the mudstones prone to degradation were classified by looking at the correlation between the obtained property values. Based on these results, we proposed laboratory and in situ test items for classification of mudstone susceptible to degradation, emphasizing the simplicity of obtaining the results. These results can be summarized as follows.

(1) The geotechnical classification method of mudstone and shale, which focuses on the fracture spacing that occurs when exposed, is consistent with the geological classification of mudstone and shale according to their metamorphic grade.
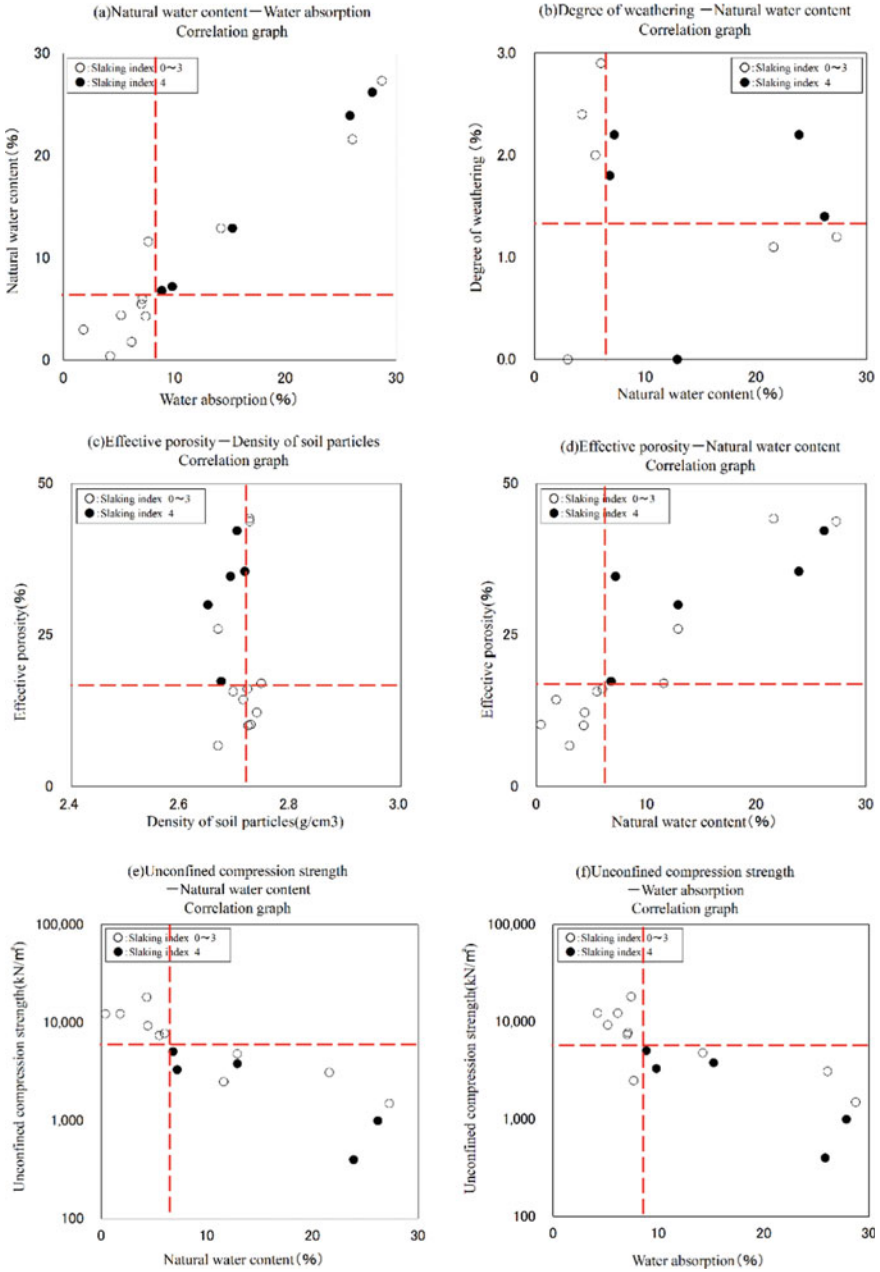
Fig. 6 Correlation graph of characteristic values that have a marked tendency to deteriorate

(2) Physical and chemical properties that are highly correlated with the susceptibility of mudstone to degradation include natural water content ratio Wn, water absorption Q, effective porosity, degree of weathering Wd, Ignition loss Li, and unconfined compression strength qu.

(3) Muddy rock with natural water content $Wn \geq 6.0\%$ and water absorption $Q \geq 8.0\%$ may be susceptible to degradation.

(4) Muddy rock with weathering degree $Wd \geq 1.3$ and natural water content $Wn \geq 6.0\%$ may be easily degraded.

(5) Muddy rock with soil particle density $\rho s \leq 2.72\text{g/cm}^3$ and effective porosity $\geq 17\%$ may be easily degraded.

(6) Muddy rock with natural water content $Wn \geq 6.0\%$ and effective porosity $\geq 17\%$ may be easily degraded.

(7) Muddy rock with natural water content $Wn \geq 6.0\%$ and uniaxial compressive strength $qu \leq 5000 \text{ kN/m}^2$ may be easily deteriorated.

(8) Mudstones susceptible to degradation include chlorite and smectite, which are universally swelling clay minerals.

(9) Natural water content ratio test, soil particle density test, water absorption test, effective porosity test, Ignition los test, uniaxial compression test, needle penetration test, and X-ray diffraction analysis are effective methods to classify mudstones susceptible to degradation.

References

1. 1:50,000 Geological Map of Japan, Hyuga-aoshima with Explanatory Text, Geological Survey, Japan (1958)

2. Uda R, Yasufuku N, Ishikura R (2021) Stability evaluation of cut slope reflecting stratigraphic and weathering characteristics. In: Procedings of Western Branch of JSCE, vol 317–318 (March 2021)

3. Yamaguchi Y, Nakamura Y, Nakamura M, Hakoishi N, Yamaya M, Kato Y (2005) Verification of design strength of soft rock foundation for dams by needle penetration test. J Japan Soc Eng Geol 46(1):20–27

4. Kohno M, Maeda H (2010) Relationship between cylinder(longitudinal)point load strength and uniaxial compression strength for smectite-bearing fine tuffs in a soft and semi-hard rock boundary area: example of the upper Miocene Ikutawara formation from the Ikutawara-minami landslide area landslide. J Japan Landslide Soc 47(1):17–25

5. Adachi T, Ogawa T (1980) Mechanical properties and failure croterion of soft sedimentary rock. vol 295. pp 51–63

6. Kikuchi H, Kawamura H, Furukawa K, Okuzono S, Tayama S (1998) Based on long-term measurements cut-off slope weathering progress and collapse possibility. J Japan Soc Civil Eng 588(VI-38):151–164

7. Taga N, Tayama S, Okuzono S, Yagisawa T (1991) Long-term measurements on weathering progress and stability of cut slopes. J Japan Soc Civil Eng the Japanese Geotech Soc; Soil mechanics and foundation engineering, vol 39-6(401). pp 41–47

8. Okuzono S (1978) Weathering of cut slopes and their correction. J Japan Soc Civil Eng The Japanese Geotechnical Society; Soil mechanics and foundation engineering 26–6(244), pp 37–44

9. Chigira M (1988) Chemical weathering of mudstone of the Pleistocene Haizume Formation, Niigata Prefecture, Central Japan. J Geol Soc Japan 94(6):419–431
10. Chigira M (1992) Soft rock weathering. J Japan Soc Civil Eng the Japanese Geotech Soc; Soil mechanics and foundation engineering 40–8(415), pp 71–79
11. Nishi K, Furukawa K, Ogawa T, Nakagawa K (1993) Procedure for judgement of slope stability and evaluation of slope-failure factors during heavy rain. J Japan Soc Civil Eng 480(VI-21):127–136
12. Nishi K, Furukawa K, Ogawa T, Nakagawa K (1994) A system for forecasting cut-off slope collapse during continuous heavy rain. J Japan Soc Civil Eng 498(VI-24):95–104
13. Yamashita K, Tanaka S, Tochio T, Hamada M (2021) Fundamental properties of Hatazu Shale, Kijima Group, and strength changes associated with slaking. In: The 56th geotechnical engineering research conference, collection of lectures
14. Otsuki H, Nishi K, Okamoto T, Tanaka S (1981) Time-dependent characteristics of a mudstone. ISRM Symposium(Tokyo), Theme1, pp 113–118
15. Murata H, Hyodo M, Yasufuku N (1987) Compressive and shear characteristics of undisturbed decomposed Granite soils paying attention to the degrees of weathering. J Japan Soc Civil Eng 382(III-7):131–140
16. Xiangyu W, Yamashita K, Yasufuku N, Ishikura R (2022) Study on evaluation of weathering degree of Miyazaki mudstone focusing on ignition loss. J Japan Soc Civil Eng
17. Furukawa Y, Fujita T (1994) Estimation of the degree of weathering of decomposed granite soils distributed in the Abukuma mountains and their characteristics for banking materials. J Japanese Geotech Soc Report of Papers 34(4):121–33

Single Pile Behavior Under Repeated Horizontal Loading

Yuka Sakoda, Atsushi Mohri, Yoshiaki Kikuchi, Shohei Noda, Tetsuo Okuno, Hirokazu Sugiyama, and Kiyoshi Fukutake

Abstract Over the years, several marine structures with pile foundations have been proposed. Typically, such structures are repeatedly subjected to horizontal loading along numerous directions and at various load levels under the effects of waves or winds. However, the current Japanese design method examines these structures at the maximum load of virgin loading and rarely considers the deformation change of the pile owing to repeated loading. In this study, repeated horizontal loading experiments were conducted on single piles to examine the deformation behavior of such piles with respect to the loading directions and the preceding repeated loading. The maximum load was fixed, the minimum load was varied in each experimental case, and the unloading ratio (= minimum horizontal load/maximum horizontal load) was varied. Consequently, in the positive ratio, the increase in the ground surface displacement corresponded with the increase in the number of cycles. However, in the negative ratio, unexpected changes were observed in the behavior of the piles during monotonic loading. The results of the ground surface displacement and the bending moment distributions in the two-stage loading experiments, with regard to the behavior of piles subjected to preceding repeated loading demonstrated that, the considerable attention should be paid to the behavior of piles at the maximum load level when subjected to repetitive actions at different load levels. In particular, when the preceding load was smaller, the effect of the preceding load was negligible.

Keywords Single pile · Pile foundation · Repeated loading

Y. Sakoda (✉)
Pacific Consultants Co., Ltd, 3-22, Kanda-Nishikicho, Chiyoda-ku, Tokyo, Japan
e-mail: yuka.sakoda@tk.pacific.co.jp

A. Mohri
Port and Airport Research Institute, 3-1-1, Nagase, Yokosuka, Kanagawa, Japan

Y. Kikuchi
Tokyo University of Science, Yamazaki 2641, Noda, Chiba, Japan

S. Noda
Nishinippon Institute of Technology, Aratsu 1-11, Kanda-machi, Miyoko-gun, Fukuoka, Japan

T. Okuno · H. Sugiyama · K. Fukutake
Shimizu Corporation, 3-4-17, Etchujima, Koto-ku, Tokyo, Japan

1 Introduction

Several marine structures with pile foundations have been proposed over the years, and such structures are subjected to repeated horizontal loads in numerous directions and at various load levels under the effects of waves or winds. However, the current Japanese design method examines these structures at the maximum load of virgin loading and rarely considers the deformation change of the pile caused by repeated loading. Notably, Single Pile Structure (SPS) [1–4] has been proposed as examples for considering repeated loading in Japan. This is designed to make use of the property that piles are easy to deflect, sand a part of the energy absorbed at the berthing is shared by the pile, resulting in significant pile deformation. To establish a design method for SPS, studies have examined the behavior of single piles under repeated horizontal loads and that of single piles under large deformations such as the ground becoming plastic [1, 2]. Additionally, previous studies [3, 4] have revealed that the behavior of single piles differs depending on whether repeated loads act as virgin loads or elastic load levels. However, the behavior of piles when subjected to repeated horizontal loads has not been completely studied.

This study investigated the deformation behavior of single piles subjected to repeated horizontal loads from multiple directions. The following two items were examined: (1) The effect of unloading load level on deformation behavior of pile (Series 1), and (2) the effect of the preceding repeated load level on pile behavior during subsequent repeated loading (Series 2). First, when horizontal loads are applied repeatedly to the pile, we must consider the conditions where the load returns to zero after one load cycle, a second load acts before returning to 0, and repeated loads are applied while the load is applied in the opposite direction. Secondly, in a storm, the size of the waves gradually increases, upon reaching a peak in the middle of the storm, and then gradually decreases. To simplify this, if a small, repeated load is initially applied followed by larger repeated loads, it is necessary to consider how the effect of the earlier repeated loads would be generated. In contrast, after the wave peak has passed, the piles are subjected to smaller repeated loads; therefore, it is necessary to consider the behavior of the piles in this case. The experimental conditions for Series 2 are based on these issues.

Each series of experiments were carried out at different pile embedment lengths, and the effect of the pile embedment length was studied. This paper describes the results of repeated loading experiments on a long pile with sufficiently long pile embedment length.

2 Experiment Outline

2.1 Experimental Equipment

The experiments were conducted using different steel sand boxes in Series 1 and 2. Dry Tohoku silica sand #5 ($\rho_s = 2.640$ Mg/m^3, $e_{max} = 0.818$, $e_{min} = 0.522$, and D_{50} = 0.567 mm) was used, and the model ground was prepared using the air pluviation method. The steel sand box used in Series 1 was 1580 mm long, 800 mm high, and 400 mm wide, and a 600 mm thick ground layer was created (Fig. 1). The steel sand box used in Series 2 was 1200 mm long, 600 mm high, and 400 mm wide, was and a 500 mm thick ground layer was created.

A steel plate (750 mm long, 40 mm wide, 2.3 mm thick, SS400 and $E = 2.05$ $\times$ 10^5 N/mm^2) was used as the model of the single piles and installed in the center of a steel sand box with an embedment length of 500 and 600 mm. The piles were subjected to static horizontal loading at a height of $+$ 50 mm from the ground surface using displacement control (displacement rate of 4 mm/min at the loading point). The load at the loading point and the horizontal displacements at three points on the pile were measured during the experiments. Strain gauges were attached to both sides of the piles at 25 and 20 mm intervals in the ground and the air, respectively, to measure the bending strains.

In the case of repeated loading, the behavior of the piles presumably differs owing to different loading cycles. In particular, in saturated grounds, such as underwater, it is assumed that if the loading is applied at relatively fast cycles, the excess pore water pressure will rise, and the piles will continue to be loaded before they dissipate in time. However, as the experiments was conducted on dry sand ground in the first step of this study, it was not possible to assume changes in the excess pore water pressure in the surrounding ground due to repeated loading, so the loading speed was set to be relatively slow and satisfactory for quasi-static conditions.

In these experiments, the soil layer thickness differed for different steel sand boxes, however, the length of embedment of a pile was equal in both series, ensuring that the length of embedment was sufficient for long piles.

Fig. 1 Schematic diagram of the experimental model setup
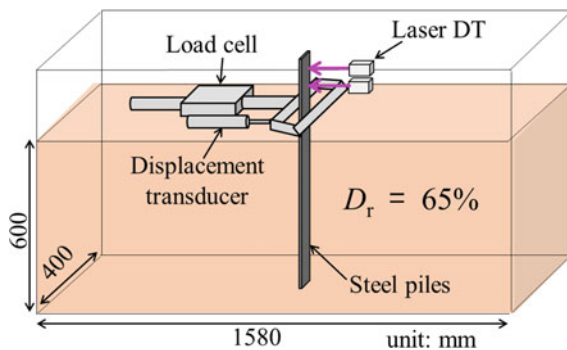
2.2 Experimental Conditions

Figure 2 shows an image of the time history of the loads from the repeated loading experiments for Series 1 and 2. In Series 1, the maximum load was fixed at 70 N and the minimum load was varied in each experimental case (Fig. 2a). Here, the unloading ratio α (= minimum horizontal load/maximum horizontal load) was considered as the ratio of the minimum and maximum horizontal loads and was varied between 0.5 to −1. Table 1 shows the experimental cases. In these experiments, the number of repeated loadings was set to 10. In Series 2, the experiments were carried out at different levels of repeated maximum loading in two stages, with the unloading ratio α fixed at 0 (Fig. 2b). That is, 10 cycles of repeated loading were performed at a load level that was β times the repeated maximum load in the second stage, followed by another 10 cycles of repeated loading in the second stage. β was selected between −2 and 2, as given in Table 2. In the case of β = 0, there was no loading in the first stage, and the load was repeatedly applied for 10 cycles at the maximum load level of the second stage. In the case of β = 1, only the second stage of repeated loading was repeated for 20 cycles.

3 Examination Method

The bending moment on the pile was measured using strain gauges, and the bending moment distribution was obtained using the third-order smoothed spline function [3], the deflection distribution was calculated by integrating the bending moment second order and dividing by the flexural rigidity *EI* of the pile.

Additionally, the coefficient of the subgrade reaction was obtained from the pile head load–displacement relationship at the initial loading, based on the subgrade reaction model of the PHRI method of the type S model [5].

$$p = k_s \cdot x \cdot y^{0.5} \tag{1}$$

a) Series 1   b) Series 2
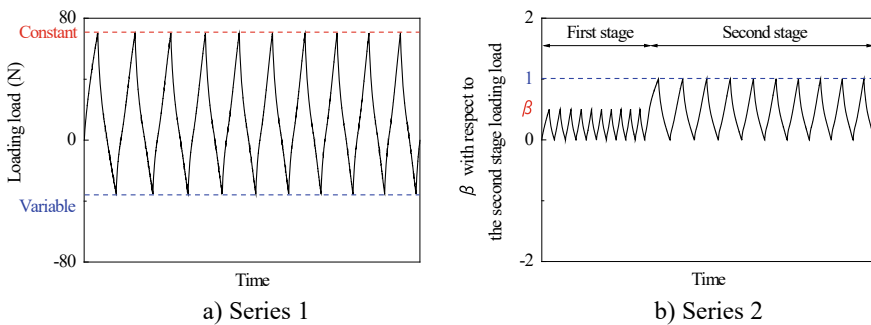
Fig. 2 Time history

Table 1 Details of the experimental cases in Series 1

Case	Unloading ratio α	Maximum horizontal load (N)	Minimum horizontal load (N)	Relative density (%)	Coefficient of subgrade reaction k_{s} (kN/m$^{3.5}$)
1-a	0.5	70	35	67	8000
1-b	0	70	0	74	8600
1-c	−0.3	70	−21	Measurement failure	9800
1-d	−0.5	70	−35	67	9500
1-e	−0.6	70	−42	65	9200
1-f	−0.8	70	−56	56	9400
1-g	−1	70	−70	67	9200

Table 2 Details of the experimental cases in Series 2

Case	β with respect to the second stage loading load	Load levels of the first stage (N)	Load levels of the second stage (N)	Relative density (%)	Coefficient of subgrade reaction k_{s} (kN/m$^{3.5}$)
2-a	−2	−60	30	82	9500
2-b	−1.5	−45	30	79	9000
2-c	−1	−70	70	82	13,000
2-d	−0.8	−56	70	81	12,000
2-e	−0.5	−35	70	77	13,000
2-f	−0.2	−14	70	82	12,000
2-g-1	0	0	30	80	10,000
2-g-2	0	0	30	77	15,000
2-g-3	0	0	30	85	13,000
2-h-1	0	0	70	74	8600
2-h-2	0	0	70	78	12,000
2-i	0.1	7	70	78	9200
2-j-1	0.2	14	70	66	8500
2-j-2	0.2	6	30	83	12,000
2-k	0.3	21	70	66	9000
2-l-1	0.5	35	70	63	8000
2-l-2	0.5	15	30	84	11,000
2-m-1	0.8	56	70	63	8000
2-m-2	0.8	24	30	86	12,000
2-n-1	1	30	30	77	15,000
2-n-2	1	30	30	85	13,000
2-o	1.2	36	30	76	15,000
2-p	1.5	45	30	79	15,000
2-q	2	60	30	81	18,000

where p is the subgrade reaction per unit area (kN/m^2), k_s is the coefficient of the subgrade reaction in the type S model (kN/m$^{3.5}$), x is the depth from the ground surface (m), and y is the pile deflection at each depth (m).

4 Examination Results

4.1 Effect of Unloading Load Level on Deformation Behavior of Pile (Series 1)

Figure 3 shows a representative example of the relationship between the loading load and the ground surface displacement for Series 1. The degree of change in the ground surface displacement of the pile at the maximum load as the number of loading cycles increased depends on the unloading ratio α. The degree of change increased when the unloading ratio α was between 0.5 and -0.5 and decreased when the unloading ratio α was -1.
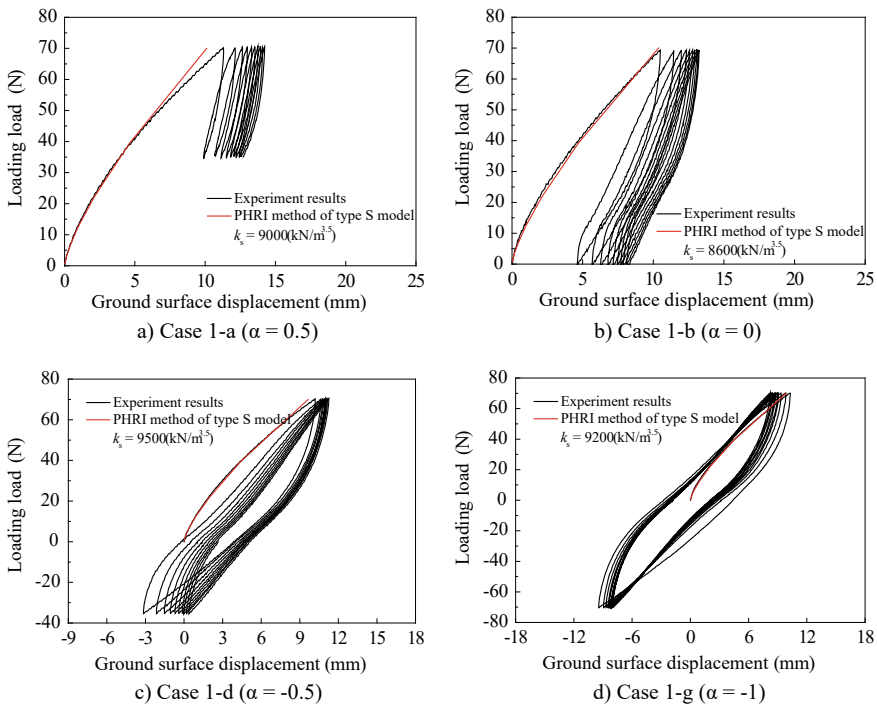

Fig. 3 Relationship between the loading load and the ground surface displacement (Series 1)

Figure 4 shows the relationship between the ground surface displacement ratio (y_{0n}/y_{01}) and the cycles at maximum load. The ground surface displacement ratio is calculated by dividing the displacement y_{0n} at the nth maximum load by the displacement y_{01} at the monotonic loading (1st cycle). As shown in Fig. 4, when the unloading ratio α was 0.5 and 0, the ground surface displacement increased as the number of cycles increased, and the growth rate from y_{01} was almost the same. In contrast, when α was negative, the growth rate from y_{01} decreased as α decreased. For all unloading ratios α, the rate of change of the displacement ratio (y_{0n}/y_{01}) per repetition decreased as the number of cycles increased. Accordingly, Fig. 5 shows the relationship between the ground surface displacement ratio at the 10th cycle maximum load (y_{010}/y_{01}) and the unloading ratio α. As seen in the figure, when α is greater than 0, (y_{010}/y_{01}) is hardly affected by α. However, when α is negative, (y_{010}/y_{01}) changes with α, and decreases to (y_{010}/y_{01}) = 0.8 for $\alpha = -1$. This indicates that if a pile is subjected to positive and negative horizontal loads during one loading cycle, the greater or lesser negative unloading ratio α affects the elongation of the pile displacement, whereas if a pile is not unloaded negatively, α has no effect on the elongation of the horizontal displacement of the pile.

Figure 6 shows the bending moment distribution at the 10th cycle maximum load in the experiment for all unloading ratios α. For reference, the bending moment distribution at the 1st cycle maximum load is shown as a dashed line. The results show

Fig. 4 Relationship between the ground surface displacement ratio (y_{0n}/y_{01}) and the cycles
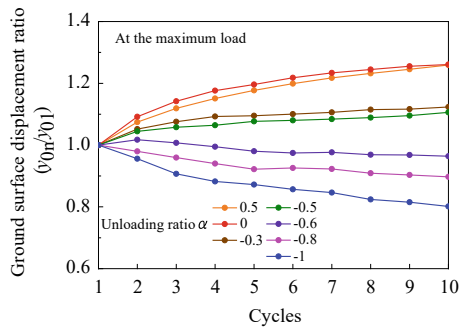
Fig. 5 Relationship between ground surface displacement ratio in the 10th cycle (y_{010}/y_{01}) and the unloading ratio α
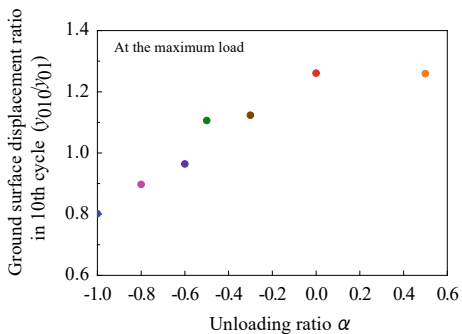
Fig. 6 Bending moment
distribution at the 10th cycle
maximum load
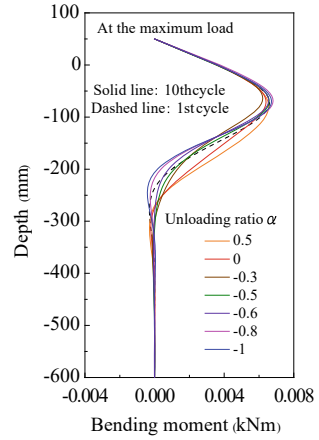
that the bending moment distribution in the 10th cycle from a depth of approximately
-100 mm to -300 mm, which is the maximum bending moment generation depth
l_{mmax}, varies as α varies, and is different from the bending moment distribution in the
1st cycle. The changes in the ground surface displacement due to repeated loading,
as shown in Figs. 4 and 5, are due to changes in the bending moment distribution in
this section, thereby indicating that the deflection behavior of the pile changes from
relatively deep sections owing to the difference in the unloading ratio α.

As shown in Fig. 6, the maximum bending moment changes as α changes. Figure 7
shows the ratio of the maximum bending moment at the maximum load for each
repeated loading with reference to the maximum bending moment in the 1st cycle
(M_{maxn}/M_{max1}). It can be seen that the maximum bending moment owing to repeated
loading changes slightly at the 2nd cycle, but then hardly changes at all.

Fig. 7 Relationship between
the maximum bending
moment ratio ($M_{maxn}/$
M_{max1}) and the cycles
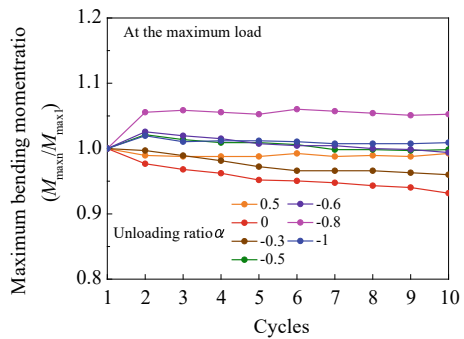
4.2 Effect of the Preceding Repeated Load Level on Pile Behavior During Subsequent Repeated Loading (Series 2)

We examined the effect of the preceding repeated loading on the subsequent repeated loading. As given in Table 2, when $|\beta|$ is large, the second repeated load level is different from when $|\beta|$ is small owing to the convenience of the experimental equipment. However, when the effect of such a change in the repeated load level in the second stage was examined, particularly with regard to the displacement elongation trend, there was little difference in the elongation of the displacement as the number of repeated loading cycles increased. The fact that the influence of the load level in the second stage can be neglected by taking appropriate ratios for comparison even at different load levels can be attributed to the fact that the conditions of the piles used to satisfy the conditions for the long piles.

Figure 8 shows the relationship between the loading load and the ground surface displacement for the cases $\beta = 0.5$, 2, and -2. In the case of $\beta = 0.5$, as shown in Fig. 8a, the maximum displacement at the maximum load in the repeated loading of the first stage increased as the repeated load increased; however, that of the second stage was largely unaffected by the repeated loading of the first stage. Conversely, in the case of $\beta = 2$, as shown in Fig. 8b, the maximum displacement at the maximum load in the repeated loading of the second stage was strongly influenced by the maximum displacement in the first stage and was smaller than the maximum displacement in the first stage at the maximum load, thereby indicating elastic behavior. In the case of $\beta = -2$, as shown in Fig. 8c, the ground surface displacement was negative at the first maximum load of the second stage owing to the repeated load level of the first stage. The subsequent repeated loading resulted in a positive movement of the ground surface displacement; however, the overall, positive displacement was small. These loading load-ground surface displacement relationships indicate differences in the displacement of the second stage for different values of β. Figure 9 shows how the surface displacement at the maximum load in the second stage varies with β, the vertical axis denoting the ground surface displacement ratio ($y_{0\beta n}/y_{001}$) and the ground surface displacement ($y_{0\beta n}$) at the nth ($1 \leq n \leq 10$) maximum load loading during the repeated loading of the second stage after the repeated loading of the first stage at each β divided by the ground surface displacement (y_{001}) at the first maximum load during the second stage at $\beta = 0$. As shown in Fig. 9, when $|\beta| \leq 1$, ($y_{0\beta n}/y_{001}$) does not depend significantly on β, and when $|\beta| > 1$, ($y_{0\beta n}/y_{001}$) depends on β. In addition, when $\beta > 1$, ($y_{0\beta n}/y_{001}$) decreases with repeated loading, whereas when $\beta < -1$, ($y_{0\beta n}/y_{001}$) increases with repeated loading.

Figure 10 shows the results of focusing on the ground surface displacement ratio ($y_{0\beta 1}/y_{001}$) at the first maximum load of the second stage owing to different values of β. As shown in Fig. 10, the ground surface displacement ratio increases as β increases. However, for $\beta < -1$ and $\beta > 1$, ($y_{0\beta 1}/y_{001}$) changes significantly with β, whereas for $|\beta| < 1$, ($y_{0\beta 1}/y_{001}$) is almost constant, between 0.95 and 1.17. However, when $\beta < -1$, the influence of the preceding repeated load reduces the ground surface

a) Case 2-l-1 (β = 0.5)

b) Case 2-q (β = 2)

c) Case 2-a (β = -2)
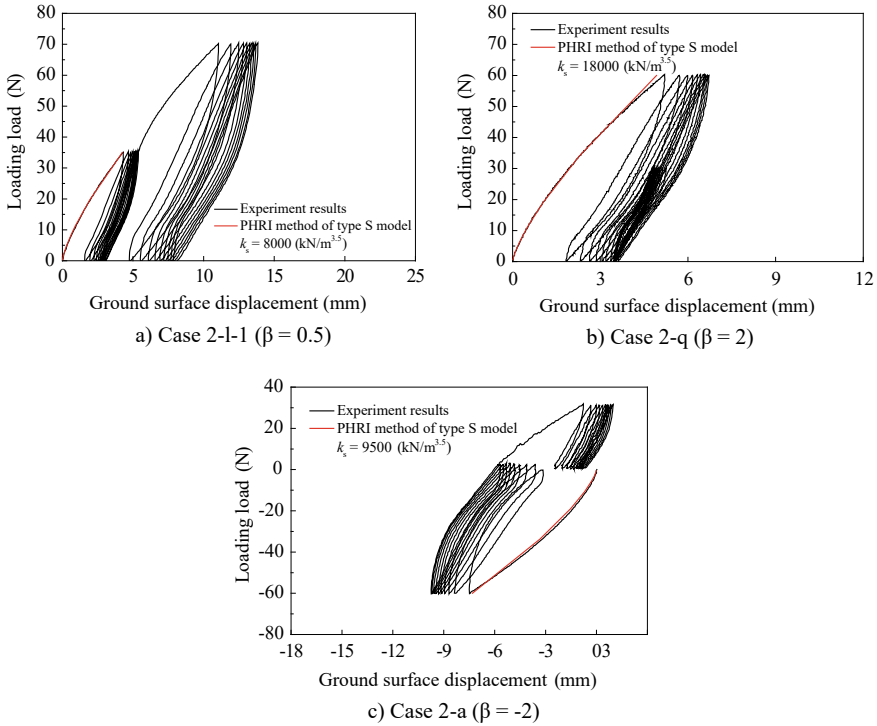
Fig. 8 Relationship between the loading load and the ground surface displacement (Series 2)

Fig. 9 Relationship between the ground surface displacement ratio ($y_{0\beta n}$/y_{001}) and the cycles
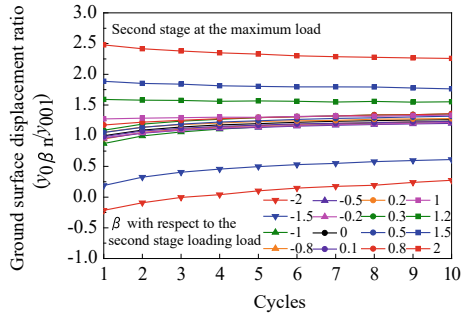
displacement owing to the repeated loading of the second stage, with the effect being greater for smaller β. When $\beta > 1$, a much larger ground surface displacement is achieved owing to the repeated loading of the second stage compared to that for $\beta = 0$.

Figure 11 shows the growth of the ground surface displacement when the second stage load was applied repeatedly for 10 cycles. The vertical axis denotes the change in the ground surface displacement of the 10th and 1st maximum loads of the second stage ($y_{0\beta 10} - y_{0\beta 1}$) divided by the ground surface displacement at the first maximum

Fig. 10 Relationship between the ground surface displacement ratio of the second stage 1st cycle ($y_{0\beta 1}/y_{001}$) and β with respect to the second stage loading load
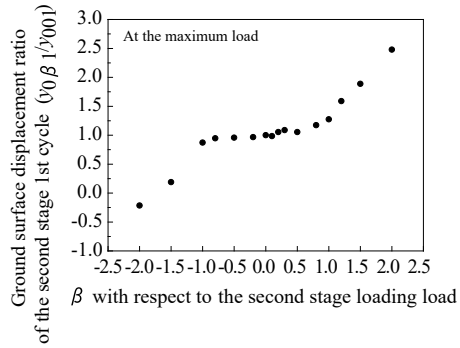
Fig. 11 Relationship between the amount of the change in the ground surface displacement in the second stage ($y_{0\beta 10}-y_{0\beta 1}$)/($y_{001}$) and β with respect to the second stage loading load
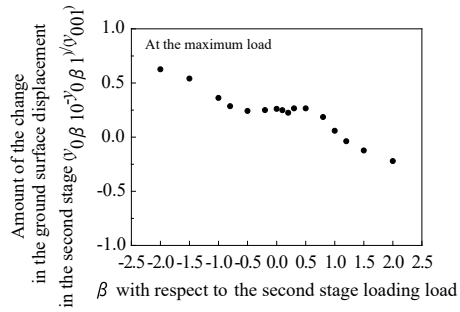
load in the second stage at $\beta = 0$ (y_{001}). As in Fig. 10, for $|\beta| \leq 1$, the change in ($y_{0\beta 10}-y_{0\beta 1}$)/($y_{001}$) with a change in β is small. For $\beta < -1$, the change is in the direction of the increase in the displacement owing to repeated loading, whereas for $\beta > 1$, the change is in the direction of the decrease in the displacement.

Therefore, if $|\beta|<1$, the ground surface displacement at maximum load during the repeated loading of the second stage is hardly affected by the preceding repeated loading, even if it is affected by it. However, when $|\beta|>1$, it remains strongly influenced by the first stage. Additionally, the effect of repeated loading on the maximum load level is pronounced for piles subjected to repeated horizontal loads at different load levels. When it is subjected to the repetitive action of different load levels, most attention should be paid to the behavior of piles at the maximum load level. In particular, when the preceding load is smaller, the influence of the preceding load is hardly noticeable, and when it is greater, the overall behavior is strongly influenced by the repetitive loading of the preceding maximum load; however, the repetitive loading of the subsequent load slightly decreases the influence of the maximum load repetition.

5 Conclusions

In this study, we conducted repeated horizontal loading experiments on single piles to examine their deformation behavior with respect to the loading directions and the preceding repeated loading. The conclusions of this study are as follows: (1) The effect of unloading load level on deformation behavior of pile: When the unloading ratio α (= minimum load/maximum load) was positive, the amount of increase in the ground surface displacement as the number of cycles increased was generally the same. However, in the negative range of the unloading ratio α, the manner in which the ground surface displacement increased depended on α. The bending moment at the shallow part up to the depth at which the maximum bending moment generation depth l_{mmax} showed little change in the bending moment distribution owing to repeated loading, and the maximum bending moment remained almost unchanged even after repeated loading without being affected by the change in α. The change in the bending moment in the depth direction was influenced by the degree of the subgrade reaction, and the difference in the subgrade reaction generated from a depth of approximately l_{mmax} to l_{m1}, which could be the reason why the elongation of the displacement of the pile at the maximum load during repeated loading differed for different α. (2) The effect of the preceding repeated load level on pile behavior during subsequent repeated loading: The results of the ground surface displacement and bending moment distributions, with regard to the behavior of piles when subjected to preceding repeated loading, indicate that most attention should be paid to the behavior at the maximum load level when subjected to repetitive action at different load levels. In particular, it was found that when the preceding load was smaller, the influence of the preceding load was hardly noticeable. When the preceding load was greater, the overall behavior was strongly influenced by the repetitive loading of the preceding maximum load; however, that of the subsequent load slightly decreased the influence of the maximum load repetition.

References

1. Kiuchi S, Morinaga K, Takahashi M, Hirose T, Sakaki N, Suzuki M (1988) Fundamental study on the design method of SPS (Single Pile Structure). In: 13th symposium on ocean development, pp 331–336 (In Japanese)
2. Kiuchi S, Matsushita M, Takahashi M, Kakee M, Isozaki S, Suzuki M (1990) Full-scale loading tests on the behavior of SPS driven into sandy ground and subjected to horizontal loads. In: 15th symposium on ocean development, pp 107–112 (In Japanese)
3. Kikuchi Y, Takahashi K, Suzuki M (1992) Lateral resistance of single piles under large repeated loads. Report of the Port and Harbour Res Institute Ministry of Transp 31(4):33–60
4. Kikuchi Y, Takahashi K, Suzuki M (1993) Lateral resistance of single piles under large repeated loads. Proc Civil Eng Ocean 9:337–342
5. Shinohara T, Kubo K (1961) Experimental study on the lateral resistance of piles (Part 1)—lateral resistance of single free head piles embedded in uniform sand layer. Monthly Reports of Transport Technical Res Institute 11(6):169–242

Visualization of Seepage Behavior in a Model Ground Around Sheet Pile Using μ-Focused X-Ray CT System

Hikaru Mouri, Takahiro Sato, Toshifumi Mukunoki, and Jun Otani

Abstract River levees are used for not only flood control, but also for flood inundation. In recent years, river floods caused by short duration torrential rains and large typhoons have occurred in Japan. The principle that river dikes must be constructed using only soil is still followed. This is due to the availability of materials, the fact that the structure does not deteriorate, and the ease of restoration if the structure fails. Meanwhile, the entire function of a continuous dike can be lost when a localized weak point causes a breakout. In this study, an experimental apparatus was developed to investigate the formation of "localized" water channels at the boundary between unsaturated soil and steel sheet piles in a river dike, which is caused by the fluctuation of water level in the river due to rainfall. A seepage test was performed using the experimental apparatus, and the results confirmed that the permeability increased with the penetration of the steel sheet piles. In addition, an analysis of CT images showed an increase or decrease in the pore space in the model ground. Changes in the modeled unsaturated ground was successfully visualized using a X-CT scanner.

Keywords Water channel · Torrential rain · River dike · X-ray CT

H. Mouri
Graduate School of Science and Technology, Kumamoto University, Kumamoto, Japan

T. Sato · J. Otani
Kumamoto University, Kumamoto, Japan

T. Mukunoki (✉)
Faculty of Advanced Science and Technology, Kumamoto University, Kumamoto, Japan
e-mail: mamukunoki@kumamoto-u.ac.jp

1 Introduction

1.1 *Background and Objectives*

River levees are used for not only flood control, but also for flood inundation. In recent years, river floods caused by short duration torrential rains and large typhoons have occurred in Japan. The principle that river dikes must be constructed using only soil is still followed. This is due to the availability of materials, the fact that the structure does not deteriorate, and the ease of restoration if the structure fails. Meanwhile, the entire function of a continuous dike can be lost when a localized weak point causes a breakout. It is generally believed that most dike failures are caused by water overtopping river dikes. Based on soil mechanics, localized weakness is caused by three main factors [1]. The first is the overtopping of the dike, as shown in Fig. 1. The pattern shows dike failure caused by river water overtopping the dike and soil scouring inside the dike when the water level in the river increases due to rainfall, etc. The second type of dike failure is shown in Fig. 2 [2, 3]. This pattern occurs when the river water level increases due to rainfall and an increase in the infiltration surface of the dike, resulting in the fluidization of the soil in the dike. The third is dike failure caused by erosion, as shown in Fig. 3 [4]. This pattern is caused by the scouring of soil on the outer side of the river dike due to repeated increase and decrease of the river water level over many years in addition to abrupt heavy rainfall. Although cross-sectional expansion, drainage, and surface covering methods have been used to strengthen dikes against such weaknesses, dike breaching due to flooding remains rampant.
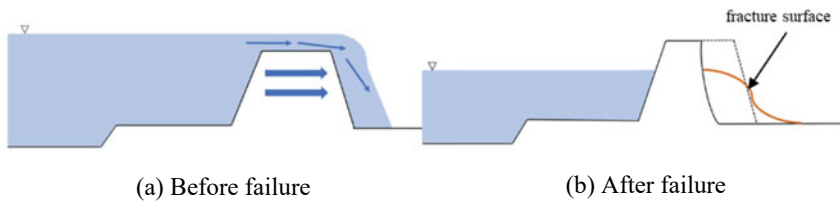

(a) Before failure   (b) After failure

Fig. 1   River dike breakage due to overtopping

(a) Before failure   (b) After failure
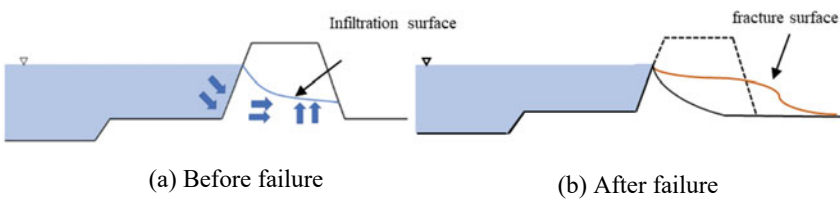
Fig. 2   River dike breakage due to seepage

(a) Before failure   (b) After failure
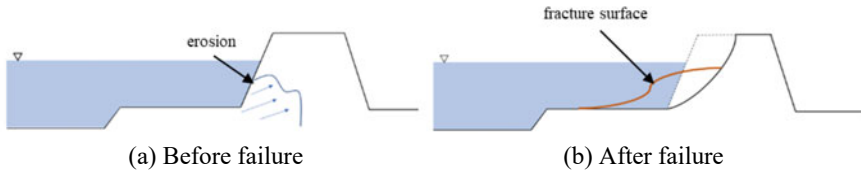
Fig. 3   River dike breakage due to erosion

Several countermeasures using steel sheet piles have been proposed for reinforcing soil structures and have been shown to be highly effective in preventing seepage failure and liquefaction at the model test level. The safety of a dike is enhanced significantly by the continuous construction of steel sheet pile walls to prevent base leakage, seepage, and erosion, as well as to prevent local weaknesses in the soil that may occur due to insufficient geotechnical information. However, questions arise regarding the current dike reinforcement technology using steel sheet piles, including the deterioration of members due to long-term use, the compatibility between the members and the ground inside the dike, which is subject to deformation due to the unequal settlement of the foundation ground caused by an elevated dike, and repair works after a disaster occurs.

The purpose of this study is to address these questions and to propose a steel sheet pile method for strengthening river dikes. As shown in Fig. 4, an experimental apparatus was developed for the case where steel sheet piles are driven into the shoulder of a dike, with emphasis on whether water channels are formed by the repetition of seepage and drainage at the boundary between the unsaturated ground and the steel sheet piles in the dike due to fluctuations in the river water table caused by rainfall. First, we conducted a one-way seepage test to clarify the behavior of the sheet pile boundary when a foreign object such as a steel sheet pile is penetrated into unsaturated soil. Additionally, we used micro-focused X-ray computed tomography (μ-focused X-ray CT hereinafter) scanner to evaluate the possibility that fine grains and air bubbles, which are constituents of soil and water, are involved in the formation of localized water channels, including piping.
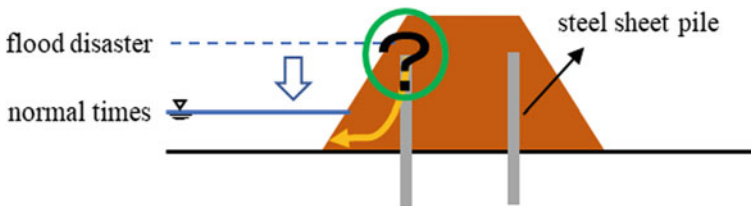

Fig. 4   Questions regarding long-term use of steel sheet pile construction methods

2 Outline of Experiment

2.1 *Development of Experimental Apparatus*

Acrylic soil tanks manufactured using rigid material were used in the preliminary experiments. The soil tanks were placed under an overburden pressure but not under a lateral pressure during the experiment. Because the sides of the tank are fixed surfaces, the behavior of the soil in the ground differs from its actual behavior due to the effect of the side walls. Using μ-focused X-ray CT to clarify soil–water interactions in dikes renders it difficult to conduct experiments where the ground depth is assumed due to the limited size of the soil tanks and the overburden pressure. We developed a model pile penetration–permeation apparatus that can apply pressure isotopically to the model ground without the effects of the side walls of the soil tank and can conduct experiments assuming the ground depth.

The triaxial compression apparatus measures stress based on water placed in a triaxial pressure chamber and an isotropic pressure applied to the specimen from a state in which pressure is applied to the water. By applying a confining pressure to the model ground, the test was conducted under conditions similar to actual conditions, which overcomes the disadvantages of conventional shear and compression tests. We considered the possibility of adapting this mechanism to a model pile penetration–permeability experiment apparatus.

A schematic illustration and photograph of the newly developed model pile penetration–permeability experimental apparatus is shown in Fig. 5. The specimen used for the apparatus was prepared using a rubber sleeve such that the specimen can deform laterally and be isostatically pressurized using air pressure. This allows the effects of the rigid lateral walls of the specimen to be disregarded and model tests with conditions similar to actual ground conditions to be conducted.

3 Model Experiment to Clarify Interaction Between Soil and Steel Sheet Piles

μ-Focused X-Ray CT System

X-ray CT allows the density distribution of a material to be visualized via the absorbing X-ray beam coefficient. In other words, the density changes before and after a mechanical or hydraulic test with erosion can be visualized as digital images. In this study, the μ-focused X-ray CT scanner (XT H 320, Nikon) installed at the Kumamoto University in 2021 was used. Figure 6 shows photographs of the entire scanner and the X-ray shield room. The X-ray CT scanner uses Nikon's unique micro X-ray source to enable high-resolution and high-definition inspections and analyses of large aluminum components and high-density metal components. Furthermore,
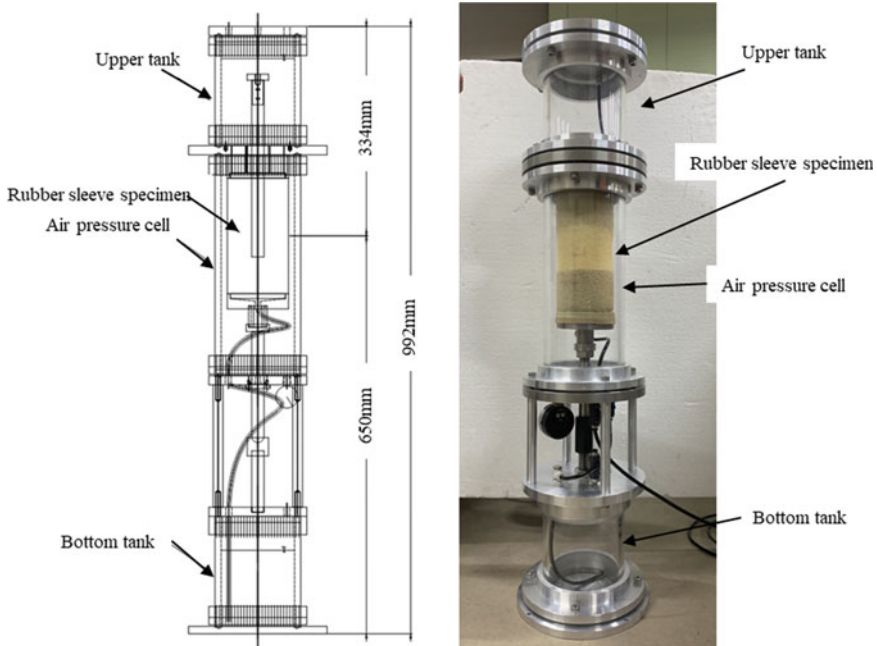
Fig. 5 Specifications of the experimental apparatus
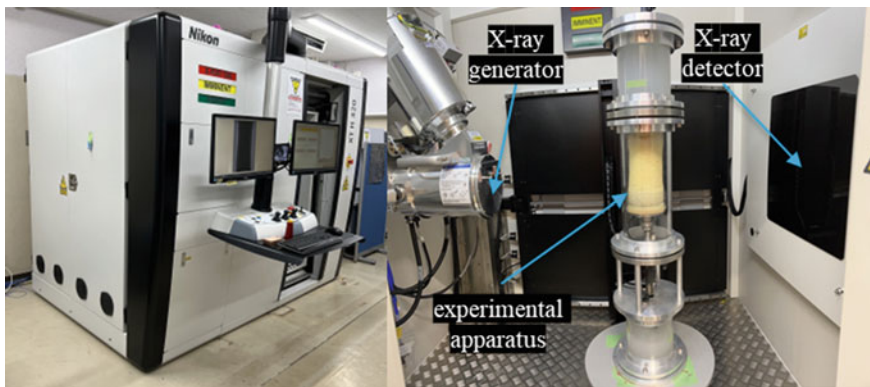
Fig. 6 Photographs of the X-ray CT scanner and shield room

the CT scanner allows noncontact and nondestructive inspections, unlike conventional cutting inspection, thus significantly reducing the inspection cost and time. The specifications of the CT scanner are shown in Table 1. The maximum power was 320 W, the scan area was φ 300 mm, the maximum sample weight was 100 kg, and the detector was a flat panel detector.

Table 1 Specifications of X-ray CT scanner used in current study

	Nikon XTH 320
Maximum voltage	225/320 kV (standard)
Maximum power	225 W (225 kV reflection type)
	225 W (320 kV reflection type)
Imaging area	φ300 mm
Mountable workpiece size	φ300 × H600 mm
Maximum sample weight	100 kg

Experimental Procedures

Figure 7 shows a conceptual diagram and photographs of the newly developed experimental apparatus. We first used Kumamoto silica sand and a mixture of silt and Kumamoto silica sand to learn about the behavior of the ground around sheet piles when foreign objects such as sheet piles are penetrated into unsaturated ground. Kumamoto silica sand sieved with a grain size of 1 to 2 mm was used in the experiment. The fine-grain content of the mixed sand was 10%, which was determined by referring to the literature [2]. The mixed sand was mixed with 5% iron powder by weight as a marker for X-ray CT imaging. Subsequently, image analysis was performed to elucidate seepage flow. The particle parameters of the mixed sand are shown in Table 2, and the grain size distribution graph is shown in Fig. 8.

The following procedures were performed in the experiments.

(1) The specimens were prepared in a dry state using the vibratory method, and the mixed sand layer was sandwiched in between the coarse-grained layers. This allows the movement of fine grains to be visualized when observing the inside of the specimen using X-ray CT by separating the coarse grain and mixed sand layers.

(2) Water with a pore volume (V) of 738.2 cm^3 was flowed in the specimen. This ground condition was defined as the initial state in this study.

(3) Water with a volume of 0.5 V was allowed to percolate vertically upward multiple times until a steady state was achieved based on the measurement of the outflow volume.

(4) The seepage test was terminated at the steady state, i.e., when a constant flow rate was confirmed, and the steel sheet piles were penetrated using an automatic loading device. In this experiment, a U-shaped model steel sheet pile with sides measuring 20 mm and a thickness of 3 mm, as shown in Fig. 9, was used. The penetrating speed was set to 10 mm/min, and the penetration length was 170 mm.

(5) Water with a volume of 0.5 V was infiltrated multiple times from one direction.
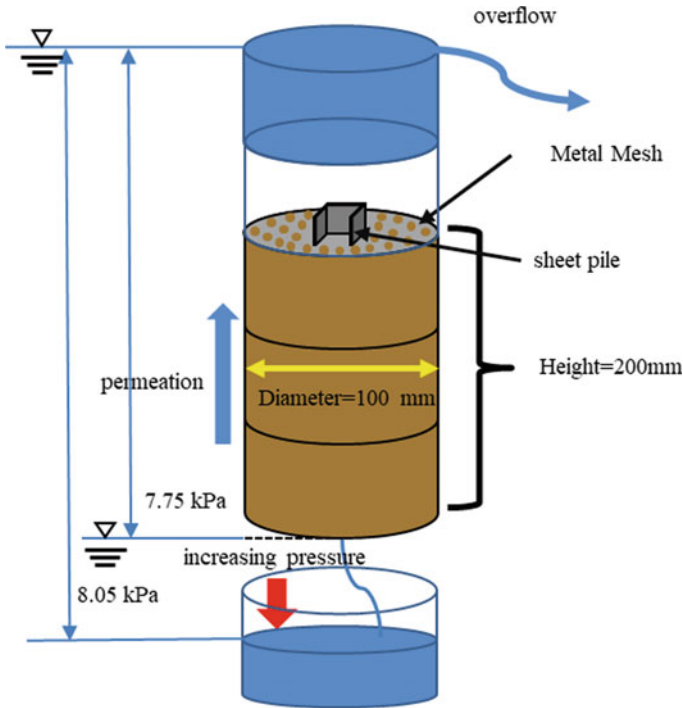
Fig. 7 Conceptual diagram of the experimental apparatus

Table 2 Soil particle parameters

Geotechnical materials	Particle density (t/m^3)	Maximum dry density (t/m^3)	Minimum dry density (t/m^3)
Kumamoto silica and slit	2.630	1.571	1.197
	2.640	1.305	0.944

4 Results and Discussion

4.1 Change in Flow Quantity

Figure 10 shows the change in flow quantity based on the current experiment. The flow quantity was almost twice higher after steel sheet pile penetration as compared with before penetration. This indicates that the penetration of the model sheet pile into the ground may have caused flow localization and formed water channels at the boundary between the member and ground. Herein, flow localization refers to an increase in the pore space due to the dispersion of fine grains, as well as an increase

Fig. 8 Grain size
distribution graph
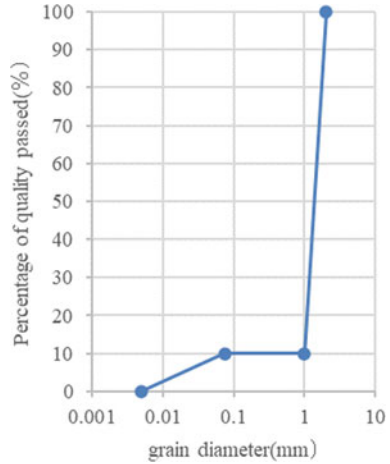
Fig. 9 Sheet pile geometry
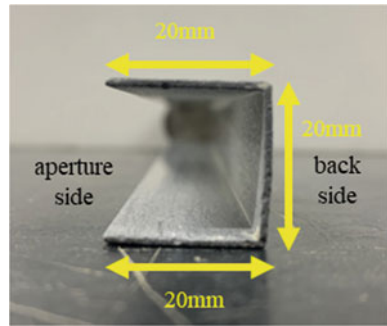
in the area where water can pass through after the penetration of the model sheet pile. However, evaluating this flow localization qualitatively and quantitatively via seepage tests is difficult; therefore, a comparison with CT images must be performed.

5 Evaluation of Specimen Behavior Based on X-Ray CT Images

Figure 10 shows a profile of flow volume at each pore volume. After the penetration of the sheet pile, the flow volume increased significantly. We defined the x- and y-axes as shown in Fig. 11 herein. Figure 12 shows a CT image in the x–z axis plane and Fig. 13 shows its zoomed-in version. The CT image shows no significant change from step A to step B before sheet pile penetration. Meanwhile, from step B to step C, the penetration of the steel sheet pile pulled in the entire ground, thus causing the gap between the sheet pile and unsaturated ground on the aperture side to increase
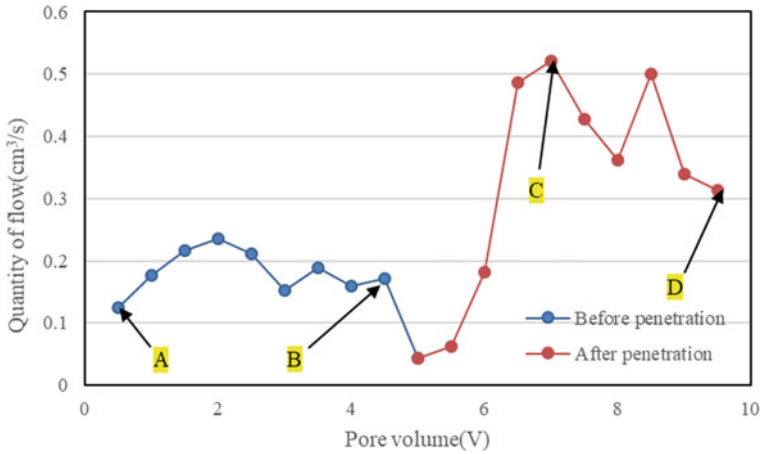
Fig. 10 Change in flow quantity
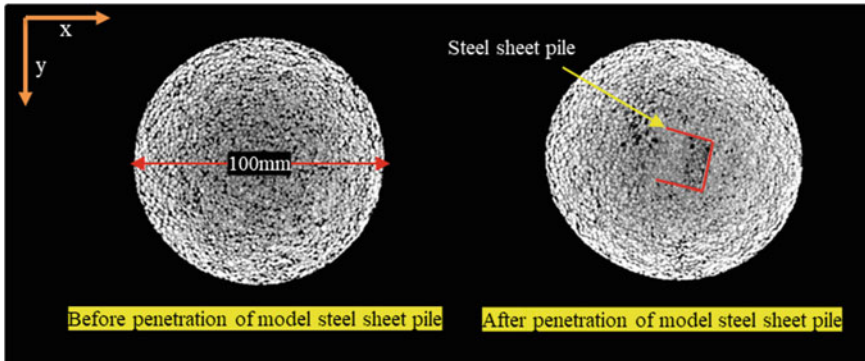
Fig. 11 Definition of x- and y-axes

from step C to step D. This indicates that fine grains may have been transferred from the vicinity of the boundary between the sheet pile and unsaturated ground. A comparison of the CT images from step B to step D shows that the change in the pore structure of the specimen on the aperture side of the steel sheet pile is more significant than that on the back side. However, whether this phenomenon is caused by the shape of the sheet pile must be elucidated.

Figure 14 shows a CT image in the y–z plane and Fig. 15 shows its zoomed-in version. Similar to the image in the x–z plane, no significant pore space change was observed from step A to step B, and the entire ground was pulled in by the penetration of the sheet pile from step B to step C. From step C to step D, the gap in the area surrounded by the steel sheet pile increased.

Fine grains and water or the presence/absence of fine-grain runoff and water channel formation were difficult to distinguish based on the CT images shown in
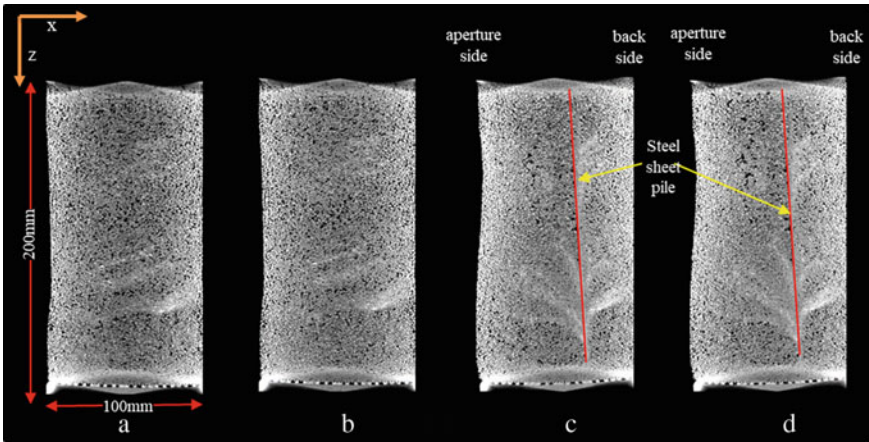
Fig. 12 Cross-sectional CT image in x–z plane
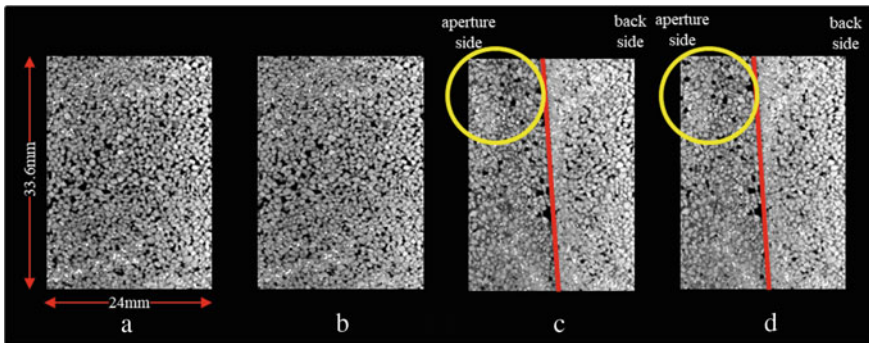
Fig. 13 Zoomed-in CT image in x–z plane
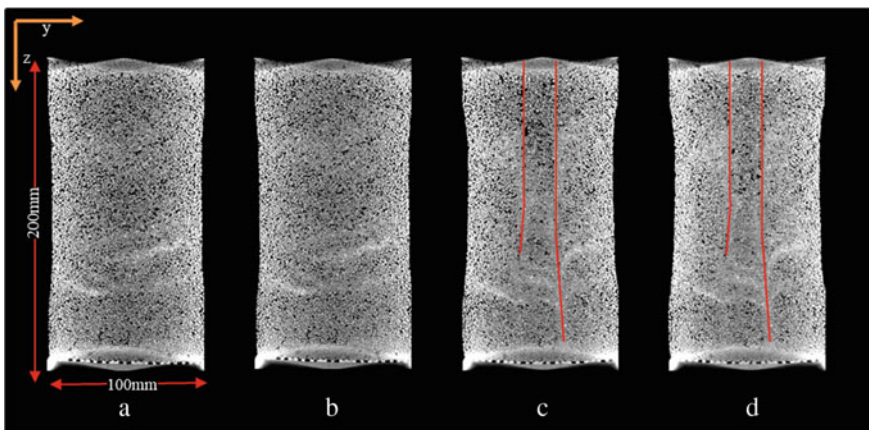
Fig. 14 Cross-sectional CT image in y–z plane
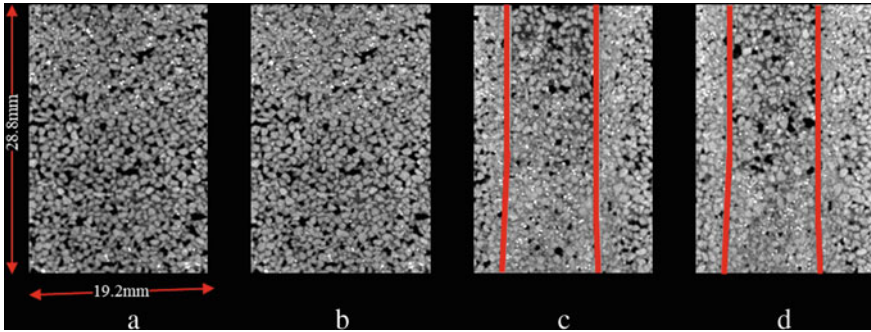
Fig. 15 Zoomed-in CT image in y–z plane

Fig. 15. We plan to investigate the presence or absence of fine-grain outflow and water channel formation via image analysis. The distance between the X-ray irradiation source and the specimen can be reduced such that image analysis can be performed more effectively via multilevel processing.

6 Summary

In this study, an experimental apparatus was developed to investigate the formation of water channels at the boundary between unsaturated soil and steel sheet piles in a river dike, which is caused by the fluctuation of water level in the river due to rainfall. A seepage test was performed using the experimental apparatus, and the results confirmed that the permeability increased with the penetration of the steel sheet piles. In addition, an analysis of CT images showed an increase or decrease in the pore space in the model ground. Changes in the modeled unsaturated ground was successfully visualized using a μ-CT scanner. Future experiments should be conducted under conditions similar to those of the actual site. Additionally, we intend to investigate the effects of the shape of the sheet piles and the number of permeations on the amount of fine-grained runoff and the average permeability.

References

1. Foster M, Fell R, Spannagle M (2000) The statistics of embankment dam failures and accidents. Can Geotech J 37:1000–1024
2. Polemio M, Lollino P (2011) Failure of infrastructure embankments induced by flooding and seepage: a neglected source of hazard. Nat Hazard 11:3383–3396
3. Xiao Q, Wang JP (2020) CFD-DEM simulations of seepage induced erosion. Water
4. Meyer W, Schuster RL, Sabol (1994) Potential for seepage erosion of landslide dam. J Geotech Eng 1211–1229

Socio-Economic and Environmental Aspects in Sustainable Construction

Development of Ground Freezing Method Using Natural Refrigerants and Its Application

Kosuke Maejima, Hiroshi Soma, and Yuta Shioya

Abstract This paper presents a newly developed ground freezing method in Japan. Instead of HCFC or HFCs, it uses NH_3 and CO_2 for freezing; both are natural refrigerants. Thanks to the use of natural refrigerants, the new method (CO_2 freezing method) is not only good for the environment but also more effective in ground freezing than the conventional method. The two fundamental experiments conducted to verify the effectiveness of the ground freezing by natural refrigerants, and the outlines and the results are shown in this paper. Moreover, the application of the CO_2 freezing method is also shown. The application was ground improvement work for shield tunneling at a depth of about 66 m, and the first use of newly developed flat-shaped perforated freezing pipes. Finally, the most recent experiment is introduced. It was a long-distance pumping experiment of CO_2 refrigerant, and its purpose was to expand the scope of application to respond to social demands in Japan for use of a great depth underground. The result proved that CO_2 refrigerant could be circulated in the distance of 1500 m from the plant to the freezing area, instead of about the typical 100 m.

Keywords Artificial ground freezing · Natural refrigerant · Shield tunneling

1 Introduction

Nowadays the tendency to use a great depth underground is increasing in Japan because available public spaces are getting less, especially in urban areas. By a Japanese statute, 'a great depth underground' is defined as 'a depth of 40 m or more below'. At such depth, there is a high risk of groundwater flooding occurring during construction work such as shield tunneling, therefore ground improvement is needed. However, general ground improvement using cement may not be adopted because ground and/or construction conditions are very difficult at such great depths. In such case, a ground freezing method is utilized.

K. Maejima (✉) · H. Soma · Y. Shioya
Chemical Grouting Co., LTD, 2-2-5 Toranomon, Minato-Ku, Tokyo, Japan
e-mail: k-maejima@chemicalgrout.co.jp

The ground freezing method is a technique for freezing the soil and uses two types of refrigerants. The primary refrigerant cools the secondary refrigerant in the plant, and the secondary refrigerant is circulated in the freezing pipes placed in the ground improvement area, then the soil is frozen. The frozen soil cuts off water perfectly and the strength of frozen soil is much higher than that of a soil cement column. Although the ground freezing method seems very useful, the conventional method has a huge problem. It uses CFCs (HCFC) or CFCs alternative (HFCs) as the primary refrigerant (the secondary refrigerant is $CaCl_2$ aqueous solution). HCFC and HFCs are regarded as greenhouse gases; therefore, their use must be avoided.

This paper presents a newly developed ground freezing method (CO_2 freezing method) in Japan, which uses natural refrigerants instead of HCFC or HFCs. It uses NH_3 as the primary refrigerant and CO_2 as the secondary refrigerant with some advantages over the conventional one. The outline of the CO_2 freezing method is shown in Chap. 2. In this paper, some experiments and application are also shown. Chapter 3 shows two fundamental experiments of the CO_2 freezing method, and Chap. 4 shows its application in ground improvement for shield tunneling. Chapter 5 introduces the most recent experiment. To respond to social demands to use a great depth underground, a refrigerant needed to be circulated in longer pipes, and then the experiment conducted to verify its possible use. The result shows that CO_2 refrigerant can be circulated in the distance of 1500 m from the plant to the freezing area, instead of about the typical 100 m.

2 Outline of Ground Freezing Method Using Natural Refrigerants

2.1 Characteristics of the System

The CO_2 freezing method uses NH_3 as the primary refrigerant and CO_2 as the secondary refrigerant; both are natural refrigerants (Table 1). Instead of HCFC or HFCs, using natural refrigerants is not only good for the environment but also more efficient to make the frozen soil. Liquefied CO_2 is circulated in the freezing pipe and deprives the heat of the soil, then a part of CO_2 is gradually vaporized and returned to the refrigerator in a gas–liquid mixed phase (Fig. 1). In other words, while the conventional method uses only the sensible heat of $CaCl_2$ brine for freezing, the CO_2 freezing method uses the latent heat of the vaporization of CO_2 as well as the sensible heat. By using the latent heat, the heat exchange rate per unit flow rate of the CO_2 freezing method increases to 60 times the conventional method.

In addition, the properties of liquefied CO_2 are more suitable for freezing than that of $CaCl_2$. Liquefied CO_2 is cooled to -45 °C by maintaining its pressure about 0.8 MPa in the refrigerator, while $CaCl_2$ aqueous solution is cooled to -30 °C, hence the CO_2 freezing method can make frozen soil more quickly than a conventional one; in short, the ground freezing construction period will be shortened.

Table 1 Comparison of refrigerants between conventional method and CO_2 freezing method

	Conventional method	CO_2 freezing method
Primary refrigerant	HCFC/HFCs	NH_3
Secondary refrigerant	$CaCl_2$ Brine	CO_2

Fig. 1 Schematic diagram of ground freezing method using natural refrigerants
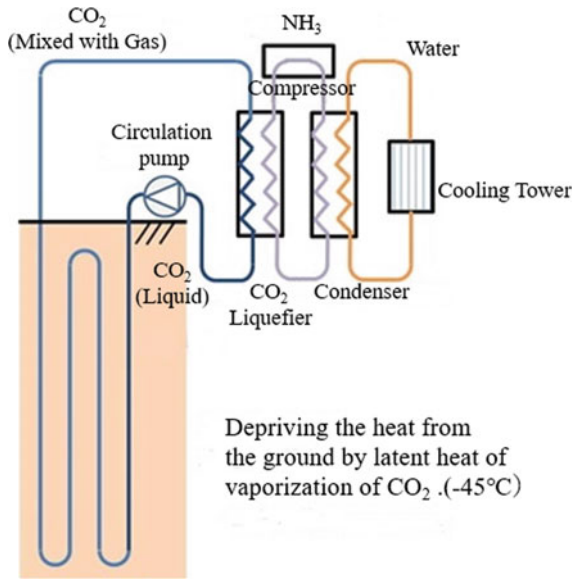
2.2 Equipment

The equipment of the CO_2 freezing method is superior to that of the conventional method. As the kinematic viscosity of liquefied CO_2 is about 1/90 of that of $CaCl_2$ brine, the freezing pipe can be much smaller, and the pumping flow rate can be lower. Figure 2 is a newly developed freezing pipe. It is a flat-shaped perforated pipe made of aluminum, the thickness of which is about 5 mm; therefore, it is easy to install in the ground by human power (Fig. 3). Moreover, it can be made to a designed length, and thus it can be used without welding, while conventional pipes must be welded at construction sites.

As well as the pipe, the refrigerator was also improved (Fig. 4). Since its size is about half that of the conventional one, it can be installed in the shield tunnel and the width is narrow enough not to stop the other construction works. Thanks to this point, the construction period will be shorter still.

In addition, reducing the flow rate leads to decreased power consumption; it is about 60% of the conventional one. For the ground freezing method, its cost greatly depends on the power consumption, hence the CO_2 freezing method will reduce not only the construction period but also the cost.

Fig. 2 Flat-shaped perforated freezing pipe
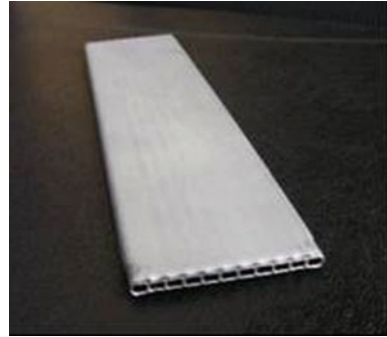
Fig. 3 Installing freezing pipe by human power

Fig. 4 Refrigerator in shield tunnel
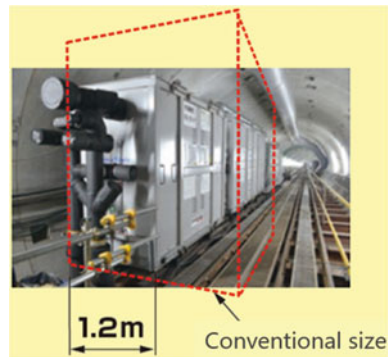
3   Fundamental Experiments

3.1   Small-Scale Soil Tank Experiment

To prove the freezing ability of natural refrigerants, two fundamental experiments were conducted [1]. The outlines and the results of them are discussed below.

The first experiment was a small-scale soil tank experiment, which was conducted in comparison with the conventional method. Table 2 shows the experimental cases, and Fig. 5 shows the schematic diagram. Case 1 was the conventional method, and Case 5 was the totally new method. The simulated soil was saturated sand. To verify the freezing ability of the flat-shaped perforated pipe, there were three types: a double pipe (the conventional method), one flat pipe, or two flat pipes in the guide pipe filled with water (the new methods). Each flow rate depended on the pump's maximum rate. In each case, the period of circulating the refrigerant was 7 days, then the frozen soil was excavated, and its size was measured.

The result is shown in Figs. 6, 7, 8, and the rightmost column of Table 2. The totally new method (Case 5) made the largest frozen soil at the fastest speed. In addition, its power consumption was lower than that of the conventional one (Case 1). Thus, the result validated that the CO_2 freezing method was more efficient than the conventional one.

Table 2 Experimental cases

Case	Freezing pipe	Refrigerant	Refrigerant's temperature (°C)	Flow rate (L/min)	Frozen soil's diameter (the result) (mm)
1	Double pipe	$CaCl_2$	−30	50	810
2	Double pipe	CO_2	−30	10	850
3	One flat pipe	CO_2	−30	1	640
4	Two flat pipes	CO_2	−30	2	700
5	Two flat pipes	CO_2	−45	2	1050

Fig. 5 Schematic diagram of experiment
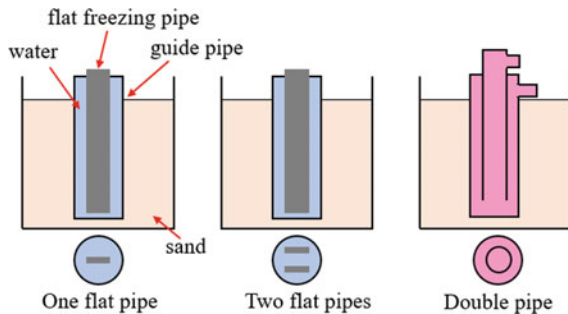
Fig. 6 Excavated frozen soil

Fig. 7 Radius of frozen soil–time relationships (one flat pipe type (case 3) took a long time to fill with water; therefore, the start of circulation was delayed)
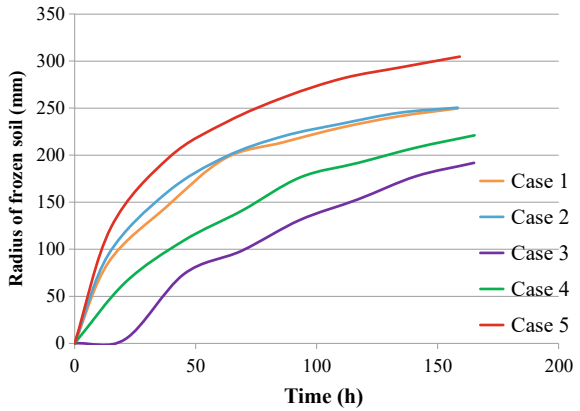
Fig. 8 Accumulated current value–time relationship
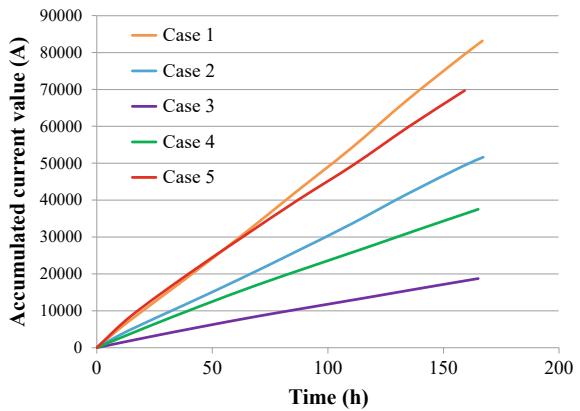
3.2 Simulated Pit Experiment

Following the soil tank experiment, the simulated pit experiment was conducted. It was a full-scale experiment, and its purpose was to test flat freezing pipes with two types of installation: one was two flat pipes in the guide pipe (the center of Fig. 5), and the other was flat pipes attached to the sheet pipe walls (Fig. 9). The latter was expected to be more efficient in ground freezing by using a flat-shaped freezing pipe.

The two types of freezing pipes were placed in the simulated pit ($5 \times 5 \times 5$ m), and then it was filled with saturated sand (Fig. 10). The ground freezing's parameters were determined by the result of the soil tank experiment: CO_2 temperature was -45 °C, and flow rate was 2 L/min. The period of circulation was 28 days, and then the frozen soils were excavated.

Fig. 9 Attached flat pipes on steel sheet pile

Fig. 10 Plan view of the soil tank
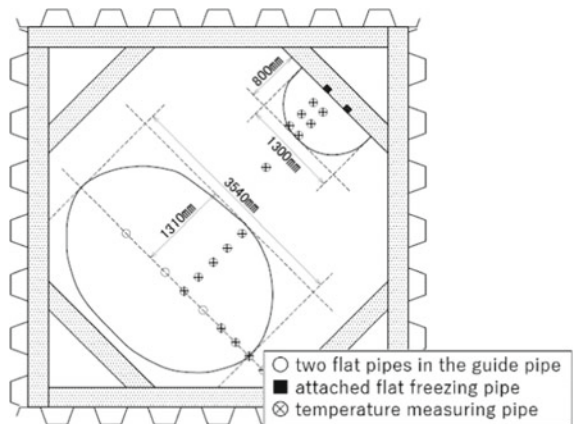
Fig. 11 Excavated frozen soils (left–guide pipe type, right–attached type)

The excavated frozen soils are shown in Fig. 11. The half thickness (radius) of the frozen soil of the guide pipe type was 1.31 m, and that of the attached type was 0.8 m. Both were almost planned sizes, and the result validated that the attached flat freezing pipes could be effective.

4 Application for Shield Tunneling

As a part of the construction of the sewage treatment facility in Japan, the CO_2 freezing method was adopted for ground improvement for shield tunneling to connect the arrival shaft [2]. The construction depth was about 66 m below ground level and the groundwater pressure was very high (about 0.65 MPa), which required not only the shield but also the frozen soil for cutting off water. It was the first work to apply the CO_2 freezing method by the attached flat freezing pipes.

Figure 12 is the schematic diagram of the project. The ground freezing area was divided into three areas; the first and second frozen soils were made at the cross-passage area intersecting the shaft walls to prevent the leakage of groundwater, and the third was made inside the arrival shaft area to prevent the first and second from melting by the following heat input work.

Thanks to the flat shape, it was very easy to attach the freezing pipes to the shield tunnel walls by adhesive; therefore, the preparing work time was much shorter than before (Fig. 13). The period for making frozen soils of the designed sizes was 8 days, and the period of maintaining them was 29 days. With the frozen soil by the attached flat freezing pipes, shield tunneling to the arrival shaft was accomplished.
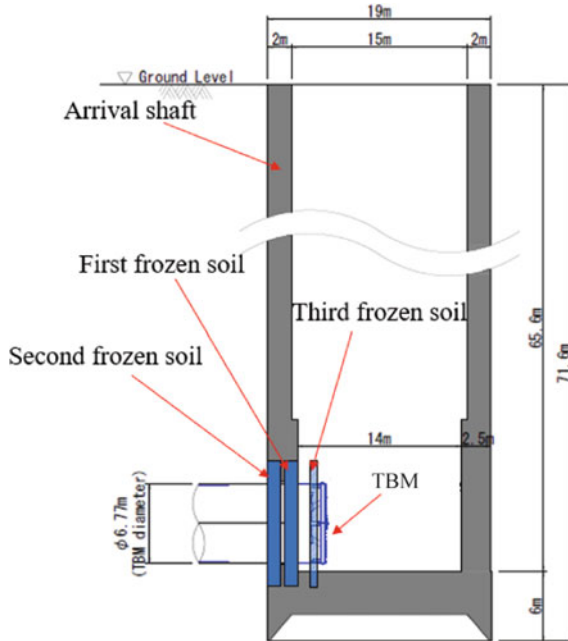
Fig. 12 Schematic diagram of project
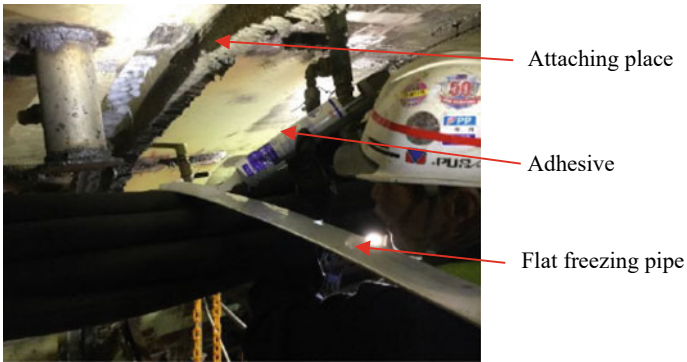
Fig. 13 Attaching flat freezing pipe

5 Long-Distance Pumping Experiment

5.1 Outline of the Experiment

In recent years in Japan, with an increasing number of projects using a great depth underground, construction work is getting more and more difficult; one of the reasons is that existing structures on/under the ground are complexly combined. So that the CO_2 freezing method can be applied to such cases, its pipe length must be much longer to detour the existing structures.

The long-distance pumping experiment was planned to verify the possibility of circulating CO_2 refrigerant in the distance of 1500 m from the plant to the freezing area, instead of about the typical 100 m. Differing from $CaCl_2$ brine, liquefied CO_2 refrigerant is gradually vaporized during pumping; therefore, it had not been circulated in such a long pipe. The pipes were divided into three sections lengthwise: send-pipe, freezing pipe, and return-pipe. Both the send-pipe and return-pipe consisted of main pipes 1450 m long and branch pipes (Fig. 14). They were connected to three types of flat freezing pipes on the ground: case 1–one pipe 50 m long, case 2–one pipe 50 m long, which is bent every 5 m, case 3–connecting 60 pipes 0.8 m long (Figs. 15, 16 and 17).

Fig. 14 Main pipes (two sets of 264 pipes of 5.5 m)

Fig. 15 Placing 50 m long freezing pipe

Fig. 16 Freezing pipe bent every 5 m

Fig. 17 Connecting freezing pipes

Fig. 18 Frosted pipe from each case (left–case 1, center–case 2, right–case 3)

During circulation of CO_2 refrigerant, the pressures in each pipe were measured. Whether CO_2 at a certain temperature is liquid or gas depends on its pressure; liquefied CO_2 at −45 °C vaporizes at the pressure below 0.8 MPa [3]. If the proportion of gas in CO_2 refrigerant becomes large, it cannot be pumped in the pipe, hence the experiment was conducted while controlling CO_2 pressure to be 0.8 MPa.

5.2 Result

In each case, CO_2 refrigerant was successfully circulated at −45 °C in the distance of 1500 m (Fig. 18). The measured pressures were maintained above 0.8 MPa and there was almost no difference between the three cases. This result means that the bends of the pipe or the connecting sockets hardly affected pumping; therefore, when the attached flat freezing pipes are needed for ground freezing, they can be placed in various ways depending on the construction-related conditions: bending, connecting, or a combination.

6 Conclusions

This paper showed the characteristics of the ground freezing method using natural refrigerants (CO_2 freezing method) through the experiments and its application. The CO_2 freezing method do not use HCFC or HFCs as a refrigerant, hence it can be regarded as a technique for a sustainable society. This paper also showed that the CO_2 freezing method is not only good for the environment but also more effective than the conventional method by using natural refrigerants. Moreover, the long-distance pumping experiment proved that this method could circulate CO_2 refrigerant in the distance of 1500 m from the plant to the freezing area, which should expand the scope of application of the method. The method will contribute to the efficiency of construction projects in a great depth underground.

References

1. Soma H, Ariizumi T, Shioya Y (2016) Ground freezing technique using CO_2. In: 26th proceedings of tunnel engineering, JSCE, II-10, pp 1–8. Tokyo (in Japanese)
2. Okazaki T, Matsuura M, Sugiyama J, Suenaga T (2019) Report of a safe and successful shield tunneling which used the freezing method and a receiving room together at great depths and under high water pressure. In: 29th proceedings of tunnel engineering, JSCE, II-4, pp 1–11. Tokyo (in Japanese)
3. Liquefied Carbon Dioxide Handling Textbook (2020) Japan Industrial and Medical Gases Association, Tokyo (in Japanese)

Estimation of Inundation Mitigation Potential Due to Time Variability in Japan

Sora Maruta and Seiki Kawagoe

Abstract Climate change has led to an increase in precipitation and the number of rivers exceeding their flood levels in all regions of Japan. It is pointed out that the amount of precipitation and the frequency of flooding will continue to increase in the future, and there is concern that the number of disasters that cannot be prevented simply by improving river channels will increase. In recent years, basin-based flood control measures have been promoted in Japan to reduce flood damage throughout the entire basin, and estimating the effect of water storage outside the river channel can help in the planning of basin-based flood control measures. In this study, data on off-channel water storage capacity for paddy fields, parks, and school reservoirs were collected on a national scale, and their functions were evaluated. In Fukushima Prefecture, the contribution of internal and external water storage was determined in consideration of future population changes, and priority areas were selected for countermeasures.

Keywords Watershed management · Off-channel storage · Storage effectiveness

1 Introduction

It has been confirmed that the amount of precipitation and the number of rivers exceeding the flood risk level have increased due to climate change [1]. From 1976 to 1985, the average number of annual rainfall events of 50 mm or more per hour was 174, while from 2010 to 2019, the average was 251, an increase of about 1.4 times. This trend is similar for rainfall events of 80 mm or more per hour and 100 mm or more per hour [2]. According to the IPCC Sixth Assessment Report (Intergovernmental Panel on Climate Change AR6), it is unequivocal that human influence has warmed the atmosphere, ocean and land, and extreme events are expected to increase in magnitude and frequency as the warming progresses [3]. In recent years, it has been promoting watershed flood control, in which all stakeholders work together to

S. Maruta · S. Kawagoe (✉)
Fukushima University, Kanayagawa1, Fukushima 960-1296, Japan
e-mail: kawagoe@sss.fukushima-u.ac.jp

prevent flood damage by considering the entire watershed from the catchment area to the inundation zone as a whole in Japan. In 2021, the Law on Basin Flood Control [4] will come into effect, which outlines measures to prevent flooding as much as possible, to reduce the damage target, to mitigate damage, and to quickly restore and reconstruct the area, in addition to strengthening the planning and system for basin flood control. In order to prevent flooding as much as possible, it is important to understand the amount of storage in the river basin in addition to the in-channel flow rate. In a study on off-channel storage, Shimura calculated the storage effect of paddy fields for the whole of Japan, covering an area of 3.17 million m^3 of paddy fields in 1975 [5]. Assuming that all paddy fields in Japan have been maintained and that the waterlogging depth standard for paddy fields is uniformly 0.30 m throughout the country, he showed that the storage capacity is approximately 9 billion m^3. For flood inundation analysis including off-channel storage, Kawaike et al. (2018) conducted a flood inundation simulation in the Nakahama sewage treatment plant in Osaka City, including off-channel storage in residential areas, schools, and parks, and mentioned the calculation of maximum inundation depth and inundation reduction effects [6]. Although there are analyses that calculate storage in paddy fields throughout Japan or that anticipate off-channel storage effects for specific areas, there is no established method for calculating off-channel storage and evaluating its functional for the entire country.

Therefore, in this study, we compiled data on off-channel storage on a national scale and evaluated its function. Based on the data, we attempted to understand the changes in water storage contribution due to demographic changes in Fukushima Prefecture, and to select priority areas for countermeasures.

2 Data and Methods

2.1 Analysis Methods

Three options were selected as the target off-channel storage: paddy fields, parks, and schools. The water storage potentials of these options were determined on a watershed basis, and water storage potential maps were created for the entire country. It was calculated the maximum hourly precipitation over the whole of Japan. Then, it was estimated the hourly precipitation reduction effect due to storage by taking the ratio of the maximum hourly precipitation to the storage potential. In addition, the contribution of internal and external water storage due to climate change and social environmental change was evaluated for Fukushima Prefecture using population data according to socio-economic scenarios.

2.2 Land Structures and Facilities Condition

The concept for estimating paddy storage was based on Shimura [5]. The storage volume was obtained from the area of paddy fields and the depth of waterlogging. Because storage varies depending on the topographical structure, paddy fields were classified into three categories: plain areas, sloping areas, and alluvial fan areas, and the storage volume was calculated after setting the waterlogging depth standard for each. As a general paddy field, the upper width was set to 0.40 m, the lower width to 0.60 m, and the height to 0.30 m, based on the Ministry of Agriculture, Forestry and Fisheries of Japan's Land Improvement Project Planning and Design Standards [7]. The verification by Masumoto [8] also indicates that plain areas serve as a ground that can actively store floodwaters [8]. Therefore, 0.30 m was set as the standard depth of flooding, and 0.27 m was set as the possible storage depth by subtracting 0.03 m of the required depth of flooding for the heading period from the standard depth of flooding of 0.30 m. Here, the heading period refers to the time when 40–50% of the ears have emerged in the ear-forming crop. This is the time of year when they need the most water. In sloping area, the same level of storage as on plain cannot be expected because the water circulation on sloping land is faster than on plain. Hayase et al. [9] conducted an evaluation of the flood prevention and mitigation functions of rice paddy dams in sloping paddy fields and confirmed that the maximum flooding depth was 0.19 m [9]. Onishi et al. [10] evaluated the storage characteristics of paddy fields on sloping terrain based on actual measurements, and found that the waterlogging depths ranged from 0.11 to 0.20 m [10]. Therefore, the sloping area was assumed to have a waterlogging depth standard of 0.10 m, which is lower than that of plain areas. The possible storage height was set at 0.7 m, which was obtained by subtracting the required waterlogging depth of 0.03 m for the heading period. The alluvial fan area is included in the sloping paddy field, but it is not included in the depopulated area, and the paddy fields are actively maintained for paddy cultivation. Thus, it is expected to store more water than the sloping paddy field. Therefore, the waterlogging depth standard was set at 0.20 m, and the possible storage height was set at 0.17 m after subtracting the required waterlogging depth of 0.03 m for the heading period.

How to storage in parks and schools can be classified into two main types: surface storage by excavating the parcel surface, installing impervious walls around the parcel, or raising the wall surface with fill, etc., and installation of underground rainwater harvesting tanks. Because both storage methods involve storage on a single fixed flat surface, they were not classified according to topography, as was the case with paddy fields storage. According to the guidelines of the Japan Rainwater Harvesting and Infiltration Technology Association [11], the possible storage height in a park is 0.30 m. Kawaike et al. [6] calculated the storage area to be 60% of the total area of parks and schoolyards, and the possible storage height to be 0.30 m. Based on these results, the storage area was set to 60% of the total park area and schoolyard area, and the possible storage height was calculated to be 0.30 m.

2.3 Weather Condition

Maximum hourly precipitation for entire Japan was estimated based on data from the Japan Meteorological Agency's AMeDAS database of maximum hourly precipitation and mean temperature (warm season normal, analysis period: 1991–2021) for 871 stations. Regression lines and coefficient of determination values were calculated using the least-squares method (Eqs. 1 and 2).

If the regression line is $y = ax + b$, then

$$a = \frac{\sum_{n=1}^{n}(x_i - \overline{x})(y_i - \overline{y})}{\sum_{n=1}^{n}(x_i - \overline{x})^2} \tag{1}$$

$$b = \overline{y} - a\overline{x} \tag{2}$$

where n: total number of bivariate data (x, y), x_i: warm season mean temperature at each location (analysis period 1991–2021), y_i: maximum hourly precipitation at each location, $\overline{x}$: mean value of warm season mean temperature, $\overline{y}$: maximum hourly precipitation at each location.

By fitting a regression line to the mean temperature of the warm season normal of the 2010 mesh climate values, they were estimated maximum hourly precipitation with a spatial resolution of 1×1 km covering all of Japan, confirming the regional nature of rainfall. Warm season mean temperatures are set from April to November, when the coefficient of determination with maximum hourly precipitation is the highest.

2.4 Population Data According to Socio-Economic Scenarios

In order to understand the effects of climate change in the future, it is common to use scenarios that assume future conditions. Special Report on Emission Scenarios (SRES) has been used in studies on the costs of global greenhouse gas emission reduction measures and the effects of climate change on ecosystems and human society. However, SRES does not reflect the increase in economic power of emerging countries such as China and India because the base year is 1990. Also, it does not explicitly take into account emission reduction measures. In response to these issues, the IPCC Fifth Assessment Report (AR5) developed and adopted the Representative Concentration Pathways scenario (RCPs). It is an emission scenario corresponding to future greenhouse gas concentrations. It is characterized based on the magnitude of the impact of greenhouse gas concentrations on the increase in radiative forcing, with four scenarios: RCP8.5, RCP6.0, RCP4.5, and RCP2.6. It is pointed that climate change impacts vary with population and socio-economic changes in addition to those due to greenhouse gas concentrations considered in the RCPs scenarios. The IPCC AR6 adopts a scenario that combines the RCPs scenario used in the AR5 and the

Shared Socio-Economic Pathways scenario (SSPs), which assumes future trends in socio-economic development. The SSPs scenarios divide the world into five regions, and five scenarios, SSP1 to SSP5. These scenarios are set according to the two axes of difficulty of climate change mitigation measures and adaptation measures.

Since this study is conducted in Japan, it is used the Japanese SSPs scenario in this study, which is a downscaled version of the global SSPs scenario developed in the IPCC AR6. The Japanese SSPs is consistent with the global SSPs and is based on the description by O'Neill et al. [12] in the global SSPs scenario. We selected SSP1 (sustainable) for RCP2.6 and SSP5 (fossil fuel dependent) for RCP8.5, following the highest priority key scenarios of O'Neill et al. [12]. We used population data based on the Japanese SSPs narrative scenario developed from the procedure of Chen et al. [13]. In order to determine only the effects of climate change, we set a status quo fixed scenario in which the current social conditions are assumed to continue until the year 2100. In this study, the year 2015 was used as the base year. It was classified into three periods; 2050 (base year), 2050, and 2100.

3 Results

3.1 Storage Potential Map

The nationwide storage volume was about 3.68 billion m^3 for paddy fields, 340 million m^3 for parks, and 0.55 billion m^3 for schools. In the case of paddy fields storage, the estimated volume was 9 billion m^3 in Shimura [5], but in this study it was about 3.68 billion m^3 nationwide, a significant decrease of about 5 billion m^3 (Fig. 1a). There are many areas where the storage volume exceeds 10,000 m^3, with the western Hokkaido, Tohoku, Kanto, and Hokuriku regions in particular having high potential. On the other hand, the eastern part of Hokkaido and the Seto Inland Sea side of the Chugoku region had low potential. The total storage capacity of the park was about 340 million m^3, which is small compared to paddy field storage due to its area (Fig. 1b). However, in metropolitan areas such as the Tokyo, Chukyo, and Kansai areas, the storage volume was expected to exceed 10,000 m^3. The storage volume in schools was found to be about 0.5 billion m^3, which is not as large as that of paddy fields and parks (Fig. 1c), but in the Tokyo metropolitan area, the storage volume was over 10,000 m^3, and the storage volume was uniform throughout the country. The areas with large total storage capacity (i.e., paddy fields, parks, and schools) were generally located in the northern part of Japan, with storage exceeding 1 million m^3, especially in western Hokkaido, Tohoku, Hokuriku, and Kanto regions. On the other hand, the areas with low storage potential were located on the Seto Inland Sea side of Chugoku region (Fig. 1d). The temporal resolution was added to the total storage potential map to obtain the spatiotemporal storage effect, and it was found that the storage effect by off-channel storage is high in western Hokkaido, Tohoku,
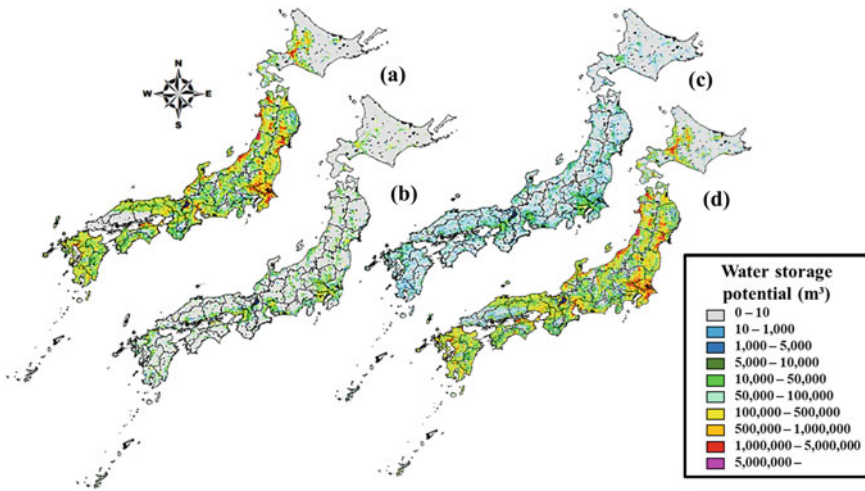
Fig. 1 Spatially located potential map (m^3). **a** represents the paddy storage, **b** the park storage, **c** the school storage, and **d** the total storage potential

Hokuriku, and Kanto regions, while the effect is not so great in the Inland Sea side of Chugoku region (Fig. 2).

3.2 Analysis Results for Fukushima Prefecture

In Fukushima Prefecture, we attempted to identify priority areas for countermeasures based on the total reservoir volume and social changes in population. Figure 3 shows the distribution of total storage volume in Fukushima.

As of 2015, 33.9% of the watersheds had no population, while the remaining 66.1% of the watersheds had a population of approximately 1.7 million. In terms of population trends over time, the proportion of watersheds with no population did not change for both SSP1 and SSP5. Basically, it is indicated that watersheds with a population distribution as of 2015 tended to increase or decrease in population. Therefore, it was not possible to determine the contribution of water storage that changes depending on the unpopulated area. The basin population in Fukushima Prefecture showed a decreasing trend in both SSP1 and SSP5, but there was almost no difference in the basin population among the social change scenarios.

When the society is under SSP1, the total population of Fukushima Prefecture in 2015 will decrease from about 1.7 million to about 1.1 million in 2050 and to about 440,000 in 2100 (Fig. 4a). When the population in 2015 is set as 100%, the population of SSP1 will decrease to 64.2% of the total population in 2050 and to 25.7% in 2100 (Fig. 5a). Based on these population decline rates, off-channel storage in areas where the population decline rate is less than 35.8% in 2050, i.e., where the
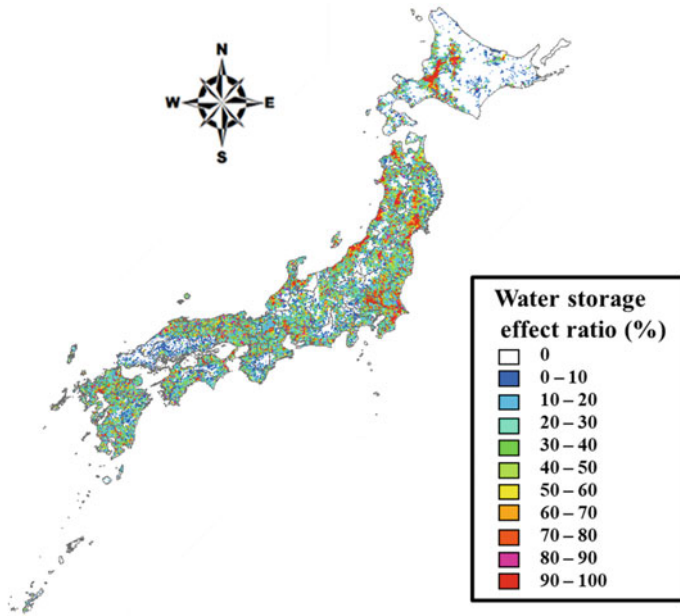
Fig. 2 Distribution of water storage effect ratio
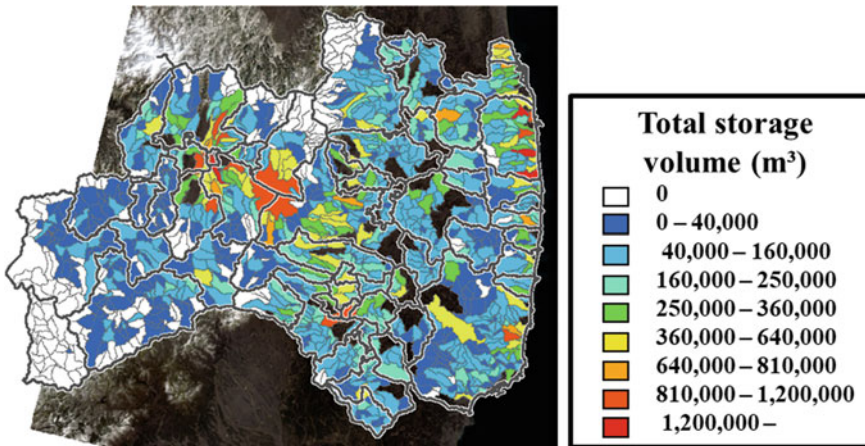
Fig. 3 Total storage volume in Fukushima prefecture (m³)

population decline is relatively small, is expected to contribute to water storage to mitigate damage from internal flooding. On the other hand, off-channel storage in watersheds with a high rate of population decline or no population contributes to water storage for reducing external water. Similarly, it can be considered when the society transitions in SSP5.
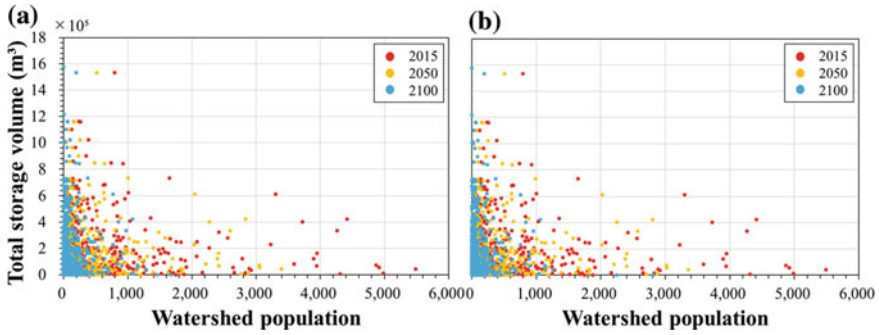
Fig. 4 Relationship between basin population and total storage (m^3) at each SSP in each year. The dots represent each basin, with the SSP1 in **a** and the SSP5 in **b**
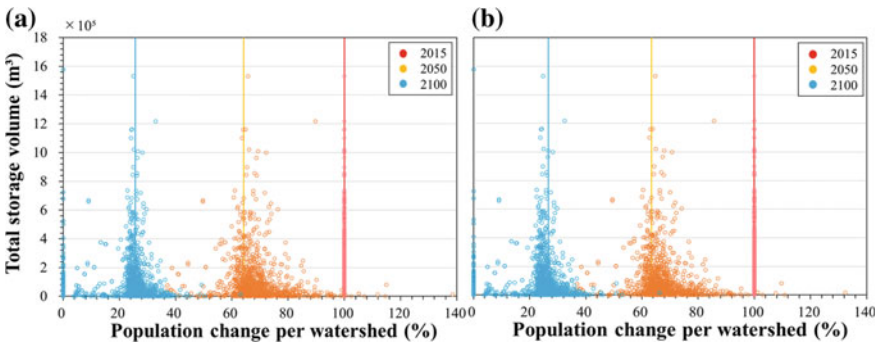
Fig. 5 Relationship between the rate of change of the basin population (%) and the total storage (m^3). ○ represents each watershed, with **a** the SSP1 and **b** the SSP5

In SSP1 and SSP5, there are some areas where the population increases in 2050. Although the population decreases in all watersheds in 2100, these watersheds are likely to have a significant investment effect on the storage options.

4 Consideration

It was determined the amount and distribution of off-channel storage for paddy fields storage, park storage, and school storage throughout Japan by developing a database of off-channel storage on a national scale. By fitting maximum hourly precipitation, into total storage potential, we were also able to determine the effect of reducing hourly precipitation throughout Japan. In the case of paddy field storage, Shimura's estimate of 9 billion m^3 of storage [5] was significantly reduced to approximately 3.68 billion m^3 in this study. This is due to the decrease in the area of paddy fields in

Japan. Comparing the area of paddy fields in 1975 used by Shimura (1982) with the area of paddy fields in 2016 used in this study, the area decreased by approximately 600,000 ha. Shimura (1982) used a uniform nationwide waterlogging depth standard of 0.30 m. In this study, paddy fields were divided into plain areas, sloping areas, and alluvial fan areas, and waterlogging depths were set at 0.30, 0.10, and 0.20 m. For these reasons, we consider that the estimation was significantly reduced. Paddy field storage is the largest off-channel storage potential of the three storage options considered in this study, and is expected to be effective in many watersheds if implemented in society.

In areas with low storage effectiveness, it is required development of other storage options and measures to increase the storage effectiveness of paddy fields, parks, and schools. In order to do so, it is necessary to understand the land structures that can be used as off-channel storage options in the area and to establish the conditions for such options. In addition, it is possible to increase the depth of waterlogging in parks and schools depending on their development.

The priority areas for off-channel storage in Fukushima Prefecture are watersheds where the population will temporarily increase in 2050 for both SSP1 and SSP5. However, since the storage capacity of these watersheds is almost nonexistent at present, it is necessary to strengthen measures for off-channel storage. In this case, it is necessary to take into account the decrease in population in 2100.

5 Conclusions

In this study, we developed data on the intrinsic water storage capacity outside the river channel of a national scale, which can be used for basin flood control planning, and evaluated the function of this capacity. Based on the data, priority areas were selected in Fukushima Prefecture. The results are as follows:

(1) We selected three off-channel storage options (paddy, park, and school), and determined each potential. We also estimated the hourly precipitation reduction effect due to storage.

(2) The storage potential of paddy fields storage is about 3.68 billion m^3 nationwide, and it is the most effective storage method for off-channel storage.

(3) The storage potential of parks and schools was not as large as that of paddy fields, but these have the effectiveness in metropolitan areas such as the Tokyo, Chukyo, and Kansai areas.

(4) Spatial off-channel storage was effective in the western Hokkaido, Tohoku, Hokuriku, and Kanto regions, where the total storage volume was large, consistent with watersheds with high storage effectiveness.

(5) It was found that the areas where off-channel storage is vulnerable and where the consideration of countermeasures is prioritized are on the Seto Inland Sea side of the Chugoku region. In particular, Hiroshima and Yamaguchi prefectures were the priority areas for watershed flood control.

(6) In Fukushima Prefecture, there are watersheds where the population of both SSP1 and SSP5 will increase in 2050. However, since the population will decrease in all watersheds by 2100, it is necessary to develop countermeasures that take future operations into consideration.

In the future, in areas where off-channel storage effectiveness is insufficient, it will be necessary to examine and verify the effectiveness of storage options other than the three targeted in this study. In addition, the potential map created does not take the discharge process into account, which may result in an underestimation of the storage effect. Therefore, it is necessary to examine the storage effect by adding drainage processes such as drainage ditches and sewage systems in paddy fields. Furthermore, it is necessary to consider adaptation measures to climate change by adding climatic conditions throughout Japan.

References

1. Ministry of Land, Infrastructure, Transport and Tourism (2018) Study group on flood control functions of dams for more frequent extreme heavy rainfall events
2. Ministry of Land, Infrastructure, Transport and Tourism (2018) Toward the flood control functions of dams and the enhancement of information in preparing for the frequent occurrence of extremely heavy rainfall—Recommendations of the study group on the flood control functions of dams in preparing for the frequent occurrence of extremely heavy rainfall—Reference Material
3. Ministry of Education, Culture, Sports, Science and Technology, Japan Meteorological Agency (2022) Report of working group I of the IPCC sixth assessment report summary for policymaker
4. Ministry of Land, Infrastructure, Transport and Tourism (2021) Act for partial revision of measures for flood damage of specified urban rivers (Act No. 31, 2021)
5. Shimura H (1982) Evaluation of flood control function of paddy fields and paddy fields. J Agricult Civil Eng Soc 50(1):25–29
6. Kawaike K, Nakagawa H (2018) Mitigation Effects of On-site storage facilities on pluvial inundation in highly urbanized area. J Japan Soc Civil Eng Ser B1 (Hydraulic Engineering) 74(4):1537–1542
7. Ministry of Agriculture, Forestry and Fisheries (2013) Land improvement project planning and design standards and operation and explanation plan "rice field development (Paddy Field)" draft
8. Masumoto T (1998) Paradigm shift in the evaluation of water storage function of paddies and in watershed management. J Hydrol Water Resour 11(7):711–722
9. Hayase Y (1994) Evaluation of paddy field's functions for flood control and a proposal of their enhancing project. Transact Japanese Soc Irrigat Drain Reclam Eng 62(10):943–948
10. Onishi T, Horino H, Mitsuno T (2004) A case study on storage property of terraced paddy fields. Transact Japanese Soc Irrigat Drain Rural Eng 230:53–59
11. Association for Rainwater Storage and Infiltration Technology (2009) Addendum to the technical guidelines for watershed storage facilities, etc. (Draft)

12. O'Neill BC, Kriegler E, Ebi KL, Kemp-Benedict E, Riahi K, Rothman DS, van Ruijven BJ, van Vuuren DP, Birkmann J, Kok K, Levy M, Solecki W (2015) The roads ahead: narratives for shared socioeconomic pathways describing world futures in the 21st century. Global Environ Change
13. Chen H, Matsuhashi K, Takahashi K, Fujimori S, Honjo K, Gomi K (2020) Adapting global shared socio-economic pathways for national scenarios in Japan. Sustain Sci 1–16

Evaluation of the Erosion Control Performance and Vegetation of Natural Vegetation Recovery Promotion-Type Mat Incorporated with Soil Algae (BSC Mat)

Nobuyuki Kohno ⬛, **Aki Matsumoto, Mineto Tomisaka, Tetsushi Ozeki, and Kohei Araki** ⬛

Abstract In this study, we evaluated the erosion control performance and vegetation of natural vegetation recovery promotion-type mat incorporated with soil algae (BSC mat). The tests were conducted by applying rainfall of 50, 100, and 150 mm/h to the slope for 30 min, respectively, and evaluating the ratio of soil loss in the unprotected soil to that in the soil covered by it (soil loss ratio: SLR). The results showed that the SLR was 192, indicating that it had a higher erosion prevention function compared to the unprotected soil. In addition, we observed the vegetation by natural invasion and measured soil loss on an outdoor embankment slope in the field test. The number of invasive plants in the mat was about 2.5 times higher than that in the unprotected slope, and the plants were established evenly in the whole area, unlike the unprotected slope where vegetation was found only in the eroded area. The amount of soil loss in the BSC mat plots was less than 1/4500. It was indicated that the mat formed vegetation faster and better than the unprotected soil, and that the amount of soil loss was also suppressed.

Keywords Erosion control · Soil loss · Natural vegetation recovery promotion

N. Kohno (✉) · A. Matsumoto
 Research and Development Division in Sales Department, Takino Filter Inc., 904-16 Hayama 2 Chome, Kudamatsu-Shi, Yamaguchi 744-0061, Japan
e-mail: kouno@takino.co.jp

M. Tomisaka
Okinawa Branch Office, Engineering Department, Nippon Koei Co., Ltd., Kohtoku Building 2F, 3-5-1, Tsubogawa, Naha-Shi, Okinawa 900-0025, Japan

T. Ozeki
Environment Department, Nippon Koei Co., Ltd., 5-4, Kojimachi, Chiyoda-Ku, Tokyo 102-8539, Japan

K. Araki
Department of Civil Engineering and Architecture, National Institute of Technology, Tokuyama College, Gakuendai, Shunan-Shi, Yamaguchi 745-8585, Japan

1 Introduction

In recent years, landslides have become more frequent and severe due to climate change and other factors. To prevent such landslides, concrete shotcrete, structures such as slope frame work, and vegetation are commonly used to protect slopes. Vegetation is effective as a countermeasure against global warming because it can be expected to absorb and fix CO_2 through the use of plants such as trees. In the field of revegetation, there is an increasing demand for the use of plants that are native to the region, especially local strains (a group of native species that share a common genotype in a certain region), in consideration of the conservation of biodiversity and local ecosystems [1]. In this background, attention is being paid to natural invasion promotion methods for revegetation through the establishment of seeds that naturally fly to the area. The "BSC method" has been developed to make a biological soil crust (BSC) with cyanobacteria, green algae, filamentous fungi, lichens, and bryophytes form, which appear at the beginning of vegetation succession, and promote natural invasion by applying soil algae along with fertilizers to the bare ground surface [2]. The soil algae used in the BSC method are not classified as non-native species because they are globally distributed, do not interbreed with native species due to asexual reproduction, and thus are considered to have no impact on the natural environment [2]. In Okinawa Prefecture, the BSC method was found to be effective in preventing red soil runoff [3]. The effectiveness of the BSC method has also been confirmed not only in Japan but also in overseas countries such as Nepal. However, the BSC method is basically applied under environmental conditions (ground environment, water environment, weather conditions, etc.) in which ordinary revegetation work can be applied, but because it takes time for the BSC to form after application, there was a problem that the materials sprayed by heavy rainfall and the other events are run off. To solve this problem, the "BSC mat" was developed by incorporating soil algae into the erosion control mat. This is the mat that promotes natural invasion by utilizing the advantages of both materials. In this paper, both the field test and the small-scale rainfall test according to ASTM standard were conducted to investigate the slope protection effect by BSC mat.

2 Field Test

2.1 Test Method

A 7 m long embankment with a slope of 30° was constructed on a southwest-facing slope at the site of National Institute of Technology, Tokuyama College in Shunan-shi, Yamaguchi, using the decomposed granite soil. Table 1 shows the physical properties of the soil used. Wooden boards were placed at 90 cm intervals on the soil to create a total of six plots. The test began on May 28, 2021, with unprotected soil as the control plot and two plots each of erosion control mat A and BSC mat as the test plot.

Table 1 Physical properties of soil

Soil particle density	ρ_s	g/cm³	2.648
Maximum dry density	ρ_{max}	g/cm³	2.002
Optimum moisture content	w_{opt}	%	6.1
Mean particle size	D_{50}	mm	1.1
Uniformity coefficient	U_c	–	21.4
Initial void ratio	e_o	–	0.448

Picture 1 shows the installation of the test mats, and Fig. 1 shows the structure of the test mats. The erosion control mat A and BSC mat are composed of polyethylene netting and polyester non-woven fabric. The thickness of both mats is approximately 10 mm. Natural vegetation was observed on the left side of the test plot, while the right side was cured with blue sheets, and no natural vegetation was observed. Containers were placed at the lower end of each plot to measure the amount of sediment that is flowed out due to rainfall. The growth of soil algae and natural vegetation invading from the surrounding area were also investigated.
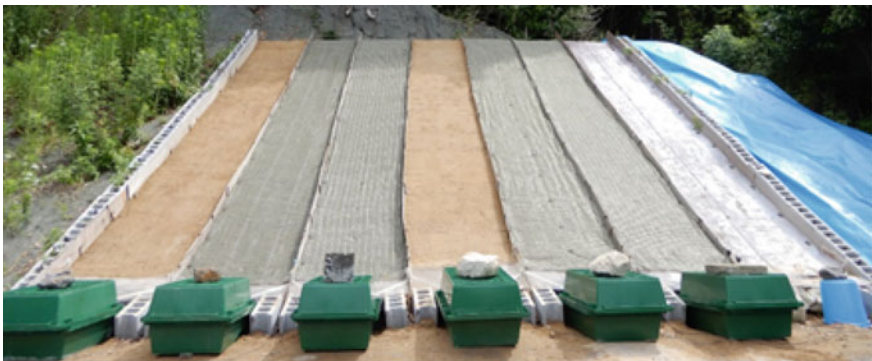
| Unprotected soil_1 | Erosion control mat A_1 | BSC mat_1 | Unprotected soil_2 | Erosion control mat A_2 | BSC mat_2 |

Picture 1 Installation status of test products

a) Erosion control mat   b) BSC mat
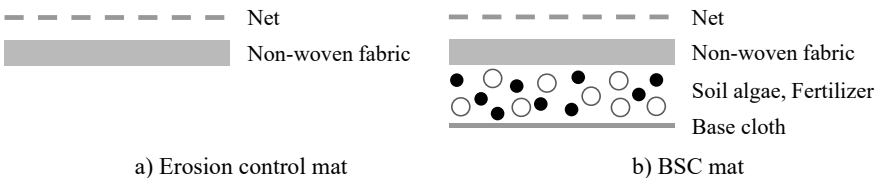
Fig. 1 Structure of test products

2.2 Test Result

Erosion control. Rainfall on June 3–4, six days after start of the test, caused the collapse of unprotected soil_1. Rainfall began around noon on June 3 and intensified during the night, peaking at 32.0 mm per hour at 3:00 a.m. on June 4 and continuing until early afternoon. The accumulated rainfall from the beginning of the rainfall was 137.5 mm. The collapse of bare ground_1 occurred at 2:04 a.m. on the 4th. The collapse of bare ground_1 occurred from the center of the slope, and the amount of sediment flowed out exceeded 18 kg. On the other hand, no slope deformation was observed in the test site. The average sediment discharge was only 31.6 and 1.4 g for the erosion control mat A and BSC mat, respectively, supporting the high erosion control effectiveness of the mats immediately after installation. Unprotected soil_2 collapsed due to the heavy rainfall from July 7 to 9, when the total rainfall was 162.9 mm over the three days. About 9 kg of soil was discharged from unprotected soil_2 at 18:00 on July 7, and unprotected soil_2 was considered to have collapsed at this point. Figure 2 shows the amount of sediment discharged from the control and test areas. Unprotected soil_1 shows the amount of sediment discharged until June 4, when it collapsed. The slope condition is shown in Picture 2. Compared to the collapsed unprotected soil, the erosion control mat A and BSC mats in the test area showed no significant deformation, and the amount of sediment discharge was small. In particular, the average sediment discharge of the BSC mat was less than 1/4500 of the unprotected soil average, confirming its high erosion prevention effect.

Vegetation. Figure 3 shows the vegetation coverage during the five-month period. The number and species of invasive plants in the control and test areas were surveyed in early November, five months after installation. The slope conditions during the first five months after installation are shown in Fig. 3, the number of invasive plants in Fig. 4, and the number of plant species in Fig. 5, respectively. As shown in Picture 3, almost no vegetation was observed until two months after installation, and the number of plants gradually increased from three months after installation. The vegetation coverage of the BSC mats at 5 months after installation was relatively higher than that of the unprotected soil and erosion control mat A (Fig. 3, Picture 3). In particular, the vegetation coverage of the BSC mats increased from September to October, although the fact that the precipitation in October was very low (0.7 mm), making it difficult for vegetation from the surrounding area to invade and grow. The number of invasive plants was about 2.5 times greater than that of unprotected soil, and woody plants (mallotus bark) were the only species found in the test area on BSC mat_1. It is confirmed that plants native to the area surrounding the test slope had invaded the BSC mats, and that natural vegetation had been established. The reason for the large number of invasive plant species in unprotected soil_1 may be due to the invasion from the slope on the left side of the slope. The vegetation in the unprotected soil is biased toward areas where the slope has become loose and soil hardness has decreased, such as soil failure scars, whereas the vegetation in the BSC mats showed relatively unbiased plant establishment throughout the entire area. Although the evaluation method [4] for the natural vegetation recovery method defines the
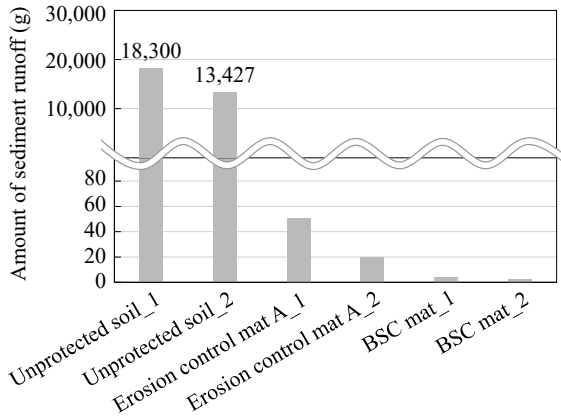
Fig. 2 Amount of runoff sediment

| Unprotected soil_1 | Erosion control mat A_1 | BSC mat_1 | Unprotected soil_2 | Erosion control mat A_2 | BSC mat_2 |

Picture 2 Collapsed state (July 7, 2021)

evaluation at six months after construction, the evaluation was conducted at five months after installation because rainfall is scarce after November and plant invasion also decreases due to lower temperatures.

BSC formation. Observation of the BSC mats at 17 days after the start of the test showed that soil algae (green algae) had grown widely on the non-woven fabric, and the mats were generally green in color. When the BSC mat was turned over and the back of the mat was observed after five months, it was confirmed that soil algae were distributed over the entire area, although the concentration was different. Microscopic observation of soil samples taken from the back of the BSC mats showed that the soil particles were covered by soil algae. This situation was not observed in the unprotected soil and erosion control mat A. It was considered that BSC formation by soil algae had progressed in the BSC mat test area.
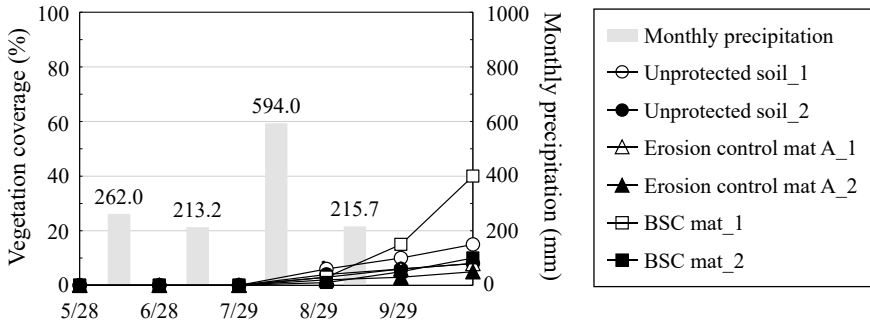
Fig. 3 Vegetation coverage

3 Bench-Scale Rainfall Test

3.1 Test Method

In this paper, bench-scale rainfall tests were conducted in accordance with the American Society for Testing and Materials (ASTM) standards, which are developed and published by ASTM International (formerly known as the American Society for Testing and Materials), an American standards organization. Although ASTM standards are voluntary, they are widely accepted internationally and are used as standards for regulations in many countries around the world. Based on the bench-scale rainfall test (ASTM D7101) in the ASTM standard, the modified rainfall test apparatus of National Institute of Technology, Tokuyama College, was used.

The tests were conducted with rainfall intensities of 50, 100, and 150 mm/h applied to the slopes every 30 min and evaluated by the ratio of soil loss in the control area (unprotected soil) to soil loss in the test area (covered with erosion control material), that is soil loss ratio (SLR). Tests were conducted on unprotected soil (control plot) and on erosion control mats B and C and BSC mats (test plots). The erosion control mats B and C have the same structure as erosion control mat A shown in Fig. 1 and are composed of a polyethylene net and a non-woven fabric made of polyester fiber. The thickness of both mats is approximately 4–7 mm. The soil used in the test were the same as those used in the field test. An outline of the test apparatus is shown in Fig. 6. The ASTM D7101 test apparatus has three lanes, and three soil cores are placed in one rainfall event, but the used test apparatus has two lanes and two soil cores are placed. Therefore, the test is repeated two times for one rainfall event, that is, four soil cores are used in one rainfall event. The test procedure was as follows.

Soil with an optimum moisture content of $\pm 2\%$ was compacted into a soil core at a degree of compaction Dc = $90 \pm 3\%$. The test apparatus with two soil cores was set up on a 3:1 (horizontal: vertical) slope (18.43°). The control plot (unprotected soil) was subjected to a rainfall intensity of 50 mm/h, and runoff water was collected for 5 min in the collection buckets placed at the end of each slope. This process was

| Unprotected soil_1 | Erosion control mat A_1 | BSC mat_1 | Unprotected soil_2 | Erosion control mat A_2 | BSC mat_2 |

Picture 3 Slope states after 5 months

Fig. 4 Number of invasive plants
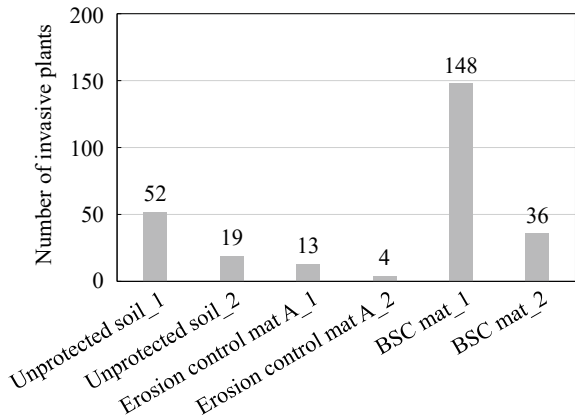
Fig. 5 Number of plant species
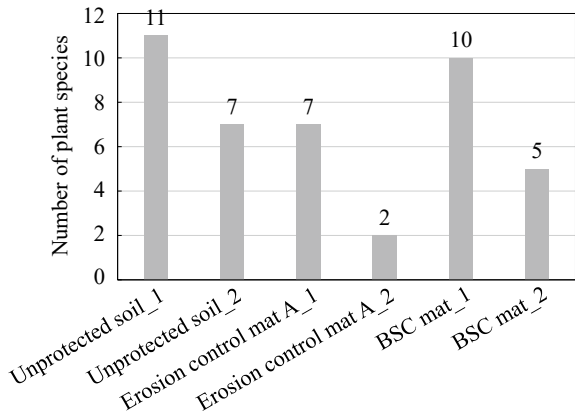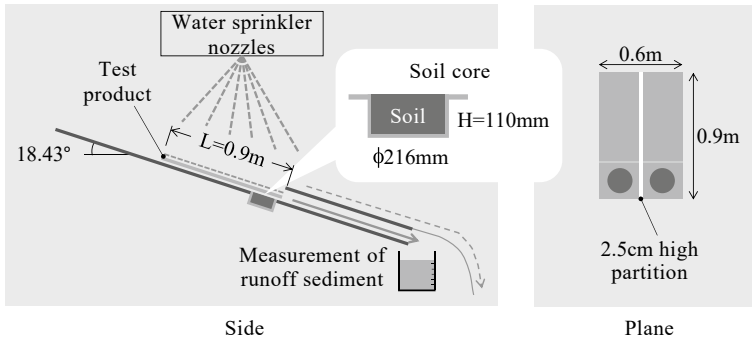
Fig. 6 Schematic diagram of test apparatus

a) Unprotected soil   b) BSC mat
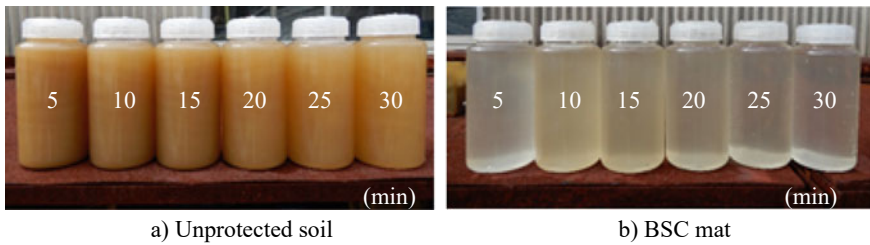
Picture 4 Appearance of runoff water at 100 mm/h

repeated until 30 min, so that six runoff water samples were collected for one lane. A series of operations was conducted twice. Rainfall intensities of 100 and 150 mm/h were applied in the same way. The collected runoff water samples in the collection buckets were settled over night, the supernatants were discharged, dried with dry oven, and the total sediment runoff mass (average cumulative sediment runoff mass) was calculated. The test areas were set up under the following conditions. Erosion control mats B and C: After the soil cores were placed, erosion control mats B and C were laid over the whole lanes. BSC mats: The soil cores, on which the BSC mats had been placed, were placed in the outdoor greenhouse for 4 weeks to allow the formation of crusts in the soil cores. The soil cores, on which the crusts had been formed, were placed, and then the BSC mats were laid over the whole lanes. The rainfall tests for test plots were conducted by the same procedures as the control plots. For the test plots, the obtained average cumulative sediment runoff values were corrected for the mass per unit area of the BSC mats, erosion control mat B and C, respectively. The value of average cumulative sediment runoff of the unprotected soil divided by average cumulative sediment runoff obtained in the test plots was defined as the soil loss ratio (SLR) for each rainfall intensity. The SLR was calculated from the corrected sediment runoff obtained from the regression curves based on the measured values of each rainfall intensity and sediment runoff.

3.2 Test Result

The amount of sediment runoff from the BSC mats was corrected for the presence of organic matter, such as soil algae, by measuring the loss on ignition (Table 2). The amount of sediment runoff and SLR are shown in Table 3. It shows that the amount of sediment runoff in the test plot was extremely small compared to the unprotected soil in the control plot. The average SLR of the BSC mats was higher at 192, compared to 128 and 68 for the erosion control mats B and C. This is considered to be presumably due to the increased erosion prevention effect of BSC formation. In addition, the average SLR of American-made erosion control mats ranged from 5.0 to 14.0 according to the results of tests conducted in the U.S. to the same way [5]. Therefore, it is indicated that the SLR of the BSC mats is extremely high. Appearance of runoff water samples showed that the turbidity of the BSC mats was lower than that of the unprotected soil (Picture 4). As shown in Table 2, the sediment runoff of the BSC mats may include soil algae and fertilizers that were flown out from the BSC mats placed on the top of the test apparatus during the test, so the values in Table 3 show corrected ones.

Table 2 Analyzed result of ignition loss

Category			Ignition loss (%)
Mat	Debris etc		9.1
BSC layer (BSC + Fertilizer)	Algae		
	Fertilizer	Dissolution	33.5
		Suspension	57.4
Soil particle			

Table 3 Amount of runoff sediment and SLR

Rainfall intensity (mm/h)	Amount of runoff sediment (g)				SLR		
	Control plot	Test plot					
	Unprotected soil	Erosion control mat		BSC mat	Erosion control mat		BSC mat
		B	C		B	C	
50	88.6	0.9	1.6	0.8	105	50	106
100	203.2	1.5	1.7	1.1	127	66	177
150	465.9	3.1	5.8	1.6	152	87	294
Mean	–	–	–	–	128	68	192

4   Summary

In this paper, field and bench-scale rainfall tests were conducted to investigate the effectiveness of BSC mats in protecting slopes. The results of the tests are as follows.

The number of invasive plants in the BSC mats was approximately 2.5 times that of unprotected slopes, and the vegetation was evenly distributed throughout the slope, unlike bare slopes where vegetation was observed only in the eroded areas. The average sediment runoff of the BSC mats in the field test was less than 1/4500 of the average one in the unprotected soil. The average soil loss ratio (SLR) of the BSC mats was 192, indicating that the mats have a high erosion prevention function. In the field test, the BSC mats formed vegetation faster and better than the unprotected soil, and the amount of sediment runoff was also reduced. In the bench-scale rainfall tests, the high erosion prevention effect of the BSC mats was also confirmed. As indicated by these test results, the BSC mats are more effective in protecting slope surfaces than general erosion control mats. In order to improve the invasion ability of vegetation with BSC mats, we are planning to study the specifications of nets to improve the trapping of flying seeds. In this small-scale rainfall test, the slope was set to 18.43° in accordance with ASTM D7101, which is a very gentle slope compared to typical slope gradients in Japan [4]. When the slope gradient was varied in the test of the same standard, it was shown that the sediment runoff of the test sample increased as the slope became steeper [6]. Based on this, it is necessary to consider the selection of test conditions that match the slopes of embankment and cut slopes in Japan.

References

1. Junichi I (2022) Necessity of revegetation with plants of local genetic lineage: Effects on ecosystems caused by use of foreign native species. J Japanese Soc Rev Technol 47(3):351–354
2. Shimomura S, Tomisaka M, Shimada M, Kobayashi Y, Fujisawa H, Kurihara J, Sakurai W, Tagata S, Ozawa K, Nagumo F, Hoshikawa A, Nakano T (2007) Experimental studies on the effectiveness of natural microorganisms on the ground surface at controlling erosion. Nippon Koei Tech Forum 15:21–29
3. Rui K, Kazutoshi O, Maki M, Hisako F, Mineto T, Hiroyuki M (2018) Identification of soil erodibities for an application of WEPP model with biological ground cover by algae and fungi. Proceed Japan Soc Civil Eng G (Environment) 74(5):I_233-I_239
4. Japan Road Association (2009) Handbook of road work-Guidelines of cutting and slope stabilization works, p 266

5. Sprague CJ, Sprague JE (2016) Testing and specifying erosion control products. In: Conference XXXXVI international erosion control association, San Antonio, TX
6. Midha VK, Suresh Kumar S (2013) Influence of woven structure on coir rolled erosion-control products. Geosynthetics Int 20(6):396–407

Roles of Coarser-Grained Soil Layers in Capillary Barrier System

Mai Sawada , **Mamoru Mimura, and Shigemasa Murai**

Abstract Water diversion occurring at the interface between finer- and coarser-grained soil layers is referred to as capillary barriers, which are used for soil covers to restrict water infiltration into waste facilities and improve slope stability. However, methods for selecting optimum soils for capillary barriers have not been established. This study aims to develop measures to select optimum soils for capillary barriers by focusing on the roles of coarser-grained soil layers. Water diversion occurring at the bottom of a sandy soil layer exposed to the atmosphere, which corresponds to a capillary barrier when the pore spaces of the underlying coarser-grained soil layer are infinitely large, is investigated via rainfall tests and numerical simulations. The results reveal that the porewater pressure at the soil–atmosphere interface where water diversion occurred is close to or less than the air entry value but remains negative. This indicates that the negative porewater pressure is a key component for the water diversion at the soil–atmosphere interface, thus providing a novel perspective on the mechanism of capillary barriers. Capillary barriers can be caused by negative porewater pressure generated at non-contact zones between finer- and coarser-grained soil layers. Essentially, the role of coarser-grained soils can make a soil–atmosphere interface by installing spaces under the finer-grained soil layer. This study is useful for reconsidering the mechanism of capillary barriers and developing reasonable measures to select optimum soils.

Keywords Unsaturated seepage flow · Water retention · Boundary condition

M. Sawada (✉)
Tokyo Institute of Technology, 2-12-1-M1-9 Ookayama, Meguro-Ku, Tokyo, Japan
e-mail: sawada.m.af@m.titech.ac.jp

M. Mimura · S. Murai
Kyoto University, C1-2 Kyotodaigaku-Katsura, Nishikyo-Ku, Kyoto, Japan

1 Introduction

Unsaturated seepage flow restricted at the interface between finer- and coarser-grained soil layers is referred to as a capillary barrier. Water is diverted by the capillary barrier and flows downward when the soil layer interface is inclined, as shown in Fig. 1a. Capillary barriers are used for soil covers in toxic waste facilities to reduce contaminated water by restricting water infiltration into the facilities. Additionally, soil covers with capillary barriers are useful for preventing rainfall-induced slope failures.

Water diversion by a capillary barrier is explained using the difference in permeability between finer- and coarser-grained soils [1]. In unsaturated conditions, soil permeability significantly decreases as the degree of saturation decreases because air-filled pores are nonconductive channels to the water flow. Thus, at the soil layer interface where a capillary barrier is formed, the permeability of the coarser-grained soil with low water retention remains lower than that of the finer-grained soil when the matric suction is higher than the intersection, as shown in Fig. 1b. Theoretical and empirical equations were proposed and validated by rainfall tests that measure the length of capillary barriers to quantify the water diversion capacity of capillary barriers. The distance from the upstream end to the breakthrough point of a capillary barrier was estimated using the coefficients of permeability and water retention curves of finer- and coarser-grained soils, rainfall intensity, and slope of the inclined layer [2, 3]. Seepage flow analysis using finite element (FE) method was performed, and the usefulness of capillary barriers for stability improvement of slopes was investigated to evaluate water diversion capacity under a natural climate with unsteady rainfall [4, 5].

Numerous earlier studies have reported that the water diversion capacity of capillary barriers is significantly affected by the hydraulic properties of the finer- and coarser-grained soils, and it is improved when the soils with contrasting hydraulic
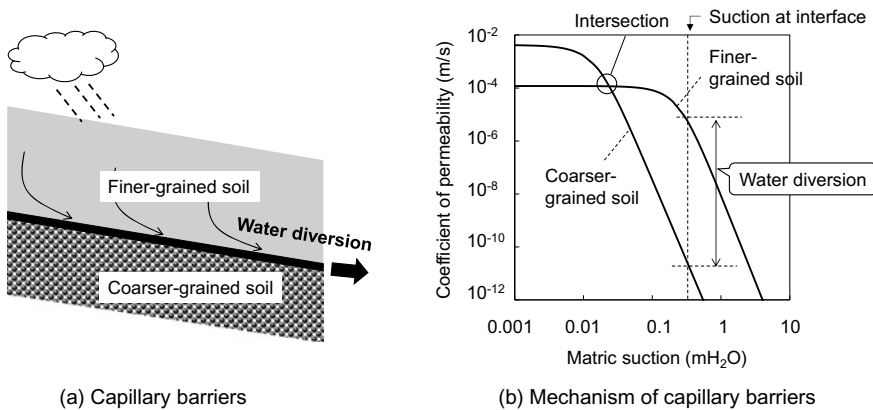

(a) Capillary barriers   (b) Mechanism of capillary barriers

Fig. 1 Water diversion by capillary barriers

properties are used. However, methods for selecting optimum soils for capillary barriers have not been established. This study focused on the roles of coarser-grained soil layers in the capillary barrier system. The water retention of coarser-grained soils must be minimized to maximize the water diversion capacity of capillary barriers when the permeability-based mechanism shown in Fig. 1b is adopted. Essentially, coarser-grained soils with larger pore spaces are more effective. Thus, the water diversion occurring at the bottom of a sandy soil layer exposed to atmosphere was investigated using physical model tests that simulate rainfall infiltration, which corresponds to a capillary barrier when the pore spaces of the underlying coarser-grained soil layer are infinitely large. Furthermore, the experimental results of the rainfall tests were numerically simulated to elucidate the boundary conditions at the soil–atmosphere interface where water diversion occurred. This study provides a novel perspective to the mechanism of capillary barriers and is useful for developing reasonable measures to select optimum soils for capillary barriers.

2 Materials and Methods

2.1 Rainfall Test

Figure 2 shows a schematic view of the rainfall test. A sandy soil (sand: 88.8%, silt: 7.4%, and clay: 3.8%) with a natural water content of 11.4% was compacted at a dry density of 1.74 g/cm^3 on the shelf installed in the soil box. The height of the shelf was 20 cm from the bottom of the soil box. A metal shelf plate with densely arranged holes with a diameter of 1 cm was placed on the shelf, which did not restrict seepage water from the soil model. However, the right end part with a length of 10 cm supported by a plastic plate attached to the soil box was impermeable. A polyester mesh with an opening of 512 μm was lined on the plate to prevent the soil from falling through the holes. The soil was compacted layer by layer until the total thickness became 15 or 30 cm. The thickness of each layer was 5 cm. Six moisture sensors (EC-5, METER, Inc.) were installed at the points shown in Fig. 2.

After the completion of soil compaction, the soil box was tilted at 5° or 10°. Artificial rainfall at a constant rainfall intensity was applied to the soil layer for 24 h. The rainfall intensity was set at 4 or 8 mm/h by varying the water head in the rainfall simulator set above the soil box. The soil box had two outlets at the downstream edge. The upper outlet collected diverted water at the bottom of the soil model, whereas the lower outlet collected seepage water from the soil model. The drainage from each outlet was measured using electric scales during a test. After a 24 h-rainfall test, the soil was quickly removed from the box and water content was measured at the nine points using oven-dry method, as shown in Fig. 2. Table 1 lists the test conditions.
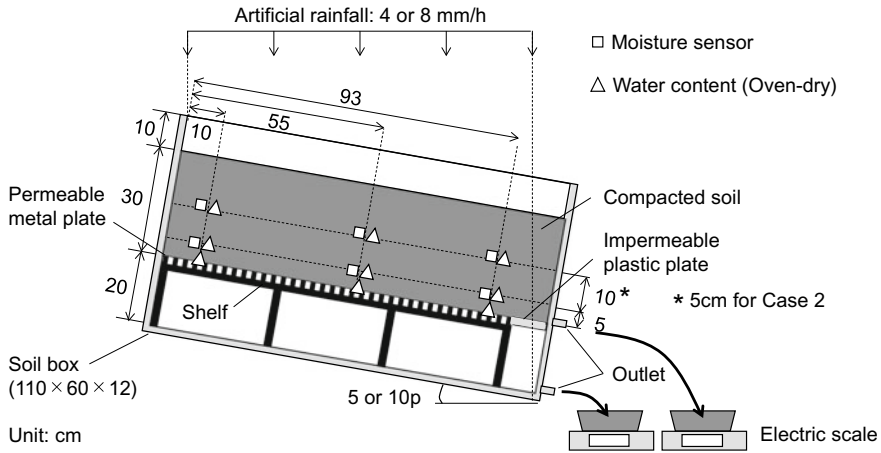
Fig. 2 Schematic view of rainfall test

Table 1 Test conditions

	Case 1	Case 2	Case 3	Case 4
Soil thickness (cm)	30	15	30	30
Slope (°)	10	10	5	10
Rainfall intensity (mm/h)[*]	4 (5.4)	4 (4.7)	4 (4.5)	8 (9.8)

[*]Values in parenthesis represent measured rainfall intensity

2.2 Seepage Flow Analysis

Rainfall tests were numerically simulated using the FE code AC-UNSAF2D [6], which implements Richard's equation. Figure 3 shows an FE model of the soil model, and Fig. 4 presents the results of the water retention test for the tested soil. Matric suction was controlled using the hanging column method and pressure plate method within a range of 10 mH$_2$O. The apparatus and procedure of the water retention test are presented by Sawada et al. [7] in detail. The water retention curve was expressed using the van Genuchten model [8]. The parameters, α and n, were determined to numerically simulate the measured moisture distribution in the soil model assuming that matric suction varies between the main drying and wetting curves during the rainfall test. The coefficient of permeability in the saturated condition was set to 1.18×10^{-4} m/s, and the coefficient of permeability in unsaturated conditions was estimated using the Mualem model [9].

A seepage boundary condition, which is a combination of constant flux and head boundaries, was applied to the bottom surface of the soil model divided into Zones A and B. The boundary condition works as a zero-flux boundary (i.e., impermeable) when the matric suction at the boundary is less than a threshold matric suction,
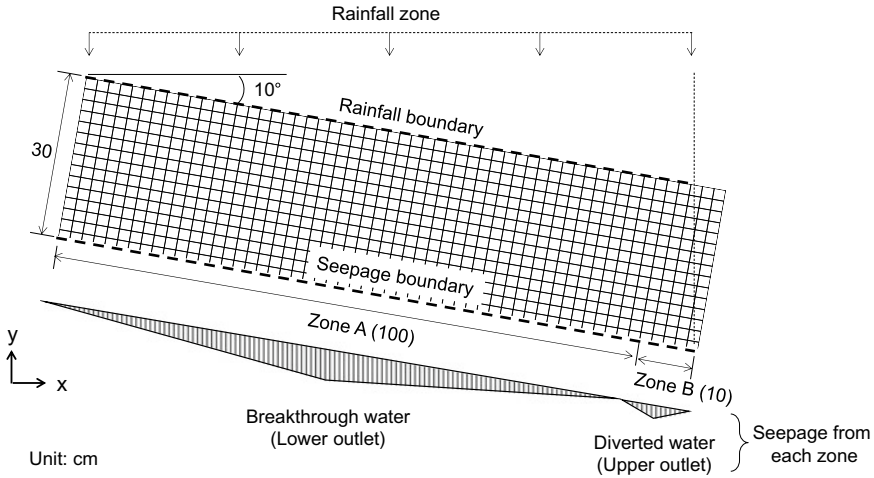
Fig. 3 FE model (cases 1 and 4)
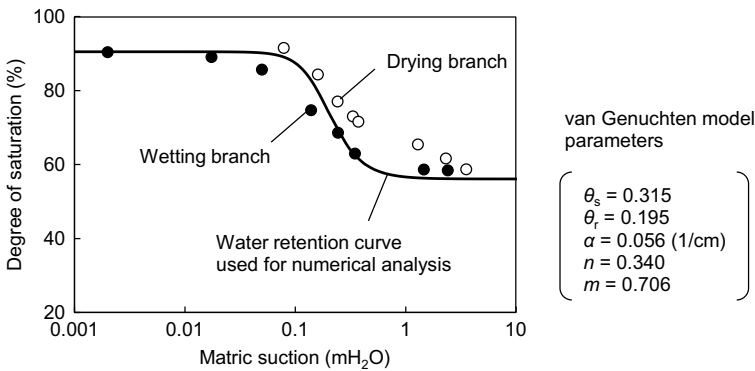
Fig. 4 Water retention curve for tested sandy soil

whereas it works as a boundary of which matric suction is constant at the threshold and water seeps from the bottom of the soil model. A zero-flux boundary was applied to the updip and downdip boundaries. The breakthrough water in Zone A corresponds to the water collected at the lower outlet in the rainfall tests, whereas the seepage water from Zone B on the plastic plate corresponds to the diverted water collected at the upper outlet. The threshold matric suction was determined by trial-and-error method for the calculated flux from Zones A and B to be equivalent to the measured drainage from the outlets.

3　Results and Discussions

3.1　Experimental Results and Numerical Simulations

Figure 5 shows the comparison of the time series of measured and numerically simulated drainage rates from outlets. The percentage described in each graph represents the ratio of the measured drainage volume from each outlet to the total measured drainage volume at steady state. The water infiltrated into the soil layer was completely diverted at the bottom and drained from the upper outlet in Cases 1 and 2. However, in other cases, water was partially diverted, and breakthrough water was collected at the lower outlet. The discrepancies in the early stage of drainage can be attributed to the difference in the outlet structure between the physical and numerical models. The 2D numerical model defined the water drainage from the upper outlets using the potential seepage boundary in Zone B, rather than modeling the 3D pipes.

These results revealed tendencies similar to those for capillary barriers. Sawada et al. [10] performed rainfall tests on the same sandy soil layer compacted on a gravel layer under the conditions listed in Table 1. Perfect water diversion was achieved in Case 1, whereas a decrease in soil layer thickness or slope or an increase in rainfall intensity reduced the water diversion capacity of capillary barriers. However, the influence of thickness was relatively small. This indicates that the water diversion at the sand-gravel interface (i.e., capillary barriers) occurs even if the underlying gravel layer is removed and the bottom surface of the sand layer is exposed to atmosphere. However, the soil–atmosphere interface is not an impermeable boundary. Essentially,
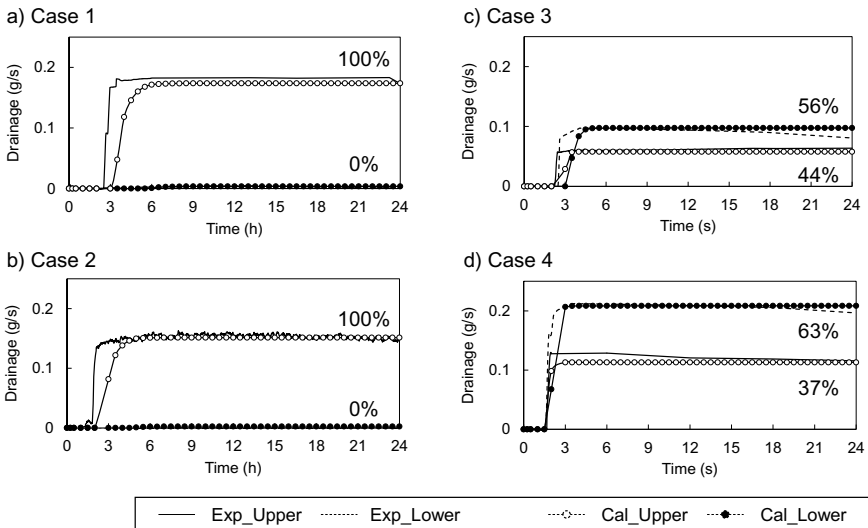

Fig. 5 Measured and numerically simulated drainage from outlets

capillary barriers can be independent from the hydraulic properties of the gravel layer when the pore spaces of the gravel layer are large to some extent. This leads to the reconsideration of the roles of coarser-grained soil layers in the capillary barrier system.

3.2   Boundary Conditions at a Soil–Atmosphere Interface

The experimental results were numerically simulated using seepage boundary conditions, which control flux from the boundaries using threshold matric suction to elucidate the mechanism of the water diversion at the soil–atmosphere interface, particularly the boundary conditions at the bottom surface of the soil model. Figure 5 shows that the measured diverted water from the upper outlet, and the breakthrough water from the lower outlet were consistent with the numerically simulated values. The starting time and amount of breakthrough water were significantly affected by the threshold matric suction.

The threshold matric suction for each case was plotted on the water retention curve, as shown in Fig. 6. This shows that the thresholds were close to or less than the air entry value, but larger than zero. The thresholds were validated by comparing with the matric suction at the bottom of the soil model estimated from the measured water content after each test based on the water retention curve. The threshold was mostly equivalent to the estimated matric suction. Essentially, the bottom of the soil model where water diversion occurred was saturated. However, the porewater pressure remained negative. The negative porewater pressure is a key component for the water diversion at the soil–atmosphere interface, which enables water retention in the soil and prevents breakthrough. This water diversion mechanism can be applied to capillary barriers when the pore spaces of the coarser-grained soil layer are sufficiently large. The water diversion by capillary barriers can be caused by negative porewater pressure that generates at non-contact zones between the finer- and coarser-grained soil layers (i.e., soil–atmosphere interface), and not by only the low hydraulic conductivity of coarser-grained soil layer in unsaturated conditions. Essentially, the key role of coarser-grained soil layers in the capillary barrier system can be installing spaces under the finer-grained soil layers. Additional rainfall tests on soils with various air entry values are needed to examine the generality of the boundary conditions at the soil–atmosphere interface. Additionally, further discussions on the comparison of water diversion occurring at the finer-coarser-grained soil layer interface and soil–atmosphere interface are useful for elucidating the mechanism of capillary barriers and developing measures to select optimum materials for capillary barriers.
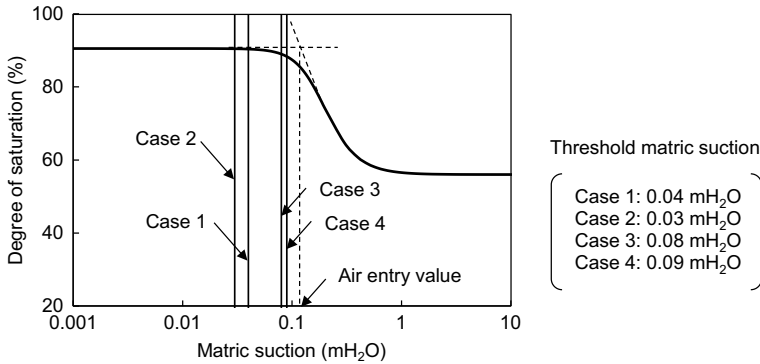
Fig. 6 Threshold matric suction at soil–atmosphere interface

4 Conclusions

This study aimed to develop measures to select the optimum soils for capillary barriers by focusing on the roles of coarser-grained soil layers. Water diversion occurring at the bottom of a sandy soil layer exposed to the atmosphere, corresponding to a capillary barrier when the pore spaces of the underlying coarser-grained soil layer are infinitely large, was investigated by rainfall tests and numerical simulations.

The experimental results revealed that water diversion similar to capillary barriers occurred at the soil–atmosphere interface. The water diversion and breakthrough were influenced by the slope and rainfall intensity, which were numerically simulated by applying boundary conditions that control flux from the boundaries using a threshold matric suction to the soil–atmosphere interface. The numerical results revealed that the porewater pressure at the soil–atmosphere interface was close to or less than the air entry value but remained negative when water diversion occurred. This indicates that the negative porewater pressure is a key component of the water diversion at the soil–atmosphere interface.

The mechanism of water diversion can be applied to capillary barriers, which are caused by negative porewater pressure that generates at non-contact zones between the finer- and coarser-grained soil layers, not by only the low hydraulic conductivity of coarser-grained soil layer in unsaturated conditions. Essentially, the role of coarser-grained soils can be generating a soil–atmosphere interface by installing large spaces under the finer-grained soil layer. This novel perspective is useful for reconsidering the mechanism of water diversion of capillary barriers and developing reasonable measures to select optimum soils although additional rainfall tests are needed.

References

1. Ross B (1990) The diversion capacity of capillary barriers. Water Resour Res 26(10):2625–2629
2. Steenhuis TS, Parlange JY, Kung KJS (1991) Comment on "the diversion capacity of capillary barriers" by Benjamin Ross. Water Resour Res 27(8):2155–2156
3. Kung KS (1990) Preferential flow in a sandy vadose zone: 2 mechanism and implications. Geoderma 46(1–3):59–71
4. Li Y, Satyanaga A, Rahardjo H (2021) Characteristics of unsaturated soil slope covered with capillary barrier system and deep-rooted grass under different rainfall patterns. Int Soil Water Conserv Res 9(3):405–418
5. Scarfone R, Wheeler SJ, Smith CC (2022) Numerical modelling of the application of capillary barrier systems for prevention of rainfall-induced slope instability. Acta Geotechnica 1–24
6. Akai K, Ohnishi Y, Nishigaki M (1977) Finite element method unsaturated seepage in soil. Proceed Japan Soc Civil Eng 264:87–96
7. Sawada M, Sumi Y, Mimura M (2021) Measuring desiccation-induced tensile stress during cracking process. Soils Found 61(4):915–928
8. Sawada M, Mimura M, Yoshimura M (2016) Infiltration control in historical tumulus mounds using capillary barriers—experimental and analytical study on the mechanism of capillary barriers. J Japan Soc Civil Eng Ser C 72(2):101–116 [in Japanese]
9. van Genuchten MT (1980) A closed-form equation for predicting the hydraulic conductivity of unsaturated soils. Soil Sci Soc Am J 44(5):892–898
10. Mualem Y (1976) A new model for predicting the hydraulic conductivity of unsaturated porous media. Water Resour Res 12(3):513–522

Technology to Reduce Environmental Impact of Jet Grouting Technology

Junichi Yamanobe, Toshiyuki Kamata, Kazutoshi Ishikawa, Toshiaki Jin, Yosuke Watanabe, and Keisuke Ohkubo

Abstract Jet grouting technology has been applied worldwide since the 1970s to improve soft ground. This paper discusses the reduction of environmental impact achieved by a technology to treat waste mud (hereinafter referred to as "spoil return") generated in jet grouting technology, as well as that achieved by contributing to the longevity of buildings. We also discuss in-situ remediation using water jet technology. The in-situ remediation method using jet grouting technology combined with bioremediation technique is an innovative soil remediation method applicable to clayey soil, which is difficult to be treated by conventional in-situ remediation methods.

Keywords Jet grouting · Bioremediation · Over-spilled uncemented column · Pile foundation · Soil contamination

1 Introduction

Jet grouting technology was developed in the 1970s and has been applied worldwide. The main feature of this method, which was basically developed by Yoshida and Yahiro [1], is that cement is agitated and mixed with in-situ ground by cutting the ground with a high-pressure fluid. This technology is now widely used in temporary construction work (e.g., support during excavation and tunnel construction) around the world. In recent years, this method has been applied to various projects for permanent construction work (e.g., ground liquefaction countermeasures and seismic reinforcement of foundations). However, jet grouting technology has an environmental problem in that spoil return of approximately the same volume as the injected solidifier slurry is discharged, and in many cases, spoil return is transported off-site and disposed of as industrial waste.

This paper introduces two technologies: one is to extend the service life of buildings by repairing and reinforcing pile foundations using the advantage of jet grouting technology, which can be applied to narrow areas; and the other is to reduce and

J. Yamanobe (✉) · T. Kamata · K. Ishikawa · T. Jin · Y. Watanabe · K. Ohkubo
Chemical Grouting Co., Ltd., Minato-Ku, Tokyo, Japan
e-mail: j-yamanobe@chemicalgrout.co.jp

effectively use spoil return, which is a problem of jet grouting technology, thereby contributing to environmental protection. We also present an in-situ remediation method that combines the features of jet grouting technology with bioremediation technique. This in-situ remediation method reduces the amount of contaminated soil to be transported off-site and also reduces the extent of construction work by taking advantage of the features of jet grouting technology, thereby reducing overall construction costs and environmental impact.

2 Jet Grouting Technology for Ground Improvement

2.1 Jet Grouting for Repair and Reinforcement of Pile Foundations

The problems facing buildings in Japan include insufficient utilization of foundations at the time of building renewal, aging, and earthquake damage due to delays in seismic reinforcement of foundations. In urban redevelopment projects, use of existing piles is being promoted due to the difficulty of pulling out and removing them. Jet grouting technology is characterized by its ability to be applied in narrow areas and its use of fluid for ground cutting. Due to this characteristic, as shown in Fig. 1, repair and reinforcement can be performed on the top of a single pile foundation by working from two diagonal directions [2]. In this section, we present an overview of the repair and reinforcement work performed on a reinforced concrete housing complex that sustained damage at the pile heads during a large earthquake, including information on the pile foundation specifications and soil improvement column layout. We also provide a comparison of CO_2 emissions between the case of repair and reinforcement work and the case of demolition and new construction.

Practical Application Example. The building is a five-story reinforced concrete residential complex built in 1983. The piles are PHC piles of 600 mm in diameter and 39 m in length. The pile top of the building was damaged by the 2016 Kumamoto earthquakes, but no damage was observed in the superstructure. Repair and reinforcement work was carried out on the pile foundations of this building as shown in Fig. 2. The repair and reinforcement work was conducted using the same jet grouting technology for soil improvement, regardless of pile damage. The depth of the soil improvement was deeper than the damaged area confirmed by an integrity test of some pile. The design strength of the soil improvement columns was 2000 kN/m², and the required designed quality was satisfied as shown by an inspection conducted in accordance with the "Guideline of Design and Quality Control of Ground Improvement for Buildings [3]."

For the case of the demolition and new construction of the reinforced concrete housing complex, the size of the newly constructed building was assumed to be the same as that of the present building. The CO_2 emissions for the new construction were
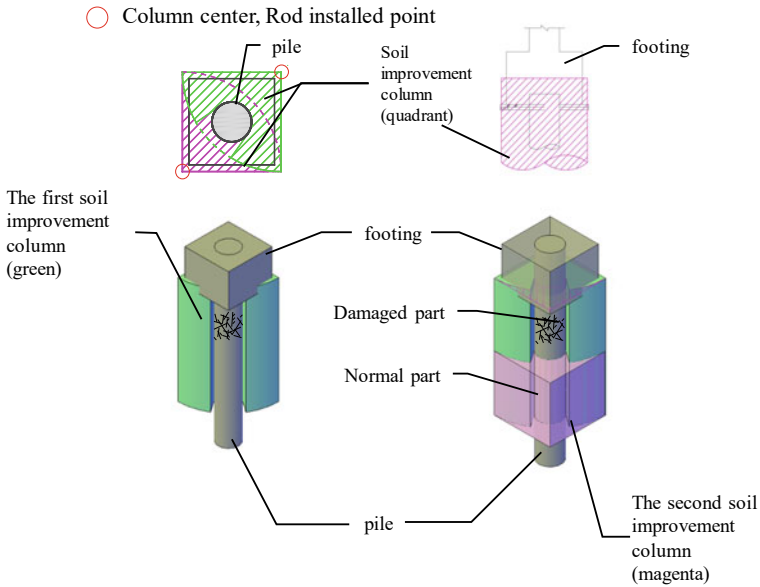
Fig. 1 Schematic diagram of repair and reinforcement of pile foundation
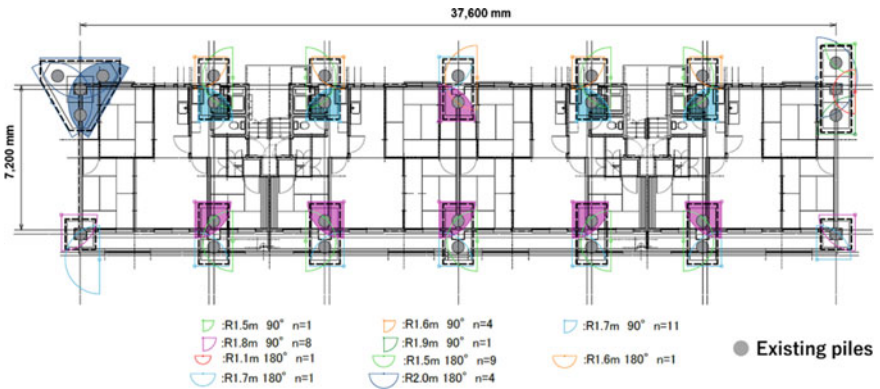
Fig. 2 Soil improvement columns layout

based on the CO_2 emissions per floor area according to Kimoto et al. [4]. The CO_2 emissions from the repair and reinforcement work using jet grouting technology were calculated according to the "Guideline of Using Existing Piles [5]" and the "Greenhouse Gas Emissions Accounting, Reporting and Publication System [6]." As a result, it was estimated that the repair and reinforcement work using jet grouting technology would reduce CO_2 emissions by about 35% compared to the demolition and new construction.

2.2 Jet Grouting Technology for Reducing Construction Waste

The ground cutting performance of jet grouting technology has improved with its development, and the amount of spoil return discharged per unit volume of improvement column has been reduced. However, the amount of spoil return still remains to be solved. Therefore, we are exploring a reuse jet system to reduce the amount of spoil return discharged. Normally, spoil return discharged in jet grouting technology is carried off-site either in unconsolidated state or after solidification, and therefore, the amount discharged directly corresponds to the amount of spoil return discharged. The reuse jet system, on the other hand, incorporates equipment for processing spoil return into a mixing or conventional plant, making it possible to recycle and reduce the spoil return generated. In this section, we introduce an example of recycling and reduction using the reuse jet system.

Practical Application Example. The reuse jet system was applied to a site as a countermeasure against liquefaction directly below a levee. Figure 3 shows the construction plan view and cross-section, and Fig. 4 is the flow diagram of the reuse jet system. The spoil return discharged from the site was sorted and treated into mud and muddy water; the sorted and treated mud was transported off-site to a disposal site as industrial waste; and the muddy water was reused as mixing water for the solidifier.

The reuse jet system reduced the amount of spoil return discharged at the site by approximately 40% compared to the planned amount, and the number of vehicles used to transport the spoil return was also reduced by 42%. The amount of water used
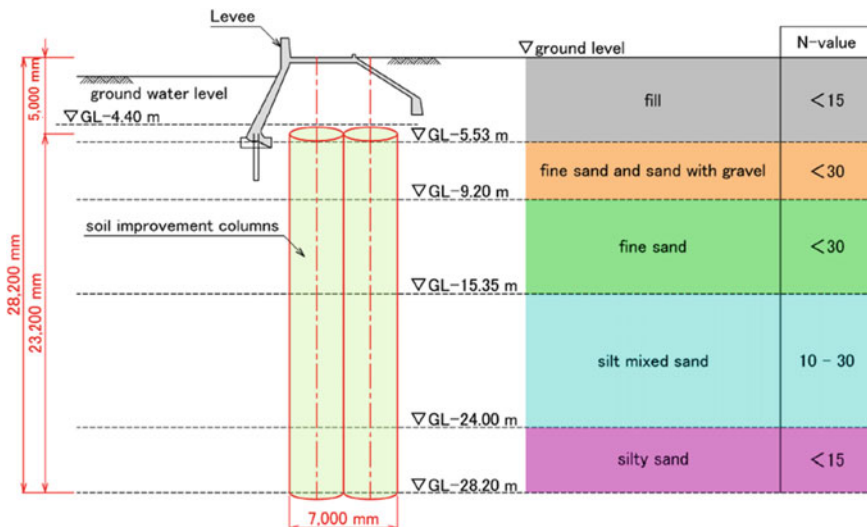
Fig. 3 Construction cross-sectional view
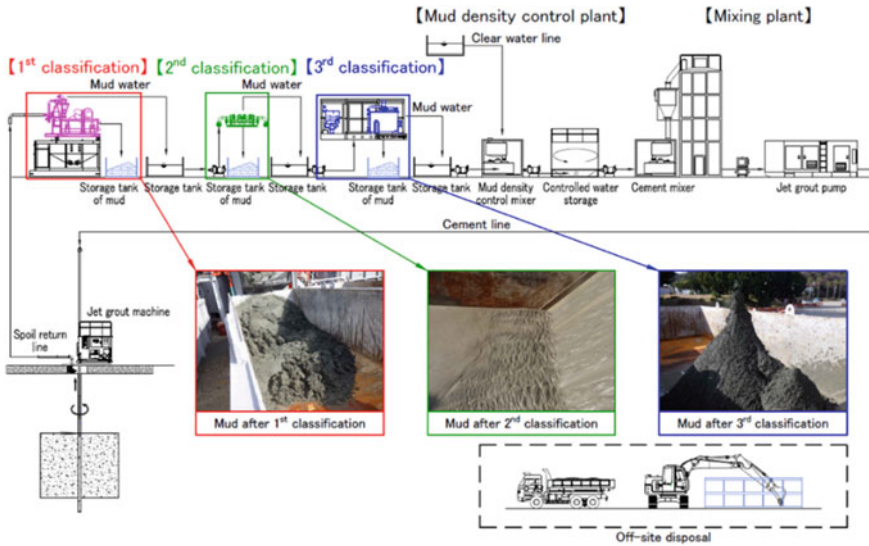
Fig. 4 Flow diagram of the reuse jet system

for mixing was also reduced by 30% by reusing some of the spoil return as mixing water for the solidifier. The quality of the soil improvement columns was evaluated by diameter and strength of the columns. The improvement column diameter was measured by taking boring cores at the top 50 cm from all the columns, and the improvement column strength was measured by taking cores along the entire length of the column and conducting a uniaxial compression test on the cores. As a result, all the top cores were sampled, and the column diameter target of 3.5 m was satisfied. The uniaxial compression test showed that the target strength of 2160 kN/m^2 was met for all cores. These results indicate that the reuse jet system enables the reuse of the muddy water in the spoil return as mixing water and satisfies the quality required for countermeasures against directly below a levee liquefaction.

2.3 Technology for Effective Use of Spoil Return

Compared to other cement-based soil improvement methods, jet grouting technology uses more material and generates more spoil return, resulting in higher greenhouse gas emissions. If the spoil return can be effectively utilized in other construction work, such as backfilling, the environmental impact can be reduced by avoiding production of additional work. This section introduces a quality control method for the effective use of spoil return and an example of its application.

The quality (strength) of the spoil return discharged in jet grouting technology mainly depends on the amount of solidifier added. Therefore, the strength can be

evaluated by measuring the Ca content of the solidifier in the spoil return. We thus investigated the strength by measuring the Ca content in the spoil return. Figure 5 shows the relationship of the Ca content with the amount of solidifier added and the uniaxial compressive strength of clayey soil measured in a laboratory mixing test. The figure shows that the Ca content correlates with the uniaxial compressive strength and the amount of solidifier added. This suggests that it is possible to estimate the strength from the Ca content in the spoil return.

For the effective use of spoil return, its density and Ca content were set as quality control items. The uniaxial compressive strength was estimated from the relationship between the two items. Figure 6 shows the relationship between uniaxial compressive strength and Ca content for different densities of assumed spoil return mix measured in a laboratory mix test. In Fig. 6, the intersection point between an acceptable strength border line and each density line was determined, and the three points obtained were plotted on a graph of the relationship between density and Ca content to draw an acceptable strength border line, as shown in Fig. 7. The graph area above and to the right of the line is the acceptable range, and below and to the left is the unacceptable range. We present below an example of quality control of spoil return using the acceptable strength border line given in Fig. 7.

Practical Application Example. This project, associated with an urban development project, involved the demolition of an existing building with its basement floor preserved and the soil improvement of the foundation for the construction of a new building. The construction period was shortened by implementing the soil improvement work from the first basement floor and first floor using small equipment in parallel with the demolition of the upper floors of the existing building. The density
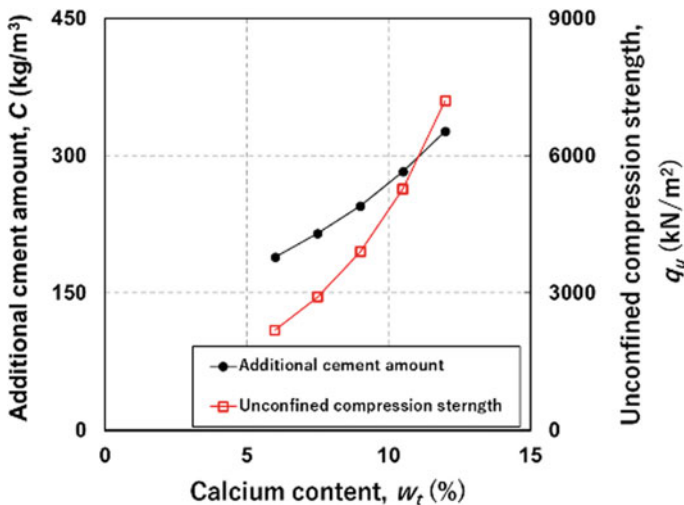
Fig. 5 Relationship of Ca content with uniaxial compressive strength and amount of solidifier added

Fig. 6 Illustration of acceptable strength border line
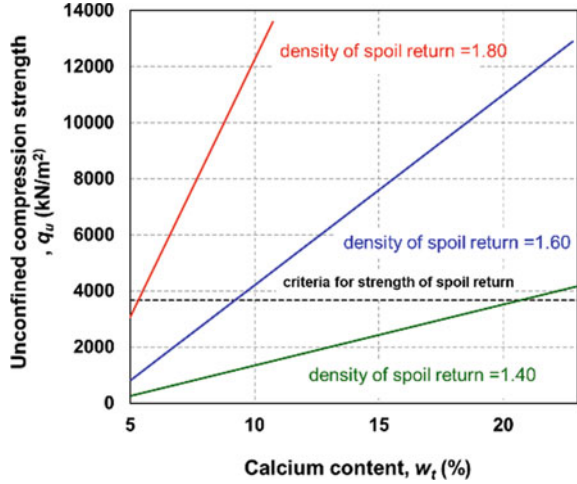
Fig. 7 Acceptable strength border line and strength judgment graph
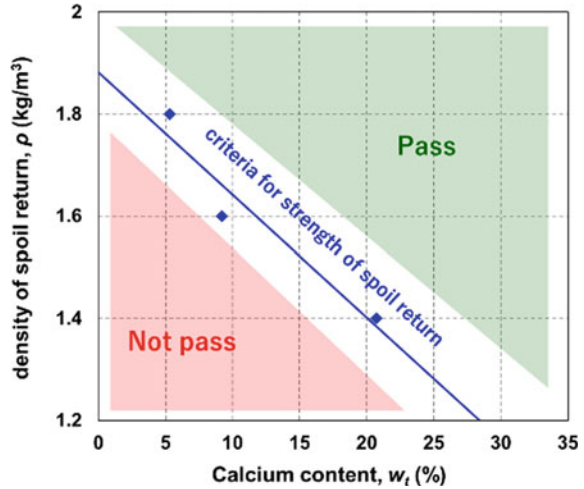
and Ca content of the spoil return generated in jet grouting technology were measured, and only the material that satisfied within the acceptable range of strength was used effectively as backfilling material for underground pits and other areas on the basis of the acceptable strength border line shown in Fig. 7. The spoil return in the unacceptable range was disposed of as industrial waste, namely construction waste. As a result, the amount of construction waste discharged from the site was reduced by 2800 m^3 from the planned 7500 m^3 to 4700 m^3, a reduction rate of 37%.

3   In-situ Contaminated Soil Remediation Method Using Jet Grouting Technology

3.1   BioJet Method

This remediation method (hereinafter referred to as "bioremediation") uses a water jet technology, which is a feature of jet grouting technology, to cut soil and inject a microbial activator into the ground to decompose contaminants in-situ. The target contaminants are volatile organic compounds (VOCs). Because VOCs have a higher specific gravity than water, they can easily permeate into the ground and cause widespread contamination along the flow of groundwater. Conventional bioremediation methods are difficult to apply to low-permeability layer because they involve installation of a well at the contaminated site and injection of a microbial activator into the well. Figure 8 shows the principle of BioJet method. It is a patented bioremediation method developed with EOS Remediation in the United States, in which microorganisms are activated in the soil to decompose VOCs. It uses a hydrogen release compound as a microbial activator. The hydrogen release compound is decomposed by microorganisms in the soil to gradually release hydrogen, which is then used by the microorganisms to decompose and detoxify VOCs through dechlorination.

In the remediation method using the hydrogen release compound, which is characterized by the activation of microorganisms by hydrogen, it has been reported that the diffusion range of molecular hydrogen can be expressed as a function of time even if the target soil has low permeability. Therefore, by injecting the hydrogen release compound into low-permeability layers through slits provided at regular intervals, hydrogen diffuses widely and uniformly into the soil. The molecular diffusion of hydrogen in the low-permeability layers activates microorganisms living in the surrounding area and promotes VOCs decomposition. This method has the ability to reduce environmental burden due to the following features: it can be applied in
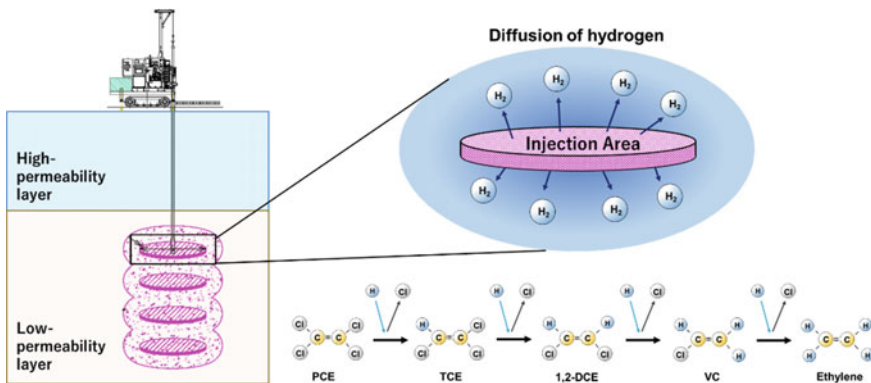

Fig. 8 Principle of BioJet method

narrow construction areas using small construction machines, and the amount of waste generated is small because the injection of the compound reduces the extent of ground cutting.

Practical Application Example. As a recent example of construction work, we introduce the site of a partially operating plant in Tokyo where soil contamination by VOCs originating from plant operations was verified. As remediation work had to be conducted inside an operating plant and small machines had to be used in narrow areas, BioJet method was adopted to take advantage of the characteristics of jet grouting technology. The total site area was approximately 9300 m^2, and the area where the technology was applied was approximately 2000 m^2. Figure 9 shows an example of soil analysis results and a soil columnar section at a survey location. The site had already been remediated by pumping water and injecting a hydrogen release compound from a well, and the aquifer sand layer had been well remediated. However, with only the pumping and well injection, contaminants remained in the low-permeability layers below GL − 6 m. Table 1 shows the results of gas chromatographic photo-ionization detector (GC-PID) analysis of soil samples collected after the remediation work. It was found that the concentration of contaminants had decreased 3.5 months after the work and had met the soil pollution criteria 6 months after the work.

Comparison of CO$_2$ Emissions Between the Excavation/Removal and BioJet Methods. There are two main methods to remedy soil contamination: excavation/removal and in-situ remediation. In the excavation/removal method, a large amount of energy resources are consumed for off-site transport and disposal of contaminated soil, and greenhouse gases including CO$_2$ are emitted as a result. On the other hand, BioJet method has many advantages: the amount of off-site transport can be reduced

Depth (GL)	Substance (mg/L)					Depth	Soil type
	PCE	TCE	cis−1,2−DCE	VC			
−4.0m	ND	ND	ND	ND		4	
−5.0m	ND	ND	ND	ND		5	sand
−6.0m	ND	0.025	0.16	0.11		6	
−7.0m	ND	0.013	0.090	0.12		7	silt mixed sand
−8.0m	ND	0.13	0.20	0.11		8	
−9.0m	ND	0.033	0.12	0.050		9	
−10.0m	ND	0.11	0.021	0.004		10	silt
−11.0m	ND	0.021	0.006	ND		11	
Soil Pollution Criteria	0.01	0.03	0.04	0.002			

PCE : tetrachloroethylene
TCE : trichloroethylene
cis−1,2−DCE : cis−1,2−dichloroethylene
VC : chloroethylen
black number : satisfying
red number : not satisfying

Fig. 9   State of contamination at each depth

Table 1 Changes in VOCs contaminant concentrations

Substance		TCE (mg/L)			cis-1,2-DCE (mg/L)			VC (mg/L)		
Measurement time		Before injection	3.5 months after	6 months after	Before injection	3.5 months after	6 months after	Before injection	3.5 months after	6 months after
Depth (GL-m)	− 5.0	0.003	ND	ND	0.015	ND	ND	ND	ND	ND
	− 6.0	0.004	ND	ND	0.78	0.20	ND	0.33	0.12	ND
	− 7.0	0.005	ND	ND	0.97	0.017	ND	0.26	0.008	ND
	− 8.0	0.014	ND	ND	0.96	0.018	ND	0.22	0.001	ND
	− 9.0	0.006	ND	ND	0.36	0.004	ND	0.11	ND	ND
	− 10.0	0.005	ND	ND	0.10	0.006	ND	0.021	ND	ND
	− 11.0	0.003	ND	ND	0.003	ND	ND	ND	ND	ND

to less than 1/10 of that for the excavation/removal method; in-situ remediation is possible with the addition of only 0.5% in volume of the remediation agent relative to the remediation volume.

We calculated CO_2 emissions using the "Environmental Impact Quantification Tool for Soil Contamination Countermeasures [7]" distributed by the Bureau of Environment of the Tokyo Metropolitan Government. The same construction conditions were used to postulate a model for both the excavation/removal and BioJet method. The results of the calculations using the quantification tool showed that BioJet method can reduce CO_2 emissions by approximately 60% compared to the excavation/removal method. The results indicate that BioJet method can reduce CO_2 emissions compared to the excavation/removal method by reducing the amount of fuel used and the extent of heavy equipment operations and by reducing the amount of off-site transport substantially.

4   Conclusions

As some of our efforts to reduce the environmental impact of jet grouting technology, we have presented technologies for extending the service life of buildings through pile foundation repair and reinforcement; reducing and effectively utilizing spoil return; and remedying contaminated soil.

In the repair and reinforcement technology for pile foundations, jet grouting technology has made it possible to extend the service life of buildings and reduce CO_2 emissions by taking advantage of its features such as workability and use of small machines.

As regards the technology to reduce the amount of spoil return, we have found that the reuse jet system can be applied effectively to reduce the amount of spoil return and the amount of water mixed with the solidifier slurry.

We have also presented the results of reusing the spoil return generated in jet grouting technology as backfilling material in the foundation of a new building while checking the quality of the spoil return. These technologies have enabled the reduction and effective utilization of spoil return, which would otherwise have been carried off-site as construction waste.

As regards the soil remediation technology, we have presented an in-situ VOC remediation method that applies jet grouting technology for cohesive soil layers. This method not only reduces the amount of chemicals used, but also reduces the amount of construction waste compared to conventional methods. In particular, CO_2 emissions during construction can be significantly reduced compared to the excavation/removal method.

While the need for jet grouting technology is increasing for infrastructure and building construction, it is a method that discharges construction waste. As shown in the examples presented here, this technology has been developed in recent years to reduce the amount of spoil return. In addition, jet grouting technology is suitable in

pursuing total carbon neutrality in construction due to its features such as smaller-scale construction work and shorter process time. We will continue to improve and apply this method to further recycle and reduce spoil return and curb carbon dioxide emissions, thereby contributing to the construction of a sustainable society.

References

1. Yahiro T, Yoshida H (1973) Induction grouting method utilizing high-speed water jet. In: Proceedings of 8th international conference on soil mechanics and foundation engineering, Moscow, pp 402–404
2. Kamata T, Shimamura A, Tsuchiya T (2019) Study on repair and reinforcement for pile foundation using jet grouting. In: Silvestri, Moraci (eds) Earthquake geotechnical engineering for protection and development of environment and constructions, pp 3170–3177
3. The Building Center for Japan, Center for Better Living: the guideline of design and quality control of ground improvement for buildings—soil mixing using cement material 2018 version, pp 338–352, (2018). (in Japanese)
4. Kimoto K, Ikaga T, Shintani H, Noguchi H (2009) Estimation of CO_2 emission from construction, renovation and demolition of residential buildings up to 2050. In: The 4th Meeting of the Institute of Life Cycle Assessment, Japan, pp 278–279. (in Japanese)
5. Japan Federation of Construction Contractors: the guideline of using existing piles—for current and future use. https://www.nikkenren.com/sougou/10thaniv/pdf/07-05-12.pdf. Accessed 2022/09/20. (in Japanese)
6. Ministry of the Environment Government of Japan, Greenhouse gas emissions accounting, reporting and publication system. https://ghg-santeikohyo.env.go.jp/. Accessed 2022/09/20. (in Japanese)
7. Environmental impact quantification tool for soil contamination countermeasures: https://www.kankyo.metro.tokyo.lg.jp/chemical/soil/information/grsr.files/tokyogrtoolmanual.pdf.(2018). (in Japanese)

Geological and Hydrological Aspects

A Case Study of Multi-point Temperature Logging for Effective Groundwater Drainage in High Embankment

Masanori Murai [ORCID]**, Masaya Kawata, Yuta Ichikawa, and Atsuo Takeuchi**

Abstract As is often experienced in the field of mountain ground disasters, groundwater in a formation is rarely uniformly distributed and flowing. Groundwater is composed of several fluidized layers, which are affected by the complex geological and soil conditions in the subsurface, and the water level and hydraulic head of each fluidized layer form the groundwater table. Without sufficient information on the location and depth of the groundwater flow layer, it is difficult to achieve effective results when implementing countermeasure works to lower groundwater. To prevent this from happening, it is very important to know the location of the groundwater flow layer in advance, both in plan and in three dimensions. The depth of the groundwater flow layer and its thickness can be obtained by performing a "multi-point temperature logging" developed by Dr. Atsuo Takeuchi. The greatest advantage of this logging method is that it can obtain information on the groundwater leachate layer above the borehole water level even when the water level in the borehole is extremely low. The commonly used method for detecting fluidized layers is the saline dilution method, but the information on fluidized layers is limited to the depth below the water level in the borehole. To solve this problem, logging while drilling exploratory boreholes in stages is another method, but it is quite difficult to apply because of its high cost and time burden. The built-up area under study is 30 m layer-thick embankment. Groundwater is present within the fill of this built-up area due to poor drainage. In order to ensure the stability of the embankment, groundwater exclusion using collection wells was considered. Multi-point temperature logging was conducted at two locations to determine the drainage pipe layout of the water collection wells. As a result of this survey, several groundwater seepage points and groundwater flow layers could be detected and effective drainage pipe placement could be planned.

Keywords Multi-point temperature logging · Groundwater flow layer · Groundwater drainage · High embankment

M. Murai (✉) · M. Kawata · Y. Ichikawa
Shimizu Corporation, Tokyo 104-8370, Japan
e-mail: m.murai@shimz.co.jp

A. Takeuchi
Natural Groundwater Research Institute, Otsu 520-0014, Shiga, Japan

1 Introduction

In addition to the Niigata Chuetsu Earthquake in 2004 [1], the Sanyo Expressway Disaster in 2005 [2] and the Great East Japan Earthquake in 2011 [3], there have been other recent cases of damage caused by groundwater from embankments filling streams, such as the Aizome River debris flow in Atami City, Shizuoka Prefecture [4], where illegal embankments collapsed. In Japan, the Ministry of Land, Infrastructure, Transport and Tourism (MLIT), Nippon Expressway Company Group (NEXCO), and other organizations have strengthened the descriptions of drainage measures in their technical standards, referring to the stability of embankments against rainfall and groundwater action, and the Embankment Regulation Law came into effect in May 2023.

It is well known that the stability of embankments is affected by rising groundwater levels, for which groundwater drainage works are often a promising countermeasure. Therefore, it is important to vertically determine the location of groundwater flow that affects slope stability.

Vertical groundwater logging, developed by Watari [5], is a typical method for obtaining vertical groundwater information. This method developed by Watari replaces the water in the borehole with brine electrolyte and detects the groundwater flow section from the increase in water resistivity due to groundwater inflow into the borehole. This method provides valuable data when the borehole water level is present in the borehole, but it cannot detect groundwater flow zones when groundwater is not present, such as when testing during a drought.

As a method to improve this point, Shin [6] proposed "staged pumping logging," in which borehole water is pumped up using a baler or the like to perform logging. In this method, drilling is temporarily stopped at any depth and groundwater logging is performed by diluting the salinity. Although the information obtained is valuable, it has the disadvantage of requiring a lot of time and money.

To solve this problem, Takeuchi [7] developed multi-point temperature logging as a method to obtain information on groundwater flow layers regardless of the presence or absence of the water table in the borehole. The main feature of this logging method is that it can provide information on the groundwater flow layer below the borehole water table even when the water table in the borehole is extremely low.

Multi-point temperature logging has been used for landslides and other mountain ground disasters, and for well logging during large-scale underground excavations. Multi-point temperature logging has been used in various fields, such as landslides and other mountain ground disasters, well failures, and abnormal groundwater inflow caused by large-scale underground excavation, groundwater contamination, and leaks in river embankments.

In this study, we report the results of the investigation to confirm the groundwater availability in high embankments and discuss the optimal measures for slope stability based on the investigation results.

Fig. 1 Theory of multi-point temperature logging
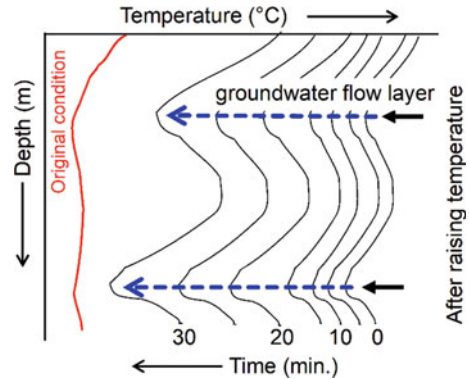
2 Theory and Method of Multi-point Temperature Logging

2.1 Theory of Multi-point Temperature Logging

The principle of multi-point temperature logging is as follows.

First, the temperature at all depths in the borehole (air above the borehole water level and groundwater below the water level) is made nearly uniform under natural conditions by injecting hot water into the borehole (Fig. 1).

If there is a groundwater flow layer at a certain depth, the temperature at that point will quickly return to the natural temperature before the temperature rises due to groundwater inflow.

In the absence of a fluidized bed, the temperature is expected to gradually return to the temperature before the temperature rises by heat conduction.

Therefore, by measuring the temperature recovery over time at each depth, it is possible to obtain information about the depth and thickness of the groundwater flow layer and its relative infiltration rate.

2.2 Method of Measurement

The following procedure was used for multi-point temperature logging (Fig. 2).

1. The borehole temperature was measured under natural conditions.
2. Hot water was pumped into the borehole through a high-pressure hose to keep the temperature in the borehole as constant as possible.
3. The temperature measurement inside the borehole was started when the temperature inside the borehole increased uniformly. Measurements were then taken every minute from 1 to 7 min and every 5 min from 10 to 30 min.
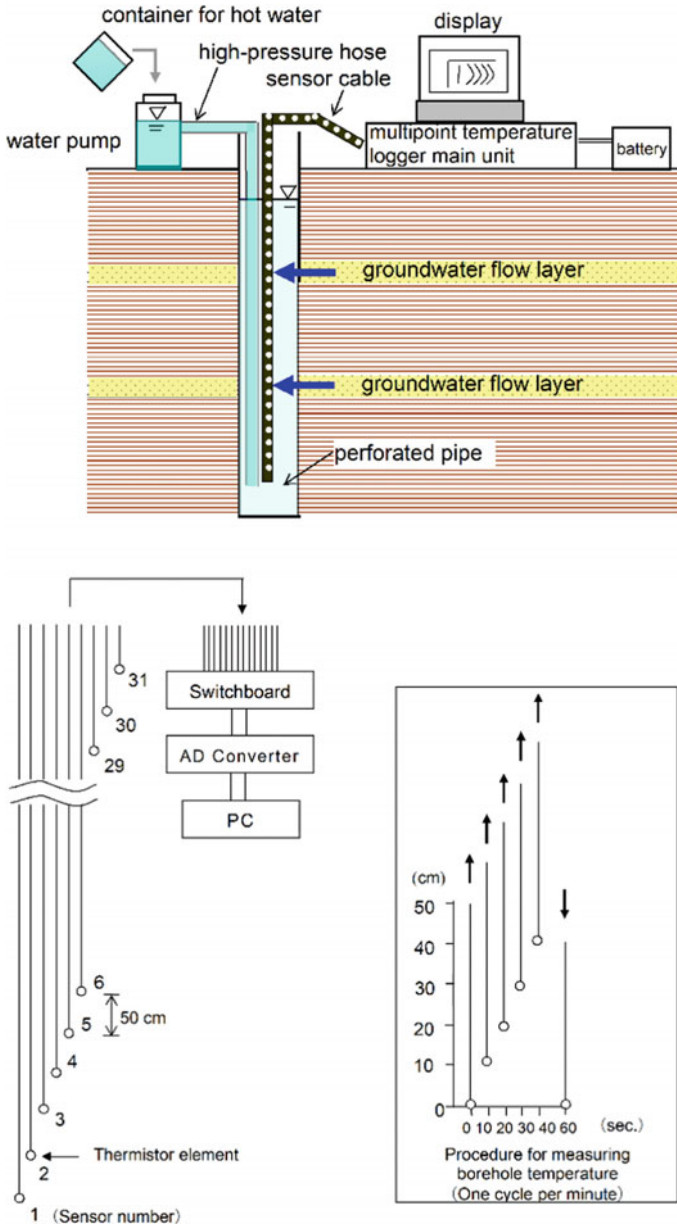
Fig. 2 Overview of multi-point temperature logging systems

2.3 Method for Detecting Groundwater Flow Beds

The results of multi-point temperature logging are expressed as a "temperature-depth curve" (Fig. 1).

Information on the depth of the groundwater flow layer was obtained by reading the point of large temperature recovery from the temperature curve in the natural state and the temperature curve at any given time after the temperature in the borehole was increased.

The "temperature recovery rate—depth curve" was then plotted, and the groundwater flow layer was determined from the magnitude of the temperature recovery rate.

The "temperature recovery rate" is calculated by the following equation.

$$\frac{(\text{Temperature at 0 min.}) - (\text{Temperature at any elapsed time})}{(\text{Temperature at 0 min.}) - (\text{Temperature in natural condition})} \times 100\,(\%)$$

When determining the groundwater flow layer, if the groundwater flow is very slow, the temperature diffusivity of the water is the criterion for determining the groundwater flow layer. In this case, the temperature recovery rate at the time of measurement 30 min after the start of observation was about 60% (50 mm diameter perforated pipe), and therefore the groundwater flow layer was determined at the location where the temperature recovery rate was greater than this. The groundwater flow with a flow velocity of about $1 \times 10\text{–}5$ m/s or higher was considered to be a fluidized bed. The groundwater flow area below the water level in the borehole was determined to be the area where the groundwater flowed out based on our previous experience and the area where the recovery rate was greater than 80%.

3 Results of Multi-point Temperature Logging

3.1 Observation Hole Specifications

The principle of multi-point temperature logging is as.

The boreholes used for logging were drilled in the center of the valley topography. The specifications of each borehole are as follows. The depth of observation hole No. 1 is 33 m. The natural water table is at GL.-15.90 m. The depth of observation hole No. 2 is 30 m. The natural water level is at GL.-20.23 m.

3.2 Results of Multi-point Temperature Logging

The logging results for each borehole are expressed as a "temperature-depth curve" and a "temperature recovery rate-depth curve" (Figs. 3 and 4). The "temperature-depth curve" indicates the situation where the elevated borehole temperature returns to its natural state, and the "temperature recovery rate-depth curve" indicates the depth to which groundwater leaching points or groundwater flow layers exist.

The temperature recovery rate-depth curve was used to determine the depth at which groundwater leached or flowed into the borehole. The evaluation of the recovery rate in the interval shallower than the water table in the borehole is based on the respective conditions, because at this stage it is not possible to simply compare the recovery rate with that in the interval deeper than the water table in the borehole.

In observation borehole No. 1, the water level in the borehole was observed around GL-15.90 m. Figure 3 shows that after 30 min of measurement time, the temperature recovery rate of more than 80% was observed between GL-5.0 m and GL-16.0 m below the water level in the borehole. It is concluded that there is a significant groundwater leaching phenomenon in this area. Geologically, the embankment is composed of sandy soil with an N value of about 1.

In observation borehole No. 2, the water level in the borehole was observed at a depth of about GL-20.23 m. After 30 min of measurement, the temperature recovery rate of more than 80% was not observed below the water level in the borehole, but more than 60% was observed at GL-13.0 m, GL-16.0 m, and GL-19.0 m. It can be concluded that there is rather weak groundwater leaching in these areas. Geologically, the dam is composed of sandy and clay soils with N values ranging from 10 to 16.
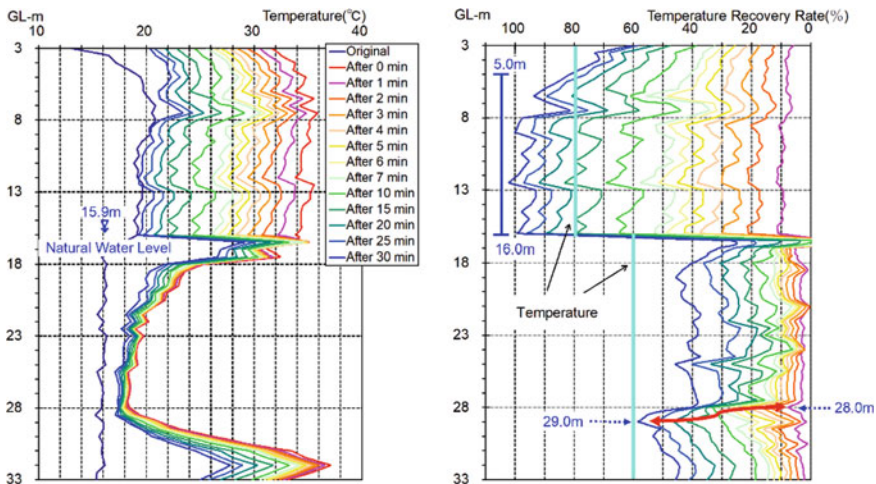

Fig. 3 Logging results for the observation hole No. 1 are expressed as a "temperature-depth curve" and a "temperature recovery rate-depth curve"
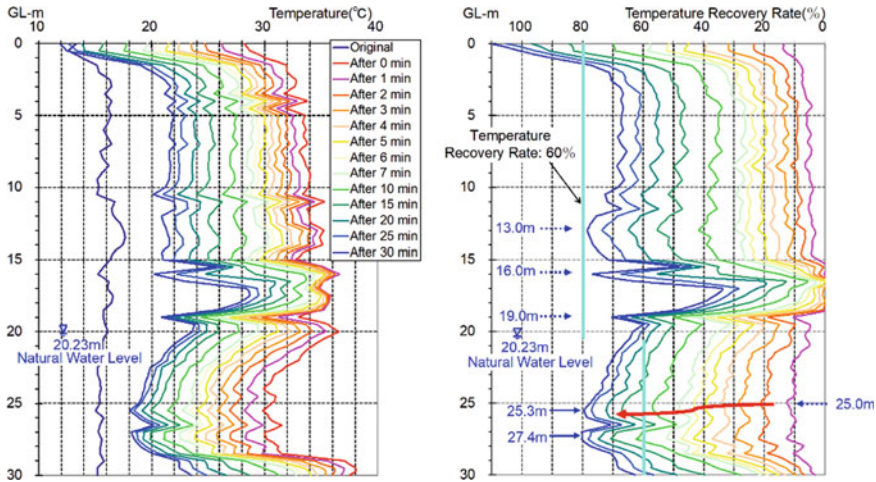
Fig. 4 Logging results for the observation hole No. 2 are expressed as a "temperature-depth curve" and a "temperature recovery rate-depth curve"

At depths below the borehole water table, temperature recovery of more than 60% is observed at GL-25.5 m and GL-27.4 m. The presence of a thin groundwater flow layer is inferred in these areas. Geologically, these intervals are clay embankments and the N value is 3 in small areas.

4 Summary and Discussion

The results of the logging indicate the following.

In observation hole No. 1, an interval of thick groundwater intrusion with a thickness of approximately 11 m was detected.

In observation hole No. 2, three weak groundwater leaching intervals and two groundwater flow zones were detected.

Based on the results of these logging investigations, the following drainage measures are recommended.

Construct a group of lateral drainage wells to eliminate groundwater in the area of GL.5 to GL.16 m.

In order to effectively eliminate groundwater flowing down the old valley, a collection well should be constructed to reach the ground level and a group of drainage boreholes should be constructed from the well to the old valley line.

Although multi-point temperature logging is a nearly 30-year-old logging method, it has proven to be effective in obtaining groundwater information in high embankments. Unlike other groundwater logging methods, this method is environmentally friendly and should be re-evaluated to achieve the SDGs.

References

1. Kataoka S, Nagaya K, Matsumoto K (2015) Analysis on damage to road embankments caused by the Mid Niigata Prefesture Earthquake in 2004. Japan J. JSCE A1 71(4):568–576. (in Japanese with English abstract)
2. Takekuni K, Hada J, Nakata Y (2018) Field Measurement of groundwater and surface water flows at embankments, and effectiveness verification of drainage facility. Japan J JSCE C 74(3):289–299. (in Japanese with English abstract)
3. Mori T, Tobita Y, Okimura T (2012) Damages of hillside embankments in Sendai City during The 2011 off the Pacific coast of Tohoku Earthquake. Soils Found 52(5):910–928
4. Chigira M, Kitamura A, Kimura K, Ichimura K (2022) Geological causes of the landslide of an embankment at the Aizome River. Atami Geosci Repts Shizuoka Univ (49):45–59. (in Japanese with English abstract)
5. Watari M, Sakai A (1965) Groundwater in landslide areas and its investigation. J Japan Landslide Soc 12(1):1–9 (1965). (in Japanese)
6. Shin YS (1976) On the "groundwater" logging serial No.1: discussions and theoretical approach thereto. J Japan Landslide Soc 13(3):16–21. (in Japanese with English abstract)
7. Takeuchi A (1996) Method for investigating flowing groundwater by temperature measurement. Kokon Shoin, Tokyo, p 480. (in Japanese)

Effect of Groundwater Filtering on Clogging of Recharge Well

Hidehiko Hayashi [ID]**, Akira Ishikawa** [ID]**, and Nobuaki Kohsaka** [ID]

Abstract At the construction site for a rainwater storage facility in Niiza City, Saitama Prefecture, the plan includes recharge groundwater into wells outside the excavation area in order to prevent subsidence in the surrounding residential areas. This paper reports on the application of a pumped filtration system for groundwater that is to be injected into recharge wells as a method to reduce clogging. Five recharge wells were constructed, three of which were recharged with filtered groundwater and two with untreated groundwater. After continuously injecting groundwater at a constant rate for about six months, the injection efficiency of the three wells recharged with treated water remained almost unchanged. On the other hand, the two wells recharged with untreated water were more severely clogged, with efficiency dropping by about 10% or less of the initial level. During the construction work, the groundwater level in an observation well outside the excavation area remained unchanged and no land subsidence was observed.

Keywords Recharge · Groundwater · Clogging

1 Background

In Niiza City, Saitama Prefecture, from 2018 to 2020, as part of a 49.5 hectares land readjustment project, an underground reservoir was constructed to temporarily store 16,500 m^3 of rainwater [1] as shown in Picture 1.

The groundwater level at the site was about 1 m below the surface and groundwater pumping was necessary during underground excavation. Subsidence can occur due to the increase in the effective stress when the groundwater level is lowered [2]. In order to prevent subsidence of the surrounding ground due to the lowering of the water level, we planned to return the pumped groundwater to the ground outside an impermeable wall. The technical challenge at that time was to ensure long-term

H. Hayashi (✉) · A. Ishikawa · N. Kohsaka
Shimizu Corporation, 2-16-1 Kyobashi, Chuo-Ku Tokyo 104-8370, Japan
e-mail: hide.h@shimz.co.jp

Picture 1 Underground reservoir under construction in 2019

water injection performance throughout the construction period. To evaluate a long-term stable recharge system, it is necessary to understand the amount of water to be injected, groundwater level, the water quality (chemical, physical, and biota), and the total suspended solids (SS) [3].

Five recharge wells were installed on site, three of which were recharged through a special filtration system [4], and two of which were filled directly from deep pumping wells. This paper reports on the long-term groundwater recharge performance of the two methods by comparing their water injection capacities.

2   Site Information

2.1   Construction Site Location

Figure 1 shows the location of Niiza City on a map. It lies on the border of Saitama Prefecture and Tokyo Metropolitan area. The construction site is close to the Yanase River, a tributary of the Arakawa River that flows from eastern Saitama Prefecture into Tokyo Bay. The topographic map shows that the elevation of the construction site is about T.P. + 12.1 m and the highest point on the surrounding land is T.P. + 25 m. From this, it can be understood that rainfall in the surrounding area can be stored in this storage reservoir.

Figure 2 shows a geological profile of the site. Down to T.P + 5 m, the layering consists of a buried soil layer (B), an alluvial gravel layer (Ag), and an alluvial clay layer (Ac). This alluvial clay layer (Ac) contains organic matter in some places. In particular, there were concerns that land subsidence due to lower groundwater levels might affect private houses and a national road to the north and east of the planned construction site. A pleistocene clay-mixed gravel layer (Dg) and a clay-mixed sand layer (Ds) are present under the Ac layer.
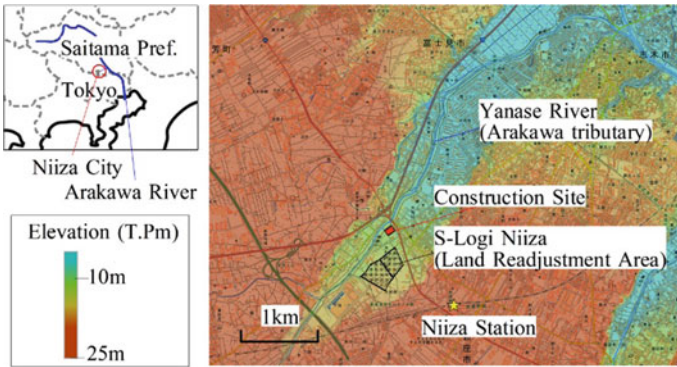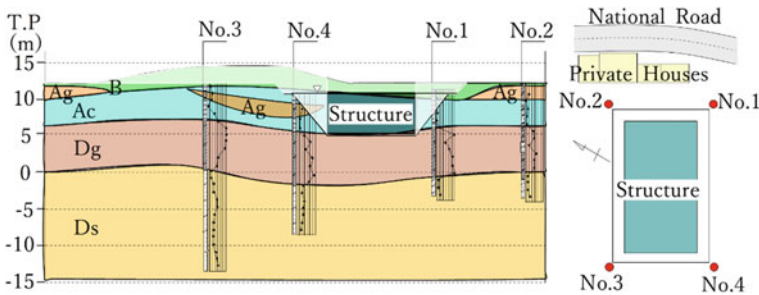
Fig. 1 Construction site location

Fig. 2 Geological section of the construction site

2.2 Design of Groundwater Treatment System

Figure 3 shows a cross section of the underground reservoir and the excavation plan. In order to minimize effects on the surrounding groundwater level, a cutoff wall with a height of $L = 15.5$ to 17.0 m was installed to reach into the Ds layer. Groundwater within the cutoff wall was pumped up from deep wells.

With the impermeable wall reaching down into the Ds layer, the hydraulic conductivity of this layer determines whether or not groundwater pumping within the impermeable wall affects the groundwater level outside.

Figure 4 shows the grain size distribution curves and the hydraulic conductivity profile of the Ds layer, which contains 5–17 wt% clay with a particle diameter of less than $d < 5$ μm. Its hydraulic conductivity varies widely from 4.9×10^{-8} m/s to 1.4×10^{-5} m/s. For the semi-3D seepage analysis, the hydraulic conductivity was set as shown by the blue line in the figure. The hydraulic conductivity of the Ds layer was set to 6.0×10^{-6} m/s.

Figure 5 shows the results of the seepage analysis. Without groundwater recharge, the water level under some private houses and national roads to the north and west
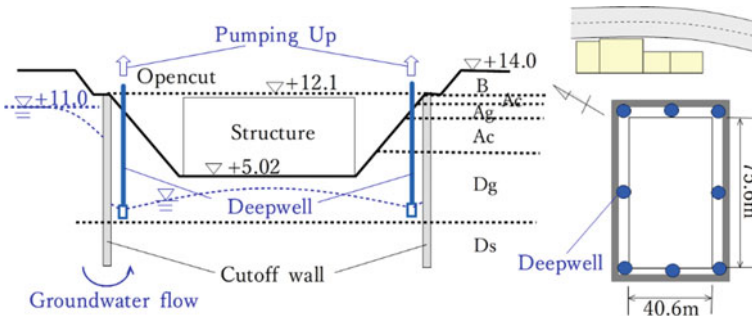
Fig. 3 Cross section of underground reservoir and excavation plan
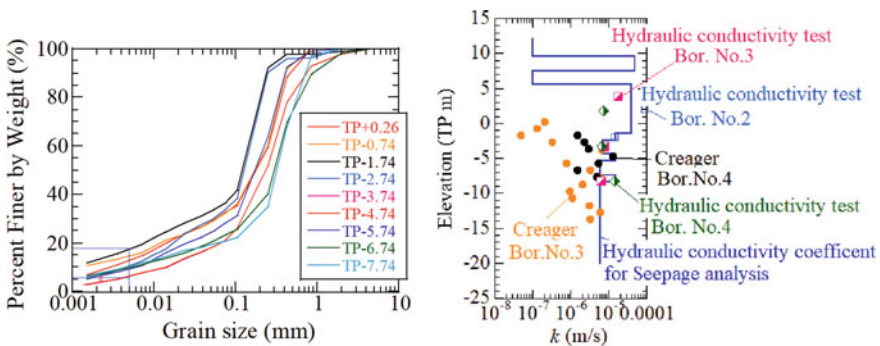
Fig. 4 Grain-size distribution curves and hydraulic conductivity profile

would drop by about 2 m. On the other hand, with groundwater recharge, the water level here would be maintained. Based on these numerical results, we decided to recharge the ground through five recharge wells.

Figure 6 gives details of the construction site recharge system. Groundwater was pumped out through deep wells DW2-7 and transferred to the first tank via the green pipeline. After passing through a second tank and a special filtering device, the treated or filtered groundwater was sent through the purple line to recharge wells RW1-3. On the other hand, DW1 and DW8 pumped groundwater and transferred it directly to RW4 and RW5 via the blue line. DW9 was not in operation and was treated as a groundwater observation well designated W-IN. Well W-OUT between RW4 and RW5 acted as a groundwater level observation well outside the cutoff wall. For backwashing, a pump was installed in each recharge well and the backwashed water was discharged through the light blue line.

Fig. 5 Contour levels of groundwater with and without recharge

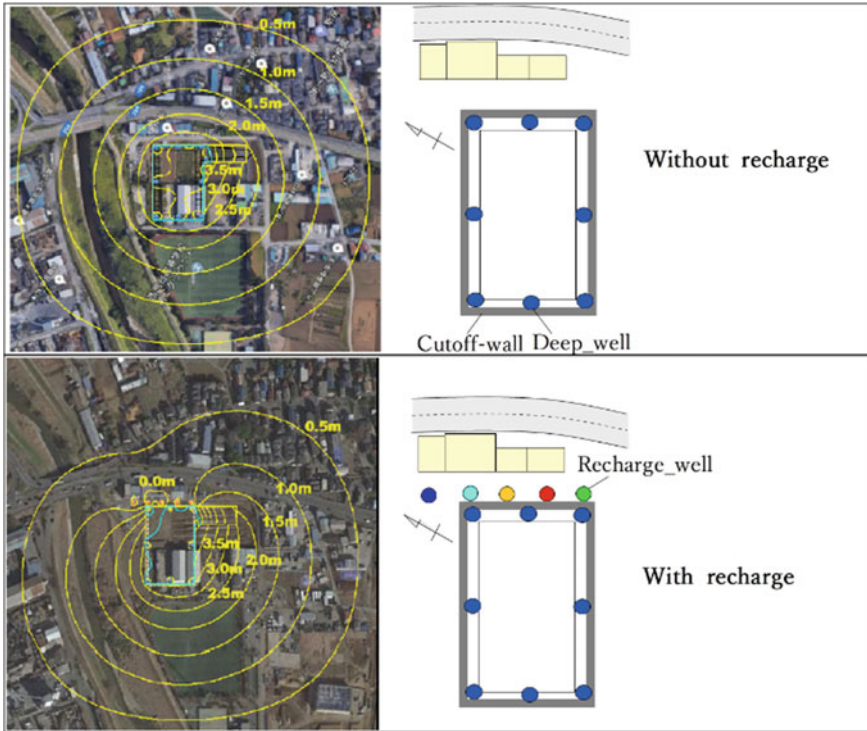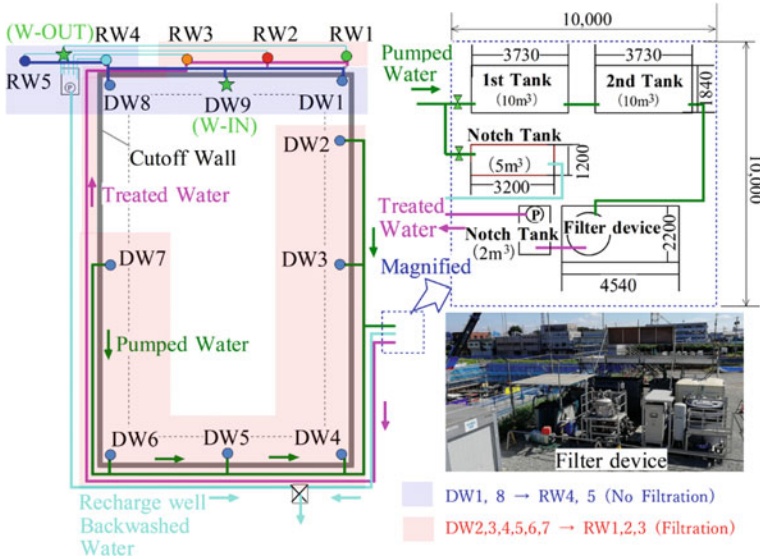

Fig. 6 Site recharge system

3 Recharge Results

Groundwater recharge began in late February 2019. The recharge rate, discharge and water level in the recharge wells, and the water level in the W-IN and W-OUT were measured every 10 min.

Table 1 shows measured groundwater (PW) and treated water (TW) quality. The main substances that cause clogging during groundwater recharge are said to be soil particles and iron oxides. These are represented by items such as Turbidity, SS, total iron (T-Fe), or dissolved iron (D-Fe) in the table. Compared with the raw pumped groundwater, values for the treated water were very low or below detection limits, showing that the filtration system was effective in eliminating these substances.

Figure 7 shows the recharge rate of each recharge well. To prevent drawdown of external groundwater, the injection rate for each well was required to be 50 L/min. RW1-3 were able to maintain this quantity all the time, while RW4 and 5 fluctuated in early March and July–September. These fluctuations were caused by air in the pipeline and are very difficult to avoid when piping directly from DW to RW.

Figure 8 shows the water level measurements of each recharge well. The numbers in the graphs represent the number of backwashes from the start of recharging. The backwash method was very simple; water was just pumped out from a recharge well for 1–2 h. It can be seen that RW1-3 were able to maintain operation with a backwash interval of about 1–2 months. On the other hand, RW4 and 5 required more frequent backwashing over time. The timing of the first backwash was 1.5 months after the

Table 1 Measured groundwater quality

| Inspection item	Unit	Sep. 5th, 2018	Feb. 12nd,2019		Apr. 16th, 2019		Sep. 15th, 2019	
		PW	PW	TW	PW	TW	PW	TW
Turbidity	FTU	2.32	6.66	0.00	0.06	0.00	–	–
pH	–	6.4	7.2	7.6	7.0	7.0	–	–
EC	mS/m	22.6	20.8	20.6	20.7	20.7	–	–
TC	mg/L	45.8	30.4	25.4	28.9	28.9	–	–
IC	mg/L	46.2	29.9	29.9	28.1	28.1	–	–
TOC	mg/L	− 0.4	0.4	0.5	0.9	0.9	–	–
SS	mg/L	2.6	17	< 1	< 1	< 1	0.63	0.09
T-FE	mg/L	0.42	0.7	< 0.05	< 0.05	< 0.05	0.07	0.03
D-Fe	mg/L	–	–	–	–	–	0.05	0.03
T-M	mg/L	0.1	0.56	0.44	0.18	0.17	0.18	0.16
D-Mn	mg/L	–	–	–	–	–	0.19	0.16
T-N	mg/L	–	3.1	0.92	0.76	0.69	–	–
T-P	mg/L	–	0.042	0.025	0.011	< 0.01	0.19	0.16
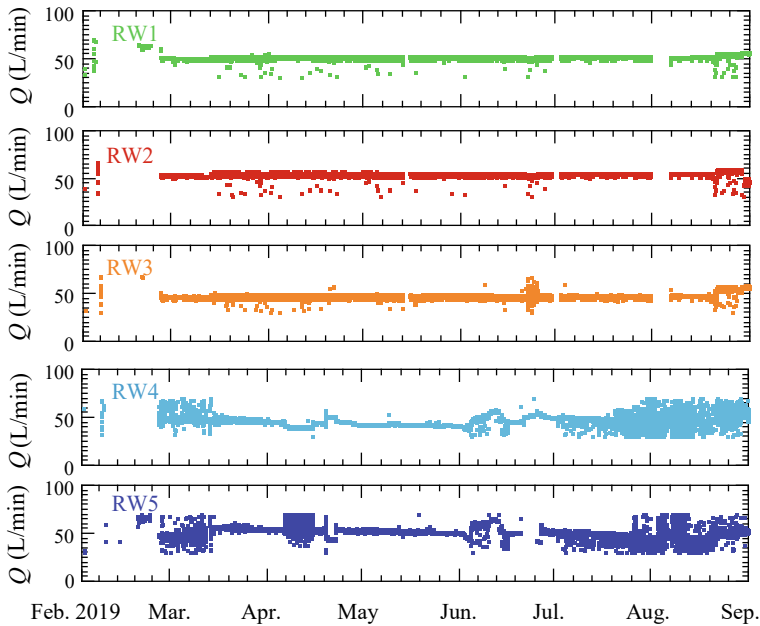
Fig. 7 Recharge flow rate of each recharge well

start of recharging, but after the second and third backwashing, the interval was reduced to just a few days.

Figure 9 shows how the water level rise rate of the recharge wells changed over time. This represents the degree of clogging of the wells or the surrounding soil layers; the groundwater would remain at a constant steady-state level if there were no clogging. The level rise in RW4 and 5 exceeded 0.1 m/day about 3 months from the start of recharging and clogging progressed thereafter. On the other hand, RW1-3 never exceeded 0.1 m/day. Their original recharge capacity was maintained.

The logarithm of the level rise rate normalized by the value of water level rise rate up to the first backwash is plotted on the vertical axis of Fig. 10. This normalizes the results by the initial performance of each well. From this figure, we can see that RW4 and 5 reached several times to 10 times the original rise rate. The wells became clogged, and the recharge capacity fell to approximately 10% of the original value.

For RW1-3, the normalized rise rate doubled in late August. However, from Fig. 7, it can be seen that the increase in recharge flow during this period affected the water level rise rate. Throughout the remainder of the recharge period, the normalized rise rate remained below 2, meaning that RW1-3 maintained their original recharge capacities.
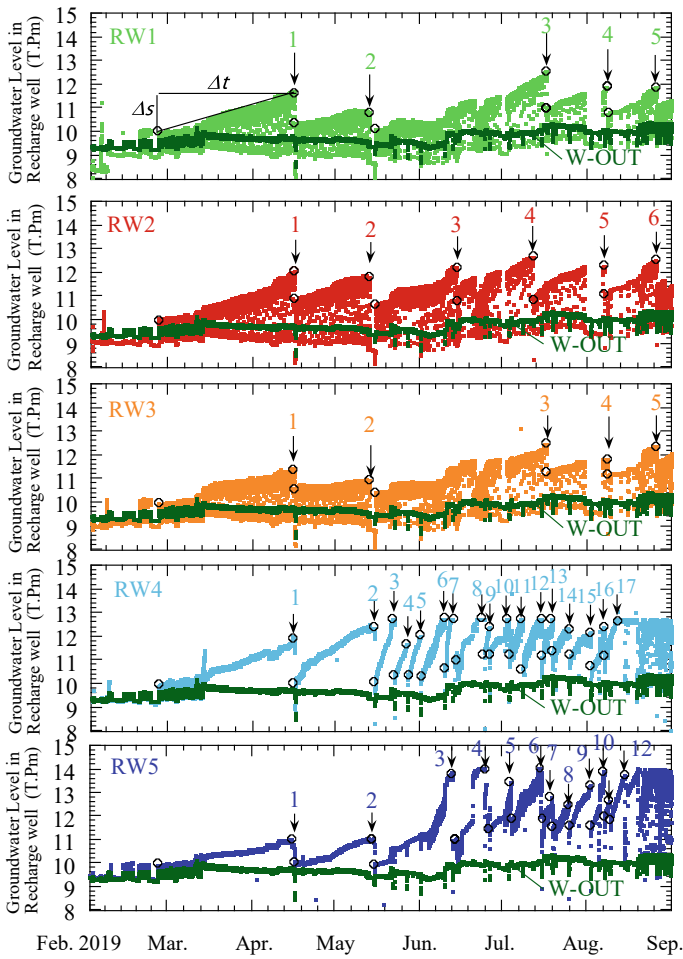
Fig. 8 Water level inside each recharge well

Fig. 9 Water level rise rate of recharge wells as proxy for the degree of clogging
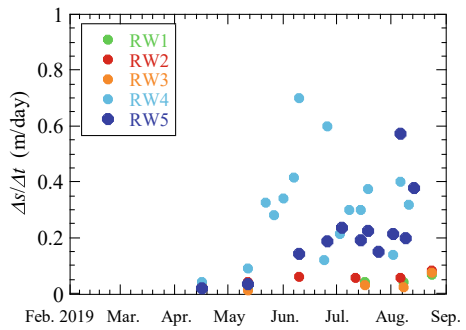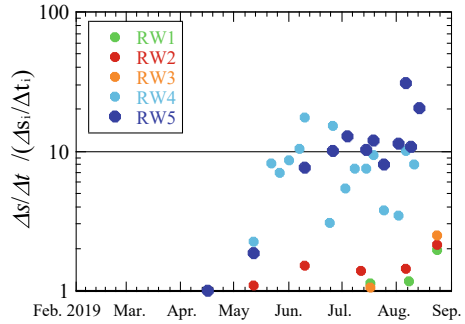
Fig. 10 Normalized water level rise rate of recharge wells

4 Conclusion

This paper reports on the field application of a pumped groundwater filtration system as a method to reduce clogging when injecting groundwater into recharge wells. The following are the conclusions obtained from the field data.

- In the treated groundwater, values of turbidity, SS, T-Fe, and D-Fe, which indicate the presence of clogging substances, were very low or below detection limits. The filtration system was effective in eliminating these substances.
- Three recharge wells fed with filtered groundwater were able to maintain the required recharge flow rate of 50 L/min throughout the measurement period, while two wells recharged without filtration saw fluctuating flow rates. These fluctuations were caused by the air in the pipeline, resulting from the direct connection of feed pipes to the recharge wells.
- The three recharge wells fed with filtered groundwater maintained a recharge rate close to the initial rate after continuous injection at a constant rate for about six months.
- The two wells recharged with untreated water had more severe clogging and the recharge rate dropped to 10% of the initial level or less.
- The groundwater level in the observation well outside the excavation area remained unchanged from before construction began as a result of groundwater recharge, as shown in Fig. 11. No ground subsidence was observed around the site.

Although treated groundwater was very clear and contained almost no clogging substances, some rise in water level in the recharge wells was attributed to clogging. The mechanism of clogging is very complicated, so the reason for this needs to be clarified in future work.
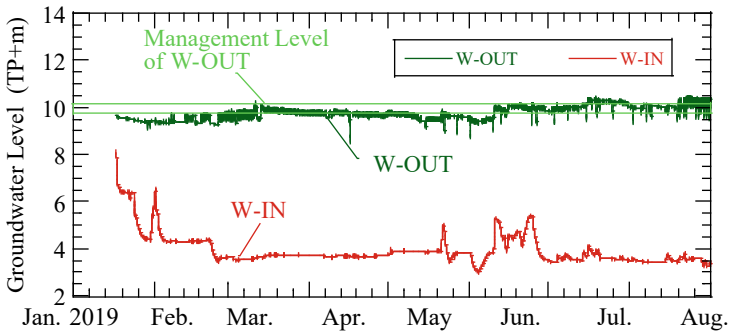
Fig. 11 Groundwater level within and outside site during construction

References

1. Ohkawado N, Kohsaka N, Minagawa K, Iida Y (2020) Countermeasures to control water level drop in surrounding area due to excavation in underground water tank construction (In Japanese). In: Proceeding o Japan Society of Civil Engineers 2020 Annual Meeting, vol 75, VI-1022. Japan Society of Civil Engineers, Online (2020)
2. Lofgren BE, Klausing RL (1969) Land subsidence due to ground-water withdrawal, Tulare-Wasco area, California. U.S. Geological Survey professional paper 437-B
3. Price D, Hart DH, Foxworthy BL (1965) Artificial recharge in Oregon and Washington, 1962. Geological survey water-supply paper 1594-C
4. Ishikawa A, Serizawa S, Hayashi H, Tasaki M, Yoda Y (2017) Ground return of pumping groundwater using spring-type filtering system (In Japanese). In: Proceeding of the 23rd symposium on soil and groundwater contamination and remediation, vol 23, S1–31. Japanese Association of Groundwater Hydrology, Okinawa, Japan

Infiltration Depth Prediction Model Considering Soil Properties and Rainfall Conditions for Aeolian Sand Subgrade

Xintong Song, Yaqi Zhang, Pengcheng Wang, Li Zhang, and Peng Jing

Abstract Aeolian sand serves as the primary filling material for highway and railway in the desert area of Inner Mongolia, China. Usually, aeolian sand subgrade is stable in the natural state. Nevertheless, the infiltration caused by rainfall events disrupts the original balance within the subgrade. The hydraulic properties of aeolian sand subgrade change substantially in a short period, which results in a decrease in shear strength and subsequent deformation or landslide of the subgrade. Based on the analysis of soil properties and structural characteristics of aeolian sand subgrade, a prediction model for rainfall infiltration depth considering soil properties and rainfall levels of aeolian sand subgrade was proposed based on the linear approach of soil water characteristic curves (SWCCs). This study further used the aforementioned prediction model to predict the infiltration depth of aeolian sand with three different dry densities under an extreme rainfall event and compared it with numerical simulation results to verify the applicability of the prediction model. This study can provide a theoretical basis for the study of the hydraulic behavior of aeolian sand subgrade soil.

Keywords Aeolian sand · Soil properties · Soil water characteristic curves · Rainfall infiltration depth

X. Song · Y. Zhang · P. Jing (✉)
Beijing University of Technology, Beijing, China
e-mail: peng.jing@bjut.edu.cn

P. Wang
Railway Engineering Research Institute, China Academy of Railway Sciences Corporation Limited, Beijing, China

L. Zhang
Baotou Railway Vocational & Technical College, Baotou, Inner Mongolia, China

1   Introduction

Unsaturated aeolian sand is a usual filling material for subgrade in Inner Mongolia, China, characterized by its uniform grain size distribution, small particles, low natural volumetric water content as well as poor water retention ability [1]. Aeolian sand subgrade is usually stable in the dry state. However, the hydraulic characteristics of the aeolian sand subgrade change significantly suffering the rainfall events, which reduces the shear strength and further leads to the decrease of subgrade stability. Numerous researches [2–4] on aeolian sand have supported this view. Therefore, clarifying the effect of rainfall infiltration on the hydraulic characteristics of aeolian sand is an essential prerequisite for understanding the deformation behavior and mechanism analysis of aeolian sand subgrade under rainfall conditions.

In this paper, based on the analysis of the soil properties and hydraulic features of aeolian sand, a prediction model of rainfall infiltration depth considering soil properties and rainfall conditions for aeolian sand subgrade is proposed by establishing the relationships between basic soil properties and parameters of the unique SWCC equations and the relationships between soil water characteristics and rainfall infiltration depth. The applicability of the prediction model is verified through numerical simulation.

2   Model Formulation

2.1   *Soil Water Characteristic Curves (SWCCs) of Aeolian Sand*

Due to the unique material properties, structural characteristics of aeolian sand subgrade and the special climate environment of desert arid regions, the variation of moisture content/saturation and suction of aeolian sand subgrade is significant under the influence of rainfall events, especially subjected to different rainfall conditions and soil properties of subgrade material. It can be well described by the soil water characteristic curve (SWCC). Additionally, dry density significantly affects SWCCs of aeolian sand owing to special grading composition.

Figure 1 presents the SWCCs [5] of aeolian sand with three different dry densities. It can be concluded that with an increase in dry density, the matric suction at the same volumetric water content increases correspondingly. For this phenomenon, Zhang et al. [5] explained that with the increase of compaction or dry density, aeolian sand is in a dense state with a small pore volume, making it difficult for moisture to be discharged [5].

Van Genuchten model [6] and a linear approach of SWCCs proposed by Jing and Nowamooz [7] were used to fit the experimental data of SWCCs for aeolian sand with different dry densities. VG model equation is as follows:

Fig. 1 SWCCs of aeolian sand with three different initial dry densities [5]
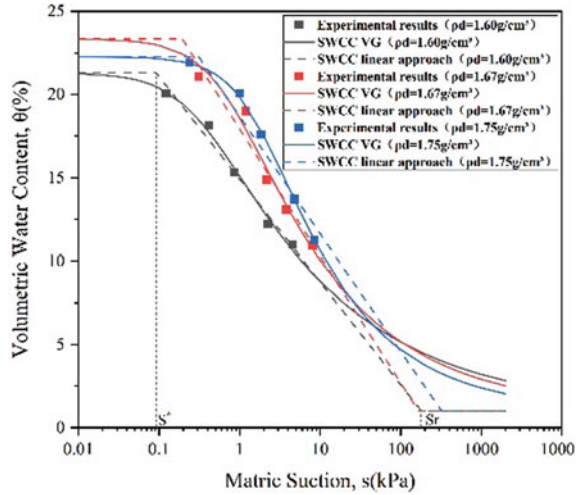
$$\theta = \theta + ((\theta s - \theta r))/(1 + (\alpha s)^\wedge n)^\wedge m, \tag{1}$$

where θ is volumetric water content; θr is residual volumetric water content; θs is saturated volumetric water content; s is suction; α is the parameter related to the air-entry suction; m, n are parameters with the relationship $m = 1 - 1/n$.

The linear method divides the SWCCs into three parts by the limited suction values S^* and Sr and simplifies each part into a linear phase. Each linear phase is expressed as [7]:

$$\theta = \theta s \,(\text{for } s \leq s^*) \tag{2}$$

$$(\theta/\theta s) = -\gamma \ln(s/s^* + 1\,(\text{for } (s^*) \leq s \leq (sr)) \tag{3}$$

$$\theta = \theta r \,(\text{for } s \geq (sr)) \tag{4}$$

with

$$(sr) = (s^*) \exp((1 - \theta r/\theta s)/\gamma), \tag{5}$$

where θ is volumetric water content; s is suction; θs is the saturated water content, θr is the residual water content; γ and s^* are parameters; sr is the residual suction.

As shown by the fitting parameters presented in Tables 1 and 2, both fitting methods demonstrate good applicability for aeolian sand. SWCCs are also shown in Fig. 1.

It can be seen from the fitting results that the air-entry suction and saturated volume moisture content of aeolian sand are relatively low and the slope of the transition

Table 1 VG model parameters for aeolian sand

Dry density (g/cm^3)	θs (%)	θr (%)	α	n	m	R^2
1.6	21.30	1	3.230	1.275	0.215	0.99
1.67	23.34	1	1.405	1.339	0.253	0.96
1.75	22.27	1	0.616	1.424	0.298	0.99

Table 2 Parameters of linear approach of SWCCs for aeolian sand

Dry density (g/cm^3)	θs (%)	θr (%)	γ	s^*	sr	R^2
1.6	21.30	1	0.126	0.092	180.451	0.97
1.67	23.34	1	0.142	0.194	166.654	0.94
1.75	22.27	1	0.138	0.310	321.897	0.94

segment of SWCC is large. It means that the water retention capacity of aeolian sand subgrade is poor and the variation of hydraulic characteristics will rapidly enter into transition segment under rainfall events, causing a rapid decrease in suction.

2.2 Normalized SWCCs Equations Considering Soil Properties

Several researches indicated that soil properties have an important effect on SWCCs of subgrade soils. Some analytical model of SWCCs using soil properties can also be found in the literatures [8–10].

In this context, based on the analysis of the meaning represented by the fitting parameters of linear approach of SWCCs and the relationship between soil properties and SWCC proposed by Jing et al. [11], it is assumed that the fine content (FC) can be correlated with the parameter s^*, the slope parameter (δ_G) of grain size distribution (GSD) introduced by Chai and Khaimook [8] is corresponded to parameter γ and the dry density have a decisive influence on saturated water content according to models proposed in the literatures and the three-phase system theory of soils.

Linear approach method is used to fit the SWCCs (Fig. 2) of tailing sand with different FC and dry density measured by Liu and Wen [12], the fitting parameters are reported in Table 3. Furthermore, the following functional relationships between soil properties and linear fitting parameters are proposed (Fig. 3):

$$s^* = A_1 \ln(FC) + B_1 \tag{6}$$

$$\gamma = [\delta_G^\wedge(A_2)]B_2 \tag{7}$$
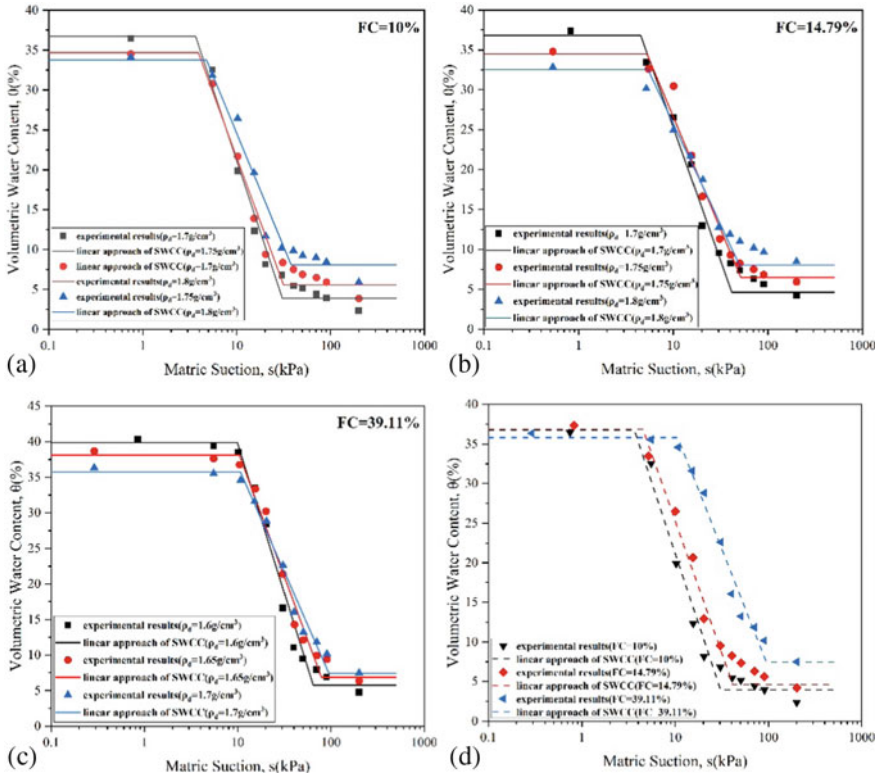
Fig. 2 SWCCs **a** of medium tailing sand; **b** of fine tailing sand; **c** of silty tailing sand; **d** with different fine content

$$\theta s = A_3 \rho_d + B_3 \tag{8}$$

where s^*, γ, and θs are parameters of linear approach of SWCCs; FC is fine content; δ_G is the slope of grain size distribution (GSD); ρ_d is dry density; A_1, B_1, A_2, B_2, A_3, and B_3 are fitting parameters.

Substituting Eq. (6–8) into linear approach of SWCCs can obtain the normalized SWCCs equations considering soil properties:

$$\theta = \theta s \, (\text{for } s \le s^*) \tag{9}$$

$$(\theta / \theta s) = -\gamma \ln(s / s^* + 1 \, (\text{for}(s^*) \le s \le (sr))) \tag{10}$$

$$\theta = \theta r \, (\text{for } s \ge (sr)) \tag{11}$$

Table 3 Parameters of linear approach of SWCCs for tailing sand

Name	Fine content (%)	δ_G	Dry density (g/cm³)	θs (%)	s^*	γ
Medium tailing sand	10	5.9	1.7	36.73	3.6478	0.4202
			1.75	34.68	3.9115	0.4027
			1.8	33.79	4.7590	0.3665
Fine tailing sand	14.79	5.5	1.7	36.83	4.5218	0.3953
			1.75	34.51	5.2627	0.3562
			1.8	32.56	5.3894	0.3390
Silty tailing sand	39.11	3.9	1.6	39.87	9.9386	0.4582
			1.65	38.13	10.4210	0.4053
			1.7	35.78	10.6846	0.3630
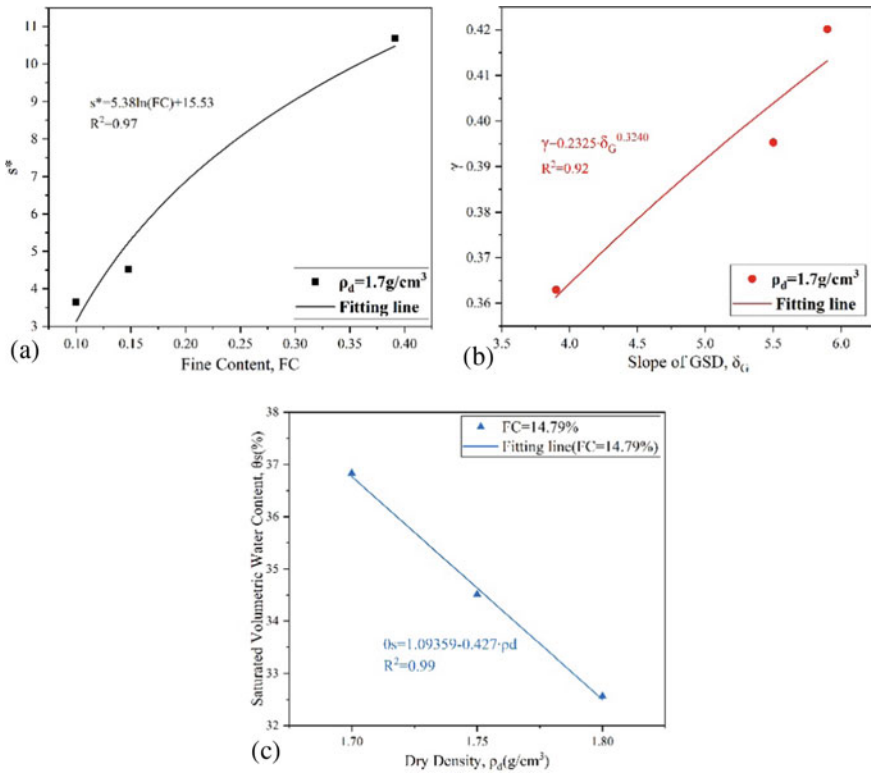
Fig. 3 Relationship between parameters of linear approach and soil properties: **a** s^* versus FC; **b** γ versus δ_G; **c** θs versus ρ_d

with

$$s^* = A_1 \ln(\text{FC}) + B_1 \tag{12}$$

$$\gamma = [\delta_G^\wedge(A_2)]B_2 \tag{13}$$

$$\theta s = A_3 \rho_d + B_3, \tag{14}$$

where A_1, B_1, A_2, B_2, A_3 and B_3 are fitting parameters.

2.3 Infiltration Depth Prediction Model

In addition to the basic soil properties of aeolian sand, rainfall condition is another decisive factor affecting the hydraulic behavior of aeolian sand subgrade under rainfall events. Therefore, based on the experimental results presented by Liu [13], this study proposes the relationship between maximum infiltration depth with rainfall intensity and rainfall duration. Furthermore, combined with the normalized SWCC parameters mentioned above, a prediction model for rainfall infiltration depth is proposed.

Table 4 presents the infiltration depths of tailing sand under different rainfall conditions reported by Liu et al. [13].

Through analyzing the experimental results of tailing sand, there exist linear and logarithmic relationships between the maximum infiltration depth (h_d) with rainfall intensity (R) and duration (t), respectively:

Table 4 Infiltration depth results of tailing sand [12]

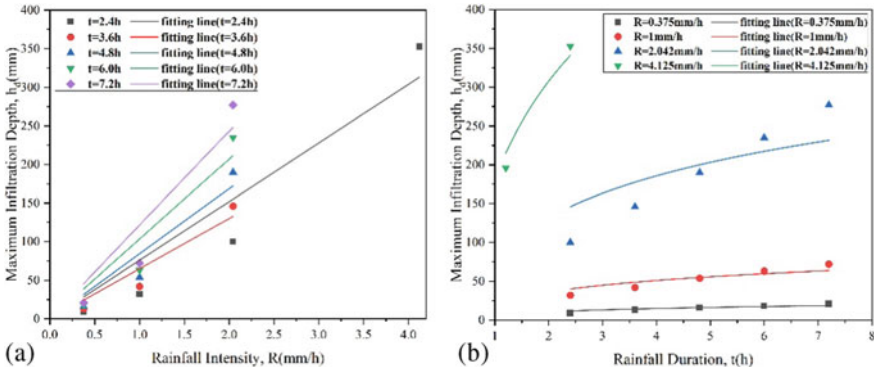| Rainfall duration, t (h)	Rainfall intensity, R (mm/h)	Maximum infiltration depth (mm)	Rainfall duration, t (h)	Rainfall intensity, R (mm/h)	Maximum infiltration depth (mm)
2.4	0.375	9	6.0	1	63
3.6	0.375	13	7.2	1	72
4.8	0.375	16	2.4	2.0417	100
6.0	0.375	18	3.6	2.0417	146
7.2	0.375	21	4.8	2.0417	190
2.4	1	32	6.0	2.0417	235
3.6	1	42	7.2	2.0417	277
4.8	1	54	2.4	4.125	353

Fig. 4 Variation of maximum infiltration depth with **a** rainfall intensity; **b** rainfall duration [13]

$$h_d = a \cdot R \tag{15}$$

$$h_d = b \cdot \ln(t) + b, \tag{16}$$

where R is rainfall intensity; t is rainfall duration; a is parameter related to rainfall duration and soil properties; b is parameter correlated to rainfall intensity and soil properties. Figure 4 shows the variation of maximum infiltration depth (h_d) with different rainfall intensity and duration.

Combining Eqs. 15 and 16, a prediction model considering both rainfall intensity and duration is proposed, as shown in Eq. 17.

$$h_d = A^* \cdot R \cdot (\ln(t) + 1), \tag{17}$$

where A^* is fitting parameter.

It is necessary to determine the parameter A^* of Eq. 17 to predict the rainfall infiltration depth. Jing et al. [11] proposed that the soil water characteristic parameters (s^*, γ, θs) of the normalized SWCCs model are related to parameter A^*. Based on it, this study further proposes a multivariate linear regression equation to establish the functional relationship between A^* and the soil water characteristic parameters as follows:

$$A^* = A' \cdot s^* + B'\gamma + C' \cdot \theta s, \tag{18}$$

where A', B', C' are parameters.

By injecting Eqs. 17 and 18, the maximum rainfall infiltration depth prediction model for sandy soil considering different rainfall conditions and soil water characteristics is acquired:

$$h_d = (A' \cdot s^* + B' \cdot \gamma + C'\theta s) \cdot R(\ln(t) + 1). \tag{19}$$

Parameters of normalized SWCCs model can be calculated with soil properties indicators, and Eq. 19 can be rewritten as:

$$h_d = (A' \cdot s^* + B' \cdot \gamma + C' \theta s) \cdot R(\ln(t) + 1) \tag{20a}$$

with

$$s^* = A_1 \ln(\text{FC}) + B_1 \tag{20b}$$

$$\gamma = [\delta_G^\wedge(A_2)]B_2 \tag{20c}$$

$$\theta s = A_3 \rho_d + B_3, \tag{20d}$$

where R is rainfall intensity; t is rainfall duration; A', B', C' are fitting parameters.

3 Model Validation and Prediction

In this study, an infiltration depth prediction model considering both material properties (fine content, dry density, and grain composition) and rainfall levels (intensity and duration) is proposed based on experimental results of tailing sand in the previous chapter. Similar to aeolian sand, tailing sand also possesses characteristics of fine particles and low weight that can be blown by wind [14]. As mentioned in the previous chapter, basic physical properties such as dry density and particle size distribution have significant impact on hydraulic behaviors. The grain size distribution of tailing sand and aeolian sand is similar, with particles concentrated between 0.075 mm and 0.25 mm in size; furthermore, their dry densities are also generally within the range of 1.6 g/cm^3 to 1.8 g/cm^3. As shown in Fig. 5, aeolian sand and tailing sand have similar normalized SWCCs within this dry density range. Therefore, it is postulated that the prediction model proposed in this study based on the experimental data of tailing sand can also be applied to aeolian sand.

To validate the proposed infiltration depth prediction model, an extreme rainfall level is considered based on the monitored rainfall events in Inner Mongolia and applied on a subgrade structure filled with aeolian sand. The rainfall infiltration depth of aeolian sand subgrade with different initial dry densities is firstly predicted using the proposed prediction model (Eq. 20). Subsequently, a numerical simulation of the aeolian sand subgrade was conducted using a finite element model under the same conditions.

Both model prediction results and simulation results are summarized in Table 5. In addition, the comparison curve between the predicted values and the simulated values is shown in Fig. 6.
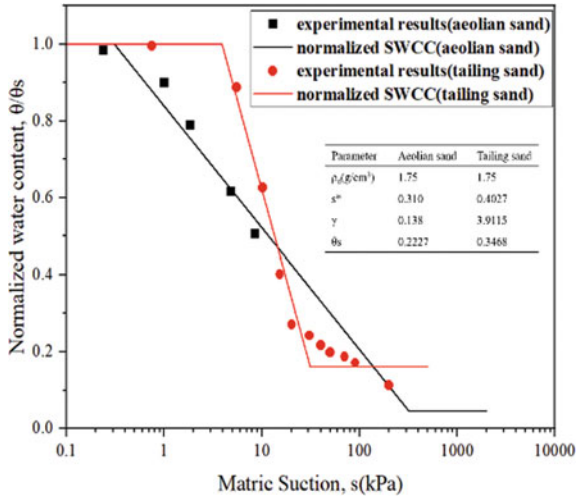
Fig. 5 Normalized SWCCs of tailing sand and aeolian sand

Table 5 Comparison of the predicted and simulated rainfall infiltration depth

Fine content (%)	δ_G	Dry density (g/cm³)	Rainfall duration (h)	Rainfall intensity (mm/h)	Predicted h_d (m)	Simulated h_d (m)
4.96	4.66	1.6	6	8.28	1.02	1.9
		1.67			0.95	1.6
		1.75			0.86	1.3

Fig. 6 Predicted and simulated maximum infiltration depth with different initial dry densities
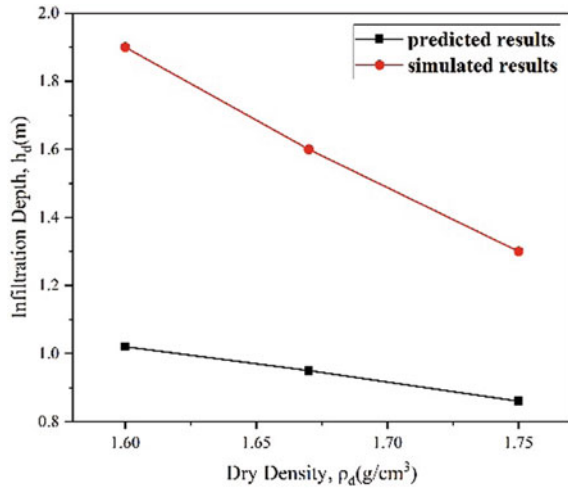
Both the predicted values and simulated values indicate that under the same extreme rainfall conditions, the maximum infiltration depth is negatively correlated with dry density. When the initial dry density is 1.6 g/cm^3, the infiltration depth is the largest. This is because the denser structure of aeolian sand subgrade has the smaller permeability coefficient. There are differences between the prediction and simulation results. This is due to the assumption supposed during the model formulation, which is that rainwater will not continue to infiltrate downward until the upper aeolian sand layer becomes saturated. Nevertheless, the simulation results indicate that even when the upper aeolian sand is in an unsaturated state, the rainwater still infiltrates downward, leading to a higher actual infiltration amount than predicted model, resulting in simulated infiltration depth being greater than the predicted values. Despite all this, this attempt to describe the infiltration depth under rainfall events is still applied in certain cases.

4 Conclusion

The basic properties of filling materials (aeolian sand) and rainfall levels are key points to rainfall infiltration process and the water distribution in subgrade. In this study, an analytical prediction model for rainfall infiltration depth of aeolian sand subgrade was proposed by establishing relationships between basic soil properties, parameters of the normalized SWCC equations, and rainfall levels with rainfall infiltration depth. Furthermore, a numerical simulation model was applied to validate the proposed prediction model. The contrast results instructed that the proposed model is acceptable for describing the infiltration depth of aeolian sand subgrade under different rainfall levels.

References

1. Zhang H, Wang Z, Liu R et al (2015) Experimental study on aeolian sand road performance in Horqin sandy land. J Inner Mongolia Univ (Natural Science Edition) 46(3):308–312
2. Wang S (2020) Study on numerical simulation of slope stability of aeolian sand embankment on heavy haul railway. Constr Technol 49(17):46–49
3. Li H (2018) Stability analysis of Aeolian sand embankment slope under rainfall infiltration. Subgrade Eng 04:249–253
4. Huang D, Chen J, Zhang L (2016) Calculation and validation of wetting depth of infiltration in aeolian sand in arid areas based on particle model. Trans Chin Soc Agric Eng 32(14):129–134
5. Zhang H, Liu H, Li C (2020) Temperature effect of soil-water on characteristic curve of aeolian sand subgrade soil. China J Highw Transp 33(7):42–49
6. Van G (1980) A closed-form equation for predicting the hydraulic conductivity of unsaturated soils. Soil Sci Soc Am J 44(5):892–898
7. Jing P, Nowamooz H (2021) Analytical and numerical investigations on the one-dimensional permanent deformations of granular materials under repeated deviatoric loading. Eng Geol 287(2):106095

8. Chai J, Khaimook P (2020) Prediction of soil-water characteristic curves using basic soil properties. Transp Geotech 22:100295
9. Chen Y (2020) Soil–water retention curves derived as a function of soil dry density. Geohazards 1(1):3–19
10. Dolinar B (2015) Prediction of the soil-water characteristic curve based on the specific surface area of fine-grained soils. Bull Eng Geol Env 74(3):697–703
11. Jing P, Song X, Shen Y et al (2023) Hydraulic behavior of sandy subgrade under extreme rainfall in Alashan, China. Transp Geotech 42
12. Liu J, Wen S (2021) Effect of dry density and particle size on soil-water characteristic curve of unsaturated tailing sand. Chin J Undergr Space Eng 17(05):1437–1443
13. Liu Y, Ren F, He R et al (2021) Research on the infiltration law of tailings and its control method under the action of rainfall. Mining Res Dev 41(05):137–140
14. Gao B (2021) Experimental research on iron tailings used as roadbed materials. Chang'an University

Integrated Water Resources Management Considering Geologic Features Under Climate Change: Development of an Analytical Tool for Langat River Basin in Malaysia

Mitsuru Yabe, Hiroki Ohashi, and Tadashi Yoshioka

Abstract For integrated water resources management in the Langat River basin in Malaysia, which has water quality problems, we evaluated the water retention function of the forest area from a geological perspective and reflected it in a hydrological analysis model of the basin and analyzed the water resources in the target basin based on climate prediction datasets with representative concentration pathways of greenhouse gases. We also introduced a dedicated tool that stores the analysis results as a database and displays them visually on a GIS. In the analytical modeling, we found that evaluating water retention based on the geological characteristics of granite distributed over the forest area and reflecting it in the modeling contributes to the accurate identification of river discharge, especially during the dry seasons when water pollution becomes apparent. Runoff analysis on datasets with representative concentration pathways RCP2.6 and RCP8.5 for climate change scenarios revealed that the impact of climate change on changes in river flow in the Langat River after 50 years was relatively insignificant.

Keywords Water resources management · Hydrological analysis · Water retention capacity

1 Introduction

In recent years, the effects of climate change have become more apparent on the planet, with regional floods and droughts raging. The impact of these water-related natural disasters on water resources affects human social and economic activities as well as ecosystems. In such a critical situation for humanity's water security, it is essential to manage water resources at watershed levels using scientific methods from a perspective of the water cycle and to share this information among stakeholders

M. Yabe (✉) · H. Ohashi · T. Yoshioka
OYO Corporation, Saitama, Saitama, Japan
e-mail: yabe-mituru@oyonet.oyo.co.jp

in order to solve the issues of water security under climate change, which may also have geopolitical implications. To address these issues, efforts are being made to model hydrological phenomena such as rainfall, evapotranspiration, river flow, and groundwater flow faithfully at watershed levels, and to identify temporal and spatial changes in water resource quantities. For example, the MIKE series of the Danish Hydraulic Institute, the HEC series of the US Army Corps of Engineers, and the SWAT model of the US Department of Agriculture are representative examples of this. Based on these models, initiatives to forecast changes of an amount of water resources on the target basin for the future using climate prediction datasets as input values which were calculated on the basis of representative concentration pathways of greenhouse gases under climate change have been implemented [1, 2].

On the other hand, in addition to changes in rainfall and evapotranspiration due to climate change, the water retention capacity of watersheds has a significant impact on changes in the amount of water resources in the watershed. This water retention capacity of watersheds is related to land use, topography, and geology. With an eye on this point, the European Commission has developed policy scenarios for the water retention capacity of major watersheds in European countries according to land use that may change in the future and examined the impact on the amount of water resources under climate change [3]. Thus, focusing on the water retention capacity of watersheds is important for predicting the future amount of water resources.

In this study, we evaluate the function of water retention in a region from a geological perspective and reflect it in a hydrological analysis model of a watershed and describe a case study of analyzing water resources in a target basin under climate change using climate prediction datasets based on representative concentration paths of greenhouse gases as input values. In addition, we introduce a dedicated system developed as a decision support tool for integrated water resources management by sharing the analysis results among stakeholders.

2 Materials and Methods

2.1 Study Area

The target watershed is the Langat River basin, which flows from east to west through the southern part of the state of Selangor on the Peninsular Malaysia.

The location and characteristics of the watershed are shown in Fig. 1. The Langat River flows through the southern part of the Klang Valley, where the urbanization is accelerating, including the capital city of Kuala Lumpur, and is an extremely important water resource for social and economic activities in Malaysia. However, due to the rapid urbanization in recent years, its middle and lower reaches are facing serious water pollution. In particular, the water quality has deteriorated during the period of low water flow of the dry seasons, resulting in repeated water intake restrictions [4]. Furthermore, when high tide levels coincide with the periods of low-water flow of
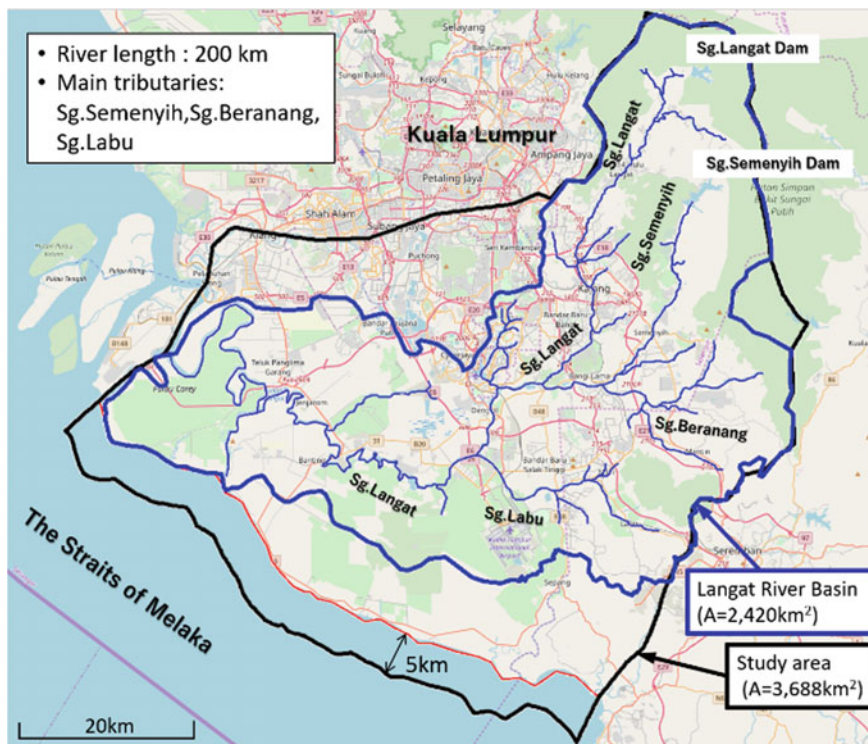
Fig. 1 Langat River basin

the dry seasons, the seawater rises up to the vicinity of the current intake facilities, leading to a decline in the water quality. Thus, grasping of the quantity of water resources, especially during low-water periods in the dry seasons, is essential for water security policy-making under climate change.

On the other hand, in the upper reaches of mountainous areas, the land use is forested, and the geology is granite. Accurate obtaining of water retention capacity in the upper reaches, where the annual precipitation is 20–30% higher than in urban areas, is important for integrated water resource management of the basin from a long-term perspective.

2.2 Methods

The hydrologic analysis model used in this study is GETFLOWS, GEneral-purpose Ter-restrial Fluid-fLOW Simulator which is one of three-dimensional runoff analysis methods using a finite difference method. The main feature of this method is that it uses Manning's equation (two-dimensional non-steady flow analysis using diffusion

waves) for surface water and Darcy's law (three-dimensional multi-phase flow analysis) for groundwater to reproduce natural interaction phenomena by coupling the two [5].

In particular, in runoff analysis during dry and low flow periods, it is important to accurately reproduce the return flows of rainwater once recharged as groundwater into rivers in order to grasp the amount of water resources under climate change. This method has been widely used in water resource management by municipalities in Japan, where geological conditions contribute greatly to groundwater availability and water supply is dependent on groundwater [6].

2.3 Building the Model and Input Parameters

Figures 2 and 3 show the analysis area and the 3D model of the target basin, respectively. Here, the elevation resolution of the digital elevation model (DEM) used was 5 m. The size of the analysis elements was set to a minimum width of 10 m in order to accurately reproduce the river flow rate in particular. The geological conditions and parameters of each formation such as a permeability coefficient including aquifer were set based on the results of previous projects conducted by the Japanese government [7].

On the other hand, a roughness coefficient as another parameter, which represents the runoff characteristics of the land surface, was determined based on land use conditions identified from the recent aerial photographs.

2.4 Input Data

Input data of precipitation, evapotranspiration, and temperature used in the runoff analysis were divided into three areas: upstream, midstream, and downstream of the target basin, based on climatic characteristics at different altitudes, such as mountainous, hilly, and low-lying areas in the basin, as shown in Fig. 4. In each area, data from representative observation stations of Malaysian government agencies such as the Department of Irrigation and Drainage were used as the input data.

The various data used were averaged for each month.

2.5 Model Calibration and Validation

Various climate data, such as precipitation, used for the modeling calibration were from 2014. Post-calibration model validation was performed for the years 2015, 2016, 2017, and 2018. The calibration and validation of the model were based on
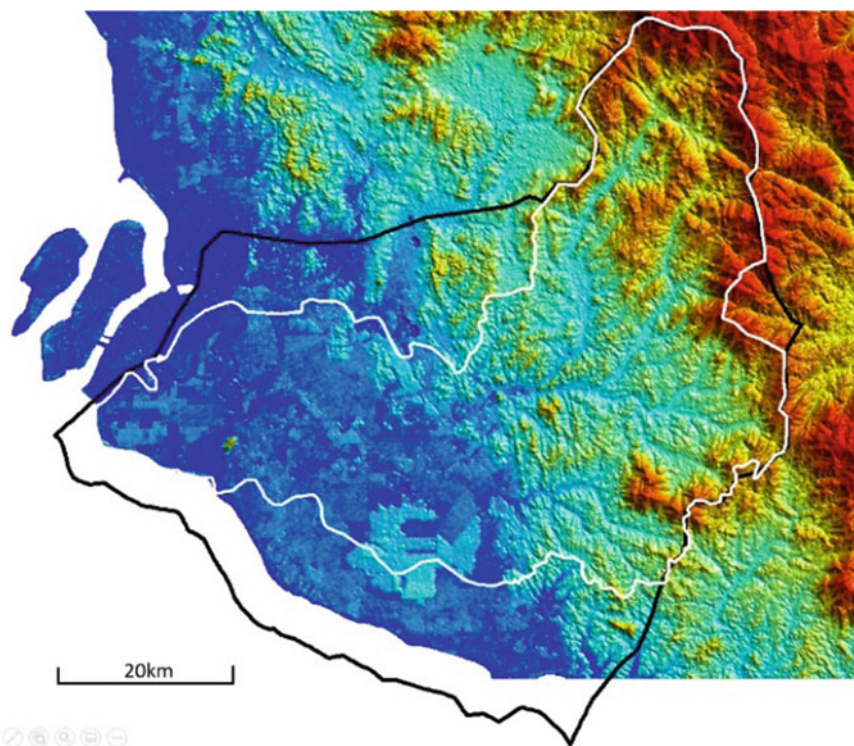
Fig. 2 Topographical data of the Langat River basin

the observed river discharge (monthly average) from Bukit Tampoi, an intake point in the middle Langat shown in Fig. 4.

On the other hand, the most important focus of the model calibration was on the water retention properties of the forest areas spreading over the mountains and hill areas, which influence the runoff characteristics of the watersheds.

The geology of these areas is mostly weathered granite, except for a thin layer of decomposed forest soil at the surface. Previous studies have shown that the weathered granite zone reaches a depth of 100 m in some places in the Peninsular Malaysia [8]. Therefore, the model calibration considered the presence of the forest soil and weathered granite in the mountains and hills.

2.6 Analysis Based on IPCC Scenarios [9]

Performing runoff analysis of the target basin for the period of fifty years from 2019 with the application of climate prediction datasets of RCP2.6 and 8.5 which are representative concentration pathways of greenhouse gases provided by IPCC on the
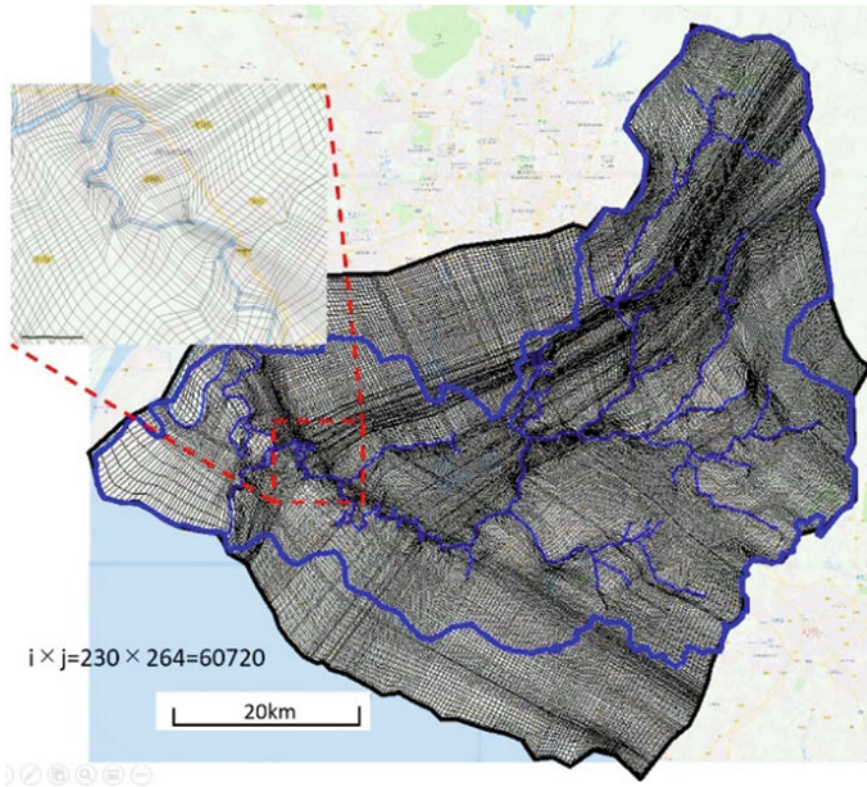
Fig. 3 Numerical model of the Langat River basin

basis of the modeling done on its calibration and validation, we examined changes of the amount of water resources, namely water demand–supply balance on the target basin.

2.7 Development of Special Tool for IWRM

The runoff analysis results were compiled into a database and stored in WROS, Water Resources Operating System as a tool developed for information sharing and decision making for integrated water resources management by stakeholders involved in water security.

WROS is a GIS-based data management system, by adding up the surface water and groundwater volumes calculated for each analysis element in GIS, the representative quantity of water such as river flow at each location and time period can be visually represented in a two-dimensional space, as shown in Fig. 5, and time-series graphs such as supply–demand balance of water resources can also be created. In
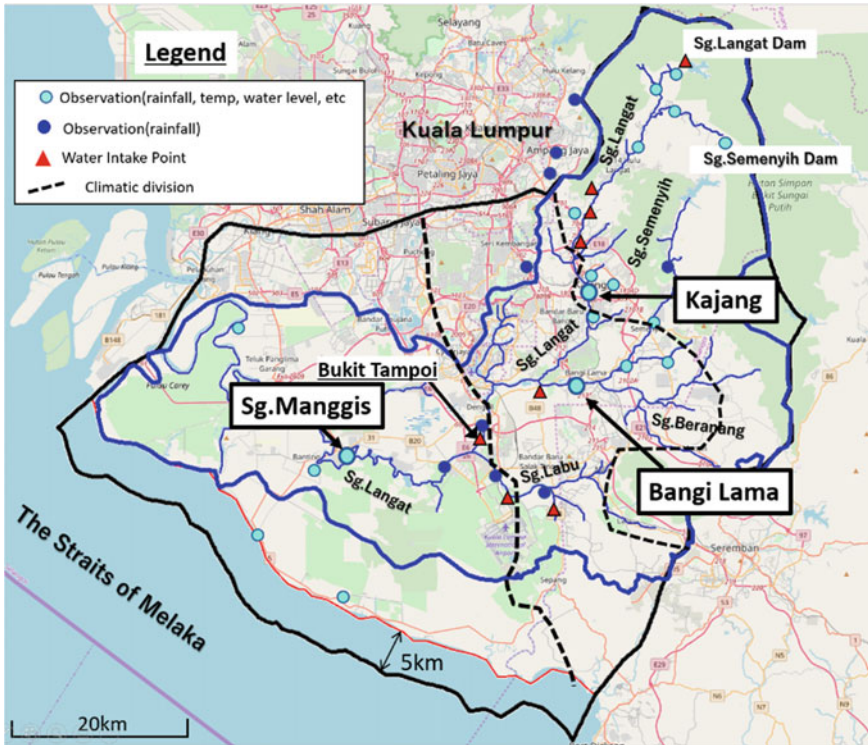
Fig. 4 Climatic division and observation points of the Langat River basin
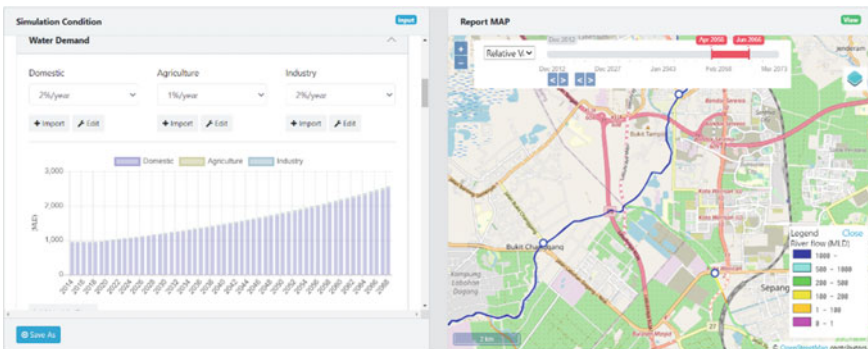

Fig. 5 Example of data display of an integrated water resources management tool, WROS

addition, WROS is equipped with GETFLOWS as an analysis engine, so by changing the analysis parameters and input conditions, it is possible to perform the predictive analysis of water resources under the influence of future changes in land use and climate change [10].

3   Results and Discussion

Figure 6 shows the calibration results of the model considering water retention in the forest area. Three cases of water retention due to the presence and varying thickness of forest soil and weathered granite were calibrated. Although there is no empirical data available to cover the entire target area, the thickness of the forest soil and the weathered granite were set to 1 m and 10 m, respectively, based on the outcrop conditions at around the site. The same values of permeability coefficient were used for each soil layer in each case, respectively, and the analysis was repeated so that the calculated values of the river flow rate at the water intake point for the dry periods in each case agrees with the measured values. As shown in the figure, in the case 3 where the forest soil and weathered granite are reflected in the model, the calculated and measured river flow rates in June and July, which correspond to the dry season in 2014 (surrounded red dotted line in Fig. 6), are most consistent, as well as reproducing well throughout the year, including other months. This suggests that rainfall in the forested area is recharged as groundwater by the water retention function of the weathered granite and is accurately reflected in the river flow as return flow. For geological features such as granite, which is easily weathered to a relatively deep level, it is important to accurately evaluate their water retention properties in order to determine the amount of water resources that accurately reflect the runoff characteristics.

Figure 7 shows a validation result of comparison of calculated and measured river flow rates from the runoff analysis from 2015 to 2018 based on the calibration model (case 3 shown in Fig. 6). It shows the comparison of calculated and measured values for about four years, except for one period in 2015 when good, measured values were not available. During periods of high rainfall, the discrepancy between calculated and measured values is relatively large. This may be due to differences in the rainfall area at that time. On the other hand, for the dry periods of 2017 and 2018 (red arrows in the figure), the calculated values show an extremely high reproducibility with respect to the measured values.

Figure 8 shows a GIS-based comparison of the calculation results of river flow rate at the Bukit Tampoi intake point in the middle reaches of the river during the dry season (July) 50 years after 2017 (2067) for each of the representative concentration pathways of RCP 2.6 and RCP 8.5 based on the calibration model. Here, the effective precipitation for RCP 2.6, given as a condition, changed little during the analysis period, while the effective precipitation for RCP 8.5 decreased by 30% by the end of the analysis period due to rising temperatures. However, Fig. 8 shows that the river flow rate for the dry season near the intake point was 289 MLD for RCP 8.5, a 4% decrease from RCP 2.6, confirming that there is no drastic change in river flow due to climate change. We presume that one of the reasons for that is the retention effect by forest soils as mentioned before.
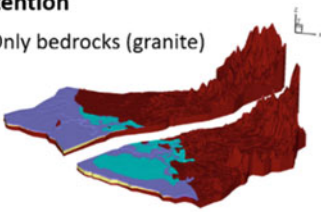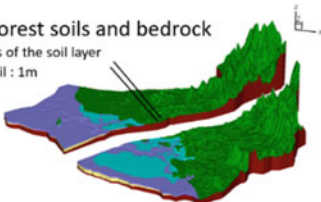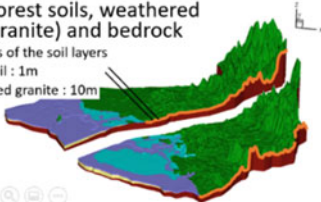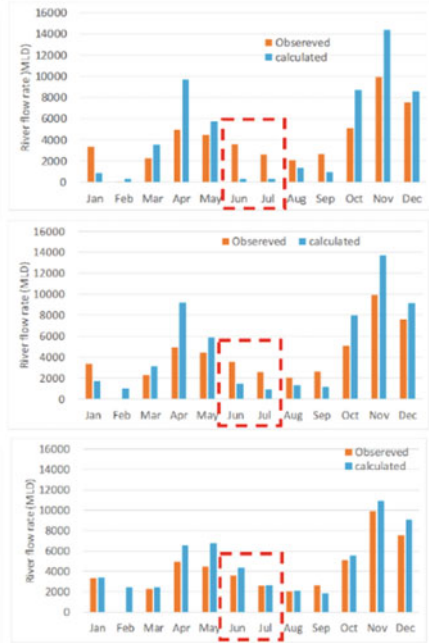
Fig. 6 Comparison of calibration results on the difference of water retention condition of forest area
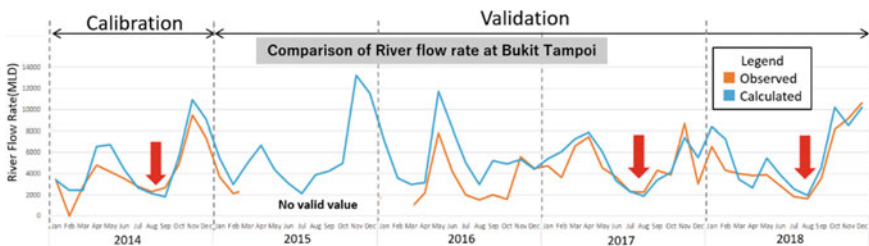
Fig. 7 Validation result of the calibrated model on river flow rate

On the other hand, as shown in Fig. 8, by visually displaying the results of the runoff analysis on a GIS, it is possible to visually and clearly explain to stakeholders the changes in water resources such as spatial river flows with taking into account of the effects of climate change.

At international conferences on water security, such as the World Water Summit, the need for information technology has been raised to correct the information gap among many stakeholders and to build consensus for solving water security issues such as floods and droughts that are likely to occur in the future in many river basins

Fig. 8 Comparison of
calculation results of river
flow rate at the Bukit Tampoi
intake point considering
climate change
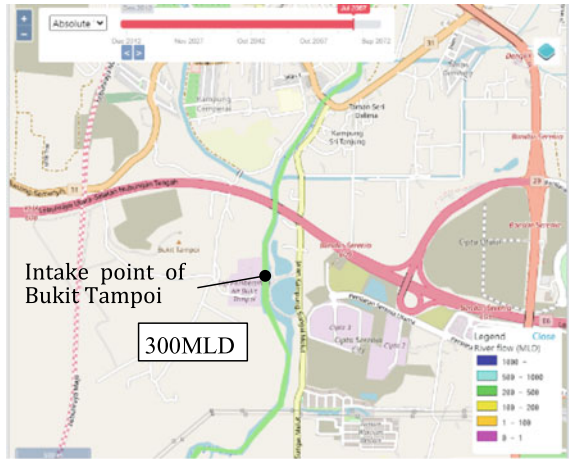
【RCP2.6】
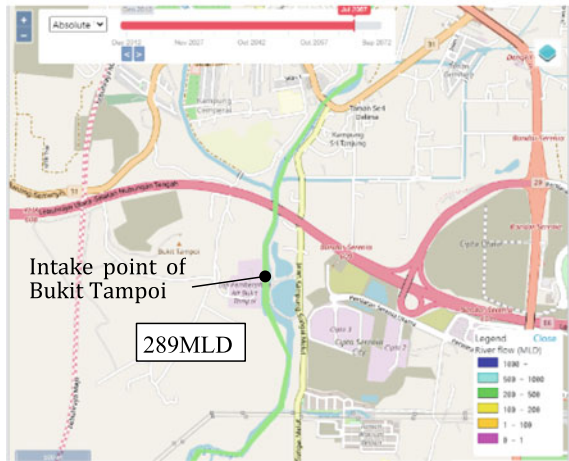
【RCP8.5】

around the world, especially in international river basins spreading across multiple
countries due to the effects of climate change [11]. As such, we believe that WROS
can directly contribute to solving such water security issues.

4 Conclusion

In this paper, we reported a case study of the Langat River basin in Malaysia, which
has water quality problems, in order to conduct integrated water resources manage-
ment, evaluating the water retention function of the forest area from a geological

perspective, reflecting it in a hydrological analysis model of the watershed, and analyzing the water resources in the target basin based on climate prediction datasets of representative concentration pathways of greenhouse gases. A dedicated tool that stores the analysis results as a database and displays them visually in GIS was also introduced.

In the analytical modeling, we found that the evaluation of water retention based on the geological characteristics of granite distributed over the forest area and its reflection in the model contributed to the accurate identification of the river flow rate, especially during the dry seasons when water pollution becomes apparent. Runoff analysis on datasets with representative concentration pathways of RCP2.6 and RCP8.5 for climate change scenarios revealed that the impact of climate change on changes in river flow in the Langat River after 50 years was relatively insignificant. Furthermore, the results show that a visual representation of spatial changes in river flow and other water resource quantities due to climate change in a GIS would be beneficial for water security.

References

1. Zhang J, Zhang M, Song Y, Lai Y (2021) Hydrological simulation of the Jialing River Basin using the MIKE SHE model in changing climate. J Water Climate Change 12(6):2495–2514
2. Duong P, Nauditt A, Nam D, Phong NT (2017) Assessment of climate change impact on river flow regimes in The Red River Delta, Vietnam—A case study of the Nhue-Day River Basin. J Nat Resour Develop 06(06):81–91
3. European Commission Joint Research Centre Institute for Environment and Sustainability: Evaluation of the effectiveness of Natural Water Retention Measures, https://ec.europa.eu/environment/water/blueprint/pdf/EUR25551EN_JRC_Blueprint_NWRM.pdf. Accessed 07 Sept 2021
4. Ahmed M, Mokhtar M, Lim CK, Majid NA (2017) Identification of water pollution sources for better Langat river basin management in Malaysia. Water 14(12):1904 (2017). https://doi.org/10.3390/w14121904. Accessed 07 Sept 2021
5. Tosaka H, Kojima K, Miki A, Chino T (1996) Numerical simulation of surface-subsurface-coupled, 2-Phase, 3-dimensional fluid behavior. J Groundw Hydrol 38(4):253–267
6. Rahman AS, Hosono T, Tawara Y, Fukuoka Y, Hazart Y, Shimada J (2021) Multiple-tracers-aided surface-subsurface hydrological modeling for detailed characteri-zation of regional catchment water dynamics in Kumamoto area, southern Japan. Hydrogeology Journal. https://doi.org/10.1007/s10040-021-02354-8. Accessed 07 Sept 2021
7. Japan International Cooperation Agency, Minerals and Geoscience Department Malaysia, CTI Engineering International Co., Ltd, OYO corporation: The study on the sustainable groundwater resources and environmental management for the Langat Basin in Malaysia (2002). https://openjicareport.jica.go.jp/pdf/11684388.pdf. Accessed 07 Sept 2021
8. Chigira M, Mohamad Z, Sian LC, Komoo I (2011) Landslides in weathered granitic rocks in Japan and Malaysia. Bull Geol Soc Malaysia 57:1–6

9. IPCC (2014) In: Pachauri RK, Meyer LA (eds) Climate change 2014: synthesis report. Contribution of working groups I, II and III to the Fifth assessment report of the intergovernmental panel on climate change [Core Writing Team]. IPCC, Geneva, Switzerland, pp 151
10. Yabe M, Ohashi H (2018) Realization of water security with visualization of water resources including groundwater. Asian Water, November/December, 20–25
11. International Institute for Sustainable Development (IISD): Budapest 2019 water summit official summary BWS bulletin 82(39) (2019)

Multiphysics Numerical Modeling of Transient Transport of PFAS

Arvin Farid and Pierrette Iradukunda

Abstract Per-and polyfluoroalkyl substances (PFAS) are a group of very persistent chemicals, labeled forever chemicals, because of their indestructibility due to their strong C-F bond. PFAS are among emerging contaminants of high concern due to their widespread contamination in the geoenvironment. PFAS are mobile, toxic, manufactured chemicals with very stable molecules and, hence, persistent in the environment. The more persistent presence of PFAS in the vadose (i.e., unsaturated) zone of soil complicates their transport due to their adsorption onto the air–water interface. The micelles formation on the air–water interface can significantly increase the retention of PFAS during its transport and turn the vadose zone into a long-term source of PFAS, slowly releasing PFAS into groundwater. This paper describes the development and testing of a one-dimensional (1D) numerical model that simulates PFAS transport, accounting for diffusion, advection, solid-phase adsorption, and air–water interface adsorption. The code is one-way coupled with a transient seepage model to account for the seepage impact on the PFAS transport, but not vice versa). After testing, the numerical model was then used to study various scenarios to evaluate the impact of solid adsorption and micelle formation on the PFAS transport.

Keywords Wildfire · Fire suppression · PFAS · Contaminant

1 Introduction

Per- and polyfluoroalkyl substances, PFAS, refer to a wide class of very stable manufactured fluorinated organic compounds [4, 25]. Thousands of PFAS compounds have been manufactured since the 1940s [4, 25]. PFAS are very stable due to their strong carbon-fluoride (C-F) bonds [9]. PFAS are very popular in industrial applications and

A. Farid (✉)
Civil Engineering, Boise, ID, USA
e-mail: arvinfarid@boisestate.edu

P. Iradukunda
Boise State University, Boise, ID, USA

commercial products such as fire resistance, dust suppression, oil repellence (due to lipophobic and hydrophobic properties). Due to their stability, toxicity, and mobility, PFAS are found as persistent source of contamination within the environment [1, 17, 20]. The most common sources of PFAS in the environment are industrial plants, leachate from landfills, sludge from wastewater treatment plants, and consumer products. Another common source is the use of aqueous film-forming foams (AFFFs) [16]. PFAS release from various sources can contaminate soil and drinking and groundwater, causing hazards to nature and humans. The most common forms of PFAS are perfluorooctanesulfonic acid (PFOS) and perfluorooctanoic acid (PFOA) [19].

There is an urgent need to understand the fate of PFAS within soil in order to assess the risk posed and ultimately remediate the environment contaminated by PFAS. This paper describes the development of a one-dimensional (1D) numerical model that couples seepage and PFAS transport through saturated and unsaturated soils. The model can account for diffusion and advection as well as the adsorption to solid phase and the air–water interfaces through various scenarios under transient seepage flow conditions. The model will be later validated using PFAS transport experimental results to help better understand ways to remove and remediate PFAS contamination.

2   Materials and Methods

2.1   Materials

The one-dimensional (1D) domain that is numerically simulated, under various scenarios of a 1D PFAS transport, is a benchtop lab-scale experimental column with a diameter of 4 cm and length of 5 cm. For the seepage model, the initial hydraulic head, H_1, at the inlet (top of the column), is maintained constant at 42 cm, and the outlet hydraulic head H_2 (at the bottom) can be either maintained at a constant value of 0 cm or be allowed to increase, hereafter referred to locked and unlocked seepage boundary conditions, BC, at the outlet. For the PFAS transport model, PFOS, with a constant concentration supply of 12 mg/L (referred to as locked transport BC) at the inlet at the top of the column. The outlet can also be simulated as locked at 0 mg/L or as unlocked to allow the PFOS concentration to increase as it permeates through the soil. This model accounts for two types of soil with equal length and different hydraulic conductivities stacked up within the column. Some parameters used in this study (summarized in Table 1) were obtained from the literature [3, 8, 12, 21, 27].

Table 1 Parameters used for numerical simulation

Parameters	Value	Unit
Bulk density, ρ_b	1.65	g/cm^3
Diffusion coefficient, D_0	5.4×10^{-6}	cm^2/s
Fitting parameter, K_f	0.055	–
Fitting parameter, N	0.85	–
Aqueous concentration, C	12	Mg/L
Surface tension, σ	71	Dyn/cm
Gas constant, R	8.314	J/^{o}K/mol
Temperature, T	293.15	^{o}K

2.2 Methods

Using the MATLAB interface, two computational models were developed for seepage and PFAS transport. The models are coupled to study the transport of PFAS with and without advection. The two models numerically linearize the transient second-order partial differential equations (PDEs) governing seepage flow and PFAS transport in order to numerically solve them. For the scenarios analyzed in this paper, a 5-cm soil column was discretized into a one-dimensional mesh. The two linearized PDEs were solved to find for the total (also known as hydraulic) head for the seepage model and the aqueous concentration of PFAS for the transport model. The forward-difference method was used to linearize the first derivatives with respect to space and time while the central-difference method was used to linearize the second derivative with respect to space [14, 15].

2.2.1 Seepage

The transient seepage flow of water within the soil is governed by the conservation of mass. If the density of water is assumed constant, the governing equation will be the conservation of water volume. Hence, the 1D governing equation can be written as [11]:

$$\vec{\nabla} \cdot v = -\frac{\partial \theta}{\partial t}, \tag{1}$$

where v is Darcy's velocity (flux), and $\theta = $ the volumetric water content, which, in turn, can be calculated as $n.S_w$, where n is the porosity of the soil and S_w is the degree of water saturation of the soil.

Darcy's law, $v = -k_z\, i$, was assumed valid for the seepage flow was applied to Eq. (1).

$$\frac{\partial}{\partial z}\left(-k_z \frac{\partial h}{\partial z}\right) = -\frac{\partial \theta}{\partial t}, \tag{2}$$

where k_z is the hydraulic conductivity, and $i = \partial h/\partial z$ is the hydraulic gradient.

On the left-hand side of Eq. (2), h is unknown while the unknown on the right side is θ. The two unknowns are related, and this relation is usually presented as the soil water-retention curve. In the absence of a soil water-retention curve, an approximate method is used where temporal variations in θ are related to the temporal variations in h based on specific/elastic capacity (i.e., retention) of water, m_v, i.e., $\frac{\partial \theta}{\partial t} = m_v \frac{\partial h}{\partial t}$.

The specific or elastic capacity, m_v, is considered ≈ 0.001 1/m for unsaturated soils and ≈ 0.00001 1/m for saturated soils (i.e., water is almost incompressible).

The partial differential equation (PDE) governing transient seepage, Eq. (2), can then be linearized using the finite-difference method over a discretized one-dimensional (1D) set of nodes and written for an arbitrary Node i as follows:

$$h_{i-1}^{t^{k+1}}\left(\frac{k_i}{dz^2}\right) + h_i^{t^{k+1}}\left(\frac{-k_{i+1}}{dz^2} - \frac{k_i}{dz^2} - \frac{m_v}{dt}\right) + h_{i+1}^{t^{k+1}}\left(\frac{k_{i+1}}{dz^2}\right) = -\frac{m_v h_i^{t^k}}{dt}, \tag{3}$$

where k_{i-1}, k_i, and k_{i+1} are the hydraulic conductivity values at Nodes $i - 1$, i, and $i + 1$, respectively, while h_{i-1}, h_i, and h_{i+1} represent the hydraulic head at Nodes $i - 1$, i, and $i + 1$, respectively, over each time step. Subscripts and superscripts represent nodes of the spatial and temporal grids, respectively. Equation (3) can then be solved to find the hydraulic (total) head for any node at any time. The modified iterative scheme can then be used to update coefficients that are nonlinear functions of the hydraulic head (e.g., the unsaturated hydraulic conductivity) using Eq. (4) [14, 15].

$$k_i = \frac{k_0}{1 + a_1 |\frac{h_i^{t^{k+1}} + h_i^{t^k}}{2} - z_i|^{a_2}}, \tag{4}$$

where $k_i =$ unsaturated hydraulic conductivity at Node i, $k_0 =$ saturated hydraulic conductivity, constant coefficients $a_1 = 1$ and $a_2 = 3$, $h =$ hydraulic (i.e., total) head, and $z =$ elevation.

2.2.2 Transport of PFAS

A series of transport mechanisms contribute to PFAS transport through saturated and vadose zones [22].

Diffusion and advection are the main mechanisms of PFAS flow. Diffusion is the spreading of the water and contaminant plume from a high hydraulic gradient and high concentration zone to zones with lower hydraulic head and concentration [10], respectively. Advection consists of the bulk movement of solutes carried by the flowing water (itself due to the hydraulic head diffusion). Both factors combined form an advection–diffusion equation as shown in Eq. (5).

$$\frac{\partial C}{\partial t} = -v_s \frac{\partial C}{\partial x} + D^* \frac{\partial^2 C}{\partial x^2}, \tag{5}$$

where $D^* =$ the apparent (effective) diffusion coefficient (cm^2/s), in Fick's second law. D^* combines the effect of tortuosity of soil and molecular diffusion, D_0; $v_s =$ the seepage velocity (cm/s) on straight line; and $C =$ the aqueous PFAS concentration (μmol/cm^3).

Like any other contaminants, PFAS can also be adsorbed to solid particles, retarding the PFAS flow. In addition, due to the charged and hydrophilic head and uncharged and hydrophobic tail, PFAS show surfactant-like properties, making them easily adsorbed to fluid–fluid interface such as air–water interfaces. There is a large air–water interface area, A_{aw}, within the vadose zone, which can affect the PFAS migration [22] and turn the vadose zone into a long-term source of PFAS release into the groundwater [7, 14, 15, 23].

The concentration of PFAS adsorbed onto the air–water interface, C_{aw}, can be calculated based on the aqueous PFAS concentration, C, in μmol/cm^2 using Eq. (6) [2, 8, 12, 18].

$$C_{aw} = A_{aw} K_{aw} C, \tag{6}$$

where K_{aw} can, in turn, be calculated using Eq. (7).

$$K_{aw} = \frac{-1}{RTC} \frac{\partial \sigma}{\sigma ln C}, \tag{7}$$

in which, $A_{aw} =$ the air–water interfacial area (cm^2/cm^3); $K_{aw} =$ the coefficient of air–water interfacial adsorption (cm^3/cm^2); $R =$ the universal gas constant (in J/$^\circ$K/mol); $\sigma =$ the interfacial tension (in dynes/cm); $T =$ the temperature ($^\circ$K). The adsorption of PFAS to the solid phase, C_s, can also be calculated using the Freundlich isotherm described in Eq. (8) [5, 6, 13, 26].

$$C_s = K_f C^N, \tag{8}$$

where both K_f and N are fitting parameters that are empirically found.

Hence, the PFAS transport is governed by molecular diffusion, mechanical dispersion, seepage-induced advection, and adsorption to solid–fluid and the fluid–fluid interfaces. This can be described using an advection–dispersion equation with adsorption terms of Eq. (9) [5, 6, 12, 18].

$$\frac{\partial (\theta C)}{\partial t} + \rho_b \frac{\partial}{\partial t} K_f C^N + \frac{\partial}{\partial t} (A_{aw} k_{a\omega} C) + \frac{\partial}{\partial z} (\theta v C) - \frac{\partial}{\partial z} \left(\theta D \frac{\partial C}{\partial z} \right) = 0, \tag{9}$$

where $\rho_b =$ the bulk density of the porous medium (g/cm^3); $v = q/\theta$ is the interstitial pore-water velocity (cm/s); $q =$ the Darcy flow flux; and $D =$ the dispersion/diffusion

Coefficient (cm^2/s). This equation be linearized over a 1D grid using the forward- and central-difference methods in time and space as follows [14, 15]:

$$
C_{i+1}^{t^{k+1}} \left(\frac{D_i \theta_{i+1}}{dz^2} + \frac{\theta_i D_{i+1}}{dz^2} - \frac{D_i \theta_i}{dz^2} - \frac{\theta_i v_i}{dz} \right)
$$

$$
- C_i^{t^{k+1}} \left(\begin{array}{c} \dfrac{D_i \theta_{i+1}}{dz^2} + \dfrac{\theta_i D_{i+1}}{dz^2} + \dfrac{\theta_i}{dt} + \dfrac{\theta_i^{t^{k+1}} - \theta_i^{t^k}}{2dt} \\[2mm] + \dfrac{v_i \theta_{i+1}^{t^{k+1}}}{2dz} - \dfrac{v_i \theta_i^{t^{k+1}}}{2dz} + \dfrac{\theta_i v_{i+1}^{t^{k+1}}}{2dz} - \dfrac{\theta_i v_i^{t^{k+1}}}{2dz} - \dfrac{\theta_i v_i}{dz} \end{array} \right)
$$

$$
+ C_{i-1}^{t^{k+1}} \left(\frac{\theta_i D_i}{dz^2} \right) - \frac{F C_i^{t^{k+1}}}{dt}
$$

$$
+ \frac{F C_i^{t^k}}{dt} C_i^{t^{k+1}} \left(\begin{array}{c} -k_{a\omega i} \dfrac{A_{awi}^{t^{k+1}}}{2dt} + k_{a\omega i} \dfrac{A_{awi}^{t^k}}{2dt} - A_{awi} \dfrac{k_{awi}^{t^{k+1}}}{2dt} \\[2mm] + A_{awi} \dfrac{k_{awi}^{t^k}}{2dt} + \dfrac{A_{awi} k_{awi}}{dt} \end{array} \right)
$$

$$
+ C_i^{t^k} \left(-k_{a\omega i} \frac{A_{awi}^{t^{k+1}}}{2dt} + k_{a\omega i} \frac{A_{awi}^{t^k}}{2dt} - A_{awi} \frac{k_{awi}^{t^{k+1}}}{2dt} + A_{awi} \frac{k_{awi}^{t^k}}{2dt} \right.
$$

$$
= C_i^{t^{k+1}} \left(\frac{\theta_i^{t^k} + \theta_i^{t^{k+1}}}{2dt} + \frac{\theta_i^{t^{k+1}}}{2dt} + \frac{-\theta_i^{t^k}}{2dt} \right) + C_i^{t^k} \left(\frac{\theta_i^{t^{k+1}}}{2dt} - \frac{\theta_i^{t^k}}{2dt} - \frac{\theta_i^{t^k} + \theta_i^{t^{k+1}}}{2dt} \right),
$$

$$
\tag{10}
$$

where $F = k_f \rho_b N C^{N-1}$. Using MATLAB, Eq. (10) was solved numerically to simulate various scenarios. Sensitivity analysis was first performed on both models (not fitting within the scope of this paper) over dt = 1 to 20 s and dz = 1 to 10 mm, which did not show any significant sensitivity over the majority of the range. i.e., at most a sensitivity < 2% when the largest dz and smallest dt were used. Thus, in the following scenarios, dz and dt are selected as 5 mm and 10 s, respectively.

3 Results and Discussion

3.1 Seepage Model Validation

First, the two models were tested using cases with well-known flow fields. Figure 1 shows the vertical profiles of the hydraulic head at different time steps (at 10 s intervals apart) for two cases. Both cases of Fig. 1 have a constant head at the top inlet (H_1 = 0.4 m). The difference is in the total head at the outlet, where Fig. 1a shows a case where a constant head of $H_2 = 0$ m is maintained at the bottom outlet— referred to as the "locked case"—and Fig. 1b shows the case where the total head H_2 at the bottom outlet is allowed to increase—referred to as "unlocked case."
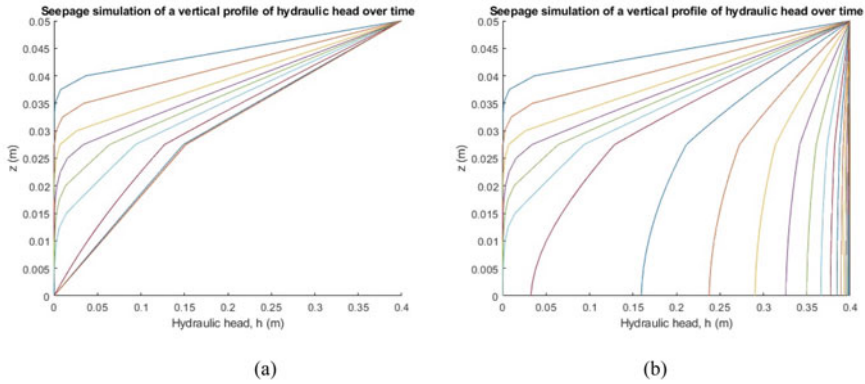
(a) (b)

Fig. 1 Vertical profile of the hydraulic head by the seepage model for **a** locked seepage outlet boundary condition and **b** unlocked seepage outlet boundary condition

The hydraulic head is maintained constant at zero for the locked case and is allowed to increase for the unlocked case. Figure 2 shows the time history of the cases of Fig. 1. Figure 2a, b shows the time history at two different points, the midpoint of the column and at the outlet. As seen in Fig. 2a, the total head at the outlet remains zero while the midpoint grows slowly. On the other hand, Fig. 2b shows that the hydraulic head at the outlet and midpoint both grow, which is consistent with the set boundary conditions [14, 15].
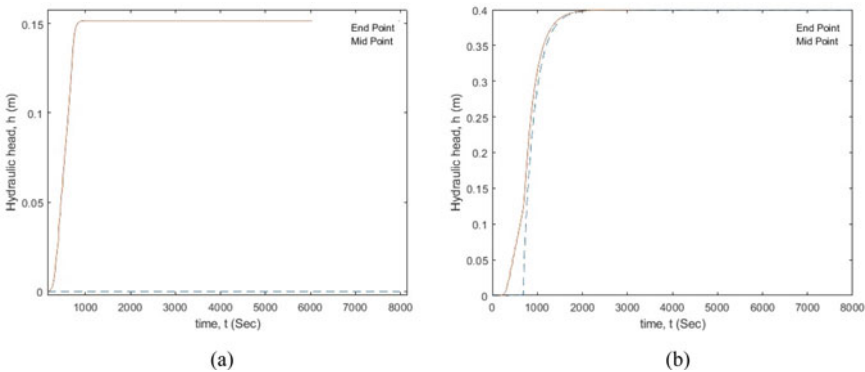

(a) (b)

Fig. 2 Time history for hydraulic head variations during by the seepage model at the midpoint and outlet for **a** locked outlet boundary condition and **b** unlocked outlet boundary condition
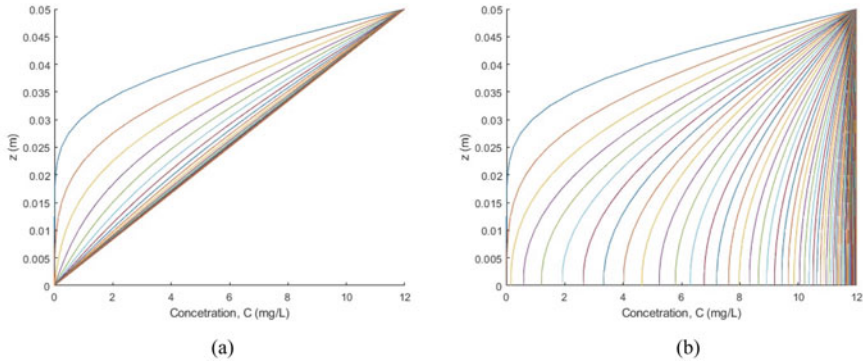
Fig. 3 Vertical profile over time of PFAS concentration for **a** constant feed at the top and freshwater at the bottom and **b** a constant feed at the top and breakthrough at the bottom, shown at time increments of 10 s

3.2 PFAS Transport

The transport of PFAS through the same domain was also simulated using the parameters mentioned in Sect. 3.1. Figure 3 shows the vertical profile of PFAS concentration at various time steps at 10 s intervals for two types of boundary conditions. The first, shown in Fig. 3a, is for a constant input concentration of a contaminant at the inlet (top) equal to 12 mg/L (referred to as locked PFAS transport BC at the inlet) and an infinite body of freshwater at the outlet (bottom), where the concentration remains 0 mg/L and is not accumulated—referred to as locked PFAS transport. The second case, Fig. 3b, shows the vertical profile over time for a constant feed of 12 mg/L at the inlet (top) and a small body of water that allows the accumulation of the contaminant and increase in its concentration at the outlet (bottom)—referred to as unlocked PFAS transport BC. In this case, diffusion advection and adsorption terms are then simulated [14, 15].

Figure 4 shows the breakthrough curves of Fig. 3a, b. The dashed red line represents the midpoint data while the dashed blue line represents the endpoint (i.e., outlet) data [14, 15].

3.3 Effect of Adsorption Coefficients on the Transport of PFAS

Figure 5 shows the effect on the transport of PFAS by the adsorption of PFAS onto solid particles. Figure 5a show the transport of PFAS without considering PFAS adsorption onto solid particles, and Fig. 5b shows a similar case with adsorption onto solid particles. It is noteworthy that in both cases, the degree of water saturation was 100% (no air and air–water interface; hence, there is no adsorption to the air–water interfaces).
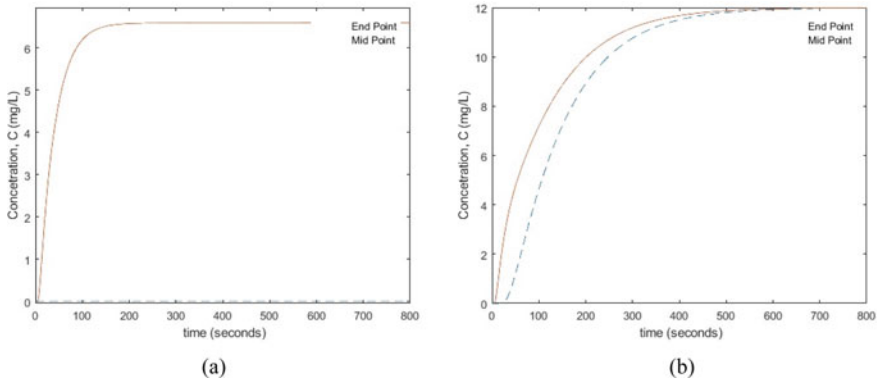
Fig. 4 Breakthrough curves for **a** constant feed at the top and fresh water at the bottom and **b** a constant feed at the top and breakthrough at the bottom
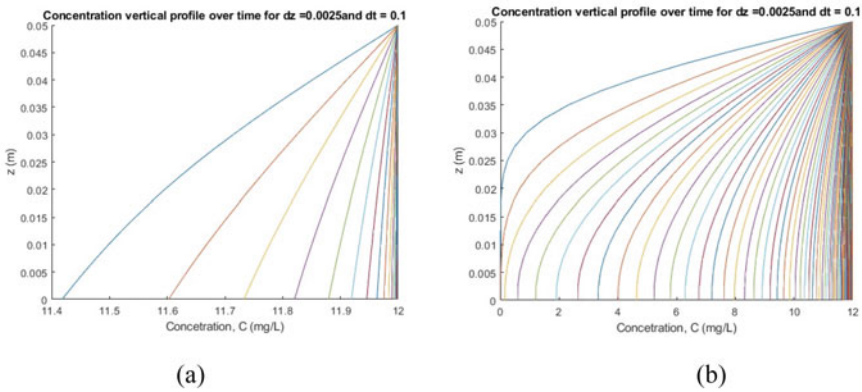

Fig. 5 Vertical profile of PFAS transport with advection and diffusion and **a** no PFAS adsorption to a solid phase, hence no retardation; **b** PFAS adsorption to solid particles and retardation

3.4 Impact of Degree of Saturation, S_w, on Transport Model

Figure 5 shows the impact of PFAS micelles formation (i.e., adsorption onto air–water interfaces), retarding PFAS transport. This is evaluated by incorporating the change in the degree of water saturation from the seepage model into the PFAS transport model. In other words, the seepage flow model is once run assuming an initial condition with fully water-saturated soil (i.e., no air). Then the same case is run using an initial condition with the soil starting fully dry and gradually saturating; hence, there will be air and air–water interfaces. The two sets of results are then fed into the PFAS transport model. Figure 6a shows the PFAS transport in a fully saturated environment with no air, and in turn, no air–water interfaces, resulting in no PFAS adsorption to those interfaces, eliminating the corresponding retardation.

Figure 6b considers the scenario where the soil is initially dry and gradually saturates; hence, there is air, and in turn air–water interfaces, resulting in PFAS adsorption onto those interfaces, leading to retardation of PFAS flow [14, 15] (Fig. 7).

Figure 5a shows how concentration moves faster through the saturated soil. Figure 5b shows that when the soil starts off dry and gradually saturates, it takes a much longer time for the PFAS concentration to move through the soil due to

(a)   (b)
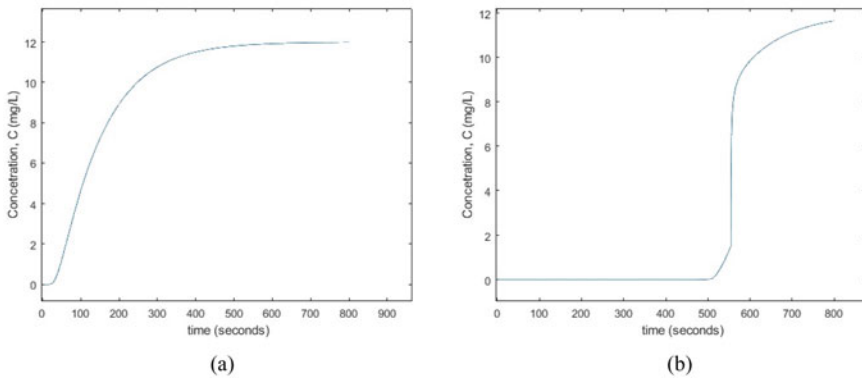
Fig. 6 Time history of PFAS transport with advection and diffusion: **a** soil is fully saturated, i.e., no air–water interfaces and, hence, no PFAS adsorption to the interfaces; **b** soil starts from dry and gradually saturates; i.e., there are air–water interfaces and PFAS adsorption to those interfaces
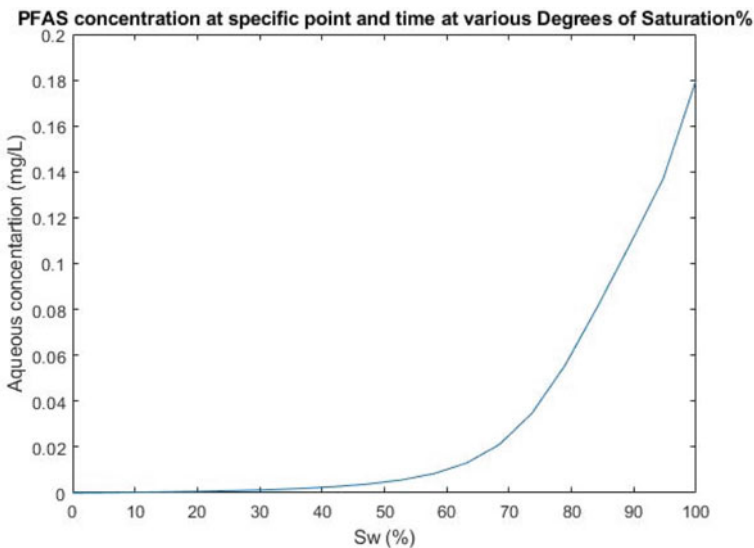

Fig. 7 PFAS aqueous concentration at Node 2 in space (5 mm below the inlet) and Node 5 in time (after 50 s) at various degrees of saturation

the existence of air and PFAS adsorption onto the air–water interfaces. Comparing Fig. 5a, b, it is seen that the breakthrough for the case with air–water interfaces starts much later but rises at a steeper slope, i.e., the breakthrough starts later but is more abrupt. The retention of PFAS in the vadose zone due to the air–water and solid interfaces is dependent on the soil matrix and the degrees of air and saturation. Higher degrees of air saturation (i.e., lower degrees of water saturation) result in the retardation of PFAS flow due to the higher retention of PFAS onto air–water interfaces due to the availability of air–water interfacial areas [19, 24]. Figure 6 demonstrates the variations in the PFAS concentration at a specific point (5 mm below the top boundary of the discretized grid) at a specific time (50 s after the PFAS is introduced into the sample through the top boundary) at various degrees of water saturation, S_w. As seen in Fig. 6, at higher degrees of water saturation, the PFAS transport is faster and vice versa [14, 15].

4   Conclusion

A one-dimensional (1D) finite-difference numerical model was developed in this work to simulate the coupled process of PFAS transport under transient seepage conditions. After describing the implemented methodology, a series of scenarios were simulated numerically, and results were shown to be consistent with the literature.

Various boundary conditions can be simulated to maintain constant to allow an increase in the hydraulic head and PFAS concentration on boundaries. For example, for the seepage model, the total heads at the inlet and outlet can be locked to remain constant to simulate constant head tests or the hydraulic head at the outlet can be allowed to raise.

The model is capable of simulating the effects of molecular diffusion, adsorption onto solid and air–water interfaces, and the degree of water and air saturation. The PFAS transport was retarded by the introduction of the adsorption onto solids and even more by the adsorption onto the air–water interface.

References

1. Ahrens L (2011) Polyfluoroalkyl compounds in the aquatic environment: a review of their occurrence and fate. J Environ Monit 13:20–31
2. Anwar A (2001) Experimental determination of air−water interfacial area in the unsaturated sand medium. New Approaches Characterizing Groundwater Flow. In: Proceedings of the XXXI IAH Congress, Munich, Germany, Sept 10−14, 2, pp 821−825

3. Araujo J, Mainhagu J, Brusseau M (2015) Measuring air-water interfacial area for soils using the mass balance surfactant-tracer method. Chemosphere 134:199–202

4. Barzen-Hanson KA, Roberts SC, Choyke S, Oetjen K, McAlees A, Riddell N, McCrindle R, Ferguson PL, Higgins CP, Field JA (2017) Discovery of 40 classes of per- and polyfluoroalkyl substances in historical aqueous film-forming foams (AFFF) and AFFF-impacted groundwater. Environ Sci Technol 51:2047–2057

5. Brusseau M (2019) Estimating the relative magnitudes of adsorption to solid-water and air/oil-water interfaces for per- and poly-fluoroalkyl substances. Environ Pollut 254:113102

6. Brusseau M (2019) The influence of molecular structure on the adsorption of PFAS to fluid-fluid interfaces: Using QSPR to predict interfacial adsorption coefficients. Water Res 152:148–158

7. Brusseau M (2020) Simulating PFAS transport influenced by rate-limited multi-process retention. Water Res 168:115179

8. Brusseau M, Peng S, Schnaar G, Murao A (2007) Measuring air-water interfacial areas with X-ray microtomography and interfacial partitioning tracer tests. Environ Sci Technol 41(6):1956–1961

9. Buck R, Franklin J, Berger U, Conder J, Cousins I, De Voogt P, Jensen A, Kannan K, Mabury S, Van Leeuwen S (2011) Perfluoroalkyl and Polyfluoroalkyl substances in the environment: terminology, classification, and origins. In: Integrated environmental assessment and management. 7:4:513. [PubMed: 21793199]

10. Freeze A, Cherry J (1979) Groundwater. Prentice-Hall, Englewood Cliffs, New Jersey, p 604

11. Fredlund D (1997) Soil Mechanics for unsaturated soils. In: China Architecture & Building Press, Beijing Shi, China

12. Guo B, Zeng J, Brusseau M (2020) A mathematical model for the release, transport, and retention of Per- and Polyfluoroalkyl Substances (PFAS) in the Vadose Zone. Water Resour Res 56. https://doi.org/10.1029/2019WR026667

13. Higgins C, Luthy R (2006) Sorption of perfluorinated surfactants on sediments. Environ Sci Technol 40(23):7251–7256

14. Iradukunda P, Farid A (2022) Multiphysics numerical modeling of transient transport of PFAS. In: Proceedings of ASCE GeoCongress 2022, March

15. Iradukunda P (2022) Multiphysics numerical model for PFAS transport within vadose and saturated zones, MS Thesis, Boise State University

16. Interstate Technology and Regulatory Council (2018) PFAS Fact Sheets PFAS-1. Washington, D.C.: Interstate Technology & Regulatory Council, PFAS Team. www.itrcweb.org

17. Krafft M, Riess J (2015) Per- and polyfluorinated substances (PFAS): environmental challenges. Curr Opin Colloid Interface Sci 20:192−212

18. Kim H, Rao P, Annable M (1997) Determination of effective air-water interfacial area in partially saturated porous media using surfactant adsorption. Water Resour Res 33(12):2705–2711

19. Lyu Y, Brusseau M, Chen W, Yan N, Fu X, Lin X (2018) Adsorption of PFOA at the air-water interface during transport in unsaturated porous media. Environ Sci Technol 52(14) :7745–7753. https://doi.org/10.1021/acs.est.8b02348. E-pub, Jun 26. PMID: 29944343; PMCID: PMC6312111

20. Rayne S, Forest K (2009) Perfluoroalkyl sulfonic and carboxylic acids: a critical review of physicochemical properties, levels and patterns in waters and wastewaters, and treatment methods. J Environ Sci Health, Part A: Toxic/Hazard. Subst Environ Eng 44:1145−1199

21. Schaefer C, Drennan D, Tran D, Garcia R, Christie E, Higgins C, Field J (2019) Measurement of aqueous diffusivities for perfluoroalkyl acids. J Environ Eng 145(11):06019006

22. Sharifan H, Bagheri M, Wang D, Burken J, Higgins C, Liang Y, Liu J, Schaefer C, Blotevogel J (2021) Fate and transport of per- and polyfluoroalkyl substances (PFASs) in the vadose zone. Sci Total Environ 771:145427

23. Shin H, Vieira V, Ryan P, Detwiler R, Sanders B, Steenland K, Bartell S (2011) Environmental fate and transport modeling for perfluorooctanoic acid emitted from the Washington works facility in West Virginia. Environ Sci Technol 45(4):1435–1442

24. Silva J, McCray J, Martin W (2020) Final report: baseline data acquisition and numerical modeling to evaluate the fate and transport of PFAS within the vadose zone. SERDP project ER18-1389
25. Wang Z, DeWitt J, Higgins C, Cousins I (2017) A never-ending story of per-and polyfluoroalkyl substances (PFAS). Environ Sci Technol 51:2508–6623
26. Wei C, Song X, Wang Q, Hu Z (2017) Sorption kinetics, isotherms, and mechanisms of PFOS on soils with different physicochemical properties. Ecotoxicol Environ Saf 142:40–50
27. Xu M, Eckstein Y (1995) Use of weighted least-squares method in the evaluation of the relationship between dispersity and field scale. Groundwater 33(6):905–908

Observations and Analysis of Vertical One-Dimensional Rainfall Seepage Flow Phenomenon

Koichi Tsubogo, Kohei Araki, Yasushi Fukuda, Keiji Kuajima, Kosuke Katayama, and Shunji Ue

Abstract Heavy rainfall due to climate change such as global warming exceeds our expectations every year in Japan, and slope failures occur due to heavy rainfall. The heavy rain disasters in Japan tend to result in human and economic loss. Therefore, in this paper, focusing on Horton's infiltration capacity theory, we have developed a proposed formula that takes into account rainfall seepage flow when bare ground or nonwoven filters are installed. We have created an artificial slope as a slope for field experiments and installed a rain gauge and a soil moisture meter for on-site measurement. Furthermore, numerical calculations were performed based on the vertical one-dimensional seepage flow phenomenon. We compared the results of numerical analysis and on-site measurement and examined the effect of the presence or absence of nonwoven filters on the infiltration capacity in the rainfall. In conclusion, when the ground surface is bare, the infiltration capacity tends to decrease due to surface erosion of the slope and the impact of raindrops. Secondly, we are able to determine the constant of the proposed formula from the field observations. Finally, if a nonwoven filter is applied to the ground surface, it has infiltration capacity and improves the water resource recharge function compared to the case of bare ground.

Keywords Seepage flow · Overland flow · Penetration characteristics

1 Introduction

In Japan, long rains or torrential downpours are on the increase due to climatic changes caused by global warming. In particular, torrential downpours bring large amounts of rainfall in a short time to a small area, and their hourly rainfall exceeds 50 mm. For example, torrential rain in northern Kyushu, in July 2017, linear rainband

K. Tsubogo (✉)
Tsubogo Computational Research Institute, Hofu, Yamaguchi, Japan
e-mail: ktsubogo@gmail.com

K. Araki · Y. Fukuda · K. Kuajima · K. Katayama · S. Ue
National Institute of Technology, Tokuyama College, Shunan, Yamaguchi, Japan

stayed in place for a long time, and torrential rain occurred for more than 6 h, leading to a disaster. In contrast, torrential rains in July 2018 were unique in that torrential rains occurred over a wide area across Japan, setting records for long-duration rainfall at many locations [1]. The number of such disasters that cause human, economic, and other losses is increasing every year due to slope failures caused by torrential rains that exceed expectations.

If the rainfall intensity exceeds the infiltration capacity, the excess rainfall cannot be seepages and flows over the ground surface. This is the Hortonian overland flow [2–4]. When a Hortonian overland flow occurs, the rainfall is not stored in the ground because the excess rainfall flows over the ground surface. Hortonian overland flow is closely related to the erosion of slopes and sediment discharges in the ground [3]. Therefore, the occurrence of Hortonian overland flow is one of the important findings in the evaluation of the erosion of slopes, infiltration capacity of the ground, and the function of groundwater recharge. Previous studies [2, 3], and [4] have generalized the point that Hortonian overland flow does not occur in slopes with sufficient vegetation because the infiltration capacity is sufficiently large. However, it has been reported that Hortonian overland flow occurs when vegetation declines (slopes become bare land) and erosion of slopes occurs [4].

One method that addresses the aforementioned problems is the use of nonwoven filters, which provide both slope protection and revegetation. Previous studies on the effect of nonwoven filters on slope protection include Fujiwara et al. [5], Tsubogo et al. [6], and Takehisa [7]. However, although many studies have been conducted on overland flow, the status of rainfall seepage into the ground has not been fully understood. Tsubogo et al. [8] attempted to formulate Horton's rainfall seepage theory using the relationship between rainfall intensity and saturated hydraulic conductivity as a discriminant condition. Furthermore, Araki and Kitamura [9] introduced the concept of a quasi-saturated degree of saturation and found that the degree of saturation in the first layer near the ground surface was greater than or equal to the quasi-saturated degree of saturation. The degree of saturation of the first layer near the ground surface was assumed to be above the quasi-saturated degree of saturation, which facilitates rainfall seepage into the ground. Tsubogo et al. proposed the equation [8] for the rainfall inflow coefficient, and also performed vertical one-dimensional rainfall seepage flow analysis. The numerical solution for the moisture content by volume in the ground was confirmed to reproduce the on-site observation values. On the other hand, the numerical solution for the quasi-saturated degree of saturation of the first layer has not been verified with sufficient accuracy.

This paper aims to improve the accuracy of Tsubogo et al.'s proposed equation by comparing the numerical results with the on-site observation results. The effects of nonwoven filters on the functional evaluation of erosion of slopes, underground infiltration capacity, and groundwater recharge are also discussed.

2 On-site Observation and Vertical One-Dimensional Rainfall Seepage Flow Analysis

2.1 On-site Observation

Whether or not a slope will collapse is highly dependent on moisture content by volume. In other words, measuring soil moisture is important in assessing slope hazard. In this paper, the north slope of the National Institute of Technology, Tokuyama College (hereinafter referred to as "Tokuyama College") in Shunan City, Yamaguchi Prefecture, which is designated as a sediment disaster warning area, is constructed on the slope was constructed as an on-site experimental slope. On-site observations are conducted by installing a rain gauge and a soil moisture meter. The on-site experimental slope was constructed on the north slope of Tokuyama College as shown in Photo 1. The slope is an artificial slope with a length of slope 7 m and a slope angle of 30°.

The soil moisture was measured using an EC-5 soil moisture sensor (METER) at 1 m from the bottom of the slope and 10 cm from the ground surface, and a data logger (Em50 data logger, METER) was installed to store the observed values. The EC-5 soil moisture sensor can measure over a wide range from air-dry to saturated soil and can accurately measure the moisture content by volume of any soil type by minimizing the effects of salinity and temperature. A tipping rain gauge was used as the rain gauge. The rainfall intensity was observed approximately every hour, and the observed values were stored in a compact flash memory card. The rainfall intensity and the moisture content by volume were observed from midnight on June 3 to midnight on June 5, 2021. The properties of the soil used in this paper are shown in Table 1.

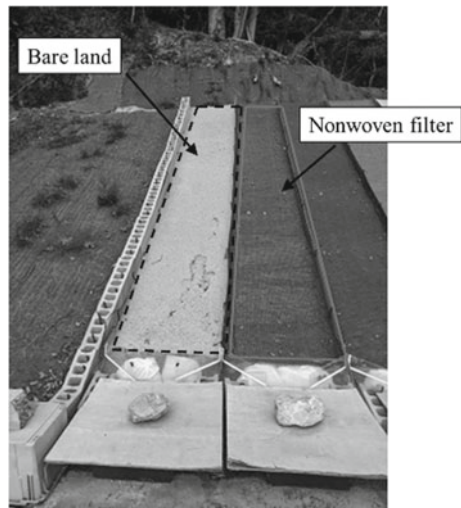**Photo 1** Example of on-site experimental slope

Table 1 Properties of the soil

Properties of the soil	Numerical value
Density of soil (g/cm^3)	2.65
Void ratio	0.448
Maximum moisture content by volume	0.309
Saturated hydraulic conductivity (cm/s)	2.0×10^{-4} to 1.0×10^{-3}

2.2 Vertical One-Dimensional Rainfall Seepage Flow Analysis

Rainfall seepage flow phenomena occur in two or three dimensions. However, in most cases, rainfall seepage is dominated by vertical flow [10]. The equation for vertical one-dimensional rainfall seepage is a variant of the governing equation for unsaturated seepage [11]. However, since there is currently no analytical method that can accurately reproduce on-site observed values, it is necessary to add correlation coefficients such as the rainfall inflow coefficient to obtain a numerical solution. Therefore, the equation for rainfall inflow coefficient [8] by Tsubogo et al. should be improved in terms of the discrimination conditions for rainfall intensity, saturated hydraulic conductivity, and quasi-saturated degree of saturation.

Richards Equation [11]

Richards presented the fundamental equation for unsaturated seepage flow.

$$\frac{\partial \theta}{\partial t} = \frac{\partial}{\partial x}\left\{k_x(\theta)\frac{\partial \psi(\theta)}{\partial x}\right\} + \frac{\partial}{\partial y}\left\{k_y(\theta)\frac{\partial \psi(\theta)}{\partial y}\right\} + \frac{\partial}{\partial z}\left\{k_z(\theta)\frac{\partial \psi(\theta)}{\partial z}\right\} + \frac{\partial k_z(\theta)}{\partial z} \tag{1}$$

As rainfall seepage is often dominated by vertical flow [10], if the x and y terms in Eq. (1) are set to 0 and the z-axis is set to positive downward from the ground surface, the vertical one-dimensional Richards' equation can be transformed into the following equation.

$$\frac{\partial \theta}{\partial t} = \frac{\partial}{\partial z}\left\{k_z(\theta)\frac{\partial \psi(\theta)}{\partial z}\right\} - \frac{\partial k_z(\theta)}{\partial z} \tag{2}$$

Where θ: the moisture content by volume, ψ: suction pressure head, assuming that the unsaturated hydraulic conductivity in the z-direction is k_z.

Setting of Soil Parameters

Brooks–Corey's equation [12], which is often used for sandy soils and is simple to treat, is used and the degree of saturation S_r is given by Eq. (3).

$$S_r = \frac{\theta - \theta_r}{\theta_s - \theta_r} = \left(\frac{\psi_b}{\psi}\right)^\lambda \tag{3}$$

The unsaturated hydraulic conductivity k_u is expressed by Eq. (4).

$$k_u = k_s \left(\frac{\psi_b}{\psi}\right)^{2+3\lambda} \tag{4}$$

Furthermore, Eq. (3) was substituted into Eq. (4) and transformed into Eq. (5).

$$k_u = k_s (S_r)^{\frac{2+3\lambda}{\lambda}} \tag{5}$$

where S_r: degree of saturation, θ_s: maximum moisture content by volume, θ_r: residual moisture content by volume, ψ_b: critical suction pressure head or air penetration value, λ: constant depending on soil type (pore size distribution index), k_s: saturated hydraulic conductivity. The maximum moisture content by volume of the on-site experimental slope is 0.309. The lower limit of the saturated hydraulic conductivity of the on-site soil, $k_s = 2.0 \times 10^{-4}$ cm/s, is used as the value of k_s. Other parameters were determined by fitting the observed value of moisture content by volume.

Discretization of the Fundamental Equations [13]

Darcy's law and the continuity equation were divided into differential as in Eq. (6), and numerical calculations were performed.

$$w_{i,i-1} = -k_{i,i-1}\left(\frac{\psi_i - \psi_{i-1}}{\Delta z_{i,i-1}} - 1\right) \tag{6}$$

$$\theta_{i,t+\Delta t} = \theta_{i,t} - \frac{\Delta t}{\Delta z}\left(w_{i+1,i} - w_{i,i-1}\right) \tag{7}$$

In this paper, rainfall intensity is given as a boundary condition for the ground surface, and its introduction into the analysis was done as follows in relation to the moisture content by volume (θ_1) of the first layer.

$$\theta_{1,t+\Delta t} = \theta_{1,t} - \frac{\Delta t}{\Delta z}\left(w_{2,1} - C_e R\right) \tag{8}$$

where θ_1: moisture content by volume in layer 1, $w_{2,1}$: seepage flow velocity from layer 1 to layer 2 (cm/s), R: rainfall intensity (cm/s), and C_e: rainfall inflow coefficient. The details of the rainfall inflow coefficient are explained in the next section, but the change in moisture content by volume in layer 1 is expressed as the difference

between seepage flow velocity from layer 1 to layer 2 and rainfall intensity seepage from the surface layer to layer 1. The maximum moisture content by volume for the on-site experimental slope is 0.309, and this value is used as the upper limit. The degree of saturation is set not to exceed 1.0 because the state of oversaturation is not considered.

Proposed Equation for Rainfall Inflow Coefficient

The equation proposed by Tsubogo et al. [8], which numerically models Hortonian overland flow, is based on the relationship between rainfall intensity (R) and saturated hydraulic conductivity (k_s), as shown in Fig. 1. If R is lower than k_s, all rainfall will seepage into the ground. On the other hand, if R is greater than k_s, rainfall will not seepage completely and will cause excess rainfall to flow over the ground surface. In this case, the rainfall inflow coefficient is expressed as k_s divided by R and formulated as in Eq. (9). The discriminant condition for rainfall intensity is given by Eq. (10).

$$C_e = \frac{k_s}{R} \beta \tag{9}$$

$$\begin{cases} R \leq k_s & : C_e = 1.0 \\ R > k_s & : C_e = \dfrac{k_s}{R} \beta \end{cases} \tag{10}$$

where $\beta (0 < \beta \leq 1.0)$ is the correction factor. The correction coefficient β is determined from the relationship between the numerical solution, the observed value, and the error in the amount of data.
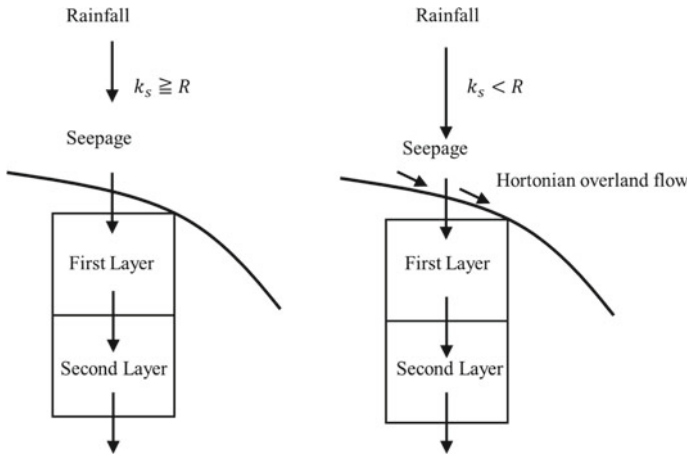

Fig. 1 Relationship between rainfall intensity and saturated hydraulic conductivity

On the other hand, the degree of saturation of soil near the ground surface under natural conditions is never 0 or 100%, but exists in an unsaturated state. Even in water retention tests, the degree of saturation at suction 0 does not reach 100% and there are several examples showing values of 75–90% (e.g., Kamiya et al. [14], Fujimori and Araki [15]). Araki and Kitamura [9] defined the quasi-saturated degree of saturation as the maximum degree of saturation taken by actual soil based on thermodynamic considerations and equilibrium conditions. The quasi-saturated degree of saturation is used as an input parameter for unsaturated seepage analysis to predict slope failure [16] associated with rainfall. Araki and Kitamura [9] proposed a method to estimate the quasi-saturated degree of saturation from the compaction curve.

The degree of saturation of the first layer, S_{r1}, near the ground surface, is assumed to be more than a quasi-saturated degree of saturation. The degree of saturation threshold (quasi-saturated degree of saturation) for the first layer is assumed to be S_{rq}. The discriminant condition for the degree of saturation of the first layer is given by Eq. (11).

$$
\begin{cases}
S_{r1} > S_{rq} & : C_e = 1.0 \\
S_{r1} \leqq S_{rq} & : C_e = \dfrac{k_s}{R}\beta
\end{cases}
\tag{11}
$$

However, the discriminant conditions in Eqs. (10) and (11) do not reveal a causal relationship between rainfall intensity and the degree of saturation of the first layer. Therefore, in this paper, Eqs. (10) and (11) are clarified as follows.

If the rainfall intensity (R) is greater than the saturated hydraulic conductivity (k_s), we improve the condition to consider the degree of saturation in the first layer and propose a new Eq. (12). The following values are used for S_{rq} and β when the numerical solution is close to the observed values.

$$
\begin{cases}
R \leqq k_s : C_e = 1.0 \\
R > k_s
\begin{cases}
S_{r1} > S_{rq} & : C_e = 1.0 \\
S_{r1} \leqq S_{rq} & : C_e = \frac{k_s}{R}\beta
\end{cases}
\end{cases}
\tag{12}
$$

Calculation Conditions

This analysis is performed on an artificial slope with a length of slope 7 m and a slope angle of 30. The rainfall inflow coefficient is used to examine the time variation of rainfall seepage into the ground with and without nonwoven filters by changing the correction factor β and the threshold value S_{rq} (quasi-saturated degree of saturation) of the degree of saturation of the first layer. The numerical algorithm is shown in the flowchart in Fig. 2.

The differential spatial and time intervals Δz and Δt were set to 5 cm and 2 s, respectively, and the Brooks–Corey equation was used for the $\theta - \psi$ and $k - \theta$ relationships, where $k_s = 2.0 \times 10^{-4}$ cm/s, $\theta_s = 0.309$, $\theta_r = 0.05$, $\psi_b = 40$ cm. The hysteresis of the water absorption and dewatering processes is not considered

Fig. 2 Numerical algorithm
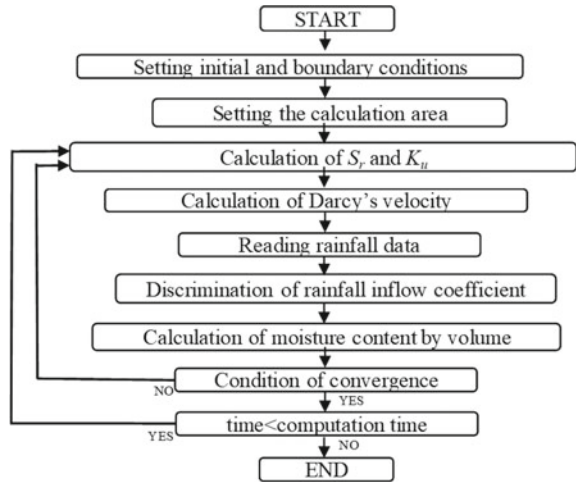
here. Initial conditions are moisture content by volume in the depth direction from the ground surface $\theta = 0.097$ for bare land and $\theta = 0.080$ for nonwoven filters.

By fitting the on-site observation values to the numerical solution, the soil type constant λ fits the observed value best when $\lambda = 2$ for both bare land and nonwoven filters from Tsubogo et al. [17]. The degree of saturation threshold (quasi-saturated degree of saturation) for the first layer was set to $S_{rq} = 0.9$ for both bare land and nonwoven filters from Tsubogo et al. [17]. The correction coefficient β is 0.2 for bare land and 0.6 for nonwoven filters by fitting the numerical solution to the observed value from Tsubogo et al. [17].

3 Analysis Results

This paper is compared with the numerical solution and observed value in the second layer of the geotechnical model. Figure 3 shows the time variation of the observed value and the moisture content by volume of the numerical solution. Figure 4 shows the time variation of the rainfall inflow coefficient. Figure 5 shows the change in degree of saturation with time. Note that only numerical solutions are shown for degree of saturation, since no on-site observations were made.

Figure 3 shows that the increase in moisture content by volume due to rainfall tends to be closer to the observed value when nonwoven filters are used than when bare land is used. Moreover, the rainfall inflow coefficient is higher for nonwoven filters than for bare land from 19 to 22 h, according to Fig. 4. Figure 5 shows that the degree of saturation of bare land increases more slowly than that of nonwoven filters during the time period when the rainfall inflow coefficient decreases. Figures 4 and 5 show that the increase in the degree of saturation of bare land slows down during the time period when the rainfall inflow coefficient decreases.
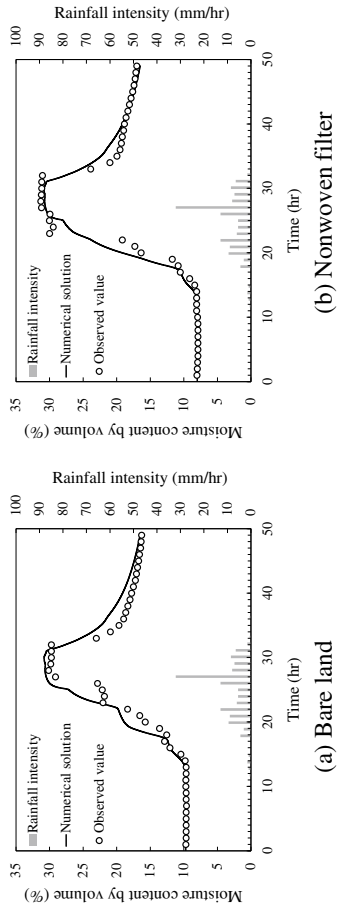
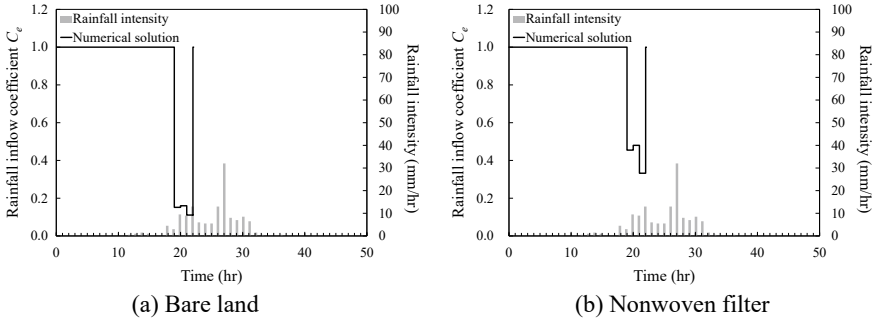**Fig. 3** Time changes in moisture content by volume

Fig. 4 Time changes in rainfall inflow coefficient

Figure 4 shows that for bare soil, the rainfall inflow for the 19-to-22-h period is about 10–15% of the total rainfall. After the installation of nonwoven filters, the numerical results are that the amount of rainfall inflow during the same period is about 33–45% of the total amount of rainfall. Excess rainfall is considered to affect the Hortonian overland flow of the slope and the seepage of rainfall into the ground. The results indicate that the installation of nonwoven filters can reduce the amount of excess rainfall by 25%. In addition, the value of β means that nonwoven filters are three times as large as bare land, the nonwoven filters are considered to have three times the infiltration capacity of bare land.

The above results indicate that in the case of bare land, the ratio of excess rainfall to rainfall is high, and the occurrence of Hortonian overland flow tends to cause erosion of slopes. On the other hand, the nonwoven filters prevent the occurrence of Hortonian overland flow, protect the ground surface, and have more infiltration capacity than bare land.
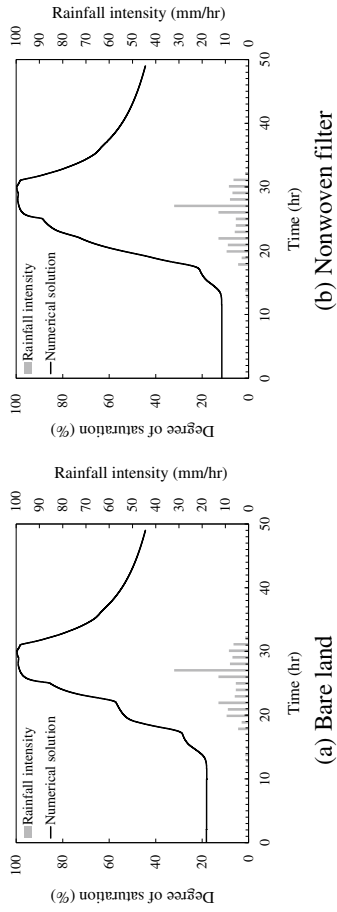
Fig. 5 Time changes in the degree of saturation

4 Conclusion

In this paper, we have improved the equation for the rainfall inflow coefficient proposed by Tsubogo et al. [8] to numerically model and numerically analyze the rainfall seepage flow into the ground when bare land or nonwoven filters are used in construction.

The findings of this paper are summarized as follows:

(1) In the case of bare land, the ratio of excess rainfall to the amount of rainfall is large and the occurrence of Hortonian overland flow is likely to cause erosion of slopes. The relationship between the amount of excess rainfall and rainfall seepage has a significant influence on the occurrence of Hortonian overland flow in the slopes.
(2) In the case of nonwoven filters, protecting the ground surface with nonwoven filters prevents the occurrence of overland flow and helps to protect the ground surface. In the case of bare land, Hortonian overland flow tends to cause erosion of slopes, which reduces the infiltration capacity.

References

1. Disaster Prevention Research Institute of Kyoto University Homepage, https://www.dpri.kyoto-u.ac.jp/web_j/publication/other/201903_gouu.pdf. Accessed 13 Oct 2022
2. Onda Y, Okunishi K, Iida T, Tsujimura M (1996) Hydrogeomorphology. Kokonsyoin, Japan
3. Miyata S, Onda Y, Gomi T, Mizugaki S, Asai H, Hirano T, Fukuyama T, Kosugi K, Sidle R, Terajima T, Hiramatsu S (2009) Factors affecting generation of Hortonian overland flow in forested hillslopes. J Japan Forest Soc, Japan
4. Gomi T, Miyata S, Onda Y (2010) Overland flow generation and the contribution on storm runoff in headwater catchments draining Japanese cypress forest. Water Science, Japan
5. Fujiwara H, Fukuda Y, Ue S, Kuwajima K, Tsunemura T (2003) Stability of slope with open type filter. Ground Engineering 21(1):23–30. Chugoku Branch of Japanese Geotechnical Society, Japan
6. Tsubogo K, Nakamura K, Yamamoto K, Ue S, Fukuda Y (2011) Study on slope protection function at rainfall of using nonwoven filter. Ground Engineering 29(1):89–97. Chugoku Branch of Japanese Geotechnical Society, Japan
7. Tokuhisa A (2020) Rainfall infiltration and failure mechanism of source head in masado slope using finite element analysis of seepage flow and full-scale field experiment. Dissertation, Yamaguchi University established the Graduate School of Sciences and Technology for Innovation, Japan
8. Tsubogo K, Araki K, Fukuda Y, Kuwajima K, Katayama K, Ue S (2022) Observations and Analysis of vertical one dimension seepage flow phenomenon. In: Proceedings of the 11th symposium on sediment-related disasters, pp 125–130. Japan Society of Civil Engineers—west, Japan

9. Araki K, Kitamura R (2005) Relation between soil compaction curve and soi-water characteristic curve for unsaturated soil. In: Symposium on geotechnical engineering, pp 83–90, Japanese Geotechnical Society, Japan
10. Ogawa S, Kishi Y, Yamada A (1990) Infiltration-discharge of rain water and translation phenomena in soil. J Japan Soc Hydrol Water Resour 3(3):25–35. Japan
11. Japan Society of Civil Engineers.: Properties of porous media affecting fluid flow. pp 53–55. Maruzen Publishing Co., Ltd., Japan (2019)
12. Brooks RH, Corey AR (1966) Properties of porous media affecting fluid flow. J Irrig Drainage 92(IR2):61–88. Proc. ASCE, American
13. Oka T, Kadoya M (1974) Rainfall infiltration and groundwater runoff in bare slope (2)—approach to runoff model. DPRI Annuals, No. 17B, pp 523–533. 1. DPRI Kyoto University, Japan
14. Kamiya K, Bakrie R, Honjo Y (2006) The measurement of air permeability coefficient of unsaturated soil with controlling water retentivity. JSCE Journal C 62(3):679–688. Japan
15. Fujimori H, Araki K (2017) An experimental consideration on permeability, compaction characteristic and failure pattern by vibration for unsaturated soils. JSCE J Earthquake Eng 73(4):I_161–I_169. Japan
16. Araki K, Kitamura R (2007) Derivation of SWCC and permeability coefficient from compaction test based on Kitamura model. In: Proceedings 3rd Asian conference on unsaturated soils (Unsat-Asia2007), pp 327–333. China
17. Tsubogo K, Araki K, Fukuda Y, Kuwajima K, Katayama K, Ue S (2022) Study on rainfall penetration characteristics of slope. In: Proceedings of the symposium on the relationship between slope failure and rainfall in Kitakyusyu 2022, Japan Society of Civil Engineers—west, pp 47–56. Japan

Seepage Model Experiment of Earth Fill Dam Due to Heavy Rains

Namihiko Tanaya, Shuichi Kuroda, Kentaro Kuribayashi, and Tadashi Hara

Abstract In recent years, a lot of small earth fill dams have collapsed by occurring torrential rain. It is considered that rainfall infiltration causes the weakening of the levee, which is accompanied by a complex of failure phenomena such as sliding and seepage, but the main cause of the failure has not yet been identified. In this paper, we conduct the model experiments in a 1G gravity field to verify the failure mechanism of small earth fill dams during rainfall. The model experiments are conducted under the assumption of continuous heavy rainfall on the levee composed of sandy soil. The experiments confirmed the development of intermittent small-scale slip failures associated with the increase of pore water pressure and pressure hydraulic head in the levee and the erosion of the slope due to rainfall. The series of results indicate that the erosive failure of the surface soil due to rapid saturation of the surface soil and the development of intermittent slip failures are the main causes of failure when highly permeable levee soils are subjected to very heavy rainfall in a continuous manner.

Keywords Earth fill dams · Heavy rains · Seepage

1 Introduction

In recent years, heavy rains have frequently caused the collapse of many small earth fill dams for agriculture in Japan, resulting in human casualties [1]. Damage to small earth fill dams caused by heavy rainfall can be classified into overflow failure, slip failure, and seepage failure, with rainfall-induced seepage failure being the most common cause of failure, according to previous damage surveys [2].

N. Tanaya (✉) · S. Kuroda · K. Kuribayashi
Eight-Japan Engineering Consultants Incorporated, Osaka-Shi, Osaka-Fu, Japan
e-mail: tanaya-na@ej-hds.co.jp

T. Hara
Kochi University, Kochi-Shi, Kochi, Japan

The results of research emphasize that environmental degradation or hydraulic fracturing cause the seepage failure in small earth fill dams during heavy rainfall and concluded that piping holes formed by the rising and falling history of the water table on the upstream slope are the starting point of seepage failure [2]. However, the main cause of failure in the affected small earth fill dams identified in Japan's heavy rain in July Heisei 30 was reported to be slip failure due to rainfall seepage into the levee, but the possibility of a combined disaster with seepage failure has also been pointed out, and the main cause of failure has not yet been identified [3].

The government and local governments are promoting the maintenance and rehabilitation of small earth fill dams; however, countermeasure methods such as flood discharge modification and holding levee construction are adopted in many cases. These methods are mainly focused on overflow of stored water and slides on downstream slopes, and there is room to consider safety against seepage failure, such as rapid saturation of the levee due to rainfall infiltration and formation of water channels. To promote efficient rainfall countermeasures for the approximately 160,000 small earth fill dams in Japan, it is necessary to elucidate the areas where levees become most vulnerable during heavy rainfall and the mechanisms leading to seepage failure.

In this study, we conducted rainfall infiltration model experiments in a 1G gravity field to analyze the factors that cause levees to become brittle during heavy rainfall. In this experiment, we analyzed the pore water pressure change in the levee and the failure behavior of the levee under heavy rainfall.

2 Experimental Conditions

2.1 Test Equipment and Geomaterials

An infiltration model test in a 1G gravity field is conducted to verify the failure behavior of a small earth fill dam during a rainfall event. A model cross-sectional view of this experiment is shown in Fig. 1. This experiment is conducted in a water tank (4100 mm wide, 1520 mm high, and 550 mm deep), which is made to simulate a small-scale model. The dimensions of the model are based on the assumption of the scale of the earth fill dam as it actually exists, and the cross section (height 500 mm, inclination of slope 1:1.8) is set considering a scale factor $\lambda = 1/20$. Table 1 shows the relationship between the parameters and the similarity law in this experiment [4].

The levee is made of a 9:1 ratio of silica sand No. 7 and Kasaoka clay, with a controlled water content ratio of about 15%. In this experiment, we used sandy soil composed mainly of sand as the levee to reproduce the sandy soil that has caused the most seepage failure in small earth fill dams from past damage cases [2].

The grain size accumulation curve and compaction curve of the levee are shown in Figs. 2 and 3. The fine-grain content Fc of the levee is 16.0% and is a non-plastic sandy soil classified as fine-grained sand (JGS 0051-2020) [5]. The density condition
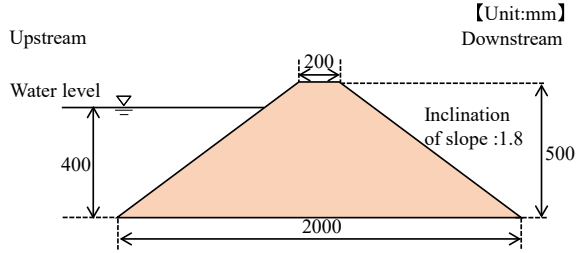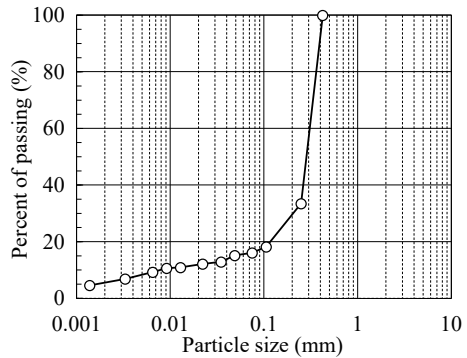
Fig. 1 Model cross-sectional view

Table 1 Law of similarity

Parameter	Real/model	Scale
Length	λ	20
Density	1	1
Time	$\lambda^{0.75}$	9.5
Pore water pressure	λ	20
Pressure head	λ	20
Deformation	$\lambda^{1.5}$	89.4

Fig. 2 Grain size accumulation curve of soil of levee

of the levee is based on the degree of compaction that was determined in research to have experienced seepage failure during heavy rainfall [3], and the levee is fabricated with a target degree of compaction $Dc = 90\%$. The levee is prepared by placing soil mixture with a controlled water content into a water tank and compacting it manually using a special rammer.

The levee is divided into five layers in the direction of height for density control, and we ensured that the required density is achieved with the prescribed amount of soil input in each layer. The water level is set at 400 mm, equivalent to 4/5 of the vertical height, and is adjusted to ensure a constant water level at all times by installing a drainage outlet upstream. Rainfall of 100 mm/h is applied from above the levee using an artificial rainfall device. The height of the rainfall device is adjusted to ensure that the raindrops are evenly distributed over the entire surface of the levee.
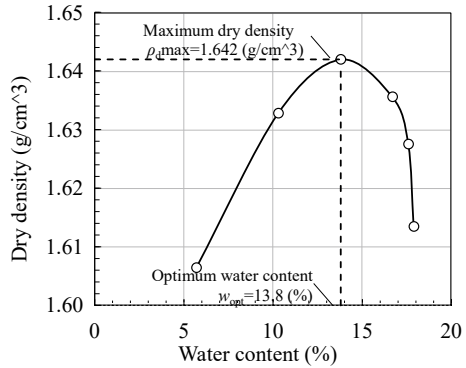
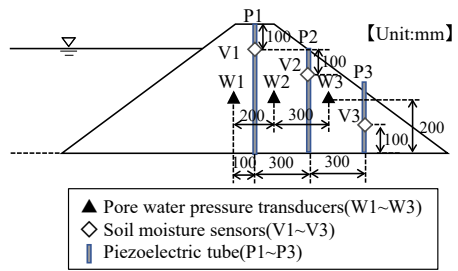**Fig. 3** Compaction curve of the soil of levee

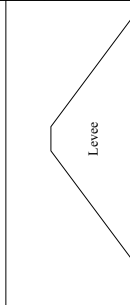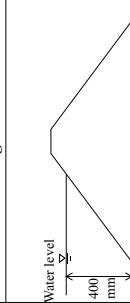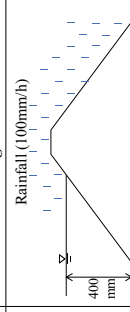
Fig. 4 Measurement points

The layout of the measurement points is shown in Fig. 4. In this experiment, pore water pressure gauges and soil moisture gauges are placed inside the levee at regular intervals inside the levee to focus on changes in water pressure and moisture content inside the levee during rainfall. In addition, an aluminum piezoelectric tube with a perforated hole (φ5 mm) is placed inside the levee and connected to a differential pressure gauge to measure the difference in hydraulic head during the experiment.

2.2 Experimental Procedure

In this experiment, seepage experiments are conducted by storing water before allowing rainfall to act on the levee under steady-state conditions. The experimental procedure is shown in Table 2. After constructing the levee in a water tank, water is allowed to flow into the upstream of the levee up to 4/5 (400 mm) of levee height. After confirming that the values of pore water pressure and pressure head in the levee are in a stable condition during the seepage experiment, the experiment is shifted to a rainfall experiment. Rainfall is applied intermittently from above the dam using an artificial rainfall device.

In the rainfall experiment, the boundary condition for rainfall action is set from the point of contact between the reservoir surface and the upstream slope to the

Table 2 Test procedure

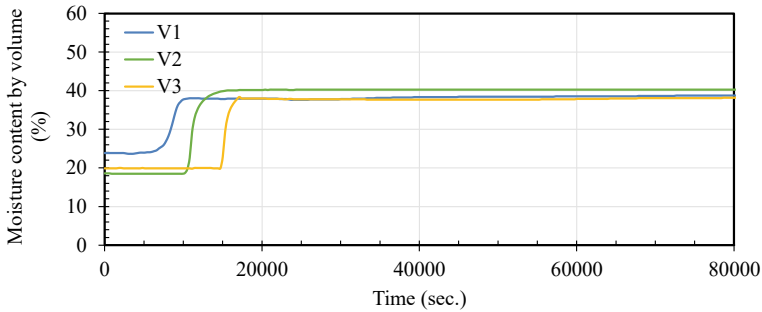| 1.Model making	2.Experiments on seepage from water storage	3.Experiments on seepage from water storage and rainfall
Levee	Water level 400 mm	Rainfall (100mm/h) 400 mm

Fig. 5 Time history of moisture content by volume on seepage experiments

downstream slope edge. The rainfall is applied from above the levee with a rainfall intensity of 100 mm/h using a rainfall device with a silicon nozzle that is designed to rotate and spray water at high speed.

3 Experimental Results

3.1 Seepage Experiments

Figure 5 shows time history of moisture content by volume of levee after the inflow of stored water. The measurement interval is 1 time/5 min. Moisture content by volume of levee immediately ranged from 19.8 to 23.4% after the start of water storage, and each value showed a rapid increase in moisture content by volume of levee up to 15,000 s after the start of water storage inflow. Thereafter, no significant changes in volumetric water content were observed at any of the measurement points, and the water content remained almost at its maximum value.

The water level in the levee at intervals of 20,000 s, obtained from the measurements of pore water pressure and pressure hydraulic head, is shown in Fig. 6.

The water level in the levee showed a tendency to vary from 20,000 to 60,000 s due to the suction of unsaturated soil, but after 80,000 s, the values of pore water pressure and hydraulic head tended to stabilize, indicating that the steady-state condition due to water storage before rainfall was reproduced, and the rainfall experiment was conducted.

3.2 Rainfall Experiments

Time history of the incremental change in pore water pressure during the rainfall experiment is shown in Fig. 7. The measurement interval is 1 time/5 s. The pore
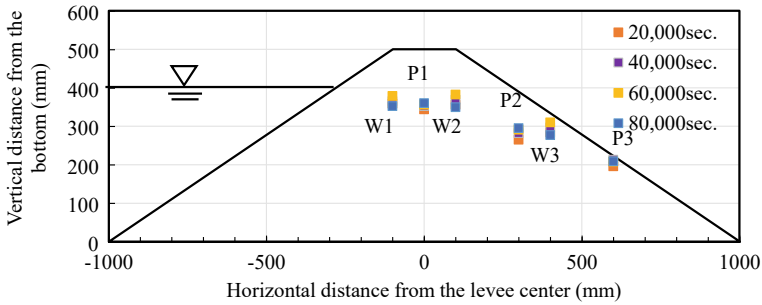
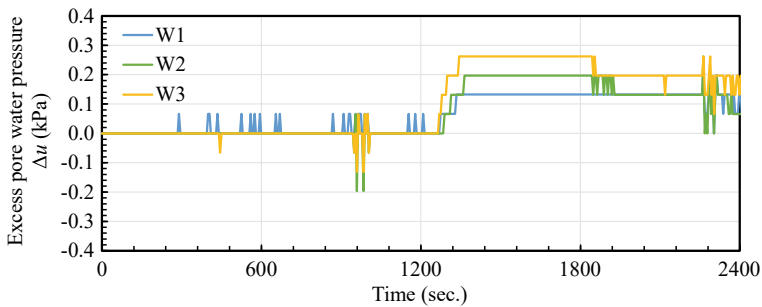**Fig. 6** Water level of the levee on seepage experiments

Fig. 7 Time history of excess pore water pressure on rainfall experiments

water pressure shows a tendency to increase rapidly at almost the same time for each instrument at about 1260 s after the start of rainfall, and all reach their maximum values within 120 s. The pore water pressure gauge W3, which is installed at the most downstream side, shows a rise of 0.26 kPa in 100 s from 1260 to 1360 s. Considering the installation depth of each measuring device, it is determined that at W3, the levee has lost effective stress at 1360 s and is almost saturated.

Time history variation of the increment of pressure hydraulic head is shown in Fig. 8. The measurement interval is 1 time/1 s. The pressure hydraulic head gradually increases at about 500 s after the start of rainfall in the piezometer P2, which is located near the midpoint of the downstream slope. In the piezometer P1 installed at the upstream side, the pressure hydraulic head does not change for a certain period from starting the rainfall, and after about 1200 s, the hydraulic head tends to increase. The pressure hydraulic head becomes negative in the piezoelectric tube P3, which is installed at the most downstream side. This is thought to be due to a temporary decrease in the pressure hydraulic head on the downstream slope, where erosion has a greater impact.

Time history of moisture content by volume over time during the rainfall experiment is shown in Fig. 9. The volumetric water content did not change significantly at any of the measurement points. On the other hand, the pore water pressure in the
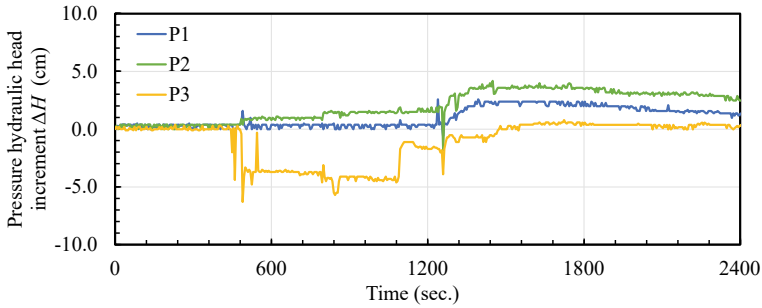
Fig. 8 Time history of pressure hydraulic head on rainfall experiments
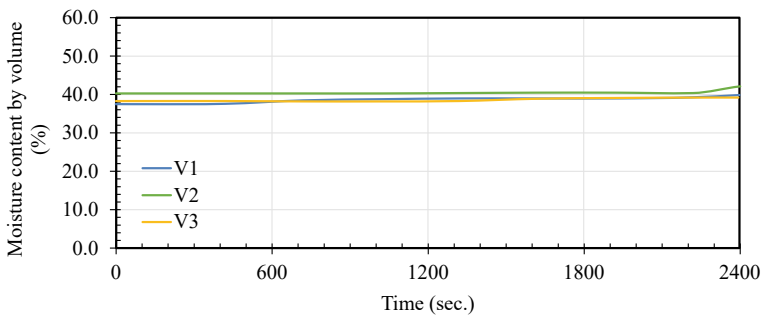

Fig. 9 Time history of moisture content by volume on rainfall experiments

levee tends to increase after the start of rainfall. Therefore, it is considered that the area where the soil moisture meters were installed was saturated by the infiltration of stored water before starting the rainfall.

Cross-sectional shape of the levee and water level during the rainfall experiment is shown in Fig. 10. In this figure, the 100 mm square grid lines and the water level distribution in the levee at that time are shown. Figure 10b shows that at 600 s after the start of rainfall, a vertical depression of about 100 mm is observed from the midpoint of the downstream slope to the bottom of the slope. Figure 10c shows that at 1800s of rainfall, the downstream slope has collapsed, and 100–200 mm of vertical depression could be observed from the downstream top to the bottom of the slope. This may be due to the development of erosion by raindrops, as well as the rapid saturation of the downstream slope observed in Figs. 8 and 9, which lowered the shear resistance of the levee, resulting in intermittent small-scale slides.

Figure 10d shows that the erosion extended to the top edge area after 2400 s, and the stored water flowed downstream starting from the point where the local top edge soil mass collapsed.

Table 3 shows the relationship between the maximum hydrodynamic gradient between the measuring instruments during the rainfall experiment and the time at which the values were extracted. The hydrodynamic gradient i is obtained from

(a) Before starting the rainfall

(b) 600 seconds after the rainfall

(c) 1800 seconds after the rainfall
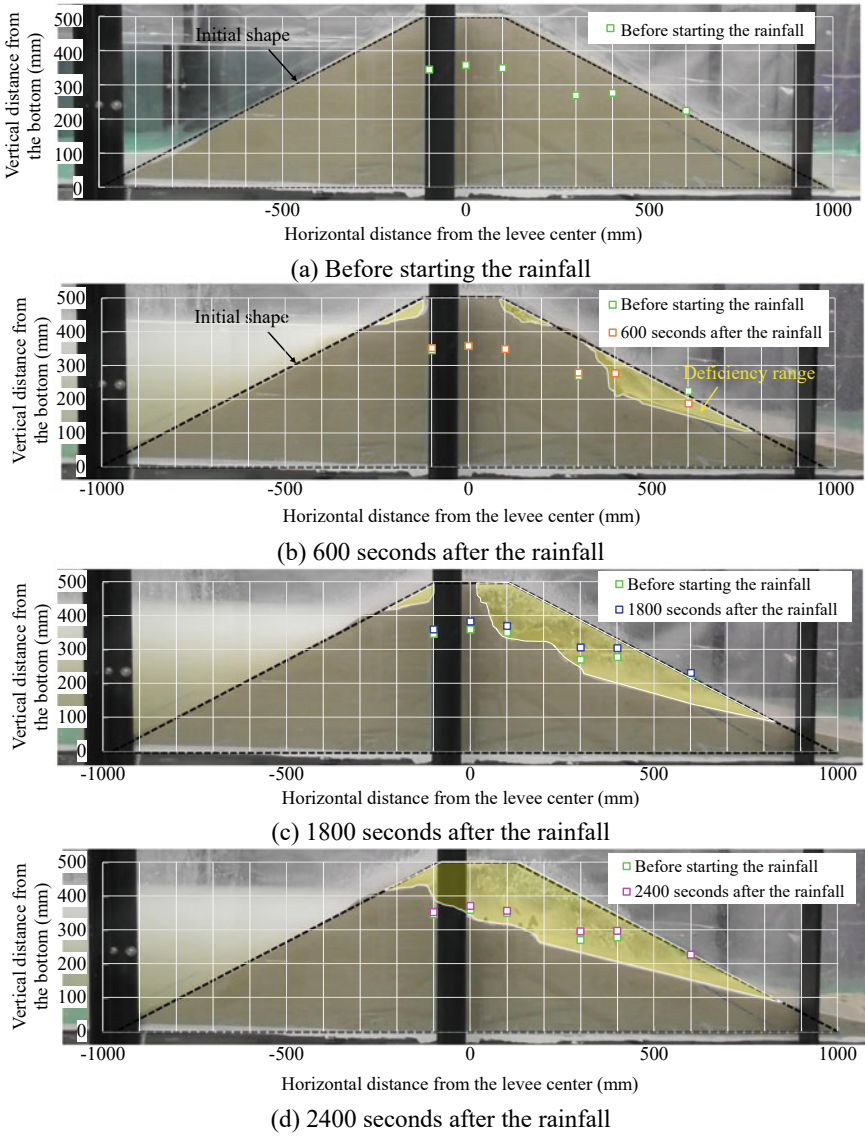
(d) 2400 seconds after the rainfall

Fig. 10 Cross-sectional shape of levee and water level during rainfall experiment

the following equation, assuming that the values are calculated at the measuring instruments where the hydraulic head values are obtained.

$$i = \Delta H / h \qquad (1)$$

Table 3 Maximum hydraulic gradients and the time

Gauge No.	W1 ~ P1	P1 ~ W2	W2 ~ P2	P2 ~ W3	W3 ~ P3
Time (s)	1250	1250	1450	1450	500
Maximum hydraulic gradients	0.39	0.38	0.61	0.62	0.58

where

i hydrodynamic gradient
ΔH water head difference (mm)
h horizontal distance (mm)

The maximum hydraulic gradient was 0.62 between W2 and P2 on the downstream slope at 1450 s after the start of rainfall, and the same value was observed between P2 and W3 near the middle of the slope at the same time. On the other hand, the maximum value of 0.58 was observed between W3 and P3 on the downstream slope at 500 s, indicating that strong seepage force was generated by rainfall in the area with a short seepage channel length. The hydrodynamic gradients at W1-P2 and P1-W2 just below the upstream slope and top edge were 0.38–0.39, indicating that the water level rise was smaller than that at the downstream slope.

According to Japanese technical data on river levee, the index value for safety against seepage failure at the downstream slope is a hydraulic gradient of 0.5 or less ($i < 0.5$) [6], and in this experiment, hydrodynamic gradients exceeding the index value were observed from the mid-slope of the levee to near the bottom of the slope, suggesting that rainfall caused localized seepage failure within the levee and induced intermittent slip failures on the slope.

4   Conclusions

In this study, we conducted rainfall infiltration model experiments in a 1G gravity field were conducted on a small earth fill dam levee composed of highly permeable sandy soil, and discussed the factors that cause the levee to weaken during heavy rainfall. The following conclusions were obtained.

(1) The rainfall infiltration model experiments showed that pore water pressure increased significantly on the downstream slope of the levee, and that the levee could not retain its initial shape due to intermittent erosion of the surface soil and development of slip failures, resulting in a failure mode in which the levee deformed significantly. The hydrodynamic gradient between the measurement devices installed on the levee suggested that a large seepage force was exerted mainly on the downstream slope, and that a localized seepage failure may have occurred.

(2) Focusing on the hydrodynamic gradient between the measurement devices installed in the levee, it was considered that a large seepage force was exerted mainly on the downstream slope, suggesting that a localized seepage failure may have occurred.

The results of this study are expected to be applicable to levee that is vulnerable to rainfall. Since some of the existing reservoirs in Japan contain a large amount of fine grains, it is necessary to conduct further experimental investigations on levee with low permeability and to consider the effects of differences in material properties of the levee on stability during heavy rainfall.

References

1. Ministry of Agriculture, Forestry and Fisheries, Future plans for reservoir countermeasures in light of the torrential rainfall in July, 2018 and other factors, pp 1. Japan (2018)
2. Toshikazu H (2005) Research on heavy rainfall disasters in agricultural reservoirs. In: Agricultural engineering research Institute Report No.44, pp 143–145
3. Ministry of Agriculture, Forestry and Fisheries, Land improvement project design guideline reservoir development, Japan (2015)
4. Japan Institute of Country-ology and Engineering, Guidance for structural investigation of river levee (Revised Edition), Japan (2014)
5. Japanese Geotechnical Society. Method of classification of geomaterials for engineering purposes, Japan (2020)
6. Japan Institute of Countryology and Engineering, Guidance for structural investigation of river levees (Revised Edition), Japan (2014)

The Use of Field Water Retention and Ambient Temperature for Developing the Soil Water Characteristic Curve

Randhilini Liyanage, Ahmad Mousa, Ankit Garg, Fauziah Ahmad, and Vivi Anggraini

Abstract The integrity and performance of geo-infrastructures have been receiving growing attention in the last two decades. Differential settlements are critical forms of distresses that lead to loss of functionality and even failures. Differential settlement is typically initiated by uncontrolled waste dumping and uncompacted fills coupled–exacerbated seasonal volumetric soil changes triggered by wetting and drying cycles. Therefore, it is paramount to continuously monitor load-deformation patterns without interrupting usage. It is also vital to consider the effect of vegetation and meteorological factors on soil properties. More data is needed to build robust correlations between basic soil properties/characteristics, vegetation, weather, and hydraulic properties of soils. Despite recognizing the significance of the long-term effects of vegetation and climate on soil's behavior, very modest effort has been invested in developing intelligent systems and models that allow for the prediction of soil parameters in relation to water retention and stress-deformation characteristics using the input of vegetation and atmospheric parameters. This study uses field and laboratory testing to develop a predictive model encompassing quantified environmental and vegetation factors. The program employed field monitoring sensors measuring soil water potential and soil moisture with varying proximity to the vegetation. Real-time data collected by the field sensors and thermal imaging assisted in postulating a quantified relation between a radial fluctuation of the soil suction from the tree roots and the vegetation parameters. Upon laboratory verification, these relationships were processed to develop a graphical model to represent the quantification of the varying soil suction with climatic and vegetative parameters.

R. Liyanage · A. Mousa · V. Anggraini (✉)
Monash University Malaysia, Bandar Sunway, Selangor, Malaysia
e-mail: vivi.anggraini@monash.edu

A. Mousa
University of Nottingham Ningbo China, Ningbo, China

A. Garg
Shantou University, Guangdong, China

F. Ahmad
Universiti Sains Malaysia, Penang, Malaysia

427

The model's outcome supports the design of geotechnical infrastructure, especially through evaluating soil water retention without disrupting the natural habitat.

Keywords Climate change · Water retention · Vegetated soil

1 Introduction

1.1 *Problem Statement and Hypothesis*

The availability of suitable land for construction in Malaysia has become limited due to rapid urbanization. Consequently, disasters due to differential settlement and slope instability could be imminent, especially in regions prone to high precipitation [1]. It is paramount to assess the effects of vegetation and meteorological factors on soil properties and the mobility of water within soil and ground stability without disrupting the natural environment and artificial structures [2]. Established studies and research need more extensive data collection to verify the relationships between soil properties and the impact of the soil-vegetation-atmospheric continuum on soil hydraulic properties or in developing intelligent systems and models for predicting soil water retention parameters through the input of vegetation and atmospheric factors [3]. This study, therefore, sets out to measure the fluctuations in the soil water retention characteristics curve and quantify the effects on soil properties under complex vegetation and climatic conditions. The quantification was carried out through laboratory and field investigation. The impact on soil suction through atmospheric parameters was analyzed in the field. The data revealed from this investigation could be adopted as the building blocks to establish a predictive model to allow for the sustainable and diligent long-term monitoring of the changes in soil properties under complex climate and environmental conditions. Such a model could support the design of geotechnical infrastructure, primarily by evaluating soil water retention without disrupting the natural habitat.

1.2 *Study Area*

A site located at Sunway South Quay, Petaling Jaya, Selangor, Malaysia, was selected for this study. The site is located within reclaimed land that used to be a tin mining quarry in the late 80s. The topography and the surrounding vegetation of the site are quite suitable for monitoring the water retention of soil. The deep-rooted trees allowed the assessment of the influence of vegetation on the hydraulic parameters of the soil. The site is quite accessible, which reduces the cost associated with testing. Samples were collected from an urban slope for mapping the change in soil matric potential across a slope. Samples at depths of 20, 40, and 60 cm were collected at
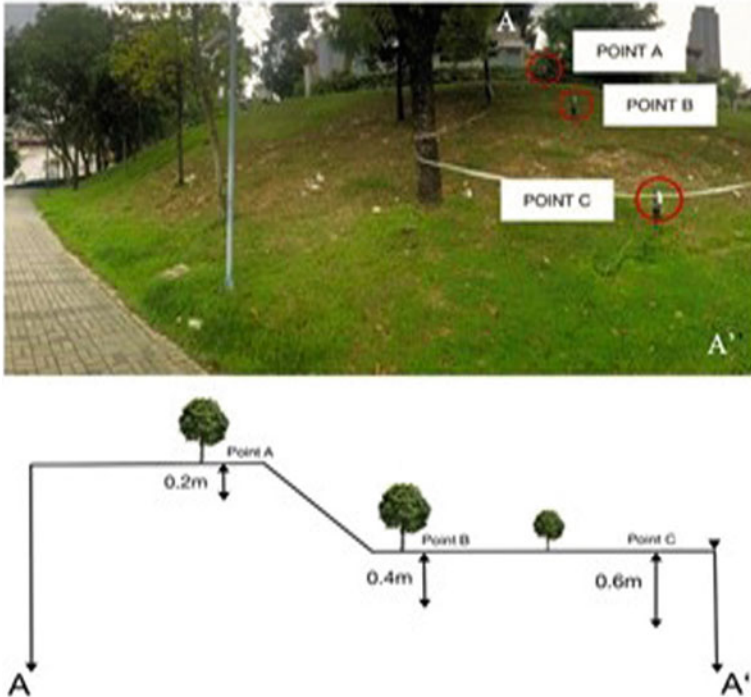
Fig. 1 Locations on-site at the required depths for sample collection containing sections A-A′

points A, B, and C, respectively, along the selected slope (see Fig. 1). The variation in root depths along the slope allows us to assess the impact of the vegetation on the hydraulic parameters.

1.3 Materials and Testing

Prior land use indicates that upper soil strata consisted of backfill soil. The following tests were conducted to determine the index soil properties according to the ASTM standards:

- Sieve analysis test (ASTM: D6913/D6913M)
- Specific gravity test (ASTM: D854-14)
- Sand cone test (ASTM: D1556/D1556M-15e1)
- Gravimetric moisture content test.

The property tests are conducted for samples at the depths specified at points A, B, and C (see Fig. 1). Multiple trials were conducted at each point, and the average was obtained to ensure accuracy. Table 1 summarizes the basic properties of soil.

Table 1 Summarized soil properties at each root depth

Property	Point A (20 cm)	Point B (40 cm)	Point C(60 cm)
Moisture Content (%)	6.68	7.78	9.76
Specific Gravity, G_s	2.63	2.67	2.63
Bulk Density, (kg/m^3)	1593	1526	1462
Dry Density, (kg/m^3)	1493	1416	1332
Void Ratio, e	0.76	0.89	0.97
Degree of Saturation (%)	23.08	23.45	26.34

1.4 Procedure

Field Investigation. The sensors at each location were collated into one system at each station. The information collecting system records the data every hour for 24 h and stores it within its design and can be retrieved manually through the data logger.

Experimental Work. Proctor compaction and one-dimensional consolidation tests were conducted to characterize the physical and mechanical properties of the collected samples. Initially, the optimum moisture contents and maximum dry densities were determined. Material finer than 0.075 mm sieve was used for this purpose. The compaction test is conducted in accordance with ASTM-D698–12. Oedometer tests were conducted for soil specimens passing through the 0.075 mm sieve and 4.75 mm sieve. The one-dimensional consolidation test is conducted following ASTM-D2435/D2435M.

Numerical Analysis. The soil water characteristics curve was obtained in the lab due to the extreme variability in the results. Therefore, the numerical model in the software SEEP/W was employed to determine the SWCC. The software utilizes several empirical equations through multiple regressions developed by analyzing an extensive collection of measured SWCCs. SEEP/W uses input parameters such as basic soil parameters, grain size distribution, and Atterberg's limits to determine the SWCC through the application of the Fredlund–Xing best fitting unimodal [9].

2   Results and Discussion

2.1 Soil Properties

The values derived meet the conditions—$C_u < 6$ or $C_c < 1$ or $C_c > 3$ and therefore are classified as **poorly graded sands (SP)** [4] (see Fig. 2).

It is recognized that is an increase in the void ratio from Point A to Point C as the depth increases; this may be attributed to the percentage of the fine present at
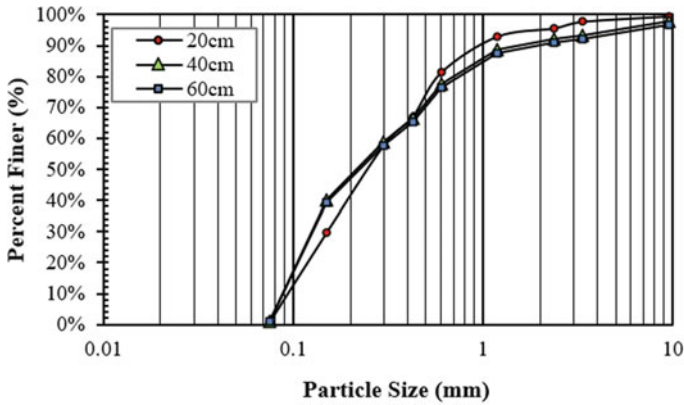
Fig. 2 Particle size distribution comparison between varying depths

each location which promotes small pores through the soil strata and contributes to a greater void volume [5]. Therefore, a decreasing bulk density across the site locations is recognized, and the more significant number of voids would insinuate a lower soil mass per unit volume. The maximum dry density for the depths also follows a similar trend with a decreasing value as root depth increases. Furthermore, by analyzing the variation in moisture content retained in, the soil we can identify an increase from 20 to 40 cm, which can be attributed to the surface getting closer to the body of water on site. Despite the locations from which the samples collected moved closer to the groundwater table, the degree of saturation increased by only 3.26%. This can be attributed to the root-water uptake by the vegetation present, which removes moisture from the ground and ensures that soil doesn't reach saturation at the same rate as non-rooted soil and preserves the soil suction and shear strength of the soil mass.

2.2 Modified Proctor Compaction

The maximum dry densities (MDD) for the samples at 20 cm, 40 cm, and 60 cm depths passing through the 0.075 mm sieve were determined to be 2.094 g/cm³, 2085 g/cm³, and 2.085 g/cm³, respectively. The corresponding optimum moisture contents (OMC) for the samples at 20 cm, 40 cm, and 60 cm depths were determined to be 7.9%, 8.7%, and 8.7% respectively. While the maximum dry densities (MDD) for the samples at 20 cm, 40 cm, and 60 cm depths passing through the 4.75 mm sieve were determined to be 2.094 g/cm3, 2085 g/cm3, and 2.085 g/cm3, respectively. The corresponding optimum moisture contents (OMC) for the samples at 20 cm, 40 cm, and 60 cm depths were determined to be 7.9%, 8.7%, and 8.7%, respectively. A distinctive trend of decreasing maximum dry density and increasing optimum

Table 2 Calculated values of coefficient of volume compressibility (m_v), compression index (C_c), and recompression (swell) index (C_s) for the material passing the 0.075 mm sieve

Sample	m_v (kPa)$^{-1}$	C_c	C_s
Point A (20 cm)	0.000058	0.0098	0.00058
Point B (40 cm)	0.000129	0.0321	0.00116
Point C (60 cm)	0.000266	0.0963	0.00698

Table 3 Calculated values of coefficient of volume compressibility (m_v), and compression index (C_s) for the material passing the 4.75 mm sieve

Sample	m_v (kPa)$^-$	C_c
Point A (20 cm)	0.000236	0.00416
Point B (40 cm)	0.000270	0.00392
Point C (60 cm)	0.000180	0.02658

moisture content from a depth of 20 cm at Point A to a depth of 40 cm at Point B and then the values remaining stagnant at a depth of 60 cm at Point C.

2.3 One-Dimensional Consolidation

Oedometer tests were conducted for soil specimens passing through the 0.075 mm and the 4.75 mm sieve collected at points A (20 cm), B (40 cm), and C (60 cm), respectively. The data gathered was evaluated for the variation in compression and swelling indexes and volume compressibility with the variance in the specimen depth and the effect of the root characteristics. The parameters were calculated after establishing the void ratio versus effective stress relationship from experimental data. Tables 2 and 3 summarize the results of the consolidation tests for the material passing 0.075 mm and 4.75 sieves, respectively.

2.4 Hydraulic Conductivity

The hydraulic conductivity was calculated utilizing the empirical relationship established by Watabe [6] through the compressible parameters from the oedometer tests for soils passing through 0.075 mm sieve and the 4.75 mm sieve for the respective depths and are summarized in Table 4. The hydraulic conductivity was also derived by utilizing grain distribution test results for varying depths [7]. The values for the

Table 4 Derived hydraulic conductivity values

Sample	Oedometer (< 0.075 mm)	Oedometer (< 4.75 mm)	Hanzen (1892)	Kozeny–Carman (1927)	Breyer (Ishaku [7])
Point A (20 cm)	7.86E − 05	7.77E − 05	8.91E − 05	8.55E − 05	8.39E − 05
Point B (40 cm)	6.83E − 05	6.86E − 05	7.87E − 05	7.37E − 05	7.47E − 05
Point C (60 cm)	6.39E − 05	9.35E − 05	7.57E − 05	6.92E − 05	7.24E − 05

*Units (in m/s)

coefficient of volume compressibility, compression index along with recompression-swelling index show an apparent increase with depth. The compression index calculated from the slope of the virgin compression curve as well as the coefficient of volume compressibility indicates that the soil would be more prone to settlement.

The hydraulic conductivity calculated through oedometer results and derived through Watabe [6] empirical relationship shows an increase in hydraulic conductivity from 20 cm depth to 60 cm depth. This effect is triggered by compressibility as the increase in soil's compactness with depth obstructs water flow and thus reduces the hydraulic conductivity. Since the compressibility parameters were derived at its maximum dry density and the optimum moisture content (smallest possible pores size), this would not reflect the true soil structure on site. However, the hydraulic conductivity is relatively consistent across methods. One can deduce that the minimum pore size at maximum compaction would not have varied drastically from that encapsulated through the empirical relations [7]. On the other hand, the hydraulic gradient derived is based on the particle size corresponding to the 10% finer passing [7]. It shows a decreasing hydraulic gradient with increasing root depth. A smaller particle size corresponding to the 10% finer passing would indicate that the packing arrangement has finer or smaller pores. The percentage difference between each method and the hydraulic conductivity derived from the oedometer test were calculated and graphically presented for comparison.

This revealed that for soils passing the 0.075 mm sieve at depths of 20, 40, and 60 cm, and for those passing the 4.75 mm sieve at depths of 20 and 60 cm, the hydraulic conductivities estimated are quite consistent with those estimated using the oedometer results [7].

2.5 Soil Water Characteristic Curve

The grain size distribution and SEEP/W were utilized to estimate the air entry value (ψ_{AEV}) and the residual suction (ψ_r) values. The saturated water contents were adopted in accordance with the degree of saturation in the prior section. The gradation used for the soil water characteristic curve (SWCC) was based on the sieve analysis

Table 5 Air entry and residual suction values for varying depths

Sample depth (cm)	Air entry value, ψ_{AEV} (kPa)	Residual suction, ψ_r (kPa)
20	2.9	19
40	3	22
60	3	24

tests. A value of 23% for the liquid limit of the sample was adopted according to the literature [8]. The air entry value ψ_{AEV} and the residual suction ψ_r value at the respective root depth are summarized in Table 5.

Through the derivation of SWCC curves utilizing the grain size distribution data, it was recognized that as the root depth increases there's a slight variation in the air entry value. At the same time, there is an increase in the residual suction value. The air entry value is the value of suction that transitions the soil from saturated to unsaturated as it moves the air into the most significant pores of the soil strata. In contrast, the residual suction is the large suction change required to remove additional water from the soil [9]. Therefore, as the fine content increases from 20 to 60 cm, the pores minimize and make the suction of water out of the inter-particle voids more resistive. The residual suction is more sensitive and increased by a greater margin than the air entry value, which remains virtually constant. As the air entry value and residual suction increase, the suction range for which the soil stays in the transition phase or two-phase zone where it is unsaturated increases.

2.6 Climatic Parameters

The data from the following stations and sensors at the respective depths and distances were extracted at 0.1 m depth and 0.5 m distance from the base of trees at points A, B, and C. The data was logged and collated hourly from 02/06/2022 to 08/07/2022. This data was processed through pivot tables to get an average value for each day for times between 8:00 am and 6:00 pm. This period was selected to capture the maximum sunlight hours and 6:00 pm to 7:00 am, which is the time that experiences the least sunlight. For all the stations across the site, soil suction shows a similar trend where soil suction increases with decreasing soil moisture for mornings and evenings. Soil moisture reached less than 10% across all three stations. It was observed that the minimum soil moisture content increases from Station 1 to Station 3 as the area gets close to the body of standing water. The values of suction reach notably large values. This could be due to increasing temperature, evaporating soil moisture from the ground, and the vegetation siphoning up groundwater during high temperatures. This is consistent with the variation of soil temperatures with matric suction trends (see Fig. 3). The highest temperatures are recorded during morning hours. They are the highest at Station 3 as it experiences the minor shading effect and is not within the canopy as Station 1 and Station 2.
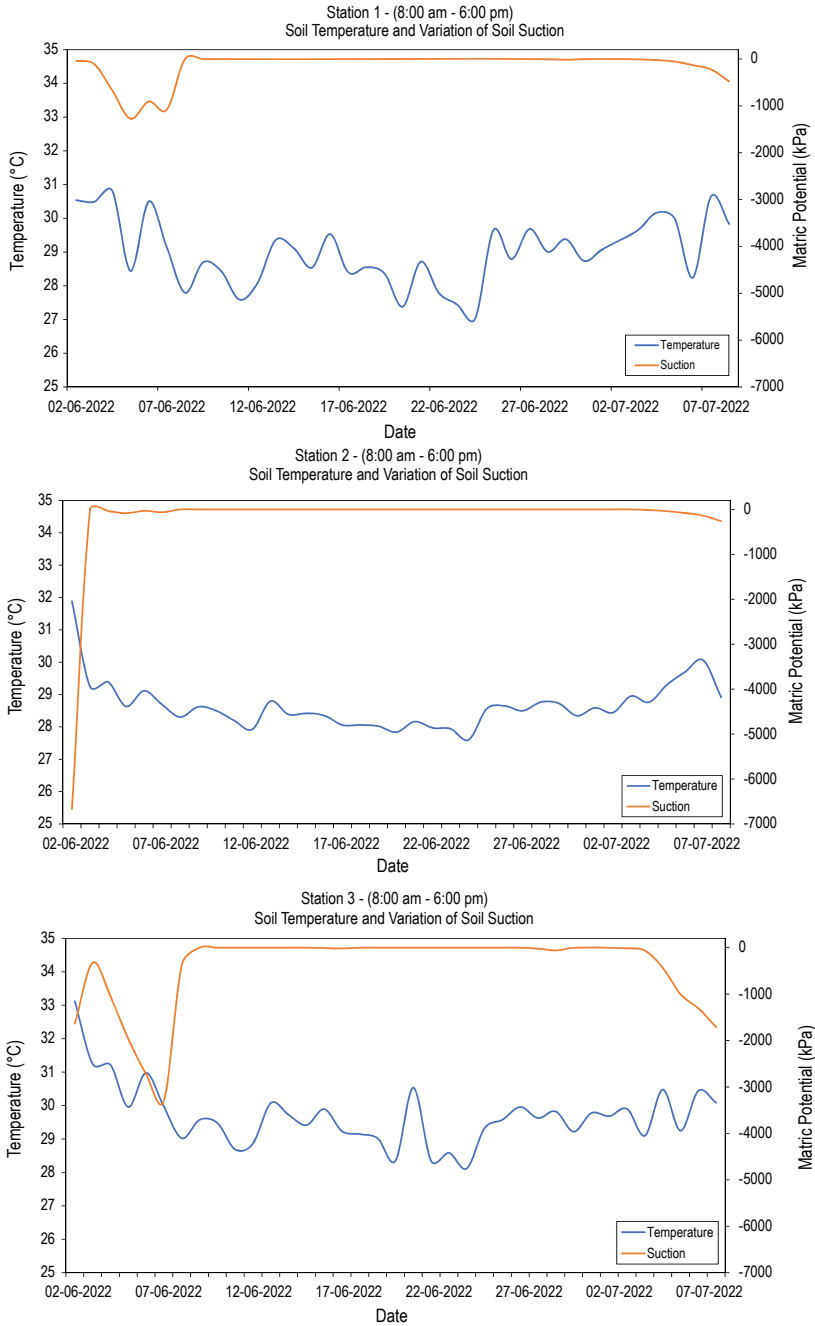
Fig. 3 Soil suction and soil temperature variation for dates from 02/06/2022 to 08/07/2022 of Stations 1,2,3

3 Conclusion

Laboratory and field investigations were conducted at an urban slope located in Sunway South Quay near a standing water body. The study aimed to understand the influence of natural conditions, such as vegetation parameters and climatic conditions, on soil's hydrological parameters. Laboratory tests were conducted to characterize the soil. Only a 3.26% increase in the degree of saturation was noted with increased proximity to the water body and piezometric surface, which can be attributed to root-water uptake and soil-atmosphere effect. The increased void ratio is due to an increase in soil's fineness from Point A to Point C so there would be more small pores through the soil structure that would add to a greater void volume. The hydraulic conductivity was derived through compressibility parameters such as the coefficient of consolidation and volume compressibility using an empirical relationship by Watabe [6] and cross-validated by empirical relationships based on Ishaku et al. [7]. Decreasing hydraulic conductivity with increasing root depth was recognized, as the roots disrupt the water seepage through the root-water uptake closer to the tip of the roots. This induces matric suction and increases the shear strength.

The soil water characteristic curve was derived from SEEP/W using grain size distribution data for the three root depths. It gave a consistent value of 3 kPa for the air entry value and 19 kPa, 22 kPa, and 24 kPa for residual suction at depths of 20 cm, 40 cm, and 60, respectively. The increase in fines and reduction in pore size indicates greater suction required for water particles to be pushed out of inter-particular voids. Finally, the field data investigation revealed that the soil suction increased with a decreasing soil moisture content and rising temperatures. The suction values reach very high, which can be attributed to the sensors being placed right at the base of the tree roots. It may also flag the suction effect due to the root-water uptake coupled with soil moisture evaporating from the surface, thereby reducing the soil moisture content in soils and increasing the negative porewater pressure.

References

1. Holcombe EA et al (2016) Urbanisation and landslides: hazard drivers and better practices. Proc Inst Civ Eng Civ Eng 169(3):137–144
2. Garg A, Leung AK, Ng CWW (2015) Transpiration reduction and root distribution functions for a non-crop species Schefflera heptaphylla. CATENA 135:78–82
3. Le TMH et al (2013) Rainfall-induced differential settlements of foundations on heterogeneous unsaturated soils. Géotechnique 63(15):1346–1355
4. Carrier III (2003) WD: Particle size distribution of lunar soil. J Geotech Geoenvironmental Eng 129(10):956–959

5. Xu P, Yu B (2008) Developing a new form of permeability and Kozeny-Carman constant for homogeneous porous media by means of fractal geometry. Adv Water Resour 31(1):74–81
6. Watabe Y, Yamada K, Saitoh K (2011) Hydraulic conductivity and compressibility of mixtures of Nagoya clay with sand or bentonite. Géotechnique 61(3):211–219
7. Ishaku JM, Gadzama EW, Kaigama U (2011) J Geol Min Res 3(4):105–113
8. Soil Consistency (1990) Foa.org. Food and Agriculture Organization of the United Nations. https://www.fao.org/3/a0541e/a0541e.pdf
9. Fredlund DG, Xing A (1994) Equations for the soil-water characteristic curve. Can Geotech J 31(4):521–532